

# REMOTE SENSING APPLICATIONS to GROUNDWATER

A.M.J. Meijerink

With contributions by

D. Bannert

O. Batelaan

M.W. Lubczynski

T. Pointet



# REMOTE SENSING APPLICATIONS to GROUNDWATER

**A.M.J. Meijerink**

With contributions by

**D. Bannert  
O. Batelaan  
M.W. Lubczynski  
T. Pointet**

The designations employed and the presentation of material throughout the publication do not imply the expression of any opinion whatsoever on the part of UNESCO concerning the legal status of any country, territory, city or of its authorities, or concerning the delimitation of its frontiers or boundaries.

Published in 2007 by the United Nations Educational,  
Scientific and Cultural Organization  
7, Place de Fontenoy, 75352 Paris 07 SP (France)  
Composed by Marina Rubio, 93200 Saint-Denis  
Printed by UNESCO

IHP/2007/GW/16  
SC-2007WS/43

© UNESCO 2007

*Printed in France*

In 2002, the World Summit on Sustainable Development recognized that the scarcity of water information in many developing countries was one of the main obstacles to achieving sustainable development and attaining the Millennium Development Goals. The alarming degradation of water monitoring systems and the obsolescence of in situ measurement equipment in developing countries necessitated additional new solutions to improve water governance based upon reliable and timely water information.

Earth Observation technologies and water cycle observation can help fill these gaps. Different aspects of current global changes affect the water cycle; satellite remote sensing provides a valuable global overview that can monitor changes in rainfall, extent of water bodies, vegetation and – at a more local level – help to identify zones with groundwater potential. The keys to ensuring that Earth Observation data and services are accessible to water resource studies practitioners are education and training – as well as availability of the necessary tools and information resources.

Groundwater plays an important role in the world: it feeds springs and streams, supports wetlands, and maintains land surface stability. Groundwater is a significant global resource, comprising 96% of the Earth's unfrozen freshwater, as well as being the main water source in many water-scarce areas. The application of satellite remote sensing to groundwater studies presents many challenges. This manual offers guidance to the many free tools and resources available to practitioners, with information on their proven applicability in practice. It also incorporates examples from various application projects, providing the reader with an excellent panorama of the different applications of Earth Observation data for groundwater management.

UNESCO and the European Space Agency (ESA), through their different applications and education programmes, support the development and promotion of good practices in the use of Earth Observation technology to overcome the water information gap that exists in many developing countries. As an example, the AQUIFER project of ESA is developing different information products based on data from the ENVISAT Earth Observation missions to improve the transboundary management of two large aquifer systems in North Africa. UNESCO's International Hydrological Programme (IHP) is providing methodological and technical advice for the better management of these groundwater resources through a series of projects. UNESCO's International Geoscience Programme is contributing to capacity-building efforts for the application of satellite information.

The European Space Agency's ERS and ASAR data have been widely used in analysing ground surface movements caused by pumping or recharge of groundwater, in addition to interpretation of hydrogeological features. The new generation of satellite systems will improve capacity. New scientific missions, such as ESA's SMOS mission will provide fresh data on soil moisture, while the upcoming sentinel series will observe the Earth at high resolution, thereby opening the door to new applications and information services, also for use in the context of groundwater management. The use of gravity data supplied by, for example, the GOCE and GRACE missions, is another recent development that shows great potential for monitoring large scale changes in groundwater.

The lack of qualified specialists to exploit these new capacities is recognized as a major constraint to the successful implementation of remote sensing applications programmes, particularly in developing countries. There is therefore a pressing need to facilitate knowledge and technology transfers, especially to Africa, where in many areas the lack of water is a serious constraint to development and scarce information limits proper management of the resource. Towards that end, UNESCO's International Hydrological Programme and the European Space Agency have cooperated with other space agencies, UN organizations and African partner organizations, which

use satellite data within the framework of the TIGER project, to develop a network of experts to strengthen the scientific base and work towards developing sustainable satellite-based information services to support water resources management. Although global in scope, this manual was devised as a contribution to the TIGER project.



**András Szöllösi-Nagy**  
The Deputy Assistant Director General  
for Natural Sciences  
Secretary of the International  
Hydrological Programme  
UNESCO



**Stephen Briggs**  
Head of the Earth Observation Science  
and Applications Department  
European Space Agency,  
ESA Centre  
for Earth Observation (ESRIN)

# ACKNOWLEDGEMENTS

The introductory chapter is written by D. Bannert and A.M.J. Meijerink. The case study on Cape Vert, Senegal (section 6.2.2) is a contribution by T. Pointet. The extensive case study on karst in Viet Nam (section 9.5) is written by O. Batelaan, while Chapter 11 on Image data and groundwater modelling is by M.W. Lubczynski and A.M.J. Meijerink. The latter author is responsible for the remaining text of the book.

The author and contributors thank UNESCO staff, in particular Dr A. Lipponen and also Dr A. Aureli, of the Division of Water Sciences, for their initiative, organizing meetings for the contributors, coordination and supplying information. D. McDonald is thanked for taking care of the final editing.

The Directorate of the International Institute for Geo-information Science and Earth Observation (ITC) offered office space and facilities while writing this book and several staff members of ITC provided material and critically read certain sections. Much of the content is derived from studies carried out during the long affiliation of the author with ITC and with students and colleagues of various institutions worldwide, all of whom are gratefully acknowledged.

Prof. J.J. de Vries is thanked for his review, and so are the authors who permitted use of figures; they are mentioned in the captions and references.

The constructive comments to chapters 11 and 12 by J. van der Gun are gratefully acknowledged.

<b>1</b>	<b>INTRODUCTION</b>	<b>15</b>
1.1	Why this book?	15
1.2	About this book	15
1.3	Availability of remote sensing images and image processing software	16
1.4	About the contents	17
1.5	Remarks	21

## REMOTE SENSING DATA AND TECHNIQUES

PART I

<b>2</b>	<b>PROCESSING OF MULTI-SPECTRAL IMAGES</b>	<b>23</b>
2.1	Introduction	23
2.2	Parts of the electromagnetic spectrum used for recording images	23
2.3	Use of aerial photography	24
	2.3.1 General aspects	24
	2.3.2 Scale, stereo and relief displacement	25
2.4	Multi-spectral data	26
	2.4.1 A digital image	26
	2.4.2 DN's and energy interaction	28
	2.4.3 Examples of relative spectral signatures	28
	Soils 29	
2.5	Image enhancement methods	30
	2.5.1 Histogram operations	30
	2.5.2 Lineaments	32
	2.5.3 Filters for the enhancement of lineaments, 'high pass filters'	32
	2.5.4 Automated lineament detection	37
2.6	Colour composites	37
	2.6.1 Red Green Blue (RGB) colour system	37
	2.6.2 Hue Saturation Intensity colour system (ISH or IHS)	38
2.7	Transformations often used in hydrogeologic interpretation and data extraction	39
	2.7.1 Principal component (PC) transform	39
	2.7.2 Ratioing	41
2.8	Radiometric correction	42
	2.8.1 Conversion of DN's into radiances	42
	2.8.2 Correction for solar irradiance	43
2.9	Vegetation index	44
	2.9.1 Applications	44
	2.9.2 The NDVI transform	44
	2.9.3 Comparing NDVI images of different dates	46
	2.9.4 Other Vegetation Indices	47

2.10	Multi-spectral classification	47
2.10.1	Applications	47
2.10.2	Simple classification	48
2.10.3	Supervised classification	49
2.10.4	Supervised classification algorithms	51
2.11	Stereo satellite images	53
2.12	Image Combination or Fusion	53
2.13	Final remarks	54
	References	55

### **3 GEOMETRIC ASPECTS, USE OF DIGITAL ELEVATION MODELS, GIS 57**

3.1	Introduction	57
3.2	Digital elevation model	57
3.2.1	Structure, TIN or Raster	57
3.2.2	Acquisition of a DEM	58
3.3	Map projections	59
3.4	Two-dimensional transforms	61
3.4.1	Georeferencing	61
3.4.2	Geocoding	61
3.5	Three-dimensional transforms	62
3.5.1	Transfer of data	62
3.5.2	Monoplotting	62
3.5.3	Ortho-image	63
3.5.4	Creation of DEM using automated photogrammetry	63
3.6	Use of Geographical Information System (GIS)	63
3.7	Summary and conclusions	65
	References	65

### **4 RADAR IMAGES 67**

4.1	Introduction	67
4.2	Radar images	67
4.2.1	Imaging principle	67
4.2.2	Commonly used imaging radar bands	68
4.2.3	Microwave polarizations	69
4.2.4	Microwave and object interactions	69
4.2.5	Data formats	70
4.2.6	Distortions in radar images	70
4.2.7	Speckle	71
4.3	Interpretation aspects of radar images	72
4.3.1	Terrain analysis	72
4.3.2	Lineament mapping	73
4.3.3	Geologic interpretation	73
4.3.4	Ground penetration	74
4.4	Image fusion	76
4.5	Stereo radar images	79
4.6	3D information and precision measurement of land subsidence by radar interferometry	79
4.6.1	SAR Interferometry (INSAR), SRTM DEM	79
4.6.2	Hydrogeological application of SRTM data	80
4.6.3	Differential INSAR: Land subsidence and uplift	80
4.6.4	Implementation and outlook	83



4.7	Radar altimetry, LIDAR, Laser	83
4.8	Soil moisture and radar/microwave remote sensing	84
4.8.1	Image interpretation	84
4.8.2	Volumetric soil moisture	85
4.9	Summary and conclusions	86
	References	86

## **5 THERMAL IMAGES 89**

5.1	Introduction	89
5.2	General aspects	90
5.2.1	Derivation of the surface temperature differences of water	90
5.2.2	Thermal contrasts caused by outflow of groundwater, submarine groundwater discharge	93
5.2.3	Estimation of discharge of submarine springs	95
5.2.4	Estimation of discharge of hot springs in a lake	96
5.2.5	Thermal anomalies in rivers	97
5.2.6	Groundwater emergence along a fault	97
5.2.7	Outflow of springs on land	98
5.2.8	Relief enhanced by a thermal image	98
5.3	Rock emissivity mapping	99
5.4	Use of thermal imagery for evapotranspiration, hydrogeological applications	100
5.5	Summary and conclusions	100
	References	100

## **HYDROGEOLOGICAL APPLICATIONS IN VARIOUS TYPES OF TERRAIN**

**PART II**

## **6 HYDROGEOLOGICAL IMAGE INTERPRETATION 99**

6.1	Introduction	103
6.1.1	Geological and geomorphological interpretation	104
6.1.2	Drainage density and permeability	104
6.1.3	A practical guide	105
6.2	Hydrogeological interpretations of sedimentary rock terrain	107
6.2.1	Example 1. Area around Kalava, Andhra Pradesh, India	107
6.2.2	Example 2. Cape Vert peninsula, Senegal	109
	References	111

## **7 TERRAIN CONSISTING OF UNCONSOLIDATED DEPOSITS 113**

7.1	Introduction	113
7.2	Geomorphology, Quaternary geology and hydrogeological properties	113
7.2.1	Fluvial deposits and landforms	113
7.2.2	Eolian deposits	114
7.2.3	Lacustrine deposits	115
7.2.4	Coastal deposits	116
7.2.5	Glacial and periglacial deposits	116
7.3	Image interpretation at sub-regional scale, overviews	116
7.3.1	Identification of aquifer, Area around Pati, Central Java, Indonesia	116
7.3.2	Effects of past climatic change on fluvial and tidal deposits, Area in SW Gujarat, India	117

7.3.3	Interpretation of local aquifers, Cauvery delta, S India	119
7.3.4	Eolian, fluvial and marine deposits, Mozambique	120
7.3.5	Verification of modelling response, Kalahari Sands and Zambezi floodplain, Zambia	121
7.3.6	Regional setting and study of a groundwater related problem in the Pampas region of Argentina	122
7.4	Alluvial fans	125
7.4.1	Origin	125
7.4.2	Interpretation of thickness	126
7.4.3	Hydrogeology	126
7.4.4	Alluvial fans and hydrogeology of a subsidence basin, N. Iran.	128
7.4.5	Effect of tectonics and example of Eastern Doon Valley, N. India	130
7.5	Summary and conclusions	132
	References	132

## **8 VOLCANIC TERRAIN 135**

8.1	Introduction	135
8.2	Specific volcanic terrain	135
8.2.1	Some volcanic landforms	135
8.3	Stratovolcanoes	138
8.3.1	Hydrogeology	138
8.3.2	Upper, middle and lower volcano	138
8.3.3	Image interpretation, flow systems and simple modelling	141
8.3.4	Springs in volcanic terrain	142
8.3.5	Interpretation of lineaments	144
8.3.6	Lineaments and springs in Amboseli, Kenya	145
8.3.7	Limitation of lineament analysis in Rift area, Ethiopia	147
8.4	Flood basalt terrain	147
8.4.1	Introduction	147
8.4.2	Image interpretation of structural elements	149
8.4.3	Geomorphological interpretation and image processing	153
8.4.4	Image interpretation and conceptual model of possible sub-regional flow system	154
8.5	Summary and conclusions	156
	References	156

## **9 KARST TERRAIN 157**

9.1	Introduction	157
9.2	Surface karst	158
9.2.1	Karst landforms and images	158
9.2.2	Recharge aspects	161
9.3	Covered karst	162
9.3.1	Examples of collapse sinkholes and shallow subsidence	162
9.3.2	Covered karst aquifer, example of Borunda, Rajasthan, India	163
9.4	Image processing and interpretations of sink-spring relations	164
9.4.1	Example in Dinaric karst	164
9.4.2	Example of a karst area in Romania	165
9.5	Remote sensing studies of karst terrain in Viet Nam	168
9.5.1	Introduction	168
9.5.2	Lineament extraction	170
9.5.3	Lineament analysis	171
9.5.4	Lineament-length density and specific capacity	172

9.5.5	Lineament-length density and prediction of underground flow paths	171
9.5.6	Extraction of karstic depressions	172
9.6	Summary and conclusions	174
	References	174

## **10** CRYSTALLINE BASEMENT TERRAIN **181**

10.1	Introduction	181
10.2	Segmentation of the terrain; hydrogeomorphological units	182
110.2.1	Example 1. Area in SE Zimbabwe	182
10.2.2	Example 2 Burkina Faso, area around Dori	185
10.3	Lineaments	186
10.3.1	Interpretation aspects	187
10.3.2	Image Processing	187
10.3.3	Lineaments, fractures and drainage lines	188
10.3.4	Effect of scale	190
10.4	Geomorphology	191
10.4.1	Planation levels: Relicts of the geological past	192
10.4.2	Pediments and inselbergs (bornhardts)	193
10.4.3	Weathered areas	194
10.4.4	Dambos	199
10.5	The tectonic setting	200
10.5.1	Image interpretation of the structural geology	203
10.5.2	Limitations of structural image interpretation	206
10.5.3	Use of geophysical survey	207
10.6	Recharge aspects	207
10.7	Example of ophiolite terrain	209
10.8	Preliminary well siting, two examples	209
10.8.1	Example from Cote d'Ivoire	209
10.8.2	Example from Burkina Faso	210
10.9	Analysis	212
10.9.1	Updating geological maps, well yields and lithology	212
10.9.2	Lineament maps and descriptive statistics	213
10.9.3	Prominence and type of lineaments and well yields	213
10.9.4	Lineament azimuth and well yields	214
10.9.5	Analysis approaches	215
10.10	Hydrogeological mapping and use of GIS procedures	216
	Approach (A)	216
	Approach (B)	216
10.11	Summary and conclusions	217
	References	217

## **DATA HANDLING AND APPLICATIONS** **PART III**

### **11** REMOTELY SENSED DATA AND GROUNDWATER MODELLING **221**

11.1	Introduction	221
11.2	Remote sensing data	222
11.3	Defining the conceptual model	224

11.4	Setting up a numerical groundwater model	224
11.4.1	Model grid	224
11.4.2	Setting model boundaries	227
11.4.3	Spatial input data (model parameters)	228
11.5	Spatio-temporal model input data	231
11.5.1	Potentiometric surface (hydraulic head)	231
11.5.2	Evapotranspiration	232
11.5.3	Groundwater recharge	232
11.5.4	Contribution from sinks and sources	233
11.5.5	River discharge in ungauged catchments	233
11.6	Summary and conclusions	233
	References	234

## **12 REMOTELY SENSED INFORMATION FOR GROUNDWATER MANAGEMENT 237**

12.1	Introduction	237
12.2	Scope for further groundwater development	237
12.2.1	Introduction	237
12.2.2	Rapid appraisal of scope for groundwater development in crystalline areas	238
12.3	Estimation of the net draft	239
12.3.1	Groundwater use by estimation of crop water use with empirical method	239
12.3.2	Groundwater use by estimation of crop water use with surface energy balance method	240
12.4	Examples of groundwater monitoring and economic aspects	241
12.4.1	Monitoring	241
12.4.2	Economic aspects	241
12.5	Groundwater allocation	244
12.5.1	Urban development	244
12.5.2	Mapping urban growth	244
12.5.3	Urban land use and spatial pattern of population density	245
12.6	Pollution of groundwater by agriculture and vulnerability of groundwater to contamination	247
12.6.1	Non-point pollution	247
12.6.2	Specific point pollution	249
12.7	Groundwater dependent ecosystems, water accounting	249
12.7.1	Taking stock	249
12.7.2	Study of trends using sequential images	250
12.7.3	Water accounting	250
12.8	Summary and conclusions	251
	References	252

## **13 SITE SELECTION FOR MANAGED AQUIFER RECHARGE 255**

13.1	Introduction	255
13.1.1	Artificial recharge	255
13.1.2	Some economic considerations	256
13.2	Recharge schemes based on ponding of runoff within the drainage system	257
13.3	Recharge schemes based on diversion of flash flows	258
13.3.1	Flood-spreading schemes: Concepts and types	258
13.3.2	Procedure for selection of suitable areas and sites for flood-spreading schemes	262
13.4	Main factors	264
13.4.1	Episodic catchment runoff	264
13.4.2	Magnitude of natural recharge by transmission loss	267

13.4.4	Chemical water quality	269
13.4.5	Permeable infiltration areas	272
13.4.6	Presence of suitable aquifers below infiltration areas	273
13.4.7	Sediment	276
13.4.8	Topography and land use	278
13.4.9	Flood damages	279
13.4.10	The screening process	280
13.5	Summary and conclusions	281
	References	281

## **14 GENERAL THEMES 283**

14.1	Introduction	283
14.2	Rainfall	283
14.2.1	Introduction	283
14.2.2	Qualitative rainfall patterns	283
14.2.3	Estimation of rainfall amounts	284
14.3	Evapotranspiration	285
14.3.1	Hydrogeological applications	285
14.3.2	Surface energy balance	285
14.3.3	Simplified, semi-automated approach	286
14.3.4	From instantaneous ETa to time series	286
14.3.5	Accuracy and outlook	287
14.4	Vegetation and groundwater	287
14.4.1	Introduction	287
14.4.2	Species recognition and water use	288
14.4.3	Areal estimates of evapotranspiration by other methods	290
14.4.4	Plant indicators for groundwater quality	290
14.5	Recharge	290
14.5.1	Interpretation, qualitative approaches	290
14.5.2	Locating areas with strong recharge	291
14.5.3	Mapping of relative recharge units	293
14.5.4	Patterns of rainfall recharge with satellite based rainfall and evapotranspiration	293
14.6	Soil moisture	294
14.6.1	Multi-spectral, thermal and gamma radiation data	294
14.6.2	Soil moisture and recharge, a discussion	294
14.7	Wetlands, areas with shallow groundwater tables	295
14.7.1	Introduction	295
14.7.2	Mapping of wetlands	296
14.7.3	Estimation of wetland evapotranspiration	299
14.7.4	Interpretation of shallow groundwater conditions	299
14.7.5	Salinization/alkalinisation	301
14.8	Groundwater status measured by satellite gravity data	302
14.9	Use of hyperspectral images	302
14.10	Summary and conclusions	303
	References	303

## **APPENDICES 307**

1.	List of acronyms	307
2.	Overview of sensors	309

## 1.1 Why this book?

This book is written for those who wish to become acquainted with the use of remote sensing for groundwater studies, be it exploration for well sites, for evaluation of groundwater resources, or for the management of groundwater, requiring processing of data. It is written from the point of view of a hydrogeologist-practitioner.

Emphasis is placed on the interpretation of images of diverse geologic terrain in warm climates, and on extraction of hydrogeologic information, for which knowledge of the basics of digital image processing techniques is required. As mentioned below, satellite images can be downloaded free of charge and recently open source software for remote sensing and GIS has been made available as via the internet (see below). Therefore, use of remote sensing is now available to anyone dealing with groundwater.

The synoptic views and time series offered by aerial photography and satellite data are eminently suitable as a source of information for the management of groundwater.

Apart from the qualitative approaches in image interpretation, the use of various sensors that provide data of quantitative nature are introduced, such as; elevation data, precise radar measurement of surface deformation due to pumping or recharge, concentrated submarine groundwater discharge, actual evapotranspiration in space and time, and measurement of soil moisture.

Although the need for a complete hydrogeological survey and exploitation of all available data sources has been stressed for decades, remote sensing methods and data extraction from remotely sensed data, especially Earth resources satellite image data is still not widely used. Lack of knowledge and insufficient experience in image interpretation still today hampers the proper use of these important data. This book will help to raise awareness for the use of remote sensing data, which is still needed in many organizations dealing with groundwater.

## 1.2 About this book

An attempt is made to be comprehensive, which implies that some subjects are introduced in brief terms only, particularly those which are of indirect use for studies of a practical nature and those which require specialist knowledge in processing of remotely sensed data.

Most of the text is devoted to qualitative approaches, particularly image interpretation of diverse geologic terrains from an Earth science perspective. The synoptic view offered by images allows for the study of surface features related to the interaction of surface and groundwater. In hard rock terrain success rates can often be increased by drilling close to lineaments identified by visual interpretation; relative recharge patterns can be mapped by interpretation and can be quantified in a second stage.

Interpretation must be based on hydrogeological knowledge; for example, groundwater intake areas on higher and permeable ground are accompanied by discharge areas in adjoining lower terrain, and with that knowledge one looks for features on images that place a groundwater flow system in a spatial context. A number of examples are given in this book.

Simple (cross-sectional) modelling may also help in understanding features seen on images, while image data can provide input in setting up the model. Examples are also discussed here.

Although exploration of groundwater remains important, particularly considering the lack of good drinking water in many regions, over the last decades attention has shifted to groundwater management. Remote sensing provides much of the spatial data needed to understand the interactions between surface water and groundwater.

A numerical groundwater model is an important instrument in making decisions about wise management of groundwater, and it is fortunate that more studies are becoming available on the use of remotely sensed information as inputs in such models. A chapter is devoted to the subject, where the various geophysical techniques that can provide inputs for modelling are discussed.

Furthermore, site selection for managed aquifer recharge (artificial recharge) schemes is included because such schemes are badly needed to mitigate further depletion of groundwater, especially in aquifers used for irrigation.

Attention is also given to the relationship between groundwater and the environment. Remote sensing data provides information on spatial patterns of groundwater dependent vegetation or salinization and is often the only source to study the history of change.

Concerning general image interpretation, an important aspect is that such interpretations do not require specialist software or specialist services to handle complex remote sensing processing (e.g. measurement of changes in land surface). Hydrogeologic image interpretation and evaluation of results do require a background in Earth science or knowledge of the interaction between surface water and groundwater. It is emphasized that hydrogeological image interpretation should be confirmed through follow-up fieldwork and needs consultation of existing hydrogeologic data, because interpretation is often a matter of inference.

Tribute should be paid to the staff of many local offices and consultant services in groundwater exploration and development, who undertook much of the practical application of remote sensing. Their objectives were to find suitable sites, develop wells and lay down the results in departmental reports, rather than publish their methods in scientific journals. In fact, plotting information obtained from local drillers about successful and dry wells on images is a good start in hydrogeological image interpretation for the development of groundwater.

### 1.3 Availability of remote sensing images and image processing software

A variety of satellites and sensors offer spatial data that can be used, in one way or the other, for groundwater studies. Until a few years ago, the costs of acquisition of satellite images hampered their general use in hydrogeology. However, Landsat TM-ETM images (30 m. resolution) of fairly recent date can now be downloaded free of cost, or obtained at low cost (see Tables 1.1 and 1.2).

<i>Web site</i>	<i>Available data</i>
Global Land Cover Facility (University of Maryland, USA) <a href="http://glcf.umiacs.umd.edu/portal/geocover/">http://glcf.umiacs.umd.edu/portal/geocover/</a>	Free downloads Landsat TM & ETM+ and 742 compressed mosaics and SRTM
Google Earth	Free online 'natural colour' TM or higher resolution images, perspective views
USGS <a href="http://landsat.usgs.gov">http://landsat.usgs.gov</a> <a href="http://edcns17.cr.usgs.gov/EarthExplorer/">http://edcns17.cr.usgs.gov/EarthExplorer/</a>	Landsat 7 ETM+ to purchase, browse and order worldwide cover of Landsat TM/ETM+ scenes, EO-1 ALI data (table 1-2 for costs)

**Table 1-1. Free and low cost satellite scenes, medium resolution**

<i>Instrument</i>	<i>Costs (US\$)</i>	<i>Resolution</i>	<i>Swath (km)</i>
Landsat-7 ETM+	475 (April 1999-May 2003) 275-300 (after May 2003)	15, 30m, 60 m*	180
Landsat-4 and -5 TM	425 (1982-2005)	30	180
ASTER	80	15, 30, 90m*	60
EO-1 ALI	250	10, 30 m*	37

\* depending on band. Table 1-1 Costs < US\$ 500 of satellite scenes.

**Table 1-2. Costs (early 2007) of medium resolution satellite images**

In addition, specific satellite-based products, such as digital elevation models of the Shuttle radar mission (SRTM), decadal SPOT vegetation indices and soil moisture maps are available via the internet. It is expected that more products will be made available.

An overview of the main particulars of current satellites and sensors used in hydrogeological studies is given in the Appendix 2.

As of 1 July 2007 open source, free of cost PC-based software for digital image processing and Geographic Information System (GIS) operations is available for download). Another PC based remote sensing software, is the Bilko package, developed by the UNESCO-Bilko project, United States Geological Survey (USGS) provides free software for UNIX systems.

Free PC-based packages for image processing and GIS processing:

**ILWIS** (Integrated Land and Water Management Information System) of the International Institute for Geo-information Science and Earth Observation (ITC), Enschede, The Netherlands

Download from: <http://www.itc.nl/ilwis/default.asp> In cases of slow internet connection, downloading may be done in modular fashion. Help files and tutorials are available to assist new users.

**BILKO** remote sensing processing software can be downloaded from:

<http://www.noc.soton.ac.uk/bilko/>.

Although the tutorials pertain to oceanography and coastal management, the routines can be applied to hydrogeological studies.

## 1.4 About the contents

A wide range of applications of remote sensing are discussed and illustrated in this book. This is reflected by the 14 chapters, which are grouped in three parts.

### PART I

This part deals with more technical aspects, although some interpretation elements are included.

#### *Chapter 2: Image processing*

The methods discussed may be regarded as the toolbox of a hydrogeologist who uses digital remote sensing images, in particular multi-spectral ones. Where possible, the hydrogeological relevance of some of the techniques is illustrated. Apart from general image enhancement techniques used to obtain the 'best' image(s) for interpretation, attention is given to filtering methods for enhancement of lineaments, which play an important role in the search for groundwater in the hard rock terrain (crystalline basement, basalt terrain and karstic limestone terrain) that covers a large proportion of the continents. A few spectral classification methods and vegetation indices are explained, as these are of use in providing information for groundwater management and budget studies, such as estimating net drafts of aquifers used for irrigation, estimation of pollution loading, and vegetation-groundwater interactions.

#### *Chapter 3: Geometric aspects, Use of digital terrain models, GIS*

This chapter deals with geometric transformations required to match satellite data with existing data sources, notably topographic and geological maps, positions of boreholes, and springs and other thematic data.

Acquisition and use of satellite-based Digital Elevation Models (DEM) is included because of references to regional hydrogeologic studies making use of DEM. Derivatives of DEM, such as slope maps or maps with depressions can be combined with other data of hydrological relevance in GIS. Some typical GIS applications for analysis of groundwater occurrences are also included. It is assumed that the reader is familiar with basic GIS principles.



**Chapter 4: Radar images**

This chapter is devoted mainly to data obtained via active radar. The essentials of radar imaging principles are introduced in order to understand the nature of the radar images that may be used for interpretation of structures and geomorphology affecting groundwater occurrences and flow, with or without combination with multi-spectral images (image fusion). In desert terrain radar images can penetrate thin (0.5–3 m) sand covers to reveal fossil drainage and rock structures.

Of more general use is the ability of specific processing of radar images for altimetry and interferometry to produce DEMs and to measure with high precision deformation of the surface of aquifers, which may be due to recharge and pumping. Land subsidence is a well-known problem in many large cities situated on unconsolidated deposits.

Developments in determining soil moisture using passive radar are also mentioned.

**Chapter 5: Thermal images**

Radiometric principles are mentioned in order to arrive at temperature differences in water in degrees Celsius (or Kelvin), which may be used for the detection of concentrated groundwater discharge in coastal waters, lakes and rivers. Some examples of thermal images for general interpretation are given. The use of thermal satellite image data for the estimation of spatial patterns of actual evapotranspiration is discussed in Chapter 14.

**PART II**

This part is devoted to discussing and illustrating the use of images in various types of geologic terrain.

**Chapter 6: Hydrogeological image interpretation**

In this chapter the role and principles of hydrogeological image interpretation in general are discussed and their application is highlighted by means of two cases pertaining to folded and faulted sedimentary rocks.

**Chapter 7: Terrain consisting of unconsolidated deposits**

In the past era of geological mapping this terrain, if consisting of Pleistocene deposits, was often treated in a cursory manner or left to Quaternary geological specialists or geomorphologists. However, since much groundwater occurs in this type of terrain, it is deserving of greater attention. Image interpretation is perhaps the only way to map the various types of deposits in an efficient manner, at least at a reconnaissance scale and several examples are given. Once the overview is obtained, hydrogeological data and specific features must be considered in order to understand the occurrence and behaviour of groundwater. Waterlogging with associated salinization often occurs in this type of terrain and a case showing the contribution of remote sensing is included.

Of special interest are alluvial fans. These are often important sources of groundwater with specific recharge and where surface features, as observed on images, can be related to a groundwater flow system in the fan.

**Chapter 8: Crystalline basement terrain**

The variety of landform-soil associations and land cover, often related to type of crystalline rock or to past weathering, can be grouped into hydrogeomorphological terrain units by image interpretation. In an indirect manner, it is possible – if not likely – that groundwater occurrences are associated with the units, because each unit has specific recharge and storage characteristics of the weathered zones. Attention is given to interpretation of the weathered zones, recharge conditions, and to the areas where the so-called dambos are found. In such areas, evidence of groundwater seepage may be interpreted on images.

Because primary rock porosity is negligible, groundwater also may occur in large fractures, especially when surrounded by weathered rocks that receive recharge water. These large fractures are commonly indicated by lineaments on satellite images and aerial photographs. Not all lineaments contain water; this can be true even for prominent ones due to a variety of reasons. Tectonic models have been used in attempts to distinguish open fracture systems from closed ones and the principles of such models are discussed. Associations of higher well yields with certain orientations of lineaments are often a manifestation of open fractures. However, in many areas the tectonic history and latest stress field may not be well known, while fillings of fractures can obliterate or

preclude such an association. When well yield data is adequate, analysis lineament properties may serve a useful purpose, and an overview of analysis methods and results are mentioned.

In practice one may be faced to locate sites for dug wells or boreholes near villages, or local institutions, whether or not ground geophysical survey can be done, and two examples are included to illustrate how image interpretation can be used for site location.

### ***Chapter 9: Volcanic terrain***

Examples of some volcanic landforms and interpretations of hydrogeologic properties are discussed in this chapter. The main hydrogeology of stratovolcanos is illustrated by differentiation of groundwater uptake in the upper volcano, transient flow in the middle volcano, and groundwater discharge in the lower volcano. Simple cross sectional groundwater modelling is used with information of some volcanoes in West Java, Indonesia, to place features seen on images in the context of flow systems. The significance of lineaments can be placed in the same context.

Hydrogeologic conditions of terrain consisting of flood basalt are illustrated with geomorphological and structural interpretations of areas in India, with references to studies by Indian authors.

### ***Chapter 10: Karst terrain***

Surface karst and covered karst features, including an aquifer, are illustrated on images of different scales. Limitations concerning the interpretation of dolines using satellite images are discussed. For two areas, images are studied for sink-source relations, based on published data. In one case the link was evident from alignment of sinkholes, but for the other area the relation was not obvious, despite the employment of images of different resolution and image processing techniques.

A well-documented study of two karst areas in Viet Nam highlights the role of lineaments. These were extracted using interpretation of stereo airphotos and an automated method. The set retained for analysis, after sifting for geological relevance, was used to determine lineament-length density and lineament frequency; association with specific capacity of boreholes was also studied, for which a lineament-length density map was prepared. Lineament-length density is considered as an indicator for the degree of rock fracturing, which is also a prerequisite for development of cavernous passages. A routine is developed to automatically find probable subsurface conduits, which was then confirmed by tracer tests.

For one of the studied areas, automated determination of karst depressions was obtained using a method based on shadows of depression walls and a DEM-based method.

## **PART III**

This part features crosscutting themes.

### ***Chapter 11: Image data and groundwater modelling***

An overview of some studies made in this domain, which has attracted attention in recent years, is given by way of introduction and the role of remote sensing is specified. The major steps in groundwater modelling are then discussed with reference to input of both remote sensing and geophysics. Such input is a useful complement when direct geological observations, for example from drilling, and groundwater level measurements, are scarce. After the development of the conceptual model, using information provided in other chapters in this book, the steps in setting up the numerical groundwater model are: defining the grid, setting of model boundaries and spatial input data (model parameters), mentioning the type of airborne and ground geophysics for the estimation of parameter values.

Temporal information of spatial input for transient modelling is discussed, with reference to what remote sensing may contribute to changes in potentiometric surface, groundwater evapotranspiration, recharge, sinks and sources and river discharges.

### ***Chapter 12: Information for groundwater management***

As is well known, groundwater levels are declining in many areas because pumping exceeds recharge, with due consequences for water supply, agricultural production and groundwater-dependent ecosystems. Often, total net extraction amounts are not known, and this is where remote sensing can provide information.

A rapid assessment method for estimating the scope for further exploitation in hard rock areas is given. Net drafts of aquifers used for irrigation can be estimated with remotely sensed data, either by an empirical method using multi-spectral crop classification and crop water use factors, or by using satellite data for the surface energy balance method to assess the evapotranspiration. The latter method formed the core of a system designed for monitoring – in fact policing – overuse of groundwater by individual farmers.

An example of economic considerations is given where remote sensing was used to inventory land use dependent on groundwater followed by appraisal of economic returns.

Groundwater pollution is another widespread concern. With remote sensing the rapid growth of urban areas often with large unplanned extensions – and the various classes of urban land use can be inventoried.

With some census data, population or household densities can be estimated and pollution loadings assigned to the categories, for directing hydrochemical field sampling.

Remotely sensed information for other aspects of groundwater management, such as artificial recharge, protection of groundwater-dependent ecosystems, and groundwater-related salinization is discussed in the last two chapters.

### ***Chapter 13: Site selection for managed aquifer recharge schemes***

The problem of declining groundwater resources in aquifers may be alleviated by artificial recharge. Out of the variety of possible schemes, the role of remote sensing in locating suitable sites for two types of schemes is discussed and illustrated. The first type makes use of structures within a catchment to temporise the flow of runoff so that greater infiltration can take place than is the case without obstructing measures. Examples from a basalt catchment and a catchment underlain by crystalline rocks with alluvial deposits illustrate locations of possible sites on the images.

The second type of scheme discussed is based on flood spreading. Three sub-types are differentiated. Remotely-sensed information for a multi-criteria analysis for site selection is discussed and illustrated.

The economic attractiveness of flood spreading schemes if other benefits, such as flood protection are considered, is also discussed.

### ***Chapter 14: General themes***

In some regions the spatial distribution of rainfall is poorly known, while rain gauge networks are often degrading. Spatial rainfall information based on satellite data is accessible via the internet.

An important step forward in hydrological application of satellite data is the possibility to calculate actual evapotranspiration using the surface energy balance method (SEB) with a minimum of ground data. The gist of the method is mentioned because of the importance of knowing the actual evapotranspiration for groundwater budgets.

Use of groundwater by vegetation, phreatophytes and deeply rooted trees in semi-arid regions, has attracted attention over the last decade or so. The use of remote sensing in a few aspects of vegetation-groundwater interaction is discussed.

Although recharge amounts cannot be determined by remote sensing methods, the spatial patterns of relative recharge can be estimated either by using various interpreted terrain characteristics.

Areas with high soil moisture due to shallow groundwater can often be interpreted on multi-spectral and thermal images. Much research has been devoted to the use of radar and microwave data for the determination of soil moisture, which has resulted in monitoring of relative surface soil moisture; products for which are available on the internet. Comments are made regarding the use of such data for recharge of deeper groundwater.

In most wetlands surface water interacts with groundwater and therefore attention is given to the mapping and monitoring of wetlands and areas with shallow groundwater.

Satellite gravity data for monitoring changes of groundwater storage in very large aquifers is also mentioned.

## **1.5 Remarks**

It is hoped that this book will stimulate readers unfamiliar with the application of remote sensing to groundwater to make use of the possibilities it has to offer studies in this area.

Jha and Chowdary (2007), in the Special Issue on Remote Sensing of the Hydrogeology Journal, mention five

factors that impede the use of remote sensing in developing countries. Of these impediments, (1) distribution of remote sensing data and (2) high costs, are now, at least in part, resolved by the availability of downloadable, free Landsat TM and ETM data ([www.geocover.org](http://www.geocover.org)). Impediment (3), expensive RS and GIS software has been removed by the availability of free ILWIS packages. For impediment (4), poor knowledge about RS and GIS techniques, it is hoped that this book will alleviate the situation as far as remote sensing is concerned. Impediment (5) pertains to infrastructure for training. Although this book is not an instruction manual, the examples provided might entice readers to embark on exercises with downloaded images using the above-mentioned software, which include help and tutorial files. In any case, hydrogeological image interpretation is a matter of experience, obtained through actual practice. The last two impediments, negligence in proper water monitoring and the plethora of GIS file formats, are beyond the scope of this work.

For overviews of the use of remote sensing in groundwater some review articles are listed below.

### *Review articles*

- Becker, M.W. 2006. Potential for satellite remote sensing of ground water. *Groundwater*, Vol.44(2), pp. 306–18.
- Brunner, P., Hendricks-Franssen, H-J, Kgotlhang, L. and Kinzelbach, W. 2007. Remote sensing in groundwater modelling. *Hydrogeology Journal*, Vol. 15(1), pp. 5–18.
- Hoffmann, J. 2005. The future of satellite remote sensing in hydrogeology. *Hydrogeology Journal*, Vol. 13(1), pp. 247–50.
- Jha, M.K. and Chowdary, V.M. 2007. Challenges of using remote sensing and GIS in developing nations. *Hydrogeology Journal*, Vol. 15 (1), pp 197–200.
- Meijerink, A.M.J. 1996. Remote sensing applications to hydrology: Groundwater. *Hydrological Sciences Journal*, Vol. 41 (4), pp. 549–61.
- Waters, P., Greenbaum, D., Smart, P.L. and Osmaston, H. 1990. Applications of remote sensing to groundwater hydrology. *Remote Sensing Reviews*, Vol. 4(2), Harwood Academic Publishers GmbH, pp. 223–64.

## Processing of multi-spectral images

### 2.1 Introduction

The objectives of this chapter are to introduce and discuss:

- Basic aspects of aerial photographs, multi-spectral digital images
- Some image processing methods that can enhance certain features of hydrogeologic interest
- Transformations for extraction of information of hydrogeologic relevance
- Selected methods for spectral classification of land cover (vegetation, soil/rock) units and illustration of their use in groundwater studies.

For those new to the subject, it is useful to introduce some technicalities, and an attempt is made to provide illustrations with hydrogeologic significance. The use of images in specific subjects, such as comprehensive image interpretations in various types of terrain, recharge, groundwater modelling and groundwater management, is discussed in later chapters.

The basics of aerial photography are kept to a minimum because this topic is covered in many accessible handbooks. However, in the chapters dealing with hydrogeologic subjects, interpretation of aerial photographs takes a more prominent role.

Thermal and radar images are discussed in the next two chapters.

A selection of digital processing methods is made to highlight those commonly used in applied hydrogeologic studies. These are discussed at some length as multi-spectral images of all parts of the world can now be downloaded free of cost – in particular archived Landsat Thematic Mapper data of some years ago (see Appendix 2).

### 2.2 Parts of the electromagnetic spectrum used for recording images

Panchromatic (black and white, B&W) or colour aerial photographs taken from aircraft or space, prior to the advent of digital aerial cameras make use of sensitive emulsions and need processing in a photographic laboratory.

Satellite images record the Earth's surface in digital format and thus we need certain techniques to render the digital data visible. Several options are available, each for a purpose, and these will be discussed here.

The imaging instrument on board the satellite or aircraft has various sensors that record the energy reflected or emitted from the Earth's surface in various parts of the electromagnetic spectrum, called 'bands' or 'channels', therefore we speak of *multi-spectral* images.

Figure 2.1 shows what parts of the electromagnetic spectrum are used for recording images.

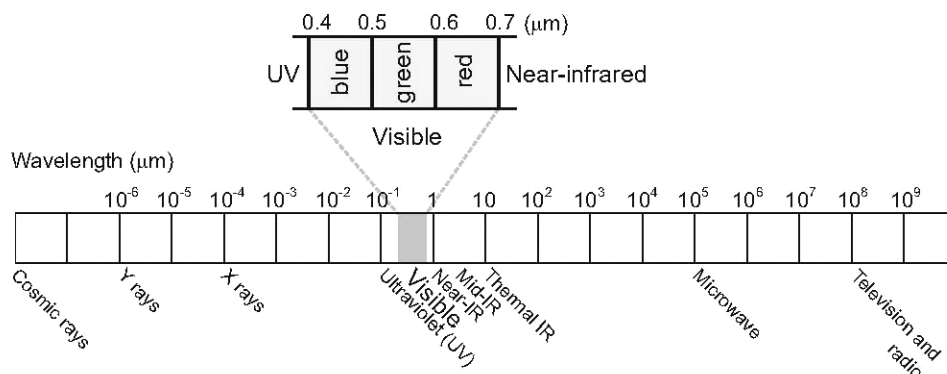


Figure 2-1

Electromagnetic spectrum

In this text, attention is given to the visible-near infrared and shortwave infrared (or far-infrared) part of the spectrum, also called the optical part, the thermal domain (thermal infrared, TIR) and the microwave or radar domain.

For general interpretation and data extraction for hydrogeologic purposes much use is made of the visible and invisible near infrared part of the spectrum, as many examples discussed in this book will illustrate. Some main applications are: (1) interpretation of geology, geomorphology/soil geography and land cover for evaluation of recharge and groundwater flow systems, (2) the detection in crystalline basement, karst and other terrain of lineaments, with which groundwater occurrence is associated, (3) estimation of net groundwater drafts for irrigation and other groundwater management aspects.

Of special importance is the thermal infrared part: the emission of long-wave energy, related to the surface temperature of water bodies, vegetation, soils or rock outcrops. Freshwater flowing out along the coast, for example along major fractures or faults, may be detected on the image if there is a temperature contrast between the up-welling fresh groundwater and the surface water of the sea. Furthermore, thermal data offers a possibility of determining the actual evapotranspiration component of groundwater budgets and some other aspects.

The longer wavelengths are used for the recording of radar images in various bands, which are denoted by capitals, for example, C band, L band, X band, and so on. We differentiate *active* and *passive* microwave (or radar) systems, explained below. Use of these bands has the advantage that images can be made in cloudy conditions (important in the humid regions) and at night. Radar images (aircraft and space images) have been successfully used for (hydro)-geologic studies and lineament mapping.

The radar domain is also used for precise height measurements by radar altimetry and for detecting small changes of altitude in time sequences. Land subsidence and uplift due to groundwater pumping or recharge respectively, can be detected by interferometry, using two or more sequential radar images or radar data from stereo-missions.

A variety of applications of various sensors in different terrains are given in later chapters.

## 2.3 Use of aerial photography

### 2.3.1 General aspects

For a long time (1930s to 1970s), aerial photographs (AP) were the only images used in practice. They were and still are important, because of:

- High spatial resolution. Depending on scale, which is a function of flying height and focal length of the aerial camera used, ground features in the range of 0.5 to 2 m can be seen. Such details are important in detecting the dips and strikes or rocks, details of dissection, emergence of groundwater in ephemeral river beds, vegetation differences caused by groundwater seepage, different type of alluvial deposits, and so on.
- Stereovision. Because of the approximate 60% overlap, 3D views of the terrain can be created by placing two successive photographs under a stereoscope. The heights in the terrain are usually exaggerated by a factor of 2 or more, which helps in the detection of small differences in relief. For that reason slopes and dips appear steeper than in reality. Apart from 'in-depth' interpretation requiring a background in Earth science, stereovision also serves such practical purposes as judging whether drilling equipment can reach suitable drilling sites.
- Availability. APs were and are used to make topographic maps, after the introduction of photogrammetry worldwide in the mid 1950s. Existing AP covering any part of the country can usually be obtained at relatively low cost, whereas high resolution satellite imagery remains expensive. Although some countries have restrictions on the issuing of APs (despite the fact that satellite imagery with a resolution of 1 m is available commercially), older sets are often available as they have lost their military relevance. Although land use and infrastructure may have changed since the date the image was taken, the geology and geomorphology will not have, with the exception of some dynamic geomorphological features.
- Aerial surveys can be flown to customer specific requirements, for instance the time of acquisition, area, scale, and other important parameters.
- The images can be used as they are; no computer processing is required.

Generally, a systematic coverage of an area is flown, as illustrated in Figure 2.2.

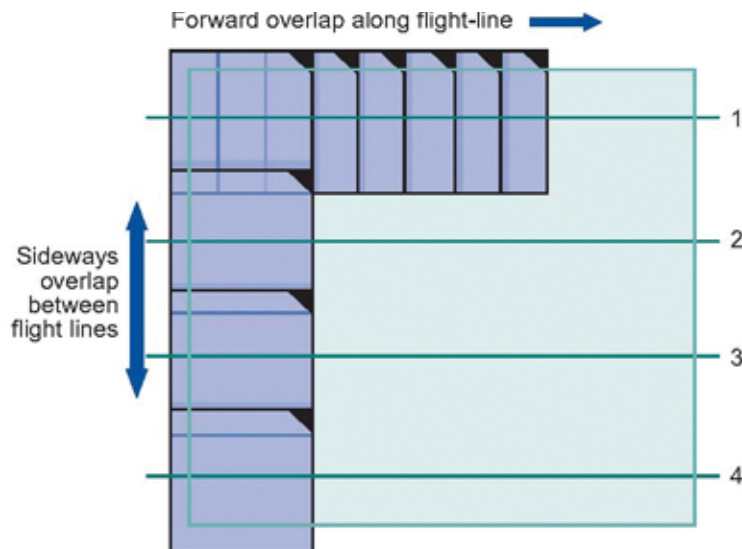


Figure 2-2

Example survey area for aerial photography.

Note the forward overlap allowing stereovision and sideways overlap for full coverage.

Source: Horn and Grabmeyer, 2004.

Colour aerial photographs have only very limited additional value compared to good quality panchromatic (B&W) APs. In fact, for general hydrogeologic interpretation an undue dominance of green colours of vegetation is unwanted. In tropical countries often pan-chromatic films in combination with orange or red filters have been used that are sensitive to the near infrared part of the spectrum; this aggravates the dominance of the vegetation in the photograph. The colour version of the films, also sensitive for near-infrared, was developed primarily to detect vehicles painted in green partially hidden beneath canopies. Green vegetation shows up in reddish tones on these photos, whereas green paint does not. The term ‘false colour’ or ‘camouflage detection’ photo has a military origin.

Modern airborne surveys make use of digital cameras so the data is available in digital format. The same can be obtained, at a lesser quality, by scanning with high resolution existing analogue airphotos. Filtering techniques may enhance joint and fracture patterns, emergence of groundwater in riverbeds, and so on.

### 2.3.2 Scale, stereo and relief displacement

#### Scale

The photo scale factor ( $s$ ) depends on the focal length ( $f$ ) of the aerial camera and the flying height above the terrain ( $H$ ):  $s = H/f$ . Thus if  $f = 152$  mm and  $H = 4,560$  m, the scale factor is 30,000 (or photoscale is 1:30,000). Focal length and flying height are shown along the margins of an aerial photograph.

#### Stereo

The stereo capability is a result of a ground object being viewed from two different positions in the overlap area of the APs, as illustrated in Figure 2.3.

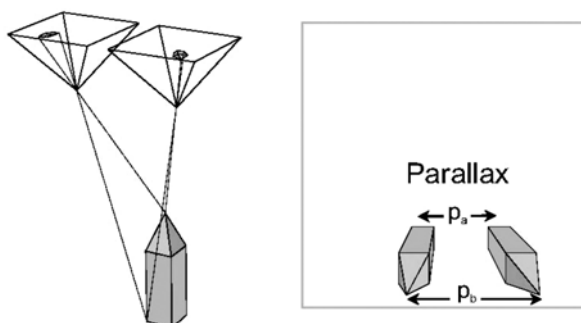


Figure 2-3

Sketch showing distance difference between top and bottom of high object (parallax) on stereopair

Source: Janssen et al., 2004

From the difference in distance between the bottom and the top of a terrain object, the height of the object can be obtained by precise measurement of the parallax ( $P_b - P_a$  in Figure 2.3.)

The contours on topographic maps are usually based on photogrammetry. As a rule of thumb, the absolute height accuracy is about 1 pro mille of the flying height. Hence, this accuracy is usually not sufficient for determining, for example, the altitude of bore holes. With large 1:5,000 scale aerial photographs, elevation data with an accuracy of 0.25 m were obtained, but seldom are such scales available, while a survey of accurate elevation with modern differential GPS systems is far more accurate and less expensive.

### *Relief displacement*

An AP is a central projection and therefore so-called relief displacement occurs, as will be clear from Figure 2.4.

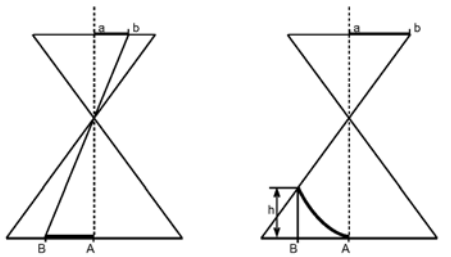


Figure 2-4

**Relief displacement: object of equal length in projection (A-B) has different length on an AP (a-b) in area with relief.**

Source: Horn and Grabmeyer, 2004

The planimetric, or projected distance A-B is the same in situation *a* and *b* in Figure 2.4, but the lengths *a-b* are different. The height of the object is *h*; *f* and *H* are defined above. There is no relief displacement at the nadir (the vertical) and displacement is greatest at the edges of the photo.

As explained below, plotting coordinates of boreholes or wells on aerial photographs requires rectification, see Chapter 3 on Geometric Aspects.

### *Digital aerial camera*

This modern type of camera uses charge-coupled devices (CCD). The camera is divided into individual sensors (pixels) and the data is available in digital format. CCDs are sensitive to wavelengths of up to 1,100 nm, which goes further into infrared than infrared sensitive photographic films.

### *Examples and literature*

No stereo AP examples are given in this text, because it is assumed that readers do not have pocket stereoscopes to hand. However, examples of monoscopical aerial photos are included in chapters of this book.

Because of the strength of aerial photo-interpretation for hydrogeological studies the reader is advised to consult the handbooks, which do contain a structured approach to photo-geology/geomorphology as well as the basics of photogrammetry required to understand the metrical and 3D aspects. A non-exhaustive list of some well-know textbooks is given at the end of this chapter.

## 2.4 Multi-spectral data

### 2.4.1 *A digital image*

The imaging system is designed in such a manner that the radiation arriving at the sensors is split into a few spectral bands or 'channels'. The widely used Landsat Thematic Mapper or ETM images are produced by a rotating mirror scanner. A scan line consists of an array of picture elements (pixels), each having a digital number (DN) also termed Digital Counts (DC), which results from the quantization of the amplified electronic signal generated by the sensor (detector). All scan lines together form a contiguous image, also termed a 'scene'. Apart from scanners, 'push-broom' systems (e.g. SPOT) are in use, which consist of a great many sensitive CCD cells, which are now familiar from digital cameras.



The pixel is the smallest unit of information in a grid cell map or image. The spatial resolution refers to the smallest spacing between two display elements or the smallest size of a feature that can be mapped or sampled. The terms ‘pixel size’ and ‘spatial resolution’ are often used interchangeably. The dimensions of a pixel on the surface of the earth depends on the system, and varies from 2 m in some commercially available systems (see Appendix) to 1,000 m (e.g. NOAA-AVHRR) or to 15 km (passive radar systems).

For many sensors, the DN, or brightness, recorded in each band is a simple linear relation of the radiance reaching the sensor. For each band, a binary number is produced, usually in the range of 0–256, so that 8 bits can be used to store one band value. The output is a scaled (integer) value of the input, which follows for all practical purposes a linear relationship.

For some purposes the DNs have to be converted into spectral radiance values measured by the sensor (in  $\text{W}\cdot\text{cm}^{-2}\text{ sr}^{-1}\text{ }\mu\text{m}^{-1}$ ), as discussed in section 2.8. For more details, readers are referred to the User Manuals of sensor systems and their websites and User Manuals or Field Guides of Image Processing packages and Chapter 5 on Thermal Images. An introductory overview to radiometric correction with references to literature is given by Parodi and Prakash (2004). A practical method for correcting Landsat TM data radiometrically, solely based on evaluation of scene information, is given by Hill and Sturm (1991).

For visual interpretation and for most classification applications it is not necessary to convert the data (in DNs) into absolute radiance units. A practical point is that often the calibration data may not be readily available. Figure 2.5 illustrates the pixels on various bands and their DNs.

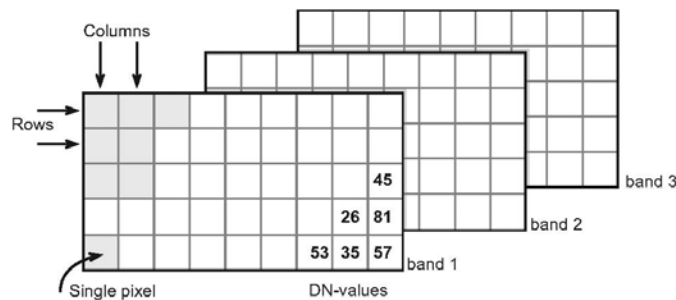


Figure 2-5

## Structure of digital images

As a matter of fact, if one acquires a digital satellite image (e.g. on CD, etc.) all one gets essentially is an ordered series of DNs for each spectral band, as shown in Figure 2.5. It is obvious that for visual interpretation the DNs have to be ‘translated’ into grey tones or colour tones; the so-called image processing (IP) software does exactly that, as well as many other similar tasks.

Since this aspect is relatively basic, a small hypothetical example is included. Figure 2.6a shows pixels with DNs of a near infrared (NIR) band of a small area consisting of three land cover types: (1) a uniform grassland (G, see Figure 2.6b), (2) a small water body (W) and (3) bush (B). Pixel size is 30 m. Sunlight is absorbed by water in the NIR band, thus the DNs of the water body are low (not zero because of some light reflected by particles in the atmosphere, and they vary from 1 to 4. Green vegetation reflects much light in the NIR band, thus the DNs are higher, but show some variation (from 18 to 21) due to differences in density and heights of the grasses, mixtures of grass species, and so on. The open bush area, with much bare soil, has reflectance values (DNs) that vary from 8 to 11.

It should be noted that pixels in the transition from one land cover type to another have intermediate DN values. These correspond to so-called ‘mixed pixels’ (M), composed of mixtures or either grass-bush, grass-water and water-bush.

In this simple example the mixture allows an even more precise estimation of the width of the water body along each line than the spatial resolution of 30 m in the example, if, and only if, one is sure that there is only grass and bush along the water body. The field evidence is known as *groundtruth*. For example, take line 4: the second pixel from the left has a DN of 7; in other words, about 1/3rd consists of water and about 2/3rd of grass; hence the estimated approximate width of the water body in that pixel is

$$\frac{2}{3} * 30 \text{ m} = 20 \text{ m}$$

The process of creating an image from digital data could consist of assigning grey tones to ranges of DNs, as is shown in Figure 2.6c. Instead of grey tones, colours can be used.

Col.	1	2	3	4	5	6	7
1	18	20	19	20	13	8	11
2	21	19	20	21	14	9	8
3	22	20	14	5	6	8	10
4	18	7	3	2	2	6	11
5	22	13	2	1	2	4	8
6	20	16	2	2	2	1	6

1	G	G	G	G	M	B	B
2	G	G	G	G	M	B	B
3	G	G	M	W	M	B	B
4	G	M	W	W	W	M	B
5	G	M	W	W	W	W	B
6	G	G	W	W	W	W	M

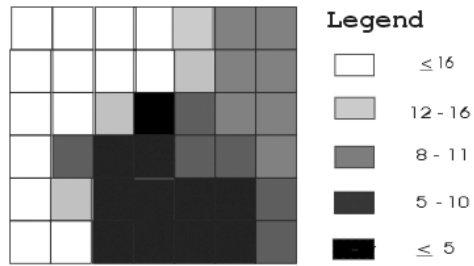


Figure 2-6

Sketch illustrating digital numbers (a) and corresponding ground cover classes (b); G=grass, B=bush, W=water, m= mixed, and assignment of grey tones (c).

This type of partitioning DN's is called *density slicing* in most IP software and is the simplest form of a *spectral classification*. It is easy to see that confusion can be caused between riparian pixels and bush area; this is the well know problem of *mixed pixels*.

### 2.4.2 DN's and energy interaction

Having introduced the DN's it is useful to remark that the DN values of a given object in the terrain are time variant, due to a variety of reasons. Atmospheric conditions during a satellite overpass change and thus so does the amount of absorption, two-way transmission, and different types of scattering. Furthermore, the surface properties of the object change with time, such as: water and chlorophyll content of leaves, soil moisture, dust and aerosols in the atmosphere, and so on. The geometry of the path sun-object-satellite sensor influences the energy received by the sensor and thus the time of year and the orientation of slopes, canopy structure, as well as some other factors. Discussion of proper radiometric corrections is beyond the scope of this book, but some physical aspects are explained in Chapter 5, Thermal Images.

Generally, for most hydrogeological work, no complex corrections are required and the relative reflection values suffice for enhancing image contents, spectral classification, and some transformations.

In case images of different dates are available, care should be taken to compare DN's after radiometric correction, but some simpler type of operations can be applied, as discussed below.

### 2.4.3 Examples of relative spectral signatures

Typical spectral reflectance curves of the ground classes 'water' and 'soil' are sketched in Figure 2.7. These are

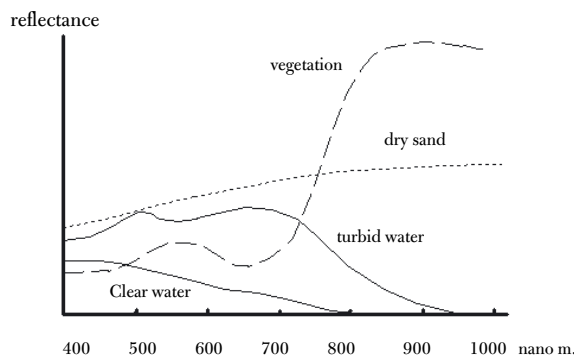


Figure 2-7

Schematic spectral reflectance curves

shown in relative form (no units on the vertical axis) because of the effects of viewing conditions, roughness, moisture, mineral content, and so on.

## Water

The reflectance properties of the class 'water' depends on whether the water is clear or muddy, whether vegetation grows in the water (papyrus, reeds) or floats on it (water hyacinth, etc.). Suspended matter, solid or biotic, significantly influences spectral reflectance. The shorter wavelengths (blue, green) can penetrate water, about 10 m in the 500–600 nm (0.5–0.6  $\mu\text{m}$  wavelength), and thus bottom reflection may contribute to the energy received by the sensor. Therefore, water bodies, not consisting of deep and clear water can have a wide range of reflectances in the visual bands.

The red wavelength is partly absorbed and those beyond in the near infrared are fully absorbed. Emergence of groundwater, for example, in ephemeral riverbeds, can therefore be best detected on the infrared band(s).

## Soils

Soil reflectance spectra exhibit in general a monotonic rise from 0.40 to 1.75  $\mu\text{m}$  (or 400 to 1,750 nm) with absorption around 1.45  $\mu\text{m}$  (Figure 2.8a). Scattering and absorption by mineral and organic matter and surface roughness determines the spectral signature, but for a given soil, the surface moisture influences the reflectance. Generally, the higher the soil humidity, the lower the reflectance.

The linear relationship between reflectance in the red and NIR parts of the spectrum of soils with varying moisture content is known as the 'soil line' (see Figure 2.8b). Deviations from the soil line have been used for vegetation indices, because pixels with green vegetation plot in the upper left part of the diagram, due to high reflectance in the NIR band.

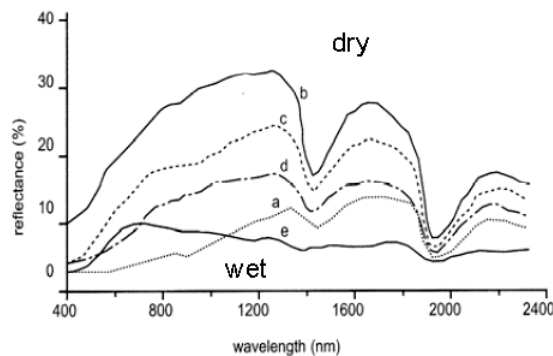


Figure 2-8a Spectral reflectance curves of some soils with different composition

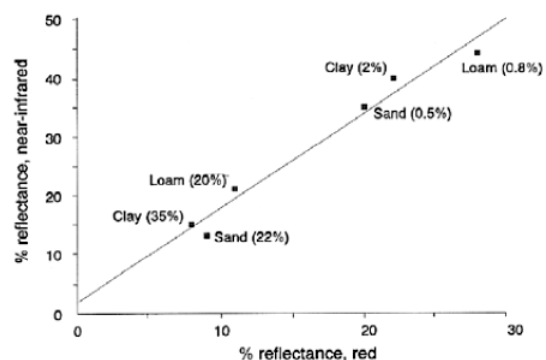


Figure 2-8b Reflectance of soils of different texture and moisture content. Curve is the 'soil line'. Source: Belward, 1991

The hydrogeological significance of lower reflection of wet soils (see Figure 2.8b) is illustrated in Figure 2.9. Shown is the NIR band of a Thematic Mapper (TM) image of an alluvial area in north India, NW of Roorkee.

Groundwater emergence takes place along a fault. North of the fault in the dry area is the intake area of a groundwater flow system. Most recharge takes place through transmission losses in the wide ephemeral riverbeds (boulders and gravels near the hills, sands and gravels downstream) and rainfall recharge in the sandy soils. This recharge drives a groundwater flow system. The discharge area of the groundwater flow system is concentrated along the fault, which brings the older and less permeable deposits (in the upthrown southern side) in contact with the more permeable younger deposits in the downthrown northern side. The coincidence should be noted of the pattern due to emergence of groundwater in the ephemeral riverbeds and that of the wet soils (darker tones, lower reflectance) due to capillary rise from a shallow groundwater table.

Geologic evidence for the faults are the uplifted, tilted older alluvial deposits (A, B and C), which have been dissected. The areas between the older and higher terrain consists of younger fluvial deposits without internal relief, on both side of the faults.

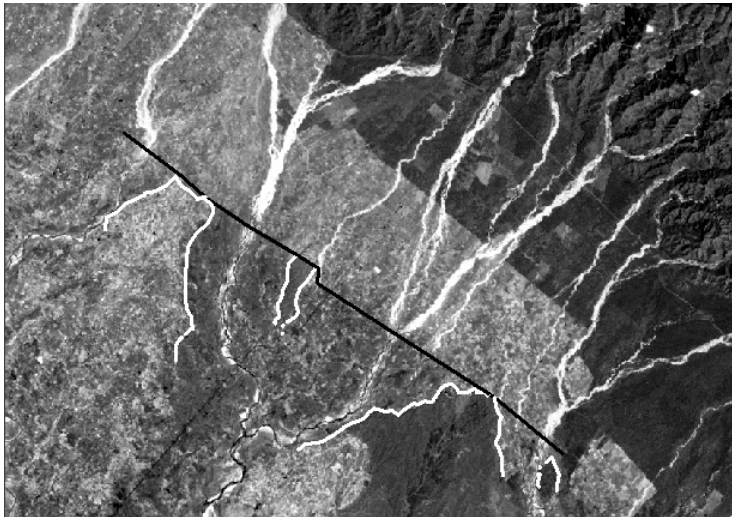


Figure 2-9

The Red band image Landsat ETM of a predominantly alluvial area in North India, showing groundwater emergence in ephemeral riverbeds along a fault (black line), and difference of reflectance of wet soils south of the fault due to capillary rise from shallow groundwater table and reflectance of dry soils north of the fault. The uplifted, tilted older alluvial deposits (A, B, C) whose margins are indicated by a white line, are geologic evidence of the fault.

Distance E-W is 24.9 km.

## 2.5 Image enhancement methods

The objective of image enhancement is to show features of interest in an enhanced manner, by applying certain operations available in the IP software. Here, we will discuss a few operations that are of use for hydrogeological studies. It should be understood that if a feature is not visible on the image, the operations would not be able to enhance the feature.

Discussed are:

- Stretching
- Filtering for enhancement of lineaments
- Ratioing
- Colour composites (RGB and HIS schemes).

### 2.5.1 Histogram operations

#### *Stretching*

This simple but effective technique is used to enhance certain features that are of interest but appear only vaguely on an overall image. For example, it is known that important transmission losses can occur on alluvial fans during episodic flow and recharge of groundwater. It is therefore useful to know the extension of the active part of the fan, that is, the part that receives occasional flood flow, as evidenced by the presence of fresh sands and gravels. Here we discuss how to enhance an image to highlight the active part.

In order to understand the way in which this can be most simply done we study a frequency plot (or *histogram*) of all the DN values of an image. Figure 2.10a shows an image (TM band 4 of an area in south Iran) with alluvial fans in the central part while the active part can be faintly differentiated from the inactive part, which has darker tones (lower DNs). South of the fans lies an area with salinity, the salt efflorescence causing high reflectance (high DNs). The salinity is due to a high groundwater level, which can be inferred from the emergence of groundwater in the riverbeds. There are also some outcrop and vegetated areas with low reflectance. A histogram of the area is shown in Figure 2.10b. Distribution seems relatively normal, but the tail ends are quite extended. The same image, after stretching to enhance difference between the active and non-active parts of the alluvial fan is shown in Figure 2.10c.

The grey levels available on the monitor range from 0 to 256, but the human eye cannot distinguish so many small gradations in grey tones. If the grey tones are equally distributed over the full range of DNs (in this case from 0 to 175), medium grey tones will dominate because the mode of the histogram lies in about in the middle range. Most of the available dark and white tones will be assigned to a low proportion of pixels at the tail ends. In order to enhance the differences in grey tones on the alluvial fan, the range of grey tones is distributed, in this case, over the range of DN 63 to DN 105. These values were obtained simply by inspecting the DNs of a number of pixels on

the active and non-active parts of the fan. It can be noted on the stretched image (Figure 2.10c) that the active part of the fan can now be discriminated with more ease, but at the expense of displaying differences in the tail ends, which show up as black or white.

In case one is interested in the saline area, stretching may also be done for the right hand side of the histogram.

In order to avoid assigning black and dark grey tones to the lower tail end and white and light grey tones to the higher end, leaving medium grey tones for most of the pixels, images are usually displayed by distributing the full range from black to white to DN values that correspond to 1% and 99% of the histogram. Most IP software does this as a default. Figure 2.10a was displayed in this manner.

Another example of the use of stretching over a narrow range of DN values is given in Chapter 5, Thermal Images, section 5.2.

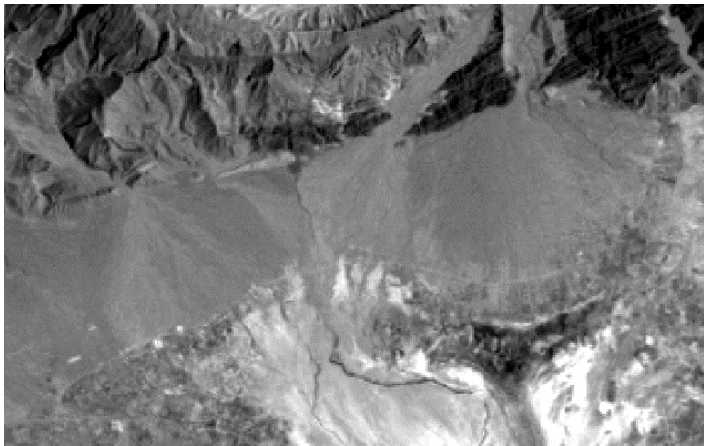


Figure 2-10a TM band 4 of area in southern Iran

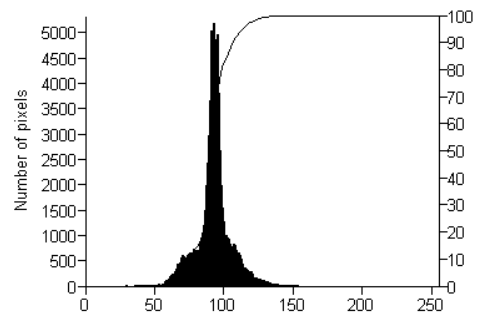


Figure 2-10b Histogram of the area shown in Figure 2.10a. Right-hand scale and solid line: accumulated %.

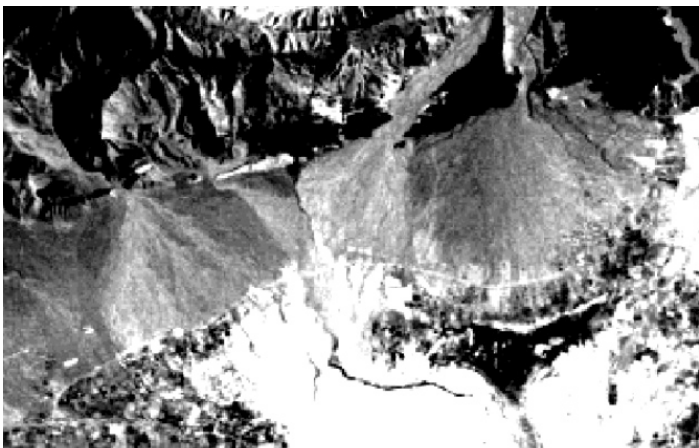


Figure 2-10c Area of Figure 2.10a, stretched between DN values 85 and 100

### *Histogram equalization and Gaussian stretch*

When an image is stretched with histogram equalization, the number of pixels with a certain value is taken into account. Input values are redistributed over a user-defined number of output intervals; in principle, all output intervals contain an equal number of pixels. When a certain image with values between 55 and 103 is stretched with histogram equalization to 256 output intervals, the minimum input value 55 is brought to output value 0, and maximum input value 103 is brought to output value 255; the other input values are divided over these 256 output intervals in such a way that each interval contains as equal a number of pixels as possible. In general, it can be said that the part of an image's histogram with the largest number of pixels is stretched more than the parts with few pixels.

Most histograms of varied areas have a more or less normal distribution and *Gaussian stretch* results in closer output intervals around the mode of distribution than the tail ends. Its effect is between that of a linear stretch and stretching by histogram equalization.

*Histogram operations for comparing multi-temporal images*

Comparison of images of different dates, but of the same band, can be improved by simple arithmetic operations based on adjusting the histograms. First, the lowest DN in the image should be zero, which is achieved by subtracting the minimum value found in the image. This is also known as ‘haze correction’ and is often required for vegetation index transforms (see NDVI, below). The next step is to locate ‘pseudo-invariant’ objects on the scene such as fresh dune sands (beaches, active dunes), large surfaces of concrete or asphalt (airports, etc.), and water bodies of some depth where water is free from suspended matter (unless NIR bands are used) and where no shadow effects occur. The DNs of such objects are noted on the images of different dates. One of the images of the time series is taken as the reference image (the master); the other ones are termed ‘slaves’. The ratio between the master-slave DNs of selected pseudo-invariant features is that used for multiplication (positive or negative value) of all the DNs in the image. This operation equalizes the DNs of the pseudo-invariant features and variations in other objects are due to variations in reflectivity.

**2.5.2 Lineaments**

Groundwater occurrence in hard rock terrain is often limited to fractures and faults; along tensional faults much groundwater can flow, sharp flexures can form a barrier to groundwater flow, and so on.

Fractures and faults are essentially linear features and therefore can be identified by visual interpretation of images. The true nature of such linear elements may not be known during the interpretation and therefore it is preferable to speak of *lineaments*. These can be defined as non-man made, more or less linear features, possibly associated with faults and large fractures. The nature of lineaments and their significance in groundwater studies is discussed in Chapter 9, Karst Terrain and Chapter 10, Crystalline Basement Terrain.

Because the surface expression of faults or fractures can be due to a variety of circumstances, visual detection and tracing by hand of linear features is performed. The operation is therefore subjective and should be regarded as a start for locating and studying possible water bearing zones. In this chapter some image enhancement techniques are discussed that assist the visual interpretation of lineaments.

**2.5.3 Filters for the enhancement of lineaments, ‘high pass filters’**

The so-called ‘high pass’, ‘edge enhancement’ or ‘sharpening’ filters are used for lineament detection. For hydro-geologic study the high pass or gradient filters are mostly used.

The functioning of a filter can be understood through the following exercise. Consider 8 pixels on a row; the first 4 have a DN of 1 due to reflectivity of land cover X, and the last four a DN of 4, of land cover Y. A so-called ‘operator’ can be applied to the row, and the operator may consist of the values -1 and 1. First the DNs of the first two pixels are multiplied with the operator and the sum is written at the second position;  $-1 * 1 + 1 * 1 = 0$ . Then the operator is shifted to pixels no. 2 and 3, then to 3, 4, and so on. It is easy to see that as long as the DNs remain the same, the result will be 0. However, when there is a change (an edge) in the example from pixels 4 to 5 the result will be different:  $-1 * 1 + 1 * 4 = 3$ , but will be zero again for the next pairs of pixels, as is shown below.

1	1	1	1	4	4	4	4	Original image
	0	0	0	3	0	0	0	Filtered image

One could decide to assign black to the value 0 and white to the value 3. The effect is that the edge marking the change from land cover X to Y is shown as a white line in a uniform dark image. The original image is thus *transformed* into a new one.

For image processing usually a 3 x 3- or 5 x 5-filter is used. The method of calculation is the same as given above, but the sum of the products is written on the central pixel. The filter then moves a pixel in x-direction and the calculation is repeated until the end of the row. The procedure is continued beginning with the first pixels of the next row, and so on.

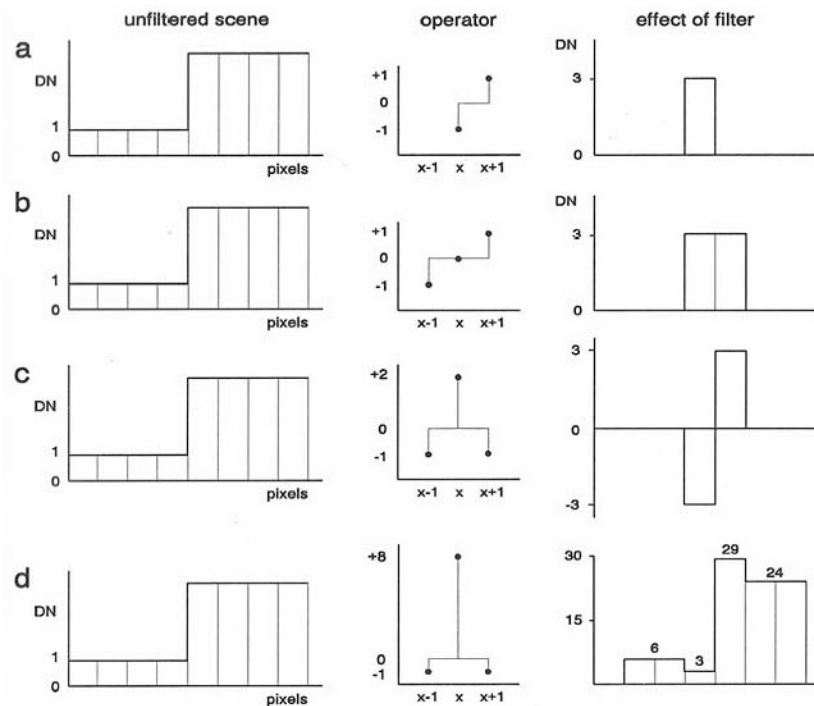


Figure 2-11

Sketch illustrating effect of high pass filters (see text)

Operators and their effects are illustrated in Figure 2.11:

- Operator **a** with two terms, shows the effect as explained above.
- Operator **b** has the same effect, but since 3 terms are used the edge effect comprises 2 pixels.
- Operator **c** results in a kind of shadow effect along enhanced contrast in the image.
- Operator **d** retains much of the original image and enhances the contrast somewhat.

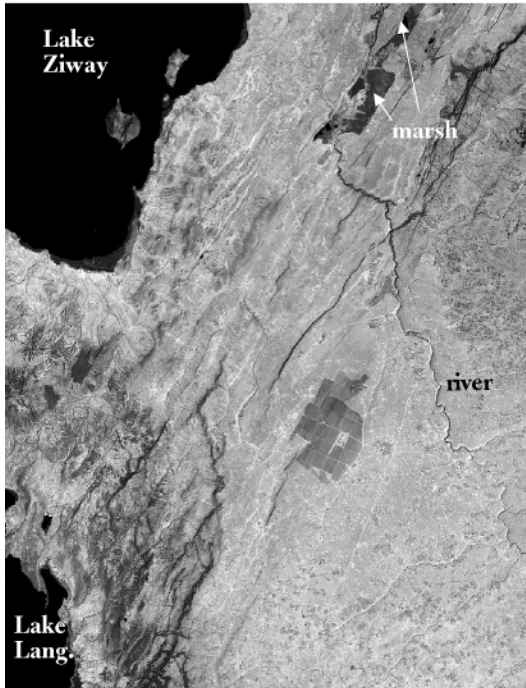
*Edge enhancement filter*

For the study of lineaments, operator (d) has the advantage that most of the original image content is retained, showing the terrain, but contrast is increased somewhat and edges are a little sharpened. Instead of the operation on one row of pixels, the filter is used for blocks of three rows and three columns, for example in a symmetrical fashion to avoid giving a-priori preference to any direction:

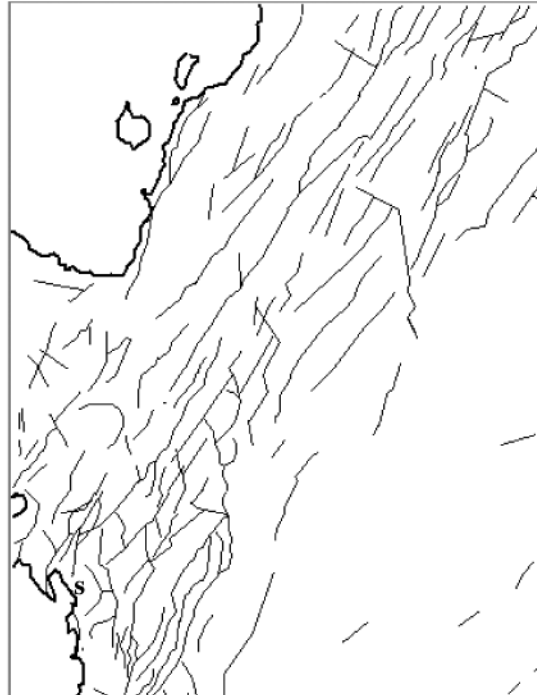
$$\begin{matrix}
 -1 & -1 & -1 \\
 -1 & 16 & -1 \\
 -1 & -1 & -1
 \end{matrix}$$

Figure 2.12a shows a small part of the eastern fault zone of the Central Ethiopian Rift, north of Lake Langano (the lake is not completely shown, it is just south of the area depicted). The above filter is selected because the fault scarps run more or less north south, while the sun at the time of recording of the image is at about 9.30 am, thus at a relatively low angle in the east, so that the scarps are in shadow. Because of the steep slope of the scarp, they have a fairly dense vegetation cover, which gives contrast to the cultivated areas or grazing lands in the gentle sloping to flat areas in between the fault scarps. Because of these two reasons the features as seen on the original image have to be retained in the image processing and by using the above filter only a little ‘sharpening’ is done.

Along the extension of one of the faults shown on the image near the shore of Lake Langano, a powerful spring was found. Interestingly, the local inhabitants said the spring (s) provided minimal water in the period prior to the 1970s. It thus seems that recent tectonics widened the fault plane and increased its capacity as a conduit of water from a river, which feeds marshes in a minor graben. Figure 2.12b indicates that faults are running from the marshes to the spring. Ayenew (2003) found that isotopic composition of the spring water was similar to that of the river. Faults of open nature are expected in a rift environment.



**Figure 2-12a** TM band 5 of a part of the central Ethiopian Rift, with edge enhancement filter, which sharpens contrast only a little. Distance E-W is 37 km.



**Figure 2-12b** Lineament interpretation, mainly tensional rift faults, using on-screen digitising with enlargement. s = spring, see text

*Filter giving full transformation of the image*

The situation is quite different in the southwestern part of the Central Ethiopian Rift, because the geology is different from that of the above example. Figure 2.13 (upper left) shows the area west of Lake Shala and it is difficult to detect lineaments. The figure shown is a black and white image of band 5 (infrared) of TM, being the image that displays lineaments best compared to the other bands, in this case, or even to false colour images comprising combinations of three bands. Because of the difficulty, a strong transformation method can be used like a Laplace filter, with operators such as (a) to (c), shown in Figure 2.11 (upper right). Written in a 3 x 3 format:

$$\begin{matrix}
 0 & -1 & 0 \\
 -1 & 2 & -1 \\
 0 & -1 & 0
 \end{matrix}$$

Because the filtered product is fully transformed, the histogram is entirely different from the original image and thus stretching has to be done. Automatic stretching between 1% and 99% may not give the best image for lineament interpretation and some experimentation with different cut-offs should be undertaken before interpretation starts. Note that little of the original contrasts, due to vegetation, rocks/soils, shadows, and so on are still present in the image, but any local contrasts in reflection values (DNs) have been enhanced. This product has been interpreted visually (the only practical way to extract lineaments), shown in Figure 2.13 (lower left).

The hydrogeologic significance can be briefly sketched as follows: the groundwater contour map of the area shows a gradient to the south and the east. Pumping tests have shown that the aquifer, composed of different rocks, behaves as a hard rock aquifer, hence poor primary porosity. There can be appreciable loss of water by fracture flow through the north-south trending lineaments and less loss of water through fractures/faults in easterly direction to Lake Shala.



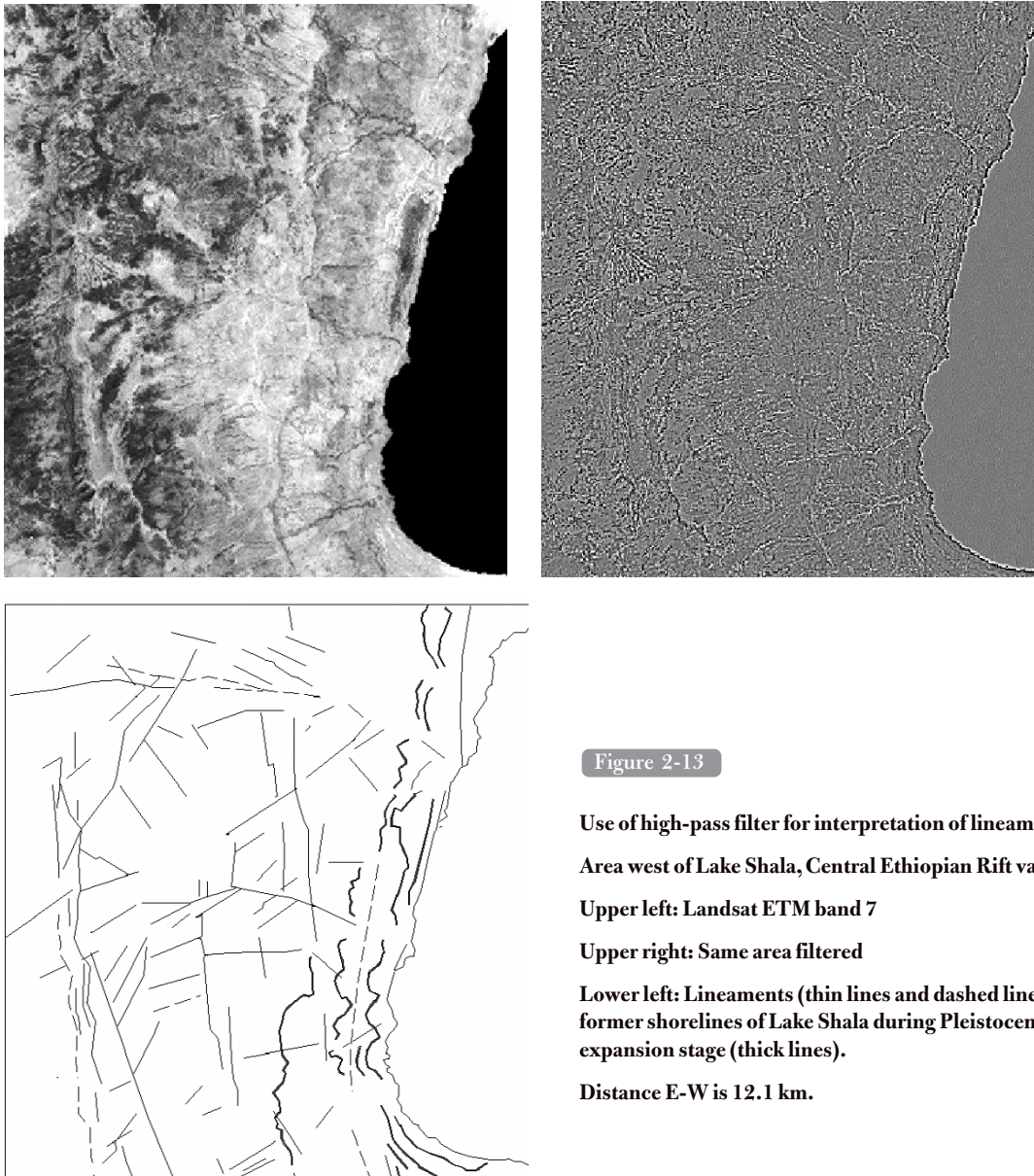


Figure 2-13

Use of high-pass filter for interpretation of lineaments.  
Area west of Lake Shala, Central Ethiopian Rift valley.

Upper left: Landsat ETM band 7

Upper right: Same area filtered

Lower left: Lineaments (thin lines and dashed lines) and former shorelines of Lake Shala during Pleistocene expansion stage (thick lines).

Distance E-W is 12.1 km.

*Other filters*

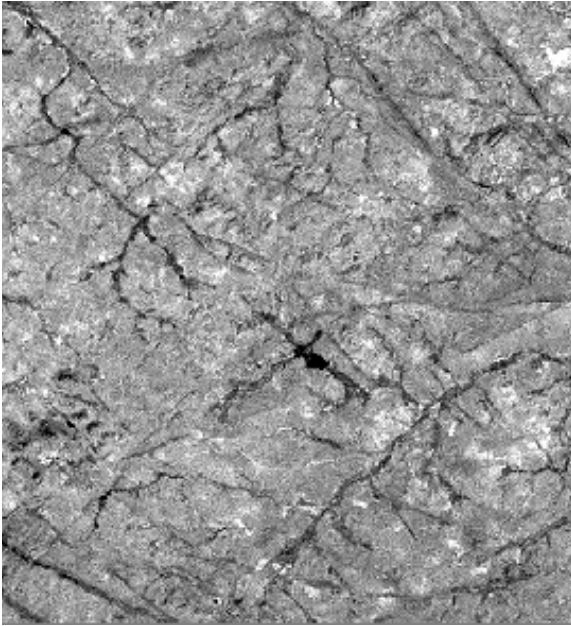
The strength of the local spectral gradient is enhanced by applying the operator in two directions (in x and y direction). The operators of some commonly used zero-sum gradient filters are shown below:

Prewitt	$x \rightarrow \begin{matrix} -1 & -1 & -1 \\ 0 & 0 & 0 \\ 1 & 1 & 1 \end{matrix}$	$y \rightarrow \begin{matrix} 1 & 0 & -1 \\ 1 & 0 & -1 \\ 1 & 0 & -1 \end{matrix}$
Sobel	$x \rightarrow \begin{matrix} -1 & 0 & 1 \\ -2 & 0 & 2 \\ -1 & 0 & 1 \end{matrix}$	$y \rightarrow \begin{matrix} 1 & 2 & 1 \\ 0 & 0 & 0 \\ -1 & -2 & -1 \end{matrix}$
First derivative	$x \rightarrow \begin{matrix} 0 & 0 & 0 \\ -1 & 0 & 1 \\ 0 & 0 & 0 \end{matrix}$	$y \rightarrow \begin{matrix} 0 & -1 & 0 \\ 0 & 0 & 0 \\ 0 & 1 & 0 \end{matrix}$
Laplace	$x \ \& \ y \ \begin{matrix} 0 & 0 & 0 \\ 1 & -8 & 1 \\ 1 & 1 & 1 \end{matrix}$	

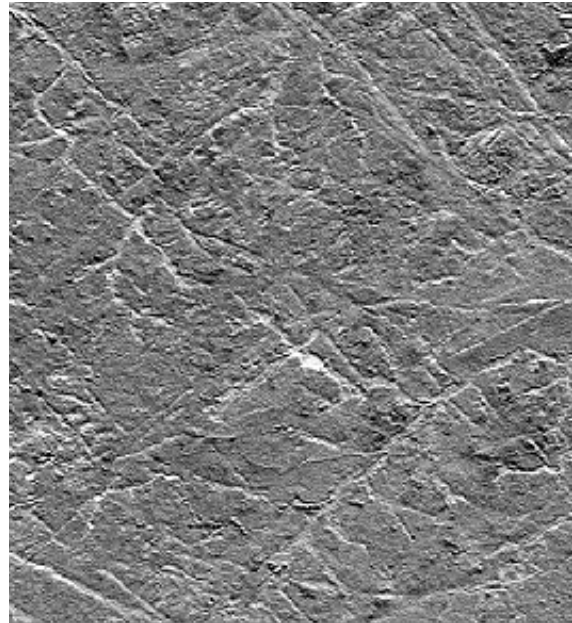
A non-filtered LANDSAT-ETM Panchromatic band with a resolution of 14.5 m of a granite area with inselbergs and other outcrops and some dolerite dykes is shown in Figure 2.14a. The regolith has generally limited thickness. Most of the drainage follows fractures. The dark area in the centre is a small reservoir. Figures 2.14b–d show the effect of the above filters.

High pass filters with a 5 x 5 kernel have also been used, but these may result in a blurring effect of sharp gradients.

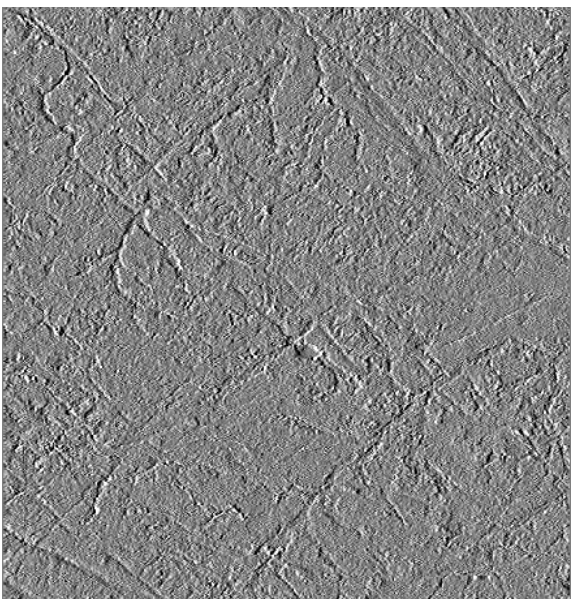
The Laplace filter calculates gradients in both x- and y-directions (second partial derivative). The effect of using the Laplace filter is that when the value of the central pixel is relatively high compared to its neighbours, the



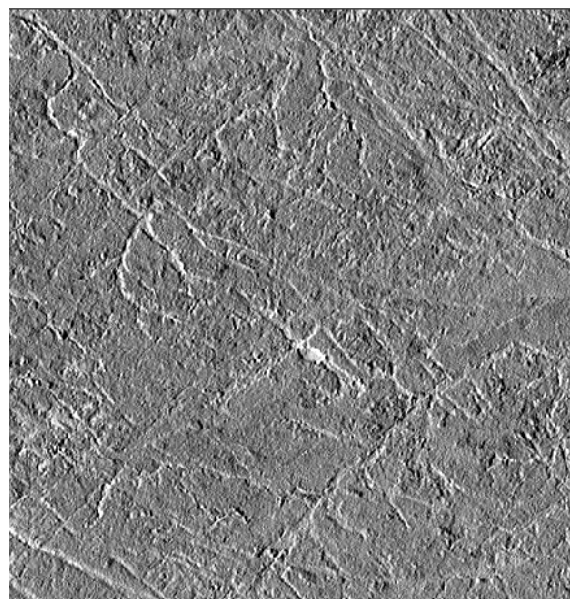
**Figure 2-14a** Granite area in central India of little weathered terrain, some inselberg complexes drainage adjusted to fractures and fractures. LANDSAT ETM Pan chromatic band



**Figure 2-14b** Same area and same band as left hand Figure 2.14a, filtered with Prewitt filter, Y direction. Distance E-W is 7.2 km.



**Figure 2-14c** First derivative filter, X direction



**Figure 2-14d** Sobel filter, X direction

value assigned to the central pixel will be even lower than its neighbours and vice versa. Thus values, which 'largely' differ from their neighbours, come out as an opposite in the output map, while areas with more or less the same pixel value 'disappear'. The Laplace filter is quite sensitive to noise.

It must be remembered that most of the common multi-spectral images (e.g. SPOT, Landsat, IRS) are recorded at around 9.30 a.m. to avoid clouds in tropical areas and to enhance morphology, as at this time the angle of the sun is relatively low. However, topographic shadow effects will benefit lineaments that run more or less perpendicular to the azimuth of the sun and attention must be paid to this fact during interpretation.

#### 2.5.4 Automated lineament detection

In the chapter on Crystalline Basement Terrain attention is paid to the criteria and sometimes indiscriminate tracing of lineaments, which are supposed to be associated with fractures. Because the process of tracing lineaments is somewhat subjective, some advocate the use of automated extraction through the employment of algorithms, such as the Hough transform (Karnieli, 1996).

A major problem is that such algorithms operate purely on linearities in contrast in an image. Thus, many features not associated with fractures, such as man-made boundaries (field boundaries, roads, fences, etc.), strike ridges, foliation directions and so on, are included. This leaves the hydrogeologist with the task of establishing one-by-one which 'linears' are associated with possible fractures and which ones are not. This is usually a more tedious and subjective operation than tracing the lineaments (on-screen digitizing) directly on images, whereby use can be made of different types of images (false colour composites, various filters, etc.) and in particular having the benefit of geological judgement.

## 2.6 Colour composites

Much of hydrogeologic application of remotely sensed images is visual interpretation, and therefore a small excursion into colour-coded combinations of bands is useful.

An understanding of some of the principles of colour and intensity information is needed for optimal image fusion, for example combining three multi-spectral bands and an orthophoto or high resolution pan chromatic satellite image (e.g. SPOT, TM band 8, IRS pan), discussed at the end of this chapter under Image Fusion.

### 2.6.1 Red Green Blue (RGB) colour system

The RGB definition of colours is directly related to the way in which monitors of computers or television sets function. The three primary colours are handled in an additive mode, and the full gambit of colours recognized by us can be displayed. Any colour can be regarded as a combination of different contributions of the primary colours Red, Green and Blue (RGB). Figure 2.15a presents a colour cube with Red, Green and Blue axes. Along each of these axes the 'amount' of a primary colour increases from 0 to 255, where 0 means no intensity (no contribution to the final colour) and 255 means maximum intensity. Each point in the colour cube thus represents a different colour depending on the amounts of Red, Green and Blue. The Grey scale is presented by a line from Black to White (dashed line in Figure 2.15a). For each Grey colour, the amounts of Red, Green and Blue are equal.

Suppose a pixel on band  $i$  has a low DN but on band  $j$  a high DN. If Red is given to band  $i$  and Green to band  $j$ , that pixel will have a green colour on a composite of bands  $i$  and  $j$ . In case a pixel has high DNs on both bands, it will appear as bright yellow on the composite (Red + Green = yellow), and so on.

It is customary to speak of a 'false colour' composite by assigning Red to the Near Infrared (NIR) band, Green to the red spectral band and Blue to the green spectral band. However, one may assign these colours to any selected bands or to transformed images.

For images of dry regions in particular, the information of some spectral bands can be highly correlated (i.e. the images look much the same). Therefore, for a colour composite it makes sense to use three spectral bands that have the least correlation to each other. IP software usually has a facility to show the degree of correlation; otherwise visual inspection of the images has to be done for the selection. As will be explained below, the 'Principal Component' transform applied to multi-band data always results in non-correlated images.

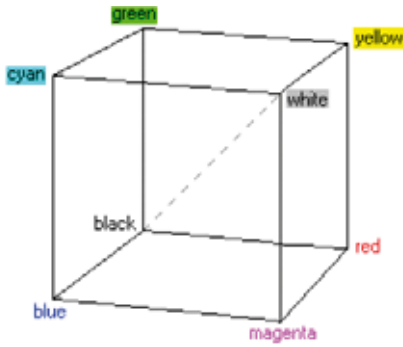


Figure 2-15a Colour cube of the Red Green Blue system and some additive colours

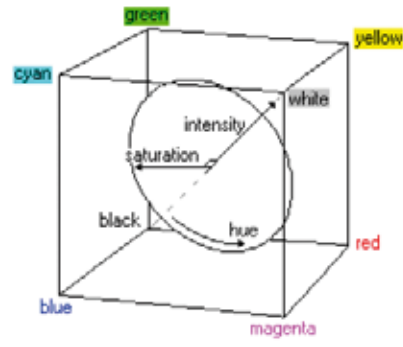


Figure 2-15b Colour cube showing also Hue, Saturation and Intensity (= diagonal)

### 2.6.2 Hue Saturation Intensity colour system (ISH or IHS)

Colours can also be defined using the Hue, Saturation and Intensity (HSI) system. Intensity describes the brightness of a colour and has a dimension of 0 to 1. The total amount of Red + Green + Blue determines the brightness and is represented by the diagonal ( $R = G = B$ ) in Figure 2.15a, from black through shades of grey to white. The diagonal represent the intensity.

Hue is the basic component of a colour and is the dominant or average wavelength. Hue refers to our perception of colour; green, orange, purple, and so on. Hue has a circular dimension from 0 to 360. It is possible to think of a plane orthogonal to the intensity axis, shown in Figure 2.15b as a circle. By moving around in the plane, the hue changes.

Saturation describes the ‘colour purity’ or the purity of colour relative to Grey and has a dimension of 0 to 1. The relative amount of Red, Green and Blue determines the Hue and the Saturation. Saturation refers to whether colour is pale or vivid; pastel colours have low saturation. At the green-red, blue-green and blue-red sides of the cube, saturation is maximal (unity or 100%). Pixels with values that would plot close to the intensity axis have low saturation and all shades of grey from dark to light have no saturation.

The transform into Intensity-Hue-Saturation system is done by algebraic operations using the three original bands as input. Most IP software includes the option of the IHS transform. Such transformations are used in image fusion, discussed later.

Figure 2.16a shows ASTER images in the IHS and RGB schemes (Figure 2.16b) of an area in Thailand. The colour assignment to both images was done in the conventional manner: Red to Band 1, Green to Band 2 and Blue to band 3. Note that the IHS colour composite has more colour information.

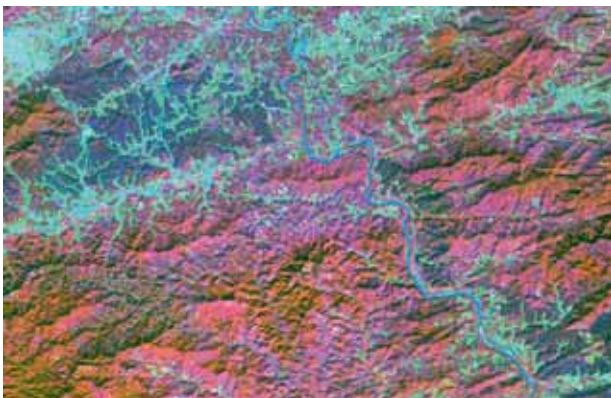


Figure 2-16a IHS image of an area in Thailand of ASTER bands 3, 2 and 1. This image has more colour information than a colour composite made in the conventional RGB scheme, shown beside

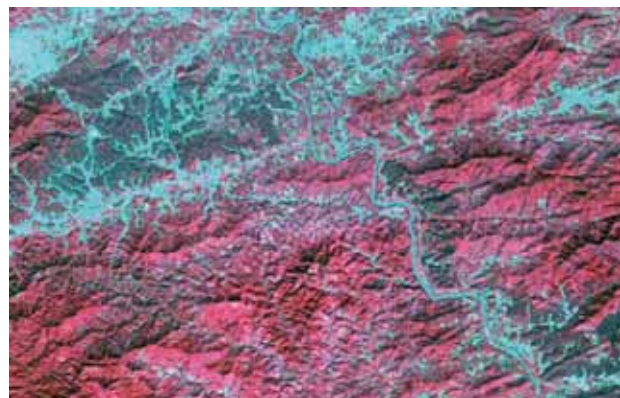


Figure 2-16b Colour composite of ASTER bands 3, 2 and 1 in the RGB scheme

### 2.6.3 Decorrelation stretching

This term means that images are brought into the Hue-Saturation scheme with constant Intensity. The saturation is stretched and hue may be adjusted by rotation; thereafter the images are transposed into the RGB scheme for display. Image processing software may include this option (sometimes termed ‘colour separation’).

## 2.7 Transformations often used in hydrogeologic interpretation and data extraction

### 2.7.1 Principal component (PC) transform

The strength of PC transform is that it is an effective method of data compression by a mathematical linear transformation. Thus, all the information contained in many spectral bands can be reduced into a few new PC images with little loss of information. The PC transform can also be regarded as a form of image enhancement.

The mathematical background of the transform is not given here, only a conceptual sketch and some salient aspects.

To sketch the principle, Figure 2.17 shows the DN's of pixels of 3 spectral bands: 1, 2 and 3. Only a limited sample of the amount of pixels is shown; all the pixels in the image would form a large cloud. Because of internal correlation of some bands this cloud is usually not a sphere, (certainly in this 3D example) but has a sort of irregular cigar or thick boomerang shape. The maximum variance corresponds to the extremities of the cloud of points or, in other words, along the axis of the cigar. The first PC can be thought of as this axis, with all the data points ‘projected’ onto the PC-1 axis; in this way we have a histogram and a PC-1 image can be made.

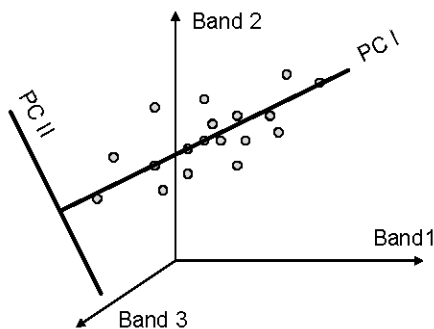


Figure 2-17

Sketch showing image data in 3D feature space and axes of Principal Component I (maximum variance) and Principal Component II (orthogonal to PC I)

Once the PC-1 is determined on grounds of maximum variance, the other PCs are fixed, being orthogonal to each other. The sketch shows only the PC-2 axis, onto which the data points are projected and thus a PC-2 image can be made and in a similar fashion so can a PC-3 image.

In the above example not much is gained by making a colour composite of PCs 1, 2 and 3 over a composite of the original 3 bands, but the situation is quite different when many spectral bands are used.

The input for Principal Components transform consists of a map list with the available bands or images from which the variance-covariance matrix will be calculated. This matrix shows how much variance there is in each of all the input bands and is used to calculate the transformation coefficients. Once the coefficients are known, a PC image (or the ‘projection’) is created by:

$$PC = c_1 B_1 + c_2 B_2 + \dots c_i B_i$$

where,  $B_1 \dots B_i$  are the pixel values (DN's) of each band used and  $c_1 \dots c_i$  the numerical coefficients. An example is shown in Table 2.1, where the bands of Landsat ETM (band 6, thermal band, omitted) were used. In this case a colour composite of PCs 1, 2 and 3 would contain 98.5% of the total variance. The table also shows that PC-1 is chiefly based on the NIR bands 5 (coefficient = 0.830) and 7 (coefficient is 0.490), and so on.

The interesting point for practical application is that the PC-1 and PC-2 images are not correlated; because of the orthogonality, they are complimentary to each other. Therefore the term ‘orthogonal decomposition’ is used in the literature. Furthermore, the PC-1 image contains most of the information because it is based on maximum

Variance per band:						
425.21	52.24	14.96	7.55	2.62	0.58	
Variance percentages per band:						
84.51	10.38	2.97	1.50	0.52	0.11	
	nig	subnig	subnig	subnig	subnig	subnig
PC 1	0.080	0.057	0.144	0.202	0.830	0.490
PC 2	-0.264	-0.117	-0.278	0.681	0.247	-0.561
PC 3	-0.618	-0.348	-0.524	-0.397	0.149	0.206
PC 4	0.159	0.024	0.121	-0.578	0.476	-0.632
PC 5	0.711	-0.220	-0.665	0.005	0.027	0.058
PC 6	-0.109	0.902	-0.413	-0.061	0.031	0.007

Table 2-1

Table showing variances per PC band and factor loadings derived from the input bands of Landsat ETM, the thermal band omitted because of different spatial resolution.

variance, followed by PC-2, PC-3, etc. The proportion of information described by a PC is termed the eigenvalue. The proportion of information from the input bands in a given PC is given by the coefficients (or 'loadings'), which vary from -1 to 1; the higher the value the more the input band has contributed. The set of loadings are called the Eigenvectors.

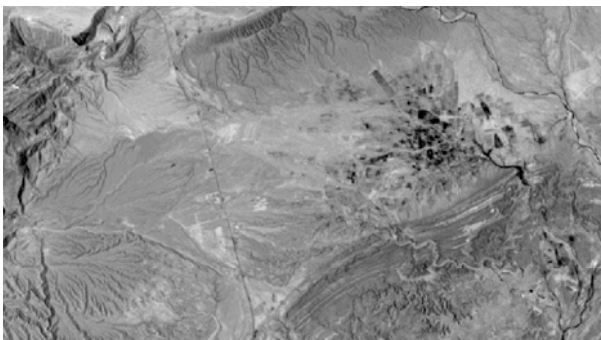
*Example 1: Enhancement of areas with transmission losses*

Figure 2.18 shows the PC-1 and PC-4 images of a semi-arid region in southern Iran, obtained from 6 Landsat TM bands (excluding the thermal band). The PC-1 had an eigenvalue of 85.4%, PC-2 of 9.4%, PC-3 of 3.3% and PC-4 of only 1.2%. Hence, a colour composite of PCs 1, 2 and 3 would contain 98.1% of the total information (variance) – effective data compression indeed. The loadings of PC-1 were all positive and therefore the image is a sort of weighted summation of the radiances (intensities or reflection values) of the original contributing bands' intensity values. For that reason the shadow effects are displayed well, showing the relief in the mountains and the adjoining dissected alluvial fans in the western part. PC-2 (not shown here) does not have this effect, because of its complementary nature.

The central-eastern part is a wide syncline forming an alluvial aquifer, which supports irrigation, as is evidenced by black toned fields, and well fields for drinking water supply (not seen on the image).

Although PC-4 contains only 1.2% of the variance, it should not be discarded because it so happens that a significant feature for recharge appears best on the PC-4 image. This is the fresh sands and gravels deposited by flash floods. In fact most of the 1.2% of information pertains to the occurrence of such fresh deposits. In a later chapter fluctuations of well levels will be given showing substantial rises in observation wells in the proximity of recent deposits. The PC-4 was stretched (see above) in such a manner to highlight the contrast between the light tones of the fresh gravels and sands and the surrounding area. Note that the deposits are not obvious on the PC-1 image.

Figure 2-18



PC-1 image Landsat TM of alluvial aquifer in southern Iran recharged by transmission loss of ephemeral streams.

Black patches are irrigated fields.

Distance E-W is 21.2 km



PC-4 image of same area, showing active riverbeds where transmission losses occur. Image was stretched to enhance recent alluvium.

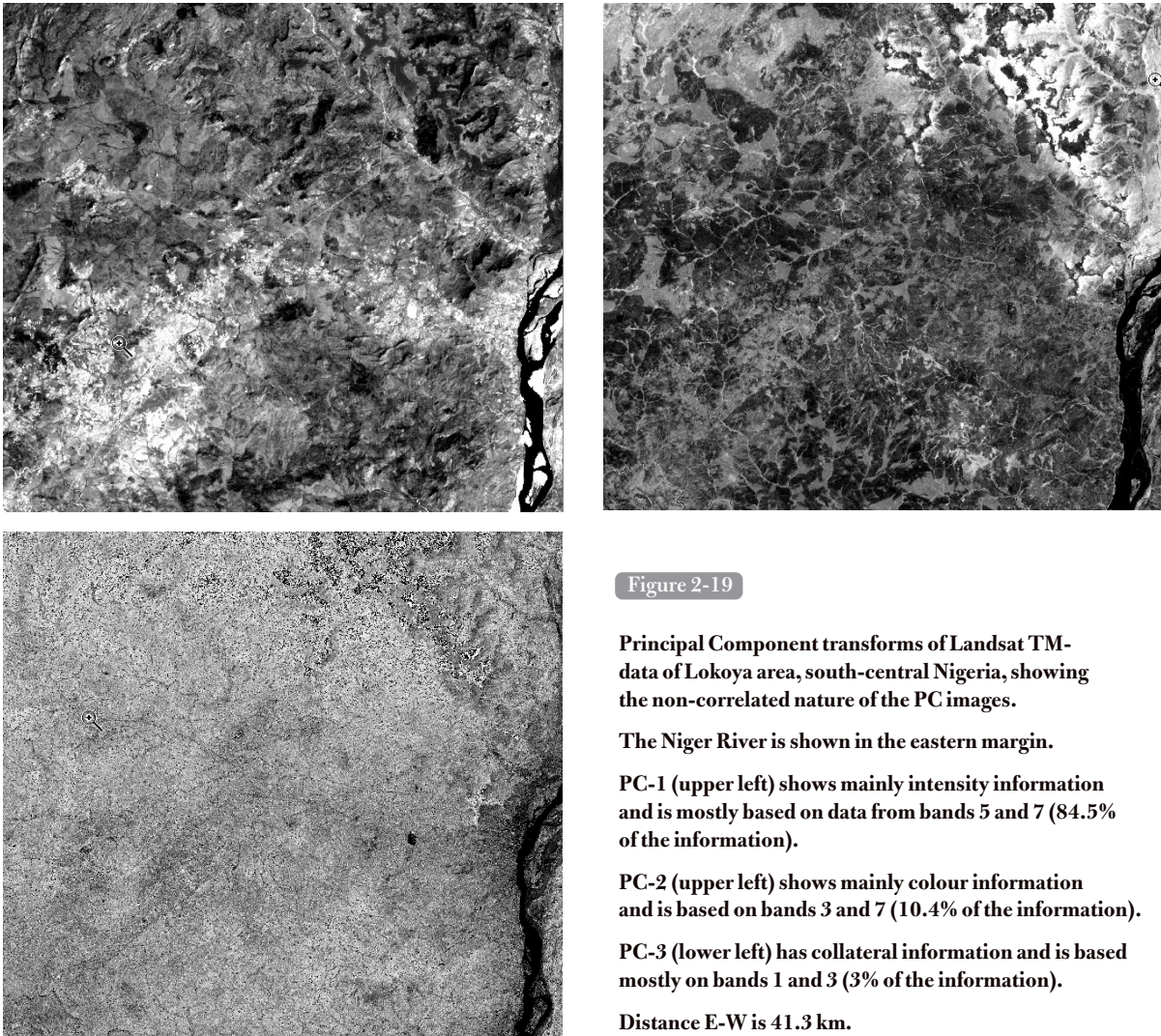
### Example 2: Area in south-central Nigeria

Figure 2.19 shows PC-1, PC-2 and PC-3 images of an area consisting of various gneisses (south-western part) and sedimentary rocks (north-eastern part), illustrating the complimentary (non-correlated) nature of the PC transforms. The text in Figure 2.19 shows the amount of information in each PC.

Burned fields (black) in the area influence PC-2 and PC-1, but not PC-3. The PC-3 image has a ‘noisy’ appearance, because of the low information content, but still has useful information (after enlargement) because the drainage network is well displayed.

#### Remark on PC transform

From the theory given above, it is evident that the PC transforms depend on the area selected. If one is interested in certain features occurring in a given aquifer, but the overall satellite scene has a large water body, the PC transform should be performed with data of a sub-scene covering the aquifer area, excluding the water body. If so desired, the entire scene can be transformed by typing the loadings or coefficients obtained for the area of interest in a map calculation.



### 2.7.2 Ratioing

This method simply consists of dividing the DN's of one band of a scene with another. What happens is illustrated in the diagram of Figure 2.20.

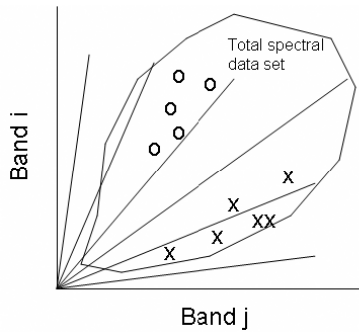


Figure 2-20

Sketch showing effect of ratioing. Feature space is partitioned in segments; grey levels are assigned to segments.

Classes (0) and (X) occupy certain segments and show up in narrow range of grey levels.

Effects of shadow due to relief are minimized by ratioing.

Empirical data has shown that certain ratios of TM images (or other sensors with the same wavelengths) and combinations of ratio images of semi-arid and arid terrain correspond to the following applications (Sabins, 1996; Jensen, 1996; Inzana et al., 2003):

- TM 3/1 = iron oxide
- TM 5/1 = mafic igneous rocks
- TM 5/7 = clay minerals
- TM 5/4 = ferrous minerals,  $5/4 * 3/4$  = mafic from non-mafic rocks
- TM 5/7 = argillites, serpentinite and alteration zones
- TM 5/7 + 5/4 + 3/1 = mineral composite
- TM 5/5 + 3/1 + 4/3 = hydrothermal composite

The rationale for deciding what ratios to take is subjective, unless larger sample sets are examined on the feature spaces of all band combinations. In practice, a trial and error procedure is used, starting with bands that are the least correlated and comparing the results with known rock types. Useful ratio images are retained for interpretation or for updating geological maps.

It may be mentioned that presence of regolith, vegetation and burned areas obliterates the effect of band ratios. For example, in the above PC example of the Lokoya area, Nigeria, the ratio images did not enable the differentiation of the igneous and metamorphic rock types shown on the geologic map based on field mapping, but the same poor result was obtained with the PC images. Only the contact of the sandstones and the basement rocks in the NE corner appeared on nearly all image products. The weathered mantle and vegetation in this area masks the lithology, but lineaments (fractures) can be interpreted. However, Inzana et al (2003) found useful application of ratio images for a large area in Madagascar, where outcrop areas were present in a generally vegetated and soil covered area.

## 2.8 Radiometric correction

As mentioned earlier, for many applications (e.g. filtering, classification using a single scene) it is not necessary to convert DNs of an image into radiance values. However, for comparison of multi-temporal images, for example vegetation indices (see below), temperature differences of water (concentrated groundwater outflow in water bodies), comparison of multi-sensor data and some other applications, the image data should be put into a common radiometric scale. The full correction procedure consists in fact of three steps:

1. Conversion of DNs into radiances
2. Correction for solar irradiance
3. Correction for atmospheric influence.

The last step is not discussed here; references are given in the chapter on General Themes.

### 2.8.1 Conversion of DNs into radiances

For the conversion the 'gain' coefficients have to be known. With the aid of simple equations all pixel values of a given band are changed from DN values into L values.

Normally, the conversion coefficients are given in the radiometric record of the header file and are unique for



each image. However since for this study the Landsat images header files were not available, such information was retrieved from the internet and related literature review.

For Landsat 4 and 5 TM images, the conversion from digital numbers (DN) to at-sensor spectral radiances can be done with the equation:

$$L = L_{\min} + \frac{(L_{\max} - L_{\min})}{DN_{\max}}(DN)$$

For Landsat7 ETM:

$$L = L_{\min} + \frac{(L_{\max} - L_{\min})}{DN_{\max} - 1}(DN - 1)$$

where L = spectral radiance at sensor's aperture,  $W\ m^{-2}\ sr^{-1}\ \mu m$  (sr is a measure of solid angle, comparable to field of view)

DN = digital number

Lmin = spectral radiance at DN=0

Lmax = spectral radiance at DN=DNmax (255)

Band	Processing date			
	From March 1st 1984 to May 4th 2003		After May 5th 2003	
	LMIN	LMAX	LMIN	LMAX
1	-1.52	152.10	-1.52	193.00
2	-2.84	296.81	-2.84	365.00
3	-1.17	204.30	-1.17	264.00
4	-1.51	206.20	-1.51	221.00
5	-0.37	27.19	-0.37	30.20
6	1.2378	15.303	1.2378	15.303
7	-0.15	14.38	-0.15	16.50

**Table 2-2**  
Landsat-5  
Spectral radiances,  
Lmin and Lmax  
in  $W\ m^{-2}\ sr^{-1}\ \mu m$

Tables 2.2 and 2.3 show the band specific calibration coefficients (source: Chander and Markham, 2003, and NASA, 2002)

Band	Processing date							
	Before July 1st 2000				After July 1st 2000			
	Low Gain		High Gain		Low Gain		High Gain	
	LMIN	LMAX	LMIN	LMAX	LMIN	LMAX	LMIN	LMAX
1	-6.20	297.50	-6.20	194.30	-6.20	293.70	-6.20	191.60
2	-6.00	303.40	-6.00	202.40	-6.40	300.90	-6.40	196.50
3	-4.50	235.50	-4.50	158.60	-5.00	234.40	-5.00	152.90
4	-4.50	235.00	-4.50	157.50	-5.10	241.10	-5.10	157.40
5	-1.00	47.70	-1.00	31.76	-1.00	47.57	-1.00	31.06
6	0.00	17.04	3.20	12.65	0.00	17.04	3.20	12.65
7	-0.35	16.60	-0.35	10.93	-0.35	16.54	-0.35	10.80
8	-5.00	244.00	-5.00	158.40	-4.70	243.10	-4.70	158.30

**Table 2-3** Landsat-7 ETM+ Spectral radiances, Lmin and Lmax in  $W\ m^{-2}\ sr^{-1}\ \mu m$

For calibrating Landsat-7 images non-desert, non-ice land surfaces, bands 1, 2, 3, 5, 6 and 7 are normally set to high gain whereas bands 4 and 8 are set to low gain, shown below.

### 2.8.2 Correction for solar irradiance

The radiance as measured by the instrument at the top of the atmosphere (TOA) is dependent on the solar

irradiance at that level. For relatively clear scenes and to avoid variations due to the variation within a year of solar irradiance, it is suggested that the radiance measured by the satellite be normalized, as calculated above, to planetary reflectance. The obtained values will then be comparable from one date to the other and allow inter-sensor comparison of images.

For all Landsat and Aster images, the top-of-atmosphere reflectance  $\rho$  (a unitless reflectance at the satellite, values of 0-1) for band  $\lambda$  can be computed by the following equation:

$$\rho_{\lambda} = \frac{\pi \cdot L_{\lambda} \cdot d^2}{ESUN_{\lambda} \cdot \cos\theta}$$

where  $\pi = 3.141593$ ,  $L_{\lambda}$  is TOA spectral radiance of the band observed by the satellite (above equations),  $d$  is the Earth-Sun distance in astronomical units,  $ESUN_{\lambda}$  is mean solar exoatmospheric irradiances for the wavelength band interval  $\lambda$  (for Landsat, see Table 2.4), and  $\cos\theta$  is the cosine of the solar zenith angle in degrees.

The distance  $d$  can be calculated by  $d=1+0.0167 \sin[2 (JD-93.5)/365]$ , where JD is Julian Day (JD is day number of the year, 1=January first). The solar zenith angle is calculated by subtracting the sun elevation (mentioned on the header file of the image) from  $90^{\circ}$  ( $\pi/2$  radians).

<i>Band</i>	<i>Landsat 5</i> <i>W m<sup>2</sup> μm<sup>-1</sup></i>	<i>ETM+</i> <i>W m<sup>2</sup> μm<sup>-1</sup></i>
1	1,957	1,969.000
2	1,820	1,840.000
3	1,557	1,551.000
4	1,047	1,044.000
5	219.3	225.700
7	74.52	82.07
8	n.a.	1,368.000

Table 2-4

Solar exoatmospheric irradiances

## 2.9 Vegetation index

### 2.9.1 Applications

A Vegetation Index aims at displaying and inventorying pixels (areas) with green vegetation. The interest for hydrogeology is

- The determination of acreages irrigated by groundwater for groundwater budget studies
- In dry areas the absence or presence of groundwater in fractures, assuming vegetation response to presence of water (see example below)
- Vegetation affects soil moisture budgets, recharge and in some areas uptake of groundwater by deep roots, as will be discussed in a later chapter.
- Areas with denser vegetation may indicate areas with higher rainfall and presence of groundwater, which may go unnoticed because of poor density of rain gauges.
- In case groundwater fluctuation causes problems, it may be desirable to study the vegetation response through a vegetation index and sequential images.

### 2.9.2 The NDVI transform

A typical spectral reflectance curve for healthy green broadleaves plants fully covering the ground is shown in Figure 2.7. Green vegetation reflects much light in the near infrared (NIR) band but not much in the red band (RED). Therefore, the simplest vegetation index is (NIR-RED) because that difference has a positive and large value much more so than would be obtained for the other land covers. Since the NIR domain is invisible to the human eye, the higher reflectance in the green band (Figure 2.7) causes us to see vegetation as green.

The low reflectance and transmittance in the visible range is caused by the strong absorption of chlorophyll pigment. Absorbing effects are less strong in the near infra-red (0.7 -1.30 μm) but reflectance and transmittance are higher. Type of pigment, leaf water content, cell-structure, thickness of the leaves and their orientation in the sun-sensor path influence the details of the spectral signature.

The state of development of plants and trees through the seasons and within the season as a function of rainfall and temperature is, of course, a source of variation in the development of vegetation and thus of the reflectance characteristics. To complicate matters, the soil background influences reflectance when the canopies do not fully cover the ground.

The difference in reflection (expressed by DN's) of the NIR and RED bands is much greater for green vegetation than the difference for bare soils, outcrops water, dried out vegetation, and so on.

An image containing pixel values of the difference is termed a vegetation index image. The 'Normalized Difference Vegetation Index (NDVI)' is widely used, where normalization is given by dividing the difference by the sum, in order to bring the range of NDVI values to -1 and 1.

$$NDVI = (NIR - Red) / (NIR + Red)$$

Pixels with lush vegetation on a NDVI image will appear as whitish tones (if such tones are assigned to high values, as is customary) and pixels with no or poor vegetation in dark grey to black tones.

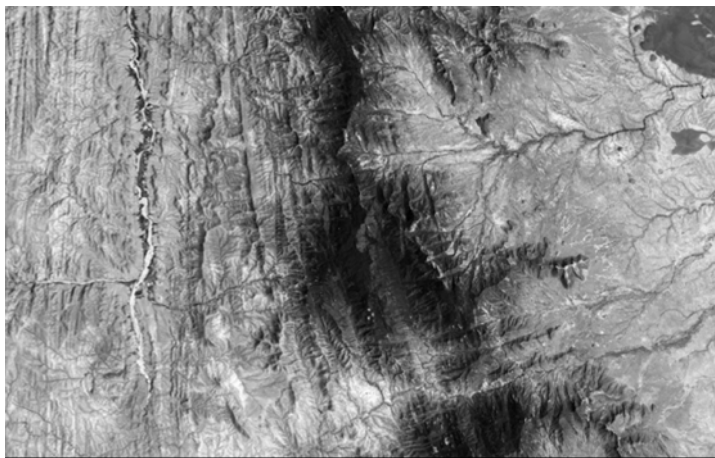


Figure 2-21a

Use of NDVI image for detecting fractures with groundwater

Samburu, N. Kenya

Landsat TM band 5

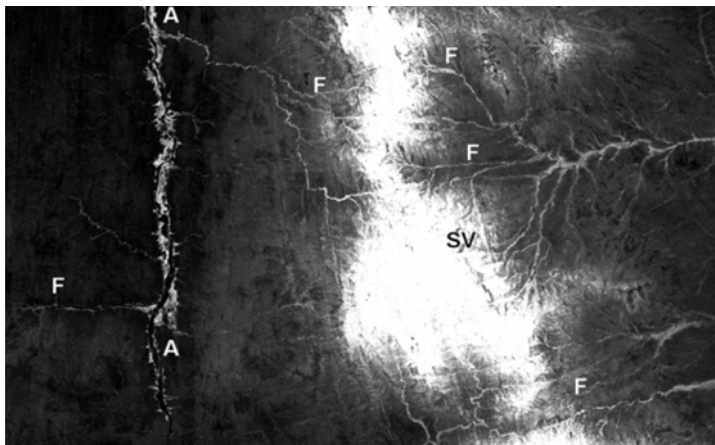


Figure 2-21b

NDVI

F = fracture with vegetation

A = alluvium

SV = strike valley



Figure 2-21c

Lineaments, interpreted from band 5 image

Often colour coding is used to split up the DNs of a single NDVI (or other) image by slicing (see earlier section). Usually, dark to light blue colours are assigned to low NDVI values, green colours to the middle values, and red shades to the high values. Such images look attractive, but have the disadvantage that gradual transition and patterns may not be apparent.

NDVI values are sensitive for the range of poor vegetation cover to just a full cover. If expressed in terms of the Leaf Area Index (LAI, the proportion of total leave area per surface unit), the NDVI is sensitive for LAI, up to LAI values of about 3. For LAI values > 4 the NDVI does not change much as it is saturated.

Internal shadows of the canopy influence NDVI; for example, the NDVI of a tropical rainforest with its irregular canopy structure, and LAI of >15 can be less than that of a teak forest plantation with LAI <15, but having a more even canopy surface.

The use of an NDVI transform for detecting groundwater bearing fractures and faults, due to vegetation response, is shown in Figure 2.21a c. The area shown is located in Samburu district, northern Kenya. The geology consists of basement rocks (gneiss is dominant), except in the extreme north-eastern corner where the basement rocks are covered by flood basalt. In the eroded western part with strike ridges and valleys, limited vegetation response is noted in only two fractures, because of poor recharge, due to low rainfall (450 mm) and fast runoff. In the high hills in the central part rainfall (some 1,000–1,200 mm, as estimated on ecological grounds) exceeds evapotranspiration for a period of about two months, and in combination with presence of thicker soils, leads to recharge and downhill flow of groundwater in the fractures. Some are indicated on the NDVI image. Vegetation in association with alluvium along rivers is due to recharge by episodic overbank flow and riverbed infiltration.

### Practical note

The DNs of the original bands of optical RS data fit within the range of 0–256 or ‘image domain’, required for display. The DNs of transformed images, such as NDVI, created by using map calculation functions, may have values beyond this range and can have negative values. Some IP software requires that these be brought into the range of the image domain by simple mathematical functions (multiplication, addition) for display.

### 2.9.3 Comparing NDVI images of different dates

The NDVI values are relative, therefore the numerical values cannot be used for determining differences in vegetation density of NDVI images of different dates. The latter is only possible after atmospheric and radiometric corrections of the original images.

Since the relation between NDVI and percentage of vegetation in a pixel is not linear, Valor and Caselles (1996) proposed the *percentage of vegetation cover map (or P<sub>v</sub> index)* which accounts for the non-linearity between NDVI and LAI and is particularly useful when percentages of bare soil or water and vegetation canopies change in time. According to the authors, the calculation of vegetation proportion P<sub>v</sub> is as follows:

$$P_v(\%) = \frac{(1 - \frac{NDVI}{NDVI_s})}{(1 - \frac{NDVI}{NDVI_s}) - K \cdot (1 - \frac{NDVI}{NDVI_v})} * 100 ,$$

$$\text{with, } K = \frac{NIR_v - R_v}{NIR_s - R_s} ,$$

where  $NDVI_v$  is the maximum NDVI value for pure vegetation and  $NDVI_s$  is the minimum NDVI value for pure bare soil in the NDVI reference image;  $NIR_v$  is the fully-vegetated pixel reflectivity in the near infrared;  $NIR_s$  is the bare soil pixel reflectivity in the near infrared;  $R_v$  is the fully-vegetated pixel reflectivity in the red; and  $R_s$  is the bare soil pixel reflectivity in the red.

In the chapter on Alluvial Terrain, an application is given of the P<sub>v</sub> index for a temporal series of satellite images in a study on water logging and salinization due to groundwater rise.

### 2.9.4 Other Vegetation Indices

Other vegetation indices have been used in groundwater vegetation studies, such as Soil Adjusted Vegetation Index (SAVI) and the Modified Soil Adjusted Vegetation Index (MSAVI).

The formulation for SAVI is:

$$\text{SAVI} = [(1 + L) (\text{NIR} - \text{RED})] / (\text{NIR} + \text{Red} + L).$$

L is a coefficient, usually taken as 0.5. By adjusting the coefficient the effect of soil influences within the measured spectra can be minimized and sensitivity to spatial changes in vegetation is enhanced. Without changes in (L) there is no difference in patterns of NDVI and SAVI. Like NDVI, SAVI saturates for LAI value of about >3.

Also used in phreatophyte studies is the Modified Soil Adjusted Vegetation Index (MSAVI):

$$\text{MSAVI} = [a(\text{NIR} - a\text{RED} - b)] / (\text{NIR} + R + L),$$

Where,  $L = 1 - 2a\text{NDVI}$ .  $\text{WDVI} = \text{NIR} - a\text{RED}$ , where  $a = \text{NIR}_{\text{soil}} / \text{Red}_{\text{soil}}$ . Coefficients (a) and (b) can be taken as variable, but in generic form MSAVI can be expressed as:

$$\text{MSAVI} = 0.5 [2\text{NIR} + 1 - \{(2\text{NIR} + 1)^2 - 8(\text{NIR} - \text{RED})\}^{0.5}]$$

A vegetation index that is related to water content in the canopy is the Normalized Difference Water Index, NDWI (Gao, 1996). The index in general form is as follows:

$$\text{NDWI} = (R_{\text{NIR}} - R_{\text{SWIR}}) / (R_{\text{NIR}} + R_{\text{SWIR}})$$

where  $R_{\text{SWIR}}$  is the reflectance or radiance in a short wave infrared wavelength channel (1.2–2.5  $\mu\text{m}$ ). For Landsat TM/ETM+,  $R_{\text{NIR}}$  and  $R_{\text{SWIR}}$  correspond to bands 4 (0.78–0.90  $\mu\text{m}$ ) and 5 (1.55–1.75  $\mu\text{m}$ ), respectively. Moderate Resolution Imaging Sensor (MODIS) on NASA's Terra and Aqua satellites now make such data routinely available.

A similar index was tested by Cettacco et al. (2001) from the SPOT vegetation sensor. They concluded that the SWIR channel was critical to estimating VWC and that the NIR channel was needed to account for variation of leaf internal structure and dry matter content variations. They and many others have also concluded that indices contrasting the SWIR channel with the NIR channel were sensitive to the mass or volume of water and not to the fractional percentage of water. NDWI is sensitive to changes in liquid water content of vegetation canopies. Atmospheric aerosol scattering effects in the 0.86–1.24  $\mu\text{m}$  region are weak. NDWI is less sensitive to atmospheric effects than NDVI. NDWI does not remove completely the background soil reflectance effects, similar to NDVI. Because the information about vegetation canopies contained in the 1.24  $\mu\text{m}$  channel is very different from that contained in the red channel near 0.66  $\mu\text{m}$ , NDWI should be considered as an independent vegetation index. It is complementary to, not a substitute for NDVI (Bindlish et al., 2006).

## 2.10 Multi-spectral classification

The objective of multi-spectral classification is to classify automatically land cover types or vegetation types by using the spectral data of several bands.

### 2.10.1 Applications

Applications for hydrogeologic studies are:

- Groundwater balance studies requiring an estimate of the irrigation draft. By using sequential images the development of the total area irrigated by groundwater over an aquifer may be related to the overall behaviour of the groundwater level in the aquifer. Estimates of water use by irrigated crops, which is the net use of

groundwater, can be made by first classifying the acreage under different crops and followed by assigning consumptive use values to each crop.

- As discussed in Chapter 14 (section on vegetation), groundwater uptake by trees has been quantified by classification of phreatophyte associations and measurement of evapotranspiration of each association. Certain tree species are indicators of groundwater and evidence has emerged that certain savannah tree species have very deep roots (over 40 m b.g.l.). In order to study the uptake of water from the vadose and saturated zone, tree species have to be identified using classification methods.
- Spectral classification may be used to extract certain types of land cover or features that are of interest to the hydrogeology, such as water logged areas indicative of (seasonally) shallow groundwater tables, river beds with important transmission losses, and so on. Multi-spectral classification of lithology may be successful in arid terrain. Soil and vegetation covers in non-arid terrain usually give rise to confusion.

### 2.10.2 Simple classification

The simplest type of classification is density slicing, discussed above. The near infrared band (NIR) could be used to determine the acreage of (groundwater) irrigated lands in a dry environment, because green crops will have high DN<sub>s</sub> (reflection), whereas the bare land or poor rangeland vegetation surrounding the irrigated fields will have low DN<sub>s</sub>.

The NDVI image could be used instead of the NIR band. Images of the thermal band(s) could also be used because by evapotranspiration irrigated fields have lower temperatures than the surrounding dry areas, but the spatial resolution of the thermal band is lower than that of the other bands.

Noting the number of pixels in the slice corresponding to irrigated lands and multiplication of that number with the squared value of the resolution will give the estimate of the irrigated land in m<sup>2</sup>. However, because of presence of mixed pixels (partly irrigated) this estimate may be refined, particularly when irrigated fields are small.

To account for the contribution of the mixed pixels the following may be done. First an upper threshold ( $T_h$ , Figure 2.22, which shows the histogram in accumulated form) of the NDVI is assessed that corresponds to pixels fully covered by irrigated crops, based on field observation. After that a lower threshold ( $T_l$ ) is estimated. Pixels with NDVI values less than that threshold are considered not to be irrigated and NDVI responses are thought to be due to various soil reflectance, bushes, weeds, and so on. The pixels between the two thresholds  $T_l$  and  $T_h$  represent pixels with partial irrigation and the interval has been divided into three classes, 1, 2 and 3, see Figure 2.22.

It can be assumed that in classes 1, 2 and 3, respectively  $1/3^{rd}$ ,  $1/2$  and  $2/3^{rd}$  of the pixel size is covered by green crops, and for  $NDVI > T_h$  all pixels are assumed to consist of green crops. The corresponding increments in each class, shown in percentages, can be converted into number of pixels and the acreage in each class can be calculated and thereafter the total acreage.

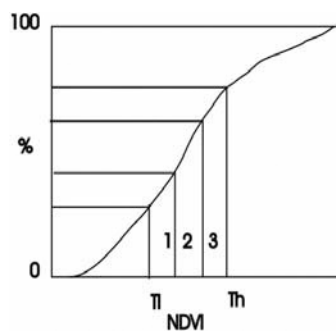


Figure 2-22

Cumulative histogram of NDVI image and three categories of mixed pixels irrigated crops/bare or fallow soil, for determination of total irrigated acreage.

The above method was applied to the Sana'a Basin (Yemen) for a groundwater study, where it was difficult to obtain the irrigated area by conventional surveys or by using census data.

The increase of the area irrigated, and thus indirectly the groundwater use, was estimated by using historical Landsat TM data and is shown in Table 2.5. The contents of that table also show the variation within a year, partly due to the dynamics of the irrigated crops, but also due to inaccuracy because of assumptions made.

<i>Date</i>	<i>Irrigated area (ha)</i>
09-03-1985	9,700
12-05-1985	11,900
06-10-1989	14,700
12-10-1994	23,200
16-01-1995	17,100
24-05-1995	26,800
01-06-1998	27,400
26-03-2000	18,400
13-05-2000	23,400
12-10-2000	27,800

Table 2-5

**Area irrigated by groundwater of Sana'a Basin, Yemen, estimated using NDVI transforms of Landsat TM images.**

**Note variation within a single year, but also the overall expansion, which is associated with lowering of the groundwater table in the basin.**

### 2.10.3 Supervised classification

Also discussed here is the so-called 'supervised classification', which means that the automatic classification of land cover is based on a sample set containing groundtruth. By land cover is meant any surface, bare soil, rock outcrops, water, vegetated areas, water, etc.

'Unsupervised' spectral classifications are also used with the aid of clustering algorithms, which group pixels that have similarity in spectral values at different hierarchical levels. The result is less variation in the image, but no clue to the identity of the objects is obtained.

First the 'training sets' are discussed and the judgement of how well classification can be done, based on inspection of the sets in scatter plots. A poor sample set always results in a poor classification, and therefore time spent on a good sample set is time well spent, but the effort should not be underestimated.

Of the many classification methods, two widely-used algorithms are discussed here.

#### *Training set*

A sample set or 'training set' is taken by selecting pixels that are known to consist of the vegetation types or rock-soil types of hydrogeologic interest. One could think of obtaining sample pixels from such classes as:

- 'irrigated areas (by groundwater)'
- 'gallery forest' or 'phreatophytes' (indicating presence of groundwater), or classes such as 'grassy Dambo areas' (which have at least seasonal shallow groundwater levels)
- areas with rapid runoff and thus no or little infiltration and recharge, such as 'rock outcrops', 'bare soils'
- 'crops irrigated by groundwater', and so on.

It should be remembered that the image data pertains only to spectral data and hopefully, spectral classes correspond to desired land cover classes. It should be noted here that classification based on training sets is only valid for the particular scene and for a limited eco-system and cannot be applied to very large regions, which may contain different eco-systems.

#### *Feature space*

The spectral properties of the sample set are examined in a '*feature space*'. This is a scatter plot of the DNs of the sample pixels of selected classes in a diagram using the horizontal axis for one spectral band and the vertical axis for another. The value in (e.g.) two bands can be regarded as the components of a two-dimensional vector: the feature vector.

When the feature vectors of ground objects of interest (e.g. irrigated fields, water bodies, large outcrops, etc.) are sampled, the sample pixels tend to form a *cluster* in feature space, as is illustrated in Figure 2.23, whereby it can be noted that the clusters corresponding to the classes are well defined and well separated from each other. Note that the spectral variation in a land cover class or cluster can differ from one class to another. In general, the class 'water' can be well clustered if the water has no suspended matter and no floating vegetation, but the class 'build-up area' is likely to be spread out in the feature space because of presence of rooftops, yards with soil, parks,

etc. Similarly, orchards without closed canopies show much variation because of mixed pixels – green leaves and soil – and variations in bare soil and weed cover.

The feature spaces also show visually the degree of correlation of the spectral bands; if the sample sets plot in an elongated narrow zone, the bands are correlated; if the sample pixels spread out over the diagram, there is less or no correlation, similar to regression analysis. In the latter case, the spectral classification is likely to be more accurate, but much depends on how well the sample pixels of a given class cluster or group together at separate positions in the feature space and the degree of overlap of the clusters in the various feature spaces formed by various combinations of spectral bands. Only if the clusters are well separated – usually valid for only a few classes will the classification be accurate.

Inspection of the feature spaces using the non-correlated PC-1, PC-2 and PC-3 images is an efficient a-priori way of judging the classification result from how well clusters corresponding to each sampled class are separated spectrally.

To obtain a good sample set, it is essential to use field data. The fact that many land cover classes other than the ones of hydrogeologic interest have to be included should also not be overlooked.

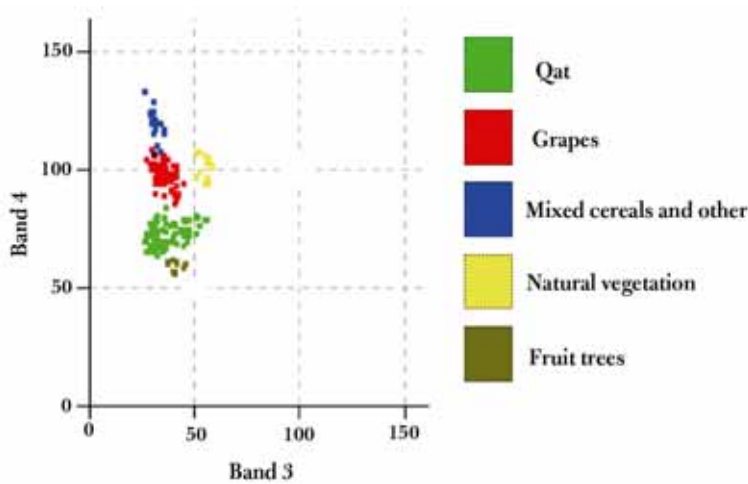


Figure 2-23

Feature space showing 5 clusters.

In this example, from Sana'a Basin, Yemen, clusters generally had no or little overlap on bands 3 and 4 of Landsat TM.

For example, Figure 2.24 shows a feature space with the DN's of all pixels in an image and the position of 5 clusters representing certain classes of hydrogeologic interest. They describe the entire data space only partially, and thus in the classification there will remain many 'unknowns' and the classification result is likely to grossly overestimate the desired classes.

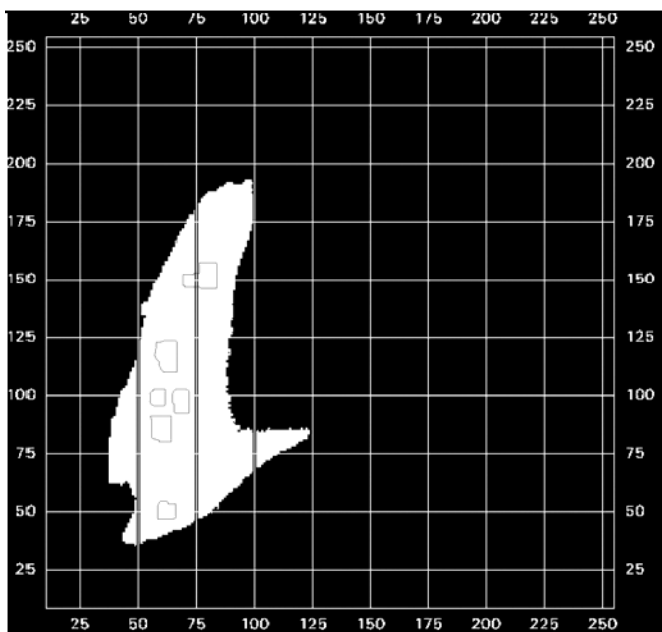


Figure 2-24

Feature space showing all pixel values in two bands and six clusters, which do not cover the full range of the data set



As has been said, usually many clusters show overlap in all feature spaces (i.e. all bands) and there is not much one can do, except using multi-temporal images, preferably of different seasons during a year and knowledge of the vegetation developments in the area of study to differentiate classes. First, the images of different dates must be accurately registered to each other (georeferenced or geocoded, see below), with deviations of less than 1 pixel. The sample pixels with their coordinates can then be used for all images. The multi-temporal images can be considered as one set and a PC analysis may be done, resulting in a new set of PCs that can be used to inspect the feature spaces. If clusters now have less overlap, the classification could be done.

It is customary to keep a sample set with groundtruth apart from the one used for classification in order to assess the accuracy of the classification.

### *Splitting and merging of spectral classes*

It may be necessary to split spectral classes in order to obtain proper clusters. For example, lakes are termed by some as ‘groundwater outcrops’, and it may be of interest to study the dynamics of the expansion of the water body. If a part of the water body consists of clear water, a part has suspended sediment or algae and another part has marsh vegetation (e.g. papyrus) or floating vegetation (e.g. water hyacinth), it makes sense to create separate classes for each of the cases, because their spectral properties are different from each other. After classification the classes can be merged into one class: ‘water’.

Similarly, a class ‘alluvial area’ should be avoided, although such areas are of direct hydrogeologic interest, in the first classification because mixed land use and vegetation may occur on alluvial areas. As in the case with some ‘water bodies’, subclasses in the alluvial areas may be made and if there is no confusion with classes in the non-alluvial areas, the subclasses can be merged finally into the class ‘alluvial areas’. Incidentally, it may be easier and more accurate to make a visual interpretation of the alluvial areas and superimpose that on the automatic classification results.

It is evident that one has to have local hydrogeologic knowledge to make the right choice, or in other words groundtruth, which can be gathered by traversing the area and noting precisely the position (i.e. pixels) and type of land cover. This task is now facilitated using GPS and geo-referenced imagery.

## **2.10.4 Supervised classification algorithms**

When a sample set is used, the classification is termed to be ‘supervised’. Essentially, a classifier examines the DN<sub>s</sub> of each and every pixel of all bands of an image and compares them with the values of the clusters of the sample set, whereafter a decision is made as to what cluster a pixel value is most likely to belong. Two major classifiers will be briefly discussed here.

Before applying a classification algorithm, make sure that the number of pixels per cluster is sufficient, a rule of thumb is  $30 \times n$  ( $n$  is number of bands). Furthermore, clusters should not overlap each substantially. If so, (1) merge classes, by expansion of the description, or (2) make spectral sub-samples and merge them after applying the classification algorithm.

### *Minimum distance to the mean (MDM) algorithm*

This classifier (also appearing under different names) uses the cluster centres and determines how far – on the feature spaces or Euclidean distances on all bands – a pixel value is from that centre, whereby the position of the other cluster centres is considered, as illustrated in Figure 2.25. The unknown pixel is assigned to that class to which is distance to the mean DN value of that class (or cluster) is least.

One of the flaws of the MDM classifier is that pixels far away from a centre of a cluster may be assigned to that cluster, as is illustrated in Figure 2.25. Therefore, a threshold value can be defined to limit the search distance, leaving pixels with much deviating values as ‘unknown’.

Setting a low threshold results in many unclassified pixels but in a more accurate result, and vice-versa.

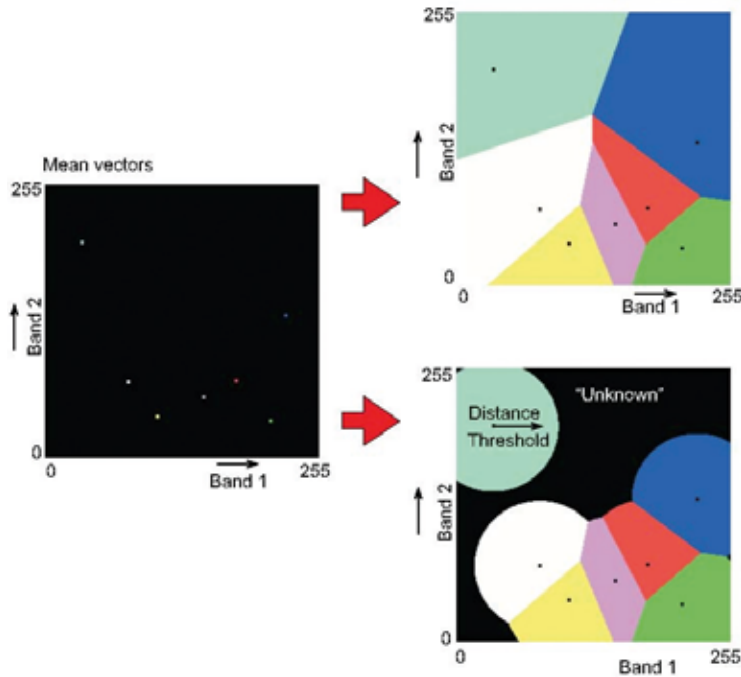


Figure 2-25

Principle of minimum distance to mean classification in a two-dimensional situation

Upper right:

The decision boundaries are shown for a situation without threshold distance

Lower right:

Decision boundaries with threshold distance

Source: Janssen and Gorte, 2004

### Maximum Likelihood (ML) classifier

This classifier considers not only the cluster centres but also the shape, size and orientation of the clusters, which is achieved by calculating a statistical distance based on mean values and the covariance matrix of the clusters. The statistical distance expresses a probability value: an unknown pixel is assigned to a cluster to which it has the highest probability. The threshold distance is illustrated in Figure 2.26.

The assumption of many ML classifiers is that the statistics of the clusters all have a normal distribution. So-called equiprobability contours are drawn around the centre of each cluster and this allows the operator to specify

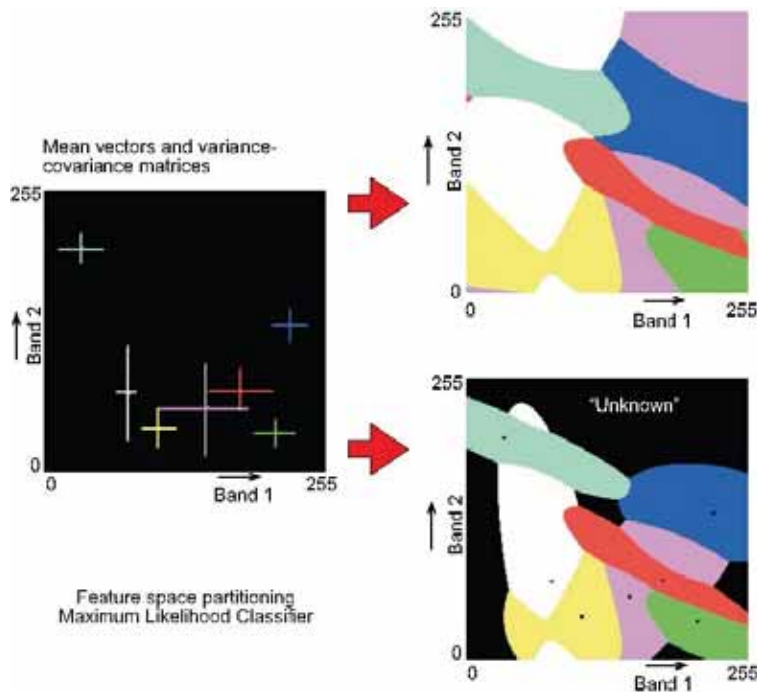


Figure 2-26

Principle of the maximum likelihood classification.

Upper right:

The decision boundaries are shown for a situation without threshold distance

Lower right:

Decision boundaries with threshold distance

Source: Janssen and Gorte, 2004

a threshold distance by defining a maximum probability value. By choosing a small threshold value, a small ellipse centred on the mean defines the values with the highest probability of membership of a class.

### *Classification accuracy*

It is customary to assess the accuracy of a multi-spectral classification by setting up a table or error matrix (also known as contingency matrix or confusion matrix) showing the number of pixels that are correctly classified and those that are not. A substantial sample set, kept apart for the accuracy assessment must be available.

## 2.11 Stereo satellite images

Stereo satellite images can be obtained from systems which use either along-track images or across-track images for off-nadir viewing and the stereopair could consist of (1) a vertical (nadir) image and an image looking forward or backward or (2) a vertical image and an across track image.

The satellite systems listed in the appendix gives further details of current stereo capability. The overlap area of adjacent satellite tracks can be seen in stereo as well.

The principle of relief displacement (parallax) for obtaining a three-dimensional view of the terrain (see section on aerial photographs) applies, which means that the height resolution is at best equal to the spatial resolution (pixel size). The worldwide DEM produced by the Shuttle Radar Topographic Mission (SRTM) uses a different principle for measuring heights, as mentioned in the chapter on Radar Images. The chapter on Metric Aspects (Chapter 3) discusses the correction for relief displacement and the creation of DEMs.

## 2.12 Image Combination or Fusion

To display three spectral bands of the same scene in a false colour composite is of course a form of image combination, but one can also add a resolution image to the composite, as a form of enhancement by providing more detail to the image.

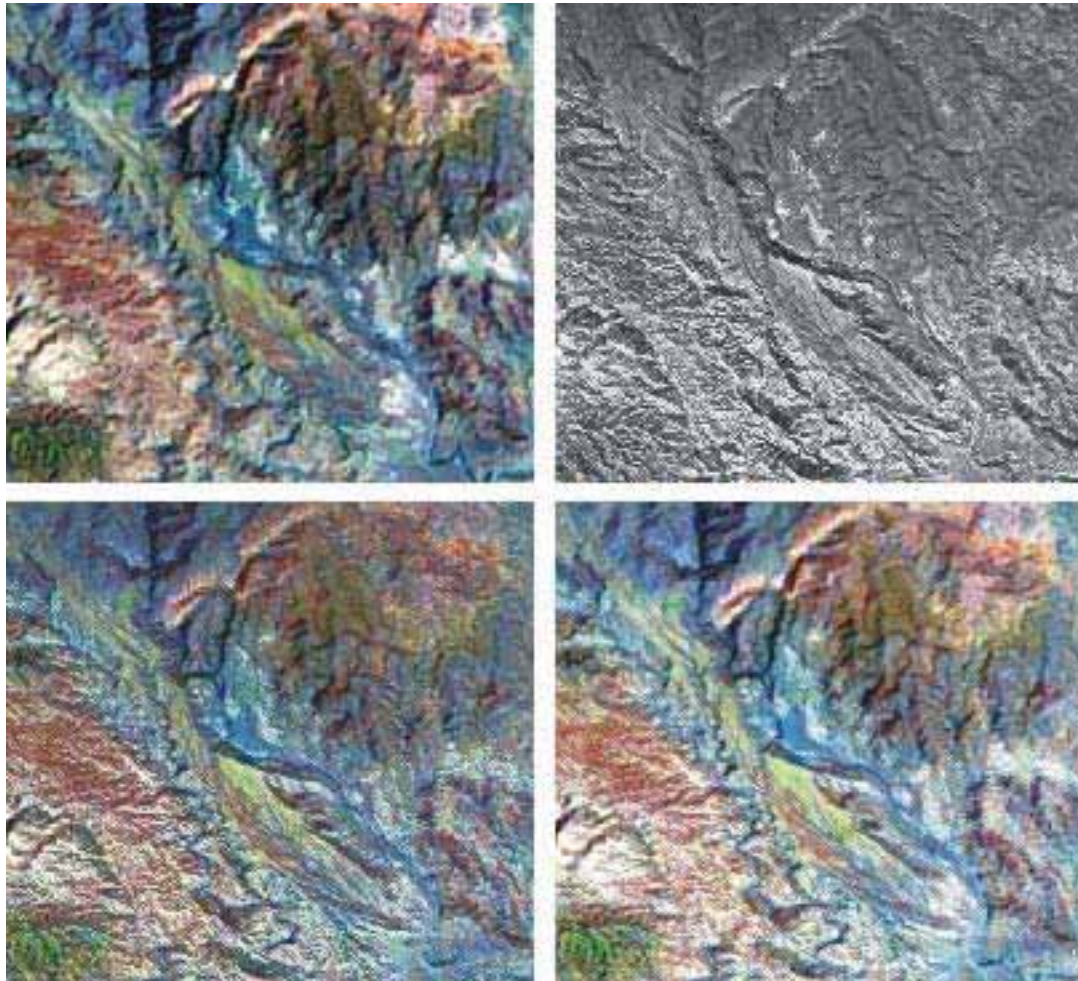
Also discussed here is the combination of three spectral images (e.g. Landsat TM, 30 m resolution) with images of higher resolution, such as an aerial orthophotograph in digital format, or Landsat TM band 8 (15 m), the Panchromatic bands of SPOT (5 m) and IRS-1C (5.8 m), or the very high resolution IKONOS (2 m) and others.

First, the images have to have the same pixel size; usually that of the highest resolution image is taken (e.g. 5 m pixel size). Second, all images have to have the same planimetric system (see geocoding discussed in a section below). To achieve both requirements, the images have to be re-sampled. Geocoding accuracy has to have accuracy at the sub-pixel level, otherwise artefacts are introduced and the image looks blurred.

Nothing really is gained by resampling a 30 m resolution spectral band into a 5 m resolution because the pixels are simply split up into 36 equal small pixels having the same spectral properties as the original pixel, but then the 5 m resolution image can be added.

It should be remembered that there are only three colour spaces available, Red, Green and Blue. The simplest way is to use two of them for the spectral bands that had originally 30 m resolution and use the remaining colour space for the high resolution image. Often the Hue and Saturation image of the HIS scheme is used for two of the images for the false colour composite and the Intensity image is the high resolution image. Figure 2.27 shows the result of this operation; Figure 2.27a is a false colour composite of LANDSAT-7 ETM of bands 7, 3 and 1, while Figure 2.27b is a mosaic of fully rectified aerial photographs (orthophotos, see below), resampled to a 5 m resolution.

The disadvantage of the method leading to Figure 2.27c is that the information of the original false colour composite cannot be retained. This is the case in the colour composite of Figure 2.27d, which contains a weighted average of the intensity information of the original false colour composite and the photo-mosaic.



**Figure 2-27** Image fusion illustrated. Upper left (a): RGB colour composite of Landsat ETM, bands 7, 3, 1. Upper right (b): orthophoto mosaic, resampled to 5 m. Lower left (c): Fused image of ETM bands, its intensity substituted with the photo mosaic using RGB-HIS colour space transformations. Lower right (d): As previous, but adding back 50% of the original intensity of TM bands.  
Source: Gorte and Schetselaar, 2004.

Here we discuss how four images can be combined in three colour spaces. As explained in an earlier section, a pan chromatic image can be considered as an intensity image ( $I'$ ). A simple algebraic operation for intensity substitution to make a fused image in the RGB space (the *Brovey transform*) is:

$$R' = \frac{R}{I} I', \quad G' = \frac{G}{I} I' \quad \text{and} \quad B' = \frac{B}{I} I' \quad \text{with} \quad I = \frac{1}{\sqrt{3}} (R + G + B)$$

where R, G and B are the contrast stretched bands (e.g. TM band 7, 4 and 2) and  $I'$ , as mentioned, is the pan chromatic image.

An alternative method for image fusion (the additive pixel method) is given in the chapter on Radar Images.

## 2.13 Final remarks

The above contains – in our view – the essential methods or tools for handling digital satellite images, which enables the hydrogeologist to prepare products for data extraction and preparation of fieldwork. After introducing some basics of digital images and image enhancements for visual interpretation, filtering methods are explained and illustrated, with particular reference to lineaments and faults, which are of importance in hydrogeologic studies.

Information derived from multi-spectral data for water budget studies and aspects of groundwater management makes use of multi-spectral classification and vegetation indices, including some methods that enable the comparison of images in time series.

As the experience in handling digital images grows, the need may be felt to expand ones knowledge of image processing techniques, for which we refer to some well known textbooks (by no means exhaustive) listed below, but also to the user manuals or field guides of image processing systems used.

General textbooks:

- General background remote sensing, digital image processing and interpretation: Lilles et al. (2004), Jensen (1996), Kerle et al (eds), 2004.
- Image interpretation in Earth science: Way (1973), Verstappen (1979), Ray (1980), Sabins (1996), Drury (2001), Gupta (2003).
- Introductions to digital image processing: Harrison and Jupp (1990), Richards (1993), Schowengert (1997), Mather (1999) and Liang Shunlin (2004) for advanced methods.

An overview of current remote sensing systems mentioned in this book is given in the Appendix, with websites added.

## References

- Ayenew, T. 2003. Environmental isotope-based integrated hydrogeological study of some Ethiopian rift lakes. *Journal of Radioanalytical and Nuclear Chemistry*, Vol. 25 (1), pp. 11–16.
- Belward, A.S. 1991. Spectral characteristics of vegetation, soil and water in the visible, near infrared and middle-infrared wavelengths. A.S. Belward and C.R. Valenzuela (eds). *Remote Sensing Applications and GIS for Resources Management in Developing Countries*, Kluwer Acad. Publ. Eurocourses, pp. 31–45.
- Bindlish, R., Jackson, T.J., Gasiewski, A.J., Klein, M. and Njoku, E.G. 2006. *Remote Sensing of the Environment*, Vol. 103 (2), pp. 127–39.
- Ceccato, P., Flasse, S., Tarantola, S., Jacquemond, S. and Gregoire, J. 2001. Detecting vegetation water content using reflectance in the optical domain. *Remote Sensing of Environment* 77, pp. 22–33.
- Drury, S.A. 2001. *Image interpretation in geology* (3rd edn), Nelson Thornes, Blackwell Science, Cheltenham.
- Gao, B. 1996. NDWI—a normalized difference water index for remote sensing of vegetation liquid water from space. *Remote Sensing of Environment* 58, pp. 257–66.
- Gorte, B.G.H and Schetselaar, E.M. Image enhancement and visualisation. *Principles of Remote Sensing*, ITC Educational Textbook Series, pp. 159–67.
- Gupta, R.P. 2003. *Remote Sensing Geology*. Springer Verlag, Berlin.
- Harrison, B.A. and Jupp, D.L.B. 1990. *Introduction to Image Processing*. CSIRO, Australia.
- Hill, J and Sturm, B. 1991. Radiometric corrections of multi-temporal Thematic Mapper data for use in land cover classification and vegetation monitoring. *International Journal of Remote Sensing*, Vol.12 (7), pp. 1471–91.
- Horn, J.A. and Grabmaier, K.A. 2004. Aerial cameras. N. Kerle, L.L.F Janssen and G.C. Huurneman (eds) *Principles of Remote Sensing, An introductory textbook*, ITC, The Netherlands, pp. 61–74.
- Inzana, J., Kusky, T., Higgs, G. and Tucker, R. 2003. Supervised classifications of Landsat TM band ratio images and Landsat TM band ratio image with radar for geological interpretations of central Madagascar. *Journal of African Earth Sciences*, Vol. 37 (1–2), pp. 59–72
- Janssen, L.L.F. and Gorte, B.G.H. 2004. Digital image classification. N. Kerle, L.L.F Janssen and G.C. Huurneman (eds) *Principles of Remote Sensing: An introductory textbook*, ITC, The Netherlands, pp. 193–206.
- Janssen, L.L.F., Weir, M.J.C., Grabmaier, K.A. and Kerle, N. 2004. Geometric aspects. N. Kerle, L.L.F Janssen and G.C. Huurneman (eds) *Principles of Remote Sensing: An introductory textbook*, ITC, The Netherlands, pp 143–58.
- Jensen, J.R.. 1996. *Introduction to digital image processing*. Prentice Hall Series, New York, pp 162–65
- Karnieli, A.A., Meisels, A., Fisher, L. and Arkin, Y. 1996. Automatic extraction and evaluation of geological linear features from digital remote sensing data using a Hough Transform. *Photogrammetric Engineering and Remote Sensing*, 62, pp. 525–31.

- Kerle, N., Janssen, L.L.F. and Huurneman, G.C. (eds) *Principles of Remote Sensing: An introductory textbook*, ITC, The Netherlands.
- Liang Shunlin. 2004. *Quantitative remote sensing of land surfaces*. Wiley Interscience, John Wiley & Sons.
- Lilles, T.M., Kiefer, R.W. and Chapman, J.W. 2004. *Remote Sensing and Image Interpretation*. (5th edn), John Wiley & Sons Inc.
- Mather, P.M. 1999. *Computer Processing of Remotely Sensed Images: An Introduction* (2nd edn), John Wiley & Sons Inc.
- Parodi, G.A. and Prakash, A. 2004. Radiometric correction. N. Kerle, L.L.F. Janssen and G.C. Huurneman (eds) *Principles of Remote Sensing: An introductory textbook*, ITC, The Netherlands, pp. 143–58.
- Ray, R.G. 1965, 1980. *Aerial photographs in geologic interpretation and mapping*. Geol. Survey Prof. Paper 373. US Governm. Printing Office, Washington DC.
- Sabins, F.F. 1996. *Remote Sensing: Principles and Interpretation* (3rd edn). Freeman & Co, N.York.
- Richards, J.A. 1993. *Remote Sensing Digital Image Analysis: An Introduction* (2nd edn), Springer Verlag.
- Schott, J.R., Salvaggio, C. and Volchok, W.J. 1988. Radiometric scene normalization using pseudo-invariant features. *Remote Sensing of the Environment*, Vol. 26, pp. 1–16.
- Schowengerdt, R.A. 1997. *Remote Sensing, models and methods for image processing* (2nd edn) Acad. Press, San Diego, London.
- Valor, E. and Caselles, V. 1996. Mapping land surface emissivity from NDVI: Application to European, African and South American areas. *Remote Sensing of Environment*, 57 (3), pp 167–84.
- Verstappen, H. 1977. *Remote Sensing in Geomorphology*. Elsevier Sci. Publ. Co.
- Way, D.S. 1973. *Terrain Analysis: A guide to site selection using aerial photographic interpretation*, Hutchinson & Ross Dowden.

# Geometric aspects, use of digital elevation models, GIS

## 3.1 Introduction

A hydrogeological study of a given area preferably uses images of different nature and dates. It can therefore be advantageous to combine images and use overlays of image interpretations with topographic and geologic maps. That data should be mutually compatible, that is, of the same map projection system. Furthermore, wells have geographic coordinates and it may be desirable to plot them on an image.

When acquiring images choices are offered as to metric formats. If not, the images should be transformed to the desired map projection system and Remote Sensing-GIS packages contain software to do that task. Therefore some working knowledge of these aspects is required.

In order to add relief to an image for 3D viewing and to perform proper geometric corrections in relief-rich terrain, a digital elevation model (DEM) is required. In this text, only an introduction is given. The general textbooks on remote sensing (see chapters on Image Processing, e.g. Lillesand et al. 2004) contain sections on geometric aspects, as do textbooks on GIS (e.g. Star and Estes, 1990; Meijerink et al., 1994; Longley et al., 1999; Georgiadou et al., 2004).

Section 3.6 on GIS application to groundwater studies is included because remotely sensed information is usually combined with other thematic data, including DEM derivatives (slope, depressions, drainage) in regional groundwater studies.

## 3.2 Digital elevation model

### 3.2.1 Structure, TIN or Raster

The structure of a DEM consists either of a Triangulated Irregular Network (TIN) or a raster structure. The concept of TINs describing the topography is illustrated in Figure 3.1.

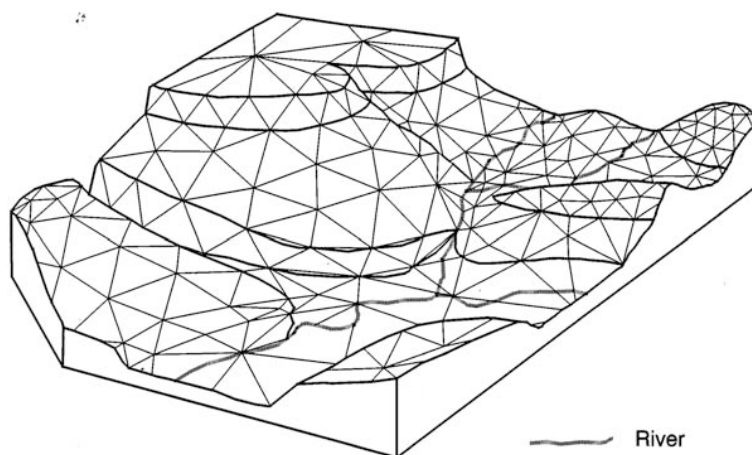


Figure 3-1

Block diagram showing  
representation of terrain by TINs

Each nodal point has stored coordinates ( $X, Y$ ) and elevation ( $Z$ ). The size and therefore the density of the TINs can be adjusted to the complexity of the terrain. TINs have the advantage of efficient data storage. Heights of terrain points within a TIN are obtained by interpolation. A DEM with a raster structure has a  $Z$  value for each pixel, of which  $X, Y$  values are implicitly known and thus has a structure that is compatible with a digital satellite image or digitized aerial photograph.

A DEM with a TIN structure can be interpolated to a regular structure, resulting in a raster DEM. Some groundwater models make use of TINs, others use a raster structure with constant or variable cell sizes.

### 3.2.2 Acquisition of a DEM

There are various ways to obtain a DEM:

- DEMs prepared by professional agencies may be purchased. The accuracy of such DEMs is generally known.
- Using a download of a Shuttle Radar Terrain Model (SRTM), discussed in Chapter 4, Radar Images. Planimetric visualization of the DEM contents can be achieved by way of contours, by shadow effect (the so-called hill-shading) or by both, using GIS functionalities.
- Before the availability of the SRTM data, DEMs were created starting with digitizing contours on a topographic map, followed by interpolation to obtain a DEM, usually in raster format. There are some problems using this method, such as low accuracy due to deformation of the paper of the topographic map – and contours are anyway cartographic generalizations. Interpolation across drainage divides or small valleys gives inaccuracies; relief features between two contours are ignored; pits or artificial steps may appear in gently sloping or flat terrain. Mitigation of some of the problems is possible, depending on the interpolation method used and by adding topographic information.
- Digital photogrammetry, developed for aerial photographs, can also be applied to stereo satellite images. SPOT, ASTER and IRS offer this possibility, while KOMSAT and AVNIR are less well-known systems. More recently, high-resolution push broom scanners provide stereo images that allow more accurate DEM generation than the first mentioned systems. The principle of relief displacement (parallax) for obtaining height information (see section on aerial photographs) applies. Software packages have been developed to create a DEM from a stereopair by automatically comparing the patterns formed by a group of pixels for their similarity. From those patterns that match on each image of the stereopair, the parallax shift is determined, from which the elevation is calculated. In cases where the algorithm mistakenly selects a group of pixels, so-called ‘blunders’ occur, which are apparent from steep ‘hills’ or depressions in the DEM. These have to be removed by the operator.

Since TERRA-ASTER images can be downloaded or acquired at low cost, the height accuracy of a DEM created from Aster images is mentioned here. Cuartero et al. (2004) investigated the accuracy of an ASTER DEM of



**Figure 3-2** DEM created from stereo aerial photographs, with visualization by way of contours and hill shading and automated determination of drainage lines. Note sinkholes in karst area at high elevation area in the central part of the image. Source: Maathuis (unpubl.).



complex terrain, using control points that could be identified on the image (often difficult) and their absolute height was measured with a differential GPS in the field. Results varied with the software used; the package of a widely used RS processing system had a root mean square error (RMSE) of 34.8 m with few blunders, while use of a specific package resulted in a (RMSE) of 12.6 m with some blunders. It should be noted that the latter accuracy is at sub-pixel level (15 m), although the DEM had 30 m resolution cells. As discussed in the chapter on Radar Images, the absolute height accuracy of SRTM DEM is 16 m and the relative accuracy is <10 m. Hirano et al. (2002) evaluated the accuracy of satellite-based DEMs (not SRTM) but used less accurate positioning of ground control points. They found RMSE ranging from 7 to 15 m for ASTER data.

DEMs from active radar systems, including the widely used SRTM data, are discussed in Chapter 4 (Radar Images). Various groundwater studies have made use of them (e.g. Leblanc et al., 2003; Münch and Conrad, 2007; Robinson et al., 2007).

High-resolution satellite systems operating in the stereo-optical domain (CARTOSAT of India, IKONOS, EARLY BIRD, EROS-A1, SPOT-5) and in the radar domain (Terra Sar) allow the production of DEMs with higher accuracy (about 2 m) than the widely used SRTM DEMs available today. It is not difficult to predict that DEMs with higher height resolution will be used for groundwater studies at local scale. The best height resolution, 10 to 30 cm after processing, is provided by airborne LIDAR surveys, but vegetation confounds the processing.

### 3.3 Map projections

The Earth is not a perfect sphere and in order to account for this deformation, various ellipsoids or spheroids have been proposed to approximate its shape. The result is that each National Survey Organization has adopted a particular best fitting ellipsoid. Thanks to advances in extraterrestrial positioning techniques the Geodetic Reference System 1980 (GRS80) ellipsoid could be realized and from that emerged the World Geodetic System (WGS84) datum. The two are identical for all practical purposes and have their origin in the centre of mass of the Earth.

The International Terrestrial Reference System (ITRS), a widely accepted spatial reference system, makes use of the centre of mass, the Z-axis points towards to the mean Earth North Pole, the X-axis is oriented to the Greenwich meridian and the Y-axis completes the right handed reference coordinate system. For practical purposes, the ITRS is identical to the WGS84.

At the national level, map projection systems have been adopted for topographic and geologic maps. A position of, for example, a borehole, is given in latitude–longitude (lat-long) coordinates and height above the national mean sea level datum.

Imagery and global GIS data are usually in formats that may not conform to the national map projection, and thus either one of them has to be transformed. Most GIS and RS processing systems have packages that can perform this task and provide background information and operation details.

A widely used worldwide standard for many satellite data is the Universal Transverse Mercator (UTM) projection, valid for areas between 84°N and 80°S, using the metric system and is based on the WGS84 ellipsoid. The Mercator projection is a conformal projection, meaning that angles and small shapes on the globe project with the same angles or shapes on the map.

#### *Longitude:*

The world is divided into 60 west to east zones of 6° of longitude in width. Zone I has its western edge on the 180° meridian (the International dateline); zone 60 therefore has its eastern edge on the same meridian. To find the grid zone for any longitude, treat west longitude as negative and east as positive; add 180°; divide by 6 and round up to the next higher number.

#### *Latitude:*

The original UTM system divided latitude zones with 8° intervals (except for high latitudes), with a letter-code, which is still in use with NATO maps and World aeronautical maps. The code starts for 80°S with *C* and ends with *X* at 84°N in alphabetical order. Letters *I* and *O* are omitted, the equator is the line between *N* and *M*.

In scientific work usually the letter-code is omitted and the reference in the direction of Y-axis is made in km distance from the origin.

For the northern hemisphere the origin is at the equator and is positive northwards. For the southern hemisphere the origin is shifted 10,000,000 m from the equator to near the South Pole and thus locations have positive values. Confusion must be avoided by indicating whether it is S (southern hemisphere) or N (northern hemisphere). Unfortunately the original letter-code also contains the letters N and S, therefore, one should take care as to what system is used.

Cartesian coordinates are used to specify locations. Each 6° longitudinal zone (1–60) has its own origin. The origin of the Y-axis is placed 500,000 m west of the central meridian of the zone, locating it in fact outside the zone because the maximum width of the zone – at the equator – is about 40,000/60 or 667 km wide. Therefore, the X coordinates of all locations are positive. The UTM grid (2 digits only) of a part of the world is shown in Figure 3.3 (for the full map, see [www.dmap.co.uk/utmworld.htm](http://www.dmap.co.uk/utmworld.htm) or other websites).

The convention is that by using 4 digits, the coordinates are given in km and by using 7 digits they are given in m (see Figure 3.4).

When the area of interest covers more than one zone the origin is placed in the westernmost zone to avoid negative coordinates. To maintain accuracy the area of interest within each zone has to be transformed to UTM coordinates, after which the transformed maps are merged.

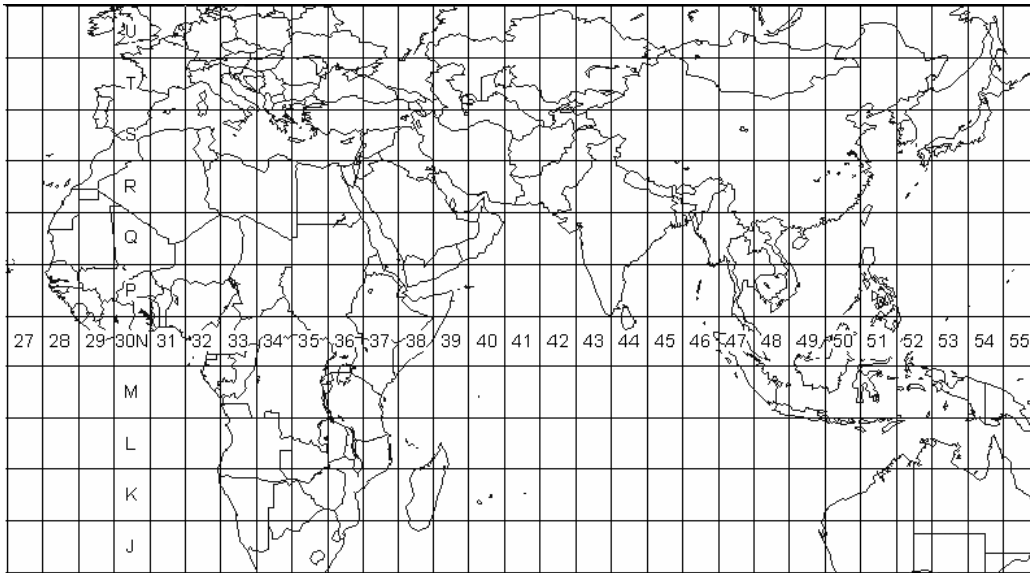


Figure 3-3 UTM grid for part of the world

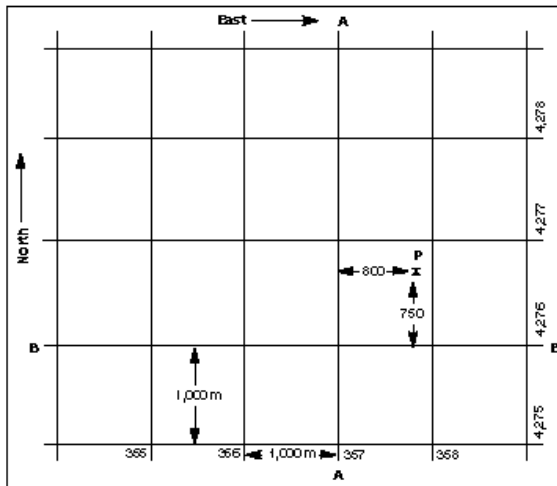


Figure 3-4

**Determining a UTM grid value for a map point**

The grid value of line A-A is 357,000 metres east. The grid value of line B-B is 4,276,000 metres north. Point P is 800 metres east and 750 metres north of the grid lines; therefore, the grid coordinates of point P are north 4,276,750 and east 357,800.

Source: USGS Fact sheet 077-01 (August 2001)

## 3.4 Two-dimensional transforms

### 3.4.1 Georeferencing

The various bands of a given image have the same geometric properties and are geometrically mutually compatible, but the image as such is generally not compatible with a given national projection system.

In order to match thematic map data of interest, such as contours, infrastructure, geologic boundaries, locations of wells and springs, etc. with the satellite image, the latter has to be 'georeferenced'. This means a geometric transformation has to be done to relate the coordinates of the image pixels (their central position) arranged in rows ( $r$ ) and columns ( $c$ ) to the map projection ( $x, y$  positions) in use. In case the satellite scene covers relatively flat terrain a simple affine transformation (first order or linear equation) will suffice.

The transformation equation is developed using a number of control points for which the  $r_i, c_i$  and corresponding  $x_i, y_i$  values have to be determined. Typical suitable control pixels are road crossings, confluence of small rivers, corners of large rectangular objects, etc. Because of the difficulty in finding suitable points and in determining the right positions of selected control pixels and to avail of points as a check, it is advised not to be parsimonious about the number of points.

After the first attempt at transformation, the error reported by the software should be checked. Usually the root mean square error (RMSE), comparable to standard deviation, is used and often expressed in terms of the pixel size. The RMSE should be less than 1 pixel in case of 20 or 30 m images. If not, another transformation method should be used or other ground control points selected. Higher order transformations require a number of ground control points that are equal or exceed the number of parameters indicated in Figure 3.5.

After transformation the map coordinates of each pixel are known, the original raster structure ( $r, c$ ) is not changed, but vector data (e.g. digitized data from a map) can now be superimposed.

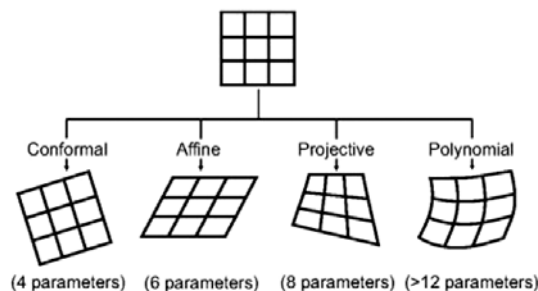


Figure 3-5

Type of transformations and the number of parameters required.

### 3.4.2 Geocoding

When images of different dates, scales or sensors have to be matched with each other and with a given map projection, a new row-column structure is required and this is achieved by so-called 'geocoding' (sometimes included in the term georeferencing).

This procedure consists of two steps:

- (1) Each new raster element or pixel is projected onto the original image or map coordinate system. For the projection/transformation higher order equations may be required to obtain desired accuracy.
- (2) A DN value for the pixel at the new position is determined, this is known as *resampling*, and three options are open; (a) a nearest neighbour algorithm that assigns the original DN value to the new pixel being closest to the original one (Figure 3.6a). If the pixel size remains the same and spectral classification is intended, this is the best good option; (b) bi-linear convolution calculates the weighted mean of the DNs of the four neighbouring pixels of the original image and assigns that value to the new pixel (Figure 3.6b); and (c) cubic convolution that applies a polynomial function based on the DNs of the 16 surrounding pixels. The latter two methods result in a smoother image, but the original spectral values are changed. Resampling is required when the pixel size has to be changed, for example to merge images of different spatial resolution.

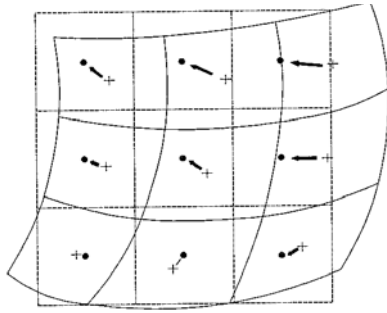


Figure 3-6a Resampling: Nearest Neighbour. Dots indicate the original value, small crosses the values used for transformed image

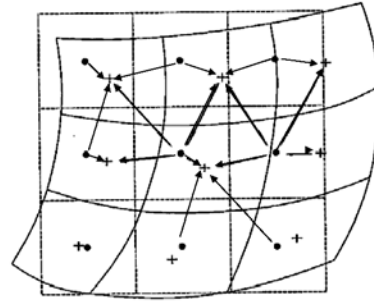


Figure 3-6b Resampling: Bi-linear. Values for transformed image are based on 4 pixel values of the original image

### 3.5 Three-dimensional transforms

#### 3.5.1 Transfer of data

When relief displacements cause positional error, which is too large to be ignored, the height dimension has to be added to the transformation. 2D transforms are adequate for most current optical RS images (Landsat, SPOT, IRS, etc.) of non-mountainous terrain, because the ratio of orbit height to terrain height is very large.

However, the transfer of information from aerial photographs (APs) to maps is not straightforward because of relief displacement and scale differences within an AP.

In case of lineaments in hard rock terrain it is important to know its precise position, for example, to make an analysis of borehole yields versus the distance of the borehole from the lineament.

A simple method of plotting is to transfer the information by hand from the interpreted AP onto a topographic map of about the same scale as the AP, by noting details of drainage, contours and land use. The accuracy depends greatly on the skill of the person doing the transfer and the amount of topographic details on the map, while often the optical instruments facilitating the plotting are no longer available.

#### 3.5.2 Monoplotting

The alternative is to scan the AP and the interpretation so that they are available in digital format. However, a high-resolution digital elevation model (DEM) with heights expressed in an adequate vertical reference system should be available. The DEM should be in the required map projection system. With a procedure called monoplotting, a number of ground control points with their coordinates are selected. A kind of georeferencing is done with corrections for relief displacement (without resampling). Monoplotting is of use when limited amounts of data from the APs (e.g. lineaments, well locations) have to be transferred to proper planimetric positions. The procedure is illustrated in Figure 3.7.

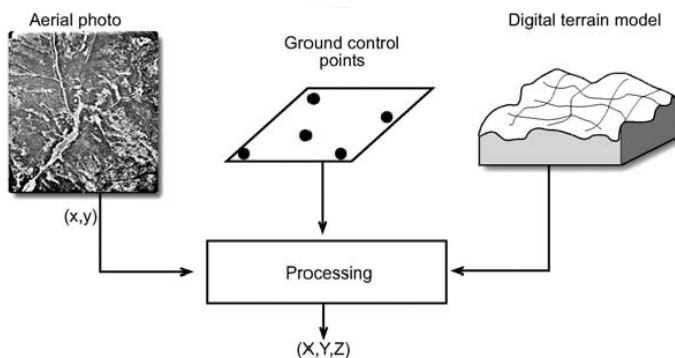


Figure 3.7

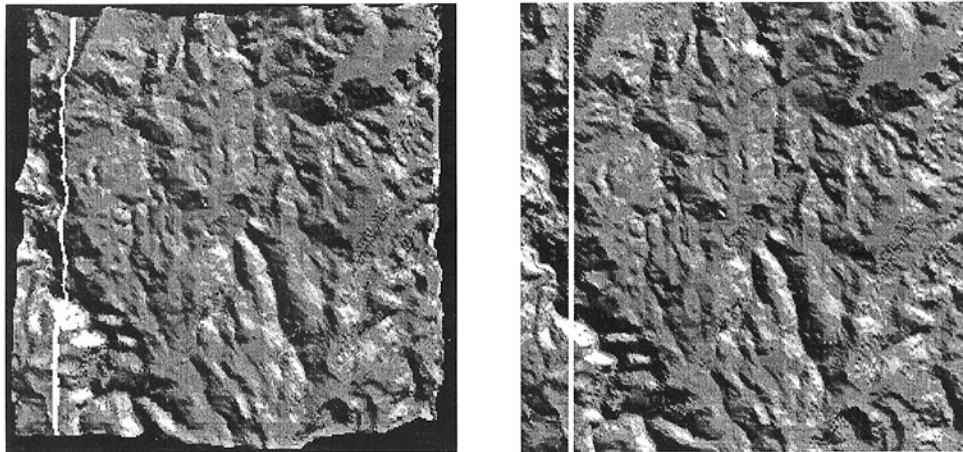
Monoplotting; transferring image interpretation to proper planimetric positions, rectifying for relief displacement.

Source: Janssen et al., 2004.

### 3.5.3 Ortho-image

An *orthophoto* or an *ortho-image* is an AP or image that is fully corrected for relief displacement, internal scale differences and other displacements. Distortion due to relief displacement is a more serious problem for APs than for satellite images, although in mountain terrain the displacement can be 5 to >10 pixels, depending on relief and system.

The procedure for orthophoto or image preparation is similar to that of monoplotting. Terrain differences are modelled by a DEM and the computer calculates the position of a pixel in the original photo for each new output pixel in the correct position, using a resampling procedure. The effect is illustrated in Figure 3.8. Specific photogrammetry software is available for the production of orthophotos or orthoimages.



**Figure 3-8** Example of transformation in orthographic projection. Relief displacement is shown by crenulated white line (left image), which has straightened on the ortho-image (right image) The image shown is a SPOT XS.

Source: Kostwinder (in Meijerink et al., 1994).

### 3.5.4 Creation of DEM using automated photogrammetry

Locations and heights of boreholes can now be accurately determined by differential GPS, but the absolute elevation requires geodetic processing of the data provided by the GPS at the location.

The example of Figure 3.2 is an orthophoto with contour lines derived from a DEM image from a stereo pair of aerial photographs. The visualization of the relief is done by generating contours and by hill shading. Drainage lines have been traced automatically by an algorithm, which looks for the local gradients and local lowest elevations. The upper part of the hill consists of massive limestone with karst development. Some sinkholes can be identified by the contours.

## 3.6 Use of Geographical Information System (GIS)

A Geographical Information System (GIS) is of great value to store, retrieve and process multifunctional and multidisciplinary data for further analysis. In fact, processing of remotely sensed data, which is generally of a spatial nature, and GIS processing are closely interlinked. Certain hydrogeological properties can be analysed in a GIS environment, such as well yields and characteristics of lineaments, karst depressions associated with conduits, or lithological units. Furthermore, the combination of remotely sensed data with hydrogeological data, such as maps showing groundwater contours, depth to groundwater, and hydrochemical data provides an improved insight into the spatial patterns of groundwater occurrences and flow and allows extrapolation of point data.

Since GIS methods have now become widely used, it is assumed here that readers are or can become familiar with the subject.

The above described geometric map or image transforms and DEM visualization are included in GIS functionalities as well as combination of data from two or more sensor systems, by using 'map calculations' (Chapter 2, section 2.9). Algorithms for obtaining derivatives of a DEM, such as a slope map and automated drainage network generation, are standard GIS functionalities, and so are the various interpolation methods for obtaining rainfall or groundwater contours from point data.

Evaluation of the hydrogeology is much enhanced by plotting on the images available hydrogeological data, such as geologic boundaries, borehole data, groundwater contours (possibly only for parts of the scene) and hydrochemistry, using suitable symbols. In particular, the electrical conductivity that can be acquired easily at many places in a field survey often provides an indication of recharge and groundwater movement. By the combination of different data sources in a GIS, the insight in the hydrogeological situation is improved.

In addition, a GIS function as distance operator may be used to analyse well yields as a function of distance from lineaments, and geologic contacts in hard rock terrain. Other factors can be included in the analysis, such as well yields as a function of lineament density, lineament azimuth, lithology, proportion of outcrops, measures of local relief, and so on, all within given distance zones of lineaments. Lineaments in crystalline basement terrain and their relations to groundwater are discussed in Chapter 8.

A map showing estimated relative recharge can be prepared by weighted combination of factors of data obtained from satellites, such as slope maps using SRTM data, vegetation through multi-spectral classification, major classes of relative soil permeability obtained by visual interpretation, and so on. Shaban et al. (2006) used GIS for a method to assess recharge as a weighted function of the factors: lineaments, drainage, lithology, karstic domains and land cover, using various sensor images, topographic and geologic maps. After that, he related the relative recharge classes to some known recharge rates.

A zonation of relative favourability zones for groundwater of an area in Eritrea was made by Solomon and Quiel (2006), using simple addition of values, ranging from 10 to 80, assigned to five relative classes ('poor' to 'very good') of four categories: lithology (including lineament density), distance to lineament, geomorphology and slope. Lineaments and lithology were mapped using Landsat TM and SPOT images, slope and geomorphic units were obtained by using a DEM, but the units were checked visually. Using the additive scores in the GIS overlay, a favourability map was produced and results were verified with well yield data. 'Very good' and 'good' zones corresponded to major lineaments, drainage channels (with some alluvium) and densely fractured basalt. The simple additive scheme was chosen because of the paucity of well yield data and pumping tests.

Tweed et al. (2007) give a good example of how remote sensing and GIS data can be used if more data is available, in this case, for mapping groundwater recharge and discharge areas in a large area in SE Australia underlain by flood basalts. With the exception of visual interpretation of aerial photographs and satellite images for stony rises and eruption points, indicative for recharge areas, and permanent wetlands, they used a time series of Landsat TM and ETM images to map discharge areas through the temporal variability of the NDVI, expressed by the standard deviation of NDVI per pixel. Both fresh and saline discharge areas exhibited a constant photosynthetic activity (indicated by NDVI) in the studied area. Topographic depressions were mapped by using a wetness index based on the slope map derived from a DEM and a map showing the break of slope, also derived from the DEM. The map with topographic depressions was overlaid with the NDVI temporal variability map and a map showing the depth of the groundwater, which was obtained using well data for interpolation of groundwater contours – in fact a groundwater DEM, and subtraction of that DEM from the DEM of the ground surface. Airborne gamma ray spectrometry was used to distinguish the less-weathered basalt (high recharge) from basalt overlain by thicker clay/soil profiles. Authors presented a map showing groundwater flow directions with permanent lakes and wetlands, rivers and depth to water table and another map showing the integrated result of groundwater discharge areas and preferential recharge areas. The discharge areas were divided into indicators that highlight groundwater flow to surface water bodies, and indicators of potential discharge areas.

Such results are important for numerical groundwater modelling, water budget analysis and groundwater management, which in that part of Australia focuses on salinity mitigation programs.

The understanding of the hydrogeology of the desert area of SW Egypt was improved by merging in a GIS, structural geological and geomorphological interpretations using radar images with a map showing slope steepness based on SRTM, hydrogeological point data and groundwater quality data (Robinson et al., 2007).

An early (1990) application of GIS to merge remotely sensed data with other data for groundwater

management was described by Karanga et al. (1990). A map of actual and near-future water demand of the Samburu district, Kenya, was prepared, using census data and drinking water requirements for people and livestock. The spatial patterns of the water demand map were based on a land cover map, using Landsat TM, in order to exclude the parts of the administrative units without occupancy. A water availability water map was made by combining a hydrogeological map, based on lineaments and weathered zones, interpreted on satellite images and aerial photographs and a map based on monthly differences of rainfall and evapotranspiration. The isohyets of the rainfall map were based on station data and vegetation pattern obtained with Landsat TM. The water demand map was compared with the groundwater availability map in order to guide the water development planning and to identify the need for storage of surface water in case it was likely that groundwater was not available

Also in the domain of groundwater management is the concern regarding groundwater dependent ecosystems. Münch and Conrad (2007) used images of different seasons to map vegetation characteristics, which they combined with maps of rainfall and several DEM derivatives, and the groundwater contours based on point data and DEM data, to analyse the base flow driven rivers, springs and wetlands in an area in South Africa.

### 3.7 Summary and conclusions

The DEMs that have become available have contributed to regional groundwater studies and it is expected that new generation of satellite-based DEMs with higher resolution will be used in local studies.

The use of DEMs compensates for the lack of height information in most satellite images. Derivatives of a DEM, such as slope steepness and presence of depressions, can be used in combination with image information of hydrogeological significance.

GIS is now widely accepted as an ideal tool to relate the spatial patterns of information provided by remote sensing with ground based hydrogeological data and this has led to GIS-based groundwater models.

A requisite of GIS operations is that all data are in compatible formats and in the same exact geographic position; hence in the same cartographic projection without effects of relief displacements or other sources or error associated with the use of image data.

## References

- Cuartero, A., Felicísimo, A.M. and Ariza, F.J. 2004. Accuracy of DEM generation from Terra-Aster stereo data. ISPRS conf. Istanbul, 2004: [www.isprs.org/istanbul2004/comm2/papers/191.pdf](http://www.isprs.org/istanbul2004/comm2/papers/191.pdf).
- Georgiadou, Y, Knippers, R.A., Sides, E.J. and van Westen, C.J. 2004. Data entry and preparation. De By (ed.) *Principles of Geographic Information Systems*. ITC Educational Textbooks Series; 1, pp. 93–125.
- Hirano, A., Welch, R. and Lang, H. 2002. Mapping from ASTER stereo image data: DEM validation and accuracy assessment. *ISPRS Journal of Photogrammetry and Remote Sensing* 1255, pp. 1–15.
- Karanga, F.K., Hansman, B. Krol, G. and Meijerink, A.M.J. 1990. Use of remote sensing and GIS for the district water plan, Samburu District, Kenya. Intern. Symp. Remote Sensing and Water Resources, Enschede, The Netherlands, IAH & Neth.Soc.RS, pp 835–48.
- Leblanc, M, Leduc, C., Razack, M., Lemoalle, J., Dagonne, D. and Mofor, L. 2003. Applications of remote sensing and GIS for groundwater modelling of large semiarid areas; example of Lake Chad Basin, Africa. *Hydrology of the Mediterranean and Semiarid Regions, Proceedings Int. Symp. Montpellier 2003*, IAHS Publ. (Red Book) No.278, pp. 186–92.
- Longley, P.A., Goodchild, M.F, Maguire, D.M. and Rhind, D.W. (eds) 1999. *Geographical information systems: Principles, Techniques, Management and Applications. Volume 1*. John Wiley & Sons.
- Münch, Z. and Conrad, J. 2007. Remote sensing and GIS based determination of groundwater dependent ecosystems in the Western Cape, South Africa. *Hydrogeology Journal*, Vol. 15 (1), pp. 9–28.
- Meijerink, A.M.J., de Brouwer, H.A.M., Mannaerts, C.M. and Valenzuela, C.R. 1994. *Introduction to the use of Geographic Information Systems for practical hydrology*. UNESCO/ITC publ. No. 23.
- Robinson, C.A., Werwer, A., El-Baz, F., El-Shazly, M., Fritch, T. and Kusky, T. 2007. The Nubian aquifer in south-west Egypt. *Hydrogeology Journal*, Vol. 15(1), pp. 33–45.

- Shaban A., Khawlie M. and Abdalla C. 2006. Use of GIS and remote sensing to determine recharge potential zones; the case of occidental Linanon. *Hydrogeology Journal*, Vol. 14 (4): 433–43.
- Star, J. and Estes, J. 1990. *Geographic Information Systems: An Introduction*. Prentice Hall. Englewood Cliffs.
- Tweed, S.O., Leblanc, M., Webb, J.A. and Lubczynski, M.W. 2007. Remote Sensing and GIS for mapping groundwater recharge and discharge areas in salinity prone catchment, south-eastern Australia. *Hydrogeology Journal*, Vol. 15 (1), pp. 75–96.
- Solomon, S. and Quiel, F. 2006. Groundwater study using remote sensing and geographic information systems (GIS) in the central highlands of Eritrea. *Hydrogeology Journal*, Vol. 14 (5), pp. 729–41.



# Radar images

## 4.1 Introduction

Hydrogeological applications of microwave or radar images pertain to the following subjects:

- Geological structures and lineaments. There are a few well-known examples of radar images in the desert revealing subsurface structures at limited depth below dry sand.
- Geomorphology and land cover.
- Dynamics of large marshes – always connected to groundwater – can be analysed using radar images.
- Radar altimetry is used for the detection of lake levels and is thus important for the study of groundwater heads and flow around lakes.
- Digital elevation models (DEMs) and precise measurement of land subsidence. Phase shifts of two or more radar images of the same area make it possible to determine with high precision changes in elevation of the land. Land subsidence, often related to pumping or recharge of aquifers, can be mapped.
- Soil moisture monitoring in a qualitative sense or in terms of volumetric moisture content of the topsoil. The spatial patterns of soil moisture and their temporal variations are of particular interest when the groundwater table is relatively shallow.

Radar data and optical sensor data have their own merits, and merging (or fusing) the two is often done in order to increase the information content of the fused image for interpretation.

A difference can be made between active and passive microwave (radar) imaging systems; both have unique all weather (cloud penetration) and day-and-night capability. For the sake of simplicity, images by active radar are referred here to as radar images, those of the passive system as microwave remote sensing.

Side Looking Airborne Radar (SLAR) was the first airborne imaging radar used for systematic radar survey of many parts of the world from the 1960s until today. The RADAM project covering Amazonian regions enabled full coverage with airborne radar data, which assisted greatly in topographic, geologic and other thematic mapping; large coverage of other countries has also been undertaken.

Satellite active radar systems for civil use became first available with NASA's SeaSat (1978) followed by SIR A (1981), B (1984) and C (1994), covering parts of the Earth. Today, several active radar satellite systems are in operation, enabling systematic coverage of the Earth, see Table 4.1.

A large research and development effort has been devoted to the use of radar and microwave remote sensing for soil moisture studies. Of particular interest is monitoring on a global scale of soil moisture with frequent repeats (days, few days), using passive microwave remote sensing systems with scatterometers. The soil moisture products, derived after complex processing, are or will be made accessible on the internet for general use, as mentioned in the section on soil moisture below.

For reasons of space, many aspects concerning the use of radar images have been dealt with only briefly. A good single book dealing with the subject is the manual by Henderson and Lewis (1998) and the chapters on geological and geomorphological interpretations by Ford (1998) and by Lewis (1998) respectively. References are given in the text for specific subjects,

## 4.2 Radar images

### 4.2.1 *Imaging principle*

A radar image is less intuitively interpretable than visual or NIR images because a radar image shows the back-scatter signal of emitted radar pulses. From the moving platform, pulses of very short duration are directed under

an angle (side looking) to the terrain by an antenna that focuses the ‘illuminated’ area into a narrow strip. The return signals are sampled with a higher frequency in time. The intensity of the return signals, which depend on terrain properties are processed and finally stored as values in pixel format along a line, see Figure 4.1. With a coordinated movement of the platform and the time between two pulses, line after line of pixels is recorded to form a contiguous image. However, some complicating factors will be discussed below. The geometry and terms used in radar systems are illustrated in Figure 4.2.

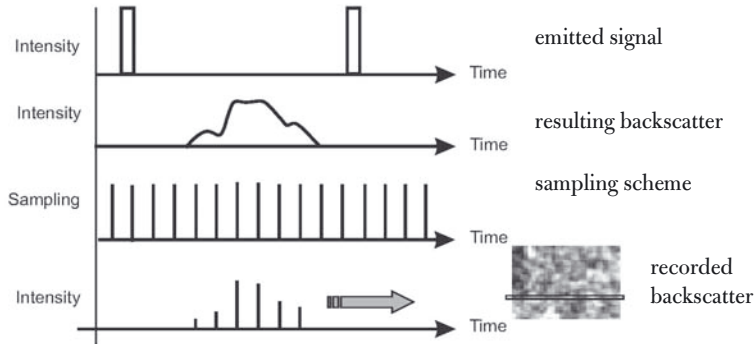


Figure 4-1

**Illustration of how radar pixels result from pulses.**

**For each sequence shown, one image line is generated.**

**Source: Pohl et al. (2004)**

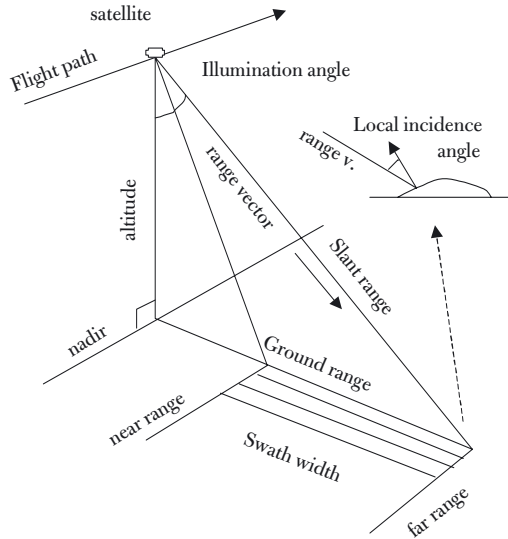


Figure 4-2

**Geometry of active radar imaging system and terms used**

Spatial resolution is determined by two components: the ground resolution across-track, which depends on the local incidence angle, and the along-track resolution. The latter depends on the antenna length. To simulate virtual long antenna lengths, the so-called synthetic aperture technique (SAR) is applied, which makes use of the Doppler shift of the return signal.

**4.2.2 Commonly used imaging radar bands**

The various bands or frequencies and their wavelengths of the radar domain are denoted by letters, as shown in Figure 4.3.

Current satellite radar systems are shown in Table 4.1. For more details the reader is referred to websites, which can be easily found by searching with the acronym of the instrument or the owner organization, or national Remote Sensing Centres or Agencies.

Airborne radar systems are operating in a wider range of bands, each with its specific information.

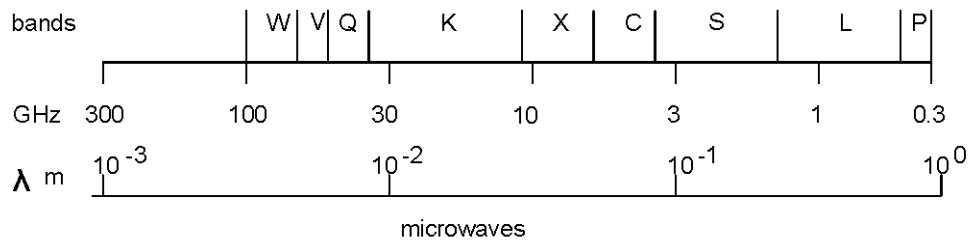


Figure 4-3 Frequency, wavelength and nomenclature of microwave region.

Satellite	Band	Swath Width km	Resolution M	Remarks	Owner
SIR A	L	50	40	2.4 days in 1981	NASA
SIR B	L	20-40	17 -58	8.3 days in 1984	
SIR C	L,C,X	15 - 90	13x26&30	2 missions, 1994	
Radarsat-1	C	50-500	9 – 100	Radarsat-2 in 2006	Canada
ERS-1	C	100	30	No longer in operation	ESA
ERS-2	C	100	30		ESA
ENVISAT-ASAR	C		30		ESA
JERS	L	75	18	No longer in operation	Japan
ALOS	L	40-70	10		Japan
SRTM	C&X		25 - 90	Space Shuttle Mission	NASA
TerraSAR-X	X	variable	1- 13		DLR
TanDEM-X				For 2m DEMs	
ALMAZ	S &C		9,6	Cosmos	USSR

Table 4-1 Active imaging radar satellite systems that have been frequently used

### 4.2.3 Microwave polarizations

Polarization of electromagnetic waves for both the transmitted and the received signals results in different images. It is customary to indicate by a first letter V or H whether the transmitted radar wave is vertical or horizontal, while a second letter V or H denotes the received radar wave.

Thus HH means horizontal transmission and horizontal reception, VH means vertical transmission and horizontal reception, and so on. The various wavelengths and polarization creates many combinations. Colour composites of radar images can be made by using different frequencies and/or polarizations.

### 4.2.4 Microwave and object interactions

The major factors that determine radar backscatter on level areas are roughness of the surface, vegetation characteristics and water contents of the vegetation and soil. Backscatter mechanisms are sketched in Figure 4.4:

- (1) smooth surface (soil, water without waves, etc.), coherent (specular) contribution dominates, little backscatter, for dry soil some soil penetration occurs;
- (2) rough surface, incoherent reflection of energy in all directions, comparatively high backscatter;
- (3) backscatter from a volume scattering medium, such as vegetation canopy;
- (4) double-bounce scattering occurs when the beam is reflected at the soil surface and vertical elements (stems, buildings, etc.);
- (5) complex scattering, forward at soil surface and diffuse in the vegetation or the reverse.

The moisture content of vegetation and soil influences the backscatter because the dielectric properties determine penetration depth in vegetation and soil. Both change in time and therefore the backscatter and consequently the contents of a radar image varies with time.

However, the above-sketched situations explain why it is possible to differentiate various vegetation complexes or associations on radar images. Smooth, bare soils can be differentiated from rough rock outcrops in dry areas, and packs of water hyacinths (much backscatter) floating on lakes or large rivers (low backscatter), etc.

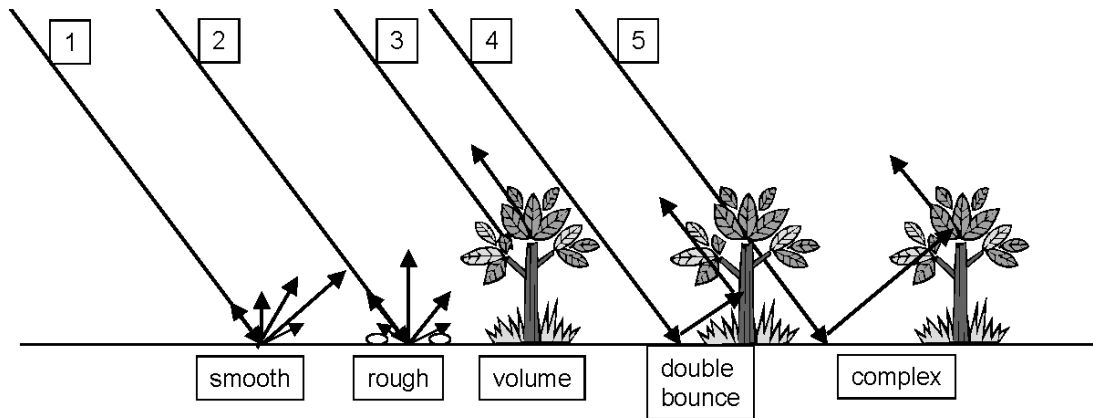


Figure 4-4 Sketch illustrating backscatter mechanisms for oblique incident radar beam.

Together with the effect of topography on incidence angle, the complexity of backscatter mechanisms explain why the derivation of quantitative soil moisture estimates is complex. A good introduction to the physical principles is given by Rott (2000).

#### 4.2.5 Data formats

The received backscatter signals in the raw data are stored in two components containing information about the phase and amplitude. The raw data is processed in different ways.

The *Single Look Complex (SLC)* format combines the Doppler shifts and range information (i.e. distance from object to sensor) for each pixel into a complex number from which the phase and amplitude belonging to a pixel can be computed.

The *Multi-look* format results from processing in such a manner that the total range of the orbit in which an object can be ‘seen’ is divided into several parts. Using the average of the multiple looks an image is produced with reduced unwanted speckle effects.

To get an image for visual interpretation, the SLC or Multi-look data are processed to produce an *Intensity* image. The spatial resolution of that image depends on the number of looks used.

Radar image products that may be used for interpretation are delivered in a format, which resembles that of a spectral image, in other words, arrays of pixels of equal ground resolution with a DN.

#### 4.2.6 Distortions in radar images

The side looking viewing geometry causes some serious geometric and radiometric distortions of radar images and one should be aware of these during image interpretation.

##### Scale distortion

Radar measures distances to ground objects in slant range, as shown in Figure 4.5 and the *scale* of the image changes from near range to far range. The image is therefore corrected and transformed to ground range geometry, but the information content of the near and far range data will be different.

##### Distortions due to relief

Imagine an area of a certain size. In case the area is located on a slope facing the platform (Figure 4.5), it will be recorded in a compressed form compared to the same area on a slope facing away from the platform. The amount

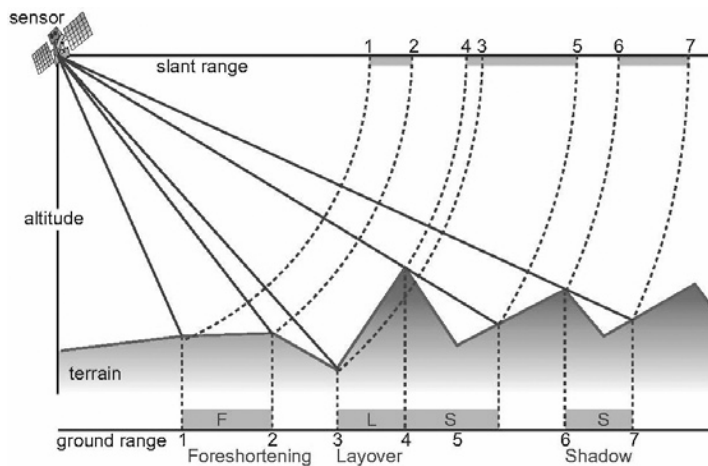


Figure 4-5

### Geometric distortions in radar images due to relief

Source: Pohl et al. (2004)

of shortening depends on the angle of the slope in relation to the incidence angle and is maximal when the slope is perpendicular to the incidence angle. This is called *foreshortening*. There will be backscatter from all parts of slopes facing the platform and because of compression, foreshortened slopes appear as very bright in the radar image.

As is shown in Figure 4.5 the radar wave reaches the bottom of a steep slope facing the platform prior to the top of the slope. Hence, the backscatter signal from the bottom will arrive earlier than that from the top and the slope is imaged upside down. This is termed *layover*.

In mountainous terrain the radar beam cannot illuminate steep slopes facing away from the platform, and thus there is no energy to be backscattered and such slopes remain dark in the image, the *radar shadow*.

### 4.2.7 Speckle

Typical of radar images is the grainy look, a salt and pepper or speckled appearance, see Figure 4.6. This is caused by interactions of the backscattered radar waves from ground objects within an area, which is included in a single pixel. Because of interference return signals can be amplified resulting in bright pixels or extinguished, resulting in dark pixels. This makes interpretation of images difficult because speckle is due to the imaging process and not to spatial variations in the terrain. Various algorithms have been developed – the so-called speckle filters – to reduce this effect. These spatial filters aim at smoothing the values of local groups of pixels, but enhancing lines and edges to maintain sharpness. Yonghong and van Genderen (1996) evaluated various speckle filters.



Example C band airborne radar image.  
Flight path to the right of images



Figure 4-6

Example X band airborne image, same area.

## 4.3 Interpretation aspects of radar images

The effects of vegetation structure/canopy wetness, soil moisture and surface roughness make the extraction of single themes (vegetation, soil moisture) from radar data complex. This might be compared with trying to solve one equation with two or three unknowns; if one is interested in soil moisture for example, the effects of other factors affecting the radar return have to be accounted for.

The interpretation of radar images for general hydrogeological studies relies on the visual differentiation of terrain patterns, due to adjustments of land cover, surface roughness and moisture to hydrogeological units. This interpretation is aided when additional data is available, such as contour maps or DEMs, geologic maps and multi-spectral images.

The sensitivity of the backscatter to (micro)topography facilitates the mapping of lineaments.

### 4.3.1 Terrain analysis

For a comprehensive hydrogeological evaluation the associations between lithology, geomorphology, soils and land cover need to be evaluated. A radar image may be helpful in taking stock or mapping such associations, which may be termed 'terrain units'.

Figure 4.7 shows an airborne radar image (RADAM project) of an area where such terrain units can be differentiated. The annotation shows the main units. The semi-consolidated sedimentary deposits lie unconformably on an erosional surface of high-grade metamorphic basement rocks, whose outcrops are seen in the central area.

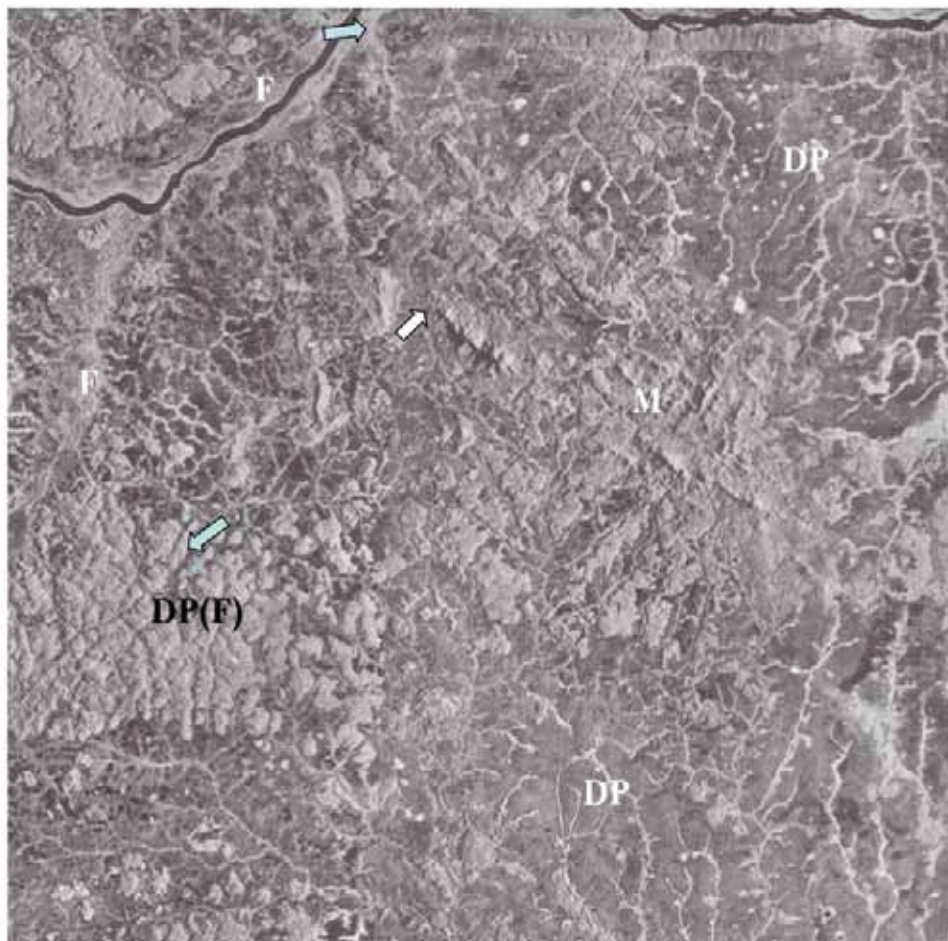


Figure 4-7

Airborne SLAR image of an area in northern Amazonia (from Radam project mosaic, sheet NA-20-X-B, Ministry of Mines and Energy, Brazil).

Arrows indicate some selected faults. DP= Dissected Plateau, flat lying sedimentary semi-consolidate deposits. Drainage pattern shows up well because of dense vegetation, uplands are deforested. DP(F)= same, but forested. F= floodplain. M= high-grade metamorphic rocks, striking SE-NW. Distance E-W is 40 km.

Of interest are also the small semi-circular landforms with strong backscatter due to vegetation. These are depressions formed by pseudo karst and indicate the existence of an internal drainage component (similar depressions are found e.g. in the Kalahari sands of Zambia, see Chapter 7, sections 7.3.4 and 7.3.5). A fault scarp is evidence for the local eastwest fault in the north.

An overview of geomorphic interpretation of radar images is given by Lewis (1998).

### 4.3.2 Lineament mapping

An example of how lineaments can appear on a radar image in a humid tropical hard rock area is shown in Figure 4.8. The arrows indicate two major directions.

Rectilinear lineaments suggest brittle rock failure (such as fractures and normal faults) and curvilinear lineaments may relate to more ductile bedrock, which has been deformed by plastic flow (shear zones, argillaceous sedimentary rocks, tuffs, etc.). Since the area shown consists of hard rocks, it is likely that the lineaments are brittle zones and thus contain and conduit groundwater. The river appears to follow fractures, suggesting limited depth of floodplain deposits.

Another example of lineaments on a radar image is given in Chapter 8, Volcanic Terrain, section 8.3.3.



Figure 4-8

Radar image of area west of Tanoe River, Ivory coast.

Lineaments are indicated with arrows (grey and white).

RADARSAT 20.06.1998 Orbit 39-248A Standard Beam Mode.

Distance N-S is 7.250 m.

Source: Bannert.

### 4.3.3 Geologic interpretation

Ford (1989) gives an overview of geologic interpretation of radar images and this interpretation is often the first step in hydrogeological investigations. Examples of how geologic features may appear on radar images are given in some textbooks and websites, but often they have been selected on the basis of their clarity and beauty. Here, an example of more commonly encountered radar image is shown – Figure 4.9, a SIR-C image of Wadi Sahba, Saudi Arabia (Dabbagh, 1996). Comparison with an existing geological map (in Dabbagh, 1996) shows that many of the contacts can be seen, although the unconformity of the *Ka* limestone (Cretaceous) and *Tu* limestone (Paleocene-Eocene) can be detected only with some difficulty. In the right-lower corner no differentiation between *Tdm* marl and limestone and the Quaternary gravels (*Qg*) is possible. The large faults can be interpreted. In the right hand part in the *Tu* area, the dark stripes could be misinterpreted as bedding traces, but these are longitudinal dunes.

The karst features indicated on the map can be recognized on the image, but this would not be possible without a priori knowledge.

Some selected lineaments have been indicated on the image. Since karst exists in the area, these lineaments could be of interest for groundwater exploration, particularly the ones in the lower left-central area, where the radar penetrates the shallow cover of sand (*Qes*) over the limestone and the relative elevation is low. In general it may be remarked that single radar images often contribute little to what can be achieved with interpretation of stereo-airphotos and multi-spectral images, except for areas where a thin sand cover obliterates the geology, as will be illustrated below.

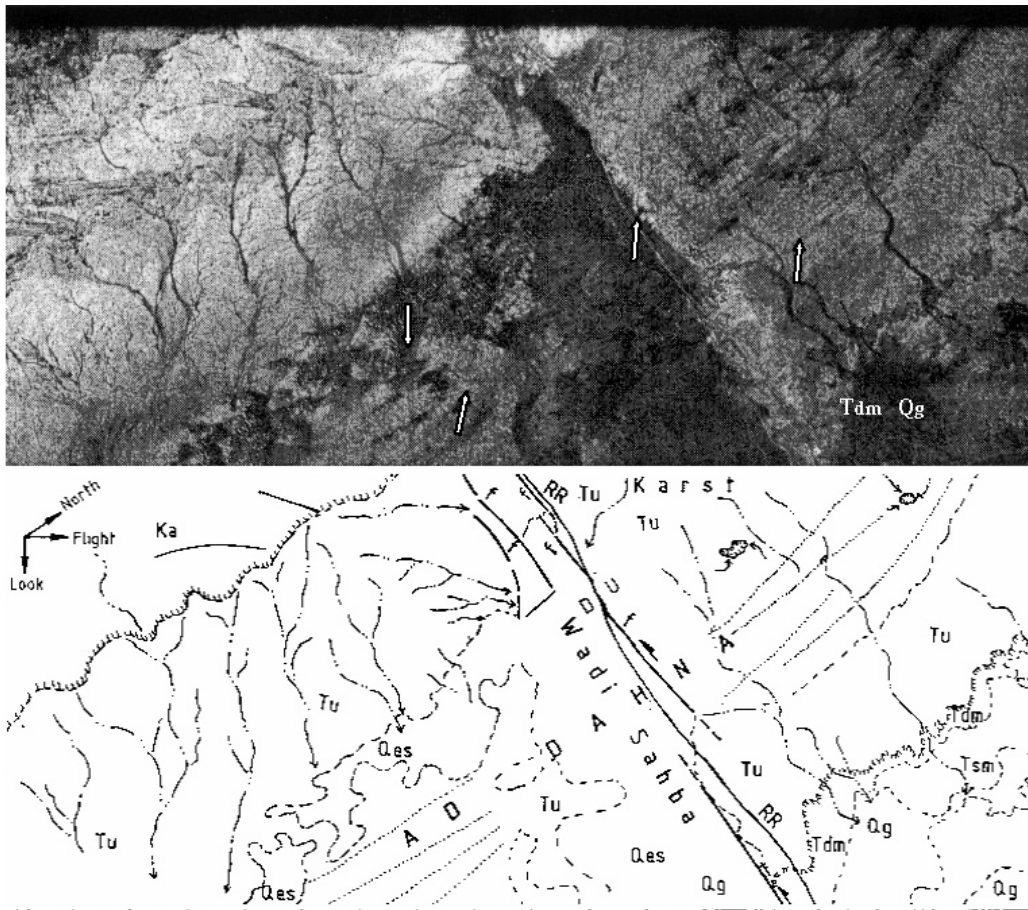


Figure 4-9 SIR-C image of Wadi Sahba area and geologic map of the area. RR is railroad, for other symbols, see text. Source: Dabbagh et al., 1996. Distance E-W is 120 km.

#### 4.3.4 Ground penetration

The longer wavelengths (e.g. the P, L bands) have ground penetrating capability and when the cover is uniform and dry, such as with a thin sand cover in a dry area, the backscatter produced by the features below the sands may show up on the radar image, see Figure 4.3. The Spaceborne Imaging Radar (SIR A, B and C, L band) acquired image data during some periods and in arid terrain revealed paleo-channels below a sand cover (ElBaz et al. 2000) prompting further investigations.

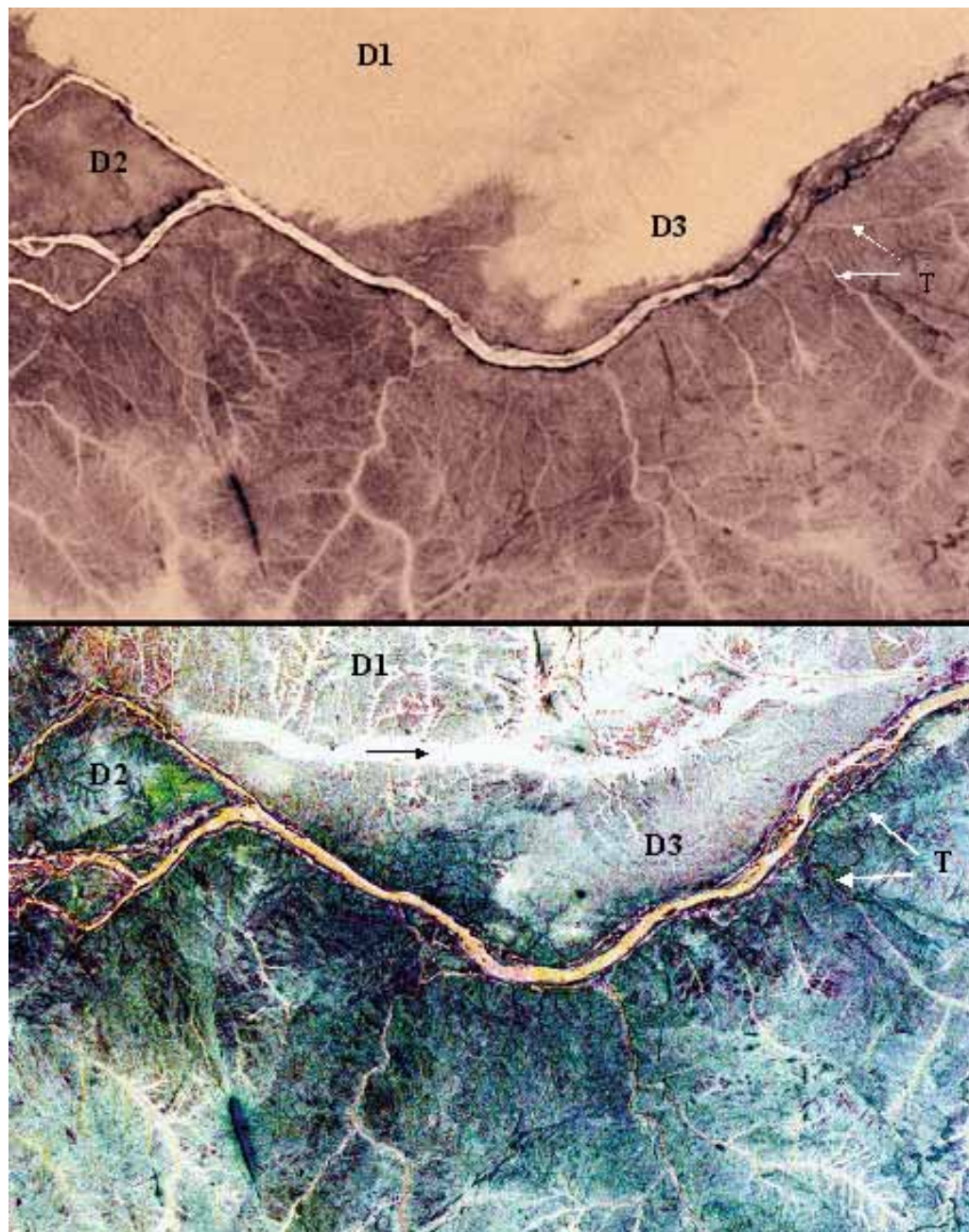
The ground penetration depth of radar depends on the wavelength used by the system, moisture content, conduction and magnetic relaxation properties of the soil. When iron-rich minerals and salts are present, or when the soil has moisture, penetration will be absent or very limited.

Elachi et al. (1984) developed a model for attenuation by the surface layers and refraction at the subsurface interface as a function of the target and sensor parameters. They noted that HH polarization at high incidence angles ( $> 50^\circ$ ) provide more information than alternative configurations. Farr et al. (1986) buried receivers in



desert sand that had some moisture, though low, and found that it is likely that subsurface features related to moisture and drainage could be detected for depths of 0.7 to 1.7 m. Experiments in Saudi Arabia using Shuttle SIR-B (L band) data indicated a maximum penetration in dry sand of 3 m (Berlin, 1986), and Schaber et al (1986) argue that penetration depth is less than 2 m for a site in Egypt and 1.5 m for the L band.

Ground-Penetrating Radar (GPR) is used to evaluate volume scattering coming from subsurface dielectric heterogeneities in cases of radar penetration of the dry sand. This evaluation is based on correlating the reflectivity of the GPR section with backscattering coefficients extracted from radar images (Grandjean et al. 2006). A structural interpretation of Radarsat images for the desert in SW Egypt was made by Robinson et al. (2007) who mention that ground penetration of the C-band used was limited to some 0.5 m in sands.

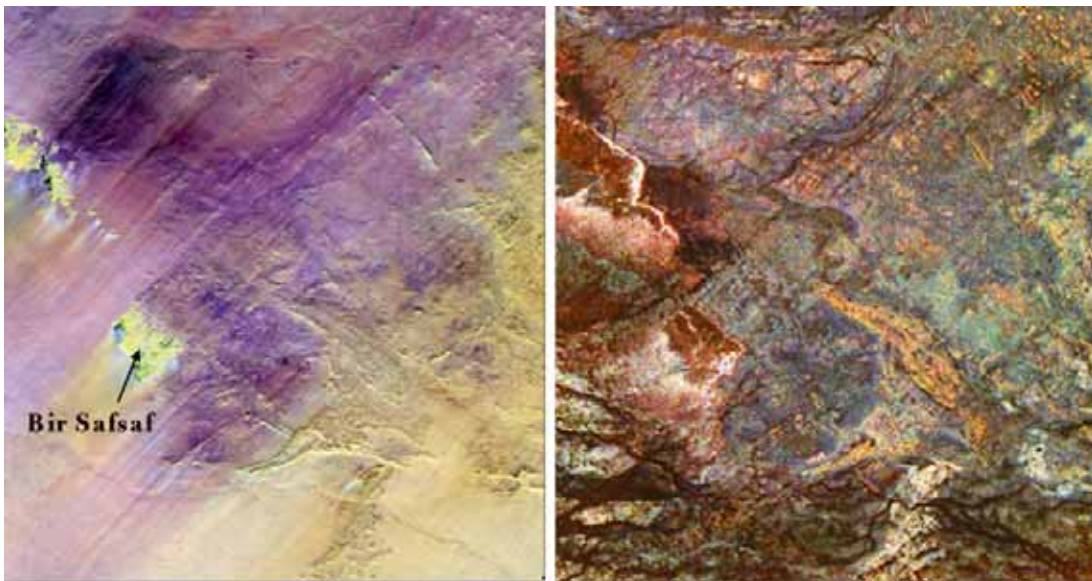


**Figure 4-10** Example of penetration of radar energy below dry sand cover, area along the River Nile, Sudan. Upper figure: Colour infrared photograph of Space Shuttle Colombia Mission Lower figure: Spaceborn Imaging Radar SIR-C/X-SAR image. Black arrow indicates former course of the Nile, visible on radar image only. Note detection of drainage patterns below sand cover at D1, D2 and D3 and thin cover (< 2m) at drainage lines at e.g. T (white arrows). Distance E-W is about 30 km. Courtesy: NASA/JPL-Caltech .

Comparison of an image based on surface reflectance with a radar image shows that a radar image in an arid environment may contain useful hydrogeological information not observed on the reflectance image, as is illustrated in Figure 4.10. The area shown is situated along the Nile River in Sudan. Of particular interest is the deposit of the former Nile River, indicated by a black arrow on the radar image, SIR-C/W-SAR of Nasa/JPL (lower image). The upstream connection with the Nile River suggests that groundwater may be present in the deposits. The former river course is not visible on the colour infrared photograph taken during the NASA Columbia Space Shuttle mission. The penetration capacity of radar is also shown by the drainage patterns near (D1) to (D3), which are also not seen on the photograph. The arrows near (T) indicate the places where sand cover in the small drainage lines is thin, probably less than 2 m. Finally, it can be remarked that the radar image displays geological information that is only partially seen on the reflection image.

Subsurface drainage patterns and fractured rock surfaces below sand covers have been found at other places, see, for example, Drury and Andrews Deller (2002), dating from past pluvial periods. However, because of the present aridity, permeable river deposits detected on radar images usually have no groundwater, except possibly perched groundwater of limited quantity.

Another example of ground penetration capability is shown in the radar colour composite of Figure 4.11, from south-central Egypt. The image on the left is an optical image from the Landsat Thematic Mapper, and on the right is a radar image from the Spaceborne Imaging Radar-C/X-band Synthetic Aperture Radar (SIR-C/X-SAR). In the Landsat image, the colours are assigned as follows: red is Band 7 (mid-infrared); green is Band 4 (near infrared); and blue is Band 1 (visible blue light). The colours assigned to the radar frequencies and polarizations are as follows: red is L-band HH, green is C-band HH, and blue is X-band VV. Some geologic structures on the surface are visible in both images.



**Figure 4-11** South central Egypt with Safsaf oasis. Left: Landsat TM colour composite (bands 7 red, 4 green, 1 blue), Right: colour composite of SIR-C/X-SAR, bands L HH red, C HH green, X VV blue. Courtesy: NASA/JPL- Caltech

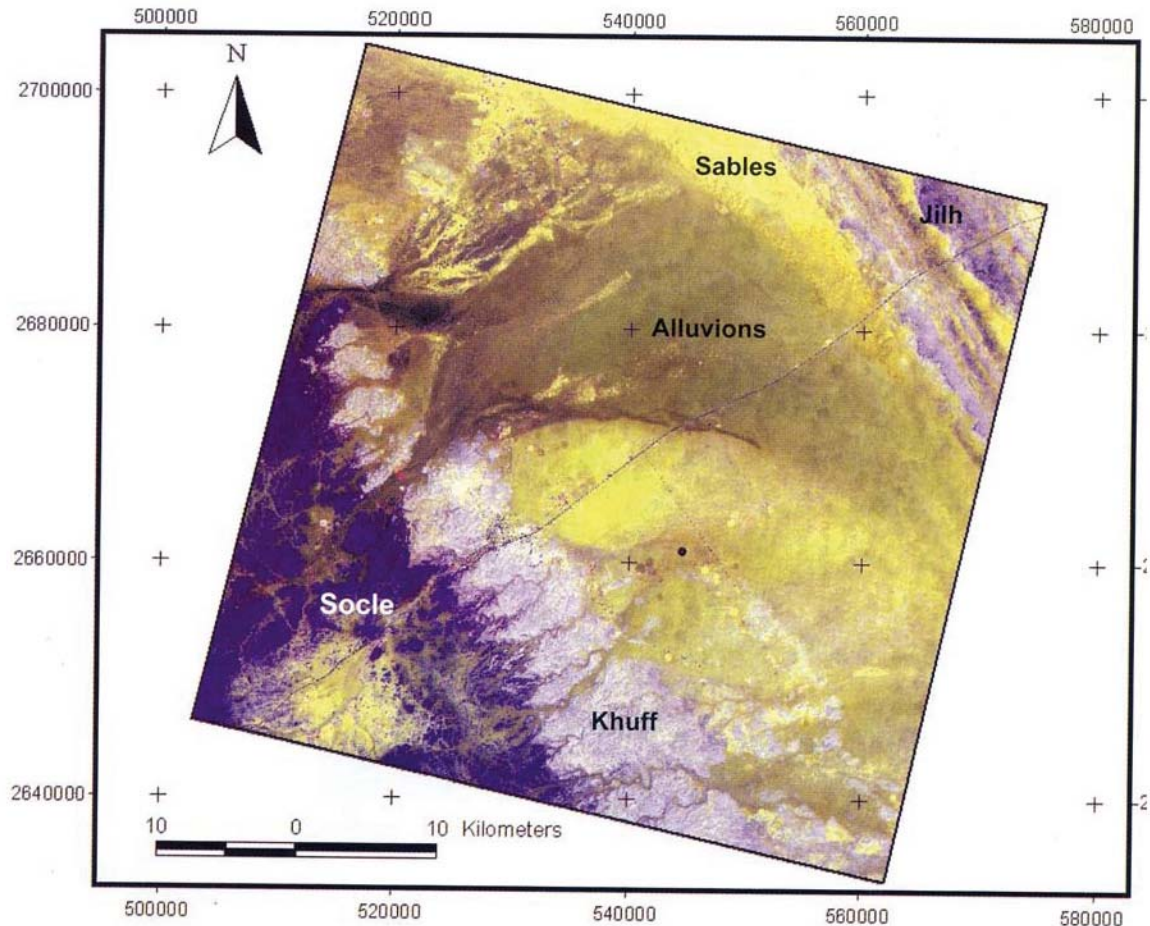
However, many buried features, such as rock fractures, fossil channels and the blue circular granite bodies in the upper centre of the image on the right, are visible only on the radar image. The Safsaf Oasis is indicated and two other oases appear in the upper left corner. Analysis as to why the oases occur at these locations requires field data concerning the regional hydrogeological setting.

## 4.4 Image fusion

Since information given by radar images is different from that of multi-spectral images, it stands to reason that a combination of the two will produce a rich source of information. The combination of radar and multi-spectral

images, also termed 'fusion' requires that both have the same geometric properties, in other words, geocoding has to be done to ensure that pixel sizes and coordinate systems are the same. This requires resampling of at least one of the images, usually the radar image. To make a radar image of hilly terrain suitable for fusion, a good DEM has to be available to place the radar pixels into the proper planimetric position because of relief distortion, as discussed in Chapter 3.

An example of fusion of radar and multi-spectral images is shown in Figure 4.12. The caption of the figure explains the features seen and their hydrogeological significance.



**Figure 4-12** Combination of Radarsat Image and False Colour Composite image of SPOT-5, (Red: NIR band XS3, Green: red band XS2, Blue: C band of radar) of an area in Saudi Arabia. Socle = impermeable basement rocks, Khuff = intake area of permeable rock dipping gently to north-east, covered by impermeable rocks (Jilh). Sands (sables) in yellowish tones; alluvium (alluvions) in brownish tones. Khuff aquifer is confined in the north-eastern half of the image. Source: O. Bachir Alami et al. (2004).

### *Image fusion technique*

It is desirable that a fused image contains information of a false colour composite consisting of three bands of multi-spectral images and the radar image, and that the hue ranges of the original colour composite are retained, because of familiarity of interpreters with such composites.

We want to fuse four images but have only three colour spaces, namely Red, Green and Blue. How can this be achieved? There are several ways of doing this (see Chapter 2, section 2.9), but a simple one is a technique known as pixel addition:

$$R' = aR + bI', \quad G' = aG + bI' \text{ and } B' = aB + bI'$$

Where  $a$  and  $b$  are scaling factors to balance the intensity sharpening from the radar image versus the hue and saturation from the three multi-spectral bands, with:

$$a, b > 0 \text{ and } a + b = 1$$

Let us assume that Red (R) is assigned to the NIR spectral band, Green (G) to the red spectral band and Blue (B) to the blue-green spectral band – the commonly used convention for a false colour image.

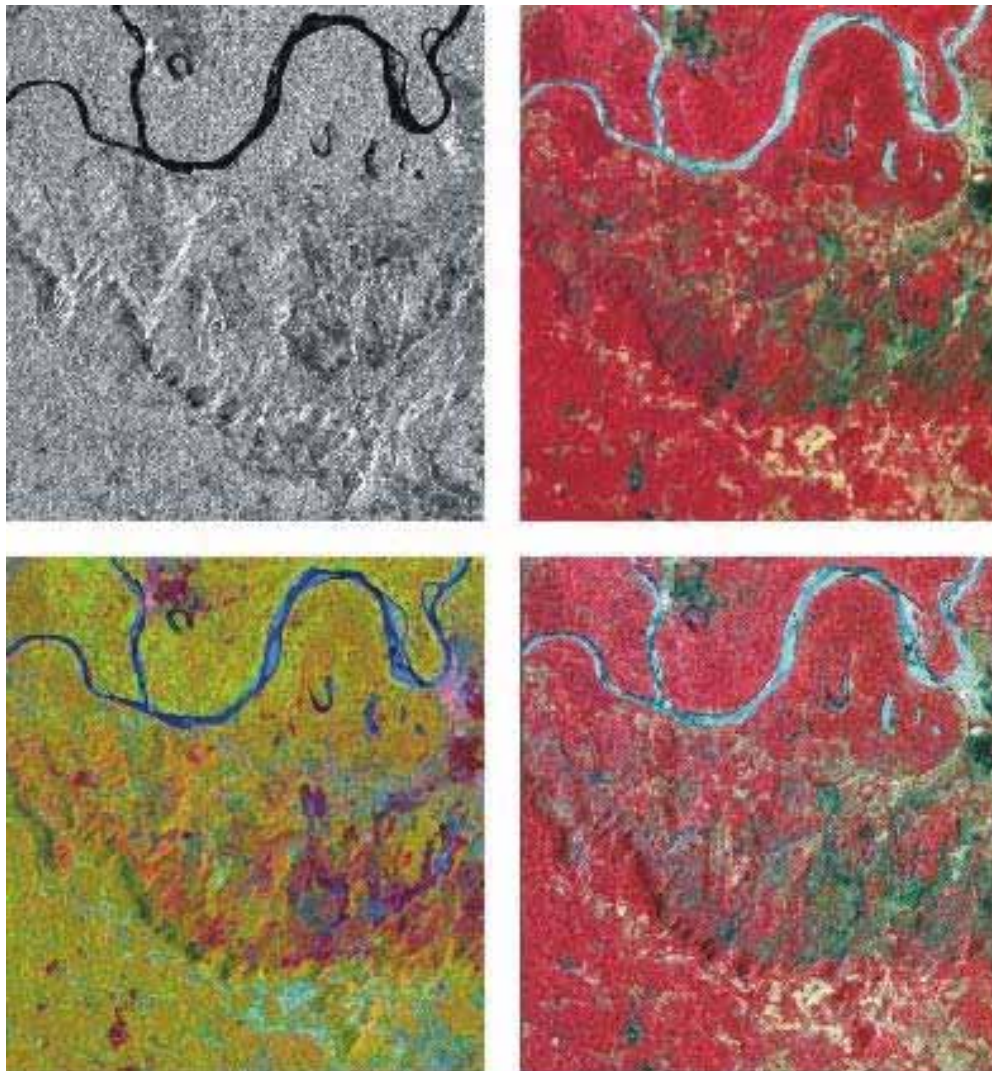
I stands for Intensity and the radar image is used because of the illumination and shadow effects due to topography, specular reflection of the radar energy over water but strong backscatter in vegetation, and so on.

Contrast enhancement (by stretching, filtering) of each of the R', G' and B' images should be applied uniformly for optimal results; after that a colour composite is displayed. It should be noted that the intensity substitute, namely the radar image, is present in all three images used for the composite.

Figure 4.13 (upper left) shows an ERS-1 SAR image of a small area in Amazonia in the south of Colombia. The upper right Figure 4.13 shows a false colour composite of SPOT 2 made in the conventional manner.

The image in the lower left is a colour composite of the radar image (in red), SPOT band 3 in green and SPOT band 1 in blue, being the simplest method of image fusion. It is not the best fusion image that can be made because neither the intensity information of the original radar image, nor the spectral information of the false colour composite is preserved adequately.

A substantial improvement in interpretability of the image after applying the pixel addition method is shown in the lower right image.



**Figure 4-13** Results of fusing SPOT and ERS-radar image images of an area in S. Colombia.  
 Upper left: ERS image. Upper right: SPOT false colour, bands 3,2 and 1 in Red, Green and Blue  
 Lower left: Colour composite ERS in Red, SPOT band 3 in Green and band 2 in Blue  
 Lower right: Three SPOT bands + Radar image by pixel addition method (see text).  
 Note that most of information of SPOT false colour image and radar image is retained.  
 Source: Gorte and Schetselaar, 2004.

## 4.5 Stereo radar images

Radar images of the same scene but taken from different positions can be viewed stereoscopically.

For a SAR, true parallax occurs only with viewpoint changes away from the nominal flight path of the radar. In contrast to aerial photography, parallax cannot be created by forward and aft looking radar 'exposures'.

Only certain radar image products are suitable for stereo viewing (see e.g. tutorial on website of RADARSAT, Canada).

## 4.6 3D information and precision measurement of land subsidence by radar interferometry

For hydrogeologists the applications of DEMs derived from radar (INSAR), particularly the worldwide coverage by SRTM (see below), are:

- to avail of relief information in regions for which only small scale maps are available,
- to drape satellite images on 3D views of the terrain (using a GIS).

The height accuracy of the DEM is inadequate to obtain topographic heights of boreholes.

Radar can produce precise elevation data; of interest are:

- changes in land subsidence that may be due to groundwater pumping or recharge, by differential INSAR
- radar altimetry of X so far selected-lakes, hence groundwater levels in the riparian zone.

### 4.6.1 SAR Interferometry (INSAR), SRTM DEM

The principle of SAR interferometry or INSAR is based on phase information of the microwave. Use is made of phase differences between corresponding pixels in two SAR images having different positions but covering the same area. The different path lengths from the two sensor positions (base line) to the object on Earth cause differences in phase. Terrain height is a function of that difference in phase, the distance between the two sensor positions and some additional orbit parameters.

The Shuttle Radar Topographic Mission (SRTM) used the so called single or simultaneous pass interferometry, because the two receiving antennas were mounted on a long mast, providing a base line of 60 m. The simultaneous recording eliminates effects of changes (moisture, vegetation) of the land objects, which do occur when radar images of different times (orbits) are used.

SRTM data in the form of DEMs are available globally between 60°N and 58°S. For non-RS specialists, SRTM data is available as a Geocoded Terrain Corrected (GTC) product, UTM projection and WGS84 ellipsoid. The global coverage so far is restricted to 3 arc-sec (about 90 m) DEMs, but for certain parts 1 arc-sec (30 m) DEM is available.

The SRTM data has to be imported into a GIS, for visualization (hill shading, contours, 3D display) and preparing derivatives such as slope maps or automated drainage network generation. Figure 4.14 shows DEM data (left) and the visualization using hill shading (right).

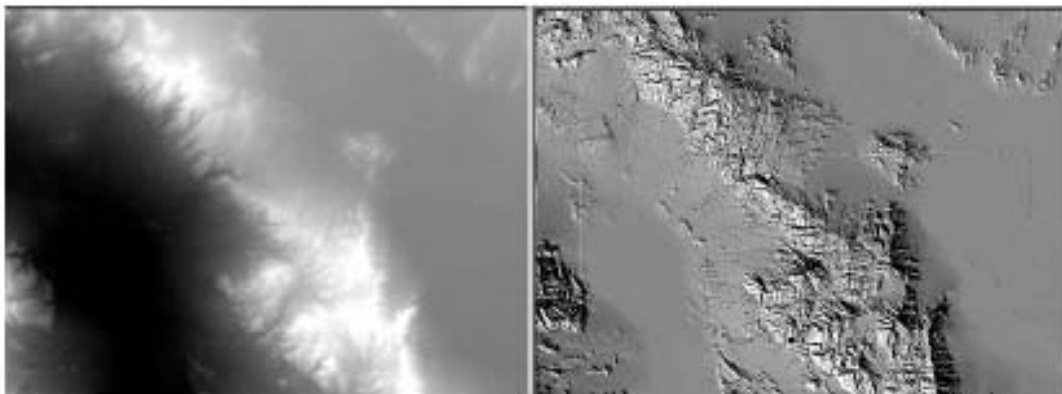


Figure 4-14 Left: DEM, grey tones correspond to elevations. Right: visualization using hill shading.

The absolute height (height above datum) accuracy of SRTM is 16 m and the relative accuracy is reported to be better than 10 m.

The next example (Figure 4.15) shows SRTM data of the Rift and adjoining highlands of a part of Rwanda and Uganda. The DEM of the example had elevations for each pixel in steps of 1 m, based on interpolation of elevation values of the original DEM. Hill shading was applied and automated drainage network generation, as well as automated catchment boundary delineation in a GIS.

Instructions for downloading and handling SRTM data are available on the internet (see references: Sijmons et al., 2005).

The DEM data generated by ERS1/2 and ENVISAT, RADARSAT or JERS is based on 'repeat or dual pass' interferometry. Two images are taken during different passes of the satellite. Because the return microwave is influenced by conditions on the ground, changes in land cover, ploughing of fields or moisture changes, etc. influence the interferogram, which is the image showing the phase differences, from which the DEM is derived. The repeat cycle for ERS2, for example, is 35 days.

For that reason, ERS1 and ERS2 were operated for a period of time in a tandem mode, that is, they passed 24 hrs after each other in similar orbits to minimize changes in ground conditions and thus increase the reliability of the DEM produced from the data.

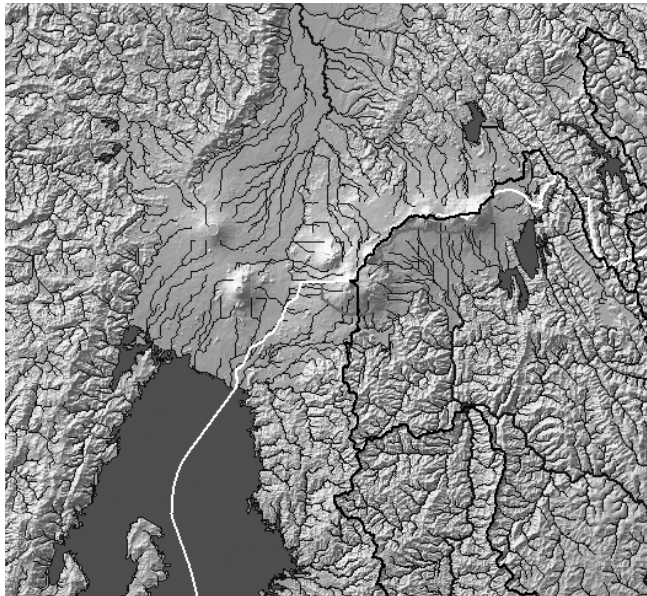


Figure 4-15

**Terrain model of NE Rwanda and SE Uganda, generated from SRTM data, downloading from Internet and imported in a GIS.**

**Spatial resolution is 90 x 90m. Image can be enlarged for local studies, see text.**

**Hill shading for relief impression and automated generation of drainage lines and catchment boundaries was done by GIS operations.**

**Source: Maathuis, ITC**

#### 4.6.2 Hydrogeological application of SRTM data

Although the image of Figure 4.15 shows a large area (regional scale), parts can be enlarged for local studies. With regard to SRTM elevation data for hydrogeological work, it should be remarked that there could be an important discrepancy between the ground level elevation of a borehole, as established by field levelling, and the pixel value of the SRTM DEM (absolute height accuracy is 16 m). However, in case more data points with absolute elevation are available, the DEM can be rectified to some degree and may then be used for estimation of elevations of ground level of bore holes for which elevation data is missing.

This estimate is probably more accurate than estimations based on interpolation between contour lines of a topographic map, especially when the contours are widely spaced. However, it is a poor alternative to differential GPS measurement of the elevation of the borehole.

#### 4.6.3 Differential INSAR: Land subsidence and uplift

Seasonally fluctuating groundwater levels or declining groundwater levels in aquifers may cause deformation at the surface, if the aquifer system has highly compressible sediments.

Very small changes in shifts of the terrain (lateral and vertical), on cm scale or a fraction of cm under good conditions, can be detected and mapped by using three SAR images of the same area acquired during different overpasses to generate two interferograms. The arithmetic difference of the two interferograms is taken to produce a differential interferogram. The elements of the latter in combination with orbit information and sensor characteristics are used to compute changes in surface elevation.

Characteristic of interferograms (or fringe maps) are the typical interference phenomena in the form of more or less regular concentric or ellipse shaped rings, displayed in colour rings of the rainbow, whereby in the centre the change of elevation is maximum and becomes gradually less towards the periphery, as is shown in Figure 4.16 which shows deformations along an active fault.

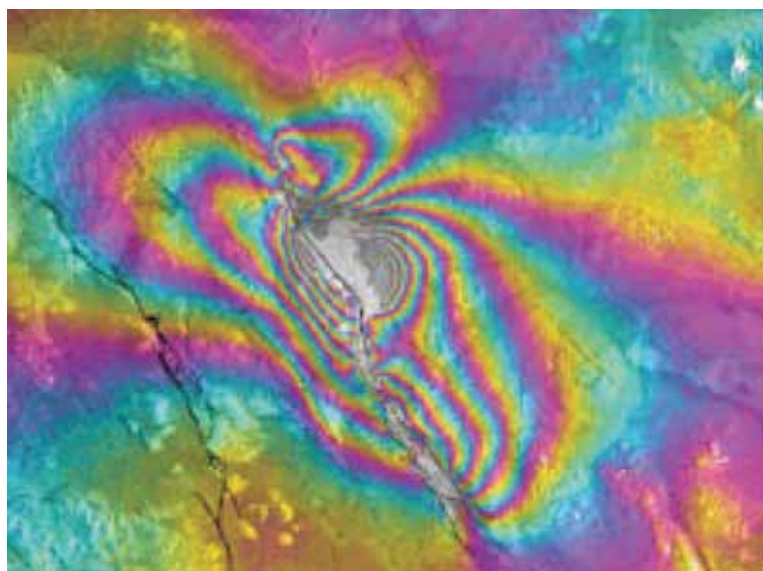


Figure 4-16

**Differential interferogram, based on an interferogram before and one after the deformation caused by tectonic movement.**

**Interference rings or fringes represent amount of deformation, coded in colour, increasing progressively towards the inner core.**

Another example is shown in Figure 4.17, which displays an ERS-1 SAR 3-pass interferogram showing land subsidence in Panama California. The image was created by Jet Propulsion Laboratory (JPL), California, and is derived from the ESA-ERS website with the following description:

The colours of the radar image represent the change in range due to surface displacement toward the satellite antenna, which is illuminating the area from the east with an incidence angle of  $23^\circ$  off the vertical. The black lines are mapped as active faults. One full colour cycle represents 5.6 cm of range change between the dates of acquisition of the radar data (20 October, 1993 – 22 December, 1995). Grey areas within the radar swath are zones where the radar correlation is lost due to steep slopes and seasonal change of the vegetation. Although surface displacement in this region is primarily due to the tectonic activity, as shown in the above image by the concentric rings visible along the western edge of the SAR swath, other features visible on the image are related to human activity such as water and oil withdrawal. Regions of ground subsidence include the Pomona (P) area (water), the Beverly Hills (BH) oil field (oil) and localized spots in the San Pedro and Long Beach airport (LBA) area (probably oil industry activity). Noticeable surface uplift is observed in the Santa Fe Springs oil field (SFS) and east of Santa Ana (SA). Surface uplift in these areas may result from the recharge of aquifers or oil fields with water, or from the poro-elastic response of the ground subsequent to water or oil withdrawal.

Interestingly, not only subsidence but also uplift attributed to recharge has been measured with interferometry. The increase in pore pressure reduces the vertical effective stress in the skeletal matrix resulting in regional uplift. Schmidt and Bürgmann (2003) presented InSar time series of an intramontane valley in the US showing subsidence and uplift and discussed the patterns in terms of the hydrogeology of the area. A part of their illustration is shown in Figure 4.18. Time series at two points (lower figure) are compared to illustrate the seasonal versus long-term deformation patterns. The points are separated by a NW-SE trending fault, which partitions the aquifer.

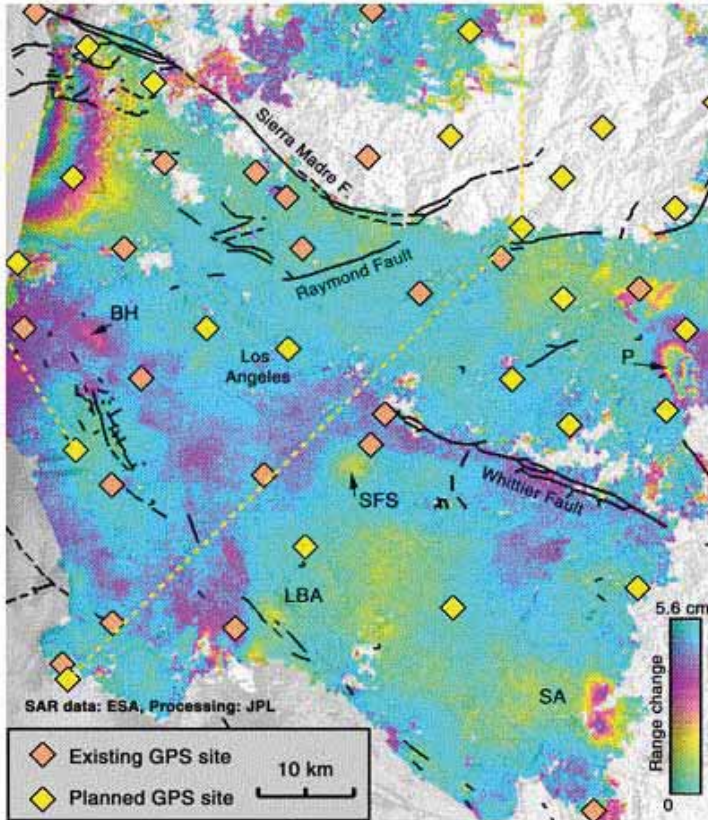


Figure 4-17

ERS-1 SAR 3-pass interferogram showing subsidence in Panama California. Image created by Jet Propulsion Laboratory (JPL), California.

Source: ESA-ERS website

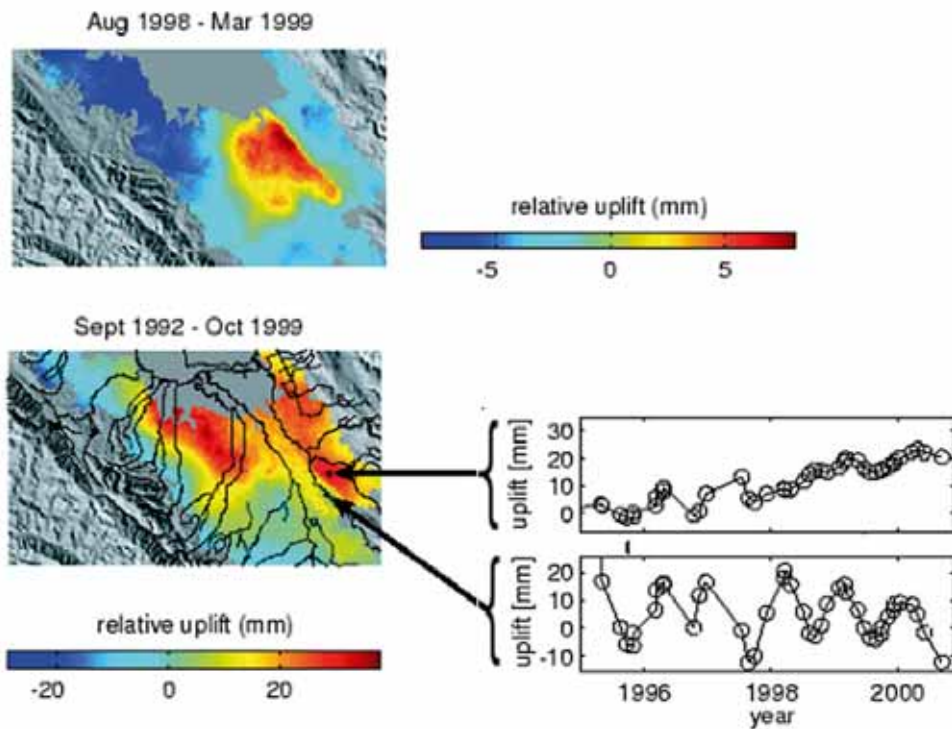


Figure 4-18

InSAR time series showing uplift and subsidence of an aquifer in Santa Clara Valley, California, U.S.A. based on ERS and Envisat data. Seasonal and long-term deformation at two points, separated by a fault, which partitions the aquifer are shown in a graph. Source: Schmidt and Bürgmann (2003) and Berkeley Seismological Laboratory.



#### 4.6.4 Implementation and outlook

Specialists undertake the preparation of interferograms and the differential interferograms. Because of the importance of deformation due to groundwater extraction and recharge, monitoring earthquakes and volcanic eruptions and subsidence due to mining or oil and gas exploitation, the technology is widely applied. Subsidence patterns have been mapped by InSAR for most of the major cities where the problem arises.

From a hydrogeological point of view, the data provided by interferometry opens new insights as to the behaviour of groundwater vis-à-vis the elastic properties of an aquifer. The deformation patterns derived by InSAR provide a basis of knowing where to do stress-strain analysis of the aquifer. Seasonal water level fluctuations and deformation patterns have been used to map the elastic storage coefficients of an aquifer (Hoffmann et al, 2001). Once these are known it is theoretically possible to detect groundwater level fluctuation from deformation.

Hoffmann et al (2003) used land subsidence data in inverse modelling and found significant improvement between simulated and observed land subsidence, both in terms of magnitude and spatial extent. However, the ability of the model to adequately reproduce the subsidence over only the few years used in their study was impaired by the fact that the simulated hydraulic heads over small time periods are often not representative of the actual aquifer hydraulic heads. They mention that error in the simulated aquifer heads constitute the primary limitation of their approach.

### 4.7 Radar altimetry, LIDAR, Laser

A radar altimeter uses the two-way time delay between pulse emission from the platform and the echo time received by the satellite system, unhindered by time of the day, weather or canopy cover. It is not an imaging device, but measures the elevation of the surface by taking account of the precise height of the satellite above a reference ellipsoid. Each returned height is an average of all surface heights found within the footprint of the altimeter. The footprint area is the smallest for water bodies during calm weather (e.g. lakes or rivers without waves) and ranges with the systems used so far between 200 m and a few km. However, the newer generation of altimeters aims at accuracy at elevations of 10 cm or less. Several factors affect the accurate recovery of height data from inland water echoes, which needs specific processing.

Using the repeat cycles of the satellites (10 to 35 days, depending on the system), hydrographs of a number of lakes have been prepared and are maintained. Figure 4.19 shows an example (from the USDA website) of relative lake height variations computed from TOPEX/POSEIDON (T/P) and Jason-1 altimetry (for the period after 2002) with respect to a 10-year mean level derived from T/P altimeter observations. The top panel displays the raw height variations (open circles denote potential icy or calm-water conditions, large error bars may denote noise or dry lake-bed conditions), while the height variation time series in the lower panel has been smoothed with a median type filter to eliminate outliers and reduce high frequency noise. An example of lake level heights by radar altimetry is shown in Figure 4.19.

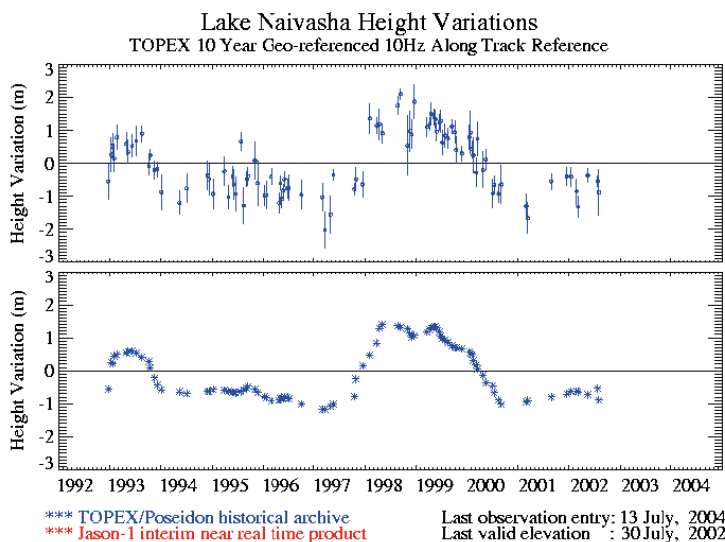


Figure 4-19

**Record of 10 years  
of lake level variations from  
TOPEX/POSEIDON  
and Jason-1 altimetry  
of Lake Naivasha, Kenya.**

Source: USDA/NASA

The variation of the level of Lake Naivasha is mainly due to inflow of the Malewa and Gilgit rivers. From a groundwater point of view the lake has a saddle position, that is, the groundwater table slopes away to the north and south (Becht 2004, see Chapter 12, section 12.5), with minor groundwater inflow from east and west. The head difference of about 2 m is therefore important in transient modelling of the groundwater outflow from the lake.

Together with the European Space Agency (ESA), De Montfort University (UK) developed a system to obtain an estimation of River and Lake height from both ERS and Envisat data. De Montfort University (DMU) developed an automated system to produce two types of products called River Lake Hydrology product (RLH) and River Lake Altimetry product (RLA).

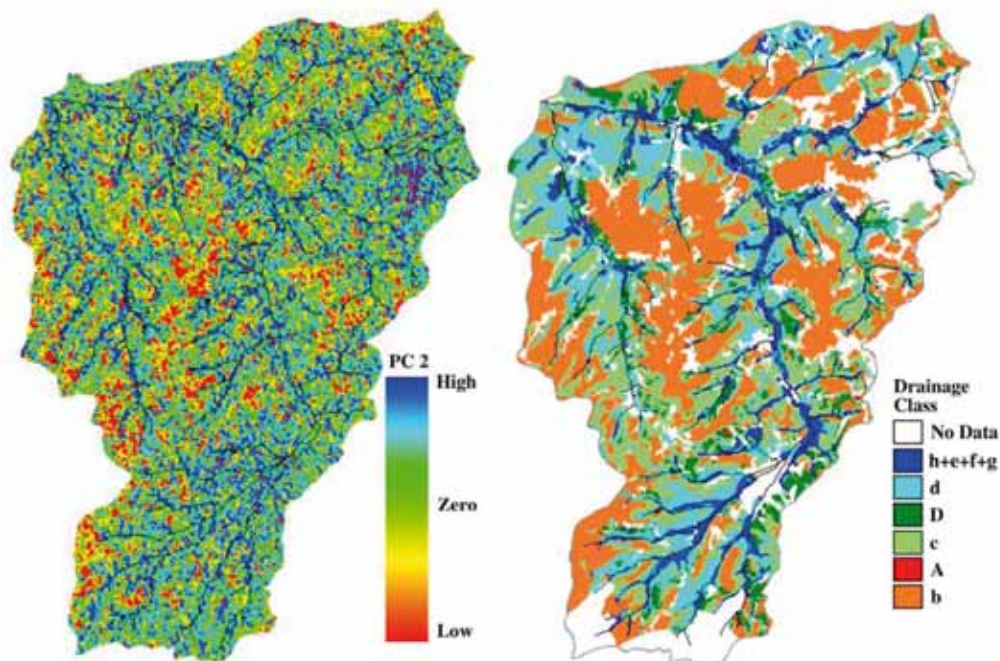
Heights can be mapped by using laser beam returns; airborne LIDAR systems are now used routinely for preparation of DEMs with a height accuracy of less than 10-30 cm, depending mainly on the terrain and quality of the algorithms for filtering vegetation and other aspects. A laser has been employed in a satellite (ICESat) with a height resolution of 3 cm, primarily for monitoring snow and ice fields. Such accuracy offers an opportunity to edit piezometric maps when elevation data of boreholes are in doubt. The data is available for other parts of the world, but the footprint of the laser beam is 70 m sampled at 170 m spacing, restricting the use in area with relief. The handling of ICESat data requires software that can be obtained from the internet.

## 4.8 Soil moisture and radar/microwave remote sensing

### 4.8.1 Image interpretation

Interpretation of soil moisture from grey tones on a radar image is difficult because dark tones, associated with moisture in the uppermost soil, can also be attributed to reflection away from the sensor due to a smooth surface and vegetation wetness and structure and topographic effects.

The pattern of relative soil moisture in a catchment with undulating topography in Belgium was shown on the second principal component images made of eight ERS radar images of the winter period (Verhoest et al., 1998), when precipitation exceeds evapotranspiration. The image was colour coded by slicing (i.e. using a threshold value) and the drainage network was overlaid. Blue colours occurred in areas adjacent to the drainage lines,



**Figure 4-20** Left: Second Principal Component image of ERS radar time series during winter season of catchment in Belgium. Bluish colours correspond to wet conditions and poor drainage (classes shown in map).

Source: Verhoest et al. (1998).

while the well-drained interfluves appeared in yellow to red tones. It can be inferred that these differences are due to the higher soil moisture content, which influences the di-electric property of soils at the lower parts of the topography, since vegetation and surface roughness do not change much during the winter period in the area.

This interesting application, which can be done with common image processing software, has not been used, to our knowledge, in other areas.

#### 4.8.2 *Volumetric soil moisture*

##### *Active radar*

The theoretical basis for measuring volumetric soil moisture by microwave techniques is based on the large contrast of the di-electrical properties of liquid water and dry soil and the di-electric constant influences the backscatter signal of the radar pulse of the active radar systems. However, as mentioned earlier a problem is that surface roughness, depth of measurement (restricted to the uppermost soil layer), vegetation structure and wetness also affect the sensed characteristics, and these effects vary with instrument parameters, incidence angle and frequency of the radar system used.

The active radar satellite systems with wavelengths suitable for soil moisture detection with resolutions of a 20 to 30 m are the ERS 1 and 2 of ESA, ASAR on Envisat, the Japanese JERS-1 SAR and the Canadian RADARSAT, apart from aircraft systems with even higher resolutions.

Although successful experiments have been carried out, see Engman (2000) for a review, studies are in the research domain and data availability limits applications.

##### *Microwave remote sensing*

Passive radar systems, with resolutions of about 20 km, use C (6.9 GHz) and X-band observations (10.7 GHz) for soil moisture estimation. Atmospheric effects at these frequencies are minimal and it is possible to partially filter the effects of vegetation and surface roughness on the brightness temperature observations through relatively simple radiative transfer modelling (Jackson, 2003). AMSR-E observations are available globally with a relatively short (2-3 days) repeat time and will form the basis of the first globally available daily soil moisture product. Standard soil moisture products are a goal of both the NASA Aqua AMSR-E science team and the Japanese ADEOS-II AMSR programme. At the present time both programmes are refining and validating algorithms (Bindlish et al., 2006).

An overview of the systems used for soil moisture determination and its use for groundwater recharge is discussed by Jackson (2002), who mentions other uses of radar in hydrogeology as well. Hoffman (2005) reviews the developments and application of radar, mainly for soil moisture.

One step forward is the global, coarse-resolution soil moisture data (25-50 km) derived from backscatter measurements acquired with scatterometers onboard the satellites ERS-1 and ERS-2 (since 1991 and their successor) and the three MetOp satellites (2006-2020). The passive microwave radiometers and scatterometers allow better accounting for the confounding effects of vegetation and surface roughness, which affect both active and passive microwave systems. The regional maps related to soil moisture are available on the internet: (<http://www.ipf.tuwien.ac.at/radar/index.php?go=ascats>).

Since not all vegetation and roughness effects can be compensated for, the surface soil moisture maps (see cited website) are scaled between 0 (no soil moisture) to 1 (saturated). Most hydrologists require soil moisture information of the soil layer, preferably up to the rooting depths and for that purpose Soil Water Index (SWI) maps are prepared. The index is a measure of the profile soil moisture content obtained by filtering the surface soil moisture time series with an exponential function.

Wagner et al. (2006) compared soil moisture estimates based on ERS scatterometers, AMSR-E on board the AQUA satellite, and on an energy and water balance monitoring system using data from Meteosats (visible and thermal bands), with field soil moisture data collected in an area in Spain. The results show appreciable differences between the methods used but the authors conclude that the trends in soil moisture variations are well replicated, rather than the actual volumetric moisture content. The satellite data set showed much higher temporal variation than the field data, which authors attributed to the fact that the sensor measures soil moisture of the upper 2 cm (satellite data), while the soil moisture field probes were placed at 2-8 cm depth.

More about soil moisture from satellite data and comments on the use for recharge is given in Chapter 14, section 14.6.

## 4.9 Summary and conclusions

In common hydrogeological practice radar images are used for interpretation of terrain units that group vegetation associations with lithology and geomorphology and for the interpretation of lineaments. The image contents can be regarded as complementary to those of multi-spectral images and the two can be merged. The all-weather capability of radar imaging is an asset of importance for areas where clouds prevail. The ground penetration capability is limited to about 2 m in sand covers in hyper arid terrain. Under other conditions, penetration is much more limited.

The worldwide SRTM DEM data is based on SAR radar data, but height and spatial resolution limit the use for improving elevation data for boreholes of doubtful accuracy. A unique hydrogeological application is the differential interferometry, which enables the measurement of ground elevation with high precision, allowing the analysis of subsidence and uplift due to groundwater pumping or recharge respectively.

Studies have demonstrated that volumetric soil moisture can be estimated using active radar, which has the advantage of higher resolutions (30 m or so), but processing of the data is not simple due to the complex nature of the factors affecting backscatter. Furthermore, acquisition of images has an expense and the repeat cycle of the satellite limits the monitoring function.

An interesting development therefore is the effort being made to make processed soil moisture monitoring data available on the internet based on short time intervals (day, at present 3-day periods) at low resolution (25 km) using passive microwave systems.

The limited topsoil depth probed (4-5 cm for the L band and few mm for the X band) is an impediment for hydrogeological application, apart from the difficulty in obtaining absolute values of soil moisture (Kerr, 2007). As will be discussed in Chapter 14, satellite soil moisture data based on radar may have to be combined with other satellite data and soil moisture models for the estimation of recharge or evapotranspiration loss of groundwater.

## References

- Bachir Alami, O., French L., Chorowicz, J. and El Hadani, D. 2004. Modélisation géologique voluminique – Apport de la télédétection et intérêt pour la problématique des ressources en eau: cas de la région d'Al Quway'iyah (Arabie Saoudite), *Geo Observateur*, No. 13, Rabat, pp. 57–69.
- Berlin, G.L., Tarabzouni, M.A., Al-Nasser, A., Sheikho, K.M. and Larson, R.W. 1986. SIR-B subsurface imaging of a sand-buried landscape: Al Labbah Plateau, Saudi Arabia. *IEEE Transactions on Geosciences and Remote Sensing GE-24*, pp. 595–602.
- Bindlish, R., Jackson, T.J., Gasiewski, A.J., Klein, M. and Njoku, E.G. 2006. *Remote Sensing of the Environment*, Vol. 103 (2), pp. 127–39.
- Drury, S.A. and Andrews Deller, M.E. 2002. *Remote Sensing and locating new water resources*. [http://www.unoosa.org/pdf/sap/2002/ethiopia/presentations/12speaker01\\_1.pdf](http://www.unoosa.org/pdf/sap/2002/ethiopia/presentations/12speaker01_1.pdf).
- Chen, C., Pei, S. And Jiao, J., 2003. Land subsidence caused by groundwater exploitation in Su Zhou, China. *Hydrogeology Journal*, 11, No.2, pp. 275–289.
- Dabagh, A.E., Al-Hinay, K.G., Gardner, W.C. and Tawfiq, M.A. 1996, Geologic and hydrogeologic studies of Saudi Arabia under the spaceborn imaging radar-c (SIR-c) Science Plan. In: Evans D.L. and Plaut J.J. (Eds), Progress Reports Principal Investigators-Geology. <http://southport.jpl.nasa.gov/sir-c/>.
- Elachi, C, Roth, L.E. and Schaber, G.G. 1984. *Spaceborn radar subsurface imaging in hyperarid regions*. *IEEE Trans. Geosci.Remote Sensing GE-22*, pp. 383–88.
- ElBaz, F., Maingue, M. and Robinson, C. 2000. Fluvio-eolian dynamics in the north-eastern Sahara: the relationships between fluvial/eolian dynamics and groundwater concentration. *Journal of Arid Environments*, Vol. 44(2), pp 173–83.
- Engman, E.T. 2000. Soil Moisture. G.A. Schultz and E.T. Engman (eds) *Remote Sensing in Hydrology and Water Management*. Springer Verlag, pp. 197–216.

- Farr, T.G., Elachi, C., Hartl, P. and Choudhury, K. 1986. Microwave penetration and attenuation in desert soil: a field experiment with Shuttle Imaging Radar. *IEEE Trans. Geosci. Remote Sensing GE-24*, pp. 590–94.
- Ford, J.P., Blom, R.G., Coleman, J.L., Farr, T.G., Plaut, J.J., Pohn, H.A. and Sabins, F.F. 1998. Radar Geology. F.M. Henderson and A.J. Lewis. (eds) *Manual of Remote Sensing* (3rd edn) Vol. 2, John Wiley & Sons, pp. 511–65.
- Gorte, B.G.H. and Schetselaar, E.M. 2004. Image enhancement and visualization. N. Kerle, L.L.F. Janssen and G.C. Huurneman (eds) *Principles of Remote Sensing*, ITC, Enschede, The Netherlands.
- Grandjean, G., Paillou, Ph, Baghdadi, N, Heggy, E, August, T and Lasne, Y. 2006. Surface and subsurface structural mapping using low frequency radar: A synthesis of the Mauritanian and Egyptian experiments. *Journal of African Earth Sciences*, Vol. 44(2), pp. 220–28.
- Guo Huodong. 2001. *Radar remote sensing applications in China*. Taylor and Francis.
- Henderson, F.M. and Lewis, A.J. 1998. Principles and applications of imaging radar. *Manual of Remote Sensing* (3rd edn) Vol. 2 John Wiley & Sons, pp. 511–65.
- Hoffmann, J., Zebker, H., Galloway, D. and Amelung, F. 2001. Seasonal subsidence and rebound in Las Vegas valley, Nevada, observed by synthetic aperture radar interferometry, *Water Resources Research*, Vol 37(2), pp. 1551–66.
- Hoffmann, J., Galloway, D. and Zebker, H. 2003. Inverse modeling of interbed storage parameters using land subsidence observations, Antelope Valley, California. *Water Resources Research*, Vol. 39(2), pp. 1031–37.
- Hoffmann, J. 2005. The future of satellite remote sensing in hydrogeology. *Hydrogeology Journal*, Vol. 13(1), pp. 247–50.
- Jackson, T.J. 2002. Remote sensing of soil moisture: implications for groundwater recharge. *Hydrogeology Journal*, Vol. 10(1), pp. 40–51.
- Kerr, Y.H. 2007. Soil moisture from space: Where are we? *Hydrogeology Journal*, Vol. 15(1), pp. 117–20.
- Lewis, A.J. 1998. Geomorphic and hydrologic application of active microwave remote sensing. *Manual of Remote Sensing* (3rd edn) Vol. 2, John Wiley & Sons, pp. 567–629.
- Rott, H. 2000. Physical principles and technical aspects of remote sensing. G.A Schultz. and E.T. Engman (eds) *Remote Sensing in Hydrology and Water Management*. Springer Verlag, pp. 15–39.
- Schaber, G.G., McCauley, J.F., Breed, C.S. and Olhoeft, G.R. 1986. Shuttle Imaging Radar: physical controls on signal penetration and subsurface scattering in the eastern Sahara. *IEEE Trans. Geosci. Remote Sensing GE-24*, pp. 603–23.
- Schmidt, D.A. and Burgmann, R. 2003. Time-dependent land uplift and subsidence in the Santa Clara valley, California, from a large interferometric synthetic aperture radar data set. *Journal Geophysical Research*, Vol. 108, Part 9, Section 2, and [seismo.berkeley.edu/~burgmann/PAPERS/publications.html](http://seismo.berkeley.edu/~burgmann/PAPERS/publications.html)
- Sijmons, K., Reinink, G. and Maathuis, B. 2005. *SRTM – Practical Guidelines*. ITC Enschede, The Netherlands. [http://www.itc.nl/library/Papers\\_2005/tech/SRTM\\_pdf.PDF](http://www.itc.nl/library/Papers_2005/tech/SRTM_pdf.PDF).
- Verhoest, N.E.C., Troch, P.A., Paniconi, C. and De Troch, F.P. 1998. Mapping basin-scale variable source areas from multitemporal remotely sensed observation of soil moisture behavior. *Water Resources Research*, Vol. 34, pp. 3235–44.
- Wagner, W., Naeimi, V. Scipal, K. de Jeu, R. and Martínez-Fernández, J. 2006. Soil moisture from operational meteorological satellites, *Hydrogeology Journal*, DOI 10.1007/s10040-006-0104-6.
- Yonghong and van Genderen J.L., 1996. Evaluation of several speckle filtering techniques for ERS1-2 imagery. *Intern. Archives of Photogrammetry and Remote Sensing*, Vol. XXXI, Part B2, Vienna, pp. 164–69.

## Thermal images

### 5.1 Introduction

Thermal remote sensing is based on recording the electromagnetic radiation in the thermal infrared region (TIR) emitted by surface objects as a function of their temperature in two windows: 3.5–5 μm and 8.0–14.0 μm. Therefore, thermal images can be acquired during both day and night.

Various hydrogeological applications of thermal images are discussed in this chapter.

The main application was traditionally the detection of submarine groundwater discharge in coastal water. More recently, pixel-wise assessment of actual evapotranspiration has been made feasible. This requires multi-spectral satellite data including one or more thermal bands and standard meteorological data. This opens new possibilities for groundwater studies, as discussed in Chapter 12, sections 12.3.2 and 12.4 and in Chapter 14, section 14.3. Apart from these applications, thermal images have been used for lineament detection (section 5.2.8 below and Chapter 8, section 8.4.2) and for mapping of wetlands and areas with shallow groundwater (section 5.2.6, Chapter 7, section 7.4.6 and Chapter 14) and recharge.

For some applications of thermal images it is sufficient to note contrasts observed on images produced by automatic-assignment of grey values to DNs of the thermal band. However, contrasts depend on time, taking into account the daily course of the sun and thermal inertia of the ground features.

For detection of features of interest, such as the emergence of groundwater in other water bodies, or vegetated wetlands from the surrounding land, use can be made of diurnal contrasts between land and water or moist and dry soils. Figure 5.1 gives an example (Mason et al., 1972) of wetland mapping.

In other cases it was found that, because of thermal inertia, thermal images could be acquired best during early dawn up till one hour after sunrise or during night-time (Heilman and Moore, 1982). Images acquired at these times best enhance the subtle contrasts between dry and moist soils.

The best timing depends on a number of factors, such as the hydrogeological purpose (shallow groundwater tables, submarine groundwater discharges, etc), soil properties, meteorological conditions, and so on. Since thermal surveys by aircraft are expensive, field studies of radiometric surface temperatures at selected sites are recommended prior to selecting the appropriate timing.

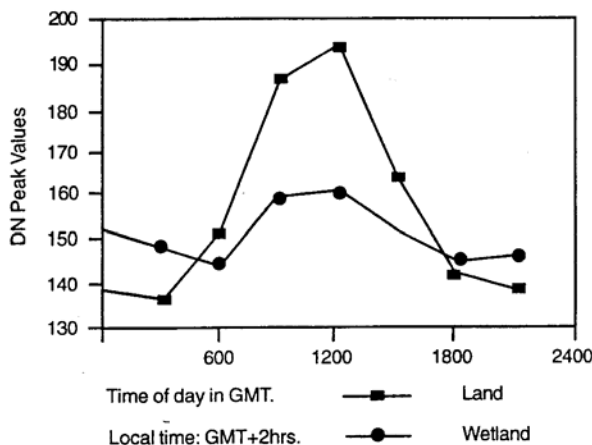


Figure 5-1

Diurnal cycle of thermal contrast between land and wetland (Sudd marsh, Sudan).

DNs from Meteosat images.

Maximum contrast was at around noon.

Inverse contrast between day and night time can also be used for classification.

Source: Mason (1992)

Comparison of a time series of TIR images, without deriving the absolute surface temperatures can be done in a qualitative manner by normalization:

$$T_n = (T - T_{min}) / (T_{max} - T_{min})$$

where  $T_n$  is the normalized relative 'temperature' of the water (between 0 and 1),  $T$  the uncorrected temperature,  $T_{max}$  the maximal temperature and  $T_{min}$  the minimal temperature. However, the DN values of the TIR image may have to be transformed into radiance values, as discussed below.

The handbooks (by e.g. Drury, Sabins, Lillesand et al.), mentioned at the end of Chapter 2, contain useful introductions to some basic physics, thermal properties of ground objects and thermal images. Manuals of Remote Sensing also have chapters dealing with thermal remote sensing, such as those by Hook et al (1999), and Hecker and Gieske (2004). Work done in the US is reviewed by Becker (2006). For reasons of space, attention here is focussed on introducing some hydrogeological applications of thermal images.

A dense stand of vigorously growing vegetation is not short of water and has an emittance that differs greatly from surrounding drier areas. Gregoire (1990) found thermal images more effective for characterizing changes in density and changes of vegetation canopy than NDVI images for larger river basins in West Africa. Wherever vegetation vigour is related to groundwater, as is likely to be observed on dry season images with shallow groundwater, the thermal images provide an indirect way to estimate the relative groundwater – soil moisture status.

Cool patches in a sandy plain in the United Arab Emirates were found on MODIS TIR images analysed for a period. These patches persisted for a week following rainfall in the upstream mountain catchments and were attributed to recharge by transmission loss, as well as transmittance through a fault zone (Ghoneim et al., 2005).

In the northern desert of Mexico, Granados-Olivas and Corral-Diaz (2003) used the thermal band of Landsat TM to locate lineaments and hydrogeomorphic features, associated with possible perched water tables. Out of a number of wells tested, the wells located on top of the lineaments had the highest yields. Leblanc et al. (2003) considered areas with lower temperature on meteorological satellite images in Lake Chad area to correspond to stagnating water and therefore areas with no or little recharge.

The use of TIR for soil moisture studies has been explored in research but the practical application to derive soil moisture from radiance is limited. This is because a number of physical soil parameters have to be known in order to model the effect of soil moisture on surface emittance. Furthermore, effects of vegetation have to be eliminated, while cloud free overpasses should be available to monitor changes.

Thermal images have been used in attempts to relate (shallow) groundwater depth to land surface temperatures. Heilman and Moore (1981) found good agreement between cool areas in night-time thermal images and areas of known shallow groundwater in the Big Sioux Basin, US, and a statistical correlation was found only after correction for the effect of vegetation on emissivity. Daytime images, however, were found to be not useful.

That groundwater depth influences surface temperatures is indicated in a study by Bobba et al. (1992) which relates warm areas in a thermal image to groundwater discharge areas where groundwater is found at shallow depths, in this case in a winter scene of Southern Ontario.

However, as Becker (2006) points out, in reference to soil heat transport studies, the applicability of night-time images for groundwater depths has yet to be critically evaluated, while the utility of daytime thermal images for the same purpose is doubtful because the subtle effects of groundwater will likely be masked by differential heating.

In some cases, thermal images do provide useful information if placed in a known overall hydrogeological context, as examples below illustrate. These pertain to emergence of groundwater along a fault in an alluvial area and differentiation of relative moisture levels in a groundwater-fed wetland or exfiltration area with shallow groundwater of a groundwater flow system in an alluvial fan (Chapter 7, section 7.4.6).

TIR images offer unique possibilities to detect outflow of groundwater in water bodies, such as rivers, lakes or coastal seas, known as submarine groundwater discharge (SGD), discussed in a separate section.

First some basic aspects of thermal images are explained.

## 5.2 General aspects

### 5.2.1 *Derivation of the surface temperature differences of water*

In case the real surface temperature has to be known, pre-processing of the data has to be done to convert the DN<sub>s</sub> to radiances and then to absolute temperature by using atmospheric correction and emissivity data.

Here, only a simplified approach for deriving temperature contrasts for water surfaces is given.

The spectral radiance curve of a so-called ‘black body’, that is, a perfect absorber and a perfect radiator in all wavelengths, has a maximum that depends on the temperature of the radiating object. The law of *Stefan-Boltzman* gives the relationship between surface temperature  $T$  (Kelvin) and total radiant energy  $M$  ( $\text{W m}^{-2}$ ):

$$M = \sigma T^4 \quad (1)$$

Thus, the colder the object, the lower the amount of electromagnetic radiation. *Wien's* displacement law states that the peak of radiation distribution will shift to longer wavelengths as the object gets colder. Compared to the reflectance domain, photons in the thermal infrared domain have low energy and therefore the spatial and/or spectral resolution is reduced (60 m for the thermal band of Landsat-7 ETM versus 30 m for bands in the optical domain).

Two atmospheric windows (3–5  $\mu\text{m}$  and 8–14  $\mu\text{m}$ ) allow most of the thermal radiation to reach satellite sensors.

Most materials do not behave as 'black bodies'; these are *selective radiators*, radiating only a fraction of that of a black body and this fraction changes with wavelength. Thus, such a radiator (ground object) may radiate significant energy in one wavelength, but not in another. This observation is of importance when working with, for example, the five thermal bands of ASTER images, because it allows discrimination of surface materials (by classification, PC analysis, band ratios, etc.).

Surface temperature is not the only determinant of radiance; it depends also on the emissivity of the material. Emissivity is defined as the fraction of energy that is radiated by a material compared to a true black body. Because most materials are selective radiators, their emissivity can change substantially with wavelength, and thus a thermal infrared spectrum of an object or material can exhibit emissivity highs and lows, just like the spectral reflectance curves, shown in the chapter on Image Processing. A cold object with high emissivity can radiate as much energy as a hot object with low emissivity.

The thermal sensor on board a satellite measures in units of spectral radiance ( $\text{W m}^{-2} \text{sr}^{-1} \mu\text{m}^{-1}$ ), where *sr* is the steradian, a unit of solid angle, related to the field of view on the sensor instrument. The amount of energy measured depends on the temperature *and* emissivity of the ground object. If the emissivity of the object in the wavelength sensitivity range of the sensor is assumed to be unity (perfect emissivity), then the ground temperature needed for the amount of radiation received can be calculated with *Planck's* law. That (calculated) temperature is referred to as the radiant temperature or 'brightness temperature' or 'top of atmosphere temperature'.

The actual or true temperature, as measured by a contact thermometer or *kinetic temperature* ( $T_{\text{kin}}$ ) is in most cases more than the radiant temperature ( $T_{\text{rad}}$ ) according to:

$$T_{\text{rad}} = \varepsilon^{0.25} T_{\text{kin}} \quad (2)$$

where  $\varepsilon$  is the emissivity.

The emissivity has to be measured in the terrain, or determined with a method that uses the thermal data in several thermal bands itself (a Thermal Emissivity Separation – TES algorithm, Gillespie et al., 1998), before the true temperature can be calculated from the satellite data. For clear water it is close to unity ( $\varepsilon = 0.99$ ), but most bare soils and rocks have emissivity values in the range of 0.80 to 0.95. This complicates the interpretation of thermal images.

However, if one is interested in local variations of surface temperature of water, such as the temperature contrasts caused by, for example, submarine groundwater discharge, DN values of thermal band(s) can be used because they are directly related to the true or kinetic temperature contrasts of the water.

The detection of springs in water bodies is a common hydrogeological application of thermal images and the question arises of how the surface temperature can be obtained from thermal images.

First the DNs of any band, and thus also the thermal band have to be converted into radiances ( $L$ ), using the equations and values listed in the table presented in Chapter 2, section 2.7.3. For the sake of convenience, the equations are written here, with substitution of appropriate values as:

$$\begin{array}{ll} \text{for Landsat 5:} & L = L_{\text{max}} / 255 \cdot \text{DN} \\ \text{for Landsat 7 ETM} & L = L_{\text{max}} / 254 \cdot (\text{DN} - 1) \end{array}$$

where  $L$  = spectral radiance,  $\text{W m}^{-2} \text{sr}^{-1} \mu\text{m}$   
 DN = digital number (i.e. pixel value of the image)  
 $L_{\text{min}}$  = spectral radiance at DN=0  
 $L_{\text{max}}$  = spectral radiance at DN=DN<sub>max</sub>

The transformation is illustrated in Figure 5.2.



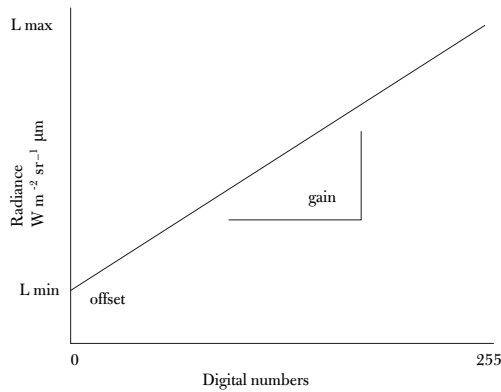


Figure 5-2

Sketch showing the linear relationship between radiance and digital numbers

Gain (slope of line) and Offset (or Bias) for each band can be obtained from header file of image and literature.

L = spectral radiance

For Landsat 5, band 6; Lmin = 1.2378, Lmax = 15.303, Gain = 0.055158 and Bias = 1.2378

For Landsat 7 ETM, band 6; Low gain\* Lmin = 0.0, Lmax = 17.04, High gain\* Lmin = 3.2, Lmax = 12.65.

[\* gains settings are changed depending on type of scene – desert or vegetated area]

The next step is to convert the radiances for each wavelength ( $L\lambda$ ) into radiant temperature ( $T$ , in  $^{\circ}\text{K}$ ) at the top of the atmosphere, under assumption of unity emissivity, by:

$$T = K_2 / \ln (K_1 + L\lambda) \quad (4)$$

where:

$K_2$  and  $K_1$  are constants, depending on the sensor. For Landsat-7 ETM+,  $K_1 = 666.09 \text{ W m}^{-2} \text{ sr}^{-1} \mu\text{m}^{-1}$ ,  $K_2 = 1,282.71 \text{ (}^{\circ}\text{K)}$ . For Landsat-5,  $K_1$  is  $607.76 \text{ W m}^{-2} \text{ sr}^{-1} \mu\text{m}^{-1}$ , and  $K_2 = 1,260.56 \text{ K}$ .

However, the interest lies in the kinetic temperature of the water surface, which cannot be derived in a simple fashion. This is because the sensor measures the radiation ( $L_{\text{sat}}$ ) that passed the atmosphere, and the radiance leaving the surface multiplied by the transmissivity ( $\tau$ ) of the atmosphere plus the radiance produced by the atmosphere, as shown in Figure 5.3. The general equation for  $L_{\text{sat}}$  is:

$$L_{\text{sat}} = [\epsilon L_{\text{bb}} + (1 - \epsilon) L_{\downarrow}] \tau + L_{\uparrow} \quad (5)$$

where  $L_{\text{bb}}$  = the black body radiation  
 $L_{\downarrow}$  = downwelling atmospheric radiance  
 $L_{\uparrow}$  = upwelling atmospheric radiance

In the case of water (emissivity is about 1) and allowing for slight error, the equation reduces to:

$$L_{\text{sat}} = L_{\text{bb}} \tau + L_{\uparrow} \quad (6)$$

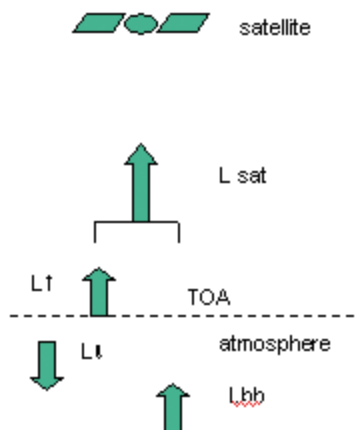


Figure 5-3

Sketch showing radiance in the thermal domain received by satellite sensor is composed of radiance from atmosphere plus radiance from water surface.

TOA = Top of Atmosphere

It is necessary to correct for atmospheric conditions in thermal remote sensing of water temperature because atmospheric transmission and absorption of long wave radiation by water vapour between the sensor and the stream surface influences remote measurements of water temperature. Atmospheric radiation effects must also be taken into account.

In order to calculate the true or *kinetic* surface temperature (in °K or °C) of the water,  $L$  and  $L\uparrow$  have to be known, and this requires use of special codes (e.g. MODTRAN4 and S6, LOWTRAN, see Parodi and Prakash, 2004, for an introduction), and use may be made of so-called 'standard atmospheres'. Simpler derivatives exist and one of them (ATCOR) is included as a package in ERDAS image processing software. The WINVICAR package also includes a customized version of the MODTRAN radiative transfer code for determining and compensating for atmospheric effects in image data. The version of MODTRAN included has been customized to allow the correction of atmospheric effects in data from certain NASA imaging instruments. The package can be obtained from: <http://www.openchannelfoundation.org/projects/WINVICAR>.

Alternatives have been proposed to obtain transmissivity ( $\tau$ ) from image data itself. However, hydrogeological interest lies in the detection of temperature differences of water bodies in rather small areas, for which  $\tau$  and  $L\uparrow$  can be assumed to be constant.

Thus with equations (3) and (4) temperature *differences* of water can be expressed in °K (or in °C by subtracting 273.16 from K).

### 5.2.2 Thermal contrasts caused by outflow of groundwater, submarine groundwater discharge

Thermal airborne scanners can register temperature differences (or contrasts) in fractions of °C. The spatial resolution depends on the flying height, but is such that thermal studies of water in small rivers can be made.

Landsat TM 5 and Landsat TM 7 with spatial resolutions of 120 and 60 m of the TIR band have a thermal resolution of 0.6–0.4°C respectively. The larger spatial resolution compared to the visual or near infrared bands is due to the weak signal of the thermal radiation passing the top of the atmosphere.

Figure 5.4 shows a thermal image made by an airborne thermal scanner of a small part of the coast of Lebanon. The scanner used has a high thermal resolution (about 0.1°C) but images have strong geometric distortion. The image shows outflow of relatively cool groundwater (about 22–23°C) into warmer seawater (27°C). Thermal anomalies were related to three types of linear geological structures that were interpreted on Landsat TM images by Shaban et al. (2005). They differentiated, in order of importance: (1) karstic galleries, (2) faults and fractures connected with inland aquifers, and (3) acute seaward dips of rocks along the coast.

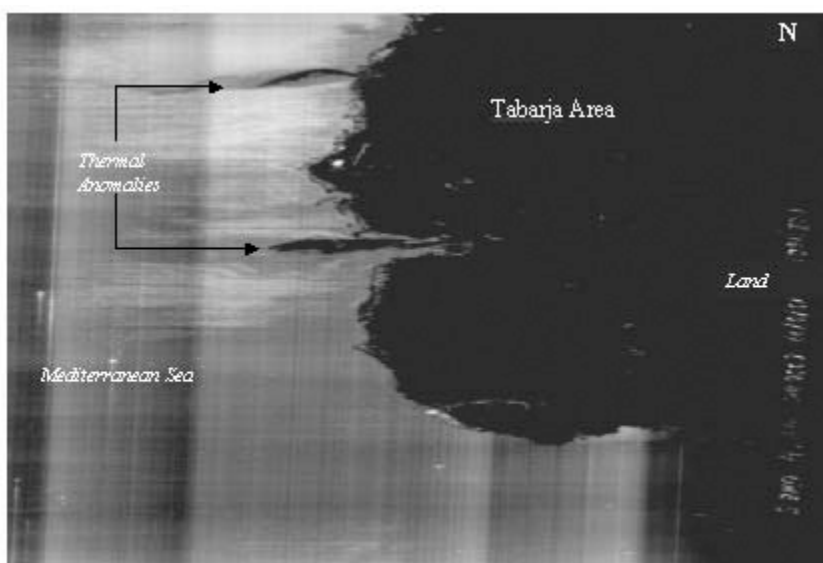


Figure 5-4

**Thermal anomalies of the coast of Lebanon caused by cool groundwater in warmer sea.**

**Aircraft scanner with high thermal resolution.**

**Image requires specific geometric correction for presentation on topographic map.**

**Width across picture is about 3km.**

**Source: Shaban et al.(2005)**

In order to observe groundwater outflow in water bodies such as rivers, lakes or seas, the outflow should create a temperature contrast (also termed anomaly) at the water surface.

A good example of the qualitative use of TIR images in finding zones of groundwater discharge in ground-water-dependent shallow lakes is discussed by Tcherepanov et al. (2005). They used time series of Landsat TM TIR to differentiate on summer time images zones with cooler water in the shallow lakes and zones with warmer water on images of the cold season. These zones were thought to be related to outflow of groundwater. The zoning was refined by considering lake mixing, lake stratification and isothermal vertical distribution. Results were embedded in local hydrogeological knowledge and fieldwork.

Submarine groundwater discharge (SGD) along coasts is a worldwide phenomenon that occurs where hydraulic gradients and permeability are sufficiently large to cause lateral and upward flow of groundwater, chiefly because of differences in density of groundwater with low salinity and seawater.

The outflow of groundwater into the sea may take place in the form of slow, diffuse flow when interstitial water is forced out. The total quantity of groundwater discharged into the sea in this manner can be substantial. However, assuming groundwater has a temperature different from that of seawater, groundwater fluxes in diffuse form are usually too small to create a temperature contrast at the surface, except perhaps in sheltered places such as lagoons. Mixing with seawater will occur so that the chances of observing thermal contrast or anomaly on images of the coast are small if not absent in cases of diffuse flow.

Groundwater may be discharged as concentrated flow by fracture flow or karst springs and possibly at an erosion window in an impermeable layer covering highly permeable fluvial deposits.

A good example of concentrated discharges of groundwater into coastal waters through karstic conduits of limestone terrain or large permeable faults and fractures, is given by Stefanouli and Tsombos (2004).

An intermittent spring was found near the shore of Sicily, Italy, and shows up as four cool pixels on one of the thermal bands of ASTER, see Figure 5.5.

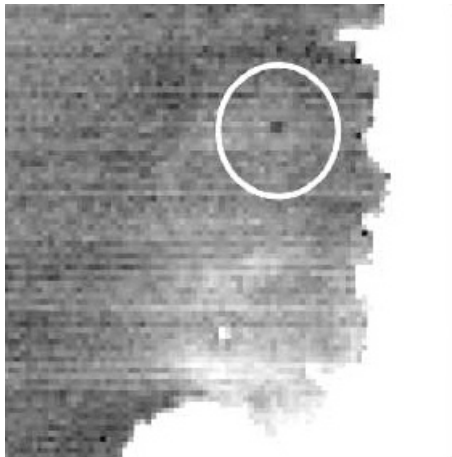


Figure 5-5

**Cool signature of a major intermittent submarine groundwater discharge off the coast of Sicily, Italy (in centre of ellipse), ASTER image, channel 14.**

**Note the influence of sensor noise**

**Image was stretched over narrow range of DN's to display contrasts due to temperature differences**

**Source: Preliminary assessment of the application of space remote sensing for SGD detection (Geosciences Consultants, Report to UNESCO IHP/Water Sciences Division, February 2003).**

The upwelling of groundwater with low salinity in seawater is mainly due to differences in density of the two types of water, while outflow at the sea bottom is governed by the hydraulic pressure of groundwater. The density of water as a function of salinity for three temperatures is shown in Figure 5.6. From the figure it can be deduced

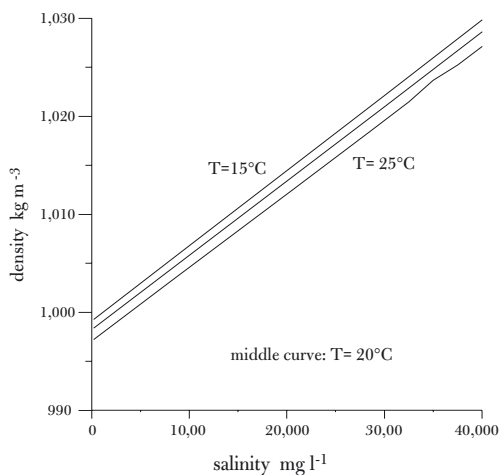


Figure 5-6

**Density of water as a function of salinity for three temperatures**

that useable groundwater, which has a salinity that is much lower (usually  $< 1,500 \text{ mg l}^{-1}$ ) than that of seawater (average is around  $37,500 \text{ mg l}^{-1}$ ), will move from the sea bottom upward to the surface, irrespective of whether it is cooler, warmer or has the same temperature as the seawater. However, detection on thermal images requires a temperature difference between the groundwater and seawater.

Quantified approaches are affected by effects of heat conductance, wind and thermal boundary layer effects, which influence thermal mixing and stratification, discussed by Torgesen et al. (2001). These effects complicate application, particularly to rivers and other turbulent environments.

### 5.2.3 Estimation of discharge of submarine springs

If groundwater has a temperature that is different from that of the seawater, the surface temperatures depend on the discharge per unit area and the degree of mixing. Gandino and Tonelli (1983) developed an equation to estimate the discharge of concentrated SGD outflows. Authors mention that results of the equation deviate by 10 to 15% of measurements on some known springs. First the thermal image (aircraft thermal scanner in their case in the  $9\text{--}11 \mu$  band) is sliced to make an isothermal map with steps of  $0.5^\circ\text{C}$ , see Figure 5.7. The spring discharge is calculated by evaluating the heat exchanged by the outlet with the sea and with the atmosphere, according to (in their notation):

$$m/t = 1/c (T_s - T_m) \{ (5 + V/1100) \sum_i A_i (T_i - T_a) + 4.95 \varepsilon \sum_i A_i [(T_i/100)^4 - (T_m/100)^4] \}$$

where:

- $m/t$  = mass of fresh water discharged per unit time ( $\text{m}^3/\text{hr}$ )
- $c$  = thermal capacity of water =  $1,000 \text{ (Cal/m}^3 \text{ }^\circ\text{K)}$
- $T_s$  = temperature of the spring outflow ( $^\circ\text{K}$ )
- $T_m$  = temperature of the sea ( $^\circ\text{K}$ )
- $T_a$  = temperature of the air at sea level ( $^\circ\text{K}$ )
- $T_i$  = temperature of the  $i^{\text{th}}$  isoradiant surface ( $^\circ\text{K}$ )
- $V$  = wind speed at the sea surface ( $\text{m/hr}$ )
- $A_i$  = area of the  $i^{\text{th}}$  isoradiant surface of the plume ( $\text{m}^2$ )
- $\varepsilon$  = emissivity of the water (for the  $9\text{--}11 \mu$  band it is about 0.9)

In this formula, the first term takes into account the heat exchanged by convection along the contact of the sea and air; the second term is concerned by the outgoing heat radiation of the plume.

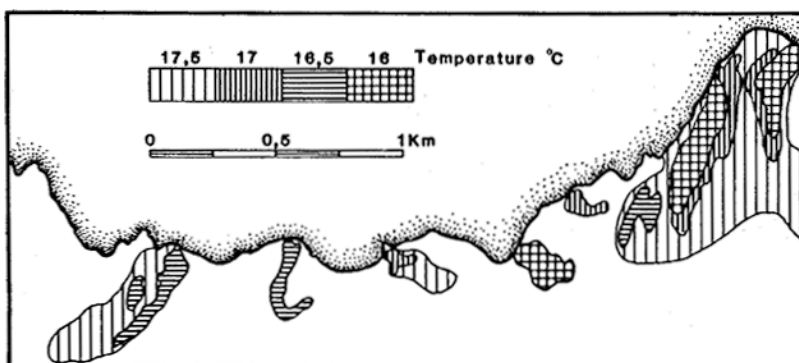


Figure 5-7

Isothermic areas in coastal sea, used to determine discharges of submarine springs.

Source: Gandino and Tonelli (1983)

#### Remarks

Because of the influence of seasonal variation in temperatures of seawater and groundwater, variation of spring discharge (some Karst springs are intermittent), variation of salinity and effects of depth and currents, SGD in concentrated form may exist, but escapes detection on thermal images. Field knowledge of the factors involved is needed to select the best timing for acquisition of images, and starting from known springs, the image may be used for finding additional ones.

The search for a concentrated SGD should of course also consider the hydrogeological conditions, such as presence of Karst limestone, large open fractures and faults and sufficient hydraulic gradients, excluding thus inland recharge areas with no or little elevation.

Usually, differences in temperature at the surface due to groundwater upwelling are small and in order to make them visible stretching (see Image Processing) has to be done over a small range of DN's of the thermal band of a satellite image. However, there is sensor noise, as can be seen on some images shown above, and this makes it often difficult to discriminate in the variation of pixel values a possible presence of relatively small springs from noise.

Anomalies can be wrongly interpreted. During the mid-60s, aircraft thermal scanning was used to survey the coast of Malta and Gozo and springs along the south coast were detected (the main locations were already known to fishermen). On the image of Figure 5.8a, anomalies (A1-2) with a large extension along the south coast of Gozo seem to be present, which would suggest an important SGD. This is unlikely because of (1) the limited size of the recharge area on land, and (2) such apparent anomalies also occur in the sea far away (Figure 5.8b; A3) from the coast. When larger areas are viewed, current patterns become apparent. The lower temperatures occurring along the south coast could well be cooler bodies of seawater passing along the coast during overpass time.

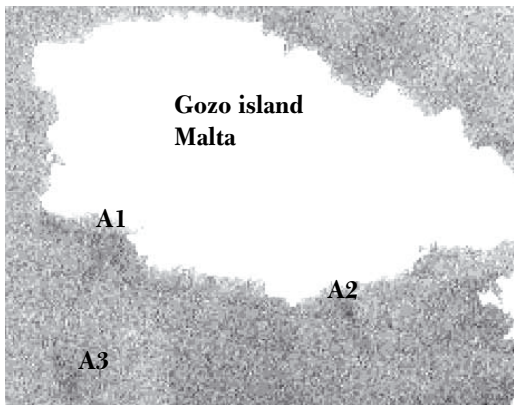


Figure 5-8a Island of Gozo with anomalies? Landsat ETM, 29-09-1999

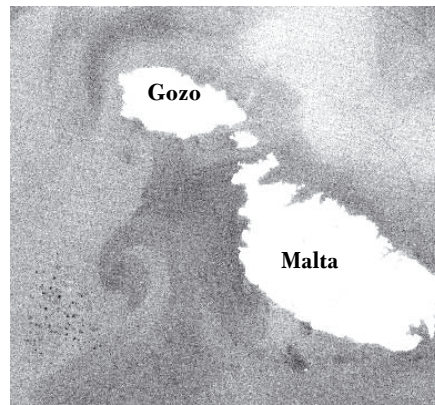


Figure 5-8b Wider view, suggesting no detectable SGD

### 5.2.4 Estimation of discharge of hot springs in a lake

A thermal anomaly observed in the TM band 6 image of Lake Ziway, Central Ethiopian Rift valley, is shown in Figure 5.9. The warm groundwater flows upward because warm spring water (estimated to be 70°C, being the averaged value of nearby hot springs on land) has a lower density than the cooler lake water. Air temperature (meteorological station west of the lake) and lake water temperatures are shown below.



Figure 5-9

Thermal image of Lake Ziway, Ethiopia, showing thermal anomalies, due to hot springs at north eastern part (S) and small spring in south-west (arrow). Anomalies along western shore are due to aquatic vegetation.

With the aid of a steady state model based on energy balances, the discharge of the north eastern springs was estimated to be around 95 m<sup>3</sup> d<sup>-1</sup>.

Image created from TM band 6 of 21 November 1989, stretched from DN 108 -116.

Surface area of the lake is 440 km<sup>2</sup>.

Maximum width of lake is 21.8 km.

A code (by Gieske in: Ayenew, 1998) was written to estimate the total discharge of the springs in the north-eastern part of the lake. The steady state model assumes that the rise in lake surface temperature is due to the vertical heat flux from the springs; exchange of heat with bottom sediments is ignored and that all heat emanating from the springs is transferred to the atmosphere through the heated lake surface.

An energy budget was made and the result for each pixel in the anomaly was integrated to yield the total energy flux ( $Q_t$ ) through the surface. The total amount of heat produced by the springs ( $Q_s$ ) is given by the product of spring discharge, specific heat of water, and the difference in temperature of the water of the hot spring and the lake water. Lake water temperatures varied during 1995–96 from 22°C to 28°C, depending on sampling location and date of sampling. By combining the equation for  $Q_s$  and  $Q_t$  the spring discharge was estimated and was around 95 m<sup>3</sup> d<sup>-1</sup>. If the temperature of the hot springs is comparable to those on land, as assumed, the calculated amount of discharged hot water is negligible in terms of the water balance of the lake, but the surface water thermal anomaly is remarkable (Ayenew, 1998).

### 5.2.5 *Thermal anomalies in rivers*

The detection of groundwater outflow in rivers needs sensors with high spatial resolution if the rivers are not very wide, and aircraft thermal scanners have been used successfully for this detection.

In temperate climates usually the winter period is selected because river water should be cooler than groundwater (as a rule of thumb, shallow groundwater in a temperate climate has a temperature which is the mean annual air temperature minus 1, in °C). Since river flow is turbulent, mixing and dilution of warm groundwater with cool river water, or the other way around, will occur in a downstream direction. The upward flux through the riverbed is small in case of diffuse flow compared to the lateral flux of river water and therefore only substantial groundwater outflows may be detected, unless detailed corrections are made for effects of reflective thermal radiation, surface roughness and turbidity. Thermal stratification may occur in deeper parts with low turbulence.

In warm climates the groundwater may have a lower temperature than the river water and this complicates the detection because the cooler groundwater tends to stay at the bottom and comes to the surface only after some distance over which mixing under turbulent conditions takes place.

Torgesen et al. (2001) in a comprehensive study conclude that ‘After taking into account the radiative properties of the surrounding environment and the physical qualities of the stream, thermal remote sensing proved highly effective for examining spatial patterns of stream temperature at a resolution and extent previously unattainable through conventional methods of stream temperature measurement using in-stream data recorders’.

### 5.2.6 *Groundwater emergence along a fault*

A LANDSAT ETM thermal image (21 October 1990) of an alluvial area in North India is shown in Figure 5.10. In Chapter 2, section 2.4.3 an image of the same area is shown with lower reflectances for moist soils in the area with shallow groundwater.

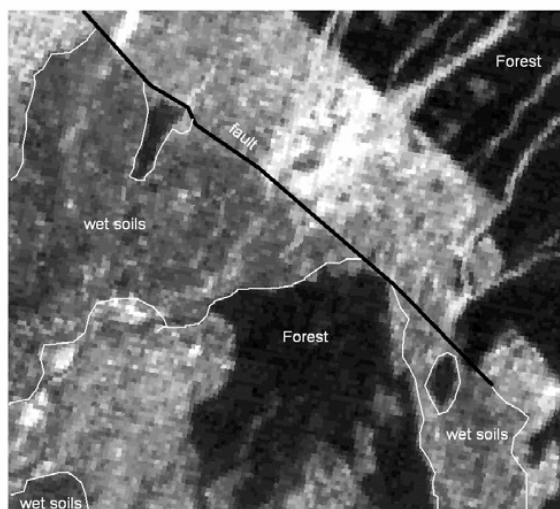


Figure 5-10

**Landsat ETM+ thermal image of an alluvial area in north India.**

**Lower temperatures (dark tones) of wet soils are due to emergence of groundwater along a fault and shallow groundwater table.**

**Uplifted older alluvium marked by white line.**

**Distance W-E is about 18km.**

The thermal image confirms the moist condition of the soil south of the fault because of capillary rise. The lower temperature (dark grey tones) is most likely caused by loss of energy by evapotranspiration. The potential evapotranspiration during the end of October is about  $3 \text{ mm d}^{-1}$ . The nights are cooler than the days, and the heat capacity of wet soils is greater than that of dry soils, therefore, thermal inertia could influence the values recorded, but are overruled by the strong cooling effect due to evaporation.

The largest loss occurs in the forested area and the lowest loss of energy in the dry riverbeds with sands and gravels or in bare fields with sandy soils. Emissivity variations due to vegetation and nature of the soils cause variations in the image, but the overall pattern can be related to the local hydrogeology. The thermal bands of two other LANDSAT images of different dates were consulted and show the same pattern.

### 5.2.7 *Outflow of springs on land*

Some powerful hot springs are found at the northern foot of Mount Kilimanjaro, in Amboseli Park, Kenya. These springs feed marshes and marshy areas in a saline plain and have appreciable annual fluctuation of discharges, but hydrometry is difficult in the marsh environment. The fluctuations can be estimated in an indirect manner, namely by measuring the total wet area using satellite data and multiplying the area with the potential evapotranspiration, as was confirmed by discharge measurements (Meijerink and v. Wijngaarden, 1997). The thermal images are suitable for this purpose, as is shown in Figure 5.11. Lower temperatures, due to evapotranspiration, are associated with open water and with the wet fringe with grasslands and low shrub. For the sake of comparison, Landsat ETM band 5 is also shown. Open water has no reflectance in this band, but the basalts in the northeast and the lavas, ignimbrite and tuffs on the foot slopes of the Kilimanjaro in the south have low reflectance in the NIR domain, just like the wet areas. A NDVI image (not shown) has low values for open water, but high values for the stands of papyrus growing in the marsh while the grasslands have varying NDVI values, depending on the amount of bare soil and the status of the vegetation. By combining an NDVI image and the thermal image, a classification of sub-areas according to their wetness and relative evapotranspiration can be made, as discussed in Chapter 14, section 14.7.2.

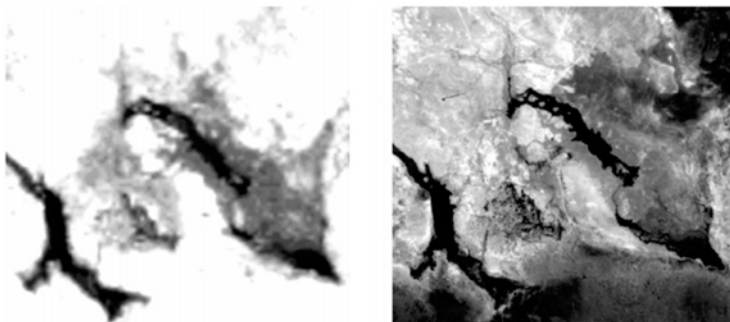


Figure 5-11

Marsh area fed by groundwater,  
Amboseli, Kenya, LANDSAT TM

Left: thermal (b6), Right: infrared (b5)

Extension of swamp (b6) is related to  
amount of discharge of springs

Distance W-E = 11.3km

### 5.2.8 *Relief enhanced by a thermal image*

The example shown in Figures 5.12a and b shows a large outcrop area with massive limestone in west-central Syria. Large faults and fractures traverse the limestone formation. Comparison of the two images show that many of them are best observed on the thermal image (resolution 57 m), partly because of topographic effects. During the overpass in the morning the sun elevation was  $66^\circ$  and azimuth  $112^\circ$  (SE), so that steep slopes facing west had not heated up and the cool pixels show up as dark ones. Some fractures or faults are more or less in the direction of the sun's azimuth and they appear on the thermal image probably because of differences in emissivity of the clay soil or vegetation in the fracture-valleys and the surrounding bare limestone. Shaban et al. (2006) found the thermal band of Landsat TM useful for identifying lineaments in western Lebanon.

The infrared band 5 (resampled resolution of 28.5 m) was selected out of the other non-thermal bands because of the display of lineaments. Note that some large lineaments seen on band 5 are not obvious on the thermal image and vice versa. Obviously both bands should be used for the study of the Karst hydrology of the area.



**Figure 5-12a** Limestone formation, Syria,  
TM infrared band 5 ETM 22-06-2000  
Distance E-W is 11.8km

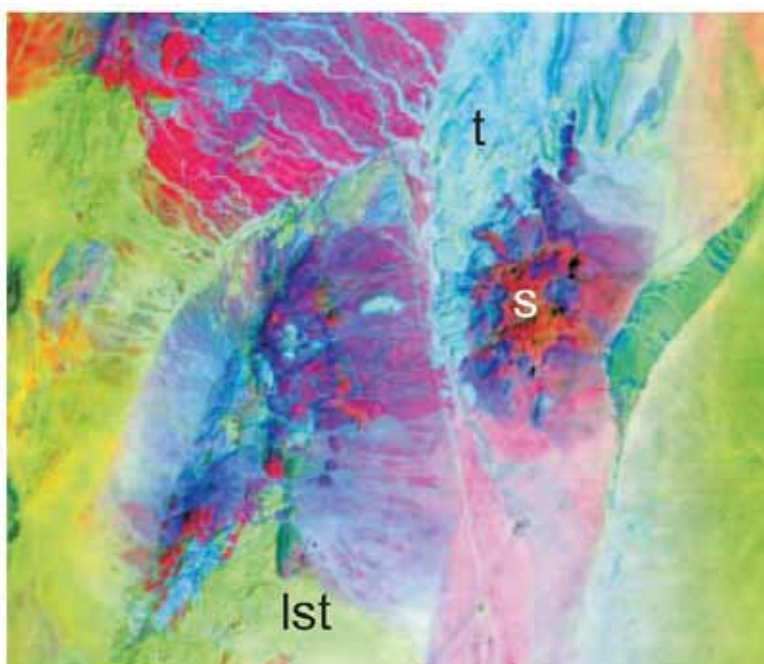


**Figure 5-12b** TM thermal band (b 6), resampled  
to same pixel size as fig.5-12a.  
Note relief features associated  
with faults/fractures.

### 5.3 Rock emissivity mapping

Thermal images can be used in the absence of vegetation to display differences of rock emissivity. An example is shown in Figure 5.13, which is based on many thermal bands of an airborne scanner (a so called hyper-spectral scanner). The colour composite is produced by stretching in the Hue-Saturation colour scheme, also known as decorrelation stretching, after which the image is put back in the RGB scheme. The mineral composition of rocks determines the emissivity spectra and allows discrimination of various rock types. A few have been annotated in the image, as shown in the caption.

The ASTER system has 5 thermal bands and false colour composites can be made with different techniques. However, if vegetation is present, it dominates the emissivity, even the scanty vegetation of semi-arid areas. In areas with scanty vegetation, it is useful to stretch principal component (PC) images based on the thermal bands. The temperature information is highly correlated in the thermal bands and thus tends to appear in the first PC, while emissivity information appears in the lower PCs.



**Figure 5-13**

False colour composite based on  
decorrelation stretching using  
thermal bands of an airborne scanner  
over a desert area.

A few rock units are annotated:

Lst = limestone

S = silicrete, as cap rock

T = tuff

From: Hecker and Gieske (2004).



## 5.4 Use of thermal imagery for evapotranspiration, hydrogeological applications

Setting up a groundwater budget requires estimating the loss of groundwater by capillary rise followed by evaporation from the soil and transpiration of phreatophytes if groundwater is at shallow depths (say, < 10m). Furthermore, in semi-arid regions trees can take up groundwater from large depths in the vadose zone and saturated zone (up to some 70 m), as was demonstrated by Obakeng (2007).

This loss is the actual evapotranspiration (ET<sub>a</sub>), which now can be estimated by satellite data and standard meteorological data, using the surface energy balance method (SEB). The method based on satellite data is termed here SatSEB, to differentiate it from SEB methods using field meteorological data such as the Bowen Ratio. The gist of the method is discussed in Chapter 14.

It must be remarked however, that the accuracy of method in dry regions with deep groundwater levels still remains to be evaluated because a discrepancy was noted between ET<sub>a</sub> values determined by SatSEB (as well as the Bowen Ratio) and deep rooted tree transpiration rates determined by upscaled sapflow measurements, as mentioned in Chapter 14.

If an aquifer is used for irrigation, the net draft (total pumped amount minus return flow) needs to be known, for the water balance and groundwater modelling, but there may be no data on amount pumped. In the sections on NDVI and multi-spectral classification, an empirical approach was discussed to estimate the net draft, but this method depends on empirical coefficients, which may not be valid for the particular area under study. By using SatSEB the (ground-)water loss on the irrigated fields could be estimated quantitatively, and that amount represents the net loss of groundwater to the atmosphere. In Chapter 12, section 12.3 an example from the Sana'a Basin, Yemen, is mentioned where Landsat TM data was used.

In our opinion, the ability to estimate the spatial and temporal pattern of actual evapotranspiration quantitatively is a major step forward in improving water balances of aquifers and preparation of groundwater management plans, not only of productive aquifers.

Applications of SatSEB are mentioned in Chapter 14.

## 5.5 Summary and conclusions

Several examples are given of thermal images showing discharge of groundwater on land and in water bodies, lineament detection (also in chapters 8 and 9) and rock emissivity mapping. A main use of the thermal imagery for groundwater studies is the detection of concentrated groundwater discharge in coastal waters, lakes and rivers. Radiometric principles are mentioned in order to arrive at temperature differences in water in degrees Celsius (or Kelvin). For groundwater budget studies, data of thermal satellite images can be used for the estimation of the spatial patterns of actual evapotranspiration, discussed in chapter 14.

## References

- Ayeneu, T. 1998. *The Hydrological system of the Lake District Basin, Central Main Ethiopian Rift*. ITC Publication no.64 (Contains computer code by A. Gieske).
- Becker, M.W. 2005. Potential for Satellite Remote Sensing of Ground Water. *Groundwater* Vol. 44(2), pp. 306–18.
- Bobba, A.G., Bukata, R.P. and Jerome, J.H. 1992. Digitally processed satellite data as a tool in detecting potential groundwater flow systems. *Journal of Hydrology*, Vol. 131(1/4), pp. 25–62.
- Gandino, A. and Tonelli, A.M. 1983. Recent remote sensing technique in fresh water submarine springs monitoring: qualitative and quantitative approach. *Methods and instrumentation for the investigation of groundwater systems. Proceedings and Informations* (Verslagen en Mededelingen) Committee for Hydrological Research TNO-CHO, The Netherlands (Committee voor Hydrologisch Onderzoek TNO-CHO), pp. 301–10.
- Ghoneim, E.M., Ozdogan, M., Al Mulla, A., Koch, M., Ahmad, K. and El-Baz, F. 2005. Thermal anomalies in eastern Arabia: implication to groundwater recharge. Paper no.44-2 Salt Lake City Annual Meeting, Geol. Soc. of Amer., Abstracts and Programs, Vol.37(7), p.107.

- Gillespie, A., Rokugawa, S., Matsunaga, T., Cothorn, J.S., Hook, S. and Kahle, A.B. 1998. A temperature and emissivity separation algorithm for Advanced Spaceborne Thermal Emission and Reflection Radiometer (ASTER) images. *IEEE Transactions on Geoscience and Remote Sensing* 36, pp. 1113–26.
- Granados-Olivas, A. and Corral Diaz, R. 2003. Fracture trace and alignment analysis for groundwater characterization. *Hydrology of Mediterranean and Semiarid regions*. IAHS Publ. 278 (Montpellier Symposium), pp. 24–28.
- Gregoire, J.M. 1990. Effects of the dry season on the vegetation canopy of some river basins in west Africa as deduced from NOAA-AVHRR data. *Hydrological Sciences Journal*, Vol. 35(3), pp. 323–38.
- Hecker C.A. and Gieske A.S.M. 2004. Thermal remote sensing. *Principles of Remote Sensing, An introductory textbook*, pp. 143–58. N. Kerle N., L.L.F. Janssen and G.C. Huurneman (eds) ITC, The Netherlands.
- Heilman, J.L. and Moore D.G. 1981. Ground Water Applications of the Heat Capacity Mapping Mission. Satellite Hydrology. Proceedings of the Fifth Annual William T. Pecora Memorial Symposium on Remote Sensing, Sioux Falls, South Dakota June 10–15, 1979, pp. 446–49.
- Hook, S.J., Abott, E.A., Grove, C., Kahle, A.B. and Pallaconi, F.D. 1999. Multi-spectral thermal infrared data in geologic studies. A.N. Rencz (ed.) *Manual of Remote Sensing* (3rd. edn) Vol.3, pp. 59–110. John Wiley & Sons.
- Leblanc, M., Razack, M., Dagonne, D., Mofor, L. and Jones, C., (2003) Application of Meteosat thermal data to map soil infiltrability in the central part of the Lake Chad Basin, Africa. *Geophys Res Lett* 30(19), Art. No. 1998.
- Mason, I.J, Harris, A.R., Moody, J.N., Birkett, C.M., Cudlip, E. and Vlachogiannis, D. 1992. Monitoring wetland hydrology by remote sensing: A case study of the Sudd using infra-red imagery and radar altimetry. Proceedings of the Central Symposium of the ‘International Space Year’ conference, Munich, Germany, 30 March – 4 April.
- Meijerink, A.M.J. and van Wijngaarden, W. 1997. Contribution to the groundwater hydrology of the Amboseli ecosystem, Kenya. J. Gibert, J. Mathieu and F. Fournier (eds) *Groundwater/surface Water Ecotones: Biological and Hydrological Interactions and Management Options*. International Hydrology Series, UNESCO, Cambridge Univ. Press.
- Obakeng, O.T. 2007. Soil moisture dynamics and evapotranspiration at the fringe of the Botswana Kalahari, with emphasis on deep rooting vegetation. ITC Dissertation no.141, Enschede, The Netherlands.
- Parodi, G.A. and Prakash, A. 2004. Radiometric correction. *Principles of Remote Sensing: An introductory textbook*, pp. 143–58. N. Kerle, L.L.F. Janssen and G.C. Huurneman (eds) ITC, Enschede, The Netherlands.
- Roerink, G.J., Su, Z. and Menenti, M. 2000. S-SEBI: A simple remote sensing algorithm to estimate the surface energy balance. *Physics and Chemistry of the Earth Part B- Hydrology Oceans and Atmosphere*, Vol. 25(2), pp. 31–37.
- Su, Z., 2002. The Surface Energy Balance System (SEBS) for estimation of turbulent heat fluxes at scales ranging from a point to a continent. *Hydrol. Earth Sys. Sci.*, Vol.5(1), pp. 85–99.
- Shaban, A., Kwahli, M., Abdallah, O. and Faour, G. 2005. Geologic controls of submarine groundwater discharge-application of remote sensing to north Lebanon. *Environmental Geology* Vol.47(4), pp. 512–22.
- Stefanouli, M. and Tsombos, P. 2004. Identification and monitoring of fresh water outflows in coastal areas: Pilot study on Psahna area/Evia Island-Greece. *Bull. Geol. Soc of Greece*, Vol. XXXVI, pp. 928–37.
- Tcherepanov, E.N., Zlotnik, V.A. and Henebry, G.M. 2005. Using Landsat thermal imagery and GIS for identification of groundwater discharge into shallow groundwater dominated lakes. *International Journal of Remote Sensing*, Vol. 26 (17), pp. 3649–61.
- Torgesen, O.E., Faux, R.N., McIntosh, B.A., Poage, N.J. and Norton, D.J. 2001. Airborne thermal remote sensing for water temperature assessment in rivers and streams. *Remote Sensing of Environment*, Vol. 76(3), pp. 386–98.

# Hydrogeological image interpretation

## 6.1 Introduction

The 'art' of image interpretation is extracting information of hydrogeological relevance from images that depict the terrain. Interpretation focuses in fact, on two interrelated aspects:

1. The (hydro)geological subsurface configuration
2. Surface features which influence recharge and show evidence of groundwater outflow.

Although interpretation work is nowadays executed on the computer screen, it should be taken into consideration that large-scale hardcopy images with a transparent overlay offer the advantage of screening the whole image during the interpretation process, allowing the interpretation to be cross-checked over the whole scene. The interpretation can then be transferred to a computer file, either manually or by scanning the overlay (Bannert, 1980).

It would be preposterous to claim that the subsurface configuration can be obtained by image interpretation, but no proper assessment of the hydrogeology can be made without such knowledge. Obviously, geological maps, sections, and drilling logs and geophysical data are required, but in the attempt to develop conceptual groundwater models it is useful to try to extrapolate the geological surface features observed on the image to the subsurface. The effort is particularly worthwhile when large-scale (say 1:25,000 or 1:50,000) geological maps are not available and few drilling records exist. The pre-field image interpretation map will make the fieldwork more efficient. Preliminary geological sections should be attempted in the initial stage of the hydrogeological survey, because this will clarify where the difficulties lie that need to be inspected in the field and by exploration drilling and geophysical survey. It is common experience that re-interpretation of images, after field data have become available, yields information not noted earlier. In other words, visual interpretation needs knowledge of hydrogeological field situations. Outcrops of the same formation may appear differently on an image, depending on the local conditions of weathering, erosion and accumulation of creep or sheet wash deposits. The vegetation on those outcrops is often profoundly disturbed by man and therefore varied in nature. Often, visual interpretation is a matter of mental filtering; deciding on what is and what is not significant. Mental filtering is in fact an iterative process; what may have been disregarded initially, may be reinstated as a significant feature at a later stage and vice versa, especially in interaction with field evidence. For this reason the term 'art' was used in the opening sentence.

The geological framework, with gross hydrogeological properties attached to the formations and layers, provides a context for the interpretation of surface features by supplying the right questions, such as:

- Do the images contain evidence of permeable conditions (non-eroded thick soils, colluvial deposits, wind blown sands, etc.) over a dipping rock sequence with good transmissivity? If so, the recharge may be high, particularly when no deep-rooted and dense vegetation is present.
- What happens to the direct runoff of large outcrop areas (e.g., inselbergs)? Does the runoff spread out in a weathered fringe zone surrounding the outcrop and thus providing recharge water or is the runoff flowing out of the area through an incised drainage network?
- If a single direction of basic dykes is noted on the image, is it so that lineaments having an angle to the dyke direction are associated with vegetation while other lineament directions have no or little vegetation? If so, the lineaments with vegetation are likely to be tensional fractures and contain groundwater.

- Appearance of water in rivulets, for example, in ephemeral beds, signifies the emergence of groundwater. If the pattern of the emergence points in an alluvial area is fairly straight, could that be a sign of a buried barrier, such as a fault bringing up rocks of low permeability, or a buried escarpment?
- If a confined aquifer is known to exist, are there signs of groundwater appearing on the surface on dry season images, possibly related to lineaments? If so, artesian conditions are likely.
- Observed disappearance of base flow in river beds indicates water loss by infiltration in permeable river bed deposits with the groundwater level below the river bed. The question then is: what happens to that water? Does it appear further downstream (a typical case of a groundwater flow system in an alluvial fan aquifer) or is it not seen again (flowing out through rock formations, large fractures)?

With the rich variety of hydrogeological situations in different climates, geology and geomorphology, many such questions can be posed, on the basis of expectations. In the practice of groundwater exploration, there is a two-way reasoning process involved in hydrogeological image interpretation: on the one hand images help in building up expectations, and on the other the basis of expectations images are scrutinized, and often re-interpreted at a later stage for groundwater-related features at the surface.

### 6.1.1 *Geological and geomorphological interpretation*

Most regions of the world have been covered by geological surveys. For that reason, knowledge of photogeology using stereo aerial photographs has dwindled. Handbooks dealing with photogeology usually start with analysis of drainage patterns and photo-tones, followed by mapping of simple structures using the photo-geological symbols for strike and dip, evident and uncertain contacts, faults (if stratigraphic evidence of displacement exists) and lineaments. These are followed by examples of more complex structures – metamorphic, igneous and other terrain.

These publications are still to be recommended to those working in areas where geological maps need updating and information at more detailed levels is required. Some well-known books dealing with geological image interpretation are mentioned at the end of the chapter on Image Processing.

This chapter includes only a few examples of structural geological interpretation in sedimentary terrain for hydrogeological purposes. Other types of terrain are discussed in later chapters.

Nowadays, geological maps are available or can be transformed into digital format and the lithologic units and structural elements can be overlaid on images, usually satellite images. This is of much help in updating and adding information by image interpretation.

Geomorphological interpretation is of importance in hydrogeological studies, especially for recharge, because of two reasons:

- Landforms are associated with soils, superficial deposits and denudational history affecting the nature and hydrogeological properties of the near surface materials, termed ‘overburden’ in engineering. As is discussed in the chapter on Alluvial Terrain, use can be made of the type of landform and the associated properties. In the following chapters many examples are given on the significance of geomorphology and groundwater.
- The proportion of rainfall available for recharge of groundwater depends not only on the permeability of soils and rocks, but also on the residence time of rainwater over groundwater intake areas. Shallow soils or soils with swelling clays (vertisols or ‘black cotton soils’), integrated drainage networks with high density, sloping areas and so on, cause rapid runoff, leaving relatively little water for recharge. Opposite conditions, whereby much water is retained, are, at least potentially, more conducive to recharge.

### 6.1.2 *Drainage density and permeability*

It has been suggested that a measure for permeability is drainage density (i.e. total length of drainage channels per unit area), in the sense that permeable conditions are associated with low drainage density and vice versa.

In the case of permeable deposits, such as wind-blown sands or fluvial terraces, low drainage density is indeed due to high infiltration, leaving little water for the formation of incised channels. However, development of drainage lines depends also on relief, or more precisely, the local base level of erosion, which is governed by tectonic or geomorphological history. Such permeable deposits can be highly dissected during a phase of incision when they have low resistance to erosion, which is generally the case of non- or semi-consolidated sands.

In fluvially eroded landscapes low drainage densities are often found on permeable rocks, such as sandstone (primary permeability) and karstic limestone (secondary permeability), but for different reasons. Soils developed on sandstone should also be permeable and resistant to erosion. In the case of karstic limestone, low drainage density is due to large depression storage and internal drainage, leaving little water for erosion by overland flow while the residual clay or clay-loam soil and certainly the limestone outcrops are resistant to erosion.

In many regions drainage density is not related to permeability of the soil/rock complex. In warm sub-humid to dry regions the dominant surface runoff takes place in the form of sheet wash over pediments. This is the case in the example of Figure 6.1 (below) where areas are underlain by shale (indicated by Ns in the image) with low permeability, without or with few drainage lines. In the chapter on Crystalline Basement Terrain, other examples of pediments – no drainage lines – on impermeable rocks are given. In fact the drainage lines on pediments or glacis consist of numerous discontinuous micro channels, too small to be detected, even on high-resolution images. This chapter also provides an example of contrasting drainage densities on the same lithology; low density on an old planation level and high density on the adjoining eroded part.

Flood basalt outcrops in the form of plateaux have low permeability but may have no developed drainage pattern. Outcrops of lava flows of more recent age may have very rough surfaces so that all rainwater is stored in numerous surface depressions, yet the rock may be impermeable.

However, low drainage density on young volcanoes can be a sign of high permeability, which is the case when the volcano is built up mainly by tuffs and agglomerates.

From above, it is evident that there are no easy rules for image-interpretation of estimated or relative permeability. In this context, it is useful to point out that empirical methods may be used for the estimation.

The well-known Runoff Curve Number method of the US Soil Conservation Service provides a practical guide for estimating direct runoff from daily rainfall records, based on a few classes of soil and land cover. An example is shown in the chapter on Artificial Recharge. The lower the estimated runoff, the higher the potential recharge.

For the Sahel, Rodier (1975) was one of the first to present tables with runoff coefficients for catchments of different sizes and rainfall zones, with an aerial photograph to illustrate the categories of ‘typical catchment permeability’.

### **6.1.3 A practical guide**

The Hydrolab expert system (Poyet and Detay, 1989; Detay and Poyet, 1990), which starts with image interpretation directed to groundwater exploration, chiefly based on stereo aerial photographs of igneous and metamorphic terrain in conjunction with basic data, field studies and geophysical exploration, was developed using data from West Africa, particularly Cameroon. The system consists of ‘rules of expertise’ (i.e. the decisional process of experts, cognitive aspects) and ‘interpretative models’ (i.e. statistical decision models). Well location is but one of a number of problems facing prospective well owners. To deal with water quality, future lowering of water levels in wells, improper construction and so on, the expert system includes decision-making parameters. However, here the concern is with the cognitive aspects of image interpretation, which include geomorphological environment, drainage pattern, position of the piezometric level (in weathered and fractured zones), jointing (fracture) systems, rock type, and extent and thickness of the weathered layer. These aspects are discussed in the chapter on Crystalline Rocks. Other cognitive aspects, not connected to image interpretation were depth of borings, climate data, geo-electrical investigation and influence of the thickness of the saturated weathered zone.

At this place, only the relations between drainage pattern and drilling-site criteria for areas with rainfall of 1,300 mm are reproduced in Figure 6.1 (from Bourguet et al., 1980, in Detay and Poyet, 1990). Several types of drainage, shown in Figure 6.1 can be recognized in images shown in Chapter 10.


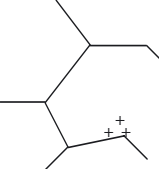
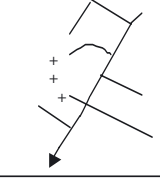



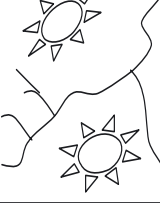
<i>Drainage pattern</i>	<i>Type</i>	<i>Morphological observations Location study criteria</i>	<i>Saprolite thickness,m.</i>	<i>Drilling success,%</i>	<i>Dug-well success,%</i>
	1	Bend and low gradient network. Floodable zones. Ferruginous cuirass. Numerous traditional dugwells. Lack of geological criteria. Location criteria: Floodable zones, lineaments, slip vein, elevation between village and 'marigot'. (Dambo)	20 - 25	16	35
	2	Polygonal network. Eroded interfluves. Many outcrops. Narrow intermittent stream. No traditional Dugwells. Location criteria: Wide and secant lineaments. Convergent faults (nodal point). Break of slope with changes in vegetation.	10 - 15	64	/
	3	Orthogonal or oblique network with high gradient. Eroded interfluves. Narrow, intermittent stream. Inselbergs, outcrops. Location criteria: Flats (saprolite>5 m., Convergent faults (modal point), Vein, Small thalweg.	15 - 20	38	52
	4	Low gradient of the network. Gneiss. Ferruginous cuirass. Many traditional dug-wells. Location criteria: Lineaments, Flats, Eroded interfluves	15 - 24	43	42
	5	Forest zone. Impossible to see drainage pattern. Granitic zone. Low gradient of the network. Ferruginous cuirass. Many dug-wells. Large drainage zones	Large	?	26
	6	Schists and granites. Zone with variable direction of the network. No dug-wells. Location criteria: Lineaments, Large thickness of saprolite, Convergent faults (nodal point).	Variable	26	No dug-wells
	7	Birimien schist with parallel lineaments. Much saprolite. Low gradient of the network	> 27	7	-
	8	Wide floodable zones. No geologic index. No dug-wells	> 60	weak	-
	9	Drainage pattern going around hill of green rocks in Birrimien schists. Location criteria: Lineaments, Faults (nodal point), Quartz veins, Small 'marigot'.	15 - 35		

Figure 6-1 Relations between drainage pattern and site location for drilling. Rainfall 1,300 mm. Source: Bourguet et al., 1980 (redrawn after table in Detay and Poyet, 1990).

## 6.2 Hydrogeological interpretations of sedimentary rock terrain

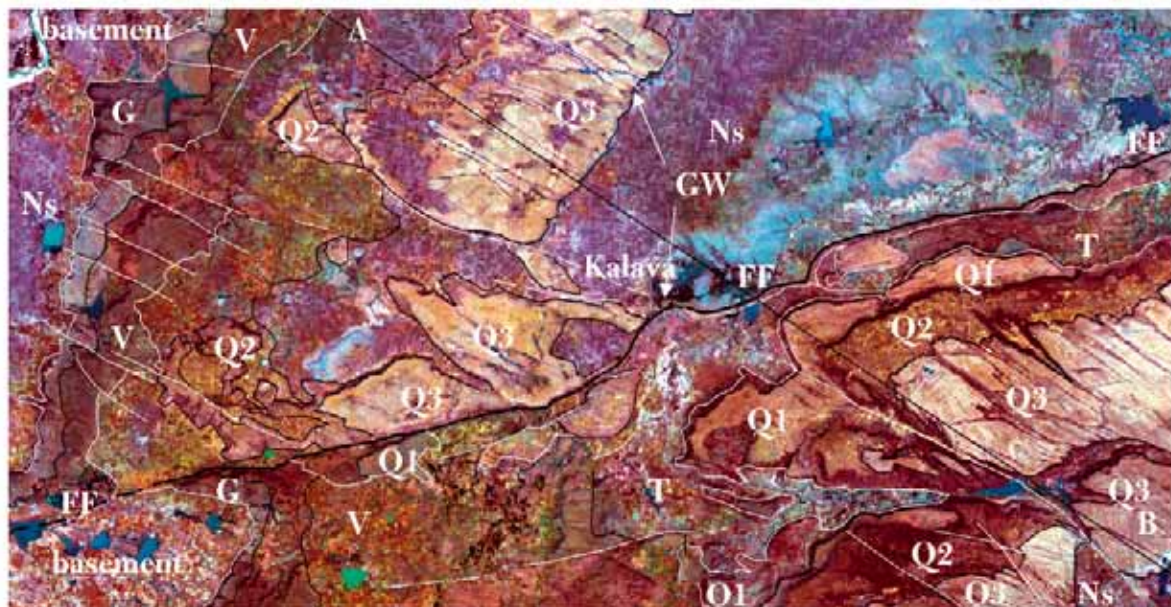
### 6.2.1 Example 1. Area around Kalava, Andhra Pradesh, India

The following example (Figure 6.2) shows how geological image interpretation and field check leads to the sketch of the geological section (A-B), see Figure 6.3, which explains the emergence of groundwater (GW) at two places.

#### *Geological interpretation and added field observations*

For a proper understanding of the geology, it should be mentioned that a larger area has to be interpreted, because there are two major unconformities in the area shown:

1. Contact of the basement and the G (Gulcheru Quartzites), V (Vempalli, dolomite, shale) formations and T, Tadpatri shales and sills,
2. Contact of a younger series of quartzites and shales, termed here Q1, Q2 and Q3 and the youngest Ns (Nandyal shales). In fact, para-unconformities exist in the younger series, and for that reasons some of the outcrops do not lie in succession but younger rocks may overlap older ones, such as the Nandyal shales (Ns), which are even found on the basement, west of the escarpment of the G formation (see Fig. 6.2). All rocks are of Precambrian age.



**Figure 6-2** Area around Kalava, Cuddapah Basin, India, TM composite (bands 5,3,1). White curved lines: unconformities. Black lines: contacts, FF fundamental fault, white semi straight lines: faults and major fractures, GW emergence of groundwater. A-B geological section (see Figure 6-3). For other symbols, see text. Distance E-W is 31.5km.

In the large, low and flat outcrop area in the northwest corner a zonation can be observed between densely cultivated area, and zones without agricultural fields. These zones correspond to very gently dipping shale beds with differing lime content.

The initial pre-field interpretation, which relied greatly on stereo-aerial photo-interpretation (Meijerink et al., 1984) of the geology left many questions unanswered, which were clarified during fieldwork, resulting in the boundaries shown on the image.

The major structures can be observed, such as the southwesterly dips of the G and V formations, the very gentle dips or flat lying Q1–Q3 beds and the large fault-cum-flexure FF. Faults and large fractures are seen in the competent rocks of the G and V formation along the western part, but their possible continuation is lost in the argillaceous rocks. The fractures in the Q3 quartzite are prominent because they have been widened by pseudo-karst and are partly eroded. However, there is no evidence that they extend deeper than the Q3 quartzite, except a few small faults in the southwest corner (between the symbols Q2 and Q3). At places some minor fractures can be seen in the Q2 and Q3 layers.

A point of interest is the asymmetric fold, whose northern flank with vertical dips (apparent on aerial photos and in the field) corresponds to the fault/flexure FF. Outside the image shown, this fault can be traced much further to the west in the basement and to the east over long distances.

The image interpretation is not straightforward because of the para-unconformities, presence of argillaceous rocks of different age, while different land covers cause variations in reflection on the image of a single formation. However, for the development of the conceptual hydrogeological model, an attempt has to be made to draw a geological section. This is not difficult to do, along the line A-B, if complexities in the Vempalle formation south of the fault FF are ignored. This is justified for the purpose here because the rocks can be considered as an aquiclude. The section is shown in Figure 6.3, with vertical scale exaggerated.

### Hydrogeology

At two places emergence of groundwater can be seen, as indicated on the image. Other water bodies are surface reservoirs.

Little water appears along the contact of Q3 and the shale Ns in the northern part, most likely groundwater that flowed in the Q3 fractured quartzite with pseudo karst (the formation is known as the ‘pinnacled quartzite’). Possibly there is a minor contribution of water from the underlying quartzite because a break of slope in the groundwater surface causes a concentrated upward flow.

A large waterlogged area occurs just north of the fault FF in the centre of the image shown. Perennial springs are found in that area. Three sources for the water can be stipulated:

1. Water (confined to semi-confined) derived from the formations Q1-Q3, driven by heads in the higher ground of the intake area.
2. Confined water from the lower quartzite G and from dolomite beds of the V formation, if the assumption is made that karstic flow can occur at such depths.
3. Water (semi confined to confined) flowing along the large fault FF, with intakes from the older quartzite, weathered parts and surface water in the basement and possibly karst water from the V formation, south of the fault.
4. The location of the emergence area is due to a combination of structural elements and to topography. Displacements of the Q3 quartzite indicate the presence of fractures/minor faults, as indicated on the image by interrupted lines, forming permeable planes for water under pressure to flow upwards.

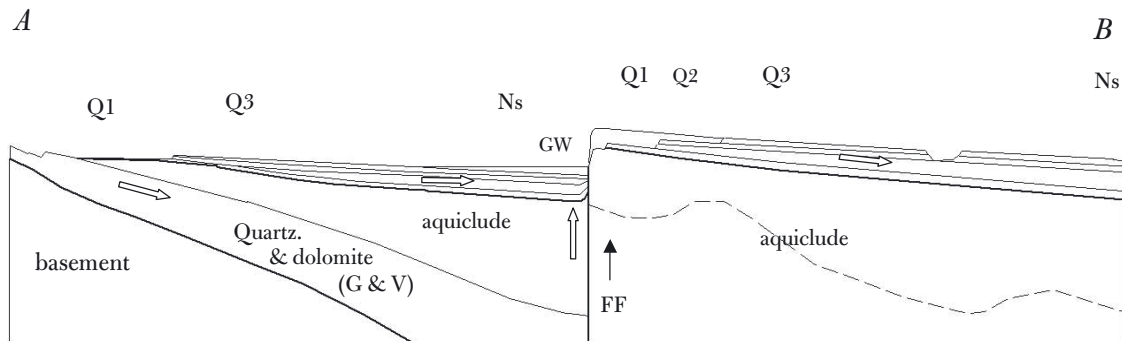


Figure 6-3 Geological section A-B explaining emergence of groundwater near Kalava, for location and symbols, see figure 6-2.

The minor faults intersect with the large fault at the emergence area and abut against the impermeable rocks across the fault and the thickening shales eastwards.

The area is also the first low area topographically encountered and the virtual piezometric groundwater surface may rise above the land surface. This is also likely for the pressure distribution along the major fault zone, with a gradient from west to east.

The relative importance of the sources of water has to be assessed by hydrochemistry and isotope studies. Also of relevance is the fact that a few springs with tepid water occur at higher elevation along the southern margin of the fault.

There is much more to say about the hydrogeology of the area, but the point to be made here is that by image interpretation (satellite and stereo airphotos) and rapid geological reconnaissance, some major aspects of the hydrogeological conceptual model can be established. From this point onwards the further details of the model



have to be developed, whereby more detailed interpretation of images, preferably at higher resolution can be of assistance.

### *Observations*

What can be learned from this example is:

- A given rock unit may have different spectral properties, depending on the land cover, as influenced by ownership (Forest department, communal grazing land, etc.). Knowing that, the units can be mapped by geological reasoning.
- Rock units, which look similar on the image, can be of different age, such as various shales.
- This should be borne in mind when attempting to sketch the geological section, on which the conceptual groundwater model relies.
- Faults and large fractures may not be seen as evident linear elements on the image, but inferred from the position of outcrops, a matter of elementary geological construction.

### **6.2.2 Example 2. Cape Vert peninsula, Senegal**

This example describes a study of the BRGM for Société Nationale d'Exploitation des Eaux du Sénégal (SONES). (Contribution by: T. Pointet.)

The objectives of the study in the Cape Vert peninsula in Senegal were to locate preferential infiltration zones, and prepare a water supply borehole drilling programme, avoiding a costly general survey of the whole region by geophysics methods (electric sounding).

The specific contribution of the remote sensing approach was the cross-combination of the stratigraphy with the fault system interpreted on SPOT satellite images. The structural analysis also made use of geological sections based on data from deep boreholes.

#### *The area*

The hydrogeological investigation is an important element for urban and tourism developments along the 'Petite Côte de Dakar', southward to the 'Cap Vert peninsula', Senegal.

Two aquifer layers contain most of the groundwater resource. Their replenishment is the consequence of the rainwater percolation on preferential zones, where the aquifer layers are exposed or are covered with pervious surficial sediments.

The deep hydrogeological pattern was poorly known. The region is intensively cut by regional faults some of them measuring several tens of kilometres, with possible vertical displacements of tens of metres, thus bringing to the surface either one or the other formation, and sometimes non-aquiferous strata. An old structural scheme was still used suggesting the region was affected by a north-south horst.

Moreover, two phenomena limit possible access to freshwater:

1. within large zones, water is saline, thus unexploitable, mainly along the sea coast and along some inland areas.
2. as a result of active groundwater exploitation, slow saltwater intrusion is provoked. The new sites for exploitation recommended in this survey are chosen to prevent acceleration of saline intrusion.

Many boreholes were drilled for phosphate exploration and provided a good amount of stratigraphic data. A preliminary project intended to cover the region with a general geophysics campaign, using an electrical sounding method, to interpolate the stratigraphy between boreholes. The fault sizes and their density and distribution suggested a more complicated pattern than a horst, and therefore it was decided to make a structural analysis with the aid of satellite images. The speeding up of the investigation phase was expected, though allowing a suitable detailed definition of the geological structure, to locate the preferential infiltration zones throughout the surface reflectance analysis, thereby helping to locate the best zones for groundwater replenishment, which could normally be the most favourable zones for shallow or mid-deep groundwater exploitations.

A first attempt to map the elevation curves for any widely distributed layer relying only on the borehole cross sections led to very complicated contours, not compatible with such a sedimentary area; in other words an unacceptable result.

*First interpretation: the geometric structure*

The salient aspects are:

1. Interpretation of the two SPOT images covering the study area permitted to delineate the 2D fault system, being the intersection of 3D fault system with the ground surface.
2. Vertical displacements can affect these faults, setting one formation at different elevation from one side to the other of a fault.
3. If the displacement is a mere vertical translation, one assumes that the formation dip, strictly along the fault, is identical from one side to the other.
4. The borehole cross-sections help to assess the local elevation of any layer, within each 'solid' polygon or compartment, delineated by a system of faults.

These four propositions framed the method for making a new structural design. The upper surface of the Paleocene aquifer was selected as the reference layer and was followed for the whole region.

Within any solid polygon this layer may have a dip, a cylindrical or even spherical-shaped surface, but from one edge to the other of a margin fault it is auto-similar, in other words, the same dip, orientation and curve radius.



Figure 6-4 The structural pattern and the distribution of infiltration prone areas

The fault identification was done on standard images, sorting out areas with dense vegetation (dark green), with sporadic vegetation (light green), with thin sand covers (light yellow) and with light silica soils (red). These elements help to locate and differentiate the run off and seepage prone areas.

In each polygon one or more boreholes were found to be suitable. From one layer to the other, the structure was supposed parallel. The faults were supposed vertical.

The method, developed over the whole zone, brought up a new scheme (Figure 6.4), where one can observe that the elevation curves of the Paleocene aquifer are rather smooth – much smoother than were suggested by the earlier scheme, and the general morphology of this surface was quite acceptable from the geological point of view and much more in accordance with a continental margin structure than with a horst structure.

By consulting the map, it became easy to measure the vertical displacement along each fault, and spot the major ones, which could create barriers across the dominant groundwater flow direction. In some cases these barriers could prevent percolation from saline zones, or on the contrary, constitute a screen between a recharge zone and an exploitation zone. It was then decided to confirm their position and displacement through geophysical prospecting. By limiting the geophysical survey to the faults, much effort was avoided.

A quick look at some 1/500,000 meteorological satellite images showed that some of these faults have major development, possibly hundreds of km.

### *Second interpretation: the surface signature and the infiltration potential*

The second piece of evidence from the satellite images was the semi-homogeneous colour (signature) within the polygons, and the contrast between two neighbouring polygons. A field survey showed correspondence of the signature with the vegetation and soil cover, the latter two being associated with infiltration, runoff and soil moisture retention. Sandy areas with little vegetation correspond to high reflectivity values (Figure 6.5), while shale surfaces with semi-permanent moisture content and grass cover, even late in the dry season, have low reflectivity (Figure 6.6).

The combination of these aspects enabled the deduction that schematically the groundwater flow ran from the plateau to the sea, starting from the infiltration areas and following the vertical aptitudes of the hydrogeological structure, partly driven by the major faults, and independent from the saline zones which were (also) controlled by the fault system.

The conclusion of the study was the selection of sites for new boreholes. A mathematical model helped to forecast the eventual risk of seawater intrusion near the coast. A piezometric map, made after the image interpretation, confirmed some bulging surface within the first unconfined aquifer under the infiltration prone areas.



**Figure 6-5 Infiltration prone area.**  
Clear soil cover, corresponding to the surficial weathering of an infiltration prone rock. No permanent grass cover and trees finding out the water in mid dip layers.



**Figure 6-6 Semi impervious areas.**  
Mainly clayey formation, allowing a semi permanent low vegetation cover, indicating frequent moisture content within the soil, and a low percolation towards deeper layers.

## References

- Bannert, D. 1980. Multidisciplinary geoscientific investigations of Landsat imagery of Upper Volta. Proc. 14th Int. Symp. Remote Sensing of Environment, Costa Rica, Vol. II, pp. 787–89. Ann Arbor.
- Bourgouet, L., Camerlo, J., Fahy, J-C, and Vaillieux, Y. 1980. Méthodologie de la recharge hydrogéologique en zone de socle cristalline. *Bulletin du BRGM*, Section III, No.4, pp. 273–88.

- Detay, M. and Poyet, P. 1990. Application of remote sensing in field engineering geology: the artificial intelligence approach. Proc. Intern. Symp. Remote Sensing and Water Resources, Enschede, The Netherlands.
- Meijerink, A.M.J., Rao, D.P. and Rupke, J., 1984. Stratigraphy and structural development of the Precambrian Cuddapah Basin, SE India. *Precambrian Research*, 26, pp. 57–104.
- Poyet, P. and Detay, M. 1989. Hydroexpert: an example of a new generation of compact expert system. *Computers and Geoscience: An International Journal*, Vol. 15(3), pp. 255–67.

# Terrain consisting of unconsolidated deposits

## 7.1 Introduction

Geological mapping in the past has often concentrated on pre-Quaternary formations, although in more recent times the Pleistocene and Holocene deposits are receiving more attention because many of the productive aquifers are situated in Quaternary deposits. Furthermore, recharge, groundwater levels and salinity problems can be associated with details of the fluvial and coastal geomorphology.

In regions where the Quaternary is little known, remotely sensed images offer a unique means of identifying and mapping the various types of deposits, as will be discussed and illustrated below.

It must be said that in many countries the Quaternary has been investigated intensively, using a wealth of data concerning borehole logs, geophysical data, various types of age determinations and so on. The research has shown that much of the sub-surface complexities have little or no surface expression, and the formations were mapped using field data and accurate topographic maps. In such areas remote sensing, such as thermal and infrared images and radar soil moisture studies can be applied to study patterns of intake and exfiltration areas due to flow systems or specific problems, such as seepage of polluted water from dumps or seepage of floodwater below dykes and so on.

In order to map Quaternary formations, it is useful to recognize the geomorphological processes that have led to deposition because of the relationship of process and type of materials. Also of interest is assessment – at least in a preliminary manner – of the overall permeability of the deposit. For that reason a geomorphological classification is discussed.

Furthermore, in some cases deductions as to the possible subsurface conditions can be made, on the basis of what can be interpreted on images, using general geological and geomorphological knowledge. For example, the effects of transgression and subsequent regression leaving sandy beach deposits, which may now be partly covered by younger fluvial deposits (e.g. the Cauvery delta example, below) can be inferred and sites can be selected for further field investigations (drilling) to ascertain the situation. Some ‘in-depth’ interpretation can be done when neo-tectonic movements have taken place, as is discussed in section 7.4.5.

Remote sensing can provide essential information on problems in flat areas with unconsolidated sediments (fluvial and eolian) having a high groundwater table, causing water logging and salinization. In such areas where digital elevation models required for land reclamation are either too crude, because accuracies of < 50 cm are desirable, or too expensive (Lidar surveys), relative elevation information can be obtained by using relations between landforms and relief, with associated vegetation, soil, hydromorphic and salinization patterns, and by studying their dynamics with sequential images.

## 7.2 Geomorphology, Quaternary geology and hydrogeological properties

The main types and characteristics are summarized and interpretation aspects are mentioned.

### 7.2.1 *Fluvial deposits and landforms*

The nature of fluvial deposits depends on the type of river.

The deposits of *braided rivers* are generally coarse-grained: boulders, gravels and sand mixtures of terrace deposits in mountain areas and along mountain fronts, where steep gradients prevail. Braiding rivers are associated with a high-bed load and strong variations in discharge and are therefore often found in semi-arid regions.

When the river has a relatively gentle gradient, deposits of braided rivers may consist of silt and sand. Because

of the unstable, braided nature and the large width-to-depth ratio of the river, the overall horizontal permeability of braided river deposits is fairly uniform.

*Meandering river* deposits have typical lateral variation of sandy and clay/silt bodies. The sandy deposits are those of scroll bars, having an inclination to the direction of the (former) channel, coarse-grained bed load deposits (sands and gravels) usually not exposed, and the sandy to silty natural levee deposits. The clayey deposits are the inter-levee basin (backswamp) deposits, clay plugs in closed-off channels. A valley fill or an aggraded floodplain consisting of meandering river deposits is therefore characterized by much lateral and vertical variation.

Deposits of rivers that are neither typical braiding nor meandering may have intermediate characteristics.

It can be expected that river terrace deposits and valley fill deposits have a more or less continuous coarse layer of bed materials left by lateral shifts of the river, and these are overlain by the finer grained (suspended load) deposits laid down during flooding. On older terrace deposits a heavier texture of the uppermost zone could also be due to soil formation (weathering of minerals, biological homogenisation, etc.).

The type of river deposit is also influenced by the provenance, in other words, the type of sediment delivered from the catchment to the river, due to lithology, relief and climate, governing the intensity and type of erosion processes. The climatic changes of the Pleistocene influenced the nature of the deposits, as illustrated in Figure 7.1, manifested as a belt of fossil braiding river deposits in juxtaposition with meandering river deposits of younger age, of which some large scroll bars can be seen separated by partly clayey swales. Because of overgrazing locally tiny dunes and deflation patterns can be seen on the air photo, indicating the sandy nature of the braiding river deposits. Many shallow wells (of up to about 8 m depth) are found in the braided river deposits, but also on the meander scrolls. Deposits in the upper right quarter of the figure were laid down by a river type that was transitional between braiding and meandering; these have been partly reworked by wind and wash and are locally covered by a thin clay blanket of flood deposits. The young levee deposits of a local river are indicated in Figure 7.1.

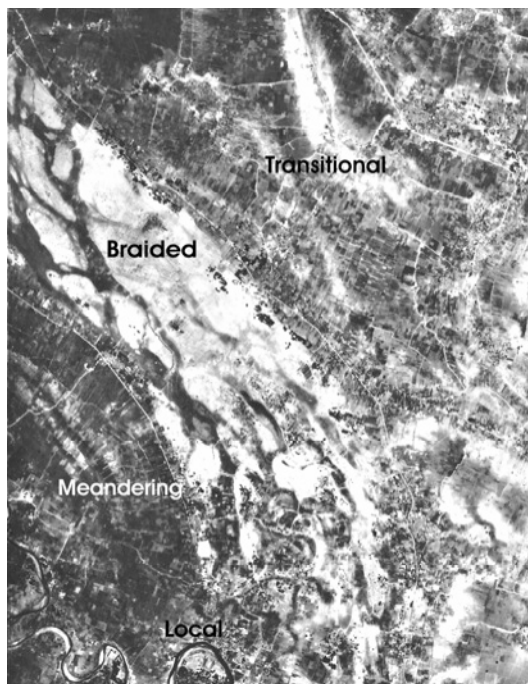


Figure 7-1

**Older floodplain deposits in the Ganges alluvial plain, India, showing change of river regime from braiding to meandering and to a transitional form.**

**On original photo deflation and microdunes can be observed on braided bars indicating sandy nature of the deposits. Meandering deposits show sandy scroll bars, and clayey swales and backswamp deposits, also found in transitional parts.**

**Change from braiding to meandering is likely to be related to climatic changes during Pleistocene.**

**Distance E-W is 8.3km.**

### 7.2.2 *Eolian deposits*

Wind-blown sands are of interest because of their permeability, facilitating infiltration and allowing storage of water (Bannert, 2004). The permeability and specific yield depends on the mean grain size, sorting and packing. The first two factors are directly related to the wind regime; strong winds transport coarse sands but also the variability of wind speeds influences the overall sorting of the deposit.

In many regions fossil sand deposits are found, which were laid down during earlier drier climatic periods and soil formation and diagenesis will have influenced their properties, particularly the older deposits. Loess is laid down in the wide fringe of desert areas, hence it is likely that older sand deposits have received loess, which by

eluviation and biological activities has entered the sands, causing tighter packing and reduction of permeability, but enhancing soil fertility.

Volcanic tuff deposits, also eolian, will be discussed in the chapter on Volcanic Rocks.

The hydrogeological properties will have to be determined by field methods, but interpretation of images can yield some information. If the various dune forms (parabolic dunes, barchans, longitudinal dunes) have a clear expression, no alteration of the sands can be expected. Such fresh forms usually have high reflection because of the high quartz content (however, gypsum dunes can occur near playas). If the dune forms are not pronounced and have less spectral reflection than fresh sands, the deposits are not recent. Reworking by occasional sheet wash may have taken place due to decreased permeability of the topsoil (loess, possibly some upward capillary transport of salts and lime) and colluvial accumulation in depressions may have taken place, which can usually only be observed clearly on stereo airphotos. Most of the older deposits have a vegetation cover.

Even a few drainage lines may have developed, which could be due to decreased infiltration with respect to rainfall intensities, or to spring sapping due to groundwater outflow at the contact of the sands and rock of low permeability below the sands.

### 7.2.3 *Lacustrine deposits*

Climatic changes in the past have caused expansion and shrinkage of lakes in many parts of the world. Lacustrine (lake) deposits consist generally of clay and silt deposits, fine-grained eolian material (tuff, loess, fine grained sand), reworked material by wave action along shores, local delta deposits, organic material and possibly diatomite deposits. At the apex of former deltas, sand bodies of limited extension and thickness may be encountered as the result of deposition due to rapid reduction of flow velocity where the riverbed load entered the lake. Wind blown sand deposits may have encroached on relict lacustrine deposits. Various remote sensing sensors (active radar, multi-spectral and thermal) have been used to map relict shorelines and associated lacustrine deposits, particularly the former extension of Lake Chad (Pachur and Rottinger, 1997; Leblanc et al., 2006).

Thermal images have been used to evaluate relative infiltration in lake deposits (Leblanc, 2003). In case lacustrine deposits are dissected, the study of slope forms of incised drainage lines may indicate cohesion of the deposits. In the Kathmandu Valley, Nepal, slumps and soil flows are associated with soft clays, which are impermeable.

Thickness of lacustrine deposits is difficult to interpret, but a good expansion of deposits covering fully sub-surface topography may indicate substantial thickness.

An example of lacustrine deposits as evidenced by former shorelines of the terminal lake Abiyata in central Ethiopia is shown in Figure 7.2.

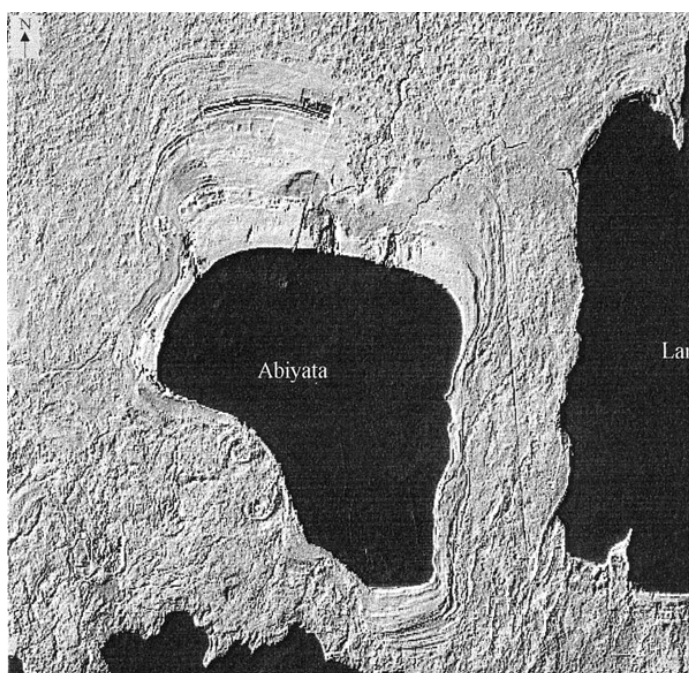


Figure 7-2

Filtered Landsat T<sub>m</sub> Pan image (14.25m resolution) of Lake Abiyata, central Ethiopian Rift, showing strandlines and lake deposits.

Black strip between strand lines and a large pit are excavations for mining salts.

Distance E-W is 34km.

Source: Ayenew, 1999.

### 7.2.4 Coastal deposits

These consist of fluvial deposits, discussed above, beach ridges and lagoon deposits.

The sandy former riverbeds usually associated with natural levees are of interest because of their permeability and good water quality, and such courses can be observed on images. They may be partly covered by suspended load deposits (clay blanket, because of aggradation of backswamps) and the former river courses (paleochannels) may only be faintly seen, but still traceable on imagery, unless fully covered by a clay blanket of substantial thickness.

An overall decrease in grain sizes from the apex of the delta in a downstream direction can be expected and such change can be noted on images by differences in land cover and hydraulic geometry of the active river. In some deltas braided river deposits (see above) near the apex gradually make place in downstream direction for a system with levees and large backswamps, with associated thick clay layers and only localized sandy river bed sediments.

The coastal beach ridges consist of sands brought by longshore transport and sands transported by wind from the beach. The thickness is highly variable, from a few metres only in case of chenier deposits, to several tens of metres. In the latter case they form good aquifers provided rainfall is sufficient to create a substantial body of freshwater to suppress the brackish water interface.

The thickness of the beach ridge/dune complex depends on sand supply and transgressive-regressive movements during sea level rise during the Holocene (see section 7.3.3).

### 7.2.5 Glacial and periglacial deposits

The rich variety of glacial and periglacial deposits which cover large parts of the Earth, the important differences of their hydrogeological properties, and presence of important aquifers would justify adequate attention, but is considered to be outside the scope of this text.

## 7.3 Image interpretation at sub-regional scale, overviews

Areas with Quaternary deposits have usually little relief and it is therefore difficult to obtain an overview and map the various types of deposits. Satellite images provide such overviews.

The interpretation and delineation of the units is based on geomorphological criteria, whereby land cover patterns may be used in case they are adjusted in one way or another to the soils and their internal drainage conditions, which are associated with the type of deposits. It is difficult to postulate the nature of the deposits and their possible thickness by image interpretation, except for general observations with regard to the type of depositional process and environment.

### 7.3.1 Identification of aquifer, Area around Pati, Central Java, Indonesia

Figure 7.3 shows a large low-lying area between a high volcano in the north and folded Tertiary rocks (marl, shale, soft sandstones) in the south with moderate relief. The slopes of the strato-volcano have been differentiated according to their position and steepness. Of interest here is the Middle Volcanic slope (M) consisting of fluvio-volcanic breccias and tuff layers with moderate to good permeability and considerable thickness while the Lower Volcanic footslope (Lo) consists of sheetwash deposits and small natural levee and channel deposits, of limited thickness. These may interfinger with the heavy textures deposits of the (neo-tectonic) depression (D) and the marshy (S) area. A drainage canal was dug to drain the swamp, but the gradient is too gentle for the drain to be effective.

Tertiary rocks dipping north form the southern fringe of the alluvial area consisting of glacial deposits, differentiated in older (UT) and younger (LT) deposits. Minor uplift and tilting along the axis of the depression took place. The uplift is evidenced by the presence of low cliffs along the coast, just NE of the area shown in Figure 7.3. The term 'glacis' is preferred here because the deposits are fine-grained due to the nature of the rocks in the provenance area and the rivers draining the hills are generally small. The overall sand content of the glacis deposits is found a little more in the upstream part than in the lower part, except for the small natural levee and channel



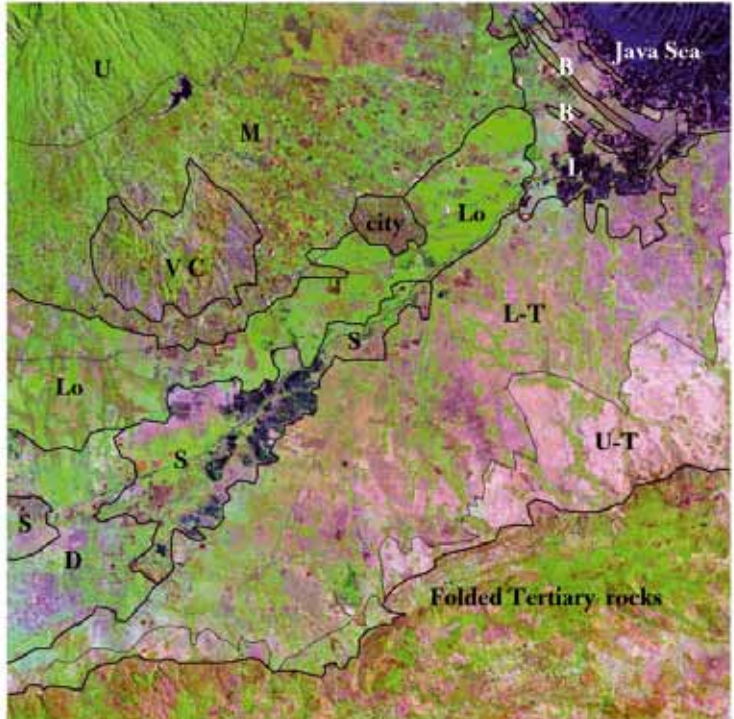


Figure 7-3

Differentiation of Quaternary deposits as related to the geomorphological origin in area around Pati, Central Java:  
 U-T = older glacia,  
 L-T = younger glacia,  
 D = depression,  
 S = swamp,  
 L = lagoon,  
 B = beach ridges,  
 Lo - lower volcanic foot slope,  
 M = middle volcanic slope,  
 U = upper volcanic slope,  
 VC = volcanic complex.  
 Distance E-W is 33.3km.

deposits. If there had been a strong gradation from coarse to fine, the term alluvial fan deposits would have been more appropriate than the term glacia deposits.

The deposits of the middle to lower volcanic slope form the only shallow aquifer in the area. No deeper borehole logs could be retrieved, but it is likely that poor aquifer conditions prevail in the remainder of the area.

### 7.3.2 *Effects of past climatic change on fluvial and tidal deposits, Area in SW Gujarat, India*

This example (Figure 7.4) is included because the type of deposits reflect climatic change from very dry, possibly with a contemporaneous low sea level to a phase which was more humid lasting during the times of the Harappan

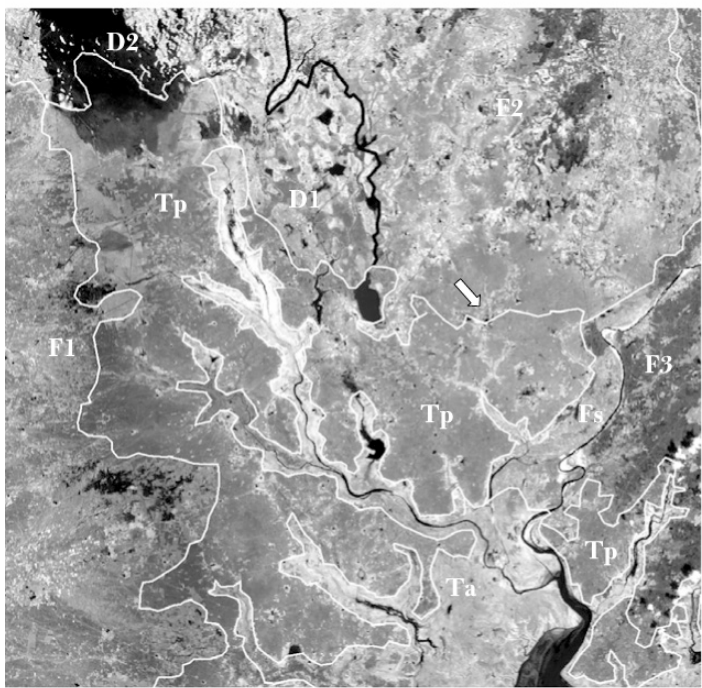


Figure 7-4

Quaternary deposits of part of SW Gujarat, India.  
 Landsat TM, PC 1 image  
 F2 = older levee-backswamp complex of precursor Sabermati River  
 F3 = younger fluvial deposits Sabermati R.  
 Fs = active floodplain  
 Tp = tidal plain  
 Ta = active tidal plain/channels  
 F1 = fluvial deposits local rivers  
 D1 = fossil dunes, partly submerged  
 D2 = same, re-activated  
 Arrow points to Lothal (see text).  
 Distance E-W is 58km.

civilisation and a change to the present semi-arid conditions, while neotectonism also played a role. The changes affect the permeability of the deposits and allow for inferring shallow subsurface conditions.

The fossil levee-backswamp complex of the former Sabermati River (F2) has been laid down during a wetter climatic period, when marshes existed in the upstream catchment of the river, which regulated the discharge (required for a meandering type of river) and sediment load. Shallow wells tap the groundwater in the levee and channel complexes (see the enlarged part, Figure 7.5), which are recharged by rainfall.

The wet period occurred after a dry one, when the eolian deposits (D) were formed. An interesting feature (location indicated by an arrow in Figure 7.4) is the presence of a manmade small basin, thought to be a harbour of the Harappan civilization (2500–1600 BC) at the village of Lothal, at the transition of a former river channel and tidal channel. Hippopotamus (now extinct in India) have been portrayed during the Harappan period, and the species can be associated with marshes, which do not occur nowadays in the catchment of the Sabermati River. The present climate is semi-arid; the present Sabermati River is braided and flash flows and river shifts occur. The sub-recent Sabermati deposits (F3) have lighter textures (sand, silt and some clay) and there is less difference in horizontal permeability than in the fossil levee-backswamp unit. The active floodplain (F3) consists mainly of silts and sands and river recharge plays a role in configuration of the fresh-saline water interface. The unit F1 consists of fluvial deposits by small rivers and these are fine-grained, while (impermeable) clays deposited by sheet wash dominate in the downstream part. During the monsoon some non-saline water infiltrates in the more permeable deposits. Evaporation in the nine non-monsoon months exceeds by far the rainfall; hence a salinity gradient towards the tidal deposits is likely in the fluvial units. The pattern of cultivated fields reveals a relative low salinity of soil water, although salt tolerant crops are grown in the lower part of unit F1.

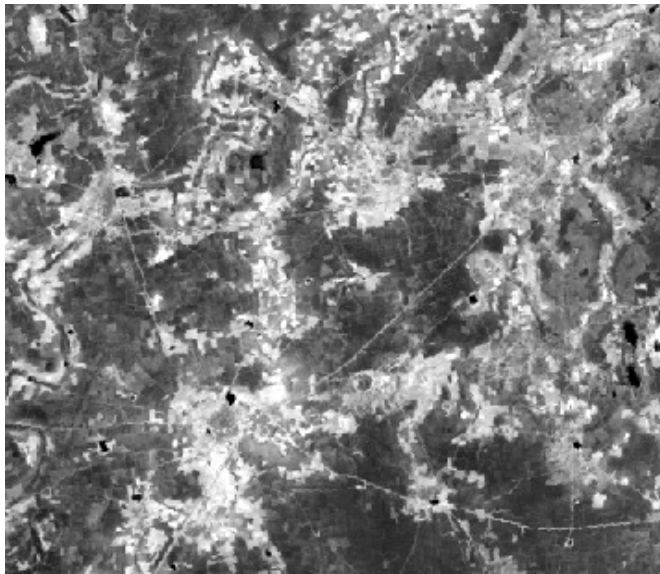


Figure 7-5

Enlarged part of area north of Lothal (see figure 7-4), showing fossil channels of meandering river, natural levee (sands) and backswamp (clay) deposits.

Shallow wells tap groundwater in the levee complexes.

Landsat TM b4.

Distance E-W is 15 km.

Saline conditions prevail in the tidal units (Tp and Ta), but also in the depression of the unit with fossil dunes (D), where small bodies of fresh groundwater are found only in the larger sand accumulations.

The presence of fossil eolian sands indicates a phase with a drier climate than the present one, probably coinciding with a low sea level during a glacial period when NE passat winds from central Asia reigned. Since the fluvial deposits overlay the eolian deposits, it is possible that below the levee and backswamp complexes wind-blown sands and/or braided river deposits are located, which are more permeable than the meandering river deposits.

The region is known for its neotectonics and seismic hazards, for example, the Bhuj earthquake, March, 2001. Lothal is now several metres above mean sea level, indicating an uplift/tilting as also evidenced by a terrace bluff between the F2 unit and the active floodplain. At places, wells turned salty after the earthquake.

For a hydrogeological study of the area the interpretation map provides information of the surface conditions only and may be used for adding data from boreholes and hydro-chemical data.

### 7.3.3 Interpretation of local aquifers, Cauvery delta, S India

This example illustrates how surface features observed on an image enables the formulation of deductions about the subsurface situation, by inferring effects of Holocene sea level rise that culminated around a few thousand years BP.

Figure 7.6 (Landsat TM, PC 1 image) shows the area with the semi-consolidated Tertiary Cuddalore Formation in the west, overlain by fluvial deposits. As can be noted on the image at some places beach ridges cut-off fluvial deposits, but at other places fluvial deposits cover the beach ridge deposits. The nearly buried and oldest beach ridge B1 in the north indicates that the former coastline was much further inland, and the pre-Cauvery River flowed to the south building up the delta in that part, and gradually shifted to the north to its present position (Meijerink, 1972). Vague traces of the possible continuation of B1 to the south are indicated by (?) on the image and it may be noted that the bend in the Cauvery River occurs where the river meets such possible sand bodies.

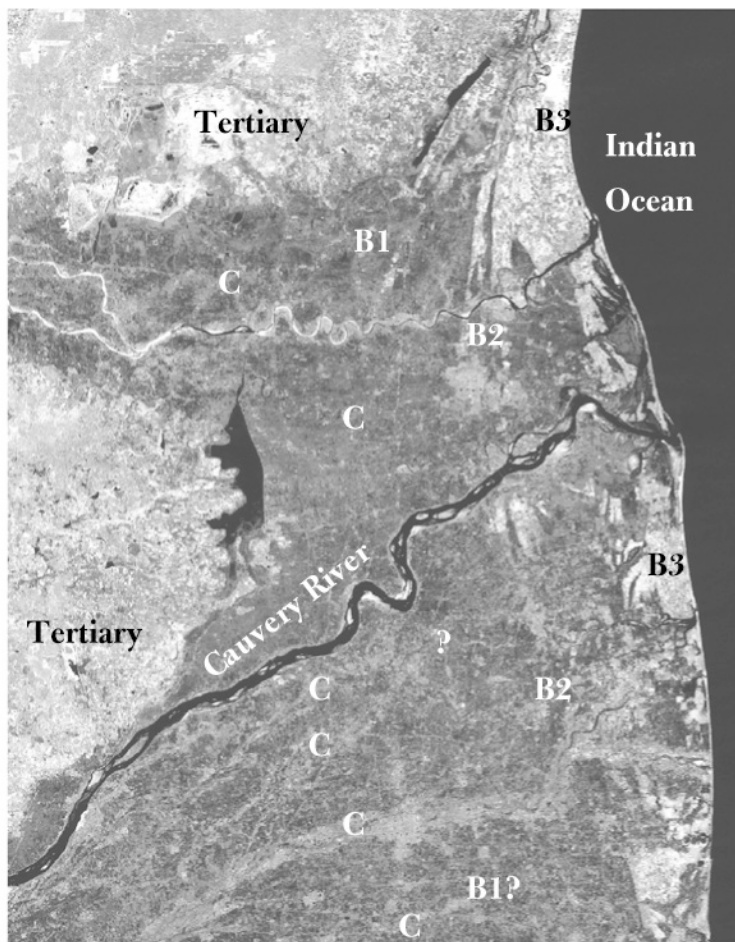


Figure 7-6

Landsat TM image of the Cauvery Delta, south India.

Beach ridge complexes:

B1, oldest, B2 intermediate, B3 youngest.

C = former channels

Distance E-W is 56 km.

Many paleo-channels can be seen on the image some of which are marked (C). The patterns suggest the fluvial sediments to be of braided or semi-braided nature and therefore fewer differences in permeability can be expected than would be the case of levee-channel and backswamp deposits. However, there is a differentiation seen between the darker toned inter-channel basins (sandy clay and silt) and the former channels with lighter tones (sandy textures).

Of hydrogeological interest is of course the subsurface geology, which is not depicted on the image, but some expectations can be made based on our knowledge that the sea level rose by tens of metres after the Pleistocene and reached levels somewhat above the present sea level around 5800 to 4800 BP and 4000 to 3500 BP, according to Mörner (1969), somewhat later (Hesp et al., 1998). To our knowledge no datings of the Cauvery beach ridges are available, but the oldest beach ridge deposits resting about 3 m a.m.s.l. near Puttalam along the east coast of nearby Sri Lanka, dated from 4100 BC (C<sup>14</sup>, unpublished).

The transgression up to B1 and its possible southward continuation, followed by smaller regressive and transgressive movements (B2, B3) must have left a more or less contiguous sand body covered partly and locally by relatively thin fluvial deposits. The situation is schematically shown in Figure 7.7 and the few available borehole logs do not contradict the hypothesis. The beach ridge complex is of sufficient thickness to be considered as a local aquifer, fed by freshwater from the fluvial deposits and rainfall.

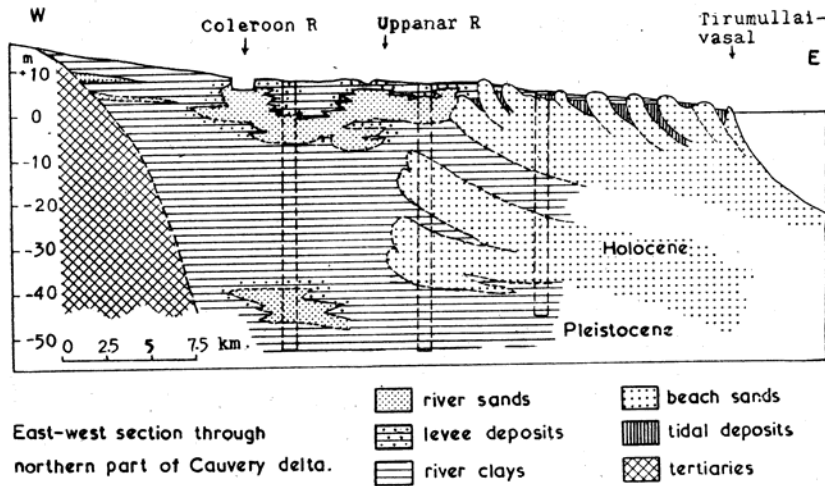


Figure 7-7

Cross section through northern part of Cauvery Delta

Source: Meijerink 1972.

### 7.3.4 Eolian, fluvial and marine deposits, Mozambique

Fossil, unconsolidated wind-blown sands covering partly former beach ridges are shown on the radar image of Figure 7.8, which is draped onto a topographic map. The colour composite is made by assigning Red-Green-Blue to different polarization images (Source: European Space Agency, ESA, image gallery). The valleys and

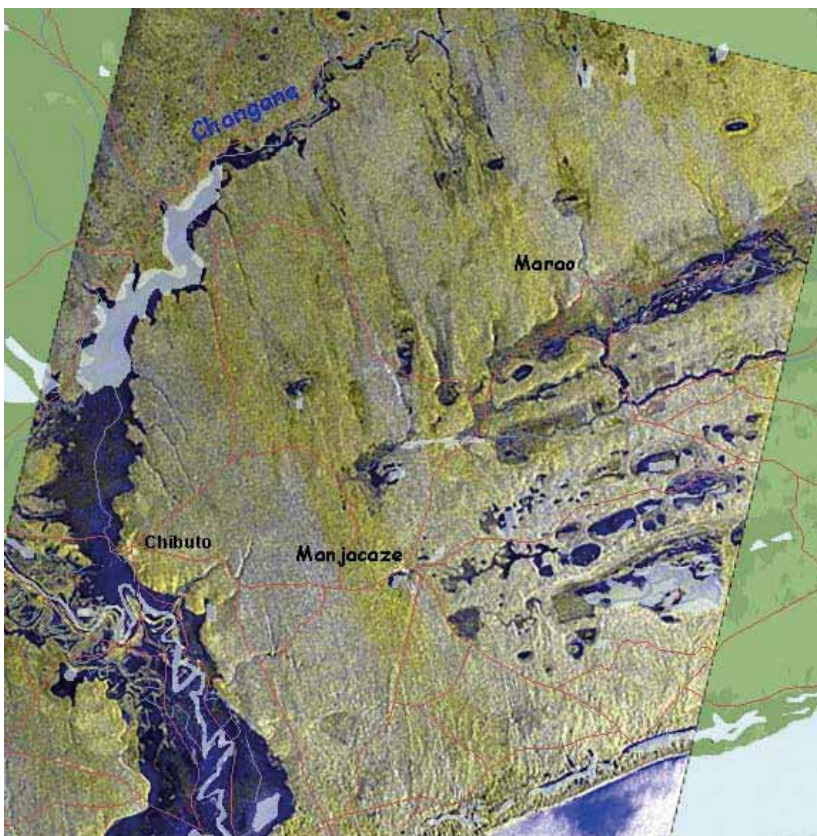


Figure 7-8

Radar image draped on map of the area NE of the Limpopo River mouth, Mozambique.

Former beach ridge and swale complexes are seen, partly intersecting the groundwater surface and thick fossil eolian sand deposits with remnants of longitudinal dunes.

Distance E-W is 109 km.

Source: European Space Agency (ESA).

floodplains of the Limpopo and Changana Rivers have been developed after the deposition of the thick sands, being probably the equivalents of the inland Kalahari Sand formation of Late Tertiary to early Quaternary age (Thomas and Shaw, 1992). Some semi-circular depressions can be seen. Such similar depressions in the Kalahari Sands in Zambia are known as pan-dambos and are thought to be ‘silicate karst’ or ‘pseudo karst’ features (McFarlane, 1995).

The groundwater surface intersects with the dambo bottoms and the swales of the beach ridge complex. At any place in the sand area the depth of the groundwater can be estimated by interpolation between the level of the floodplains and the dambo or swale bottoms.

### 7.3.5 Verification of modelling response, Kalahari Sands and Zambezi floodplain, Zambia

The image of Figure 7.9 (Landsat TM b4), Western Province of Zambia, shows Kalahari sand deposits with a thickness varying from some 80 m in the east to 130 m below the Zambezi floodplain in the west. The sands are underlain by impermeable formations (basalt and mudstones). The upland area is a few tens of metres above the Zambezi floodplain, depending on location and is bordered by a sharp terrace bluff. Semi-circular depression areas (pan-dambos) have been developed in the Kalahari sands and are considered pseudo karst features.

The hydrology of the dambos has been described and modelled by Wolski (1999), who also used a 2D groundwater model (FLOTRANS) in steady state mode along an E-W section, from the upland to the floodplain. The model section of Figure 7.10 extends to the Lui River valley, east of the area shown in the image of Figure 7.9. Based on available data, a horizontal conductivity  $K_s$  of  $3 \text{ m d}^{-1}$  was adopted and a vertical  $K_s$  of  $0.3 \text{ m d}^{-1}$ . Annual recharge was estimated by results of the chloride method and a soil water balance method, which gave different results and values between  $100$  and  $250 \text{ mm.y}^{-1}$  was used in modelling scenarios.

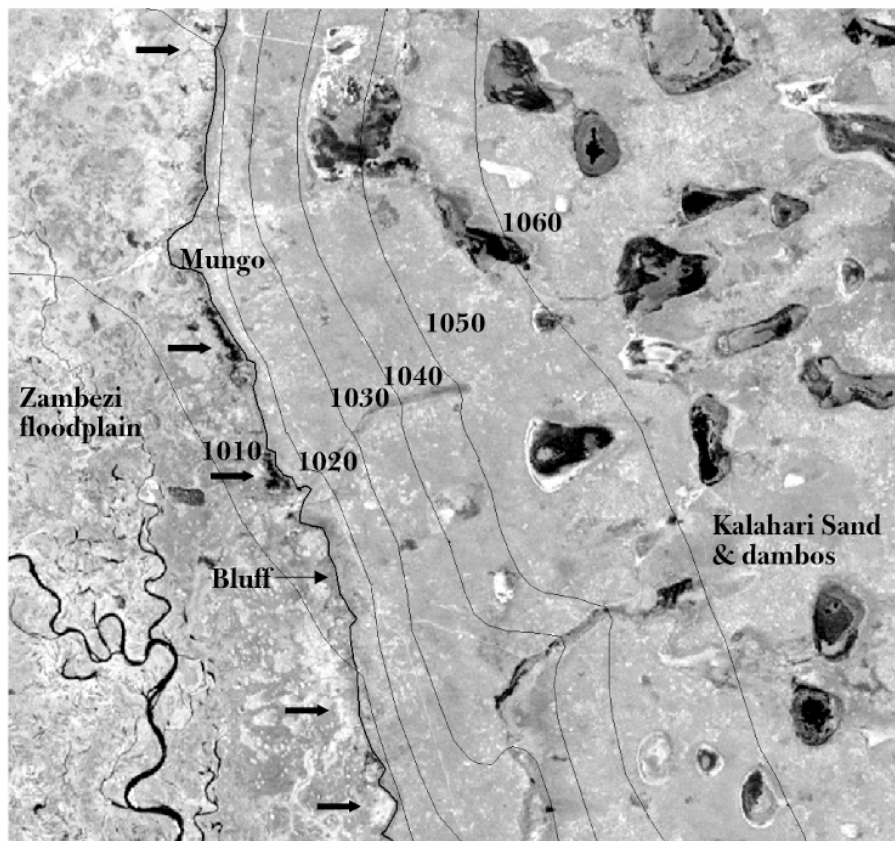


Figure 7-9

Landsat TM b4 image of sandy upland and floodplain showing narrow zone of exfiltration (water or dense vegetation, see arrows), indicated by groundwater model.

Depression areas are pan-dambos. Groundwater contours after Wolski, 1999).

Area around Mungo, Western Province, Zambia.

Distance E-W is about 40 km.

Groundwater contours, partly estimated, are shown in Figure 7.10. When drawn in a section, there is a sharp break in gradient of the groundwater surface at the bluff separating the upland from the floodplain. This results in a strong concentration of flow lines in a narrow exfiltration area in the model, as is shown in the cross-sectional model.

The question of interest now is, can this exfiltration be observed on images, and the answer is affirmative. Just west of the bluff or terrace edge, small elongated water bodies (black tones on the NIR image) can be seen, while the emergence of groundwater is also evidenced by a narrow zone of dense vegetation (white tones). Some of these have been indicated by arrows. Since image features and groundwater model results match, it can be assumed that in case of data scarcity, groundwater contours can be adjusted using the responses seen on remotely sensed images.

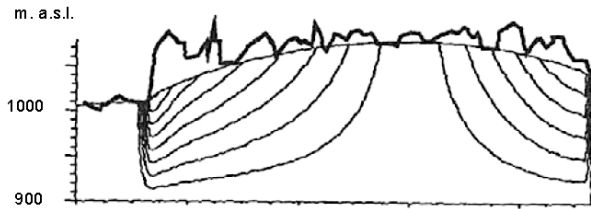


Figure 7-10

2-D model along E-W section of permeable upland and floodplain with lower permeability.

Model results in narrow exfiltration zone just west of the bluff. Image of fig. 7-9 shows western half of the cross-section.

Source: Wolski, 1999.

### 7.3.6 Regional setting and study of a groundwater related problem in the Pampas region of Argentina

A vast area consisting of thick, unconsolidated deposits, mainly of eolian origin is found in the region SE of Buenos Aires, Argentina and poor surface drainage causes problems to agriculture.

Figure 7.11 shows the location, as well as parabolic dunes in the south (with interpretation lines), longitudinal dunes in the north, and undulating sand accumulations in the remaining areas on a Landsat TM false colour image. Depressions are submerged due to rise of groundwater over the last decades.

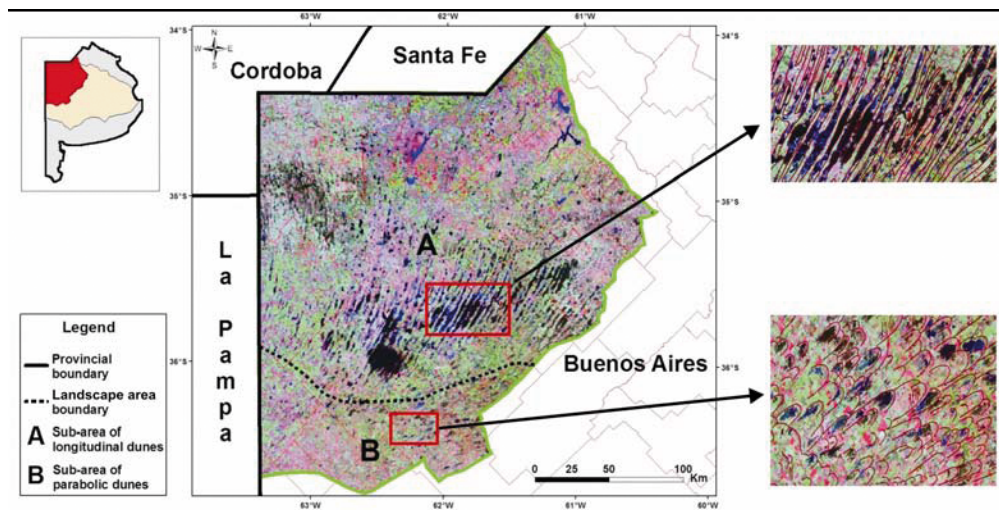


Figure 7-11 Overview of the area. Inset map A shows longitudinal dunes, inset map B shows parabolic dunes. Both are partly submerged. Source: Ludueña (2006).

The area in the northwestern corner of the Buenos Aires Province, shown in Figure 7.12, will be discussed in more detail to illustrate the use of remote sensing for taking stock of the waterlogging problem.

The following information is derived from Ludueña (2006). The thickness of the eolian deposits is large (>100 m) and consists of windblown sands with mixtures of finer grained (loess) deposits by eluviation.

The average annual rainfall during the period 1898 to 1972 was 770 mm and rose to an average of 940 mm during 1972 to 2004, causing an increase of the groundwater table. The annual potential evapotranspiration is 1,092 mm, hence more than the mean rainfall, but the actual evapotranspiration is less due to presence of bare areas in the cropping cycle, causing the rise of the groundwater table. During the dry season excess evaporation causes salinity.

Agricultural fields are found on the higher parts (often only less than 1 m above the bottom of the depressions) and a perched water table is found on the main groundwater body, which has a high salinity. The perched

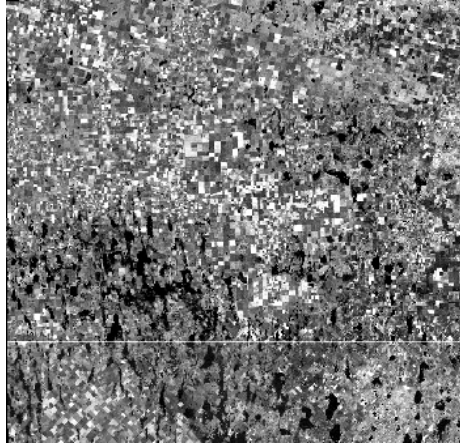


Figure 7-12

North-western part, showing transition from longitudinal dunes to undulating sand cover.

Landsat TM band 5.

Increased rainfall during the last decades caused rise of groundwater level and salinity, affecting agriculture.

Depressions shown on image are submerged (black tones). The NW corner is shown enlarged in figure 7-13.

nature is also due to the presence of an impeding horizon of pedogenetic origin found at limited depth below the surface. However, the layer of low permeability is not contiguous.

A problem for attempting remediation is the lack of accurate elevation data over large areas. The height resolution required is in decimetres or preferable centimetres, which necessitates the use of an expensive Lidar survey. High-resolution aircraft radar imagery or photogrammetry (the latter up to 25 cm accuracy) could provide a useful DEM, but is considered hitherto as beyond the means of the farming community, which lacks organizational infrastructure to realize such surveys.

For that reason, Landsat TM and Aster satellite images were used with field work, to establish relations between land cover, details of geomorphology and the dynamics of the wetness and associated salinization, in order to segment the area in units of relative height and waterlogging hazard.

Time series of Landsat TM and Aster images were processed. Figure 7.3 shows a time series of Aster NDVI images in the upper row, transformed in the  $P_v$  index images (see chapter on Image Processing) in the lower row, after radiometric correction, in order to make them mutually compatible.

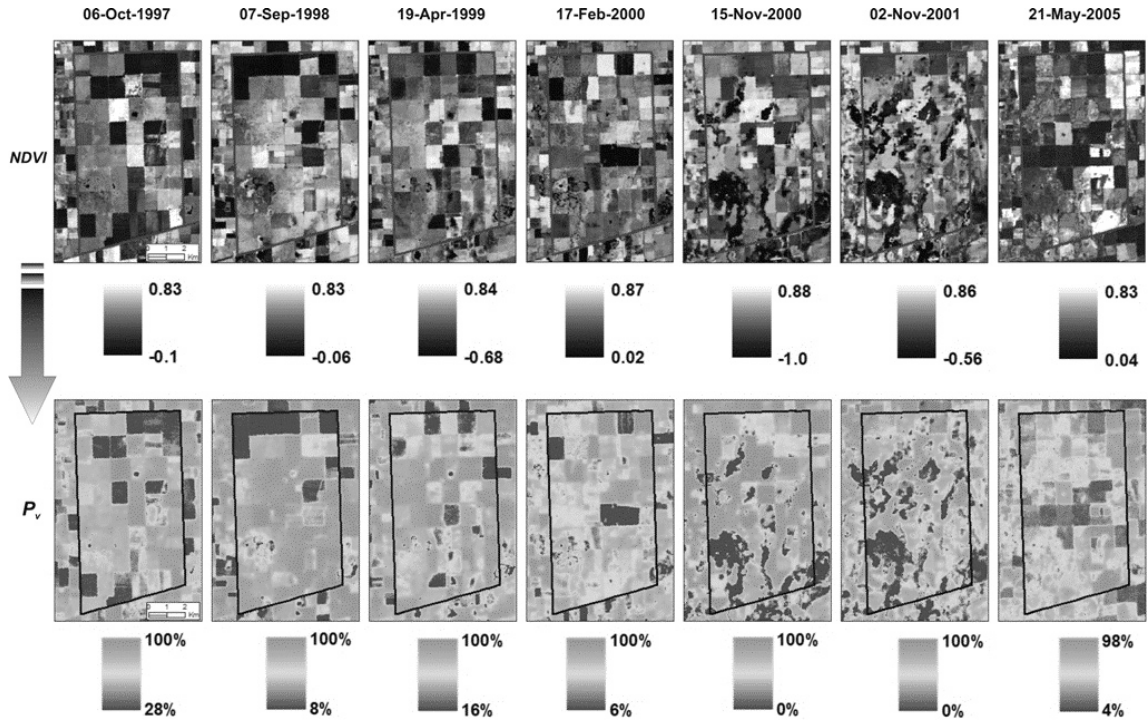
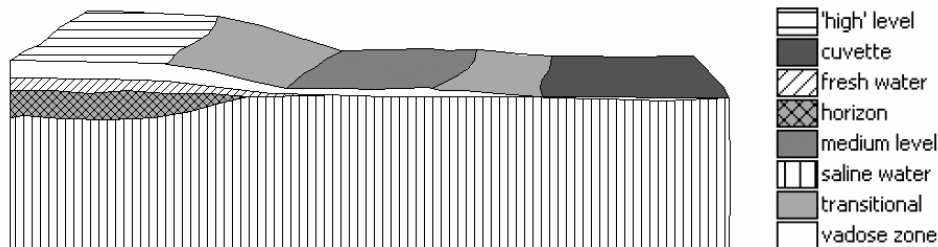


Figure 7-13 NDVI and transformed NDVI to  $P_v$  time series of ASTER of a part of the area for analysis of seasonal fluctuation of the groundwater level. Delineated area is a large farm property. Source: Ludueña (2006).

The dark tones correspond to bare soil (low % of green vegetation on the  $P_v$  index), either due to land preparation (rectangular fields) or to bare and saline patches in the depression without halophytic vegetation. In general the satellite time series shows seasonal variation and an increase of the waterlogging problem from autumn 1997 to autumn 2001. The dry season image of May 2005 suggests a lower groundwater level.

In schematic form, the four land units differentiated, shown in Figure 7.14, were interpreted visually on time series of Landsat Tm and Aster images (false colour composites, NDVI series), using patterns of land cover, including the areas with halophytic vegetation, salt efflorescence, water bodies or wet soils.



**Figure 7-14** Schematic block diagram (height and break of slopes exaggerated) showing terrain units in the Pampas region, Argentina. The ‘high’ level unit is usually 1 to 3m above the cuvette (or blow-out hollow).

Shallow groundwater table fluctuates during wet and dry season causing changes in patterns of water logging, as shown on satellite images of figure 7- 13.

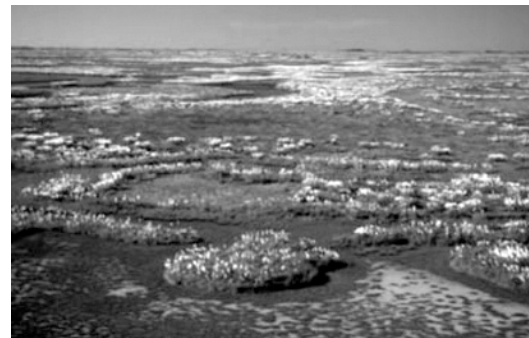
Modified after Ludueña (2006).

The cuvettes or blow-out hollows usually have permanent water logging, their transitional areas have strong seasonal water logging and saline soils and both have halophytic vegetation communities. The medium level areas have humid mesophytic prairies and meadows and alkaline soils, while the relatively high level areas are used for agriculture or have mesophytic meadows. The two field photos of Figure 7.15 give an impression of the very flat terrain and two main vegetation types.



**Figure 7-15a** Typical view of Northwest Region grass prairie.

Source: Ludueña (2006).



**Figure 7-15b** Vegetation of saline conditions in cuvettes.

Source: Ludueña (2006).

Field investigations were carried out to study the soils, vegetation types and water quality and to obtain information from local farmers as to the behaviour of the groundwater table and the associated waterlogging and salinity problems. After that the satellite images were re-interpreted to prepare the land unit map shown in Figure 7.16, which can also be considered as a kind of relative altitude map because of the known association of land unit, soil types and vegetation communities.

This example demonstrates the strength of visual interpretation of complex patterns in an area with unconsolidated deposits after field knowledge was gained and the usefulness of the monitoring role of satellite time series after adequate transformation.



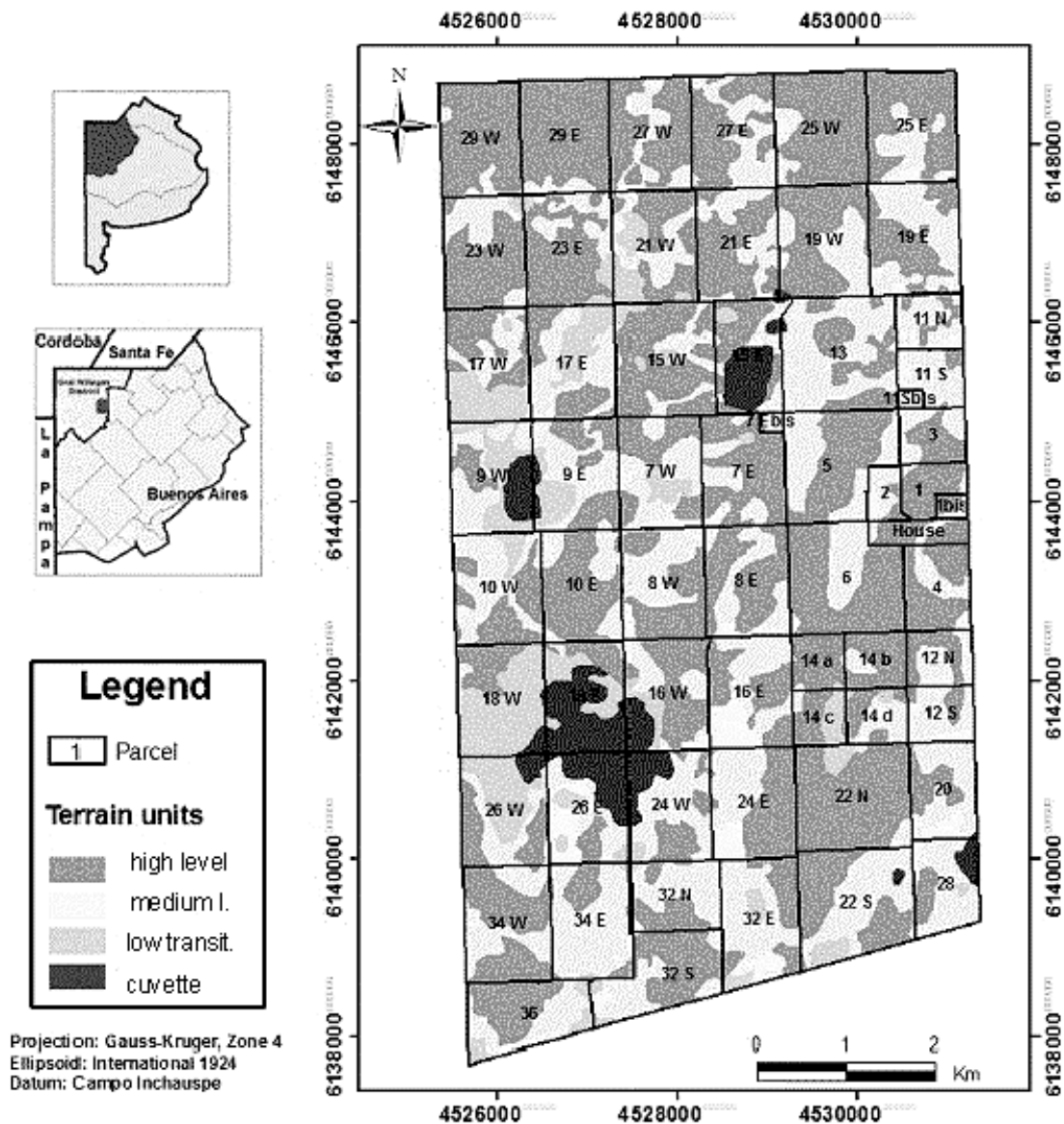


Figure 7-16 Terrain unit map of a large farm based on visual interpretation of various satellite images. The low transitional unit and the cuvette are waterlogged.  
 Source: Ludueña (2006).

## 7.4 Alluvial fans

### 7.4.1 Origin

In semi arid regions where groundwater is scarce, the alluvial fans form good aquifers, because the fan conglomerates are permeable and recharge is substantially augmented by mountain front runoff and transmission losses of (ephemeral) river flows in the upper and middle part of the fans.

Alluvial fans are formed by the deposition of bed load of rivers, which had to shift course to lower areas due to aggradation of the bed. Such frequent shifts caused the fan-like pattern. The deposition is essentially caused by a break of slope when the river leaves a mountain or hill area and enters a plain area and by transmission losses. Both reduce the transport capacity of the river.

Typical of alluvial fans is the predominance of poorly sorted coarse-grained boulders to sands (debris flow deposits), depending on provenance in the upper fan which gradually (inter-fingering) changes to somewhat finer-grained braided river deposits with more sorting in the middle part. The lower part of large fans can consist of

clays and silts because only the suspended load could reach that far, but occasional sandy lenses can occur carried as bed load during exceptional floods.

### 7.4.2 Interpretation of thickness

The thickness of alluvial fan deposits depends greatly on the tectonic history. Often a fault forms the border of the hills and plains and when repeated movements have taken place during the fan formation, the thickness of the upper fan deposits can be considerable. In case of active step faulting the thickness of the upper fan may be less. An indication of possible limited thickness is presence of outcrops in the upper fan area and such outcrops can be easily recognized on images.

In intra-montane subsidence basins, a good development of fans, absence of outcrops in the central river, and tilted and incised fanglomerates near the mountain front overlain by younger fan deposits, are indications that the thickness of fanglomerates can be substantial, and worth investigation by geophysical survey and drilling.

### 7.4.3 Hydrogeology

An alluvial fan is characterized by a well-defined flow system, which in fact, forms much of the conceptual groundwater model. The upper part of the fan is the recharge area of the flow system. The phreatic groundwater level in semi-arid regions is generally deep, but is recharged by rain, by transmission loss in the main riverbed and by runoff from small rivers from the mountain front, providing the pressure head of the system. In the downstream direction, the phreatic condition makes place for a semi-confined condition due to the presence of many clay and silt layers overlying sand and gravel lenses, see Figure 7.17.

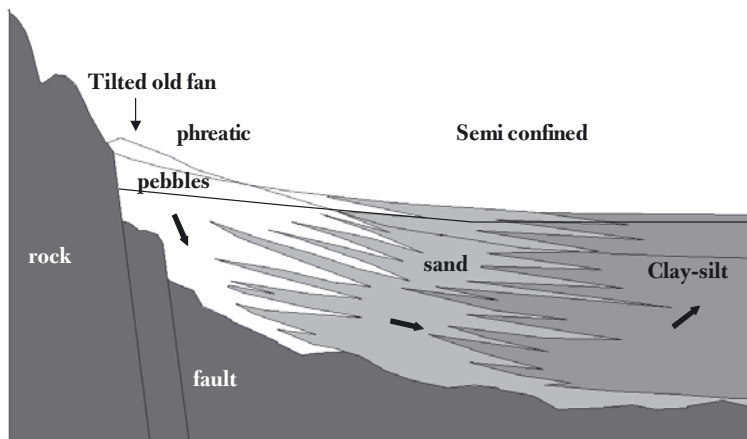


Figure 7-17

Schematic section of alluvial fan, showing change of facies from the upper to the lower fan and the groundwater flow system. Arrows indicate groundwater flow.

Hence, by recognizing an alluvial fan or fan complex (many adjoining fans along a mountain front is termed Bahada), the conceptual groundwater model is known. The next steps are to inspect the images for indications of emergence of groundwater (possibly depth of groundwater), relative importance of transmission loss and mountain front recharge by inspection of the hydraulic geometry of channels, and groundwater use for irrigation, which provides data for the groundwater budget.

These aspects will now be discussed and illustrated.

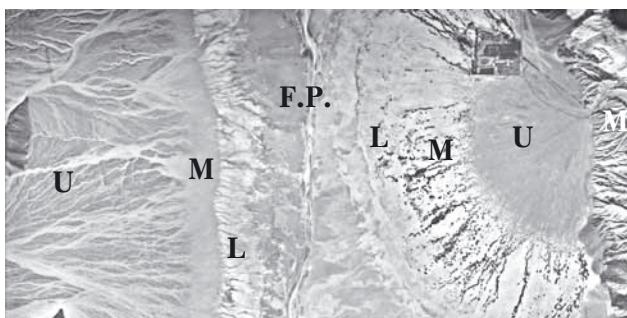


Figure 7-18

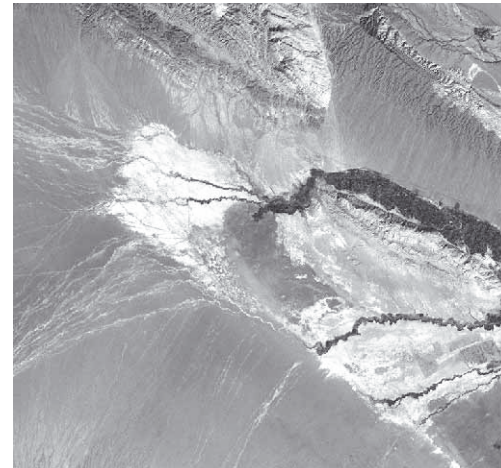
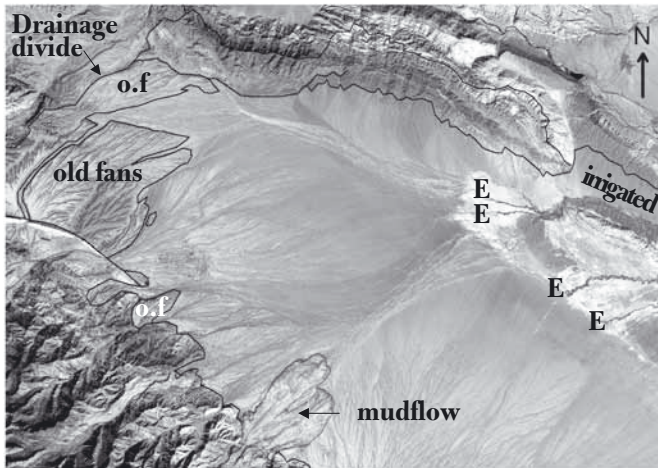
Alluvial fans in an arid region (Death Valley, USA) with distinct differences between upper (U), middle (M) and lower (L) parts, but different provenance.

Fans on the left: minor seepage on lower part. The middle part of the fan on the right is slightly dissected and has phreatophyte vegetation.

F.P. is floodplain .

Figure 7.18 shows how the details of alluvial fans are governed by provenance. Although the climate is arid (< 200 mm annual rainfall), during occasional runoff events recharge takes place through transmission loss. The fan on the left shows some ephemeral seepage lines, fed by infiltrated water from the western Panamint range (3,000 m), while the phreatophytes on the right-hand fan use water from the (weak) flow system, because recharge is insufficient to maintain permanent outflow.

Such perennial outflow occurs in the large alluvial fan complex filling a tectonic basin in Tibet (NW China), due to recharge mainly by snowmelt runoff and occasional flash flows. The fans are so large and permeable that all the surface runoff infiltrates, except perhaps runoff from very rare storms and generally only groundwater leaves the fan-area through a few springs, at the head of a few channels with dense vegetation, starting from places marked with (E) in Figure 7.19. Differential uplift along the southern flank of the basin is evidenced by dissected older alluvial fans.



Alluvial fans in subsidence basin. At E groundwater emerges. Landsat TM b5. Recharge by snowmelt runoff and flash floods is sufficient to cause perennial outflow. Note tilted dissected -old- fans and mudflow deposit. Distance E-W is 55.7km.

Figure 7-19

Enlarged part of zone with springs with dense vegetation along river course and irrigated area (dark tones) Landsat TM b3.

Hydrogeological interpretation requires the deduction of relationships between features seen on an image. Figure 7.20 shows a perennial river in semi-arid south Iran, which has formed an alluvial fan. Flood flows are contained in the incised riverbed in the upper alluvial fan but river shifts occur during flood flow at the middle part – a reason why farmers avoid this part. Because the catchment is large, floods reach the lower fan and the coastal plain beyond.

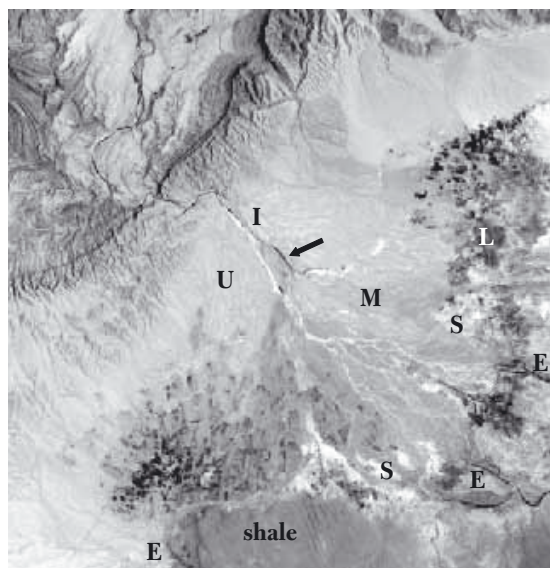


Figure 7-20

Landsat TM band 5.

Alluvial fan in S Iran with indications of relatively shallow groundwater level, due to high recharge by perennial river.

River upstream of I has water, which is lost downstream of I at the transition of the upper fan (U) and the middle fan (M). In incised branch, vegetation is seen (arrow) suggesting relatively shallow groundwater, which emerges at a few places (E) at the lower fan (L). Dark areas are fields irrigated by groundwater, partly by qanats. Shallow groundwater table at lower fan causes salinization (S).

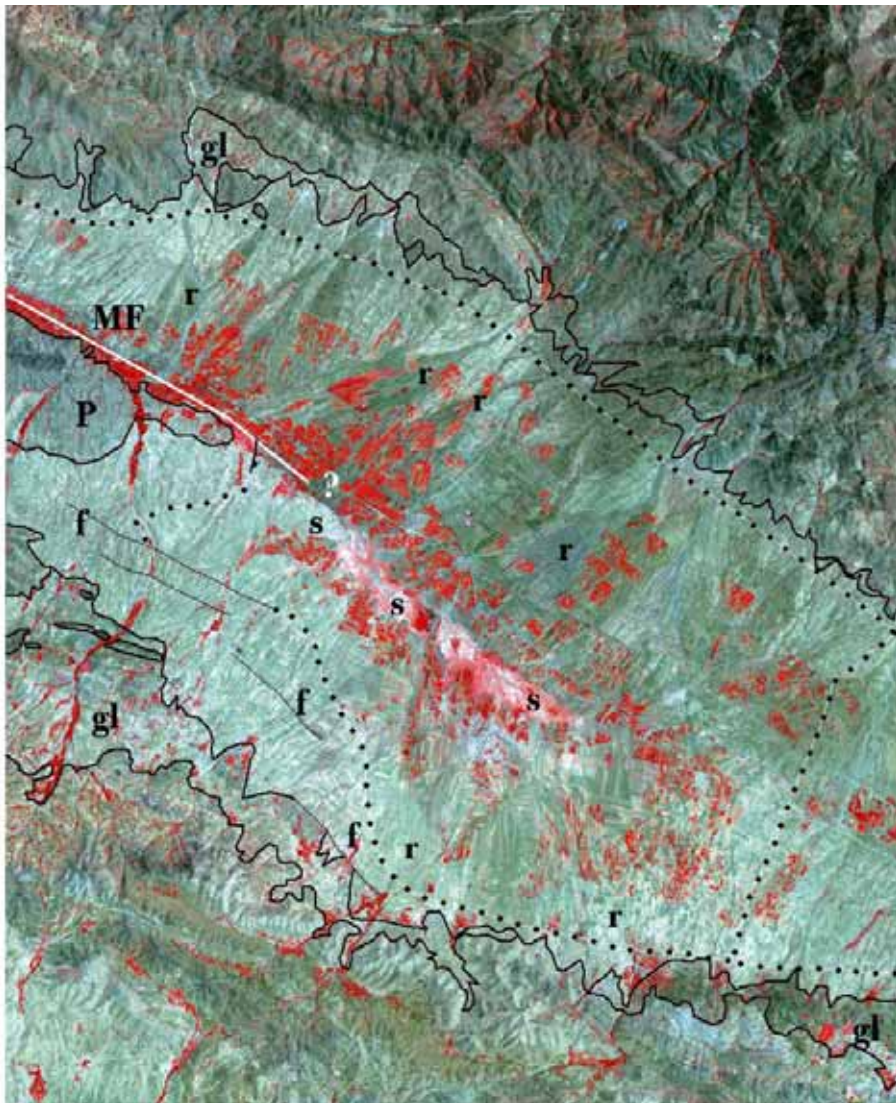
Distance E-W is 15.3km.

The image was taken during the dry season when the base flow infiltrated in the upper alluvial fan by transmission loss upstream of place (marked as I, see Figure 7.20). However, the presence of phreatophyte vegetation (small dark strip, indicated by arrow) in an incised branch makes it likely that the groundwater level in the middle fan is not too deep. This is substantiated by another observation: groundwater emerges at the lower fan and the extension of the areas with salt efflorescence (high reflection) indicates that the groundwater level at the transition of the lower to middle fan is not deeper than the capillary zone (about 2 m).

The relatively high groundwater table can be explained by the good recharge from the river and the impermeable shales and clays of the coastal plain.

#### 7.4.4 Alluvial fans and hydrogeology of a subsidence basin, N. Iran.

The following example (Figure 7.21) illustrates the contribution of image interpretation in a hydrogeological study of the aquifer formed by fanglomerates in a subsidence basin, located in the semi-arid eastern Zanzan River catchment, north Iran. A geophysical survey indicated that the central part of the basin with alluvial fill is about 200 m deep. Along parts of the margin older alluvial fans have been tilted, and the present active rivers are incised



**Figure 7-21** Soltanieh aquifer, north Iran, a subsidence basin filled with 200 m thick fanglomerates, Landsat TM false colour of bands 4,3 and 2. Mountains in the north consist of folded volcanic rocks and granites, those in the south mainly of folded sedimentary rocks. MF= main fault, f = minor faults, P = Pliocene gravel and clay beds, in anticlinal fold plunging to SE, gl = glacis and thin fanglomerates, r = some major active river beds where transmission losses recharge aquifer, s = exfiltration area with small perennial river.

Distance E-W is 34km.

near the mountain front. The high reflection of the older fans is due to lime enrichment, which in the upstream part takes the form of a lime crust with low permeability. Irrigated fields shown on the image are irrigated by groundwater only on the lower fans while irrigated fields on the middle part of the fans receive water from bore-holes and diverted snow melt runoff from the rivers during the period April and May.

Recent to sub-recent river deposits which spread out in the middle part of the northern fans do not have high reflection because of absence of lime-enrichment, and the reflection properties of the fluvial deposits are influenced by the rock types of their catchment areas, which consist of folded volcanic rocks (generally dark tones) and granite (medium grey tones) in the northern mountains, while the southern hills consist of limestone, marl and sandstone, producing the light-toned deposits of the southern fans.

The aquifer is recharged by three sources: (1) snowmelt runoff (during the period March-July) and base flow which infiltrates fully in the river beds and lasts from end of March to June, (2) flash flows, which occur after significant rain in the mountains and hills, particularly in the period March-May, and (3) rainfall recharge, particularly in the areas without lime enrichment.

The importance of river recharge is evidenced by the well hydrographs, shown in Figure 7.22, whose location is shown in the image (upper left). The three wells close to the larger rivers (nos. 1, 3 and 5) show substantial

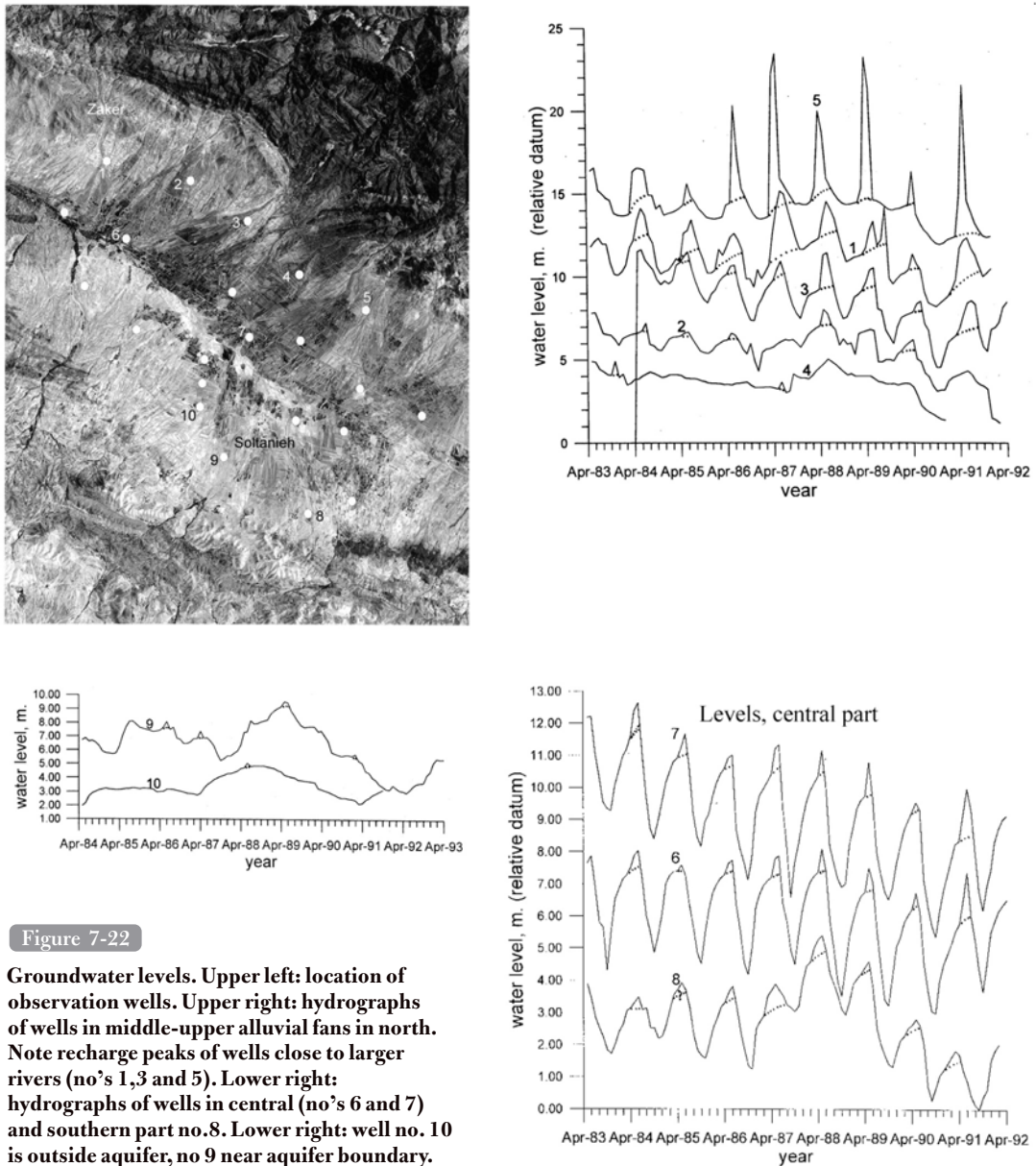


Figure 7-22

Groundwater levels. Upper left: location of observation wells. Upper right: hydrographs of wells in middle-upper alluvial fans in north. Note recharge peaks of wells close to larger rivers (no's 1,3 and 5). Lower right: hydrographs of wells in central (no's 6 and 7) and southern part no.8. Lower right: well no. 10 is outside aquifer, no 9 near aquifer boundary.

Data: Ministry of Water and Energy, Iran.

increases in the groundwater level during the period of snowmelt runoff and flash flows. By extending graphically (dotted line) the recuperation curve, recharge peaks can be identified. The two observation wells (nos. 2 and 4) located between major active rivers show little recharge.

In the central part of the aquifer, wells nos. 6 and 7 exhibit a steep drawdown in the period May–September when pumping for irrigation takes place, recuperation when pumping stops and only minor recharge peaks. Well no. 8 on a southern fan has the same pattern, but deviated somewhat during the period 1988–89.

In the central part of the basin is an area covered by grass with a shallow water table and drained to the west by a perennial, small sinuous river (visible on air photos, but not on the satellite image shown here), which, according to local inhabitants, nearly always has clear water. Hence, all but the highest flash flows infiltrate fully on the fans, because of high transmission losses in the gravels and sands of the active fans and partly because sheet-wash on the lower part is captured in the agricultural fields.

The marshy grass area is due to exfiltration of a groundwater system, as sketched in Figure 7.17.

The image proved to be of much use in defining the aquifer boundary in the southwestern part. The geological map shows most of that area as Quaternary alluvium, but interpretation of air photos and the Landsat image indicated that the alluvium consists of thin deposits on top of an erosional surface (erosion glacia), developed over older rocks of low permeability and the presence of minor faults, – shown in Figure 7.21 and substantiated by field work. In the western part the Pliocene continental deposits have different spectral properties than the Pleistocene deposits (with lower permeability) and this allowed for the interpretation of an asymmetric fold, and accordingly a deflection of the aquifer boundary, as shown in Figure 7.21. The hydrographs of wells nos. 9 and 10 reflect the correctness of the interpreted aquifer boundary; well no. 10 is outside the boundary and well no. 10 is along the margin, but within the aquifer.

A groundwater model was made of the aquifer (Bani Hashemi, 1995), whereby river recharge cells were imposed using the pattern of the recent gravels derived from the image and distance from mountain front, the interpreted aquifer boundary (considered to be a no-flow boundary) while aquifer stress was included by making an estimate of the water loss on the irrigated fields based on a multi-spectral classification of the crops and applying crop coefficient factors.

#### 7.4.5 *Effect of tectonics and example of Eastern Doon Valley, N. India*

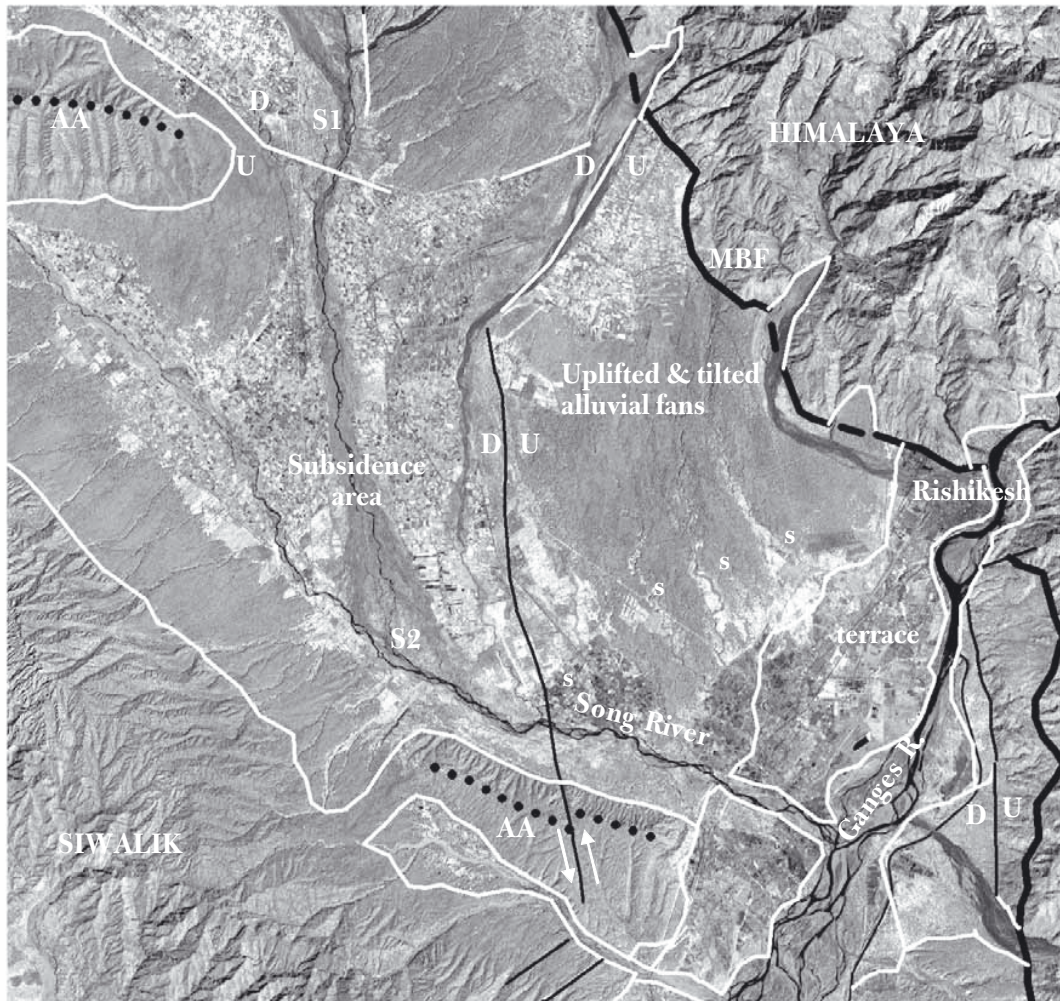
The crossings of older and younger fan conglomerates or river terrace deposits along the margin of a subsidence area are a sign of tectonic activity. The example of the alluvial aquifer in S Iran discussed in the chapter on Processing of Images, shows uplifted fans on the western margin, whereby the degree of dissection represents the relative age and the degree of uplift. As in the above example of the eastern Zanjan aquifer, important river recharge was also illustrated. Uplifted and dissected older fans are also shown in Figure 7.19 above.

It should be remembered that the older deposits along the margins of a subsidence basin have their continuation below the younger ones, whereby knowledge of the facies changes occurring on alluvial fan deposits allows some postulation of what can be expected at depth. Tectonics affecting Quaternary deposits may leave evidences on the surface, not only in the form of lineaments corresponding to faults or flexures, but also in the form of dissected deposits, widening and narrowing of floodplains, as the next example demonstrates.

##### *Eastern Doon Valley*

Pleistocene and Holocene tectonism affected groundwater in the intramontane Doon Valley in north India (Figure 7.23). In the northeast is a no-flow boundary formed by the Main Boundary Fault, a huge high angle thrust fault and Himalayan rocks bordering the fault are impermeable (slates and phyllite).

In the south the northern flank of the Tertiary Siwalik Formation is seen, with the Upper Siwalik boulder and clay beds dipping NE covered by a small alluvial fan zone. In the NW the Siwalik rocks are folded in an anticline, which is bordered by an inferred fault. Strong outflow of groundwater occurs in the wide braided Song River bed just north of the fault. The Song River further upstream of the fault is dry in the dry season because base flow from the Himalayan catchment is lost by diversion and transmission loss. South of the fault in the NW the emerged groundwater also infiltrates fully in the riverbed during the dry season over a length of a few km and the same is true for the river from the NW. However, at location S2 groundwater emerges again during the dry season and gains much groundwater discharge in a downstream direction (Meijerink, 1974). The image shown was from



**Figure 7-23** Aster VNIR B3, November 2004, image of the eastern Doon Valley, north India, showing effect of neotectonism on sedimentation, recharge and groundwater outflow (see text). Sub-recent wrench fault in the centre was first detected by shift in anticlinal axis (AA) in the Upper Siwalik Formation and could be traced further north. The fault borders an area of tilting and uplift in the east and a subsidence area with active sedimentation and transmission losses in the west.

Inferred faults are shown in white. The fault in the north crossing the Song River causes strong ( $>4 \text{ m}^3 \text{ s}^{-1}$ ) outflow of groundwater at S1. s = approximate place where groundwater appears during the dry season. U=upthrow, D=downthrow. MBF = Main Boundary Fault

4 November 2004, just a month after cessation of the monsoon rainfall. Therefore the watercourse is still contiguous.

The fault in the centre of the image shown was first noted by the shift in the anticlinal axis of the Siwalik rocks in the south during air photo interpretation and may continue to the north in the alluvial deposits of the northern rivers. East of the fault the conglomerates have been tilted and have been dissected by drainage originating on the fans and deeply (several tens of m) incised by the rivers with catchments in the Himalayas.

West of the fault subsidence took place, attracting sedimentation by coarse-grained (sands to boulders) deposits due to high flood discharges in the monsoon and the relatively steep gradients of the rivers.

There are several groundwater flow systems (ignoring the one upstream of the fault in the NW):

1. A system with the infiltration area along the northern part of the subsidence area, fed by important transmission loss and local runoff and rainfall recharge, which infiltrates nearly fully in the younger deposits. Already during November, all base flow from the mountain catchment is infiltrated in the wide riverbed. The exfiltration area coincides with the roughly E-W course of the Song River.
2. An adjoining flow system in the uplifted, tilted and dissected fans. Recharge is less than in the adjoining flow system because soil development took place, reducing infiltration. For that reason local (ephemeral) rivers

could develop and dissection take place. Exfiltration takes place in the riverbeds approximately along the line indicated by (s) and a little further downstream at the junction with the Ganges terrace deposits, where the water infiltrates again to emerge in the Ganges River.

3. A flow system in the local Siwalik fans, fed by transmission loss and rainfall recharge.

## 7.5 Summary and conclusions

The main types of unconsolidated deposits are briefly introduced as an aid to linking geomorphological features that can be observed on images to hydrogeological properties. Terrain consisting of unconsolidated deposits often has important groundwater occurrences and recharge is influenced by the nature of the surface materials, while in dry climates salinity due to shallow groundwater is associated with type of deposit (e.g. fluvial backswamp clay) or micro-relief (natural levees, dunes, beach ridges). It is difficult to map the Quaternary geology at a regional scale, as a basis for hydrogeological maps, by fieldwork only, but by image interpretation this mapping can be done in an efficient manner, as is illustrated by a few examples.

The soils of Quaternary deposits often support agriculture, but waterlogging and salinization can be a problem in some areas. Images are eminently suitable to take stock of the situation and to study the seasonal variations, as the example from Argentina illustrates.

Although image observations are restricted to surface features, some subsurface conditions may be inferred by considering geomorphological development. This is particularly so in the case of an alluvial fan, which is characterized by a groundwater flow system, due to an elevated intake area in the permeable upper part of the fan with phreatic conditions. Lateral groundwater flow is dominant in the middle part of the fan, while a semi-confined condition is common in the lower part because of presence of clay and silt layers. Upward groundwater flow in the lower fan causes appearance of water in riverbeds, seepage zones or even marshy areas, and such phenomena can be observed on images, as given by a few examples. Much of the recharge occurs in the form of transmission losses in the ephemeral riverbeds. The origin of alluvial fans is often linked to tectonic activities, which can also influence depositional patterns and associated surface permeability.

Aquifers in alluvial fans are often used for irrigation in dry climates, but groundwater levels are declining from over-use. Chapter 13 discusses the role of alluvial fans for artificial recharge schemes, which may alleviate groundwater decline.

## References

- Bani Hashemi, S.A.R. 1994. Hydrogeological study of eastern part of the Zanzanrud catchment in Zanzan Province, northwest of Iran. MSc. Thesis, ITC, Enschede The Netherlands
- Mörner, N.A. 1969. Eustatic and climatic changes during the last 15000 years. *Geologie en Mijnbouw*, No. 4.
- McFarlane, M.J. 1995. Pans and dambos of Western Province, Zambia – a preliminary consideration of their geomorphology/hydrogeology. Unpubl. Report on backstopping mission for Land and Water Management project, Mongu, Zambia.
- Leblanc, M., Favreau, G., Maley, J., Nazoumou, Y., Leduc, C., Stagnitti, F., van Oevelen, P.J., Delclaux, F. and Lemoalle, J. 2006. Reconstruction of Megalake Chad using Shuttle Radar Topographic Mission data. *Palaeogeogr Palaeoclimatol Palaeoecol* 239, pp. 16–27.
- Leblanc, M., Razack, M., Dagonne, D., Mofor, L., Jones, C. 2003. Application of Meteosat thermal data to map soil infiltrability in the central part of the Lake Chad Basin, Africa. *Geophys. Res. Lett.* 30(19), Art. No. 1998 .
- Ludueña, S.G. 2006. Farm-scale ponding susceptibility mapping for potential land reclamation assessment in large flatlands; A case study in the Salado River Basin, Province of Buenos Aires, Argentina. MSc. Thesis, ITC
- Meijerink, A.M.J. 1971. Reconnaissance survey of the Quaternary geology of the Cauvery delta. *Journal of the Geological Society of India*, Vol. 12, No. 2, pp. 113–24.
- Meijerink, A.M.J. 1974. *Photo-hydrological Reconnaissance Surveys*. ITC Publ.
- Pachur, H.J and Rottinger, F. 1997. Evidence for a large extended paleolake in the eastern Sahara as revealed by spaceborne radar lab images. *Remote Sensing of Environment* Vol. 61(3), pp. 437–440.



- Thomas, D.S.G and Shaw, P.A. 1992. *The Kalahari Environment*. Cambridge Univ. Press.
- Hesp, P.A., Chang, C.H., Hilton, M., Chou, M.L. and Turner, I.M. 1998. A First Tentative Holocene Sea-Level Curve for Singapore. *Journal of Coastal Research*, 14(1), pp. 308-14.
- Valor, E. and Caselles, V. 1996. Mapping land surface emissivity from NDVI: Application to European, African and South American areas. *Remote Sensing of Environment*, 57(3), pp. 167-84.
- Wolski, P. 1999. *Application of Reservoir Modelling to Hydrotopes Identified by Remote Sensing*. ITC Publ. No. 69.

# Volcanic terrain

## 8.1 Introduction

Hydrogeological image interpretation of volcanic terrain pertains to such aspects as: type of volcanic formations as indicated by their geomorphology, differentiation of groundwater intake and outflow areas, presence of large fractures and evaluation of the hydrogeological setting of springs. Images provide an initial basis for hydrogeological mapping, in the sense that terrain units can be differentiated, which may be associated with recharge, possible groundwater occurrence and groundwater flow systems. Whether the units can be retained or need re-grouping for the final hydrogeological map depends on results of analysis of hydrogeological field data.

As discussed in Chapter 6 on Hydrogeological Image Interpretation the value of the interpretation is strengthened by local hydrogeological data and knowledge, as will be clarified by the discussion of a number of examples.

The sections in this chapter pertain to some specific volcanic terrain and some features, Quaternary strato-volcanoes and flood basalts (Deccan Trap). Pre-Quaternary volcanic rocks, interbedded or in folded sequences, are not discussed here.

Custodio (2004) presents a concise but comprehensive overview of the hydrogeology of volcanic rocks, and Cook (2003) discusses many practical aspects.

## 8.2 Specific volcanic terrain

There are a great variety of landforms created by volcanism, depending on the type of eruption and the properties of extrusives. Thouret (1999) gives a good overview of volcanic geomorphology. The volcanic landforms are associated with types of volcanic rocks, which are highly variable and so are their hydrogeological properties. It is therefore hazardous to estimate those properties by image interpretation alone, although some can be inferred in certain cases. For example, south-east of Lake Ranau in South Sumatra is a non-dissected volcano. Despite the humid tropical climate (dense forests and coffee plantations are found on the volcano) no drainage lines are found, while springs are absent, according to the inhabitants. This can only be explained by high permeability, despite the relatively young age of the volcano, considering an annual rainfall of some 2000 mm and occurrence of high intensity showers.

### 8.2.1 *Some volcanic landforms*

One major characteristic of the volcanic terrain shown in Figure 8.1 (aerial photograph of small part of the rift valley, NNE of Lake Naivasha, Kenya) is the absence of surface drainage features, although the present annual precipitation is about 600 mm. At no place can water be detected, even in the craters, suggesting that the groundwater level is well below the surface and that overall permeability is sufficiently high to prevent much runoff and stagnation of water.

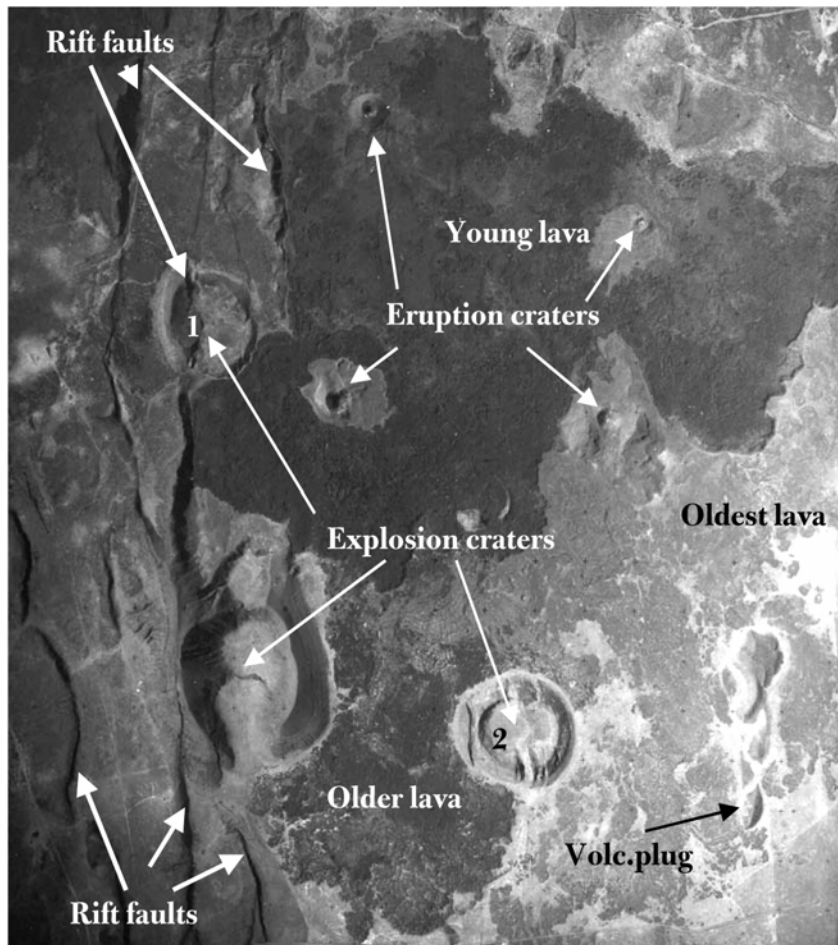
The rift faults are clearly seen; near-vertical fault walls cause a shadow effect. As can be seen on the image, faulting took place or was re-activated after formation of the young crater no. 1, while a small fault can be detected on the flank of crater no. 2. In the rift valley itself, outside the area shown in Figure 8.1, several small faults can be traced on aerial photographs.

The tensional nature of the rift faults is well known, and there is evidence that some rift faults are effective conduits of water. For example, nearby Lake Naivasha is a terminal lake that has freshwater, due to inflow of river water and outflow of groundwater, chiefly through faults. However, the presence of volcanic plugs (see image) and lava extrusions cautions against assuming that all rift faults are conduits, as some of them may be infiltrated by lava.

Lava flows can be differentiated by simple stratigraphical principles and by their freshness. A nearby lava extrusion very similar to the one shown on the image is only some 100 years old. The flow has low viscosity indicating basic lava. The typical irregular surface of such lava flows creates large surface depression storage, while

there are no signs of water stagnating for longer periods of time, which could suggest permeable conditions. It is known that lava flows develop a brecciated upper surface that is progressively pushed below the flow as it progresses and this tends to produce a relatively permeable upper and lower horizon. However, the permeability of the entire flows is unknown because porosities of basalts range widely from practically 0 to more than 75% (Cook, 2003). The large water deficit (from rainfall and evaporation) of about 1,000 mm of the area is not conducive for accumulation of surface water in depressions over longer periods for recharge. If some recharge takes place on the lava flows, it is likely to be on the bare fresh flows, whereas the older flows have a sparse but deeply rooted bush and shrub vegetation, returning water to the atmosphere.

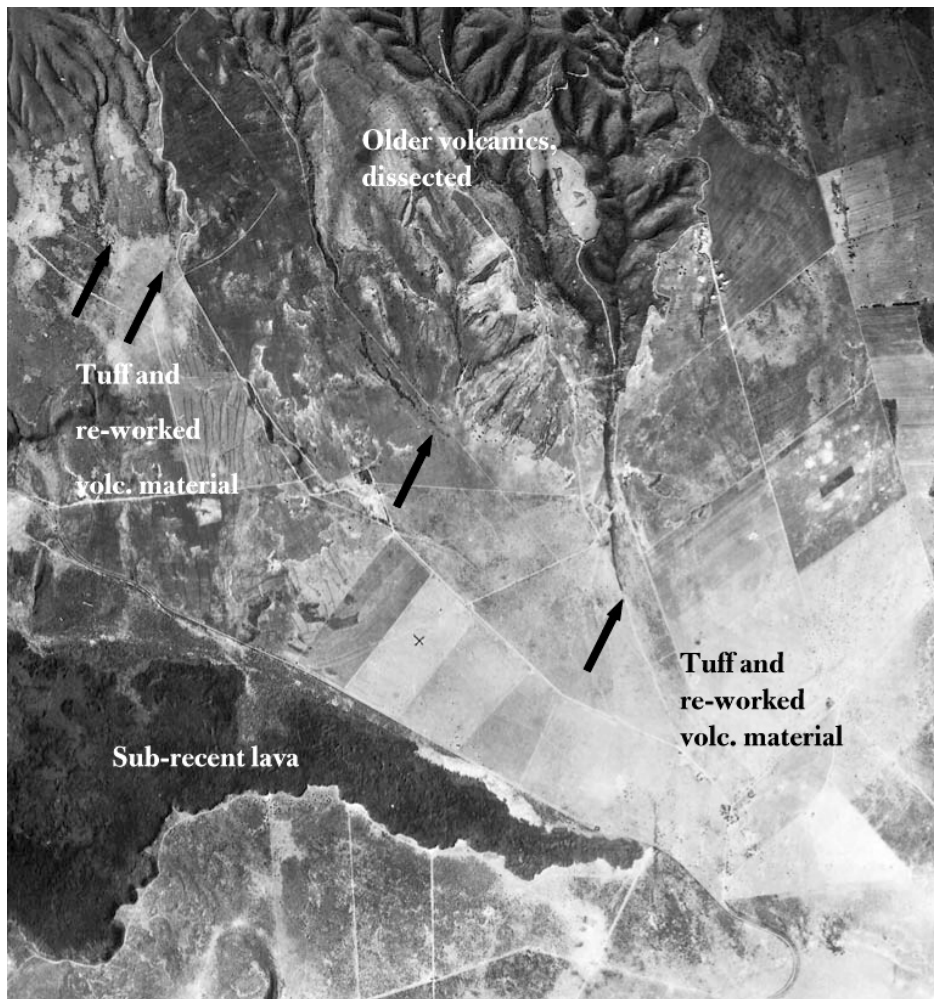
Since the lava flows abut against the explosion craters, the pyroclastic deposits (tuff, lapilli, etc.) associated with explosions, must be older than the flows and could possibly be found below the lavas and add to the overall permeability. Recharge may occur in the tuff covered and step-faulted western flank of the rift valley and part of the groundwater may flow into the rift faults.



**Figure 8-1** Aerial photograph showing volcanic landforms, Rift valley, Kenya. Absence of surface drainage indicates relative high recharge. Black lines along steep rift fault walls are shadows. Distance E-W is 8.5 km.

*Example indicating high permeability*

In the area northwest of Naivasha Lake, Kenya, ephemeral rivers draining older volcanic complexes, disappear when they reach gently sloping areas consisting of tuffs and fluviially transported tuffs and other volcanic materials, indicated as ‘re-worked volcanic material’ in Figure 8.2. The disappearance of drainage lines is a sign of permeable conditions and good recharge by runoff from ephemeral flows, but it should be noted that channel flow converted into sheetwash at the mouths of the ephemeral rivers stagnates at low places (information from local inhabitants) and is lost partly by evaporation. Presence of a relatively young lava flow (sub-recent lava), overlying an older one, adds to the recharge but by rainfall only.



**Figure 8-2** Aerial photograph (north-west of Lake Naivasha, Kenya), showing disappearance of flow of ephemeral rivers after conversion of channel flow into sheetwash (arrows) in gently sloping areas consisting of tuff and re-worked volcanic materials, due to infiltration and evaporation. Distance E-W is 8.3 km.

#### *Example of subsurface runoff in tuffs, evidenced by collapse holes*

Perhaps a less common, but interesting case, is the subsurface channel flow of groundwater in tuffs. Figure 8.3 shows a gently undulating terrain west of Lake Naivasha, Kenya, with an overall slope to the southwest, consisting of tuffs. A number of small but sharp depressions can be seen on the image (Aster false colour image).

These depressions are the collapsed roofs over subsurface tunnels, which are formed by mechanical removal of the material, known as suffosion tunnels or piping gullies. It should be remarked that the collapse holes can be best identified on stereo airphotos. By connecting the collapse holes across the topographic slope, the location of these groundwater conduits can be located, but only approximately because the tunnels are not straight. Furthermore, not all tunnels are expressed by collapse holes. For example, near site (1), two boreholes were drilled some 80 m apart; one was dry and the other one hit a tunnel and flowing water could be heard in the borehole, but without expression on the surface.

These tunnels point to the presence of permeable layers possibly former channel deposits below the tuffs, which allowed groundwater to concentrate sufficiently to cause erosion. Furthermore, there must be sufficient recharge in the older volcanic complex in the north, which has high (orographic) rainfall and in the tuff area itself to sustain strong flow of groundwater. The possibility that the tunnels were formed during an earlier pluvial period, but continue to act as subsurface drains under the present climatic conditions should also not be excluded.

The runoff does not emerge in springs in the area and it is assumed that the water flows along rift faults to far outside the area considered. Abundant traces of relatively fresh faulting can be seen on aerial photographs to the north and south of the area shown and some of them can also be noted on the ASTER image.

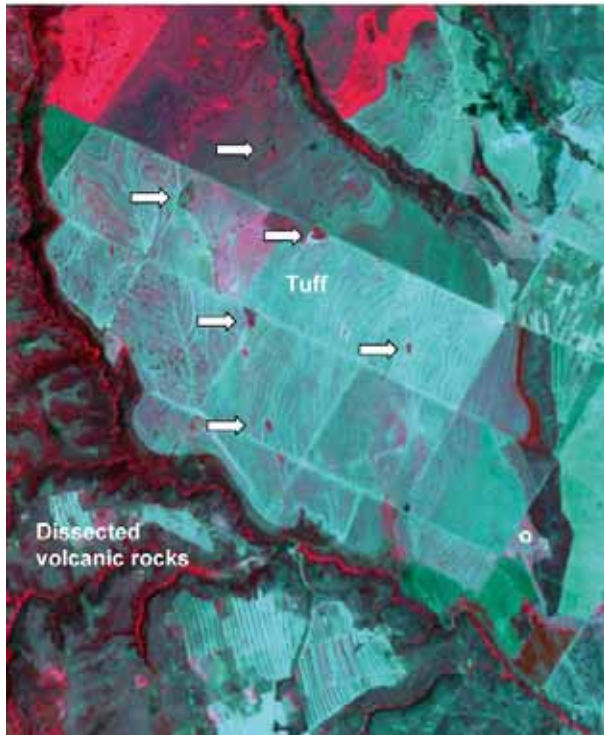


Figure 8-3

False colour image of ASTER. In area with tuff and agricultural fields, collapse holes (suffosion) are indicated by arrows (originally identified on stereo aerial photos).

Near o (southeast), two wells were drilled close to each other; one was dry in the other one – flowing – water was stuck.

Distance E-W is 6.7 km.

## 8.3 Stratovolcanoes

### 8.3.1 Hydrogeology

The relative age of stratovolcanoes in an area can be assessed by the degree of dissection/denudation; overall permeability is associated with relative age. The rocks of older and dissected stratovolcanoes tend to have lower permeability than the younger ones, because of compaction. This is due to the load of the volcano prior to erosion and internal processes due to earlier proximity to magma chambers and circulation of CO<sub>2</sub> rich groundwater at depth. Custodio (2004) terms such processes leading to reduced permeability the ‘ageing effect’.

Permeability affects surface runoff, and when peak runoff rates for a large number of rivers in Java (Indonesia) are plotted against catchment area on a graph, the catchments draining young volcanic rocks all plot below and those draining old volcanic rock above a line dividing the two, while the catchments with mixed lithology take an intermediate position. If this difference can be noted when there is a large rainfall excess (peak flows with a return period of 10 years were considered), then the effect of overall permeability will be more pronounced when rainfall is less. Obviously, young volcanoes have higher recharge and transient storage.

Aquifer characteristics of old volcanic rocks in Java, Indonesia, are relatively poor. Transmissivity is seldom more than 50 m<sup>2</sup> d<sup>-1</sup> and yields are generally in the range of 1 to 5 l.s<sup>-1</sup>, while both figures are much higher in the aquifers formed by younger rocks of stratovolcanoes (Sommen et al., 1990).

However, there can be a great variability in the hydrogeology of one stratovolcano to another, even when they are geographically close to each other. This is due to their geological history, related to depth and type of magmas, nature of the extrusives, frequency of eruption and so on. It seems that no two stratovolcanoes are identical.

### 8.3.2 Upper, middle and lower volcano

It is useful to differentiate, where relevant, a stratovolcano into three units:

- (1) The upper volcano, where slopes are the steepest; lavas and pyroclast deposits dominate. The permeability of the upper volcano depends greatly on the proportion of lavas to pyroclast deposits, which tend to be coarse grained in the upper volcano. Apart from permeable pyroclast layers, the rocks of the upper volcano tend to consist of andesite, which has a relatively high permeability.
- (2) The middle volcano, where usually fluvio-volcanics (lahar deposits) alternate with other volcanic breccias,

lavas and pyroclast beds; slopes are less steep, except when deeply dissected. The middle volcano generally has a relatively high permeability, which exceeds the overall permeability of the lower volcano, which is richer in heavy textured deposits. Perched groundwater tables are common.

- (3) The lower volcano where gradients are gentler and fluvio-volcanics are dominant, but tuff deposits can be important. The transition from the upper to the middle and to the lower volcano is always gradual. Typical transmissivities of deep wells (up to 150 m) in the lower volcanic slopes in West Java are in the range of 50 to 200 m<sup>2</sup> d<sup>-1</sup> and average well yields of 18 to 36m<sup>3</sup> hr<sup>-1</sup>. Locally, highly productive artesian aquifers may occur with self-flowing boreholes yielding up to 36m<sup>3</sup> hr<sup>-1</sup> and transmissivities of more than 500 m<sup>2</sup> d<sup>-1</sup> (Sommen et al. 1990).

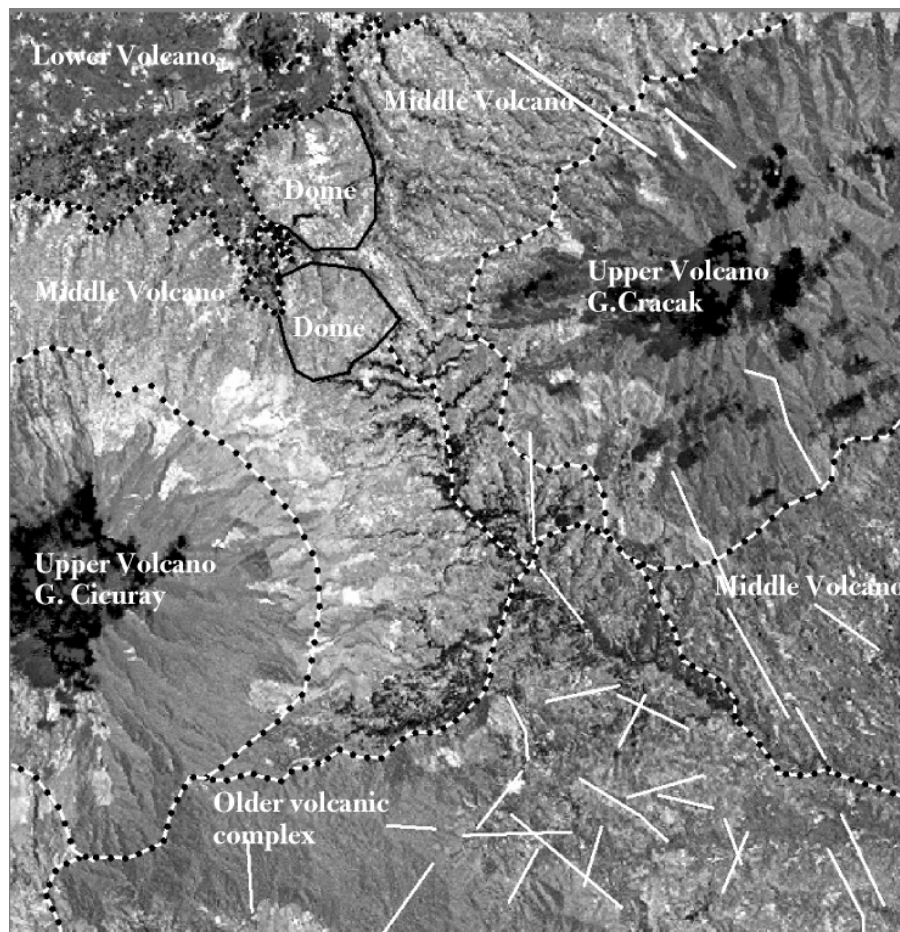
Roughly speaking, the upper volcano is a groundwater intake area. The middle volcano is a transient flow area and the lower volcano is a groundwater outflow area, but there can be strong outflow of groundwater in the valleys of a dissected middle volcano.

A few examples from West Java will be discussed.

#### *Example 1. Zonation and relative age*

An example of the zonation into upper-middle and lower parts of stratovolcanoes of different relative age, and compacted older volcanic rocks belonging to a former stratovolcano, is shown in Landsat ETM+ image of Figure 8.4.

Comparing the Cracak and Cicuray volcanoes, recharge will be greater on the little dissected upper and middle Cicuray volcano. Groundwater discharge can be interpreted from the presence of irrigated rice fields



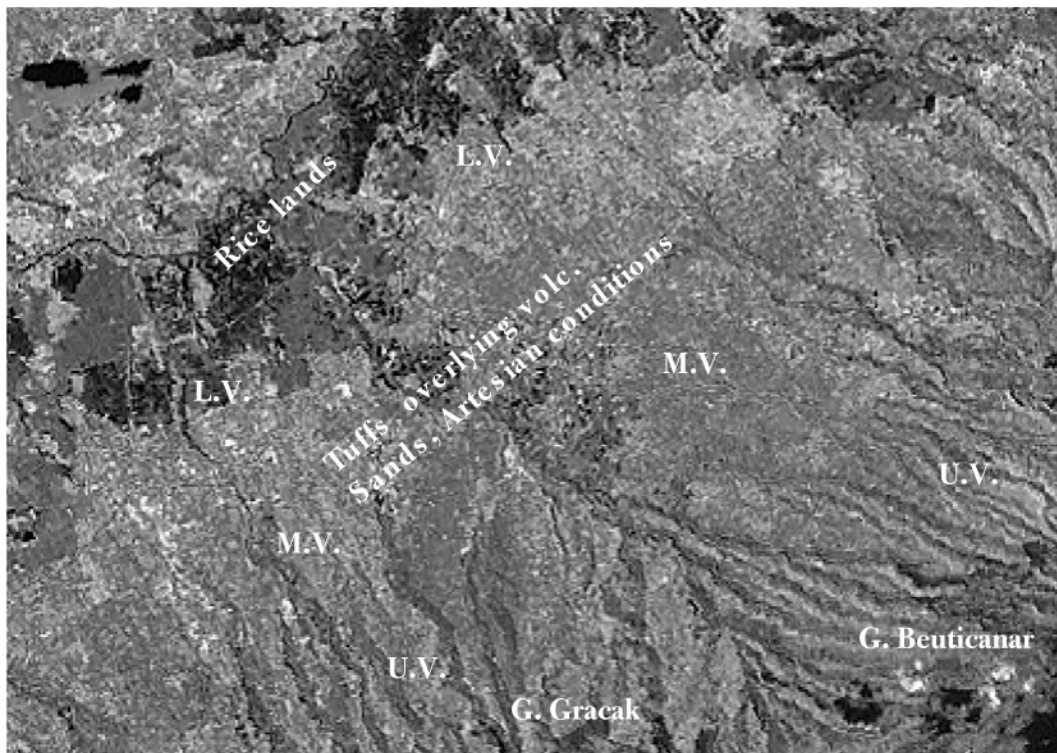
**Figure 8-4** Differentiation of stratovolcanoes into Upper, Middle and Lower parts and an older volcanic complex. Two lava domes with low permeability. White lines: major lineaments, most of them are found in the compacted older volcanic rocks. Dark areas on the Cracak volcano are cloud shadows. For hydrogeology, see text. Distance E-W is 17.4 km. Landsat ETM+ band 5.

(dark tones) on the northern flank, in valleys on the eastern flank, and along the southeastern flank near the contact with the less permeable older volcanic breccias. Major lineaments are shown on the images, drawn as white lines, and it can be noted that most of them occur on the compacted older volcanoes and are not evident on the young Cicuray volcano. Two lava domes – with low permeability – have been interpreted, the northern one was confirmed by drilling.

In fact, interpretation is based on the geomorphology but since the geomorphology is influenced by age and geology (morpho-stratigraphy, Hartono and Baharuddin, 1987), an association with hydrogeology can be made.

*Example 2, Artesian conditions*

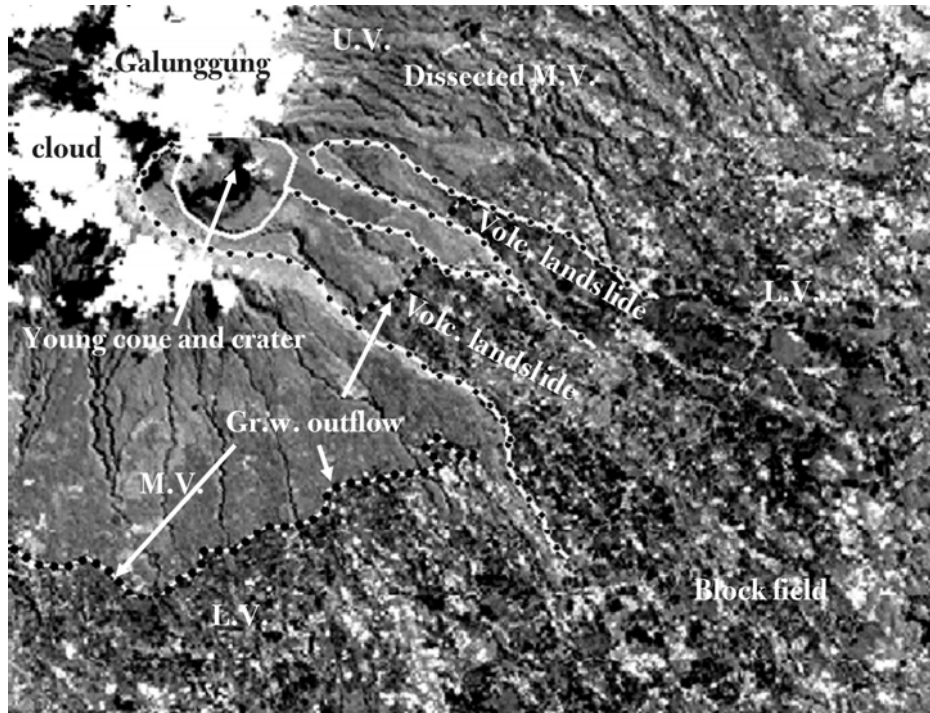
The middle and lower volcano of the northern flank of the Beutnicar-Gracak complex are little dissected, in contrast to the upper volcano. This is due to the presence of tuffs, interbedded with fluvio-volcanic layers, some of which have low permeability. Because of the hydraulic connection with the intake area of the upper volcano and the break of slope, artesian conditions occur, as indicated on the image of Figure 8.5.



**Figure 8-5** Southeast part of Garut Basin, W. Java, Indonesia. Middle volcano (M.V.) is little to non-dissected and has a cover of tuffs, which overlay volcanic sands, causing artesian conditions. Irrigated rice fields on lower volcano (L.V.) depend on groundwater discharge. Intake areas are the Upper Stratovolcanoes (U.V.) with high rainfall. Landsat TM Band 5, edge filter and stretched. Distance E-W is 12.2 km.

*Example 3, Groundwater outflow*

The southern flank of the nearby and active Galunggung volcano is little dissected, and the strong groundwater outflow, see Figure 8.6, Landsat ETM+, band 5, can be related to good recharge, particularly on the middle volcano. The line of outflow shifts on the eastern flank due to topography because a large volcanic landslide occurred. A large field of many huge lava/breccia blocks was deposited by the slide on the lower volcano (visible on stereo-aerial photographs). Such large landslides are caused by stratification and their deposits often have mediocre permeability. In the northern part of the image groundwater is discharged in the valleys of the dissected middle volcano.



**Figure 8-6** Active and permeable Galunggung strato-volcano with groundwater outflow, more or less along contour. Shift in outflow is due to topography related to a large volcanic landslide, which resulted in a field with huge blocks within lahar deposits. Groundwater outflow in dissected, older volcano in the north is in valleys. U.V., M.V. and L.V. as in Figure 8.5. Distance E-W is 12.8 km. Landsat ETM+ band 5.

### 8.3.3 Image interpretation, flow systems and simple modelling

In an attempt to understand the hydrogeology of a stratovolcano it is useful to employ numerical models of a simple nature to start with because of the many assumptions to be made.

Numerical studies of groundwater flow systems in mountainous terrain have been presented by Jamieson (1983) and by Foster (1988). In these studies free-surface methods have been developed to solve unconfined groundwater in which the position of the groundwater table is initially unknown.

The idea of modelling is to find a relation of groundwater-related features seen on images and plausible assumptions of simplified hydrogeology. In fact, it is an attempt to formulate a conceptual model and explore likely subsurface conditions. It is possible that more than one model scenario may explain features seen on the image, and this is of use in directing further investigation.

Such simple modelling was used in a groundwater study on the volcanic terrain of West Java, Indonesia (Sommen et al., 1990). The standard cross-section (2D) model used has a closed lower boundary formed by the impermeable Tertiary basement, which is found below the volcanoes. The left and right sides of the model are closed, reflecting natural flow boundaries. The upper boundary is defined by the water table, as derived from the outflow pattern seen on images (e.g. Figure 8.6), from wells or estimated using the change of perennial to ephemeral river flow in valleys in the middle-upper volcano.

Groundwater discharge is represented in the model as seepage distributed across the discharge area, rather than as concentrated groundwater outflow through springs. Local variations in surface topography, aquifer permeability and thickness of superficial deposits controlling the distribution of springs are assumed to have little effect on the overall pattern and magnitude of groundwater flow.

The model is applied to those volcanoes or parts of volcanoes where the radial drainage pattern suggests no disturbance of the groundwater flow by lava domes, adventive volcanoes on the volcano flank and so on, in order to facilitate a check on the results using well data, base flow and hydrochemical data.

The typical concave section and water table is shown in Figure 8.7 as are the sections with inflow (I), outflow (O) and throughflow (T). The figure shows some simulations whereby the configuration of the basement is changed. Other simulations use a layered sequence of beds in the volcano with estimated horizontal and vertical



permeabilities, and a combination of the two can be made, as is shown in Figure 8.8. In that particular case a set up was used with an upper layer overlying a lower one having reduced permeability and a configuration of the impermeable base that explained best the strong outflow in the middle volcano. The latter can be noted on the satellite image and from data of boreholes in the lower volcano (West East section in the area around Tasikmalaya, West Java.)

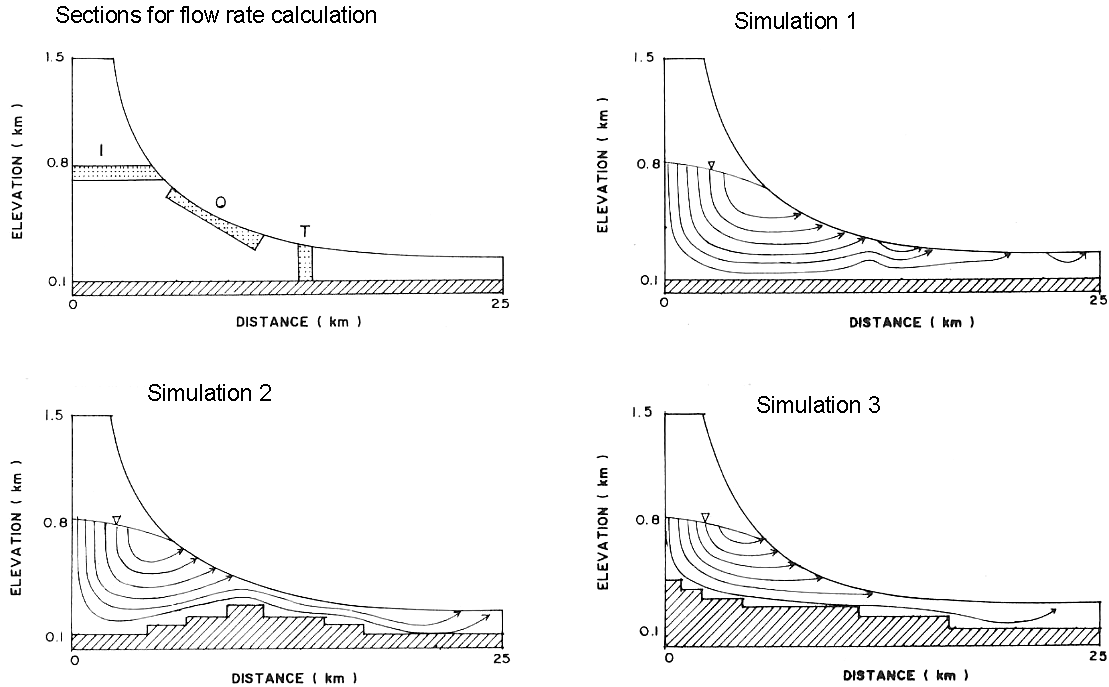


Figure 8-7 Cross sectional groundwater flow models. Upper left: Inflow (I), outflow (O) and throughflow (T) in the 2D model, and simulations whereby only configuration of the basement is changed.

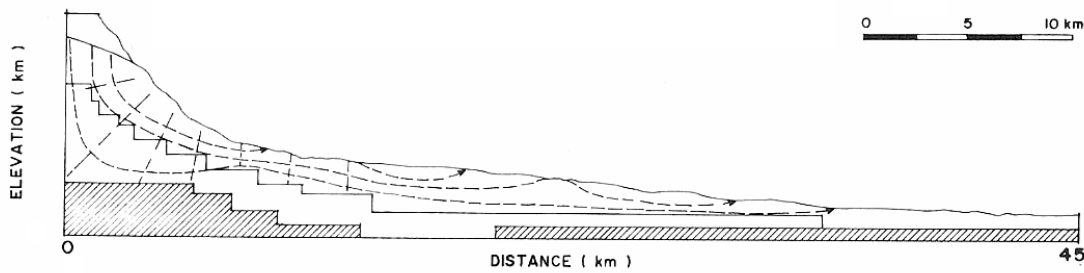
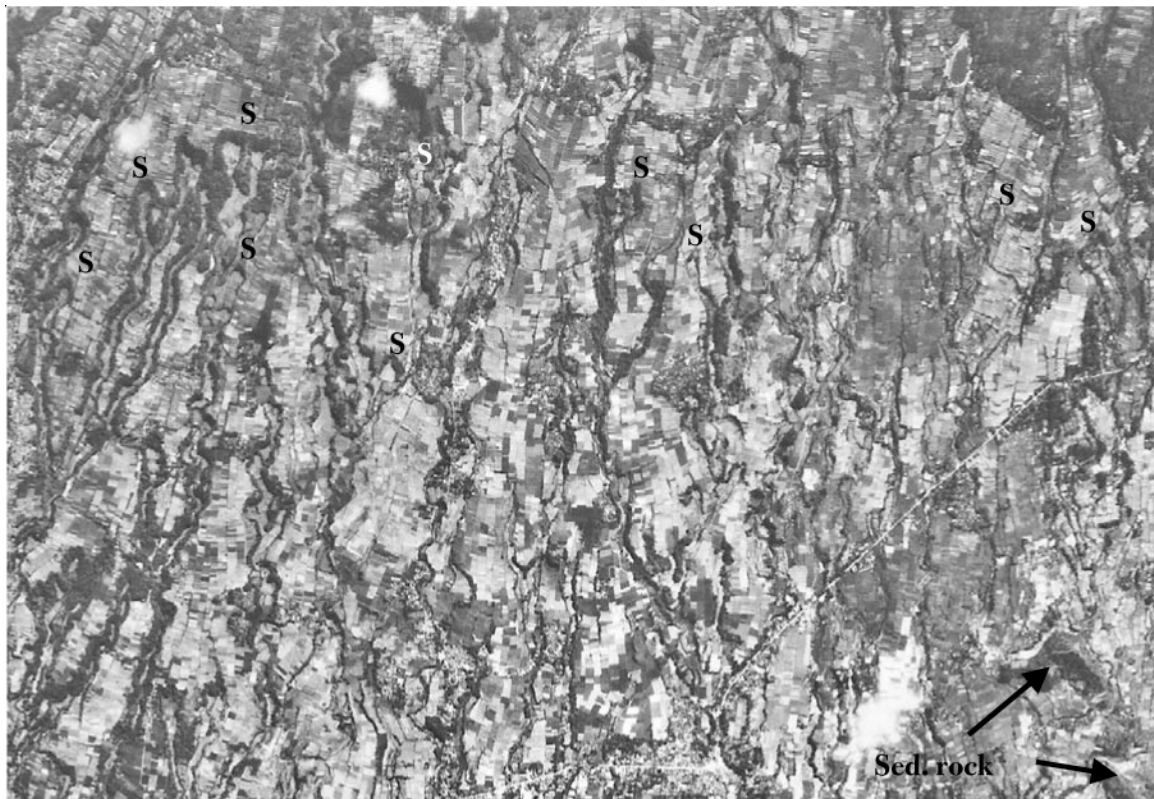


Figure 8-8 Model configuration that explained strong outflow in middle volcano, as noted on satellite image and existing hydrogeological data for the lower volcano and limited outflow in the downstream fluvio-volcanic deposits.

### 8.3.4 Springs in volcanic terrain

Interpretation of aerial photographs was used to assist in the setting up of the conceptual model of the southern flank of the large Gedeh-Pangrango stratovolcanoes in West Java. However, hydrogeological data was scarce and therefore the conceptual model was further defined by modelling of the above type, resulting in a few scenarios. To decide on the most plausible scenario, a field campaign was planned on the basis of the photo-interpretation map for base flow measurements, geological observations and measurement of electrical conductivity, starting at the junction of the upper and middle volcano and progressing downstream.

One of the questions was whether water from springs in the middle to lower volcano had their origin from local recharge or from the upper volcano. The locations of the springs are indicated by S in Figure 8.9. As can be noted they occur in a broad zone in the northern part of the image shown.

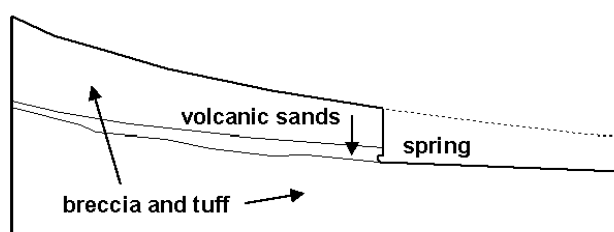


**Figure 8-9** Aerial photograph of the southern middle and lower volcano of the Gedeh-Pangranggo volcanoes, West Java, showing springs (S). Outcrops of impermeable base of the fluvio-volcanics and volcanic rocks are indicated. For explanation, see text. Distance E-W is 6 km.

It was found that the typical morphological features, namely horseshoe shapes at the heads of incised, flat bottomed valleys with rice fields, can be explained by spring sapping. Permeable layers of coarse-grained volcanic sands and gravels are interbedded with fluvio-volcanic breccias (lahar) and tuffs, as Figure 8.10 illustrates. The springs cause hollowing of the base of the small cliffs leading to rockfalls followed by removal of the sediment by fluvial action. In this manner the valleys grow in an upstream direction. The pattern of the springs and valleys seen on the image thus indicate the presence of volcanic sands below breccias beds.

The low EC values of the spring waters suggest mainly local recharge and the average spring discharge can be explained by assuming a recharge value of 30–40% of the annual rainfall in the average topographic catchment area of the springs.

The 2D groundwater model for this volcano is essentially similar to simulation 2 of Figure 8.8, although the model used was a multilayered one. Nearly all of the groundwater in the upper volcano emerges at the zone upstream of the area shown in the image, at the transition of the upper to middle volcano. For location of springs, see Figure 8.9.



**Figure 8-10**

Sketch showing a spring due to permeable layer. Valley downstream of the spring is caused by headward erosion.

For location of springs, see Figure 8.9.

### 8.3.5 Interpretation of lineaments

In volcanic terrain, wells may be located on lineaments, not only in older volcanic complexes where the secondary permeability is of importance, but also in younger stratovolcanoes.

Mulwa et al. (2005) discuss the permeability of volcanic rocks in an area in Kenya and emphasize the importance of faults, particularly in formations with low permeability, trachytes and tuffs, in their case. However, they also mention that some faults act as barriers to groundwater flow.

A more extensive discussion of lineaments as possible narrow permeable zones of fractured rocks and as groundwater conduits is given in Chapter 10.

The Landsat ETM+ false colour image of figure 8.11 shows some fractures in dissected terrain with older volcanic rocks and undulating relief. The local recharge conditions should be considered to judge possible suitability in conjunction with field observation of springs, the electrical conductivity of groundwater and so on. The image also shows some fractures, which drain the through flow from the intake areas of a relatively young stratovolcano (G. Sedakeling). The deep incision of the Cimanuk River is associated with uplift, which is related to the 'arching up' of the broad ridge of volcanoes in the central part of West Java, and it is likely that the SE NW trending lineaments are open tensional fractures. These are promising for locations of productive wells.

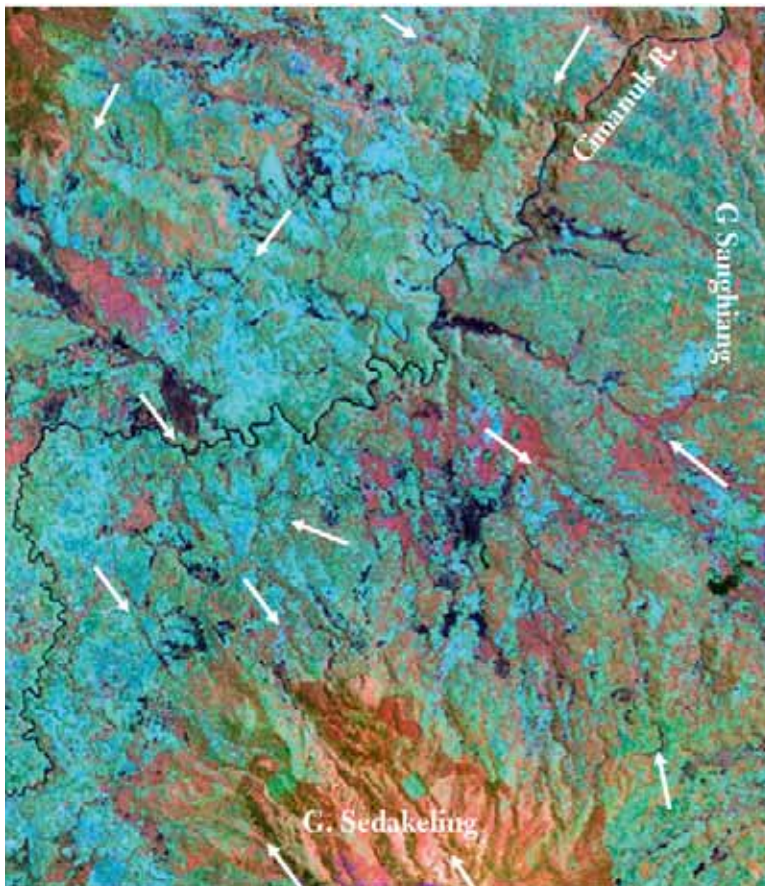


Figure 8-11

Area north of Garut Basin, showing older volcanic complex, overlain in east and south by stratovolcanoes (Sedakeling and Sanghiang)

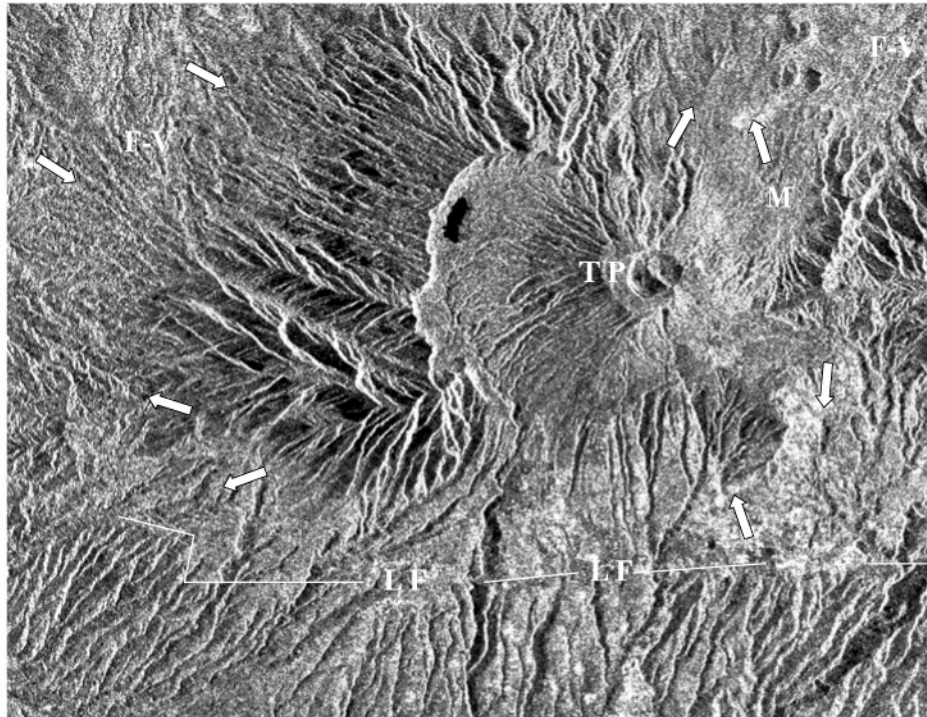
Several major lineaments are indicated (not exhaustive), which are likely to be water-bearing fractures.

The most promising lineaments are those that drain the upper-middle volcanoes.

Distance E-W is 13.7 km.

Landsat ETM+ false colour

Radar images are useful for the interpretation of lineaments, as is shown in Figure 8.12, which depicts the area around the Tangkuban Prah (TP) stratovolcano in West Java, north of Bandung. The western part of the old caldera with the younger volcano and the Lembang fault (LF) are prominent features, but so are the dissected upper and middle slopes and the volcanic landslide (M) in the northwest. A large number of lineaments can be interpreted; some prominent ones have been indicated. Their hydrogeological significance has to be assessed by fieldwork, such as measurement of base flow and hydrochemistry. However, it can be assumed that the Lembang fault acts as a barrier to groundwater flow, but that substantial flow can occur through the fractures crossing the fault under the strong hydraulic gradient.



**Figure 8-12** RADARSAR image of the area north of Bandung, West Java, showing volcanic landforms and lineaments. Some prominent ones indicated by arrows. M = volcanic landslide LF = Lembang fault. TP Tangkuban Prahua volcano in older caldera. Distance E-W is 19.5 km.

### 8.3.6 Lineaments and springs in Amboseli, Kenya

In some cases important springs occur in volcanic terrain, but it may not be obvious whether they are associated with fractures.

For example, the large fresh water springs (EC of  $<240\mu\text{S}$ ) of Amboseli Park are found at a few places along the contact of the volcanic rocks of the lower footslope of the Kilimanjaro Volcano and lacustrine deposits resting on basement rocks in south Kenya, shown in Figure 8.13.

The total annual outflow can be estimated by multiplying the wet area with the potential evaporation (Meijerink and van Wijngaarden, 1997) and therefore, by measuring the wet areas on sequential images an estimate of the variation in spring discharges can be made. These variations are not related to the rainfall in the Amboseli area, and because of the very low salinity of the spring waters, the source of the water must be sought in the high rainfall zone further up the Kilimanjaro (in Tanzania), where a dense forest vegetation is present, see Figure 8.13.

The outflow at two locations with a few springs each is contradictory of what can be expected on the basis of a cross-sectional groundwater model, similar to the one mentioned above. Model results show outflow over a wide zone upslope of the springs, but that area is fully dry; even in deeply incised valleys no water is found. Therefore, the most plausible situation is that groundwater flows relatively fast through fractures, lava tunnels and possibly narrow valley fills or permeable pyroclastic deposits, overlain by younger deposits, from the area with water excess (the forested high rainfall zone) to the springs.

The area upslope of the springs is shown in Figure 8.14. Some lineaments have been indicated on the image (white arrows), but it is obvious that no major continuous lineament reaching the spring location can be observed because young ignimbrite deposits cover the upslope area of springs S2-S3, while the extension of the N S fracture in the west cannot be traced up to the springs S1. However, it is likely that the fractures extend below the young ash flow cover.

The source of the ash flow is unknown but must be sought in one of the many young cones on the flank of Kilimanjaro. The material rushed down the incised narrow valleys and on aerial photographs ash-splay can be observed at the apex of the ash flow deposits.

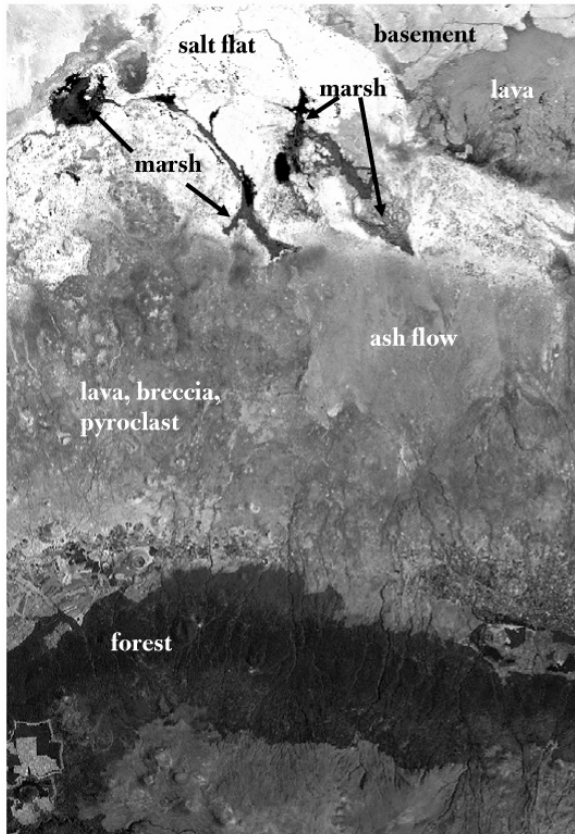


Figure 8-13

Northern flank of the Kilimanjaro volcano, Tanzania-Kenya, showing wetlands fed by large groundwater springs.

Source of the water must be sought in the zone with rainfall excess in the middle volcano, the forested area.

Flow of groundwater from that area to the springs must be rapid because of the low TDS content of the spring waters, suggesting concentrated flow.

Landsat TM b5, stretched.

Distance E-W is 31.5 km.

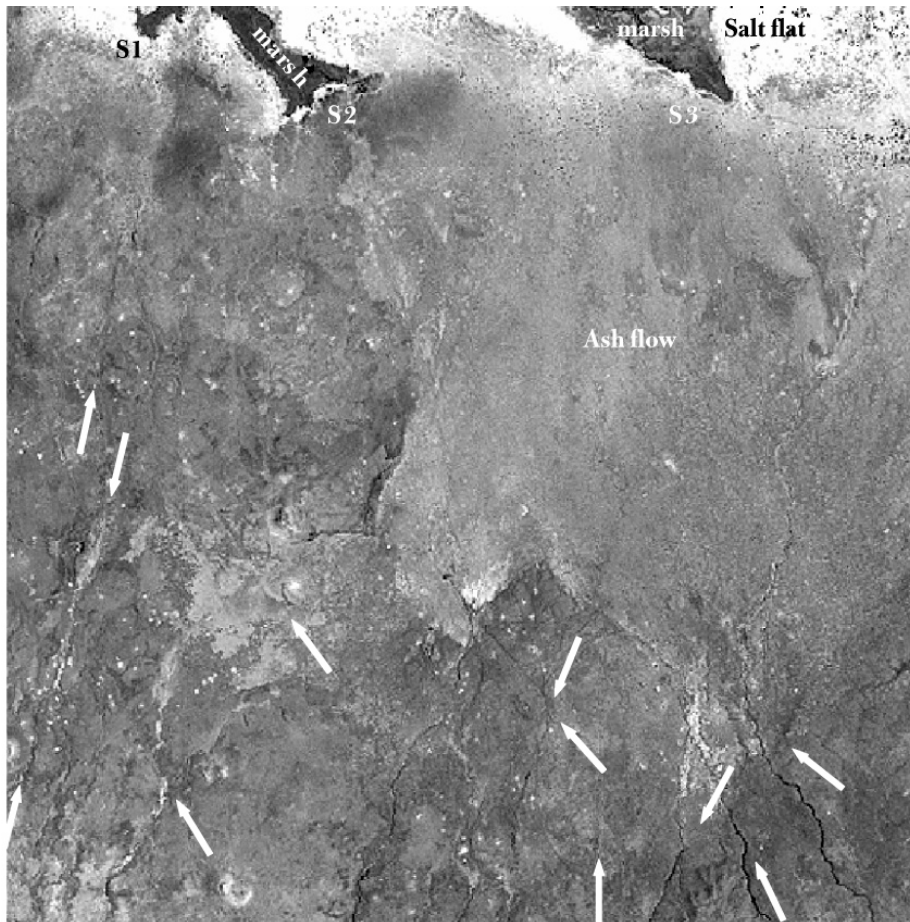


Figure 8-14 Enlargement of the area above the springs, showing fractures in the area not covered by young ignimbrite. Landsat ETM b5, edge enhancement. Distance E-W is 15.6 km

### 8.3.7 Limitation of lineament analysis in Rift area, Ethiopia

It may be useful to include another example of an area where lineament interpretation had only partial success. The area (Figure 8.15) consists of volcanic rocks (basalt and ignimbrite mainly). Some lineaments can be interpreted (see Figure 2.12b in Chapter 2) in the area west of the rift faults and the lake, but these lineaments represent only a part of the fractures present in the area as was found by drilling some successful wells hitting fractures, located by geophysical survey, not seen on images. Boreholes in non-fractured rocks were dry.

The water bodies and marshes (W) shown in the image of Figure 8.15, are groundwater outcrops in small grabens (rift in rift). Note the dry continuation of the river incised in the horst west of the rift faults. This suggests that no or little water groundwater crosses the rift faults. A regional groundwater study found strong groundwater flow along the faults, but not across them (Ayenew, 1998). In fact the perennial river loses water in the graben and that water flows in a southerly direction because water of a large spring in Lake Langano (in the south, not shown on the image) has the same isotopic composition as the water of the river traversing the area shown on the image.

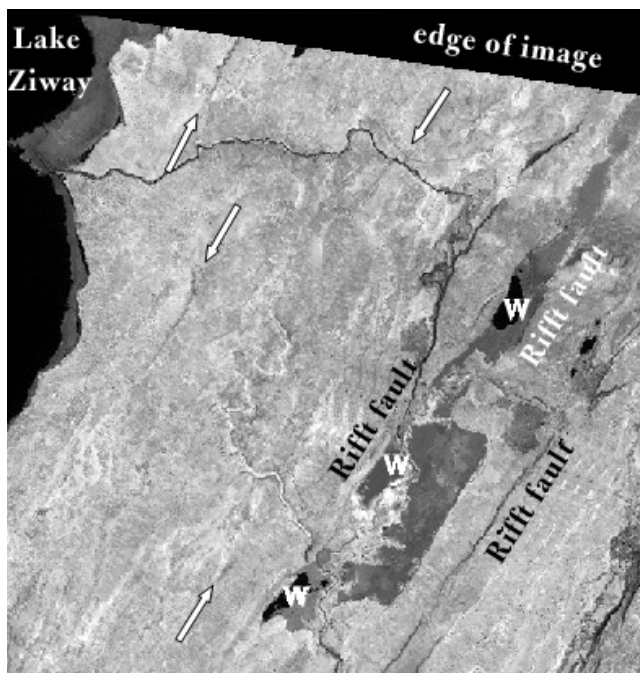


Figure 8-15

Area east of Ziway, Central Rift, Ethiopia.

Rift faults and associated wetlands are clearly shown. Only a few lineaments appear in the area (a horst) between the rift faults and the lake.

Some good wells were drilled and success was attributed to flow in fractures, some not seen on image but located by geophysics

Water bodies and marshes (W) in small grabens.

LandsatTM band 5, filtered.

Distance E-W is 16.7 km

Source: Pers. comm., Ayenew

## 8.4 Flood basalt terrain

### 8.4.1 Introduction

In order to understand and select hydrogeological relevant features in basalt terrain, some background knowledge is required.

#### *Hydrogeological rock properties*

Flood basalt terrain is characterized by the presence of tholeiitic basalt flows, which retain their mineral and physical characteristics over appreciable distances.

The features of the continental flows in India (Deccan Trap), as well as groundwater occurrences, are described by Kulkarni et al., 2000. The typical sequence is: a compact basalt, overlain by vesicular amygdaloidal basalt, which may be terminated by a red, thin tuffaceous layer and these sequences occur in thick stacks of flows. The rocks can be considered as hard rocks, and much of the transmissivity and storativity depends, in both rock units, on the density and nature of the sheet joints and the sub-vertical joints. Kulkarni et al. (2000) recognize two types of shallow groundwater systems. In system A, the vesicular basalt is outcropping and open wide diameter wells generally penetrate the underlying compact basalt only a little. In system B, compact basalt with negligible

primary porosity is found at the surface and wells have been dug into the underlying vesicular basalt. Transmissivity and storativity is higher in units in central west India with system A ( $100 - 493 \text{ m}^2 \text{ d}^{-1}$  and  $1 \times 10^{-3} - 8.5 \times 10^{-2}$  respectively) than in units with system B ( $42 - 100 \text{ m}^2 \text{ d}^{-1}$  and  $1 \times 10^{-4} - 1 \times 10^{-2}$ ). The higher yields of wells in system A allow irrigation of more hectares than those of system B.

For intramontane valleys in the lower Koyna, MP India, Naik et al (2001) mention that transmissivity values obtained are similar to those of other workers and were on average  $94 \text{ m}^2 \text{ d}^{-1}$  for highly weathered and highly jointed basalt and  $57 \text{ m}^2 \text{ d}^{-1}$  for poorly weathered and poorly jointed massive basalt.

Kulkarni et al. (2000) offer, on the basis of many observations, a conceptual model for groundwater flow in the Deccan Traps, which consists essentially of (sub)horizontal flow in the more permeable parts of the basalt flows and vertical flow through fractures to underlying permeable basalt strata.

### *Soil, weathered zone and deposits*

In warm sub-humid to semi-arid climates the soil of the basalts belongs to vertisols or black cotton soils. Under wetter conditions, deep laterites and bauxites are found. When dry, deep cracks are formed, sometimes several metres deep allowing the passage of rainwater before the cracks close. Because of the swelling nature of the clay minerals, the wetted topsoil expands during rainfall causing closure of the cracks, rendering the soil impermeable. Hence infiltration depends on aperture and stability of the cracks and spacing in time of rainfall events. Part of the infiltrated water may percolate down through fractures in the rocks below the soil; the remainder is retained as soil water held by suction. The high moisture retention of the soil makes it suitable for agriculture.

Locally, if the hydraulic gradient is sufficient, for example, near river courses, piping gullies may occur in the weathered zone draining shallow groundwater.

In non-eroded areas, the basalt often has a thick soil and the churning that takes place within the vertisol itself causes disappearance of the surface expression of fractures below the soil. Where the upper soil has been eroded partly weathered basalt is exposed and the infiltration and recharge depends on relief, degree of fracturing and porosity.

In warm non-arid climates hydrolysis is the major weathering process, and therefore vesicular basalt, which has a primary porosity and highly jointed basalt are likely to have deeper and more thoroughly weathering than massive basalt, causing higher transmissivity and storativity. Saha and Agrawal (2006) found approximately similar values for the storativity of the vesicular basalt and the weathered basalt ( $1.2 \times 10^{-2}$  and  $1.7 \times 10^{-2}$  respectively) in an area in the Deccan Traps, while the massive basalts had much lower values.

The geomorphology of flood basalt terrain consists of structural levels or terraces, and at lower positions pediments are usually formed. The structural levels reflect the differences in resistance to denudation of the vesicular and massive basalts. Little weathered basalt and shallow soil often occupy the upper pediments, which grade into more deeply weathered lower pediments, where sheetwash deposits may be present (the term buried pediment is often used). Along valleys relatively coarse-grained alluvial deposits may be present if relief is high; in pediplain areas the fluvial deposits are usually rich in clay and silt.

In deeply dissected terrain with flat lying basalts, bands of vegetation along contours may occur on slopes indicating seepage of groundwater from relatively permeable layers, but this seepage is usually very minimal. Contact springs may be found at the base of the cliffs but also in thick colluvial deposits (Naik et al., 2001), and these are generally difficult to interpret on images.

In areas with low relief, massive basalts may cause an interruption of the pediment developed over the vesicular and/or highly jointed basalt. This interruption can be subtle, as a small change of slope, but the presence of slightly weathered massive basalt may be apparent from the land cover.

Steps in the gradients of the rivers and presence of outcrops, which can be observed on images of the larger rivers, provide additional information on the weathering.

However, the geomorphological history should be taken into account when attempting to relate surface features likely to be associated with deep and thorough weathering with the inferred type of trap rock. In relatively young dissected trap terrain there could not have been sufficient time for differential weathering and erosion, development of pediments and associated retreat of basalt cliffs for rock differences to be expressed in the geomorphology. What appears in such terrain as a stack of flows of the same rock type may not be the case. High-level laterites in India are often permeable and that property protects them from erosion, so that they can be misinterpreted as massive basalt.

Interpretation of land cover is important because in dry regions groundwater is generally needed for irrigation by open wells or boreholes in the proximity of agricultural fields. Identification of irrigated fields indicates occurrence of groundwater and probable presence of vesicular basalt. Often clusters of irrigated fields can be noted, and it is possible that such clusters coincide with the intersection of the sloping pediment surface with the horizontal outcrop of vesicular basalt and zones of high fracture density.

In any case, the acreage of irrigated lands is required for groundwater balance studies, but care should be taken not to include fields irrigated by small reservoirs or lift irrigation using base flow in rivers. A vegetation index (e.g. NDVI) during the dry part of the cropping season will show the areas irrigated by groundwater, after eliminating those irrigated by surface water from rivers or reservoirs. High-resolution images can also be used, by inspecting the details of the field patterns, density of trees, etc. for mapping irrigated fields.

Dominance of rain-fed fields may point to a poor groundwater situation. Terrain units that are partly cultivated in areas with high population pressure, common in India, suggest shallow depths of weathering, while absence of cultivation and a shrub-grass cover may indicate the presence of slightly weathered basalt at the surface. Obviously, such relations are not valid in areas protected from encroachment, such as protected forestlands. Such lands usually have sharp boundaries not related to physiographic limits.

### **8.4.2 Image interpretation of structural elements**

#### *Lineaments*

Groundwater in flood basalts is often contained in fractures and faults, and these may be detected by lineaments on images.

Anomalous high transmissivity values ( $> 60\text{m}^2\text{d}^{-1}$ ) for compact basalts were found by Kulkarni et al. (2000) for wells that penetrate closely spaced linear fractures aligned with regional fracture zones. Borehole wells along or near lineaments in the Koyna watershed particularly at intersections of lineaments had substantially higher yields than those not associated with lineaments, (Naik et al., 2001), but for shallow dugwells the relation was not apparent. They also found that borewells intersecting NE trending lineaments were more highly yielding in deeply buried pediments than in the dissected plateau area.

Solomon and Quiel (2006) noted differences in permeability of basalts in Eritrea and found borehole yields to be higher near lineaments.

#### *Interpretation of regional lineaments*

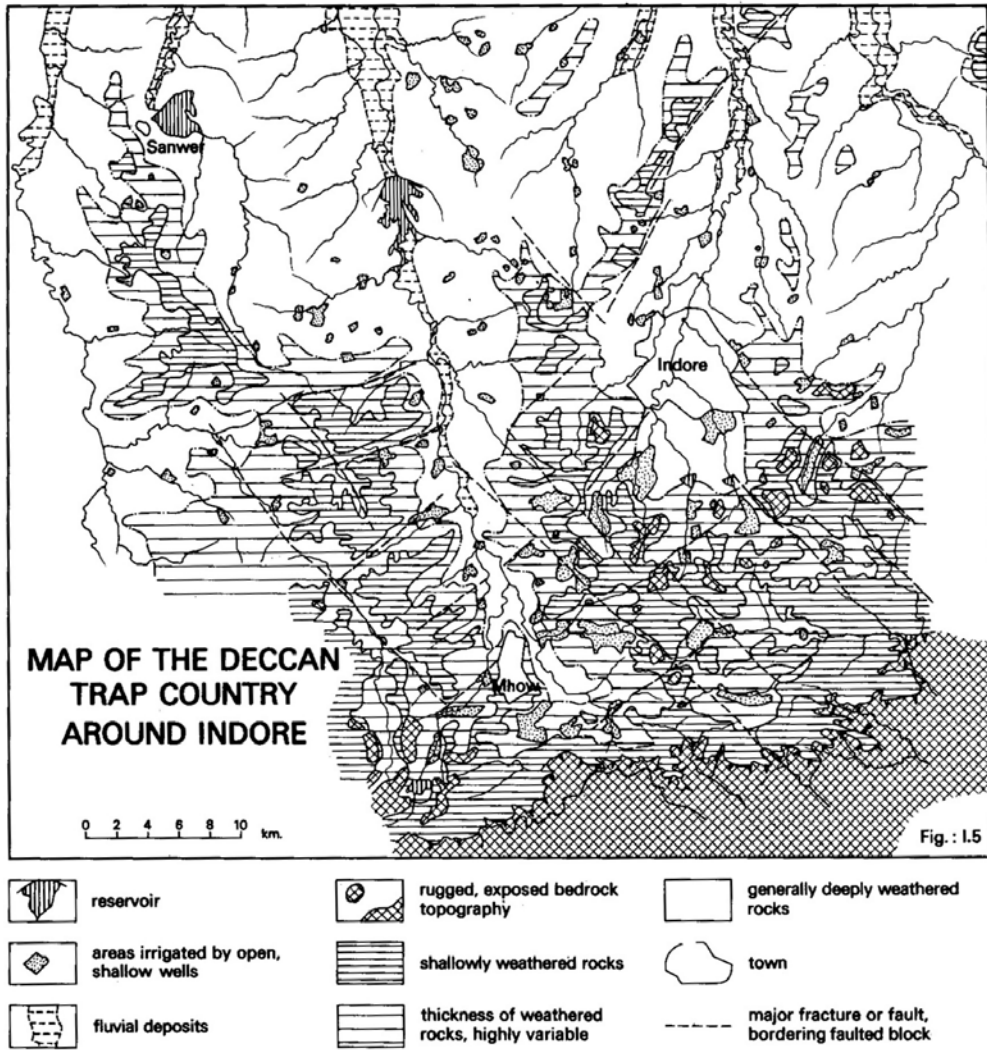
Regional fractures are usually interpreted on small-scale images of Deccan Trap terrain that show the drainage system and outcrop patterns. Lineaments in the form of long straight drainage corridors in weathered terrain are often considered as fracture zones. The same assumption may be made for lineaments consisting of straight river courses with possible-disrupted)-continuation in the form of outcrop margins and certain land cover patterns. However, the use of non-stereo, medium resolution satellite images (e.g., Landsat TM) for lineament interpretation may have a limitation, when compared with lineaments interpreted from stereo aerial photographs.

Figure 8.16 shows an area (east of Indore, MP, India) with generally gently sloping pediments and pediplains, except for some outcrop areas with low to medium relief. Stereoscopic interpretation of aerial photographs was used and results were transferred to topographic contour maps and bore-hole logs were consulted (Meijerink, 1974).

Most of the lineaments shown on the map are difficult to observe on Landsat ETM images, which can be attributed to the lack of detailed height information. On the satellite images chiefly the straight drainage features are noted, which have not been marked as lineaments on the photo-interpretation map for lack of structural evidence.

Lineaments in the form of long straight drainage corridors in weathered terrain are often considered as fracture zones. The same assumption may be made for lineaments consisting of straight river courses with possible-disrupted)-continuation in the form of outcrop margins and certain land cover patterns. By enlarging the image, most of the evidence may not be apparent. Since selection of lineaments is a subjective exercise, it may be wise to be restrictive.





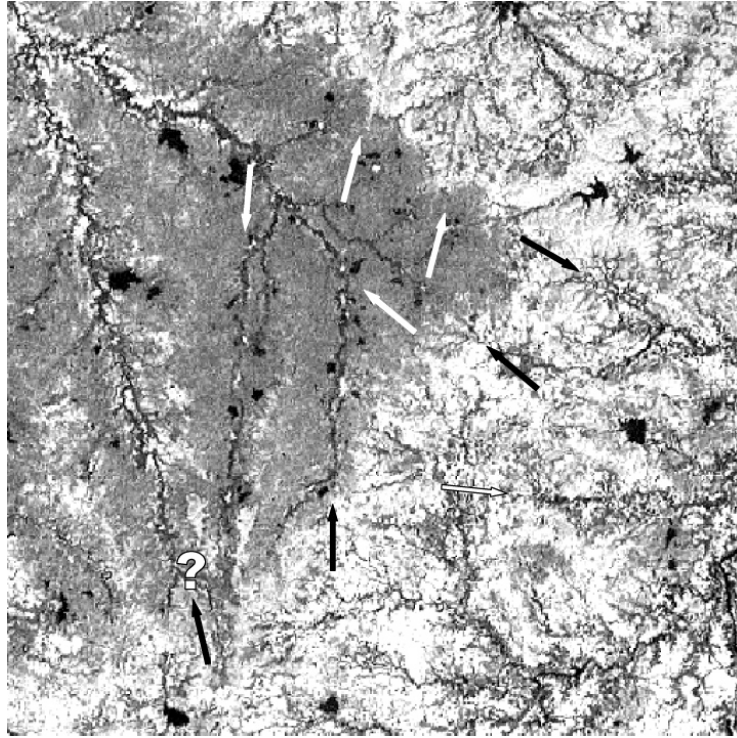
**Figure 8-16** Lineaments interpreted from stereo-aerial photos. Most of the lineaments are difficult to recognize on satellite images, for lack of height information. Straight courses of main rivers, evident on satellite images, have not been indicated on the map, because structural evidence can only be inferred.

### *Interpretation of sub-regional and local lineaments*

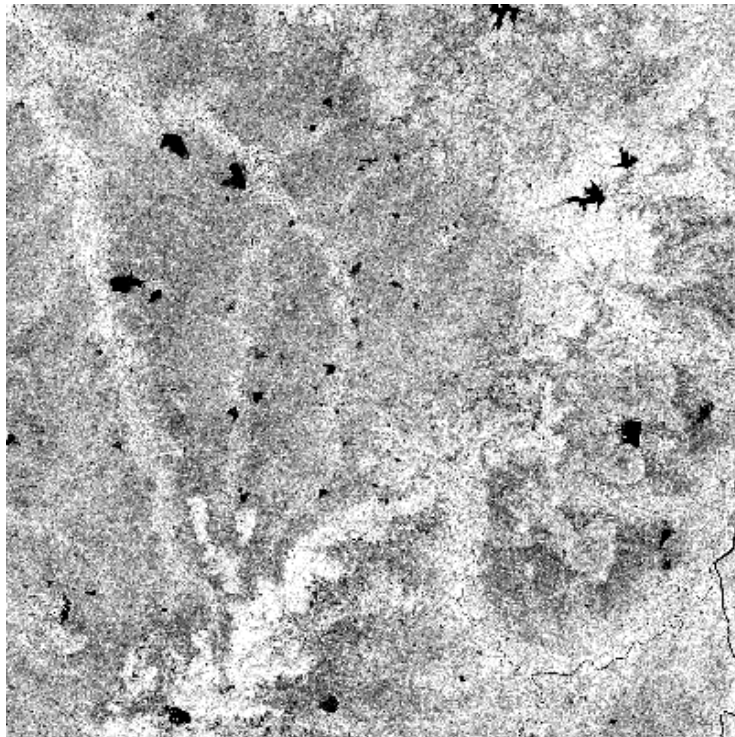
The importance of fractures in this type of hard rock was mentioned above and it is therefore worthwhile to first investigate what bands, transforms or combinations are best suitable for the interpretation of lineaments. The near infrared bands are suitable (e.g. Bands 5 and 7 of Landsat TM/ETM+), because of their sensitivity to spectral intensity variations that could be due to subtle variations in soil moisture and relief. Images created by high pass filters (Edge enhancement, Laplace, Sobel, Prewitt, etc, see chapter on Image Processing) could be used, but they have the disadvantage that the geomorphological and land use features are subdued. Often a colour composite of three bands, based on the least correlation of the selected bands is used, or a colour composite of transformed images (Principal components, NDVI, Hue-Intensity-Saturation images) but such composites may not necessarily be the best ones for interpreting lineaments.

It may be useful to inspect the thermal band, as illustrated in Figure 8.17. Without emissivity data, it is difficult to ascertain why lineaments could cause contrasts on the thermal band, but it is possible that thorough weathering resulted in different moisture content, influencing surface temperature. This is most likely to be the case for drainage lines in connection with shallow aquifer system.

Figure 8.18 shows the same area on the 14.25 m resolution of band 8 of Landsat ETM in the visual (panchromatic) domain. It is obvious that in this case contrasts are poor.



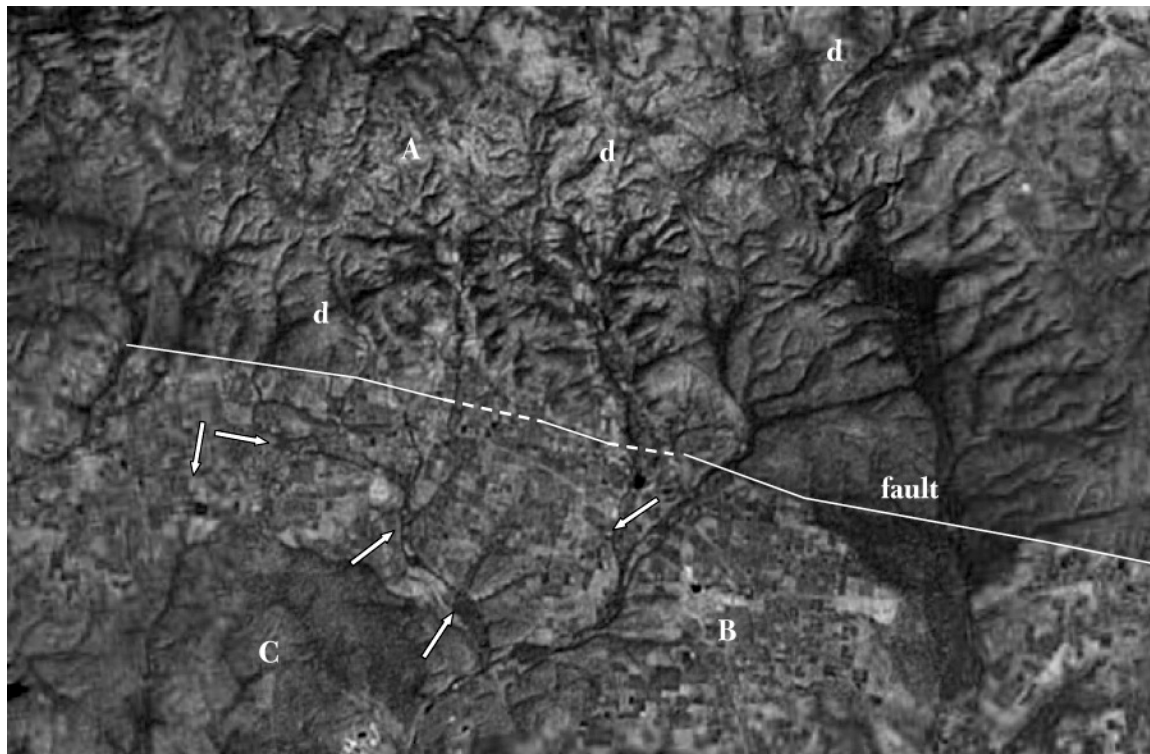
**Figure 8-17** Thermal image (Landsat ETM) of Deccan Trap terrain, east of Indore, M.P., India. Image was resampled to 28.5 m resolution and edge enhancement filter was applied. Several lineaments have been indicated. Presence of a large fracture zone over full length of river course, indicated by (?) shown on image could be questioned.



**Figure 8-18** Landsat ETM band 8 (pan-chromatic, 14.25 m resolution) of same area as shown in Figure 8.17. Note that many lineaments are not apparent, but the straight valley (questioned in Figure 8.17) may indicate perhaps a long fracture zone. Distance E-W is 23 km.

*Example structural interpretation.*

The northern part of the area shown in Figure 8.19 (north of Wardha, MP, India, Google Earth) consists of a strongly dissected plateau (A). At places traces of individual flows can be seen. On non-eroded flat parts small areas with shallow soils occur, but most of the area consists of slightly weathered basalts with no or shallow soils. Many lineaments in the dissected northern part (not indicated) are apparent and the development of drainage lines along several of them suggests that these are tensional forming zones of weakness where availability of water induced weathering prior to incision and development of drainage lines.



**Figure 8-19** Area north of Wardha, A.P., India of Deccan Trap terrain. Uplifted block in north is dissected and has no or shallow soil. Some drainage lines follow lineaments. C eroded - slightly weathered basalt, arrows indicate lineaments in weathered basalt B, d is dyke. Distance E-W is 13.3 km. (Source: Google Earth).

Dykes (d) traverse the area; these have positive relief, whereas the lineaments tend to produce negative relief. Presence of dykes may be a warning that some lineaments are intruded by dolerite, which is often impermeable.

A fault has been interpreted on the strength of the break of slope, change of relief/dissection and weathering (area B). Field patterns indicate presence of soils of sufficient depth, associated with vesicular/ highly fractured basalt. Some lineaments have been indicated in area B, because only there is groundwater needed for irrigation.

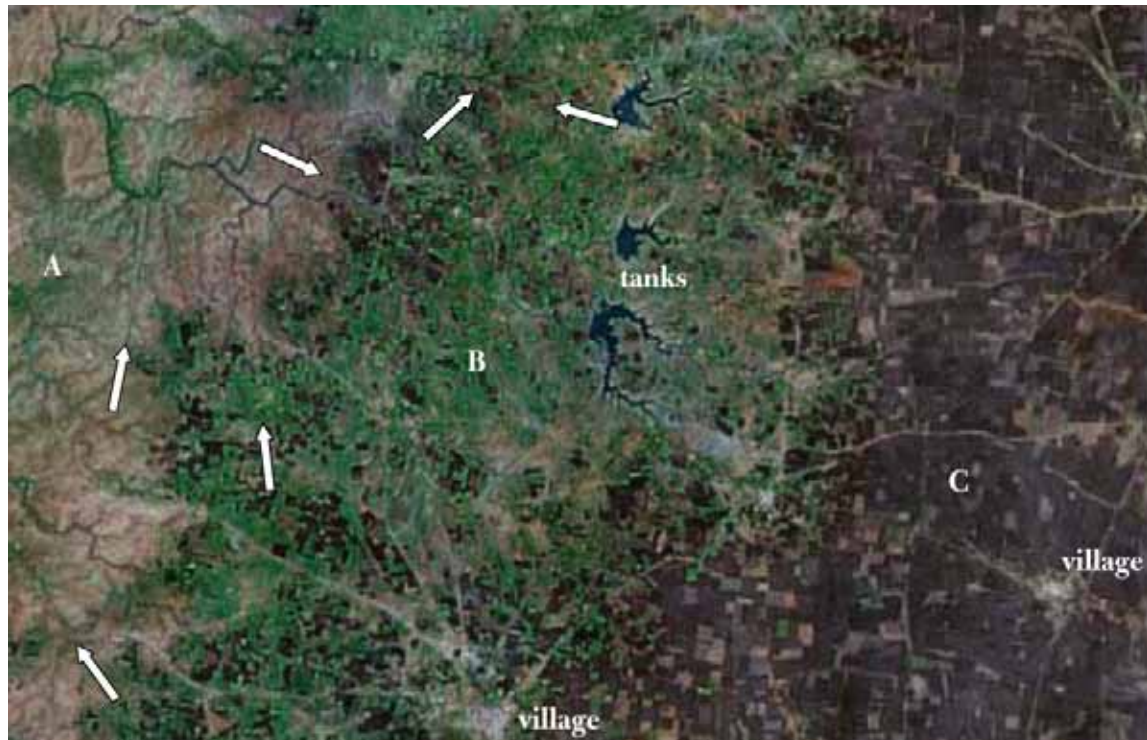
In area C the rocks are slightly weathered and have a shrub-grass cover.

The wide valleys (w) are an indication of presence of flows prone to erosion. Within the series of flows, they could be associated with higher permeability or higher storativity, but this has to be ascertained in the field.

*Example limitation of lineament interpretation*

As mentioned earlier, geomorphological development has to be considered in the interpretation, as illustrated in the Landsat ETM+ false colour image of Figure 8.20, which shows three hydrogeomorphological units.

Zone or unit A is dissected; part of the drainage network follows fractures (straight parts and angular course) and part is dendritic. At places, individual basalt flows can be differentiated with some difficulty (much easier to do so with stereo airphotos). Zone B consists of terrain with variable dissection and depth of weathering. The dark fields have crops that receive supplementary irrigation and it is interesting to note that these fields cluster along the



**Figure 8-20** Deccan Trap terrain, India (M.P), showing zonation of weathering depths and relief. A: dissected, soils absent or shallow, drainage is partly adjusted to fractures; B: intermediate zone, some dissection, weathering variable; C: deeply weathered flat to very gently sloping. Some lineaments are indicated. Many lineaments can be observed in zone A, few in zone B and none in zone C, but equal density of fracturing in all zones can be assumed. Distance E-W is 14.3 km. False colour image, Landsat ETM+.

transition of units A-B and units B-C. The presence of the clusters along the contact zones, should direct hydrogeological field investigations by selecting one or more typical transects.

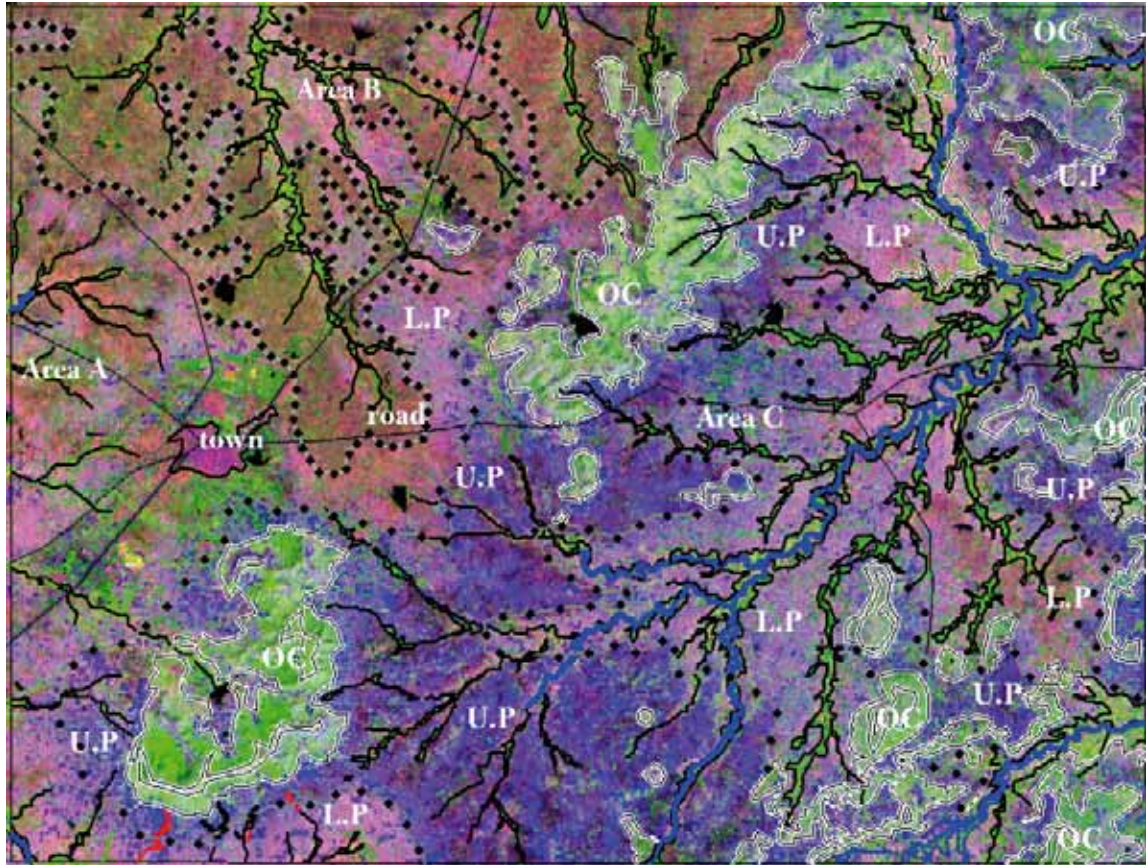
Unit C has the highest elevation and consists of a non-dissected, featureless plateau/pediplain sloping down very gently to the east, and in the area shown in the image only rainfed agriculture is found.

In units A and B some lineaments have been indicated, but none could be found in unit C because of the deep weathered zone and the nature of the soils. However, there is no reason to assume that the fracture density is different in the three zones, whose differences can be explained by geomorphological evolution. Fractures in zone C have to be found by geophysical traverses.

### 8.4.3 Geomorphological interpretation and image processing

Denudational processes (i.e. weathering and erosion) influence hydrogeology in the sense that recharge depends on kind of soil, type and relative intensity of runoff, while the weathered zone forms a shallow aquifer. Alluvial deposits may be present near rivers or ephemeral channels. Local base levels of erosion and even minor block faulting could have influenced the denudational history. Typical of much of Deccan Trap terrain of low relief is the presence of pediments or pediplains. In the case of large contiguous pediments, it is likely that the weathered zone is fairly thick, because otherwise traces of subsurface massive basalt may be observed. Interruptions in the pediment surface in the form of a strip that follows more or less the contour could indicate presence of massive basalt, and more permeable vesicular basalt is likely to be found on top (i.e. the pediment just upslope of the strip, as well as below it).

In order to make use of subtle variations in soil and land cover, which generally escape attention in the field, it is advisable to use an image for interpretation that contains as much spectral information as possible. Such an image is the colour composite of Figure 8.21, which consists of the first two principal components (PC) and the thermal band (resampled to the same pixel size as the PCs). A provisional interpretation is added. Based on details



**Figure 8-21** Composite of Principal Components I and II and thermal band of an area, east of Indore, M.P., India with low relief, except in some outcrop areas (OC) with moderate height. This image contains nearly all the information of a Landsat ETM scene. Provisional geomorphological interpretation added. Three different sub-areas may be differentiated (Areas A, B and C), Upper pediment (U.P), Lower pediment (L.P) and alluvial areas/dissected river banks.

of the drainage patterns and spectral colour information, three different areas (A, B and C) are differentiated, as well as outcrop areas (OC). In each of the three areas pediments are the dominant landform, but only in area C has the upper pediment been differentiated from the lower one. The narrow zones of alluvial deposits or dissected riverbanks have been mapped as well.

A major advantage of doing such interpretation at the start of hydrogeological investigation is that the area is inspected systematically and specific places for field checking can be listed, in order to clarify questions raised during the interpretation as to the nature of soils, weathered zones and so on.

Lineaments have to be added, but these can best be interpreted on filtered selected bands (e.g. the NIR bands, a PC I image or the thermal band).

It is only after sufficient hydrogeological data has been analysed that the significance of the geomorphological units and lineaments can be assessed.

#### **8.4.4 *Image interpretation and conceptual model of possible sub-regional flow system***

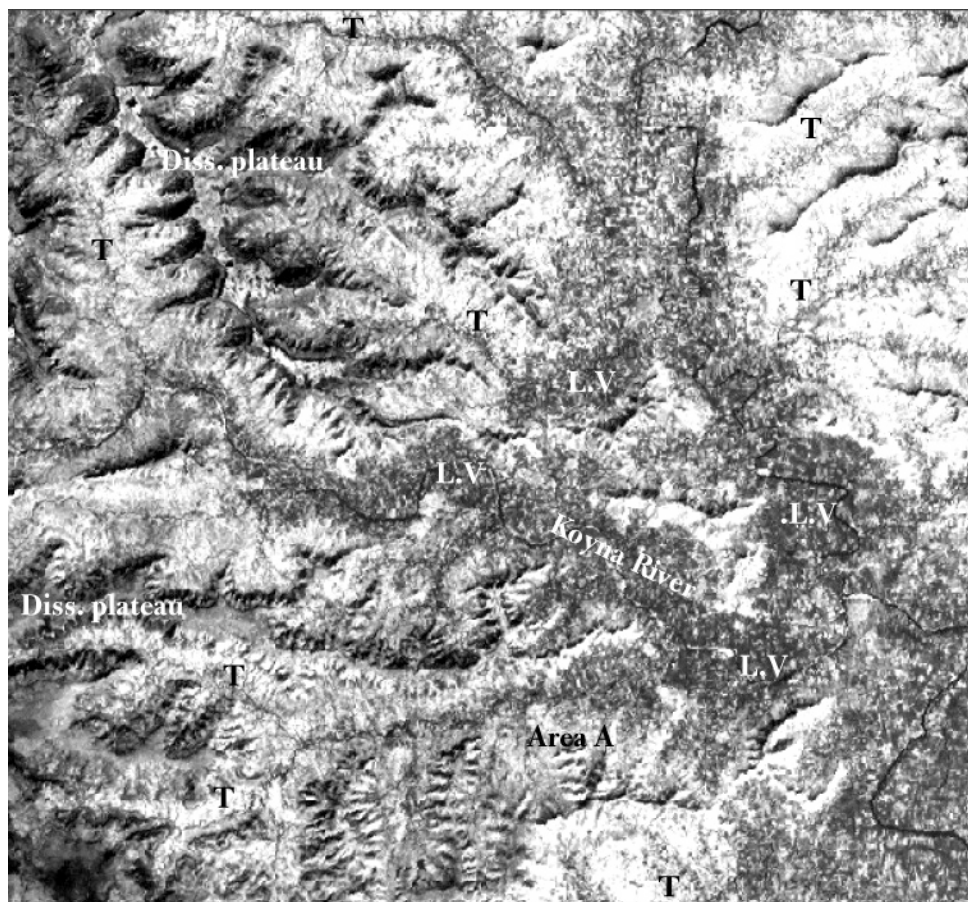
Kulkarni et al. (2000) offer, on the basis of many observations, a conceptual model for groundwater flow in Deccan Traps, which consists essentially of (sub)horizontal flow in the more permeable parts of the basalt flows and vertical flow through fractures to underlying permeable basalt strata. They remark that the relation between the shallow and deeper aquifers needs further study. In a later study in Eritrea Solomon and Quiel (2006) present the same conceptual model for flood basalts.

Looking at an overview presented by a satellite image of a Deccan Trap around the Koyna River, MP, India,

Figure 8.22, the question arises as to why there is such a small percentage of fields irrigated by groundwater in the tributary valleys compared to the proportion of irrigated fields in the gently sloping (pediments) of the valleys at lower altitude. This is noteworthy because the potential recharge areas are large in the plateau region and relatively small in the wide valleys at lower altitude. Horizontal bands of vegetation along the outcrops of flows in the hilly part suggest the presence of alternation of basalts of different permeability and some lateral seepage.

The thermal band of Landsat ETM was used for showing the overview because dark tones correspond to transpiring vegetation and moisture, but an NDVI transform of a Landsat ETM image of the month November (i.e. two months after the monsoon) was used for assessing crop responses in the cultivated areas. High-resolution images were used to inspect the extent of the cultivated lands in the tributary valleys.

Possibly, in the valley-plateau region irrigation from open wells (usually <10 m deep) makes use of local perched water tables and much groundwater percolates to lower levels through the system of fractures and vesicular basalt or inter-trappean layers. At lower altitude the system seems fully saturated and lateral sub-regional groundwater flow takes place from elevated recharge areas to the wide valleys at lower altitudes. In addition, there can be contribution of deeper confined water in the flow system. Naik et al. (2001) describe the hydrogeology of the Konya valley and present pre-and post monsoon water depths and water table fluctuations. It is interesting that on their maps, the cultivated and partly irrigated lands in the valleys near Area A (see Figure 8.22) had relatively deep water tables with large fluctuations. It can be noted that the potential recharge area around (A) is small, being the narrow ridge areas in the south and north. They also present a map showing the extent of lift irrigation along the lower Konya River, but that is only a part of the total 'wet' area shown in the figure.



**Figure 8-22** Area around Konya River, M.P., India. Area consists of stack of horizontal basalts. In tributary valleys (T) only few and small fields irrigated by groundwater are found, in contrast to the lower valleys. This may suggest sub-regional groundwater flow and relatively shallow groundwater at low altitude pediplain. North and west of area A has deepest groundwater level and seasonal fluctuation (Naik et al., 2001). The thermal band of Landsat TM was selected because dark tones in the valleys are associated with transpiring crops and moisture. Distance E-W is 41 km.

## 8.5 Summary and conclusions

Examples of volcanic landforms are discussed and shown and attention was drawn to hydrogeologic properties. The recognition of volcanic rocks depends on interpretation of the geomorphology. Recharge conditions may, in some cases, be estimated qualitatively by studying drainage features.

The hydrogeology of stratovolcanoes is discussed and zonation into upper-middle and lower volcano is related to flow systems typical of stratovolcanoes. Simple groundwater modelling may be used to clarify possible subsurface influences and explain features seen on images and related to outflow of groundwater. Older Quaternary volcanic complexes have relatively lower primary permeability than younger ones and therefore fracture flow is of importance. Lineaments interpreted on images can be related to large fractures and flow of groundwater along lineaments may be inferred from their position within a flow system.

Groundwater occurrences in flood basalt terrain are associated with weathered basalt, vesicular basalt and fractures (lineaments). Examples of Deccan Trap terrain in India are included to illustrate hydrogeological image interpretations at various scales and image types, using background knowledge of the specific hydrogeology of this type of terrain.

## References

- Ayenew, T.T. 1998. The hydrogeological system of the Lake District Basin, Central Main Ethiopian Rift. ITC Publ. 64.
- Cook, P.G. 2003. *A guide to regional groundwater flow in fractured rock aquifers*. CSIRO-Australia [http://www.lwa.gov.au/downloads/publications\_pdf/PX020312.pdf]
- Custodio, E. 2004. Hydrogeology of volcanic rocks. V.S. Kovalevsky, G.P. Kruseman and K.R. Rushton (eds) *Groundwater Studies*. UNESCO IHP-VI Series on Groundwater No. 3.
- Dewandel, B., Lachassagne, P., Boudier, F., Al Hattali, S., Ladouche, B., Pinault, J-L. and Al Suleimani, Z. 2005. A conceptual hydrogeological model of ophiolite hard-rock aquifers in Oman based on multiscale and multi-disciplinary approach. *Hydrogeology Journal* Vol. 13(5-6), pp. 708-26.
- Hartono, U. and Baharuddin, A. 1987. The use of aerial photographs in Quaternary volcanic terrains mapping. Proc. 8th Asian Remote Sensing Conference, Jakarta.
- Foster, C. and Smith L. 1988. Groundwater flow systems in mountainous terrain. *Water Resources Research*, Vol.24 (7), pp. 999-1023.
- Jamieson, G.R. and Freeze, R.A. 1983. Determining hydraulic conductivity distributions in a mountainous area using mathematical modelling. *Groundwater* Vol. 21(2), pp. 168-77.
- Kulkarni, H.F., Deolankar, S.B.F, Lalwani, A.F., Jospeh, B.F. and Pawar, S. 2000. Hydrogeological framework of the Deccan Balsalt groundwater systems, west-central India. *Hydrogeology Journal* Vol. 8(4), pp. 268-378.
- Meijerink, A.M.J. and van Wijngaarden, W. 1997. Contribution to the groundwater hydrology of the Amboseli ecosystem, Kenya. Gilbert J., Mathieu J. and Fournier F. (eds) *Groundwater/Surface Water Ecotones: Biological and Hydrological Interactions and Management Option*, Cambridge Univ. Press, pp. 111-18.
- Mulwa, J.K., Gaciri, S.J., Barongo, J.O, Opiya-Akech, N and Kijanji, G.K. 2005. Geological and structural influence on groundwater distribution and flow in Ngong area, Kenya. *African Journal of Science and Technology*, Science and Engineering Series, Vol. 6(1), pp. 105-15.
- Naik, P.K, Awasthi, A.K., Anand, A., Mohan, P.C. 2001. Hydrogeologic framework of the Deccan terrain of the Koyna River basin, India. *Hydrogeology Journal* Vol. 9(3), pp. 243-64.
- Saha, D. and Agrawal, A.K. 2006. Determination of specific yield using a water balance approach – case study of Torla Odha watershed in the Deccan Trap province, Maharastra State, India. *Hydrogeology Journal* Vol. 14(4), pp. 625-35.
- Solomon, S. and Quiel, F. 2006. Study using remote sensing and GIS in the cebntral highlands of Eritrea. *Hydrogeology Journal* Vol. 14(5), pp. 729-41.
- Sommen van der, J.J., Hasudugan, T. and Meijerink, A.M.J. 1990. Remote sensing and groundwater analysis in volcanic terrain, West Java. *Intern. Symp. Remote Sensing and Water Resources*, Enschede, The Netherlands, pp. 495-513.
- Thouret, J-C. 1999. Volcanic geomorphology – an overview. *Earth Science Reviews* 47, pp. 45-131.

# Karst terrain

## 9.1 Introduction

In studies of karst hydrology common applications of remote sensing images are:

- (1) Mapping of karst features at the surface, as these are an indication of the solubility of the rock, while features may be related to the underground karst network,
- (2) Mapping of lineaments as in many areas these are associated with cavern/fissure conduits, and
- (3) Geological mapping of carbonate rock formations because (i) cavernous conduits tend to be oriented along the structural strike, especially in regions of strongly folded rocks; (ii) bedding-plane partings provide favourable conditions of two-dimensional flow for cave development, particularly in regions with little folding and nearly flat-lying rocks; (iii) down gradient following the bedrock dip is a preferential development direction for vadose caves; and (iv) faults and their accompanied fractured zones can act as paths of high permeability and concentrated groundwater flow.

Afterwards the image interpretation results are analysed together with the available hydrogeological field data in order to improve understanding of groundwater occurrence and flow, prior to tracer tests and geophysical surveys. However, during field investigations the images are often consulted to see whether new field evidence has an expression on the surface, overlooked during the initial interpretation.

A number of examples of surface karst and covered karst are shown and some interpretations are discussed. A karst area in Romania is used to illustrate specific image processing methods utilized in attempts to find possible karst flow paths of known intake points (swallets) and resurgence springs. This case demonstrates that in some areas this can be difficult, whereas in other cases discussed and illustrated here the exercise was more successful.

Early studies of use of remote sensing in karst terrain concerned lineaments and the relation of well yields and lineaments, for example, Parizek (1967), which is now a standard analysis, next to several ground-based methods for fracture and cavity assessment, at the regional and local scale (Benson and Yuhr, 1993). Analyses of linear systems in karst terrain are discussed by Long and Derickson (1999). Other sensors, such as radar and thermal have been found useful. Dinger et al. (2002) used side-looking airborne radar imagery (SLAR, at 12 metre pixel resolution), Landsat TM imagery (30 m pixel resolution) for lineament mapping in limestone terrain as a step in well-siting.

Regional tectonic fabric, illustrated by satellite images and airphotos, of areas along the east coast of the Adriatic Sea was discussed by Kresic (1995), accompanied by interpretation maps with locations of sinks and springs. A tectonic map using existing geological data and Landsat TM interpretation was undertaken in southern Turkey by Değirmenci and Günay (1992) to explore possible subsurface flow paths in the intake-spring discharge mechanism.

Because secondary permeability dominates occurrence and concentrated flow of groundwater, analysis methods similar to those described in the chapter on Crystalline Basement Terrain, have been used in karst terrain.

Shaban et al. (2006) developed a method to assess recharge as a weighted function of the factors: lineaments, drainage, lithology, karstic domains and land cover, using various sensor images, topographic and geological maps. For lineaments, they used measures for connectivity and density. They describe a useful method for the frequency–density of lineaments, as a measure for rock fracturing, consisting of sliding windows. A window consisted of 4 squares; in each square the total number of lineaments was determined and the averaged value of all 4 squares was noted at the centre of the window, a node value. The window was shifted by one square and the procedure repeated. The resulting node values were used for contouring. The recharge potential was determined by considering interactions between the above-mentioned factors using point scores leading to a factor effect,



expressed as a percentage, resulting in five classes of relative recharge. These classes were then related to the proportion of precipitation recharging the subsurface, using other data.

Karst terrain is vulnerable to contamination because of the non-diffuse nature of groundwater flow after it has passed through the soil. Werz and Hötzl (2007) compared use of different sensors to map vulnerability of a karst aquifer in Jordan. They emphasized the importance of aerial photographs.

## 9.2 Surface karst

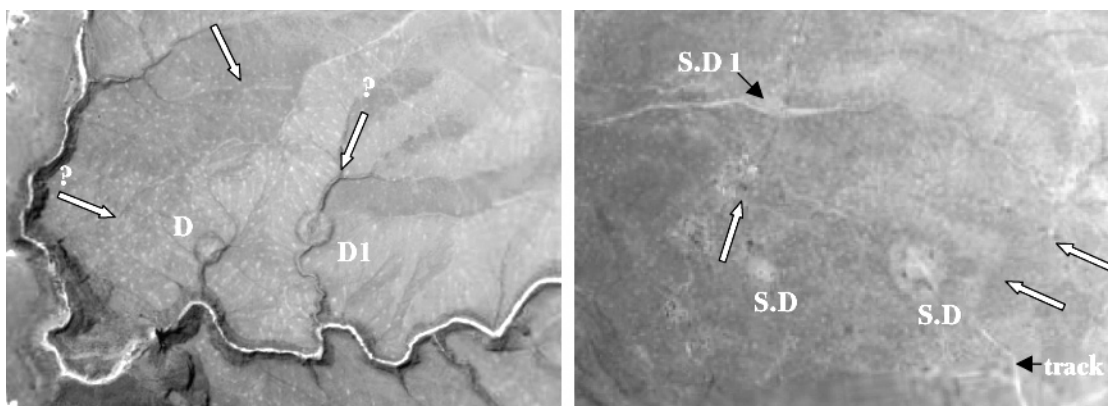
### 9.2.1 Karst landforms and images

The mapping of surface karst features of limited dimensions, such as sinkholes (or dolines), swallets, lapies, etc. requires high resolution stereo images, such as aerial photographs, and even then features such as springs and ponors or other sinks can be missed, particularly when covered by bushes or trees. Good topographic maps with adequate field verification usually contain the location of springs.

However, surface karst can be identified on high-resolution satellite images in cases of spectral contrasts due to differences of soil in the karst depression, such as residual or colluvial soil, and the limestone surrounding the depression, or due to intensity contrast due to micro-relief.

#### *Collapse dolines and solution depressions*

Figure 9.1 shows a high-resolution satellite image of Tertiary flat lying limestone in south Oman, with very sparse vegetation. The left figure contains circular collapse dolines in deeply dissected terrain and they indicate the presence of caverns below the dolines. A few kilometres to the south of this figure the terrain is not dissected and solution dolines occur in the form of minor depressions (SD, right figure), that can be observed because of soil differences. Doline D1 appears to be on the crossing of two lineaments; for doline D no evident lineaments can be seen. On the right-hand figure vague lineaments can be seen, as indicated, but the relation to the depressions is not clear, with the exception perhaps of the small doline SD1. Possibly the deep incision of the ephemeral river has created hydraulic conditions favourable for the formation of larger caves, whose roofs have collapsed, whereas in the flat terrain of the right-hand figure with the same limestone, solution processes were and are less active.



**Figure 9-1** Large scale image of Tertiary limestone, south Oman. Left: evident collapse sinkholes, circular in shape, in deeply dissected terrain. For D1, location on crossing of fractures is possible. Right: Shallow sinkholes in gently undulating terrain, visible because of differences in soil. No obvious relation to fracture can be seen, but larger lineament is indicated. Distance E-W for both images is 2.9 km. Source: Google Earth.

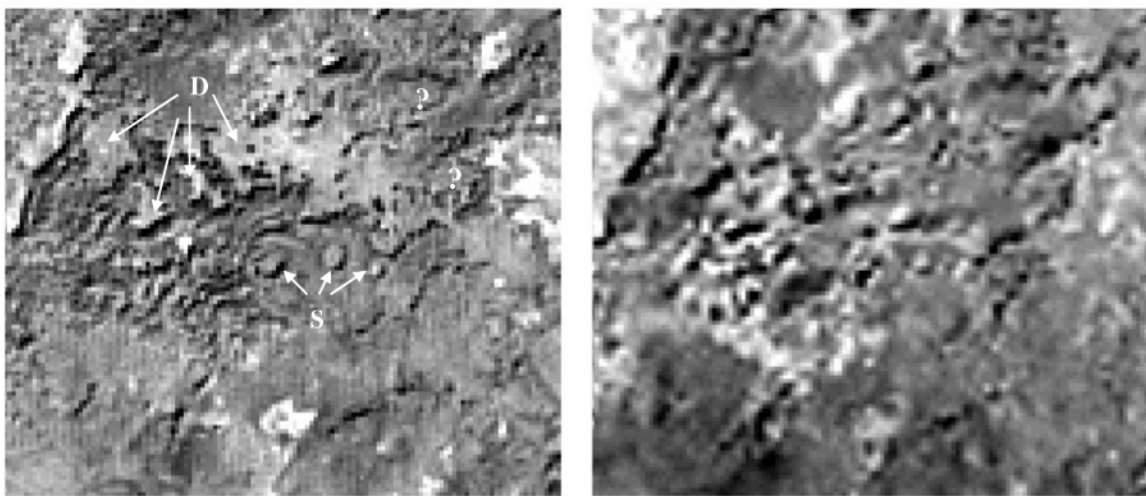
#### *Influence of resolution*

The resolution of an image is important when karst features have limited size, as is illustrated in Figure 9.2. The left-hand image is a VNIR band 3 of Aster (15 m resolution) of the Vascau Plateau in Romania, recorded in

September. Some circular and irregularly shaped dolines are indicated by shadow effects and spectral difference between residual soil/vegetation cover of the dolines with that of the surrounding limestone outcrops. The right-hand figure shows the Landsat TM band with a resolution of 28.5 m (resampled from the original 30 m resolution for geometric correction), spectrally comparable with the Aster band, of the same area taken in August and it is obvious that many features cannot be identified. The difference in reflectance must be attributed to differences in vegetation status, soil moisture and sun elevation angle. For comparison, the TM image was resampled to the 15 m resolution of ASTER and an edge enhancement filter was used for both images.

It must be remarked that many surface karst features could be missed while interpreting the Aster image monoscopically. Aster has a backward looking telescope in the VNIR (band 3B), which allows stereovision with the nadir band 3N. Stereoscopic interpretation made it possible to observe karst depressions, but since spatial and height resolution is limited, only the larger and deeper ones could be detected with some certainty. Preferably use should be made of stereo aerial photographs for accurate mapping of karst depressions or stereo very high-resolution satellite images, which are expensive to acquire.

Sections 9.4.1 and 9.5.5 (below) have more information about mapping of karst depressions.



**Figure 9-2** Left hand image: Aster band 3 (0.76-0.86 $\mu$ m, September 2001), depicting circular dolines (S) and irregularly shaped karst depressions (D), resolution is 15 m. Identification of some features is uncertain (?) and can be missed.

Right hand image: Landsat TM band 4 (0.76 - 0.9  $\mu$ m, August 2000) of the same area, resampled to 15 m. Edge enhancement filter applied to both images.

Because of the lower original resolution of the TM image (28.5 m) no surface karst features are evident. Note difference in spectral reflectance mainly due to different timing.

Distance E-W is 2 km.

### *Effect of scale*

Typical karst in the humid tropics is conical karst. For the analysis of structural and lithological effects on the hydrogeology of such karst terrain, images provide information that is difficult to obtain in the field, because of lack of oversight in the myriad of hills and dolines. Figure 9.3 shows a high-resolution satellite image of a small, mainly deforested area of the western part of the Gunung Sewu (Thousand Mountains) in Middle Java. The cultivation terraces indicate the slope in the depressions with internal drainage. Occasional surface runoff in the depressions disappears in ponors, which are generally covered by trees and high bush. Because of the large scale of the main image shown in figure, it is not apparent that the area shown is on a crossing of lineaments. The lineaments appear when a larger area is shown on a smaller scale, shown in the inset map. The ridge structure (S) could be a pressure ridge along a fault.



Figure 9-3

**Inset map: Conical karst, Gunung Sewu, Central Java.**

Two lineaments are indicated (arrows); at their crossing is the enlargement. Many more lineaments can be observed, which are considered to be fractures. S is a structural element associated with lithology and a possible fault.

V dry valley, internal drainage;

D doline,

V-D hybrid form between doline and dry valley.

Distance E-W inset map is 6.3 km

Source: Google Earth

*Interpretability*

The nature of the terrain and in some cases the date of a scene influences how well karst features can be interpreted.

In the vast and low karst plain of Nullabor, southern Australia, such overviews are indispensable for studying karst features, as is shown in Figure 9.4. The numerous sinkholes are found, usually with more or less evident alignment (D) in WNW-ESE direction, apart from those that follow the NNW-SSE direction of the karst



Figure 9-4

**Landsat ETM image of the low Nullabor karst plain, southern Australia, characterized by many small sinkholes.**

**Linear elements are:**

V narrow karst valleys;

D sinkholes linear array;

D1 lineament and sinkholes of different nature;

S structural-lithological linear feature;

? ? possible underground connection with valley in NW; gw groundwater in valley bottom.

Distance E-W is 49 km.

valley (V1). The former direction is also apparent from linear elements (S) and karst valley (V2) and is interpreted as being associated with structural-lithological variations on the strength of spectral variation related to soil-vegetation differences.

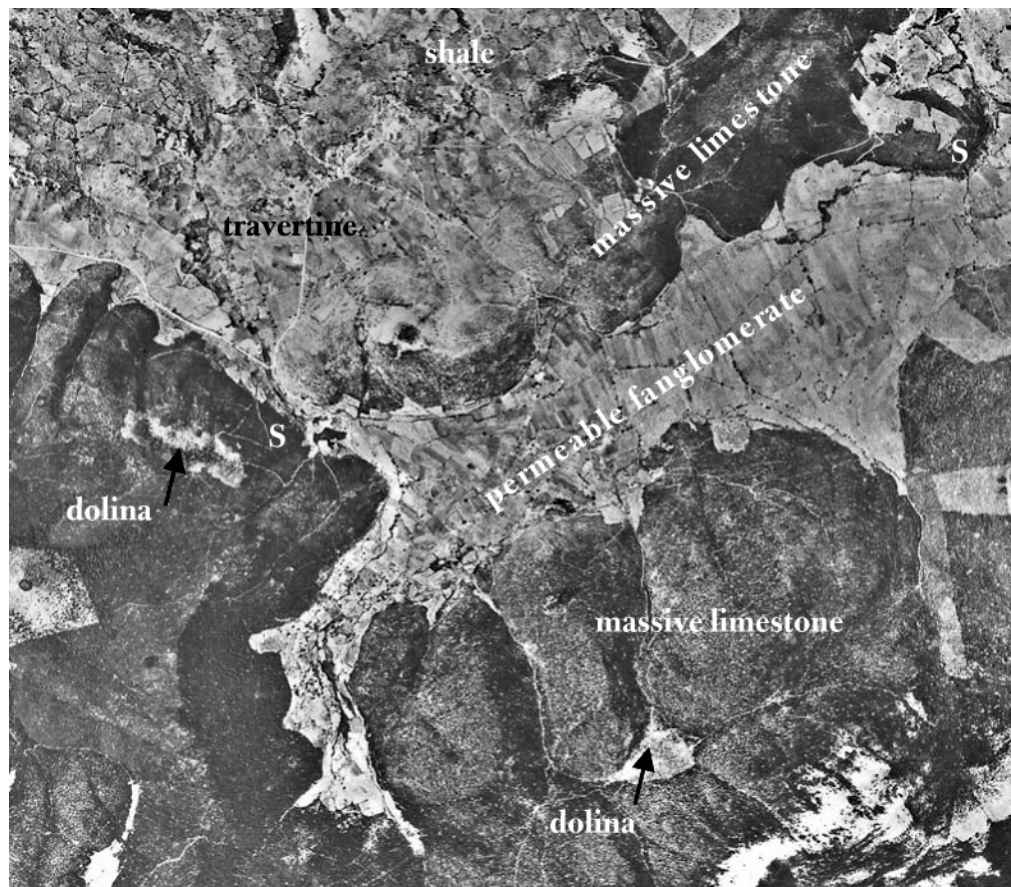
It is interesting that karst features along a different direction (D1) differ in nature from other ones, for example, the larger size sinkholes. The central one, in particular, appears also to be deep because the dark tones in the centre could be groundwater, which can also be observed in the karst valley in the SE. Perhaps there is an upstream, underground continuation of that valley in the direction of the valley V1, marked by (?).

This image also shows ‘inexplicable’ phenomena that are frequently encountered in karst terrain, such as the bend in the valley (V1), having no relation with linear directions seen in the image.

### 9.2.2 Recharge aspects

In studying a groundwater balance of a karst area the proportion of recharge in relation to surface runoff and evapotranspiration is of importance. Only rarely adequate hydrometry is available and therefore estimates of the components have to be made. A karst area may be segmented into a few terrain units depending on the proportion of surface karst prohibiting surface runoff. This is because recharge to groundwater will be highest in units with predominant surface karst features and lowest in sloping catchments where less soluble rocks (dolomite, marly limestone, etc.) crop out and where karst is mainly an underground phenomenon. Average thickness of soil cover and density of vegetation should be included in the recharge evaluation because both increase evapotranspiration loss.

As an example of the interpretation of recharge, an aerial photograph from central Italy is shown in Figure 9.5, depicting hills covered with shrub vegetation (dark tones) and consisting of massive carbonate rocks. A few irregularly shaped sinkholes indicate the presence of karst. One of the sinkholes lies on the intersection of lineaments, but not the other one. Frost weathering produced much coarse-grained debris that was transported by



**Figure 9-5** Sinkholes (dolines) in massive limestone hills. Alluvial fan deposits accumulated during cold Pleistocene periods and are so permeable that occasional runoff from the hills is fully captured. Springs (S) occur on the contact of shale and carbonate rocks. Distance E-W about 5.5 km. Aerial photograph.

snowmelt runoff during cold periods in the Pleistocene period. The debris was laid down in the intramontane valley in the form of alluvial fans and is permeable. Present episodic runoff from the hills with little fine-grained solid load infiltrates fully in the fanglomerates. The topographic catchment consisting of both the hills and the fanglomerates can be considered to have no surface runoff and runoff from the hills (possibly some 5–15% of the annual rainfall) can be added to the rainfall recharge of the alluvial deposits. The recharge on the hills may be estimated using a soil water balance model.

It is unknown whether all of the infiltrated water is discharged by springs at the outlet of the basin near the contact of the carbonates and the shales (covered partly by thin travertine deposits). Possibly water is lost by karst conduits below the fanglomerates to outside the topographic drainage basin, following lithological contacts and other structural elements, hidden from surface observation.

### 9.3 Covered karst

#### 9.3.1 Examples of collapse sinkholes and shallow subsidence

Problems due to collapse of the roofs of caverns or subsidence due to solution are well known, especially when a cover of alluvium obliterates the incipient subsurface dissolution process.



**Figure 9-6** Collapse sinkholes in river terrace deposits, near a reservoir in north Iran. Freshness of features indicates relative age: FS recent; S older; OS oldest collapses. Reservoir suffers from loss of water through karst conduits. High-resolution satellite image. Distance E-W is 1.3 km. Source: Google Earth



**Figure 9-7** Sinkholes (S) in alluvial deposits of Ebro valley, Spain, east of Zaragoza. High resolution satellite image. Only part of the sinkholes can be identified on this image, when compared with depressions, often large in size, observed on stereo aerial photographs. Distance E-W is 860 m. Source: Google Earth

Losses of water from reservoirs through karst conduits are another well-known problem and during selection of the dam site, possibly little attention was placed to interpretation of remote sensing images or aerial photographs. Evident lineaments, aligned sinkholes, particularly of the collapse types, are signs that such conduits may exist. Figure 9.6 shows some recent sinkholes in terrace deposits along the northern shore of the reservoir storing water from the upper Lars River in north Iran, close to the dam. Older collapse holes have also been indicated in the figure. During the site selection of the dam, the presence of the collapse holes was overlooked and the reservoir now loses much water through karst conduits. It is possible that the two fresh sinkholes are the result of changed hydraulic gradients due to ponding of water in the reservoir, bringing the subsurface flow and dissolution closer to the surface. This problem occurs also at other reservoirs in Iran (Ahmadipour, 2005) and other parts of the world.

Dissolution of gypsiferous and evaporitic rocks below alluvial deposits in the Ebro Valley, Spain, causes subsidence, which may be gradual or fast. Figure 9.7 shows a small part of the affected area where some of the sink-

holes can be observed. However, the high-resolution satellite image depicts only a part of them. The map of Gutiérrez-Santolalla et al. (2005), based on stereo airphoto interpretation, contains many more shallow sinkholes, often of large size, but if topography is subdued and the land fully cultivated, they cannot be identified on the satellite image.

### 9.3.2 Covered karst aquifer, example of Borunda, Rajasthan, India

This example is included to highlight the relevance of structural interpretation, which led to understanding groundwater flow in karst terrain, although the karst features are not obvious and mainly buried below an eolian sand cover.

A large structural feature was found crossing a broad syncline, which has a typical sedimentary succession starting with basal conglomerates and sandstones overlying granite basement, followed by shale and limestone including beds with syn-sedimentary slumping structures. The limestone has no surface karst, but for minor widening of joints by solution. The western part of the syncline could be mapped rapidly because outcrops and dips could be interpreted without difficulty on stereo-aerial photographs, once the nature of the rocks was determined in the field. However, the limestone area in the central part is poorly exposed because of a (fossil) eolian sand cover in a wide zone, striking NNE-SSW, at a slight angle to the general strike of the older rocks. The eastern part of the area consists of gravel deposits and sands, covering the limestone, and the few open and deep wells in that part had brackish water.

As is shown in Figure 9.8 the outcrop pattern of the limestone suggests a broad zone with likely long fractures below the sand cover, striking NNW-SSE. A high-resolution image, Figure 9.9, shows fracturing of the rocks in

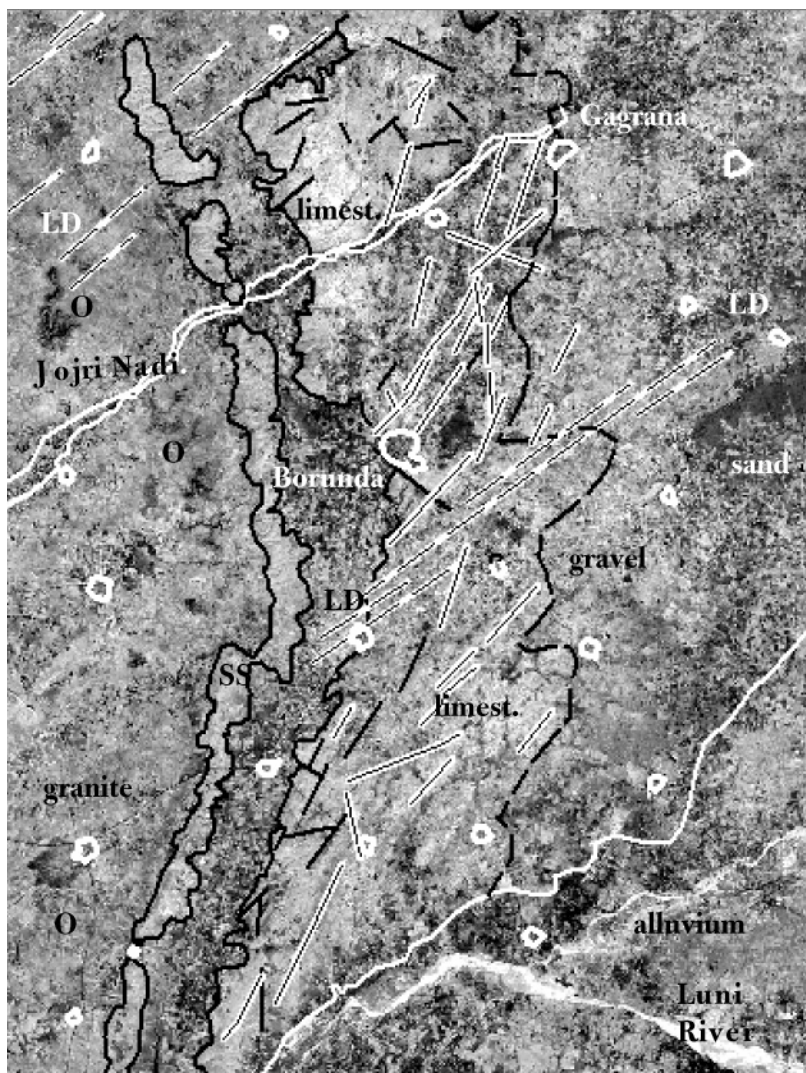


Figure 9-8

Area around Borunda, Rajasthan, India.

Landsat ETM b5.

Delineation of lithology and lineaments based on different bands, colour composites and earlier airphoto interpretation map.

Caverns partly filled with groundwater are known from Borunda and village to south, likely related to lineaments shown.

Groundwater gradient in limestone area is from NE to SW.

LD : longitudinal dune

SS : sandstone

Villages indicated with thick white line

Solid black lines: lineaments based on local contrast

Lines on white background: lineaments with sand cover

Distance E-W is 31.4 km



Figure 9-9

High resolution image NE of Borunda village, Rajasthan, India, showing limestone 1, not affected by fracturing and outcrops of limestone 2 with evident fracturing. Sand cover between limestone outcrops.

Possible large fracture covered by sand is indicated by arrow.

Groundwater gradient is from NE to SW.

Distance E-W is 4.2 km.

Source: Google Earth

this zone with the same direction. This type of fracturing is not observed in the area with contiguous limestone outcrops in the northwest, where few lineaments with different azimuth are found. The groundwater contour map, based on open wells, shows a zone with somewhat lower elevation of the phreatic surface in the broad fracture zone with a gradient from NE to SW. In addition, the TDS contents in that zone are lower than in the eastern and northern part. It is likely that groundwater flows from the NE through some karst conduits along fractures below the sand. Evidence for the existence of such conduits comprises two known, partly water-filled caverns, while the flow direction is indicated by the arrival according to the locals, of a small floating pot, which was lost in a cavern a few kilometres to the NNE.

The simplified geology is drawn on a Landsat TM band 5 with the aid of an earlier map based on photo-interpretation and field check. Two types of lineaments were used, depending on whether a sand cover is present or not. In addition, the long more or less straight course of the Jojri Nadi suggests a large lineament or fracture that has a different strike. Some longitudinal dunes have been indicated; these could be misinterpreted as lineaments, having the same direction as the Jojri Nadi.

## 9.4 Image processing and interpretations of sink-spring relations

### 9.4.1 Example in Dinaric karst

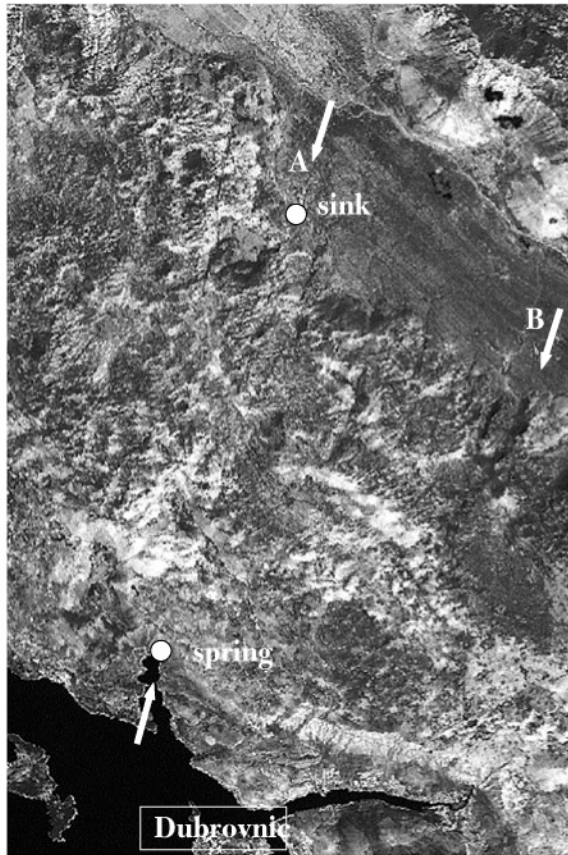
Here, relief effects are described and influence of time of the year on recognizing the likely flow path between a sink and a spring in the karst area in Bosnia-Herzegovina.

Kresic (1995) used a Landsat TM scene of the end of October 1973, and made a density slice of band 7 to obtain a map that showed in binary format the shadow effects of the rims of karst depressions. Obvious shadows along a few mountainsides were eliminated manually. The resulting map showed an evident alignment of karst depressions along a line connecting a sink and a spring, whose hydraulic connection was demonstrated earlier using dye tracers by Milanovic, (1980, in Kresic, 1995). However, the alignment is not so evident on the Landsat ETM scene band 7 of August 2000. Density slicing of band 7 of the August 2000 image did not produce the pattern shown by Kresic, which is likely to be due to the greater elevation of the sun in August compared to end October. A principal component I image of the area of Figure 9.10, containing information chiefly of the NIR bands 5 and 7 (not shown), was only marginally superior to either band 7 or band 5 for the detection of the lineament. Lineament (B) is more prominent and appears on the density slice map of Kresic, but the hydrogeological significance is not known or may not exist.

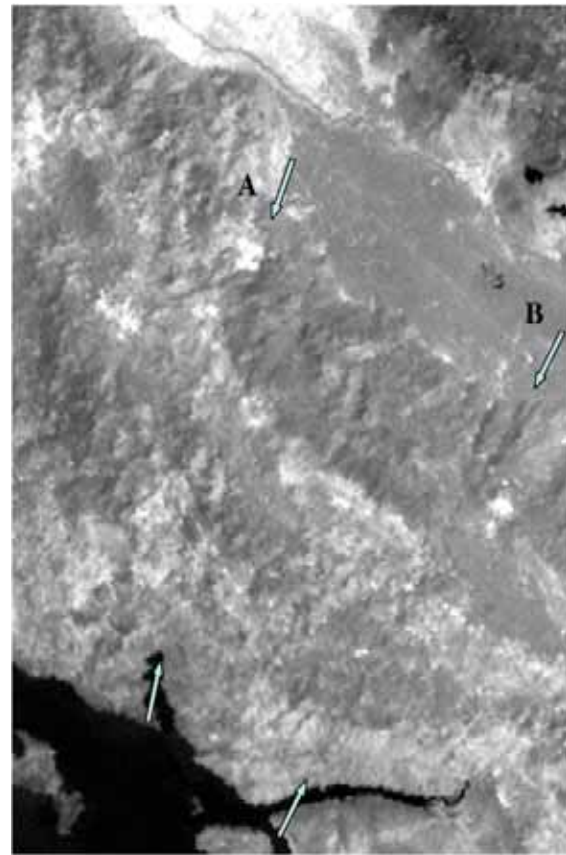
In this example a known sink-source relation could be retrieved, albeit with difficulty on band 7 of Figure 9.10. The lineaments (A) and particularly (B) can be recognized with more ease on the thermal band of the scene of August 2000, than on band 7, which may be attributed to cool rims facing away from the sun and heating of slopes facing the sun. Other lineaments (not indicated) can be observed on the images.

The large flat-bottomed karst depression (polje) with traces of the strike of the rocks can be seen in the north-eastern part with a small one in the south-eastern part.

Other examples of lineaments on the thermal band of Landsat ETM of a limestone area, is given in the Chapter 5 (section 5.2.8) and Chapter 8 (section 8.2.4).



**Figure 9-10** Dinaric karst Bosnia-Herzegovina. Lineament A, which seems interrupted on image, ETM b7 of 20 August 2000, but was detected as an alignment of dolines on density slice of an image of 31 October 1973 by Kresic (1995). Connection between sink and spring was determined by dye tracing. Other lineaments can be observed. Distance E-W is 13.3 km.



**Figure 9-11** Thermal band of ETM of same scene and area as left figure with lineament A indicated. Lineament B is also apparent on sliced B7 map by Kresic (1995), but has no or unknown hydrogeological influence.

#### 9.4.2 Example of a karst area in Romania

Tracers released in sinks in various parts of a karst area in NE Romania appeared in a few karst springs, and the question is whether flow paths could be inferred by image interpretation. Inspection of bands of a Landsat ETM image of August 2000 and an ASTER image of the month of September 2001 indicated that no evident and well-defined lineaments could be identified. Several image-processing methods were tried to explore whether or not the methods could display lineaments, lithological contacts and other geological elements, shedding light on possible flow paths.

##### Setting

The geology and hydrogeology of the area, the Vascau Plateau in NW Romania, is described by Orascano and Mather (2000). Their schematic hydrogeological map was transposed onto the images, without correction for relief displacement. The western part of the outcrop area of the carbonate rocks consists of dolomites, the central-



western part of limestone and dolomite, and the central-eastern part of limestone. Contacts between these formations are faulted or thrust (low angle). The area between the Tarina drainage and the alluvial area in the east is made up of dolomitic limestone and dolomite. The carbonate rocks, which are gently dipping in easterly directions, overlie Permian and Werfenian deposits with low permeability. A SW-NE geological section shows a series of vertical faults, some with appreciable displacements. A large number of sinkholes and dry valleys are found in the undulating plateau of the carbonate rocks. Most of the runoff from the non-carbonate rocks bordering the plateau disappears in swallet holes. Some springs are found in the carbonate terrain. Tracers were released in swallets (sinks) to determine flow directions to resurgence springs, as is shown in Figure 9.12. Letters in the figure denote sinks and corresponding springs, thus, tracers in sinks A1 to A4 emerged in spring A, and so forth.

### *Image processing and interpretation*

The aim was to select the most suitable images for discrimination of the types of carbonate rocks, recognition of faults and karst depressions, interpretation of lineaments and identification of permanent and intermittent streams. Various image-processing methods were used; histogram operations, filtering, principal component analysis (PC), ratioing, Intensity-Hue-Saturation operations and NDVI transform, and colour composites of original, enhanced and transformed bands (see chapter on Image Processing). The Landsat ETM has 7 bands and Aster 14 bands of which three are in the visible and near-infrared (VNIR) between 0.5-0.9  $\mu\text{m}$ , six in the short-wave infrared (SWIR) between 1.6-2.43  $\mu\text{m}$ , and five in the thermal infrared (TIR) between 8-12  $\mu\text{m}$ . The VNIR channels have 15 m resolution, SWIR have 30 m resolution, and TIR channels of Aster have 90 m resolution. Dolines were mapped using stereo Aster images.

The schematic geological map in the publication of Orasceano and Mather (2000) was digitized and transposed onto the images. This map contains the lithology, faults and thrusts, courses of perennial streams and some intermittent courses, locations of swallets, cold water springs, springs with thermal water and springs with gas outflow and a perennial resurgence cave. In addition, the map shows directions of subsurface flow, as the crow flies, between tracer injection and appearance in springs.

The map was overlaid on the images in order to enable comparison; see Figure 9.12. Where possible, correction for relief displacement was done by hand because no DEM of compatible resolution was available. The false colour image of Figure 9.12 consists of the three Aster VNIR bands. Because of the large difference in reflectivity of the vegetated areas and the areas with many outcrops, histogram equalization was used for all the three bands, followed by application of an edge enhancement filter.

A lineament map (Figure 9.13) was prepared by shifting the interpretation onto various types of processed images. However, no inferred continuations and possible fracture zones were considered.

### *Results*

No close association between density of dolines and lithology seems to exist in the area, but statistical analysis is precluded because of uncertainty in the interpretation map. Some alignments of depressions were found, but only at the local scale.

Despite the many spectral bands and transformed images available, lithological differences could not be differentiated and the contact and low angle thrusts could be observed locally, but only after the map was overlaid. The soil and vegetation cover masks spectral differences associated with lithology, known from arid regions. In the south-western part forest cover obliterates the contact between the carbonate rocks and the non-carbonate rocks. Most normal faults shown on the map have no or only faint expression on the images. The perennial streams could not be identified on any of the images or products because of their small widths. Filtered images of Aster band 3 (NIR) were the most useful single image for mapping lineaments, much more so than colour composites.

The interesting aspect is whether evidence exists of the flow paths between sinks and springs.

As is indicated by the block arrows in Figure 9.12, it is likely that subsurface flow follows, at least partly a SW-NE tectonic direction, mentioned by the authors. The remnant of a large drainage system in the centre (arrows near A1 and A2) was best displayed on a PC II of SWIR bands (not shown here for reasons of space) and the approximate straightness suggests a continuous fracture zone. There is a tectonic line that runs from locations D to E1 and beyond in a SE direction (not indicated on the lineament map because it is a zone, rather than a well-defined lineament). Possibly this line acts as a collector, from which groundwater flows though

fractures to the spring A in the NE at the contact between the alluvium and the carbonate rocks. For most of the other sink-spring connections, no evident continuous lineaments were found.

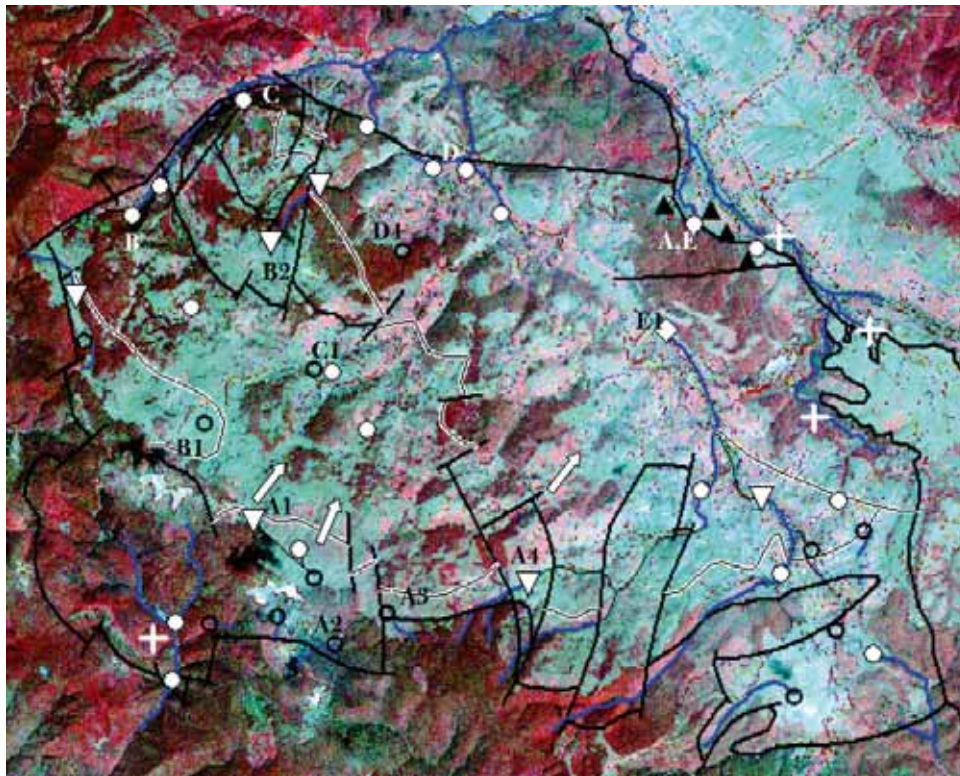


Figure 9-12

Aster false colour image of the karst area of Vascau, Romania. Distance E-W is 14.7km.

- sink
- ▽ loss in streambed
- spring cold water
- ▲ thermal spring
- ◇ perm. insurg.cave
- + gas outflow from spring
- perennial stream
- - - - - interm. stream
- contact
- fault
- thrust & contact

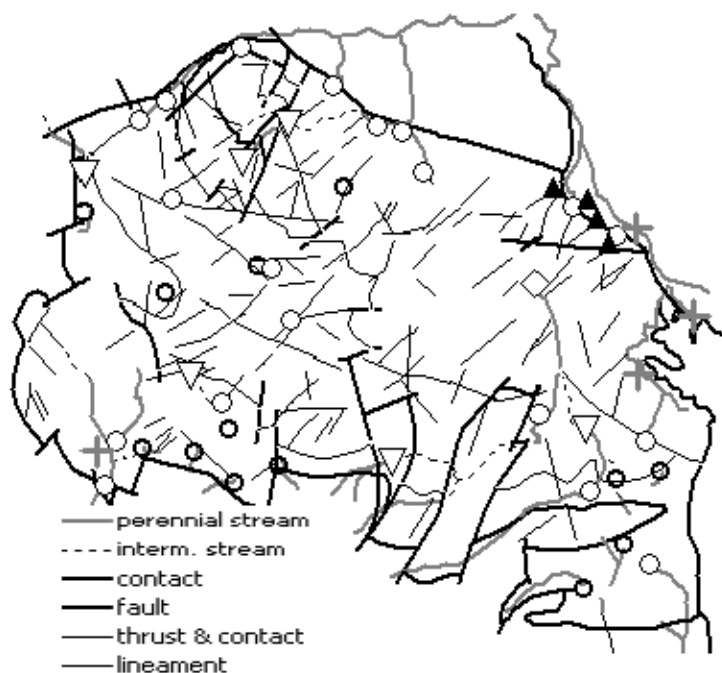


Figure 9-13

Map showing contacts, faults and hydrologic elements, of the Vascau karst area, after Orascano and Mather (2000) and added lineaments. For explanation of symbols, see Figure 9.12.

- perennial stream
- - - - - interm. stream
- contact
- fault
- thrust & contact
- lineament

## 9.5 Remote sensing studies of karst terrain in Viet Nam

Contribution by O. Batelaan

### 9.5.1 Introduction

This case study describes the Tamduong valley and Suoimuoi catchment, which are located in the northwestern part of Viet Nam (Figure 9.14). These areas are sub-basins of the mountainous Da River catchment and belong to

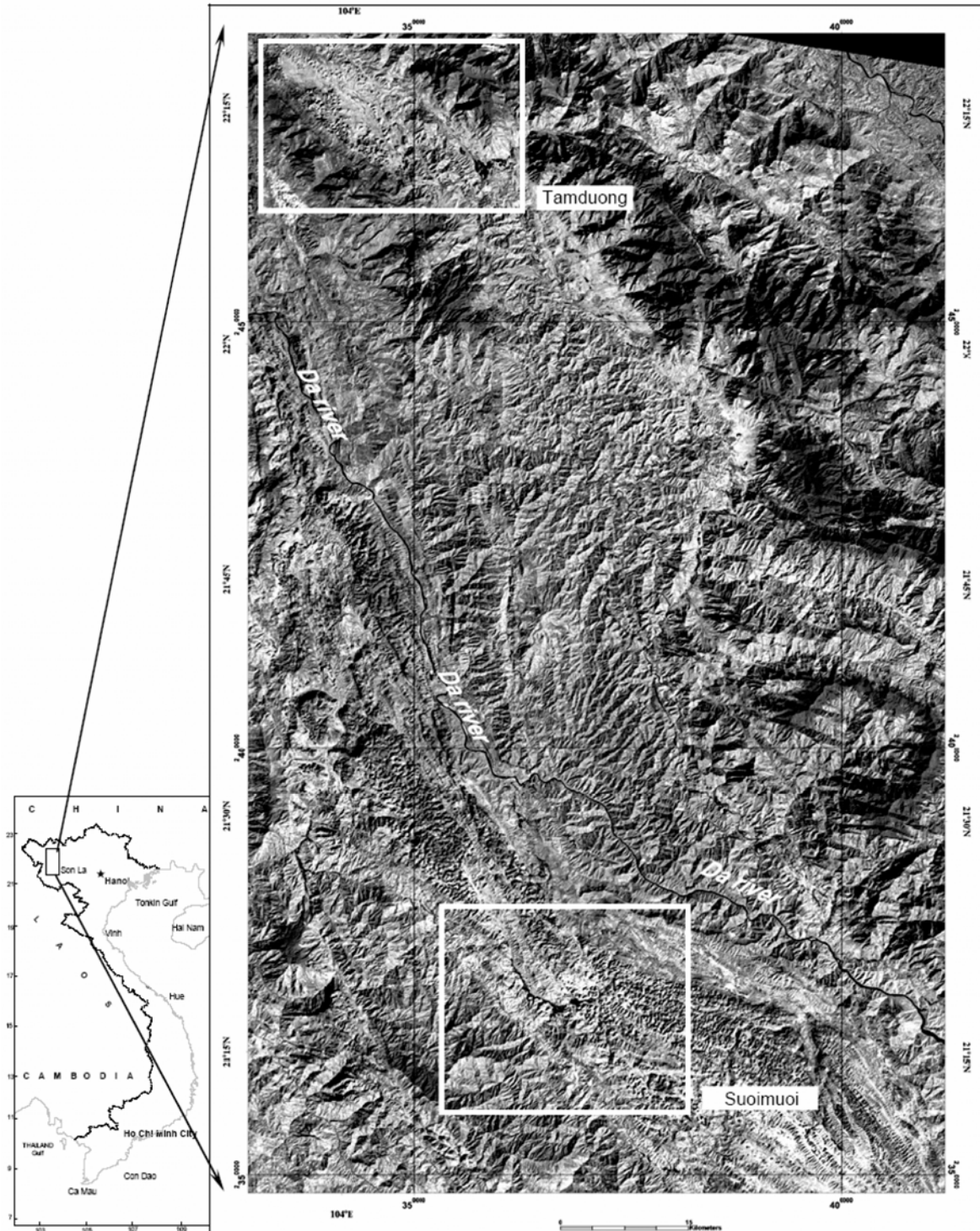
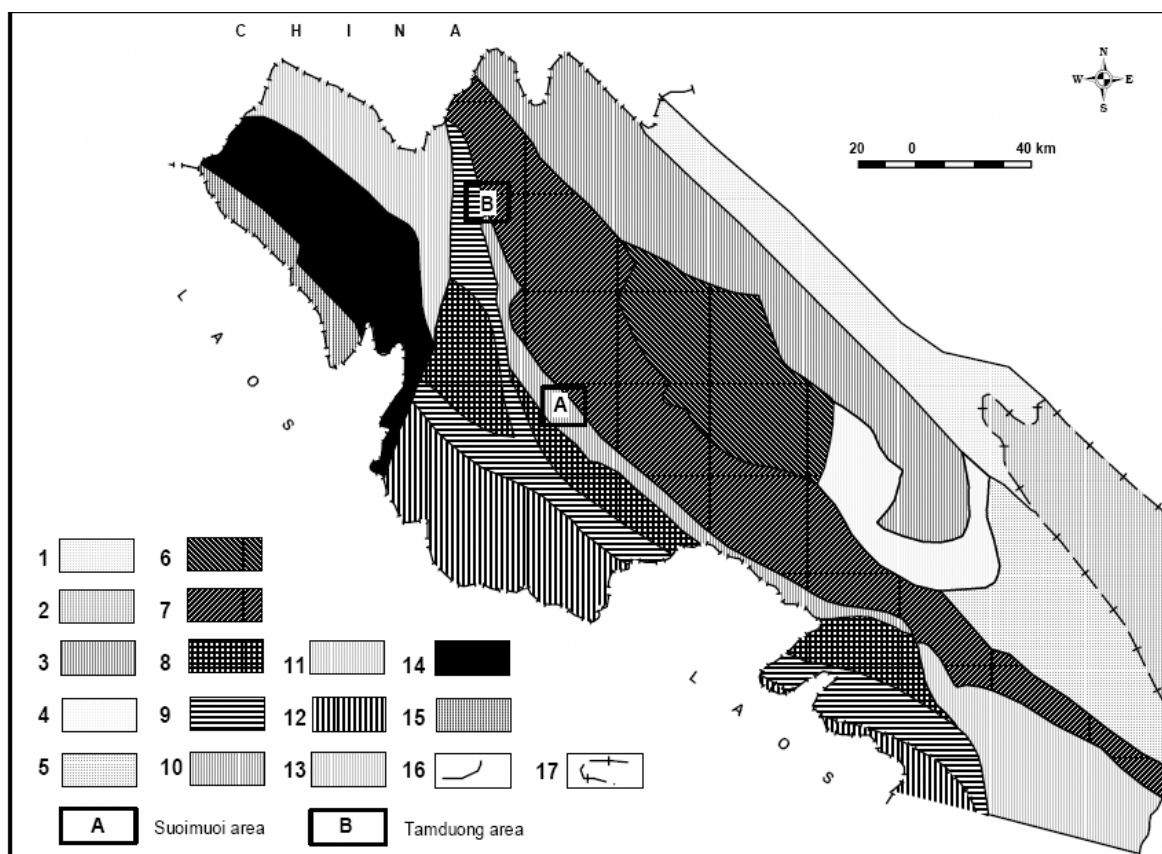


Figure 9-14 The location of the Tamduong valley and Suoimuoi study area as indicated by a white box on the background of a panchromatic Landsat ETM+ image.

the largest karstic mountain range in Viet Nam. The landscape is characterized by peak cluster depressions with blind valleys, deep dolines, narrow valleys, chained sharp peaks and many swallow holes exiting underground into caverns (Tuyet, 1998). The regional relief decreases from NW to SE. In the NW part peaks reach approximately 3,000 m altitudes, while they decrease to about 1,500 m in the central part. In NW Viet Nam continental crust consolidated since the end of the early Mesozoic, and subsequently was affected by younger tectonic movements. Within this fold belt a basin developed, composed of sedimentary volcanic rocks, terminated by siliciclastic carbonate siliciclastic sequences, which attain a thickness of 3,000 to 5,000 m. The extensional Da River basin then was affected by NW-SE oriented folding, due to Indosinian closure of the Paleotethys (beginning since the Late Permian and culminating during the Middle Triassic). The research area is located in the active zone of the Songma, Thuanchau and Songda fault zone. Folded Late Proterozoic to Middle Triassic formations, including the karstified limestones, are exposed near Son La. Since Late Mesozoic times until the present the area has been characterized by a continental regime resulting in denudation and karstification. The folded and broken limestone is fractured. The humid sub-tropical climate of the area with high rainfall and intense biochemical processes leads to the acidification of the infiltrating water and high rates of karst denudation and cave formation. Because of pulsations in the uplift, different planation levels and corresponding stages of cave formation have been formed.

Understanding of the patterns of the panchromatic image of the Tamduong-Suoi muoi study area requires a regional understanding on a much smaller scale, as given by, for example, a structural map (Figure 9.15).



**Figure 9-15** Geological structure in NW of Vietnam: 1. Precambrian seated Red River fault zone; 2. Cenozoic continental rift basin Hanoi; 3. Precambrian geosynclinal fold zone Phansipan; 4. Early Paleozoic continental margin fold zone Sinhvinh; 5. Late Paleozoic-Early Mesozoic continental margin fold zone Sinhvinh; 6. Tectonic-volcanic post collision zone Tule; 7- The Late Paleozoic - Early Mesozoic geosynclinal fold zone Songda; 8. Precambrian fold zone Namco; 9. Early Paleozoic fold zone Songma; 10. Early Paleozoic continental margin fold zone Thuanchau; 11. Late Paleozoic-Early Mesozoic continental margin fold zone Thanhhoa; 12. Late Paleozoic - Early Mesozoic fold zone Samnua-Hoanhson; 13. Precambrian reactivated fold zone in Mesozoic Pusilung; 14. Late Paleozoic-Early Mesozoic active volcanic anticlinoria; 15. Early Mesozoic post intraplate collision basin Muongnhe; 16. boundary of tectonic zones; 17. boundary of Hanoi basin. Source: Bach and Thang, 1996

### 9.5.2 Lineament extraction

Hung (2007) compared visual and automatic lineament extraction methods for Landsat and ASTER imagery for the Suoimuoi catchment. Figure 9.16 shows the results of the automatic extraction. While, the visual method is a good method for extracting geological lineaments, the automatic is an objective method and provides detailed lineaments. Automatic extraction and visual extraction are complementary in lineament detail and objectivity. Hung (2007) combines therefore both methodologies after corrections into a single GIS lineament database.

It is clear that there exists a relationship between the image resolution and the scale of study. At medium scale of study, that is, 1/50,000, the suitable pixel size is 30 m. At smaller scales of equal or less than 1/100,000, a pixel size of 80 m can be used. However, with a higher scale one needs more information in the field to extract the lineaments. Image bands of Landsat (30 m resolution) and ASTER sensors are selected in the range of VNIR (15 m resolution)-SWIR (30 m resolution). Results indicate that the best bands for automatic lineament extraction are the NIR bands, that is, band 3 of ASTER (15 m) and band 4 of Landsat ETM+. Results also indicate that ASTER data is more accurate and results in detailed lineament extraction at a scale of 1:50,000.

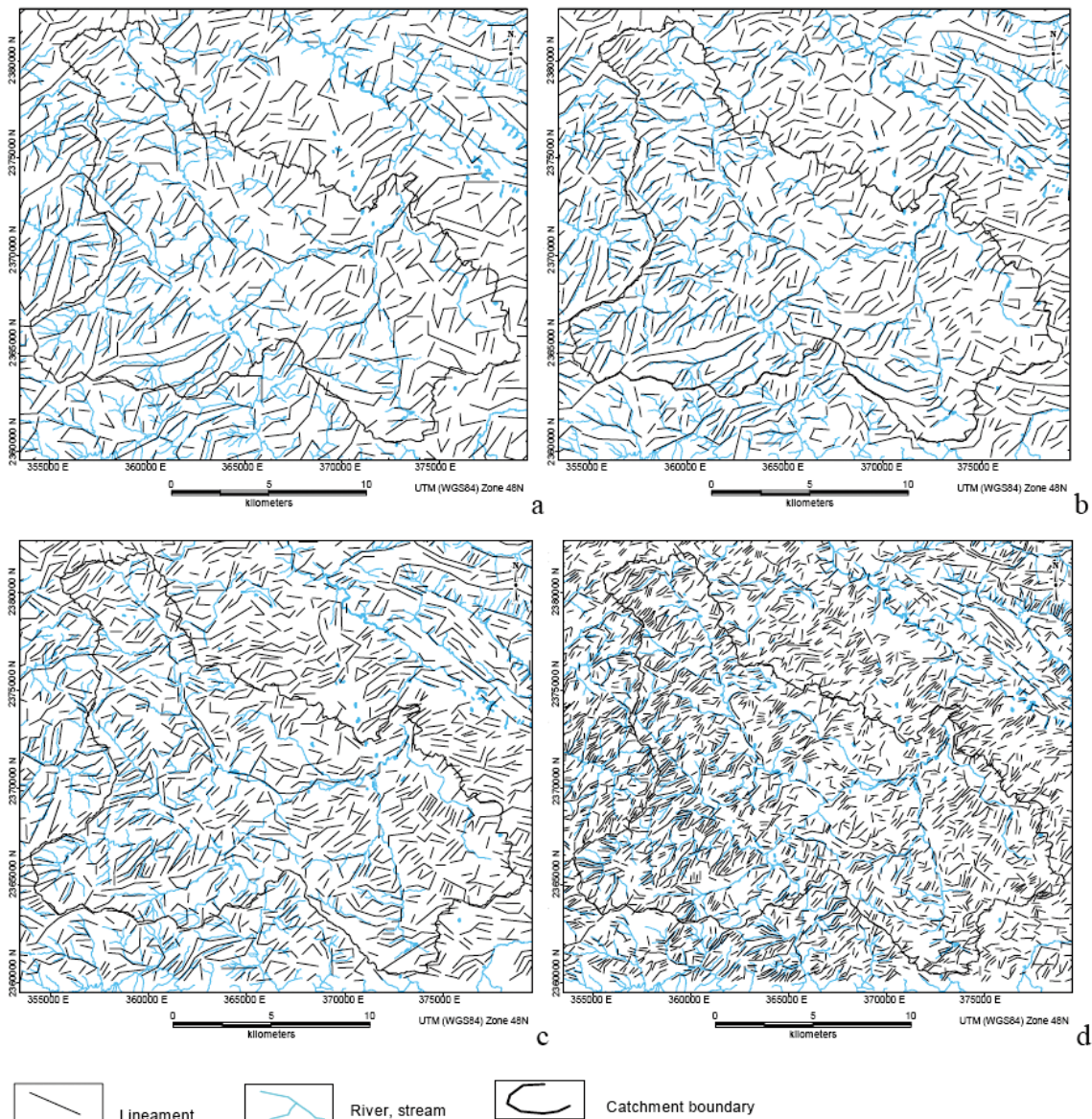


Figure 9-16 Examples of lineament maps resulting from (a) Landsat MSS band 3, (b) Landsat TM band 4, (c) ASTER band 4, and (d) ASTER band 3.

For the karstified limestone area of Suoimuoi-Nam La in NW Viet Nam, Tam et al. (2004) studied the relationship between the distribution of lineaments and borehole specific capacity. No significant spatial well yield patterns are evident in this highly fractured-karstified region. The supposition is that lineaments caused by tectonic activities affect the local variability in borehole specific capacity. Sixteen pumping tests in conjunction with a comprehensive lineament analysis are used to prove this relationship.

The first lineament source was extracted from Landsat 7 ETM imagery by two image-processing systems; ENVI32 package (for imagery pre-processing) and Geomatics PCI (for lineament extraction). A false colour (Red-Green-Blue) composite of ETM bands 4, 7 and 1 was consequently selected for lineament detection. The selected bands were contrast stretched and edge enhanced with high-pass filters to improve the detection of linear features. Directional filtering, defined on the basis of development of the regional structural geology, was also considered in the image edge-enhancement process, however this proved to be less useful. Finally, linear features were automatically extracted with the image processing system from the resulting edge-enhanced false colour composite image. The extracted lineaments were geo-referenced using an affine transformation (see Chapter 3) with 37 control points, of which the coordinates were determined by differential GPS.

The second lineament source was extracted from black-and-white aerial photographs of nominal scale 1:33,000. An experienced geologist, well trained in stereoscopic techniques, captured linear features on the photographs using stereoscopic visualization. The visualized lineaments were then transferred to a computer by scanning, and then ground registered using geo-referenced orthophotos and on-screen digitizing. In the next step, non-geological linear features were removed as much as possible from the extracted lineaments. In this process, the two lineament datasets were combined into a GIS database, where they were given a code (1) if extracted by the automatic processing and a code (2), if otherwise. The lineaments were also segmented, in other words, curves were split into straight lines; this was necessary since not all extracted lineaments were truly straight. Lineaments of less than 50 m in length were discarded, as they were too short and not significant for this study. The lineaments were classified into two groups; the first group consists of lineaments longer than 2 km, and the second group of the remaining lineaments. The removal of non-geological linear features was consequently executed for each group. For the first group, lineaments were re-observed in both satellite image and aerial photographs, and those related to non-geological linear features, such as roads, riverbanks, irrigation channels, and mountain ridges, most of which had a code of 1, were excluded from the database. For the second group, it was found that many lineaments detected by the automatic processing did not appear in the lineament dataset detected by the stereoscopic visualization. In order to verify if those detected by the automatic processing are truly geological linear features, a buffer zone of 100 m in width was constructed around each lineament coded 2; lineaments coded 1 that did not partly or fully fall within the buffer zones were re-observed on both satellite image and aerial photographs. Those that were not geologically justified (e.g. did not align along negative-relief features as ravines and valleys, boundaries between geological units, known faults and shear zones, straight portions of dry streambeds etc.) on either the satellite image or the aerial photographs were discarded from the database.

The step-by-step lineament extraction and processing described above provided confidence that the linear features being mapped were 'really geological' because they were detected through repeated trials by several observations. Geological knowledge was incorporated in the lineament detection, such that regional fractures could be justified and identified in high-resolution aerial photographs and non-geological linear features could be easily excluded from the mapped lineaments. Moreover, the combination of the two extraction methods minimized the number of missed linear features; those that had been not detected in the stereoscopic visualization were re-scanned in the automatic processing dataset and were finally justified by field observations.

Figure 9.17 shows a lineament scheme of the studied area where only lineaments longer than 1 km are included because of the small scale of presentation. A rose diagram of all mapped lineaments was also constructed (Figure 9.18), which shows that a majority of the lineaments develop in NW-SE (which is also the principal direction of the regional structure) and SW-NE (i.e. a crossing of the regional structure) directions. This can be an indication of the direction of groundwater movement in the studied area.

### 9.5.3 Lineament analysis

For the purpose of the lineament analysis, two parameters were considered: lineament-length density (Ld) and lineament frequency (Lf). Lineament-length density is defined as the total length of all recorded lineaments divided by the area under consideration; and lineament frequency is defined as the number of visible lineaments

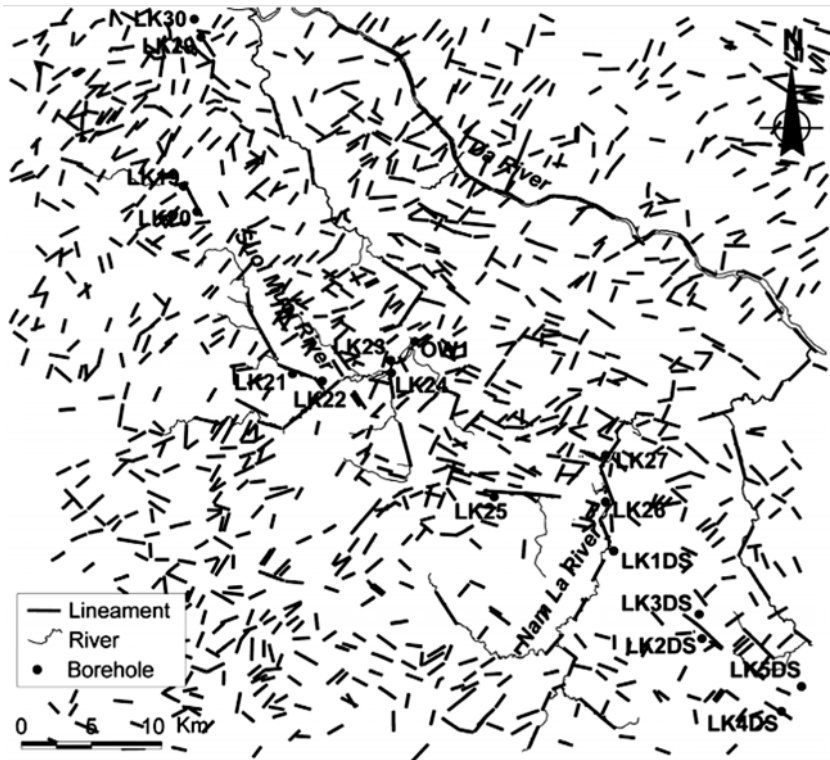


Figure 9-17

Map of detected lineaments longer than 1 km, showing location of the pumping tests and the river networks.

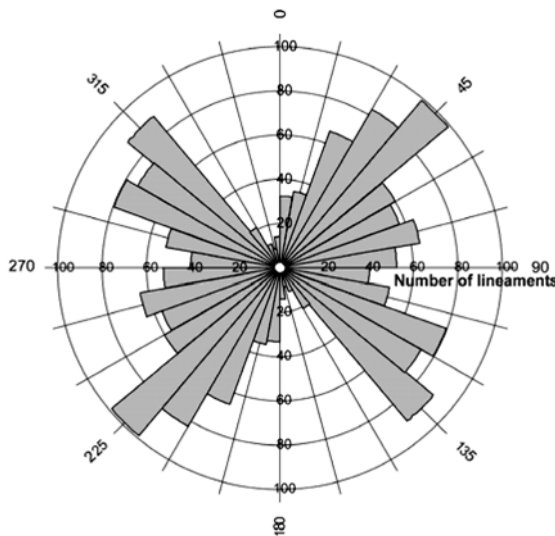


Figure 9-18

Rose diagram of detected lineaments, showing two major trends (NW-SE and NE-SW) of the lineament development.

per area under consideration (Greenbaum 1985). A grid of cells was constructed over the area of interest to compute these parameters. In addition, all lineaments falling into a circular neighbourhood (of radius 1.5 cell size) around each grid cell were taken into account in the computation, as is illustrated in Figure 9.19.

Often, the two parameters are correlated (Edet et al., 1998), and the correlation is cell-size dependent as will be shown in this study. Grids of cell sizes of 100, 200, 300, 500, 1,000 and 2,000 m were constructed, on which the values of  $L_d$  and  $L_f$  were computed. Figure 9.20 shows that as the grid cell size changes, the lineament frequency and the lineament-length density exhibit a power function relationship with the cell size. It is shown that with a grid cell size of 300 m  $L_d$  was best correlated with  $L_f$ .

### 9.5.4 Lineament-length density and specific capacity

Hence, the lineament-length density computed in the 300-m cell-sized grid is considered as a representative parameter of the mapped lineaments in the study of the lineament-borehole specific capacity relationship.

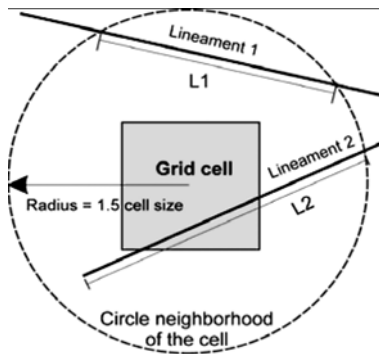


Figure 9-19

Illustration of lineament-length density  $L_d$  and lineament frequency  $L_f$  determined with GIS ArcInfo functions: the parameters of the cell is computed as  $L_d = (L1 + L2)/A$  and  $L_f = 2/A$ , where A is the area of the circle.

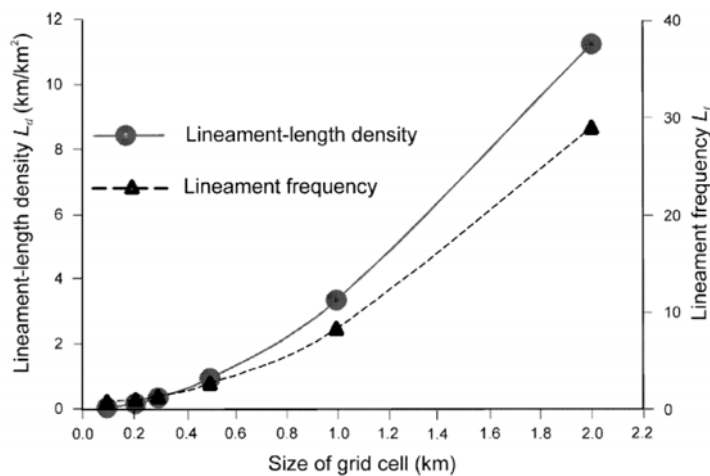


Figure 9-20

Dependence of average lineament-length density ( $L_d$ ) and average lineament frequency ( $L_f$ ) on the grid cell-size

To check how well the mapped lineaments reflect the structural geology, faults from a geological map of 1:50,000 scale were compared to the maps of  $L_d$  for a small area downstream of the Nam La catchment, displayed in Figure 9.21. A relatively good agreement between alignment of zones of high  $L_d$  values and location of the faults is observed. A more detailed analysis reveals that 66.1% of the cells located within a 300-m buffer zone around the faults have a lineament-length density higher than 0.45 km/km<sup>2</sup>; while 92.3% of the cells outside the fault buffer zone have a density value smaller than 0.39 km/km<sup>2</sup>. Therefore, zones of high lineament-length density can be used as an indication for zones of high concentrations of fractures or faults.

In the study area, the uppermost fractured-karstified zone of the carbonate rocks is the most favourable media for the karstic groundwater to reside. The thickness of this zone is about 450 m, an estimation based on the difference in topographic elevation between the sinkholes (approx. 580 m a.s.l) and the Hang Doi resurgence (136 m a.s.l) of the Nam La River (Figure 9.21). To evaluate the groundwater reserve in this zone, sixteen pumping tests were analysed.

A plot of 16 data pairs of specific capacity,  $Q/s$ , and lineament-length density,  $L_d$ , of cells based on the location of the boreholes did not relate well to lineament-length density at the scale of the entire study area. This comes from the fact that the study area is large and highly heterogeneous in geomorphology and hydrogeology. To enhance this relationship, the boreholes were classified into two groups based on a cluster analysis of parameters such as elevation of the boreholes and groundwater table, specific capacity, elevation of local discharge area, distance to a local discharge area, lineament-length density and drainage density.

Group A is comprised of seven boreholes situated in small-narrow valleys with steep slopes. The soil at these locations is dry during the dry season, but becomes moistened during the rainy season, facilitating cultivation of short-life crops. Here, the water table occurs at great depth, except in a few cases, due to a high variation of groundwater levels during summer. The boreholes have a low specific capacity and are situated far from a local river network. Therefore, one can conclude that these boreholes are situated in recharge areas with respect to the river network. Consequently, the specific capacity depends only upon the local aquifer characteristics, which is



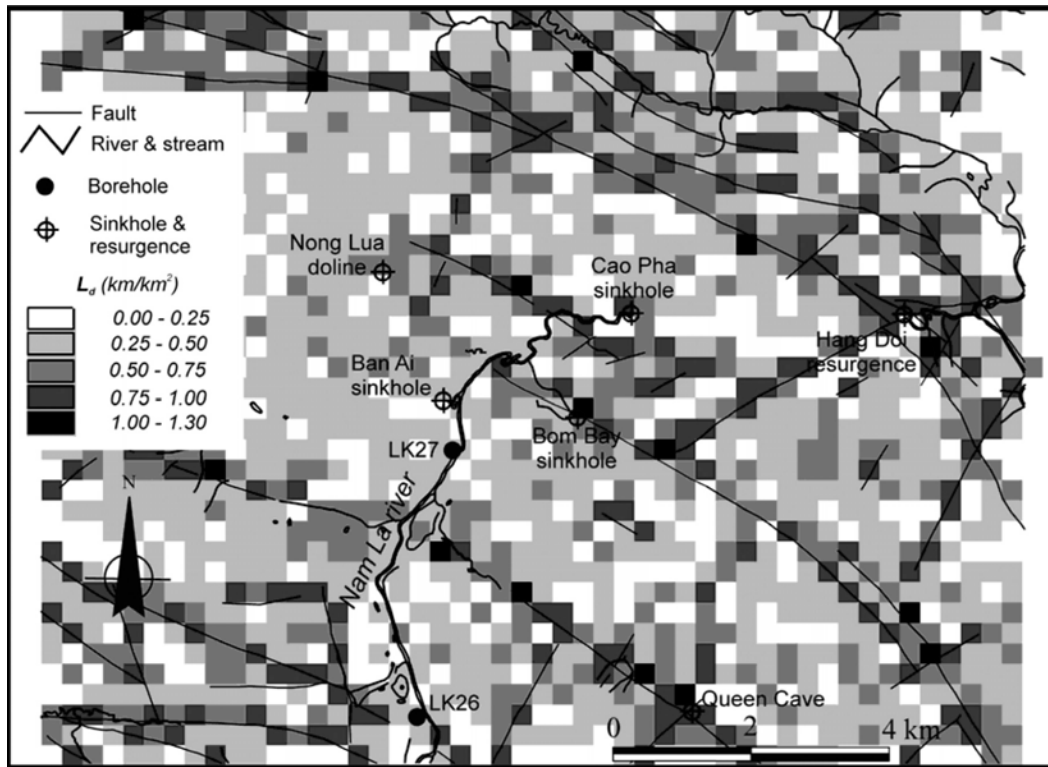


Figure 9-21 Overlay of the geological faults of the Nam La catchment outlet area, digitised from a geological map, with the 300 m cell-sized grid of lineament-length density.

revealed by a relatively good correlation between specific capacity and lineament-length density, as is shown in Figure 9.22a.

Group B is comprised of nine boreholes situated in river valleys with relatively flat terrains. The boreholes of this group are characterized by a much higher specific capacity compared to the specific capacity of group A. The boreholes are a short distance (less than 400 m) from a river. Most of the boreholes are located along river segments, where interaction between the karstic groundwater and the surface water occurs. It is shown that the closer the boreholes are to a river, the higher their specific capacity. All the above-mentioned facts imply that fractures exist in the carbonate rocks, but the Quaternary deposits cover them. This is a possible explanation of the lower

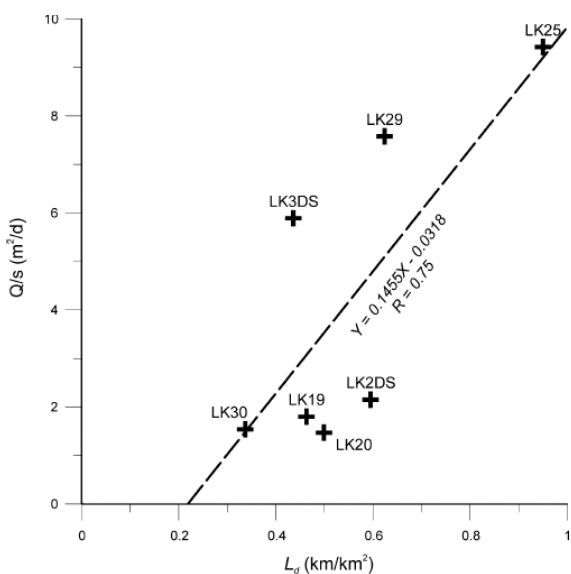


Figure 9-22a Relationship between lineament-length density and specific capacity of the boreholes of group A

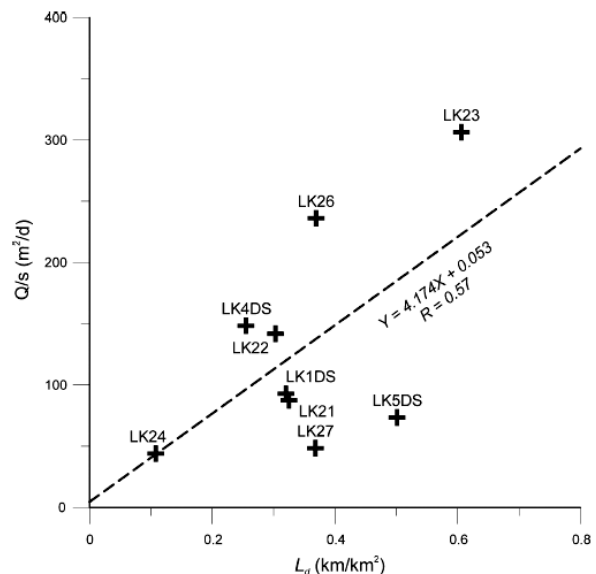


Figure 9-22b Relationship between lineament-length density and specific capacity of the boreholes of group B

lineament-length density of this group (average value for the borehole sites is 0.35 km/km<sup>2</sup>) compared to group A (averaged density is 0.56 km/km<sup>2</sup>). Consequently, the correlation between specific capacity and lineament-length density of this group, shown in Figure 9.22b, is lower than for group A.

Lineaments tend to be less detectable in discharge areas (lowland, wide and flat valleys) in contrast to the high density in recharge areas (highland narrow-mountainous ravines). In addition, the presence of a stream network in the former can act as a recharge source to the underlain karstic groundwater system. It is concluded that not only the borehole geomorphological-hydrogeological position but also the lineament distribution influences the specific capacity.

### 9.5.5 Lineament-length density and prediction of underground flow paths

Tam et al. (2005) present for the same area the result of an investigation of underground conduits, which connect the swallow holes and the resurgence of a blind river in the tropical, highly karstified limestone Nam La catchment in the NW of Viet Nam. The Nam La River disappears underground in several swallow holes near the outlet of the catchment. In the rainy season this results in flooding upstream of the sinkholes. A hypothesis is that the Nam La River resurges at a large cavern spring 4.5 km east of the catchment outlet (Figure 9.23).

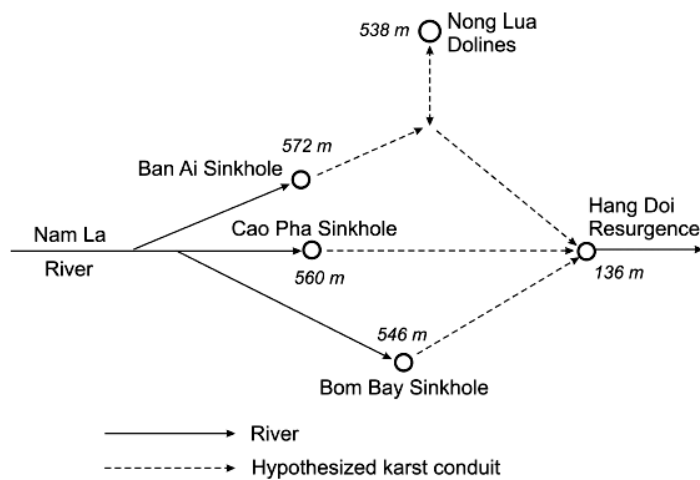


Figure 9-23

Schematisation of the Nam La swallow holes and the hypothesized connection to the resurgence, showing the elevation of the swallow holes and resurgence

Hence, routes can be delineated with the resulting density map, which connects cells of high lineament density from a source point to a destination point. A routine was written for automatic delineation of these routes. The routine works on the basis of a 3×3 cell window in which the centre cell is considered as the current routing position. The window is subsequently moved to one of the eight surrounding cells, which has the highest weighted value of lineament-length density (Ld). Ld is an indicator for the degree of rock fracturing, which is a prerequisite for development of cavernous passages. However, not only the rock fractures but also the geological structure influences the cavernous conduit development. Therefore, information on the geological structure must be taken into account during the routing, necessary, for example, in tracing a cave passage that develops along a bedding plane. A rose diagram showing the directional frequency of the lineaments was considered as a statistical means of representing the anisotropy of the fractured environment, as well as the cave development tendency on a regional scale. Therefore, the fracture anisotropy should be included to amend undesired movements of the routing window. In this study, equal influence of the local geological structure and the regional fracture development tendency on the cave development was assumed and included as a weighting factor.

Figure 9.24 shows the resulting pathways of the underground conduits estimated with the lineament-fault-cave analysis. A performed tracer test confirmed that a groundwater flow connection exists between the Cao Pha and Bom Bay swallow holes and the resurgence. It was noted that all routed underground conduits converge to the same resurgence point and exhibit a branchwork cave development pattern. It was also observed that many routed segments coincide with the direction of the faults. In addition, this analysis also indicated the likeliness of an underground passage from the Ban Ai swallow hole to the Nong Lua doline and an additional conduit that further connects to the resurgence at Hang Doi.

### 9.5.6 Extraction of karstic depressions

Kresic (1995) indicated that karstic depressions, which due to shadowing are darker than the surrounding terrain, can be enhanced by visual interpretation of Landsat MSS, TM and aerial photos. A 3D view of a R-G-B colour composite of ASTER bands 3, 5 and 1 (Figure 9.25) shows an example of karstic depressions in the Suoimuoi

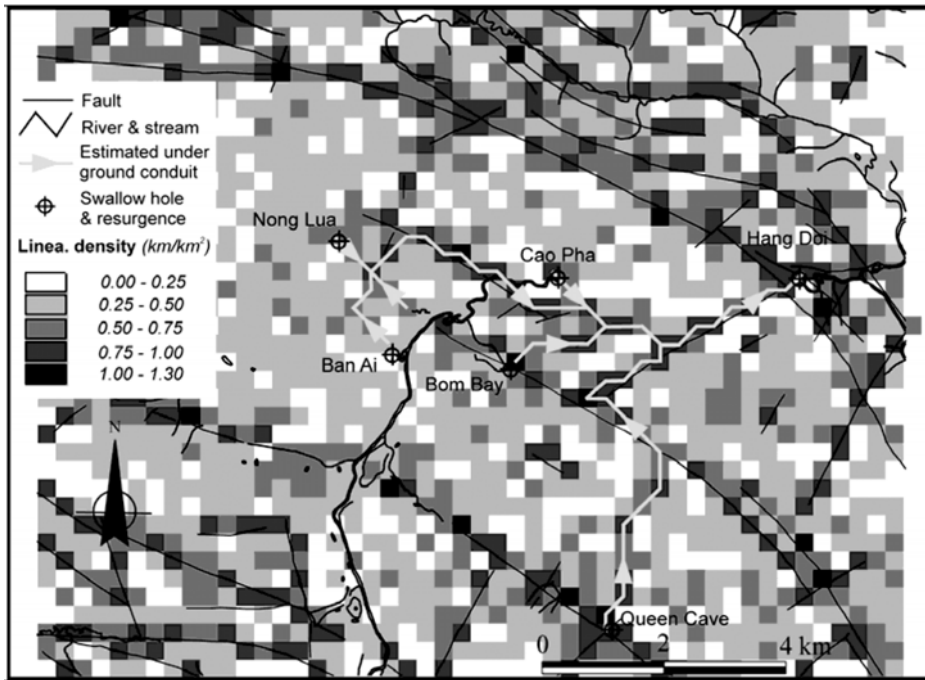


Figure 9-24

Map with lineament-length density and predicted underground flow paths; the minimum, mean, and maximum values of lineament-length density are respectively 0, 0.3 and 1.29 km/km<sup>2</sup>.

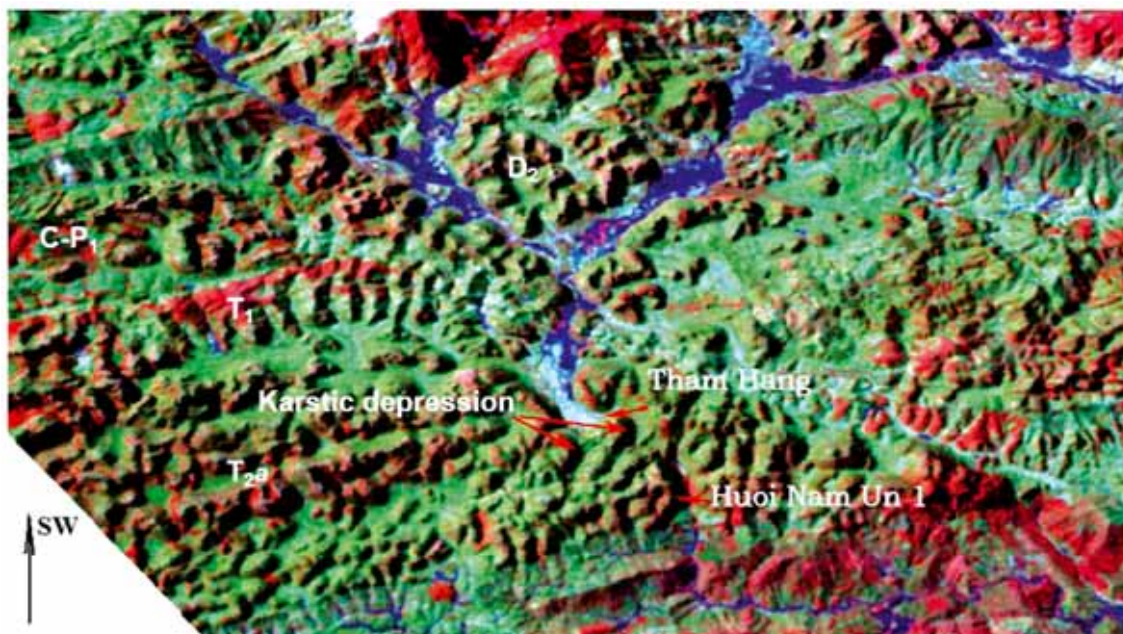
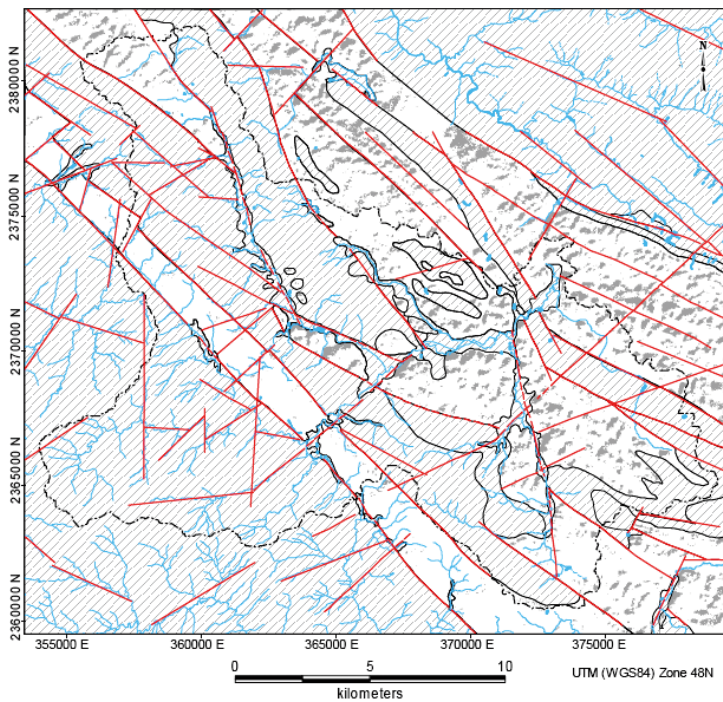


Figure 9-25 3D view of the Tham Hang sinkhole and the Huoi Nam Un 1 spring based on colour composite of B3:B5:B1 (R:G:B) of ASTER image; T<sub>2</sub>, T<sub>1</sub>, C-P<sub>1</sub> and D<sub>2</sub> are the major formations within the Suoimuoi catchment

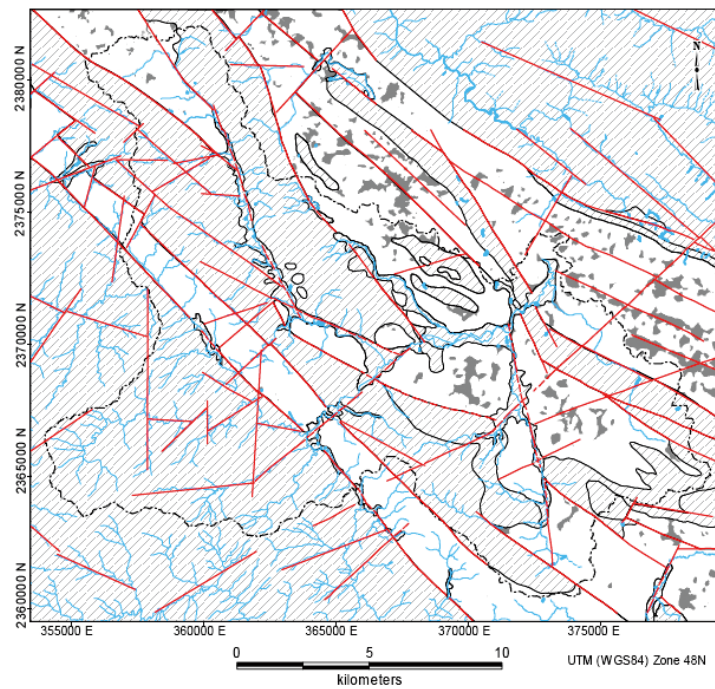
catchment. Karstic depressions can be automatically extracted when information of DEM and ASTER image analysis is combined.

Naturally, karstic depressions create straight and narrow valleys in karst areas. In satellite imagery karstic

depressions create straight, long and narrow shadows. Kresic (1995) visually detects karstic depression. However, this kind of shadow can be detected by using the ratio of ASTER band 3 divided over band 4. The ratio of band 3 to band 4 is used to predict and extract automatically karstic depressions from the ASTER imagery by using a



a



b

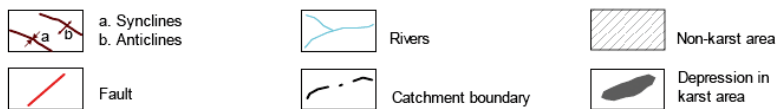


Figure 9-26

Extracted karstic depressions in the Suoimuoi area from:  
a. ASTER images, b. DEM

threshold value. In this research, the threshold for karstic depression extraction is set to 1.005, which results in karstic depressions as dark areas distributed in karstic morphology (Figure 9.26a).

By visual checking with DEM and colour composite of ASTER bands 3, 2 and 1 in the Suoimuoi catchment,

it is clear that not all of the shadows are karstic depressions. About 60% of the big and long shadows are not, however, small (less than 100 m) and circular or nearly circular shadows are very difficult to check because of complicated terrain and the limitations of image/DEM resolution. Karstic depression can be detected directly from DEM. The Fill Sink function is normally used to correct the DEM in non-karst area in order to obtain a DEM without depressions. However, this function can be used to detect depressions in the karst area. The depressions, which are detected by DEM in the Suoimuoi catchment, are given in Figure 9.26b.

Compared with the extracted karstic depressions from the ASTER image, the karstic depressions resulting from DEM are easily accepted because of higher accuracy. However, in case of lack of a DEM, satellite imagery can be used for suggesting karstic depressions. ASTER images can produce DEM themselves. Hence, they have high potential for more accurate karstic depression extraction. An alternative for mapping karst depressions is to use stereo aerial photographs for visual interpretation.

## 9.6 Summary and conclusions

Karst landforms may be indicative of underground conduit systems with groundwater. For that reason, it is important to recognize karst landforms. Some karst landforms, including covered karst, are illustrated with images of different scale. Recent collapse holes can be recognized by the freshness of their appearance on large scale images and the information is useful in studying water losses from reservoirs or areas with a risk of collapse.

Limitations in recognizing such solutional landforms as dolines or sinkholes on medium scale satellite images are mentioned. On such images the pseudo relief impression created by shadows is used for recognition of the dolines. Stereo images are much more suitable for the mapping of karst landforms, either by visual interpretation or by creation of DEMs from the images, as an example shows.

In some cases alignment of dolines, as observed on images, are associated with conduits of groundwater, as evidenced by tracer studies in the field. However, an example is included whereby the images did not yield much direct information on conduit systems.

Groundwater in karst regions requires the study of regional and local geological structures and by using image interpretation, information may be obtained with varying degrees of relevance.

## References

- Ahmadipour, M. 2005. The effect of sinkholes on leakage of water from the Sarabchenar dam, SW Iran. *Journal of Environmental Hydrology* Vol. 13.
- Benson, R.C and Yuhr, L. 1993. Spatial sampling considerations and their applications to characterizing fractured rock and karst systems. *Environmental Geology*, Vol. 20(4), pp. 296–307.
- Değirmenci, M. and Günay, G. 1992. Analysis of hydrologic relations between E irdir-Bey ehir-Su la lakes system and adjacent basin by means of remote sensing techniques (Southern Turkey). *Environmental Geology*, Vol. 19(1), pp. 41–45
- Dinger, J.S., Andrews, R.E., Wunsch, D.R. and Dunno, G.A. 2002. Remote sensing and field techniques to locate fracture zones for high-yield water wells in the Appalachian plateau, Kentucky. *Proceedings of the National Ground Water Association Fractured-Rock Aquifer 2002 Conference*, March 13–15, Denver, Colorado, and: <http://www.uky.edu/KGS/water/research/proceedings/Techniques.pdf>
- Edet, A.E., Okereke, C.S., Teme, S.C., Esu, E.O. 1998. Application of remote-sensing data to groundwater exploration: a case study of the Cross River State, southeastern Nigeria. *Hydrogeology Journal* 6, pp. 394–404.
- Greenbaum, D. 1985. Review of remote sensing applications to groundwater exploration in basement and regolith. *British Geological Survey Report*, OD 85/8.
- Gutiérrez-Santolalla, F., Gutiérrez-Elorza, M., Marin, C., Maldonado, C. and Younger, R.L. 2005. Subsidence hazard avoidance based on geomorphological mapping in the Ebro River valley mantled karst terrain. *Environmental Geology*, Vol. 48(3), pp. 370–83.
- Hung, L.Q. 2007. Integrated analysis of sub-tropical mountain karst geohydrology in NW Vietnam by field and multisource remotely sensed data, PhD thesis, Vrije Universiteit Brussel.

- Kresik, N. 1995. Remote sensing of tectonic fabric controlling groundwater flow in Dinaric karst. *Remote Sensing of Environment*, Vol. 53(2), pp. 85–90.
- Long, A.J. and Derickson, R.G. 1999. Linear systems analysis in karst aquifer. *Journal of Hydrology*, Vol. 219, pp. 206–17.
- Orasceanu, I. and Mather, J. 2000. Karst hydrology and origin of thermal waters in the Codru Monia mountains, Romania. *Hydrogeology Journal*, Vol 8(4), pp. 379–89.
- Shaban, A., Khawlie, M. and Abdalla, C. 2006. Use of GIS and remote sensing to determine recharge potential zones; the case of occidental Linanon. *Hydrogeology Journal*, Vol.14(4), pp. 433–43.
- Tam, V.T., De Smedt, F. and Batelaan, O. and Dassargues, A. 2004. Study on the relationship between lineaments and borehole specific capacity in a fractured and karstified limestone area in Vietnam. *Hydrogeology Journal* 12(6), pp. 662–73.
- Tam, V.T., De Smedt, F. and Batelaan, O. et al. 2005. Study of cavernous underground conduits in Nam La (Northwest Vietnam) by an integrative approach. *Hydrogeology Journal* 13(5–6), pp. 675–89.
- Tuyet, D. 1998. Karst geology investigation of the northwest region: Hanoi, research Institute of Geology and Mineral Resources.
- Werz, H. and Hötzl, H. 2007. Groundwater risk intensity mapping in semi-arid regions using optical remote sensing data as an additional tool. *Hydrogeology Journal* 15 (6), pp. 1031–229.

# Crystalline basement terrain

## 10.1 Introduction

This chapter discusses terrains underlain by crystalline basement rocks and dominated by secondary porosity (permeability) but locally having dual porosity, also termed 'hard rock'. The examples given pertain to areas composed of granite and metamorphic rocks and an example of ophiolites. Flood basalt and limestone areas, where secondary permeability is also dominant, are discussed in separate chapters.

Since the primary porosity of the rock is absent or is of a negligible quantity, groundwater occurrence in each climatic zone is governed by the properties of the weathered zone and by fracturing. Climatic zone means a set of rainfall and evaporative conditions, which control potential recharge.

Wright (1992), Chilton and Foster (1995) presented overviews of the hydrogeology of hard rock regions in Africa; Singhal and Gupta (1999) and Cook (2003) discuss the hydrogeology of hard rocks and an extensive review of remote sensing applications to groundwater in general, but with emphasis on hard rock applications, is given by Waters et al., 1990.

What emerges from the literature is that the fractured zone below the regolith seems to be a little more productive than the regolith itself. However, much depends on regional and local circumstances because of the complex interactions that exist between tectonic types of fractures, their density and connectivity, filling by mineral matter due to intrusion or later eluviation by clay, recharge conditions as influenced by morphometry, nature of regolith and denudational history.

Groundwater occurrence is thus highly area- and site-specific and the concept of differentiating hydrogeomorphological units with the aid of images is illustrated, because they group toposequences, other geomorphological aspects and land cover, which influence recharge and storage of groundwater.

The hydrogeomorphological approach has been used widely in India (e.g. Sreedevi et al., 2005). The importance of fractures is reflected by a discussion of recognizing lineaments in different types of terrain and a few basic general concepts of structural fracture analysis are given here, which will be a familiar matter to most but perhaps of use to those starting to build up their knowledge. Lineaments on images are likely indicators of fractures. Sander (2007) mentions that after using lineament interpretation in Ghana, the success rates in a village well programme increased from 57% to 70%, significantly reducing costs.

Weathering and general stratification from fresh bedrock to topsoil are briefly introduced, primarily to define terminology. Although the nature of the regolith cannot be assessed by image interpretation, some aspects of hydrogeological significance can be observed, while some attention is given to dambos (seasonally waterlogged bottomlands) because they are the manifestation of a denudational history, which governs the groundwater processes, partly expressed by groundwater emergence in seepage zones.

By image interpretation the various terrain types with their specific recharge and storage properties can be differentiated and lineaments can be traced, but hydrogeological appraisal depends greatly on follow-up by geophysical survey and on analysis using empirical data, namely the performance of existing wells. This is discussed in the section on analysis and in the section on GIS in Chapter 3.

The information provided in this chapter should be of assistance to those responsible for siting wells and two examples of how images can be used for siting have been included.

The use of images to assess over-exploitation of groundwater in hard rock area, as is taking place in some large hard rock regions, is discussed in the chapter on groundwater management.

## 10.2 Segmentation of the terrain; hydrogeomorphological units

Segmentation of large hard rock areas into terrain units with specific characteristics is done in the expectation that the units are associated with groundwater occurrences and processes, which may differ from one unit to another.

A hydrogeomorphological unit (HGU) comprises one or more toposequence (catena), which have certain drainage pattern(s). Hence, a hydrogeomorphological unit indirectly describes the local topography or morphometry, and the soil and weathered zone characteristics, which govern the recharge, storage of groundwater and outflow. When geology influences geomorphology, the unit boundaries should coincide with geological boundaries, because mineralogical composition, foliation and fracturing may influence hydrogeological properties.

This segmentation can be based on the system of geomorphological mapping of Verstappen (1983). The system essentially uses genetic criteria, has a lithological base, and allows for pragmatic sub-differentiation. Aspects of so-called 'land system' mapping can be included.

The HGUs are differentiated primarily on the basis of what can be seen on images, such as patterns of drainage, land cover and relief, followed by description of the catenary elements or sub-units. The latter two may be too small to be mapped individually at the scale of the HGU map (see the examples below). However, when the hydrogeological properties of sub-units are known or can be postulated, it may be advantageous to show them as separate units. Examples are impermeable outcrops or areas with many outcrops and shallow weathering, larger valley bottoms (alluvial deposits, shallow water tables, seasonally flooded, etc.), laterite caps, localized areas with fossil windblown sands and so on.

Terrain segmentation should serve practical purposes only, not be constrained by hierarchical rules and should be applied at different scales.

The hydrogeological significance of the HGUs can be assessed, usually at a later stage, when information accumulates on success rates, well performance, water level fluctuations and water quality. Even when considerable well data is available in a national or regional database, when plotted on a map or an image covering a larger area, the density often turns out to be disappointingly low, while the spatial variation of permeability and recharge is usually high in hard rock terrain.

This precludes rigid (geo-)statistical analysis and therefore, there is much to say for including hydrogeological reasoning using field observation and experience of local drillers in order to estimate differences in groundwater occurrences in hydrogeomorphological units.

Two examples of terrain segmentation will be illustrated.

### 10.2.1 Example 1. Area in SE Zimbabwe

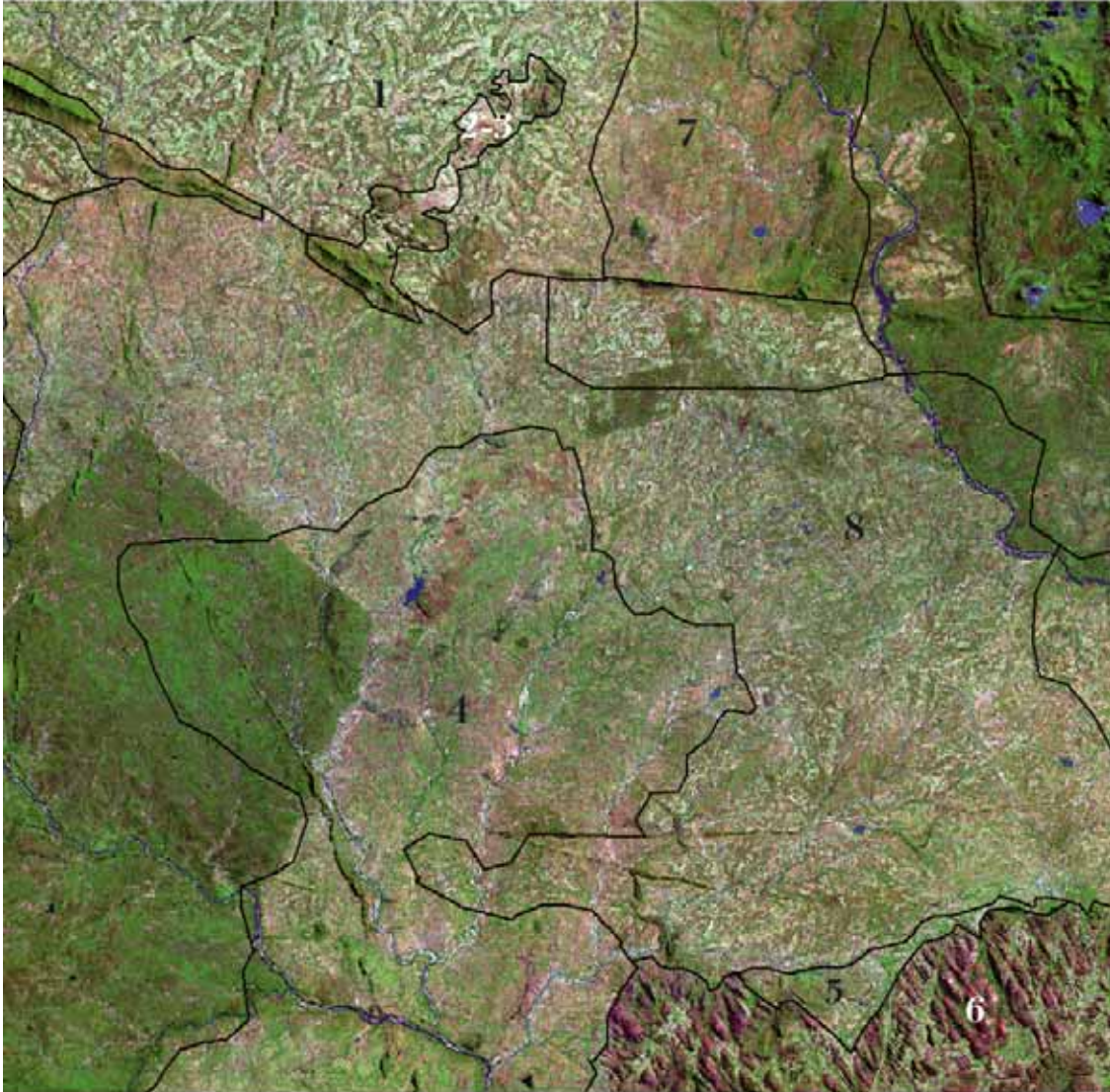
Various hydro-geomorphological units are delineated in the Landsat ETM false colour image of Figure 10.1. As can be noted, boundaries of the units can be precise, when abrupt changes in landforms occur, usually due to faulted or intrusive contacts between two different rock types, or approximate or transitional, due to the geomorphological development affecting a single rock type, as discussed in section 10.4.1.

The delineation of associations of features, grouped in a HGU, should be done on a small scale image that provides a synoptic overview. The details can be studied on larger scale images, shown below.

Important structural features, such as basic dykes, faults and lineaments are present in the image of Figure 10.1, but have not been indicated here, as the attention is focussed principally on HGUs. For many units land cover is associated with geomorphology and soil associations, but where forest cover is present the interpretation of the units relies on landforms.

Enlargements of some selected HGUs are shown in Figure 10.2, which illustrate their differences.





**Figure 10-1** Hydrogeomorphological units of granite/gneiss area in SE Zimbabwe, differentiated on the basis of patterns and local relief. Numbers refer to units shown in more detail in Figure 10.2. Landsat TM false colour of bands 5, 4 and 2, all with edge enhancement. Distance E-W is 40 km.

*Upper left:* Unit no. 1: low to medium relief, shows typical dambos (discussed in section 10.4.4) consisting of permeable interfluves (1a) and valley bottoms (1b); unit 2: shallow regolith, small outcrops; unit 3 inselberg.

*Upper right:* Unit no. 7: with foliation (schist, gneiss) shallow regolith.

*Middle left:* Unit no. 6a: steep and high outcrops, 6b valleys developed in fractures; unit 5: pediment with subunits 5a, 5b and 5c: differentiated on basis of vegetation response, possibly associated with nature of regolith.

*Middle right:* Unit no. 8: low relief with weak dambo development.

*Lower left:* Unit no. 4: low relief, association of pediments, valleys and local weak dambo development. Unit 1 is basic rock intrusion, basic dykes occur in southern part.

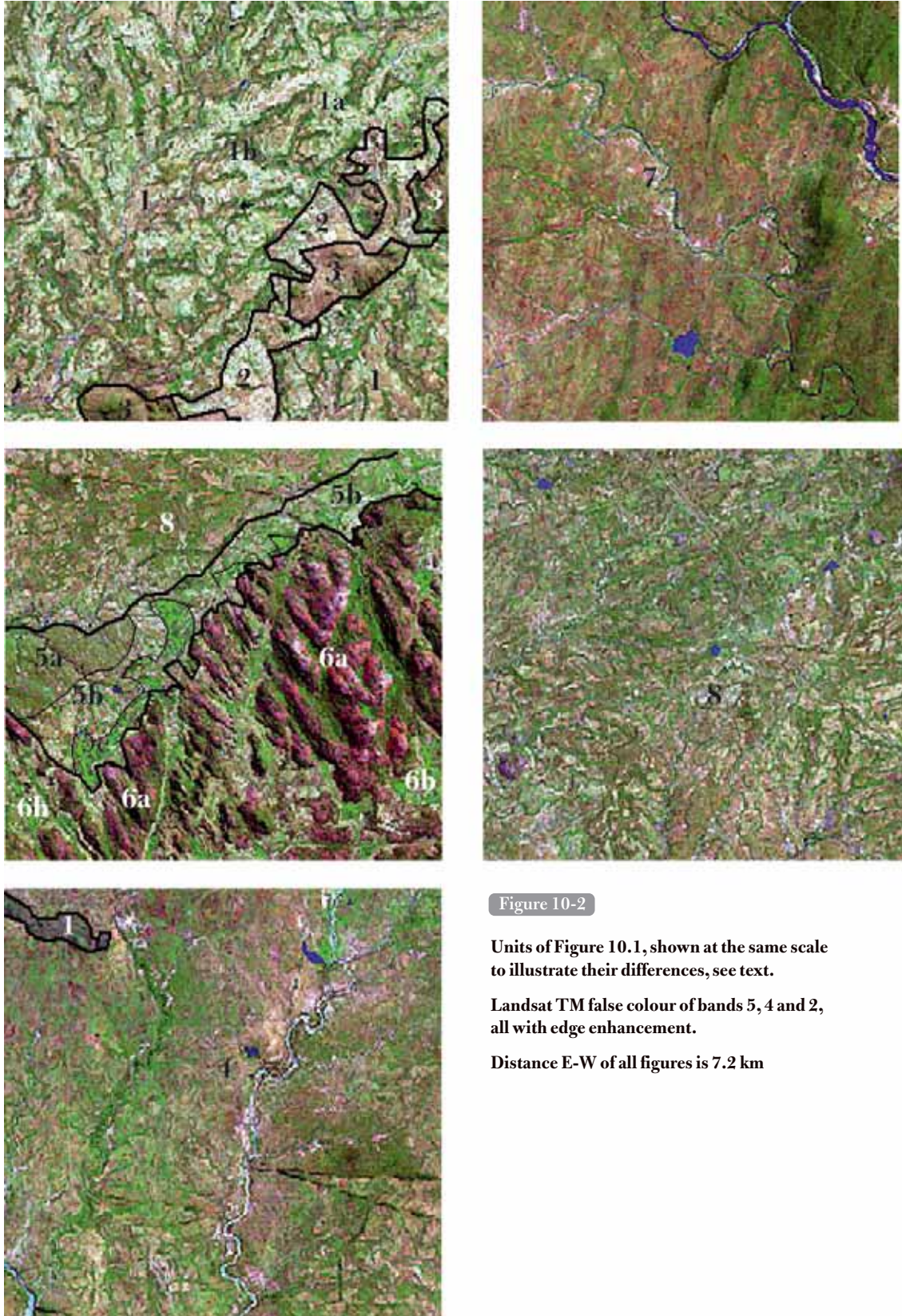


Figure 10-2

Units of Figure 10.1, shown at the same scale to illustrate their differences, see text.

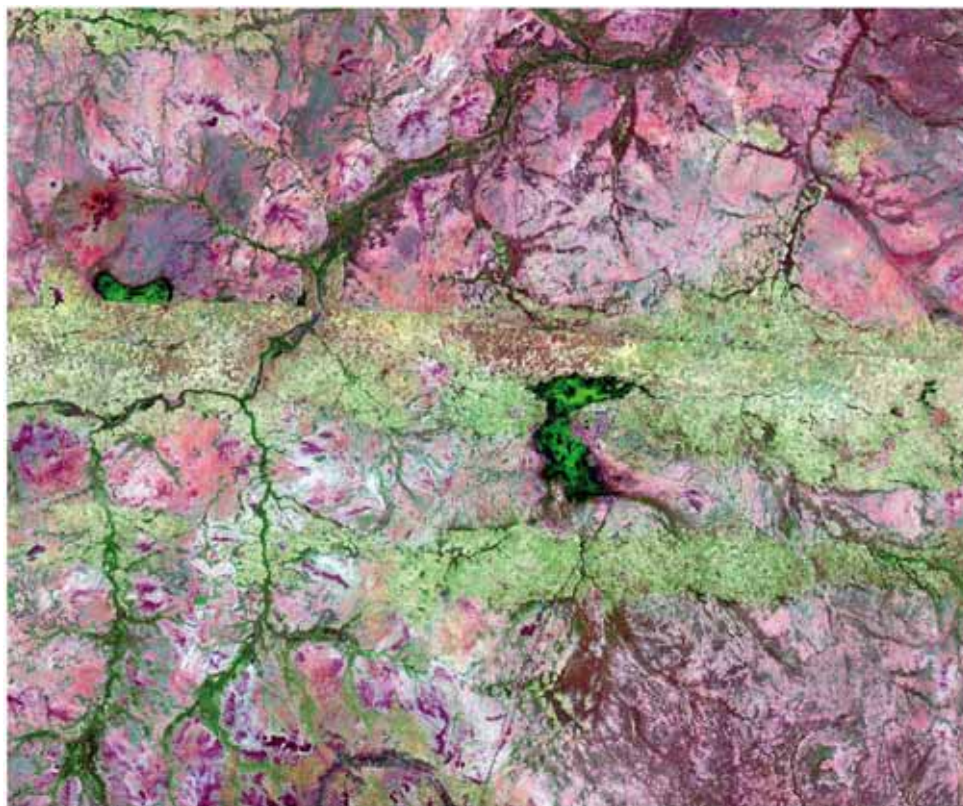
Landsat TM false colour of bands 5, 4 and 2, all with edge enhancement.

Distance E-W of all figures is 7.2 km

### 10.2.2 Example 2 Burkina Faso, area around Dori.

Much of the information is derived from Dutatre et al. (1990), who conducted a survey in the area in order to assess relative recharge, based on drainage patterns and density and suitability for agriculture. The area is underlain by hard rock, has a regolith of variable thickness, and is in parts covered by fossil wind-blown sands.

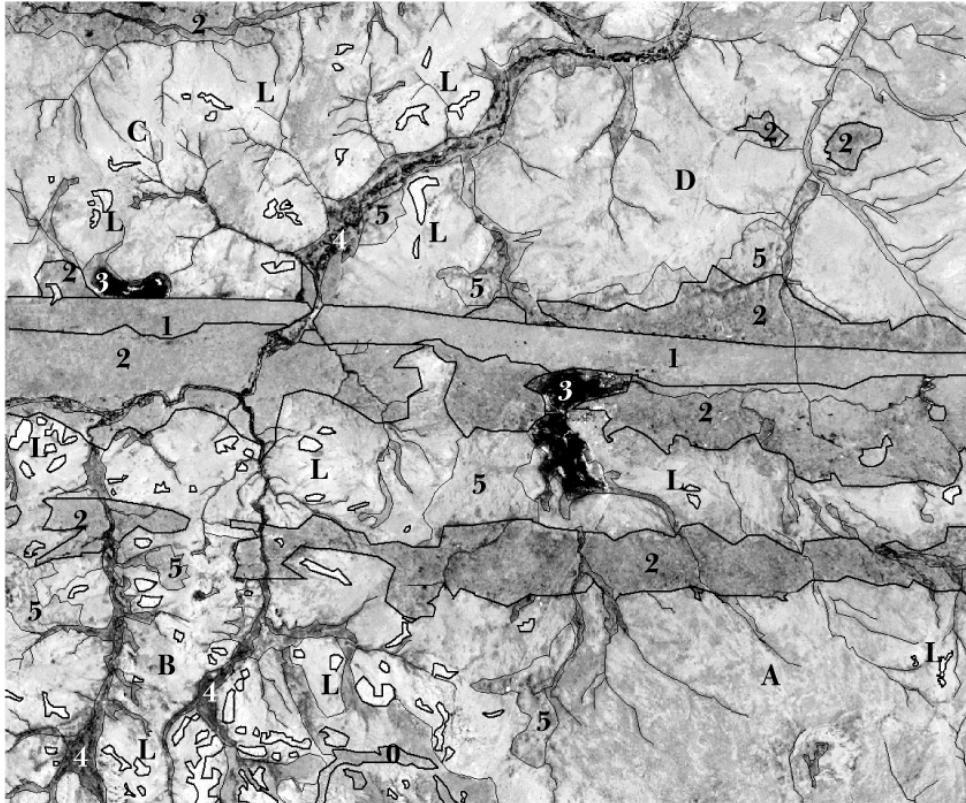
The interpretation of the HGUs is shown with a background of an NDVI image in Figure 10.3. The white tones correspond to relative dense vegetation (mainly rangeland); black tones to bare areas (soil, rock, laterite) or water. Cultivated fields are restricted to areas with a sand cover (units 1 and 2). The drainage lines drawn on the interpretation all have some vegetation response. The impermeable nature of the bedrock and the strong sheet-wash over glaxis (pediments) cause seasonally inundation of depression areas where drainage is impeded by the sands and forms a source of recharge for adjoining sands. Since sands have good infiltration, at many places the groundwater intersects with the surface in small depressions in the sands, but the groundwater is partly drained by small (ephemeral) rivers flowing north. Seasonal waterlogging on a minor scale also takes place on unit 5, which features contorted drainage and small depressions.



**Figure 10-3** False colour image (Landsat TM bands 7, 4 & 2 with edge enhancement) of the area around Dori, Burkina Faso. For interpretation, see Figure 10.4. Distance E-W is 44 km.

Of denudational units A to D, according to Dutatre et al. (1990), best relative recharge takes place on broad interfluves with low drainage density (between A and B, and in D)

The most favourable units for groundwater exploitation (possibly by gallery wells) are the sand units, particularly unit 1, which has the thickest sand cover. Some lineaments can be seen (not indicated) but are not prominent. However, after verification by geophysical survey (e.g. geo-electric surveys), extension of lineaments below or close to the sand cover could be promising sites.



**Figure 10-4** Interpretation map of the area of Figure 10.3, shown on NDVI image.  
**Units:** 1 = Longitudinal dune, thick cover of wind-blown sands. 2 = Wind-blown sand cover, partly eroded, less thick. 3 = depressions, seasonally inundated. 4 = valley bottoms, partly water logged seasonally flooded. 5 = areas with reticular and contorted drainage.  
**A** = denudational unit with strong sheet wash on long glacis, dendritic and sub-dendritic pattern  
**B** = denudational unit with shorter glacis, higher drainage density  
**C** = denudational unit with glacis and structural influences  
**D** = denudation unit with glacis and lower drainage density  
**L** = laterite cap rock and laterite remnants (small units)  
**O** = outcrop  
 For hydrogeological evaluation, see text.

## 10.3 Lineaments

Faults and fractures are linear structural elements. In hard rock terrain it is difficult to judge movement along a fault or the type of fracture (or master joints) and their hydraulic properties by image interpretation alone. Linear elements on an image of supposed association with large joints, fractures or faults are termed neutrally 'lineaments'.

Linear features have been discussed already in earlier geological texts (Waters et al., 1990). With the advent of photo-geology in the mid 1930s for oil exploration in the humid tropics, it became apparent that faults and fractures could often be observed on airphotos. An early publication on the tracing of geologic fractures and lineaments on aerial photographs was made by Lattman (1958) and its use on hydrogeology by Lattman and Parizek (1964). With the advent of satellite imagery with lower resolution than aerial photographs and smaller cartographic scales, interpretation of lineaments changed because less detail was available for analysis.

O'Leary and Pohn (1976) tried to bring more clarity to terms and concepts. They defined a lineament as: 'A mappable, simple or composite linear feature on the surface, whose parts are aligned in a rectilinear or slightly curvilinear relationship, which differs *distinctly* from the patterns of adjacent features and which presumably reflects a subsurface phenomenon'. This definition excludes man-made linear elements (field boundaries, roads, fences, etc., but could include strike ridges due to folding, other bedding planes, gneissic texture, lithological contacts and so on.

Therefore, 'subsurface phenomenon' in the above definition should ideally be replaced for the study of hard rock hydrogeology using image interpretation by 'master joints, fractures and faults'. The objection against doing so is the assumption that the geological context is known, which is usually not the case. Waters et al. (1990), argue that the term 'fracture trace' should not be used and favour Reul's (1973) term 'structure trace'. Stefouli and Osmaston (1983) further discuss definitions of lineaments and other terms.

Most lineament studies made use of multi-spectral satellite images and airphotos and the use of radar images for siting of wells in Nigeria has been undertaken by Teme and Oni (1991). It should also be mentioned that occasionally important water bearing fractures have been found by geophysics alone, and have no surface expression (Hazell et al., 1992, p 163).

### ***10.3.1 Interpretation aspects***

Detection of lineaments on images depends on their expression on the surface, which can be of a different nature, as illustrated in the following sections.

There is a degree of subjectivity in deciding whether a linear, non man-made element qualifies as a lineament. Wise (1982) wrote an ironically phrased article containing 32 rules on defining lines, arrays of lines, plotting of data and interpretation of linear patterns, meant as a warning against the indiscriminate use of linear elements. It is indeed not so difficult to find quite variable results when two or more interpreters produce a lineament interpretation of an area, using the same image. However, Sander et al. (1996) investigated the reproducibility aspect for a hard rock region in Ghana, and found that the degree of agreement was sufficient for edited lineament maps to be used for exploration.

Despite the subjectivity and uncertainty, in many cases there is no good alternative for making an inventory of fractures in a hard rock area selected for the development and management of groundwater. Field mapping would be limited by necessity to exposed areas, leaving out all parts with a weathered cover or superficial deposits. Moreover, exposed rock in the sub-humid or humid tropics is often limited to domes and inselbergs, which owe their existence to low joint or fracture densities, or to the more resistant outcrops in river beds. Field observations made at such places are likely not to be representative of the weathered areas, where the chances for groundwater occurrence are greater. However, only by field observations and examination of bore logs and performance rates, can the nature of fractures (brittle, tensile, compressional, and degree and nature of fracture filling) and the related hydraulic properties be obtained.

Furthermore, field mapping may extrapolate features on the basis of details shown on a topographic map, and thus the same type of subjectivity is introduced, as is the case with image interpretation. Image interpretation can make use of more aspects than those contained in topographic maps, assuming that good quality maps are available.

It may be good practice to set criteria for the tracing of lineaments, such as minimum length, width in case of a possible fractured zone, contiguity and prominence (strong-weak, etc.). It is evident that the scale (resolution) and type of filtering (Chapter 2) influences interpretation results.

It is also useful to consider interpretative aspects, such as lineaments associated with; drainage (with and without vegetation); soil reflectance (due to weathering); mafic dyke; other dykes (quartz, pegmatite, etc); faults (if evidence of displacement exists); interpolation- extrapolation (linear traces in continuation and between mafic dykes, stretches between or in the extension of known faults); and a category 'conjectural/ uncertain' (in case the lineation consists of diverse elements), or other criteria applicable to the particular area.

During interpretation, consideration must be given as to what kind of lineament one is dealing with and categorization may help here. The interpretation result should then be analysed, as is described in the later section (10.9) on analysis.

### ***10.3.2 Image Processing***

Most lineament analysis will be done using hardcopy enlargements of satellite imagery or on-screen digitizing of a geo-referenced image. The advantage is that the file with lineaments can be placed on various products, such as different bands or band combinations, PC transforms and NDVI transform. The latter is useful for checking whether the lineament has vegetation, which could be an indicator of groundwater.

In order to ascertain as to why a lineament is visible, it is advisable to use image processing methods that

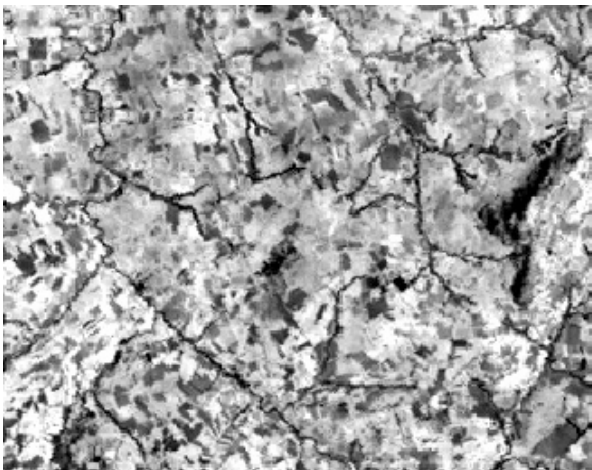
retain the spatial patterns due to vegetation, soil and rocks, with some enhancement of local gradients (see chapter on Image Processing, Use of filters). High pass filters giving full transformation should be used sparingly, for cases where fracture flow is expected but where the fractures are difficult to detect.

It is also doubtful whether diagonal directional gradient filters should be used because bias is introduced. Some researchers use an image comprising a combination of directionally filtered images and this often results in a large number of lineaments, whose significance is difficult to verify.

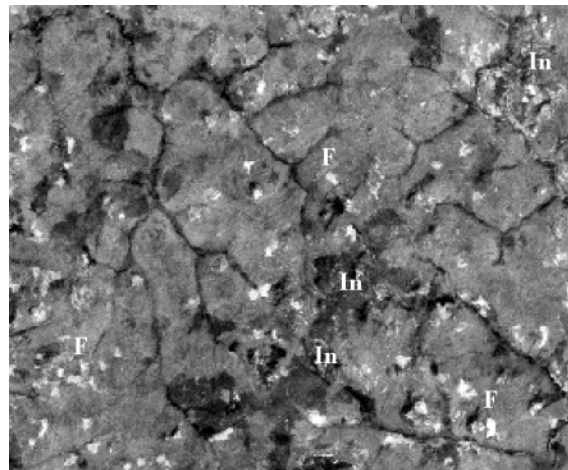
The use of automated lineament detection algorithms is not recommended because not only are man-made linear features and image artefacts included, but also bedding planes, strike ridges, gneiss bands, etc., while no differentiation is made between, for example, faults and dykes.

### 10.3.3 Lineaments, fractures and drainage lines

Because fractures are lines of weakness and are foci for weathering processes (hydrolysis in particular), drainage lines in fluviably eroded terrain often develop along paths prepared by earlier weathering. The presence and passage of water along the fracture often causes lateral and vertical expansion of weathering, hence the zone of influence expands because of the presence of groundwater in the deeply weathered fracture zone. Adjoining areas, with low fracture densities and little or no weathered overburden may be dry for large periods and thus experience less intense weathering. By erosion, the weathered overburden may be partly removed and incising rivers may make use of the fractures. This is the case in the areas of Figures 10.5 and 10.6, where the drainage lines are mainly adjusted to fractures in the granite. These appear as dark lines because of the vegetation. Interfluves are gently undulating and weathered with occasional low and small outcrops, except for high inselbergs, which rise sharply from the dissected planated surface consisting of broad convex interfluves.



**Figure 10-5** Granite country in west Kenya. Part of the drainage lines follow fractures and are clearly seen because of dense vegetation (dark tones) makes use of groundwater water in fractures. In the east and centre are large inselbergs. Landsat TM b5 (no filtering used) Distance EW is 8.5 km



**Figure 10-6** Drainage pattern adjusted almost exclusively to fractures. N. Ivory coast, LANDSAT TM b4. Three major directions: NW-SE, SW-NE and N-S with large E-W fracture in southern part. In = large outcrops/Inselberg, other dark areas are burned patches F = agricultural fields (light tones) Distance E-W is 24 km

Apart from straightness, the angle of bifurcation can be an indication that drainage lines follow fractures. In fluviably eroded terrain and isotropic rock the cosine of the bifurcation angle ( $\alpha$ ) is a function of the ratio of the tangents of the main stream gradient ( $G_m$ ) and the gradient of the tributary ( $G_t$ ):  $\cos \alpha = f(\text{tg } G_m / \text{tg } G_t)$ . Thus orthogonal bifurcation angles are found if the tributary gradient is very steep and the main gradient gentle. In the west and south of Figure 10.5 drainage lines with about equal gradients join at about  $90^\circ$ ; this is so because the fractures intersect with that angle.

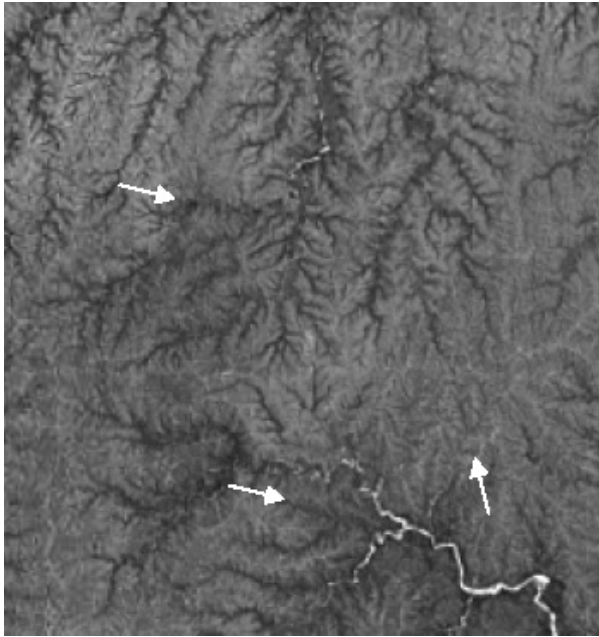


Figure 10-7

Weathered crystalline area (Malawi) having predominantly dendritic, incised, drainage pattern, but some drainage lines follow lineaments.

Straightness and bifurcation angle criteria can be used to detect lineaments (arrows)

Source: Google Earth

In case of a large fracture zone, drainage may be contained at the width of the zone, but the drainage lines may not have straight courses, particularly when fluvial deposits have accumulated in the fracture zone.

Drainage lines adjusted to fractures need not be incised by fluvial erosion but may be manifest in the form of small and gentle valleys due to solute transport of dissolved rock minerals in the weathering process along the preferential pathways created by a fracture. In case of uplift or climate change and possibly land use change (cultivation leads to increased overland flow), incision of such low order valleys can start. In many semi-arid to sub-humid areas, valley fill materials may show evidence that sequences of fill and erosion took place, and the relative age of the deposits can be established by stratigraphic principles and analysis of the materials. The older deposits often have limestone nodules (kankar) and different colours (higher chroma values of the Munsell colour charts of the soil scientists) than the younger ones.

Another example of adjustment of drainage lineaments, which corresponds to weathering along fractures, is shown in Figures 10.8a and b. The 'weathering valleys' are evident on the near infrared band of SPOT because of

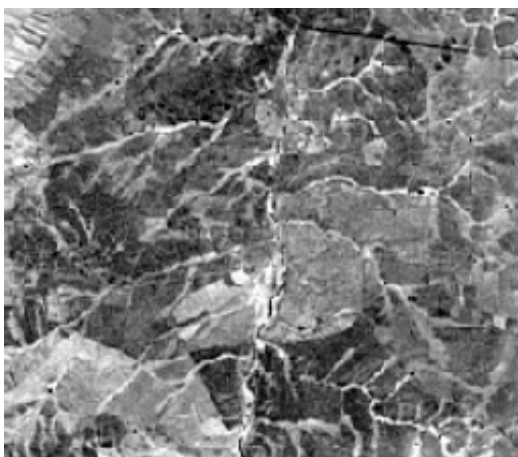


Figure 10-8a Small weathering valleys revealed by grass covered flat bottoms (light tones) in granite area, western Spain, on infrared band of SPOT. Several lineaments are seen

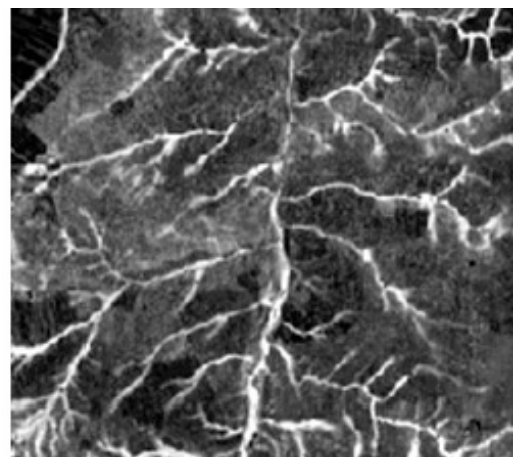


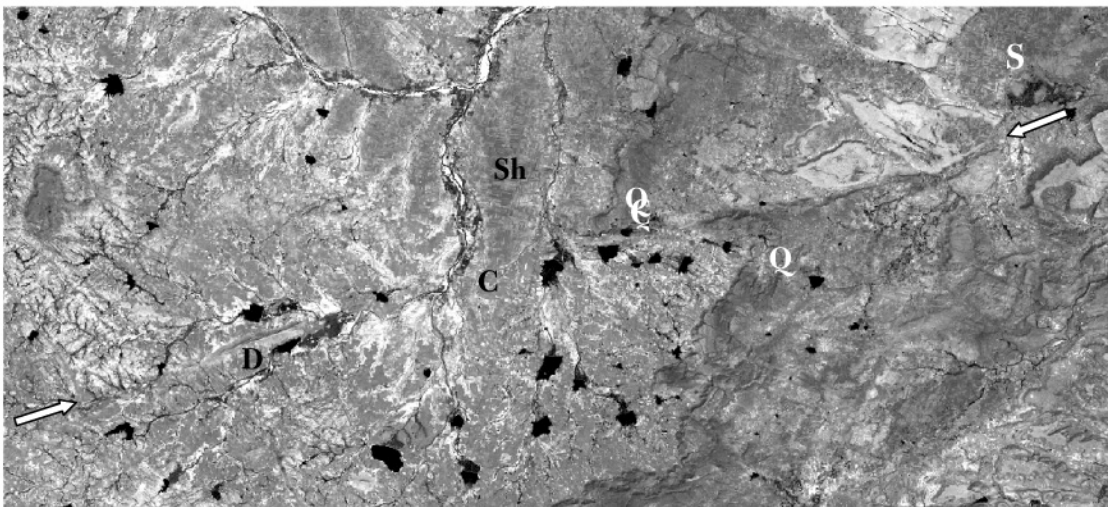
Figure 10-8b NDVI transform of same image as shown on left hand figure, having better display of vegetation contrast

Field evidence: groundwater is close to valley bottom after rainy periods. A large, approximately NS lineament, is a fault, western side down and is a main conduit of groundwater. Distance EW is 5.38 km

the presence of grass vegetation, which derives soil moisture by capillary rise from the shallow groundwater table at the date of overpass (June 1986). Dark and medium grey tones on interfluves are open forest and rangeland, with groundwater depths beyond the capillary zone. A cultivated area with mainly bare soils is dominant in the NW corner. The strength of the NDVI transform with such conditions of vegetation contrast is evident from a comparison of the two images.

### 10.3.4 Effect of scale

Rose diagrams of lineament sets generally show appreciable differences between those obtained from satellite images and those from air photos and field measurements (Bannert, 1969, Armand et al., 1983; Greenbaum, 1992; Savane, 1995; Attanayake, 1999). The differences are attributed to differences of the level of detail visible on the higher resolution of air photos and stereoscopic view and the lower resolution of satellite systems, such as Landsat TM, SPOT or IRS, and also to different timing.



**Figure 10-9** Small scale image (LANDSAT TM b5) of a large fault causing off-set of basal quartzites (Q) overlying granites. Near D is a dyke. Fault is covered near C by shale (Sh) and alluvium. Towards east the fault develops in a steep drag and continues further east, outside the image shown for >200 km. Near S water is derived from a spring along the fault and local faults trending NW. Other black areas are reservoirs (tanks). Area is south of Kurnool (Andhra Pradesh, India). Distance EW of image shown is 50 km.

An example of the use of small-scale images is shown in Figure 10.9. A long interrupted lineament (A1-A2) is shown, which corresponds to part of a large fundamental fault. Deep seismic soundings in the area south of the image shown have indicated the existence of fundamental faults, some reaching the Moho discontinuity (Kaila et al., 1979). Regional geological mapping (with the aid of photogeology) proved that the fault continues in an eastern direction (beyond the area shown) for some 200 km (Meijerink et al., 1984). Some springs occur along the eastern part of the fault, where it develops into a steep flexure, which is partly ruptured (see example in Chapter 6). In the western part the steep narrow ridge bears witness to the continuation of the fault, but parts are covered by shales of the youngest unconformable formation not affected by folding and wedging out near the fault and by alluvium of limited thickness. By using strike continuation of the fault, places for drilling could be selected, after more precise location by shallow geophysics, preferable geo-electric. On large-scale images, such as air photos of the areas where the fault trace is covered, the existence of brittle deformation of the granite basement along the fault, but below overburden, would go unnoticed. The lineament is thus partly of the 'interpolation type'.

Two other long lineaments are indicated. Lineament C1-C2 is a fault because of off-set in the basal conglomerates and quartzites (Q) of the oldest Cuddapah rocks overlying basement. Although it cannot be observed at all places, the geological evidence is, in this case, so strong that interpolation can be done. Since lineament B1-B2 is in the same direction, it is likely to be a fault as well, and interpolation may be justified.

The above example demonstrates that interpretation may fruitfully use small-scale images. However, in some cases small scale evidence be misleading, as is illustrated in Figure 10.10.



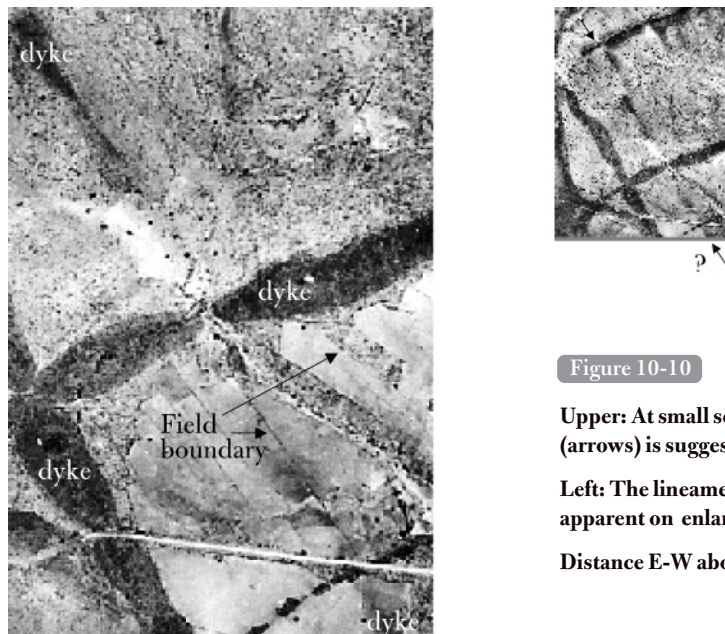


Figure 10-10

**Upper:** At small scale a lineament (arrows) is suggested.

**Left:** The lineament is not apparent on enlarged image.

**Distance E-W about 1 km**

On the small-scale air photo (upper right) it seems that there is a lineament, as indicated by arrows. However, when the image is enlarged no evidence of the lineament is seen. This example also shows field boundaries and a road. Such linear elements will be included in a data set resulting from automated lineament detection.

## 10.4 Geomorphology

A brief introduction into geomorphology of hard rock terrain and weathered zones is given, in order to understand some of the features seen on images with possible implications for groundwater occurrences.

Under *humid tropical conditions*, such as the Guinean shield in S. America, denudation (i.e. weathering and erosion) tends to produce a landscape consisting of small hills with thick and profound weathering and linear incision. Often no or little alluvium is found even along major rivers, along which outcrops may occur at places. The radar image of Figure 4.8 shows such hard rock terrain in the humid tropics. The area shown in Figure 10.6 of the north Ivory Coast (now sub-humid) has many characteristics of wet humid geomorphology, although weathering depths may have decreased by erosion. Because of high rainfall, the fractures are recharged from the weathered zone and a reasonably good success rate of boreholes close to the drainage lineaments can be expected.

Characteristic of *semi-arid conditions*, is the presence of large pediments; gently sloping planation levels with semi-logarithmic increase of slope until sharp knicklines are reached that form the border with steep slopes of bare rocks or slopes covered by boulders. Because of their widespread occurrence pediments are discussed and illustrated in a section below.

Eroded areas with thin regolith, and poor groundwater resources because of limited recharge, can usually be interpreted because of the structural geological details visible on images. If these are not seen and there is no alluvial cover, it is possible that such areas have relicts of regolith.

Under *sub-humid conditions*, denudation has usually created an undulating landscape with broad interfluvies and valleys. Nature and thickness of the weathered rocks in the interfluvies varies with rock type and evolution time. In the valleys colluvium and fluvial deposits overlie fractured rocks. After the rainy period groundwater levels often reach the surface in the valley bottoms, but rises of several metres also may occur in the weathered interfluvies because of low storativity. The water table declines due to gravity drainage and evapotranspiration and exploitable water may be restricted to the more deeply weathered parts and the fractures. Differences in fabric and mineral composition determine the hydrogeological properties, even when the main rock suite is the same, as is illustrated in Figure 10.37 (below).

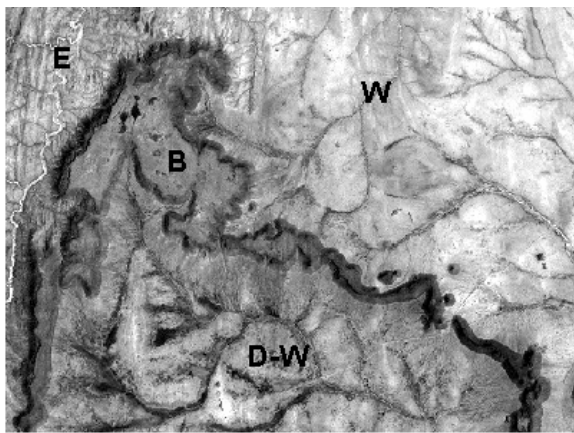
### 10.4.1 Planation levels: Relicts of the geological past

Tectonism and climatic changes in the past have caused an interaction of weathering, incision and planation, and of sedimentation. Pediments may have been weathered and dissected, while weathered hills in humid climate may have been planated during a drier climate. Wind blown sands may have accumulated on pediments creating more favourable conditions for recharge and storage.

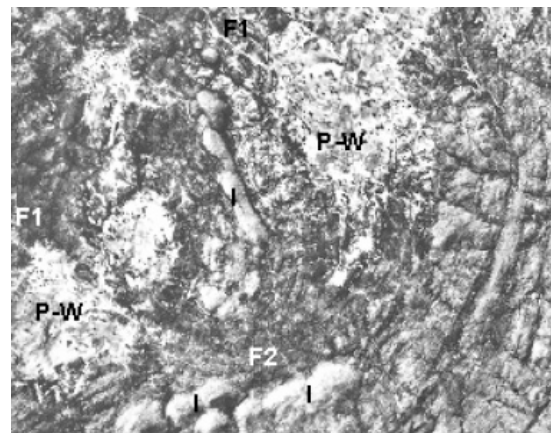
Laterite iron crusts (ferricretes) have been formed under more humid conditions and calcrete under drier climates. Lakes expanded and contracted during the pluvial and inter-pluvial periods.

In many elevated areas, now undergoing erosion, groundwater occurrence is strongly influenced by presence of saprolite and saprock on planation levels formed in the geological past. Both saprolite and fractures recharged by water infiltrated in the regolith are the sources of groundwater, while in surrounding areas at lower elevation runoff may be fast leaving little time for infiltration and fractures may have been eroded exposing bare rock or little weathered saprock.

Two examples illustrate the effects of geomorphological development.



**Figure 10-11** Past geomorphological developments has lead to four units: *W* weathered basement with some vegetation along drainage lines, indicating presence of groundwater; *E* eroded basement, barren, *D-W* weathered basement with dambo's suggesting seasonal water logging, *B* flood basalt, relief inversion by denudation. Samburu, Kenya, Landsat TM b.4. Distance EW is 24.4 km



**Figure 10-12** Remnants of weathered old planation level, *P-W* with shallow wells and water bearing fractures *F* and inselbergs *I*. The area consists of metamorphic rocks with regional folding. Eastern part is deeply eroded.  
Central India, high-resolution panchromatic image.  
Distance EW is 5.5 km

Figure 10.11 shows a part of the now semi-arid Samburu district, N. Kenya. Basalt, which then extruded in depressions, now occurs as plateaux (relief inversion). The elongated outcrop suggests outflow in a former valley. Thereafter, denudation took place, whereby the basement was lowered and the basalt outcrop area was reduced by slope retreat. The denudation could have slowed down at the level of the areas denoted with *W* and *D-W* and created an undulated landscape with broad interfluvies and somewhat incised valleys, partly along fractures. In the southern part, dambos, typical of this part of Africa, developed, and at least those in the headwaters are still present as relicts of former wetter conditions. These can be recognized by dark tones along the valleys and indicate seepage water (see section 10.4.4 for a discussion of dambos). By regional tectonic uplift a new cycle of erosion was initiated. The weathered zones were stripped off and left mainly bare rocks (unit *E*); strikes of rock units can be seen. Runoff is fast and limiting recharge so much that most fractures in this unit have no vegetation, and may not contain sufficient groundwater even for limited use.

An old planation level with a weathered hummocky (*P-W*) terrain is shown on the aerial photograph of Figure 10.12. High-grade metamorphic rocks underlie the area. Drinking water supply and supplementary irrigation depends on water drawn from the weathered zone, fractures (*F1-F2*) and more deeply weathered valleys (*F1*) along fractures or the strike of softer beds. Massive beds with minerals of low-weathering susceptibility and low

joint densities have led to the formation of inselbergs (I). After uplift the eastern part was deeply eroded and little or no weathered rock or alluvium is found in that part. Whether or not the fractures contain water in the eastern part is of little relevance because there is no human occupation and accessibility prohibits the use of drilling rigs.

#### 10.4.2 Pediments and inselbergs (bornhardts)

Inselbergs (kopjes or koppies, bornhardts, residual hills), which can be recognized on images, are found in all climatic zones, because it seems that once formed, under humid or sub-humid conditions, and exposed after erosion, they persist because of the arid microclimate of the outcrop. In some areas, such as SE Sri Lanka, steep and large residual hills have a vegetated thick regolith through which much subsurface seepage water feeds the lower fringe zone. In general, areas with many outcrops are not considered favourable for groundwater exploration because of shallow weathering depths and low recharge of possible fractures.

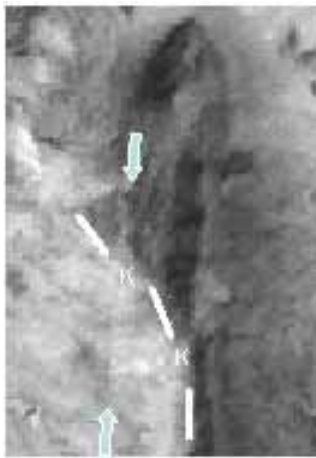


Figure 10-13

**Inselberg (dark tones) consisting of steeply folded, high-grade metamorphic rocks, bordered by pediment (light tones). The sharp topographic transition between pediment and inselberg (Knick-line, is indicated by K). Note that strike continuation (arrows) can be seen as well as a small fault on the pediment, showing evidence that the pediment is a true erosional surface.**

**The semi circular shape of the pediment is known as an embayment, which expands by slope retreat of the hills and extension of the pediment.**

**Landsat TM band 5. Distance E-W is 1.9 km.**

The pediment can cut across lithology and the same rock type may be found in a steep and bare inselberg and its surrounding pediment, as is shown in Figure 10.13.

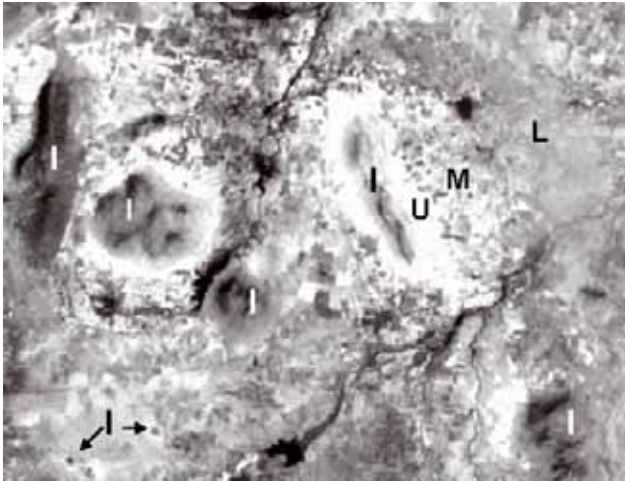
It is likely that the present pediment with little overburden, is the result of erosion under semi-arid conditions of a weathered mantle formed earlier under more humid conditions, when the regolith expanded in depth but also laterally, forming the so-called embayments.

Pediments in hard rock country often have poor groundwater storage capability, especially when the pediment consists of a true rock-cut surface (Leopold et al., 1964). The presence of thin sheetwash deposits obliterates fractures. Because of shallow soils and rapid runoff there is little recharge. However, some pediments show zonation (catena or toposequence) into an upper, middle and lower pediment, as is illustrated in Figure 10.14. On the upper pediment in that area soils are stony and shallow or absent, but in the middle zone with light textured soils a weathered zone is found. Storage and recharge are sufficient to support some open wide diameter wells, used for drinking water and supplementary irrigation of small fields. The lower pediment has heavy textured soils and no or few wells are in operation.

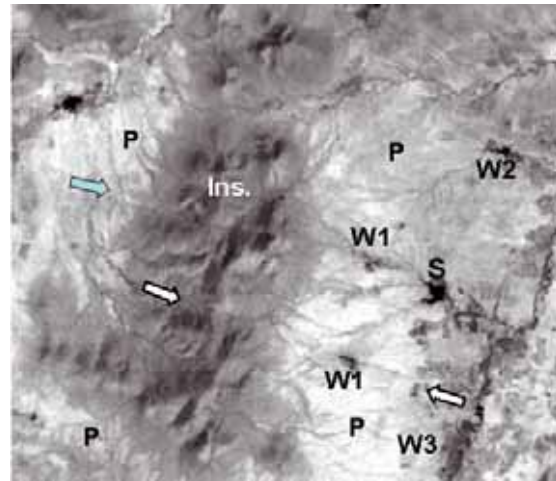
Other pediments are illustrated in Figure 10.15, which is some 80 km south of the area of Figure 10.14. Groundwater conditions are poor and limited to some large fractures (see caption of the figure) and a narrow zone along an ephemeral river, which recharges a strip with weathered rocks.

A regolith, once formed can be subjected to pedimentation when the climate changes to dry conditions, as is illustrated below (Figure 10.23, below) and where traces of fractures persist in the regolith (Figures 10.7, 10.17 and 10.23).

The regolith depth and properties of the fringe zone of inselbergs vary significantly. In the above examples from Andhra Pradesh, India, they consist of rock cut surfaces. In other areas bore holes and/or geophysical (EM) data have shown that the fringe zone can be deeply weathered (McFarlane et al., 1992; Barker et al., 1992).



**Figure 10-14** Large and small inselbergs (I) and pediments: upper (P), middle (M) and lower (L).  
Some wells in middle pediment support supplementary irrigation (small dark fields).  
Area is underlain by intermediate to basic igneous rocks and slates, boundaries not seen.  
LANDSAT TM b7. Area near Darsi, E Andra Pradesh (A.P.) India. Distance E-W is 12 km.



**Figure 10-15** Inselberg (Ins.) surrounded by pediments (P). Wells W1 (dark fields are irrigated) are located on fracture (see arrow), possibly also well W2. Few more wells (W3) are found along the small river.  
Dark area S is small tank (reservoir)  
Area consists of intermediate igneous rock.  
Location 30 km NE of Udayagiri (A.P.), India.  
Distance E-W is 10.1 km

### 10.4.3 Weathered areas

The weathered zone of hard rock, set in a geomorphological context, plays an important role in the occurrence of groundwater and therefore the extent and a few other aspects of the weathered zones should be studied on images.

The importance of the weathered zone as an aquifer has been demonstrated by a number of studies and therefore hydrogeological image interpretation of crystalline terrain may start with an attempt of a first characterization of the weathered zone.

Gently sloping areas or nearly flat areas with a contiguous weathered mantle, as evidenced by the land cover could well indicate that weathering is deep, particularly in areas with tectonic quiescence and a rainfall of 1,300 mm or more. If such areas have been stripped partially of the weathered mantle, either by uplift or due to drier conditions, or by both, the terrain is dissected, resulting in steeper slopes and at places outcrop areas can be seen. Around outcrops in some cases, partly weathered rocks may occur with relatively permeable condition, as is illustrated in Figure 10.17 (below). The land cover usually shows more variation because land use and vegetation is adjusted to differences of the soil. Because runoff intensity increases with slope steepness, recharge is less. Using data based on their hydrogeological study in central Uganda, Taylor and Howard (2000) gave transmissivity values for the deeply weathered zone in the range of  $5\text{--}20\text{ m}^2\text{ d}^{-1}$ , but only  $1\text{ m}^2\text{ d}^{-1}$  for the fractured bedrock aquifer. Recharge may be in the order of 8% of the mean annual rainfall (1,500 mm) and surface runoff of 3–5 mm. For the eroded surface and a mean annual rainfall of 1,000 mm, recharge was mentioned to be 5–15 mm, runoff 30–40 mm and the same transmissivity of the fractured bedrock aquifer.

In central Malawi, there were only slight variations in the mean yield of borehole types; those which finished in the regolith and those penetrating the hard rock had mean yields of  $198$  and  $245\text{ m}^3\text{ h}^{-1}$  respectively (McFarlane et al., 1992). Areas with very low relief and few streams but extensive dambo areas have the greatest regolith and saturated thickness and relatively high yields.

Hazell et al. (1992) compared borewells in weathered and fractured granites and metamorphics in northern Nigeria and showed that the number of successful holes ( $> 360\text{ m}^3\text{ h}^{-1}$  air-lift test) for the weathered zone wells was only slightly less (15 against 18 boreholes) in the granites, but the score of weathered to fractured boreholes was 12 to 22.

Absence of correlation was noted for regolith thickness and saturated regolith thickness and well yields for a gneiss area in Malawi and is suggestive of an overriding influence of local lithological features of the banded gneiss

rock. The same absence of correlation was found for individual regression plots for areas in Zimbabwe (Wright, 1992).

The interpreter of images of weathered hard rock terrain should be aware of the complexities that may have no or faint traces at the surface. For example, close spaced drilling for dam sites has revealed that fractures can have very deep (up to some 80 m or more) weathered materials in narrow fracture zones. Thomas (1974) described a local, closed weathered basin in hard rocks in Nigeria, as evidenced by drilling and geophysics.

### *Generalized weathered profile of crystalline rocks*

A discussion of weathering processes is beyond the scope of this book (the reader is referred to handbooks, for example, Thomas (1974), and to Wright (1992), for an understanding of terminology and for the identification of some weathering features for hydrogeological interpretation. However, a brief introduction is useful for understanding some of the images discussed below. As rocks of granitic composition have the most widespread occurrence their weathering is briefly mentioned.

A schematic view of a weathered profile (regolith) in warm (or formerly warm climates) is shown in Figure 10.16. The upper zone consists of soil and stone lines and shows much variation, depending on local geomorphology, presence of termite hills and so on. It provides generally good to medium infiltration, unless vertisols ('black cotton soil') developed when soil horizons have strong clay illuviation (downward transport of clay). Below the upper zone is a saprolite, generally consisting of silty clays or sandy clays. Thickness is highly variable but can be over tens of metres thick. Permeability is low, and specific yield depends on type and stage of weathering, but generally acts as the medium that stores groundwater, with slow release.

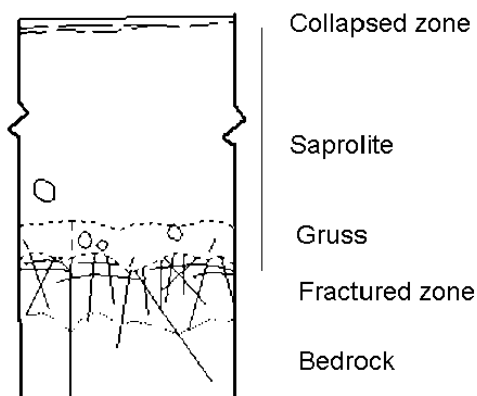


Figure 10-16

#### **Typical weathered profile of granite in warm climate**

**Upper zone consists of soil and stone line(s). Saprolite (clay, silts and sandy clay) can be several tens of m thick and has generally low permeability and low to relatively medium storage capability.**

**Lower saprolite or gruss is partly decomposed rock and together with the fractured zone (saprock) has high relative permeability but low storativity or specific yield. Permeability of bedrock only depends on deep fractures or stringers/veins.**

The zone of partly weathered rock that can be disintegrated by hand into coarse sandy, gravelly texture, still showing the fabric structure has good permeability but low storativity. Some authors use the term gruss for the lower saprolite. This layer develops particularly on coarse textured granites. Some core boulders may be present, as well as stringers of veins. There is often a gradual transition to the zone of relatively dense sub-horizontal and other fracturing, due to unloading and widening of fracture apertures by weathering, leading to relatively good permeability. With increasing depth only the larger fractures may survive causing a decrease of the overall (low) secondary permeability, but not necessarily so in all cases. The two lowest units (gruss and fractured zone) in the profile shown are also termed 'saprock'.

Wright (1992) reviews the hydraulic properties of the regolith and weathering processes; some overviews can also be found in UNESCO (1984).

### *The weathered cross section*

Areas with shallow weathering can be interpreted on images by noting dominance of outcrops and poor vegetation and possibly quartz rich shallow residuum giving high reflectance, but otherwise the thickness of the weathered zone cannot be interpreted. However, local knowledge, as the above examples of pediments illustrate, allows an approximate inference. In some cases, images may reveal aspects of the weathered cross section, for example by inspecting the fringe zones of large outcrops, as illustrated below, and certain valley bottoms (see discussion of dambos, section 10.4.4).

The lower saprolite zone (gruss) may crop out around an inselberg, possibly due to erosion of the upper clayey saprolite. Figure 10.17 shows a large granite inselberg in central India with such a fringe zone, which is slightly dissected, in contrast to the deeply weathered zone further away. The fringe zone is a groundwater intake area and because of its topographic position, boreholes just beyond the fringe zone demonstrate confined conditions, as shown in Figure 10.18. The clay-rich saprolite (or upper weathered zone) has a low permeability, in contrast to the permeable saprock or gruss layer. In this area, a few wells were reported to have flowed for a limited time after drilling.

Also of interest is that fractures traversing the inselberg continue into the weathered zone (see arrows), an indication that differences in weathering persist in that zone and affect the drainage lines, possibly by spring sapping.

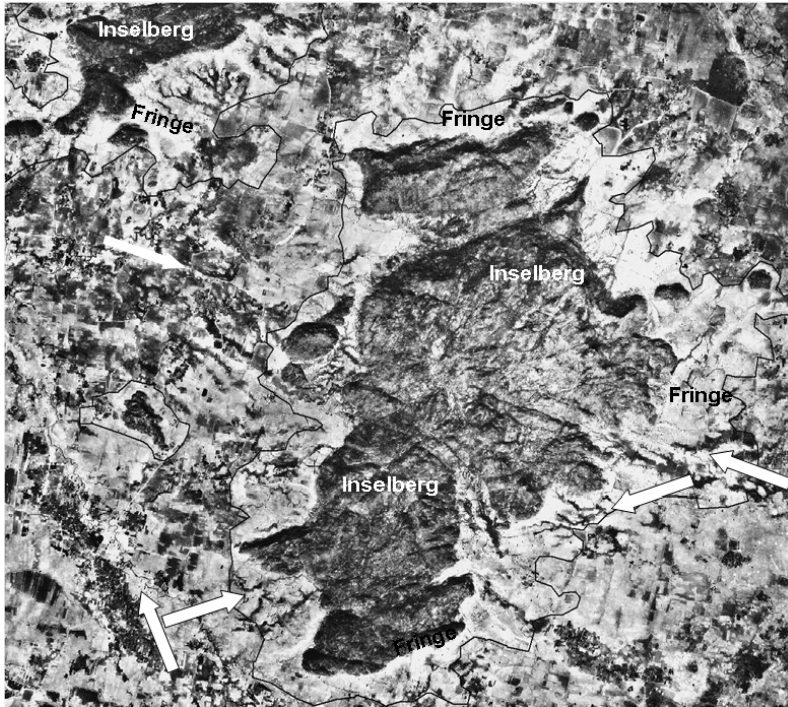


Figure 10-17

Weathering history affected by fractures in basement rock.

Aerial photograph showing large hard rock inselberg and continuation of some large fractures into deeply weathered zone.

Central India

Distance E-W is 8.6 km

The sketch of Figure 10.18 illustrates how semi-confined conditions may occur in weathered granite country. The outcrop shown is much smaller than the one in the image of Figure 10.17. The sketched situation should not be generalized because deep weathering adjacent to inselbergs has been encountered (e.g. Barker et al., 2002; McFarlane, 1992).

Generally, it is assumed that regolith thickness is associated with dense fracturing and visa-versa. It is therefore plausible that inselbergs were formed due to low fracture density (such micro-massifs are known as plinths). The assumption may imply that boreholes in the weathered area between inselbergs or areas rich in outcrops will have higher yields than those close to the inselbergs, but to our knowledge this relationship was not systematically investigated.

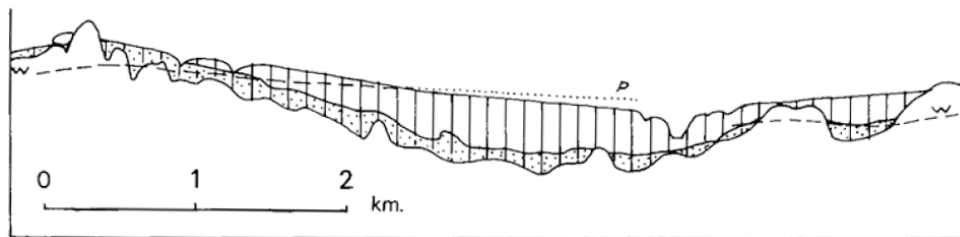


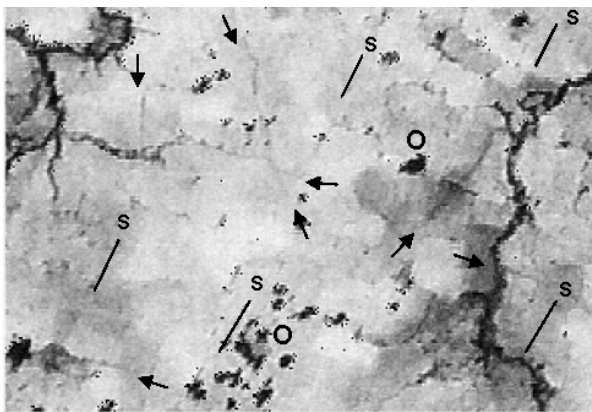
Figure 10-18 Sketch illustrating (semi)confined conditions (p is piezometric surface) in granite country due to elevated intake areas of permeable saprock (dotted) overlain by saprolite with low permeability (hatched). Pressure can also be due to tapping of inclined fracture (not shown) and loading

### *Lineaments in deeply weathered granite terrain*

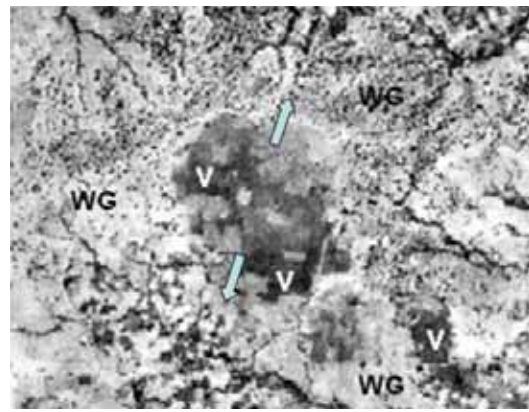
Although deep and thorough weathering usually obliterates fracture traces, in some cases they can be seen. This is of importance because one often has to find groundwater close to specified localities, often on interfluvies and a close inspection of images may reveal possible fractures. Examples at different scales are discussed.

#### Examples at local scale

The permeability of fractures or master joints and circulation of water influences the weathering, which can result in differences of soil developed on top of the fracture and the surrounding rock. This is illustrated in Figure 10.19, which shows an aerial photograph of a granite area subjected to stress, resulting in foliation, as is evident on the image. Large joints/fractures are indicated by arrows. Remnants of planation surfaces with thoroughly weathered soils, rich in clay (the areas indicated with V in Figure 10.20), can obliterate lineaments, which may be detected in eroded weathered areas (indicated with WG in Figure 10.20).



**Figure 10-19** High resolution panchromatic image, central India  
 Master joints (indicated by small arrows) that can be seen due to differences in soil formation.  
 Area consists of crystalline basement rocks. Gently undulating surface, fallow fields.  
 Arrows show possible master joints/fractures.  
 Distance E-W is 1.2 km  
 ----- s foliation  
 o outcrop with bush



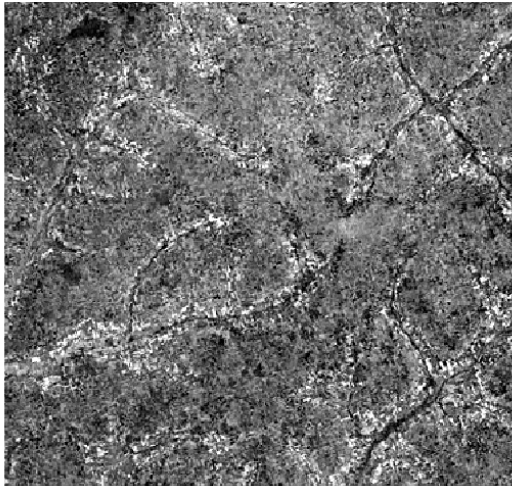
**Figure 10-20** High resolution panchromatic image, central India  
 Weathered granite area with remnant of planation level with dark clay soil (V) which obliterates lineament.  
 Distance E-W is 3.8 km

### *Examples at sub-regional scale*

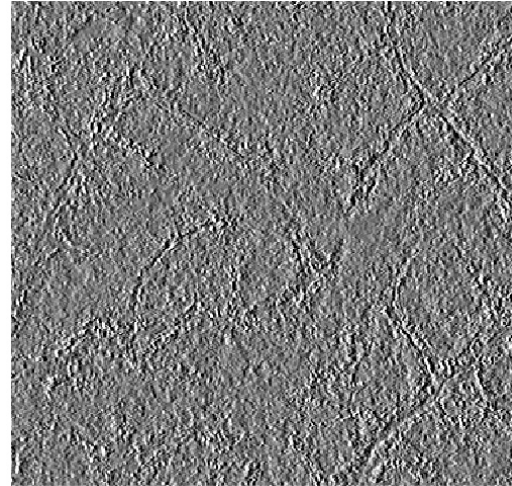
A part of the deeply weathered basement of an area in eastern Uganda is shown in Figure 10.21. It is a first Principal Component (PC1) after edge enhancement. The trellis pattern of the main drainage in the NW part suggests that drainage is developed along large fractures. However, settlements are on the interfluvies and close inspection of the (original) image reveals many faint lineaments, which can be used for directing the geophysical survey. At places many small lineaments could be seen, suggesting that there is interconnectivity of the fractures. It is obvious that accurately georeferenced images have to be used so that pixel coordinates can be used for location in the field with GPS.

Figure 10.22 shows the PC1 image after using a gradient filter in x direction. Some lineaments that extend from the valleys onto the interfluvies have been indicated, but more can be seen. These extensions are of interest as possible sites for wells, because villages and schools are located on the interfluvies.

Another example, Figure 10.23, pertains to a deeply weathered granite area along the Ken River, north-central India. Some inselbergs of varying size and heights occur, but most of the area has a regolith with variable thickness. Borehole data indicate that the topography of the bedrock below the regolith is irregular; some boreholes penetrated the regolith up to depths of 70 m. Success rates of boreholes (up to late 1970s), without geophysics and image analysis, was low (about 40%).



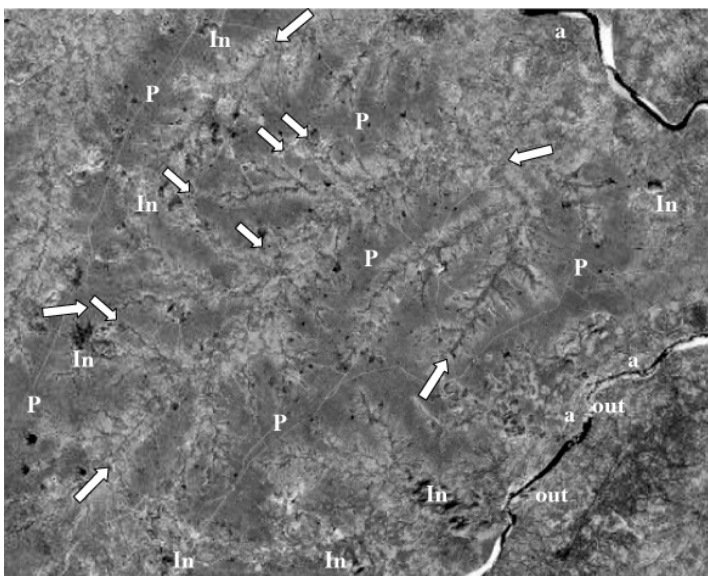
**Figure 10-21** Deeply weathered basement Iganga district, E Uganda. PC1 image of Landsat TM with edge enhancement. Trellis pattern suggests main drainage is adjusted to large fracture. Detailed inspection shows more lineaments on interfluves



**Figure 10-22** Same area as Figure 10.20, PC1, with simple high-pass gradient filter . Some lineaments indicated by arrows. Distance EW is 10.7 km

It is likely that the deep weathering originates from a wetter climate and that during a following drier period the pediments have formed, which now dominate the upper level of the topography as featureless gently sloping pediplains, developed over the regolith, except for the outcrops and dissected valleys. The presence of lime nodules (kankar) in the upper regolith bears witness to the drier climate. The contact surface of the unweathered rock and the regolith is highly irregular; close to outcrops up to 60 m deep regolith may be found. The pediplains are now subjected to fluvial dissection. The main valleys are incised up to some 30 m and have lateral belts of tributaries. The point of interest here is that some of the valleys and many of the tributaries have straight stretches and some parallelism, while they have developed entirely in the regolith. Hence, the fracture planes still existed in the regolith in the form of weathered material that differed from the bulk in terms of resistance to erosion and possibly in permeability. It could well be that they extend into the saprock or bedrock.

The uniform areas between the dissected valleys are the pediment surfaces (P in the image); these have no trace of lineaments, which are restricted to the dissected parts. Along the main river is a narrow belt of alluvium (a), not always present. Outcrops (out) are found in the riverbed at a few places. A few of the larger inselbergs are indicated (In). By photo-interpretation all outcrops in the area were mapped, but distribution seems to be random, suggesting uniform bedrock conditions.



**Figure 10-23** LANDSAT image (B & W rendition of false colour). Weathered granite area, Central India, west of Ken River (M.P.). Despite deep weathering lineaments (arrows) can be seen in dissected valley systems  
**P = pediment**  
**In = inselberg**  
**a = alluvium**  
**out = outcrop in river bed**  
 Distance E-W is 12.4 km



The photo interpretation was done prior to the advent of satellite images and did not recognize the lineaments, which can be attributed to the effect of scale.

#### 10.4.4 Dambos

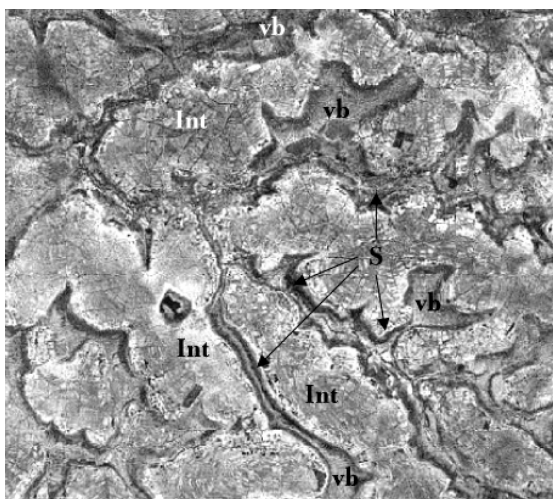
McFarlane (1989) describes a dambo as the seasonally waterlogged bottomland of the land surface, irregularly lowered by a process termed ‘etch-planation’. This involves differential leaching by infiltrated water to the extent that the saprolite collapses, leaving a thick residuum.

The dambo-catenas in the crystalline regions of sub-Saharan Africa has attracted the attention of hydrogeologists and geomorphologists (McFarlane, 1989, 1992; Mackel, 1985; Wolski 1999; and other authors) probably because of the at least seasonal presence of groundwater at the surface.

Figure 10.24 shows typical dambos on granites in the upper Nyatsime catchment (NE of Harare), Zimbabwe. The interfluves consist of light textured soils and saprolite and offer opportunity for recharge. The groundwater flows laterally into the valley but is marked by a clear and narrow zone of seepage and small springs, which can be clearly seen on the image. This seepage zone seems to be influenced by various factors. A break of slope in the groundwater surface causes concentration of flow lines just below the break; in the case of the Nyatsime dambo a geophysical survey demonstrated shallow bedrock near the seepage zone (see Figure 10.28, below). It must be noted that this is due to the adjustment of the land cover influenced by subsistence farming to soil and wetness. In adjoining commercial farmland the features are less evident or are absent because of change of lithology from granite to greenstone. The valleys have a flat bottom and are at least partially filled with swelling clays.

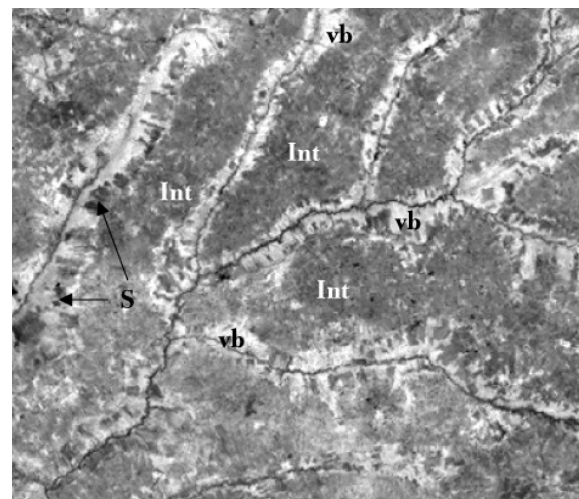
Wolski (1999) measured the base flow in the rivers and tributaries and attempted to correlate them with a number of morphometric factors and seepage area. The best, but weak correlation was a single inverse relation between proportion of valley and groundwater discharge, signifying the role of evapotranspiration from the seepage zones. A linear reservoir model for the interfluvial coupled to a non-linear reservoir model for the valley bottom could accurately simulate the base flow hydrograph of the upper Nyatsime River.

In other cases, a paleo-clay below colluvium or residuum is found (McFarlane 1992) causing a seepage zone, as sketched in Figure 10.27. The image in Figure 10.25 shows that the seepage zone (dark fields) has limited dimension and that most of the valley bottom is dry (white tones). The central drainage line has water, which can be explained by deeper flow through the saprock, and the presence of fractures as suggested by the straight nature of the drainage lines.



**Figure 10-24** Dambos of the upper Nyatsime catchment, Zimbabwe, showing interfluves (Int, fine pattern is land use), narrow seepage zones (S, black tones and flat valley bottoms vb. First Principal Component image of Landsat TM with edge enhancement.

Distance EW is 13.1 km



**Figure 10-25** Dambos in granite country in Kenya SSE of Mt Elgon. Seepage water (S) from interfluves (Int) is used for watering fields, and valley bottoms (vb) are dry except for the rivers, which have water, probably due to deeper groundwater flow through saprock (see Figure 10.25).

Parallel and straight segments of drainage lines suggest adjustment to fractures.

Landsat TM b5. Distance EW is 10.8 km

The seepage zone of the dambos of eastern Uganda (Figure 10.26) can be explained by simple intersection of groundwater surface and topographic surface. This is because the 'base level' of the groundwater is stable as it is tied with large marshes in the west (not shown). The seepage is believed to be outflow of water from the permeable grass and saprock layer. No seepage zones are found in the deeply weathered metavolcanic rocks (*Volc.*), rich in clay, in the southwest of the area shown in the figure.

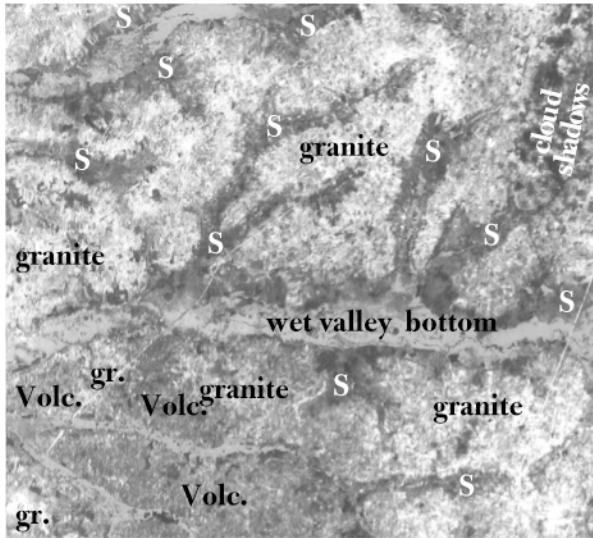


Figure 10-26

Dambos in E Uganda, West Budama, Tororo district in granite (gr) area. Wet seepage zones (S) are found on lower part of slopes. Wet valley bottom have low gradient to large marshes.

No seepage zones are found in the deeply weathered metavolcanic rocks in SW.

B&W rendition of SPOT false colour.

EW distance is 10.2 km

The conditions that explain the limited seepage and deeper flow through the fractured zone of the dambos of Figure 10.25 (western Kenya) are illustrated schematically in Figure 10.27. As mentioned earlier, Figure 10.28 shows the presence of a threshold (arrow) forcing the outflow of groundwater from the Nyatsime dambo. The bedrock configuration was obtained by geophysical survey (Mudzinhwa, 1999). Wolski (1999) made a linear reservoir model of the flow in the interfluvium and connected that to a non-linear reservoir model of the valley bottom to simulate base flow discharges.

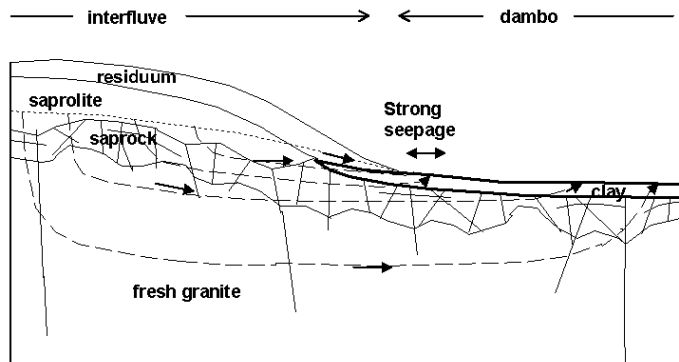


Figure 10-27 Hypothetical sketch illustrating seepage zone over paleo-clay and deeper flow feeding central part of dambo. Configuration and depth of saprolite and saprock can vary. Other configurations are known.

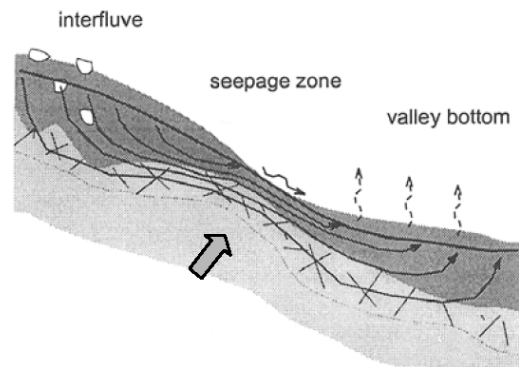


Figure 10-28 Section of Nyatsime Dambo, based on geophysical (EM) survey revealing shallow depth of permeable zone at seepage zone.

Source: Wolski, 1999

## 10.5 The tectonic setting

Some studies make structural analyses to identify the favourable fractures, taking into account the current tectonic stresses (Dutatre et al. 1990; Lachassagne et al., 2001, Bième et al., 1995; and others mentioned below).

Although it is beyond the scope of this text to deal with the structural geology of hard rocks, it may be useful to highlight a few basic aspects of the characteristics of the fracture network, which determines the flow geometry (flow dimension), in order to draw attention to features the hydrogeologist may look for on images of hard rock terrain.

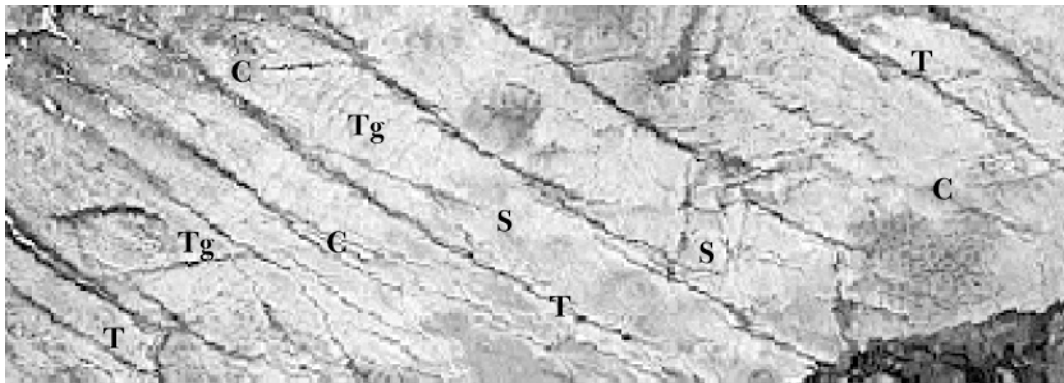
However, it should be noted, that a correlation study between lineament trends and borehole yields in SE Zimbabwe by Greenbaum (1992) did not convincingly demonstrate the existence of any favourable 'open' fracture directions. As he writes: 'Despite the tendency in the fracture related data set for slightly better success rates to occur along approximately west-northwesterly and northerly lineament directions, successful boreholes in fact occur in association with all lineament trends', and: 'Despite the geological evidence that most fractures formed as compressive shears, many now appear to provide open conduits for groundwater'.

Greenbaum explained the modern tensional fracturing by the gravitational unloading, temperature changes and lateral expansion during uplift and erosion. The near surface zone (down to several tens or possibly hundreds of metres) is one where tensile stresses are dominant and that for basement hydrogeology fractures of all types and directions in the upper zone are potentially permeable.

Greenbaum argues that the Zimbabwe craton experienced at least four periods of wrench faulting separated by relaxation and dyke emplacement. The faults and fractures should be regarded as compressive features at least at the time of their inception and may be regarded as closed structures from a groundwater point of view. He considers the hydro-tectonic models, mentioned below, as suspect.

The appreciable increase of hydraulic conductivity in crystalline rocks due to unloading up to hundreds of metre depth, as derived from observations of groundwater discharge in large tunnels, have been described by, for example, Maréchal (1999).

Evidence for opening of fractures by unloading is shown in Figure 10.29. A gently dipping (SE) thick quartzite bed (the Pinnacled Quartzite of the Cuddapah Basin) shows evident fractures and joints.

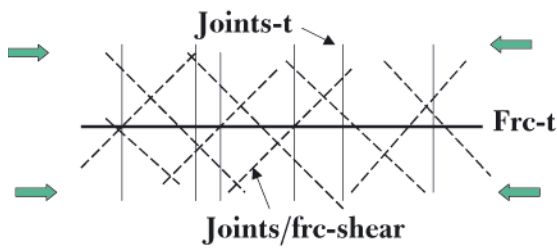


**Figure 10-29** Joint and fracture patterns on gently dipping thick quartzite bed, showing evidence of opening of compressional joints (C) by unloading. T: large tensional fractures, S: shear joints, Tg: joints due to gravitational movement of bedding plane. Pseudo karst development caused creation of fracture relief. Landsat ETM band 7 with edge enhancement. Area south of Kurnool, A.P. India. Distance EW is 10 km.

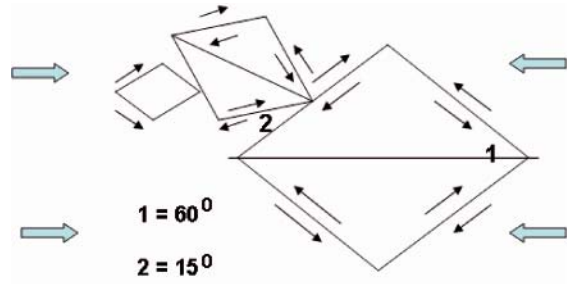
The more or less EW striking fractures (C) are parallel to the axis of an a-symmetric anticline, and are therefore genetically compressional. Widening by weathering (pseudo karst) would not have taken place if they had remained closed. The same is true for shear fractures (S). Large tensional fractures (S) are shown as are tensional joints, probably gravitational tension joints (Tg), due to incipient slippage of the bed, as some have a slightly curved nature.

A simplified sketch of the planimetry of tensional and shear fractures is given in Figure 10.30.

Under normal deformation the main stress causes rocks to fail in a brittle manner along two sets of shear fractures (conjugate shears) with acute angles to the maximum principal stress direction. Depending on the orientation of the stress ellipsoid, normal, reverse or strike-slip (wrench) type of faulting will occur. Figure 10.31 shows a scheme of Ruhland (1973) used by Boeckh (1992) for analysis of lineaments, see below.



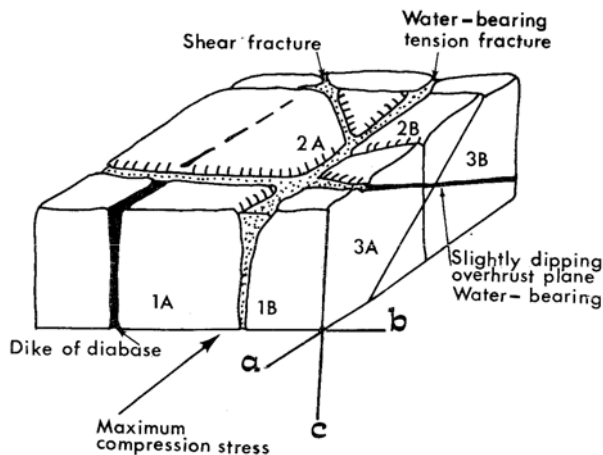
**Figure 10-30** Sketch illustrating tensile joints and fracture (Frc) and shear joints/fractures under influence of uniform stress field (principal stress indicated by block arrows) and isotropic rock conditions



**Figure 10-31** Ruhland's scheme of brittle deformation of a homogeneous rock mass  
Sinistral and dextral movements indicated (not in full). Scheme was used by Boeckh (1992).  
Block arrows indicate principal stress.

Larsson (1972 and in UNESCO, 1984) expanded on the general scheme and presented his model, shown in Figure 10.32. He considers, as a rough approximation, the different types of fractures associated with regional deformation, according to their storativity:

- Tensile joints (orthogonal to the main stress direction) related to plastic deformation. Although the jointing density can be high, the interconnectivity is usually weak and therefore the storage capability is low. Later brittle deformations have 'used' the plane of weakness at stress release and locally fractures can then be developed that have considerable hydraulic conductivity. Since interconnection remains weak, the aquifer is classified as 'poor'.
- Tensile fractures are related to brittle deformation, in the direction of the compressional tectonic force. The strike of basic dykes (lamprophyres, dolerite, etc.) is considered indicative for tensile fracture directions. No storativity is given by Larsson (in UNESCO, 1984), but from the text that follows it appears that it is variable.
- Shear fractures, related to brittle deformation are the result of differential movements of rock masses along a plane. Their planes have an angle (about 25–50°) to the direction of the principal stress. The storage capacity of shear fractures is a complex phenomenon. It seems that most, if not all shear fractures are tightly compressed by residual stress. Secondary mineralization and weathering, influenced by rock type and climate play a role in the storativity. However, in hard rocks gravel fillings have been observed in thrust faults more frequently than in vertical or sub-vertical shears.



**Figure 10-32**

**Model of rock fracturing due to brittle deformation (Larsson 1972)**

Source: Groundwater in Hard Rocks, 1984, Studies and Reports in Hydrology No. 33, UNESCO, Paris

Larsson (1984) described a field application of the model in a hard rock area in Sardinia.

Boeckh (1992) applied the concept of conjugate shears of structural geology to lineaments in Burkina Faso by geometrical analysis of the lineament map. Pairs of lineaments intersecting each other were taken and the direction of the bisector was determined and plotted against the angle of conjugate lineaments. The plot showed evident clusters of dense points and iso-density lines were drawn on the diagram. The centres of the clusters were  $90^\circ$  apart. The dominant direction of the bisector of the angle of intersection fractures is taken as an indication of the axis of maximum stress ( $\sigma_1$ ). The bisector of the dominant obtuse angles perpendicular to  $\sigma_1$  indicates the axis of minimum stress  $\sigma_3$ . Typical angles for conjugate shear formed under ductile and brittle deformation are  $90^\circ$  and  $60^\circ$  respectively (Jaroszewski, 1984). It is believed that the ductile conjugate shears are strike-slip shears formed at depth and have been brought to the surface. Following Ruhland (1973), according to Boeckh, brittle deformation is characterized by spread in the trends of the conjugate shears and offers a scheme to illustrate the spread. A rose diagram accompanying the scheme would show three major peaks, one in the direction of the principal stress and two symmetrically placed at  $30^\circ$  from that direction and two minor peaks at  $15^\circ$ , while remaining directions are present in small quantities. Shear deformation fractures are found within a range of  $135^\circ$  centred around  $\sigma_1$  ( $67.5^\circ$  each half) in the rose diagram, while tensile deformation fractures have a range of  $75^\circ$  ( $37.5^\circ$  in each half, same centre). The histogram, of angles of the bisector of lineaments in the Burkina Faso area showed a double peak, reflecting two sub-populations, with modes at angles at  $90^\circ$  and near  $60^\circ$ , considered as confirmation of the theoretical tectonic concept. By comparing the lineament analysis with geophysical data (EM) it was found that the principal structures located are genetically compatible, while elevated borehole yields were found in lineaments in the direction of the principal stress.

Obviously, the regional structural development is taken into account when studying the effect of fractures/lineaments in a given area. For example, Solomon and Quiel (2006) differentiated four lineament/fracture directions in an area in central Eritrea, shear fractures related to the Red Sea rift and associated transform faults, whereas two other directions represent dilatational fractures with  $\sigma_3$  showing maximum extension along a direction orthogonal to the Red Sea axial trend.

Fractures that are parallel to the direction of maximum horizontal compression should be more open, and conversely, those orthogonal to that direction should be more closed, therefore, the influence of the stress field is determined by the tangential component of  $\sigma_1$ , namely  $\cos \theta_i$ , where  $\theta_i$  is the angle between  $\sigma_1$  and the strike of the fracture.

Pacheco and Alenção (2002) analysed occurrences of springs in crystalline massifs in northern Portugal, using the number of springs and lengths of fractures/lineaments with different categories of orientation as input parameters. They differentiated for the characterization of fractures an extrinsic factor ( $\cos \theta_i$ ), and intrinsic factors:

- (1) shear or tensional fractures. Shear fractures are often accompanied by mylonitization, creating a zone favourable for water circulation.
- (2) deformation regimes that have generated each fracture family (fragile or ductile). Fractures resulting from fragile deformation would be more permeable because of loss of cohesion.
- (3) fracture ages; young fractures have less time to become sealed.

They used various methods for analysis (see below) and made use of the known structural development of the studies area, where three tectonic phases occurred. Particularly noteworthy is the finding that younger tectonic phases opened old fractures and faults rather than imprinting new directions favourable to spring occurrences. Pacheco and Alenção (2002) concluded 'that highest spring frequencies occur where groundwater flow is influenced by a single structural parameter (fracture length, or the angle between fracture strike and present-day stress-field orientation), whereas the lowest spring frequencies are mostly of the multiple-parameter type, that is, result from small groundwater contributions of more than one structural parameter.'

More about the hydrogeological significance of fractures/lineaments is given in the section Analysis, below.

### ***10.5.1 Image interpretation of the structural geology***

Photo-geological interpretation may lead to the deduction of the type of faults. For example, in the area shown in Figure 10.33, a normal fault and high angle faults can be interpreted, see caption. The thrust contact runs more or less along the contour, making an estimate of the angle impossible.

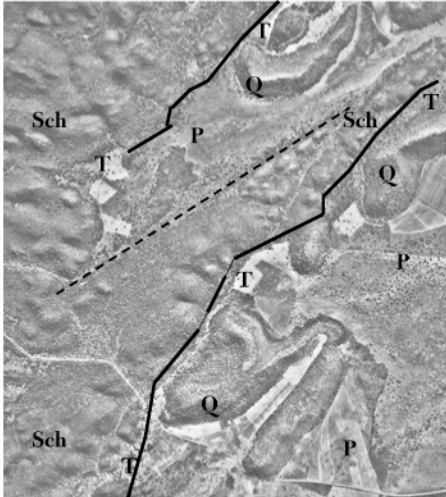


Figure 10-33

**Interpretation of type of faults**

Quartzite beds forming ridges show two folding phases. They abut locally against older schists and phyllites, indicating thrust contact (T). Quartzites are interbedded with slates, on which pediment (P) have been developed.

Normal fault is indicated by dashed line and may be the only place with limited prospects of groundwater.

Absence of drainage lines on pediments underlain by slates refutes the often postulated relationship between drainage density and permeability.

Aerial photograph of area in western Zimbabwe.

Distance EW is 3.6 km

Because of lack of sufficient exposures and indications of pressure directions and relative ages of the fractures it is useful to find places where such an analysis can be made based on image interpretation, to be followed up by fieldwork. Figure 10.34a shows an aerial photograph of such an area, with little overburden.

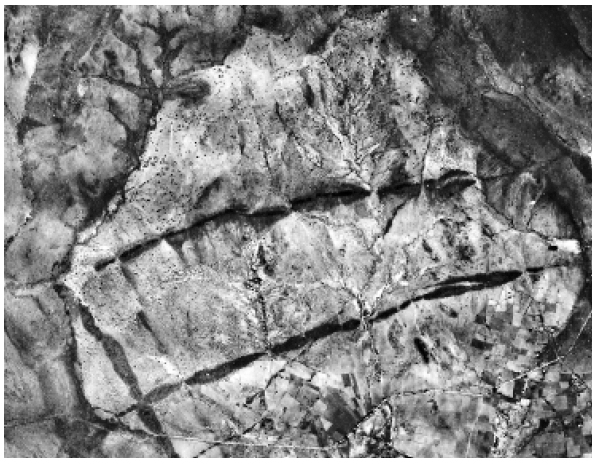


Figure 10-34a High resolution panchromatic image showing window in folded metamorphic rocks (Dharwar) exposing granite with dolerite dykes. Some deformation after dolerite intrusion took place complicating evaluation of fractures. South-west India. Distance E-W is 9.5 km.

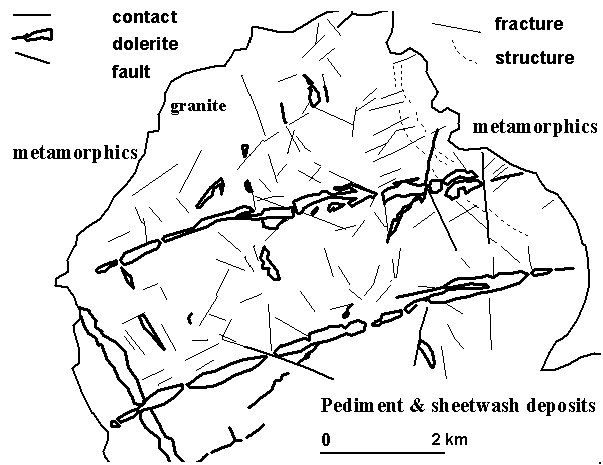


Figure 10-34b Interpretation of fractures and faults and structural elements with associated quartz reefs (field observation). Latest principal stress was ENE-WSW, possibly reactivating tension joints parallel to main dykes and shear fractures making about 40° angles to main dykes, but compressing earlier NS fractures.

A stereomodel was used for the interpretation, initially to trace all lineaments without trying to understand the type so as to avoid bias. The latter is important because if one looks for a certain direction, for example tensional fractures parallel to dolerite dykes following the model of Larsson, one tends to trace more lineaments in the 'desired' direction than an interpreter without having such knowledge would do.

The result of the interpretation is shown in Figure 10.34b and some observations on the tectonic history can be deduced concerning the nature of the fractures. The termination of the dykes at the contact of the granites and the metamorphics (mainly phyllites and metavolcanics) indicates that the dykes intruded prior to the deposition and folding of the metamorphics. The non-intrusive nature of the granite is corroborated by a thin basal conglomerate found at places along the contact (field evidence).

The dolerite intrusions occurred in different phases and it seems that the EW intrusion of the relatively thick dykes is the latest, possibly contemporaneous with the thick NS dyke. The unconformable contact shows that the granite area forms a broad anticline and it was subjected to compression in roughly EW direction, as indicated by

the overall strike of the fold axis and minor thrusts in the metamorphic rocks. It is possible that tensional fractures originating from the time of the EW dolerite intrusion were opened during the folding.

In the northeastern part quartz veins (difficult to observe on the reproduction shown) in the direction of the foliation (indicated in the interpretation map as 'structure') could bear witness that the stress affected the anticlinal granite massif. The more or less EW trending fractures can be considered as tensional. Those originating prior or during the intrusion of the latest dolerites may have been subjected to renewed tension during the later folding phase.

At one place, a small dyke, (Figure 10.35), located in the northeastern part shows evidence of shear (direction of movement indicated by arrows), but it is difficult to interpret the relative age of the shear movement.

It is interesting that thin dolerite dykes in an approximately NS direction are discontinuous and seem to be compressed, and there is some evidence of minor thrust faulting (on the stereoscopic model using the original air photos).

There is much more to say about this area, but three aspects are mentioned:

- By interpretation and use of simple stratigraphic principles and tectonic concepts hypotheses can be formulated which direct the fieldwork. One knows in advance where to look for what type of features to substantiate or change hypotheses.
- The geological history of this Precambrian area is very complex, as is true for nearly all such areas and the test of correctness of interpreted presence of, for example, tensional open fractures is the study of well yields and the results of pumping tests. It may well be that many of the old compressional and shear fractures have been opened to become tensional fractures due to unloading, as described by Greenbaum (1992).
- Interpreted fractures, their density, connectivity and lengths depend much on the local terrain conditions, such as presence of sheetwash deposits, weathered overburden and so on, which implies that analysis is representative to a limited area only.

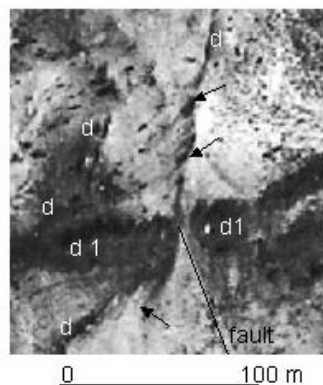


Figure 10-35

Shear fractures (arrows) causing small offsets of thin dolerite dyke. Main dolerite dyke indicated by (d1) and minor dykes by (d).

Sinistral movement along approximately NS dyke is likely.

Enlarged NE part of Figure 10.34.

A third example shows thick and massive, fine grained sandstones of western Lesotho, which have low permeability but conduits can occur along a narrow zone of contact metamorphism of mafic dykes and sandstones, where quartzite was formed. Drilling closely spaced boreholes across the sandstone-contact zone-dyke section and doing well tests (pers. comm.) confirmed this, as well as accurate measurement of the base flow in small valleys traversed by a large dyke, up and downstream of the dyke. A similar condition in S. Africa is described by Sani (1996).

Figure 10.36 shows (by black arrows) quartzite ridges on both sides of the mafic dyke (D-D). Several straight valleys must have been formed along fractures (white arrows), which are generally not parallel to the large dyke or other smaller mafic dykes (d), traversing the sandstones. It is likely that the 'drainage fractures' are open (tensional) to allow spring sapping to do its work in valley formation.

However, dense joint systems in the northern part (and in the western part) show orthogonal joints, with one direction parallel to the dyke D-D, suggesting these are tensional joints, following Larsson's model. It thus seems that tensional fractures and joint occur in many directions, and a field inspection (although cursory) indicate that these are open. It is tempting to explain so many directions as the result of broad up-doming allowing the basic rocks to intrude, although the dykes may not be of the same age. The sandstones are overlain in nearby areas by thick flood basalts, which may have been eroded in the area shown. This and uplift prior to the dissection can explain the open nature of the fractures by unloading.

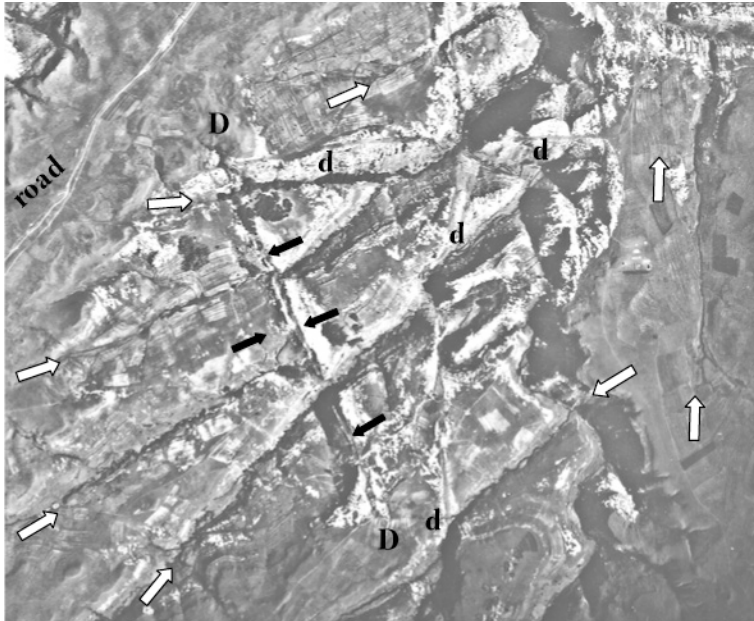


Figure 10-36

Lesotho, about 25 km W. of Maseru, aerial photograph.

Dyke of basic rock (D-D) with contact metamorphism of fine-grained sandstones adjacent to dyke into quartzite.

Resistant quartzite formed a ridge, indicated by black arrows.

Other minor dykes are indicated by (d) and large fractures along which drainage was developed indicated by white arrows.

Distance E-W about 2.75 km

The area of Figure 10.36 is well exposed because of erosion and incision, but the populated areas (where water supplies are needed) is in the lower undulating plain. Some of the mafic dykes can also be observed in the plain area by the negative or positive relief and by the soil differences and their immediate fringes have groundwater prospects.

### 10.5.2 Limitations of structural image interpretation

The differentiation of fractures types in hard rock terrain is usually difficult because most crystalline basements are old and have a complex tectonic history. Often, many mafic dykes with different directions and age are observed. There is often no stratigraphic evidence to decide whether a lineament could be a fault or a fracture. By field studies the nature of joints and fractures can be established by noting whether they are open or closed, directions of shear, mylonitization, schistosity and foliation directions. Certain directions of fractures may have been subjected to mineralization and others not. Dense parallel joints and fractures can indicate a fracture zone, and so on. Obviously, field data should lead to re-interpretation or editing of the lineaments.

Sheet joints are the (sub)-horizontal joints that are generally believed to be caused by unloading, although in some cases thermal cooling may have played a role. They are of importance for overall permeability because they occur in the upper zone connecting vertical or inclined fractures and provide flow paths from the saturated weathered zone to the fractured zone, but they cannot be observed on images.

Another limitation of lineament studies is that the dip of fractures or faults possibly associated with lineaments can seldom be determined. This is regrettable because a drill hole on the wrong side of an inclined fracture is likely to be dry or have a poor yield. Larsson's model includes inclined shear fractures or thrusts, the tectonic evaluation by Boeckh assumed that fractures are vertical.

In a few cases, there could be evidence for the inclination using ordinary geological mapping techniques. In cases where a straight lineament crosses considerable relief, the lineament is vertical. If not, by following the strike and the topography, an idea on the inclination can be obtained.

Hazell et al. (1992) describe geophysical techniques that may in certain situations allow the estimation of the dip of fractures and veins in hard rock terrain.



### 10.5.3 Use of geophysical survey

The tracing of lineaments and structural analysis is only the first step in the procedure for well-siting in crystalline basement and the result can be an indication of the most promising sites. Because of uncertainty of the nature of the lineament and error in exact location, few hydrogeologists would not advocate the use of geophysical sounding and profiling for an evaluation of the potential fracture/lineament to determine a more precise location for drilling.

It is beyond the scope of this text to discuss the merits of the various geophysical techniques that have been used in well-siting in hard rock regions. The reader is referred to Hazell et al. (1992), Barker et al. (1992), Carruthers and Smith (1992) and Sporry (2004). In Chapter 11, the use of geophysics for groundwater modelling is discussed.

## 10.6 Recharge aspects

Each region has its overall recharge condition influenced by the climate, and should be estimated by the methods for soil moisture budgets, using rainfall, potential evapotranspiration and effective depth (e.g. rooting depth) as parameters.

Although recharge conditions are acknowledged by several authors to be of importance in explaining well yields in hard rock terrain, few studies have been published on the interpretation of local recharge conditions.

What has to be judged for prospective sites, in addition to proximity of lineaments and their intersections, in a hard rock area are:

- The potential recharge area, using the local detailed topography (stereo air photos)
- Run-on conditions; runoff from higher parts (possibly outcrops) to zones near the site where at least part of the water can infiltrate. Obstructions in the form of low field bunds (dams) just upslope of the site that will facilitate induced infiltration.
- Presence of weathered zones and hydraulic gradient. The infiltration capacity and permeability are difficult to judge by image interpretation. With local field knowledge of the catenary properties and study of existing wells and their surrounding, indications may be obtained of how suitable conditions can be interpreted.
- Lateral fracture flow from higher ground.

Relatively elevated areas, rich in outcrops within a hard rock region can be considered to have doubtful prospects because of poor recharge. In such parts runoff is usually fast especially when the drainage density is high and thickness of the weathered zone is limited. Conversely, sites at lower elevation, receiving sheetwash from a relatively large (micro) catchment area and possibly flow through the saprock and fracture flow from higher parts may be judged to have better prospects.

Basement terrain may be classified on geologic maps as ‘undifferentiated basement complex’, but differentiation may be made using the details of geomorphology and this can be of hydrogeological significance, as the next example shows.

The potential recharge area, or the topographic drainage area upslope of a well, was compared with the area irrigated by each well (see Figure 10.37, upper right) within a few geomorphological units (or terrain mapping units) in a granite area in semi-arid central India. The measurements were done on stereo air photos dating from pre-1965, when there were only hand-dug open wide-diameter wells up to the upper part of the saprock and these were operated by animal traction. The size of the plots irrigated by groundwater was assumed a proxy for the well yield.

Two of such units, which are delineated on the basis of patterns, are shown in the Figure 10.37 (Landsat TM b5, upper left) at a time when electrically powered borehole-wells were introduced, irrigating locally larger plots. The graph (lower right) shows that the recharge area is correlated with the irrigated area in each of the units (also for units not shown here) and that the two sample areas have different hydrogeological properties, with unit S1 having more permeability and storage of groundwater than unit S2.

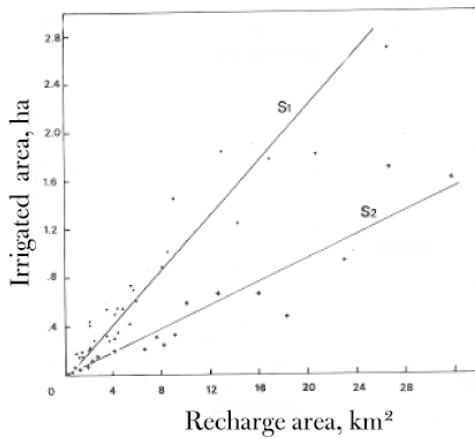
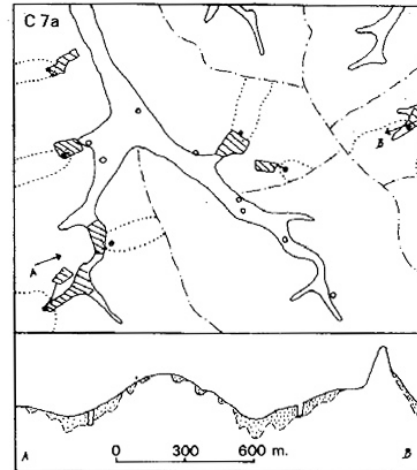
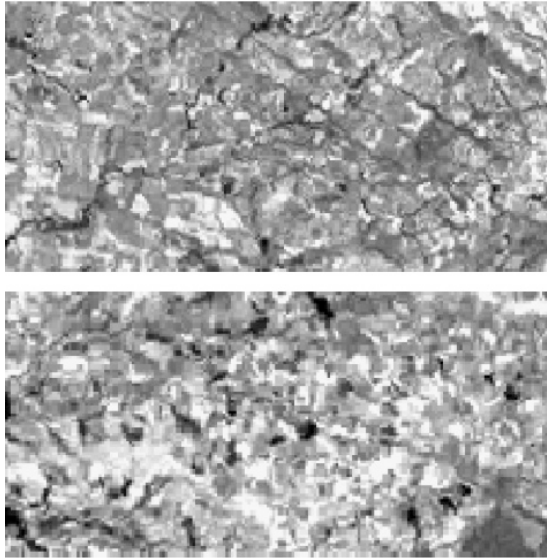


Figure 10-37

Upper left: Two different granite terrain units. Small dark fields are irrigated by groundwater (Landsat TM b5)

Upper right: Sketch showing recharge area per well and irrigated field (height exaggerated).

Lower left: Irrigated area per well as a function of recharge area measured on air photos, for two granite areas (S1, S2) near Kurnool (A.P., India) indicating different hydrogeological properties

The local relative recharge can be estimated by considering the local geomorphology and runoff, as is shown in Figure 10.38. The cluster of wells used for irrigation on the lower weathered pediment is surrounded by outcrops and pediments, which have high runoff because of the absence or shallow soils. Sheetwash reaches the lower area and infiltrates partly. Leakage from a small reservoir (tank) adds to the recharge. Despite such favourable recharge conditions, the total irrigated acreage casts doubt on the sustainability.

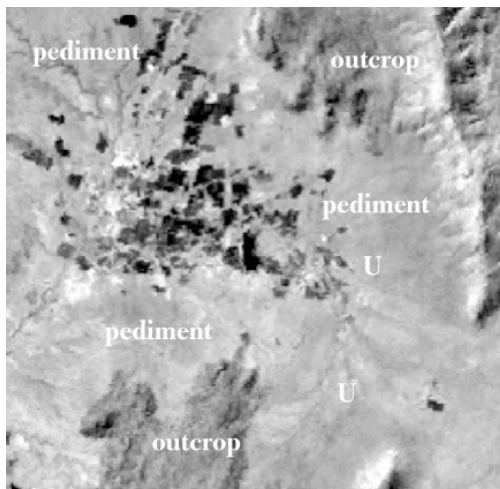


Figure 10-38

Irrigated fields (dark tones) on weathered pediment having good recharge by sheetwash and locally concentrated sheetwash from surrounding pediments and outcrops, southeast India. Landsat TM b4.

Along line U-U traces of the bedrock (contact between the two different rocks) can be seen, indicating no or little overburden at those places.

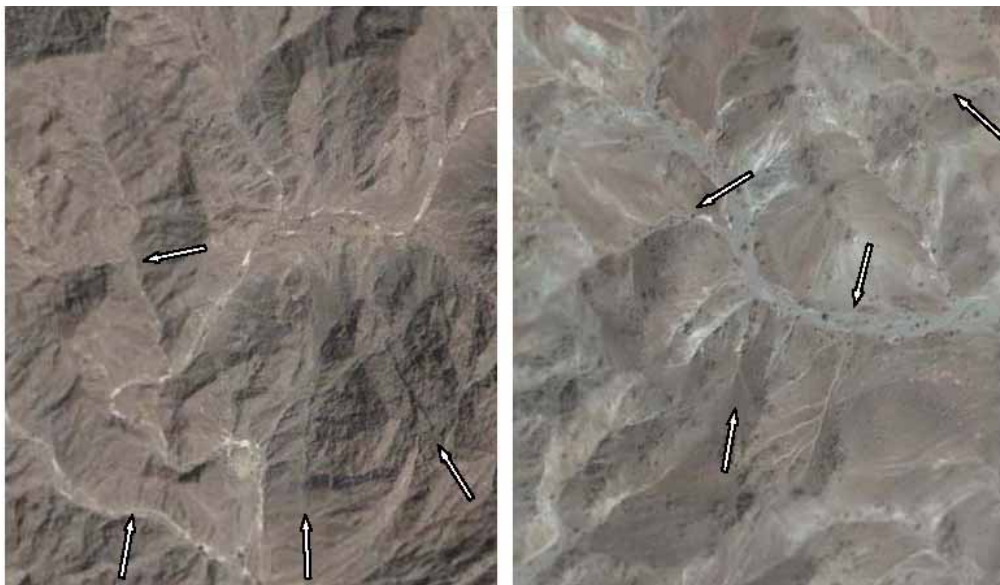
Distance E-W is 5 km.

## 10.7 Example of ophiolite terrain

When the surface features of crustal gabbro terrain and those of mantle peridotite terrain of Oman are compared on high-resolution satellite images (or airphotos), a large difference in superficial cover or overburden can be noted, see Figure 10.39. Outcrops of gabbro (right-hand image) are chiefly found at and near drainage divides. Weathered rocks and colluvium cover slopes. Due to the mineral composition of gabbro, the weathered zone is rich in clay and more trees are found than on the peridotite. These images have been selected, because a comprehensive hydrogeological study made in the area enables description of the hydrogeological significance.

Dewandel et al. (2005) attribute the difference partly to the fissuring and fracturing that took place at the mid-oceanic ridge, hence at the time of rock formation, but also at a later stage due to lithostatic decompression. However, tectonic fracturing is also present and some larger fractures are indicated on the images of Figure 10.39. The upper zone of both rock types can be considered as shallow aquifers, while the fissure permeability of the peridotite is about  $10^{-7} \text{ m s}^{-1}$  and that of the gabbro is higher, but lower than the tectonic fracture permeability, which is estimated to be  $10^{-5} \text{ m.s}^{-1}$ . Authors specify that fissures are in the range of cm-dm, while fractures have dimensions of up to kilometres. Recharge on both types of terrain appears to be similar, on the gabbro 8% of annual rainfall (chloride method) and  $7\% \pm 3\%$  of the annual rainfall (250 mm) by water balance method using runoff data from small catchments.

Authors remark that production wells, preferably in gabbro, should be sited near fractures but not within a fracture because of clay weathering.



**Figure 10-39** Ophiolite terrain in Oman; left: peridotite; right, on same scale and few km south of left image: gabbro. Note the difference in weathered mantle and presence of phreatophyte trees (dark dots). For hydrogeological significance, see text. Some large fractures indicated by arrows (more can be seen). Distance E-W, about 1 km. Source: Google Earth.

## 10.8 Preliminary well siting, two examples

A common task is finding a good site for well construction close to a specified locality. In hard rock terrain activities should start with interpretation of images by noting aspects such as: presence of lineaments, weathered zone and local topography in relation to potential recharge, accessibility and distance from the locality and possibly contamination risk.

### 10.8.1 Example from Cote d'Ivoire

For the following example, no results of local studies based on existing well data and structural analysis were available; a common situation.

Figure 10.40 shows a Landsat TM image of a granite area in northern Cote d'Ivoire with a target village.

Various types of products obtained by image processing techniques were analysed, such as colour composites of various bands, ratios, NDVI transform, Principal Component images, filtering and spectral classification. Two false colour composites of original bands after edge enhancement were considered the most suitable for the general interpretation, but for illustration in black and white, the Principal Components I and II images are the most suitable.

The PC I image shows the drainage lines with dense riparian vegetation, outcrops (better visible on false colour images), and the land cover on the broad interfluves, which consist of agricultural fields, cultivated or fallow, range land vegetation with remnants of burning. Unpaved roads/tracks can be seen, which is helpful in location and judging accessibility.

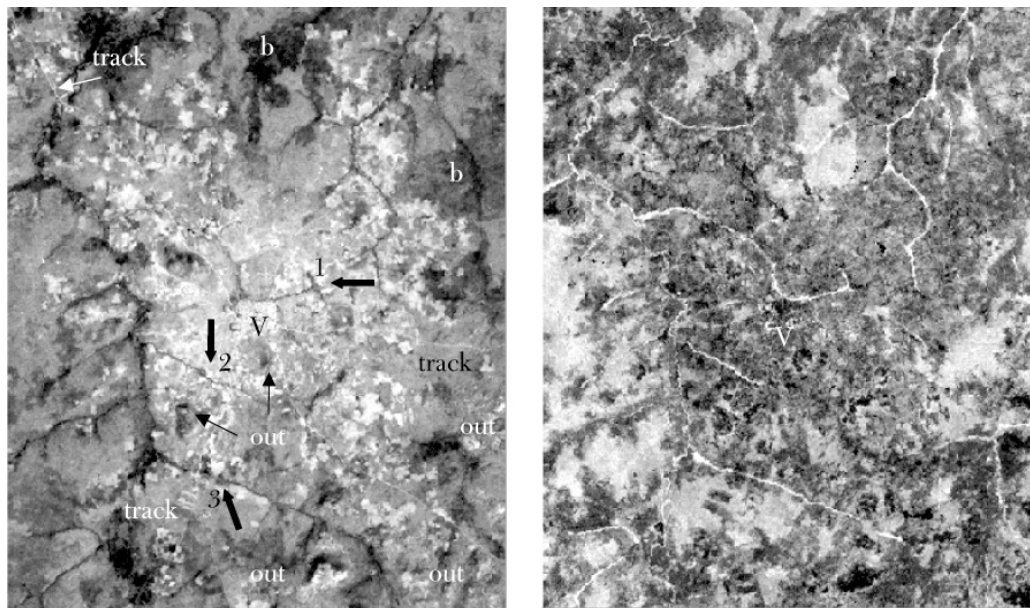


Figure 10-40

Example preliminary well siting in granite area, north Ivory Coast.

Left: PC I image with edge enhancement. V = village Out = high outcrop; b is burned area; black arrows indicate sites 1, 2 and 3.

Right image: PC II (nearly identical with NDVI), white tones indicate green vegetation.

Distance E-W is 13 km. Landsat ETM+ image

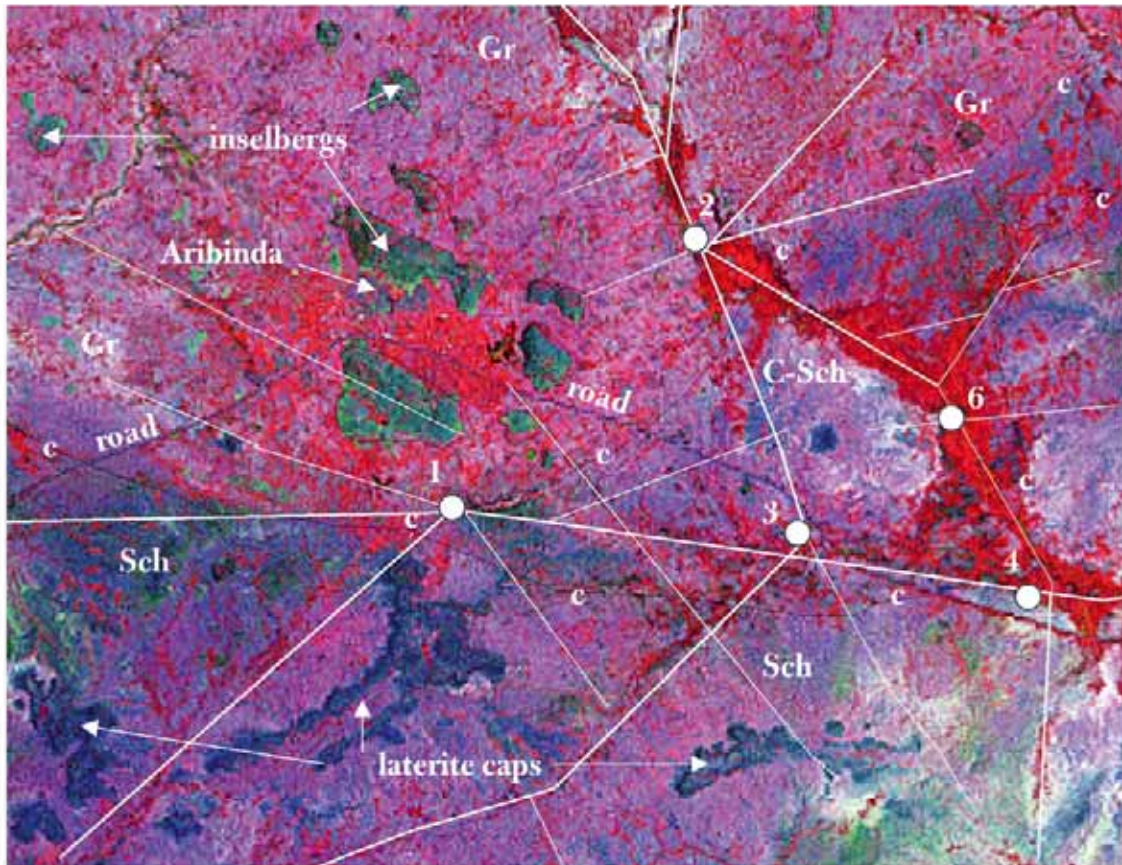
The PC II image is nearly identical to the NDVI image in this example, which is explained by a high positive factor loading of the NIR band and a negative one of the Red band for the PC II. The comparison of the drainage lines on the PC I and II image reveals where lush green vegetation is present in straight courses, indicating likely presence of groundwater in the fractures.

In the vicinity of the village, site no. 1 is preferred to site 2 because a T-junction of fractures with green vegetation is seen. The long fracture at site 3, although further away from the village may support sustained yield during drought.

### 10.8.2 Example from Burkina Faso

Geophysical survey and drilling in the close vicinity of Aribinda township in north Burkina Faso did not meet with success, and therefore the search was expanded whereby lineaments were interpreted on aerial photos and a Landsat MSS image by Armand et al. (1983). By considering overall recharge conditions and regional hydrogeological experience, the interpretation resulted in five locations for exploratory drilling after geo-electrical survey of the sites. Authors found only partial coincidence of photo and satellite image lineaments (as is often the case). The major lineaments of the map in Armand et al. (1983) have been transferred onto the Landsat ETM image of Figure 10.41.

It may be noted that some of the lineaments of their map could not or only with difficulty be recognized on the ETM images, transformed images and colour composites. The five locations are indicated in the figure. Drilling the sites, after geoelectrical survey, proved that only sites number 4 and 1 were successful. Well no. 4 stuck water at depths of 54 m and at 65 to 79 m, and the well had a yield of  $8.5 \text{ m}^3\text{hr}^{-1}$ . The success was attributed to the properties of the schist and the location on a major lineament, with good recharge conditions. Water was stuck in well no. 1 at a depth of 45 to 55 m. and the yield was  $4 \text{ m}^3\text{hr}^{-1}$ , explained by the location on the junction of two major lineaments and closeness to the contact with the granite.



**Figure 10-41** False colour image Landsat ETM+ (bands 4,1 and 5) with edge enhancements of the area around Aribinda township, Burkina Faso. Sch = schist, GR = granite, C-Sch = Calc-chloride schist, thin black line & c = geological contact. Thick white lines; lineaments interpreted on Landsat MSS, thin white lines; lineaments interpreted on aerial photographs. Interpretations by Armand et al. 1983, transferred onto TM image. Well nos 4 and 1 were successful, others were dry.

Distance E-W is 10.7 km.

The other sites were dry, despite presence of lineaments and recharge in the shallow valley system.

### *Some practical aspects of image interpretation for well siting*

The above examples illustrate that the result of image interpretation is the basis for planning of activities, in the form of follow-up work by geophysical surveys at promising places, and exploratory drilling. The images can be used for obtaining or updating other information of relevance for siting of wells, such as:

- Location of settlements and their size
- Accessibility to reach selected sites (preferably using stereo aerial photographs)
- Possible sources of pollution (mine dumps, factories)
- Flooding. As many wells will be situated in the valley bottom, their position should be well above flood limits. These limits may be interpretable on large scale (< 1:30.000) aerial photographs under stereoscopic enlargement,

- Water logging. Many hard rock regions have a strong seasonal rainfall. The groundwater table in the valleys often reaches the surface because of lateral seepage from the slopes and this causes temporary water logging. Land cover (e.g. rice fields), gradient, sinuosity of rivers-drainage lines and other features may give evidence, under stereoscopic enlargement, of seasonal water logging. More permanent water logging or salinization can usually be observed also on satellite images, particularly when local relations with vegetation types and water logging are known.

## 10.9 Analysis

Hydrogeological image interpretation in crystalline terrain is no aim in itself, but serves the purpose of locating sites or to assist in the preparation of a hydrogeological map. The hydrogeological relevance of the interpretation results has to be established by analysis and several aspects are discussed below. Particular attention is given to lineaments. GIS is a most useful tool in the analysis because plotting of wells from coordinates, measurement of distances, directions, differentiation of lineament with and without vegetation, aggregation with lithological units and so on, can be done.

What is apparent from the literature is that no universal guidelines can be given as to role of lineaments for increasing the chance of successful wells. What is valid in a given area may not be true in another area. Therefore, mapping of lineaments from images has to be followed by analysis using local field data.

### 10.9.1 *Updating geological maps, well yields and lithology*

Images can be used for updating (hydro-) geological maps, particularly if no aerial photos were used for the geological survey or when geological maps are available at small scales only.

Specific information, such as provided by gamma ray images or airborne geophysics often form important sources for updating geological maps.

In general, the updating of geological maps by image interpretation consists of adjusting boundaries of lithologic units as shown on the map and by addition of some structural information, particularly evident fractures or fault extensions. It may be remarked that images are useful for updating in particular in semi-arid regions. As mentioned in the chapter on Image Processing, ratios of bands and de-correlation for colour composites, could give useful images. In the more humid areas due to weathering and vegetation the attempt may be less successful, no matter what image processing techniques are used. It all depends on the adjustment of the details of the geomorphology and the land cover to lithology.

In crystalline basement, well yields depend on the nature of the regolith and fracturing; neither of the two is generally shown on geological maps. However, because of interrelations between rock type, susceptibility to fracturing and effect of mineral composition on weathering, some association between yields of wells and rock type may exist. Therefore, comparing statistics of well yields per major lithological unit is useful, but a wide range of yields per unit can be expected. For example, dolerite dykes are often considered as impermeable units, forming a barrier to groundwater flow, but Singhal and Gupta (1999) describe long fractured dykes supporting wells with reasonable yields.

Relationships between lithology and yields, if existing, are usually restricted to a given area. Because of the wide range, due to presence of fractures of different nature and orientation, and variations in weathering, a large number of yields have to be known to test for significant differences.

For example, Solomon and Quiel (2006) found for an area in Erytrea, that non-foliated metamorphic rocks had lower yields than foliated metamorphic rocks, and the latter equalled those of granites (about  $1.8 \text{ m}^3\text{hr}^{-1}$ ), while basalts and alluvium had 3 and  $0.9 \text{ m}^3\text{hr}^{-1}$  respectively. Several other studies have listed yields per rock type and an overview is given in UNESCO (1984).

Some information concerning the regolith can be made by image interpretation and delineation of hydro-geomorphological units, such as: areas rich in outcrops and their relative elevation; remnants of weathered planation surfaces; presence of ferricretes or laterite plateaux; zonations that may be observed in weathered areas and so on. Plotting of yields of wells penetrating only the weathered zone on the interpretation map may give an indication of what may be expected.

### 10.9.2 *Lineament maps and descriptive statistics*

It is customary to present rose diagrams or stereographic projection plots of lineaments or fractures. Generally, there are differences between the contents of a rose diagram based on lineaments interpreted on satellite images and those interpreted on airphotos (e.g. Greenbaum, 1992; Biéme, 1995). Airphotos have high resolution, are panchromatic and stereopairs visualize topographic details, so that the interpreter uses (inadvertently) different criteria for the tracing of lineaments than is the case with the lower resolution multi-spectral satellite images, such as Landsat, SPOT or IRS images.

Lineament directions can vary appreciably within distances of several km. For example, in a granite area in western Spain, rose diagrams showed association of directions with type of granite, but on a same granite type, lineament directions were different in the northern and southern part of the area examined. It was also noted that the diagram of the lineaments using aerial photos included a strong direction, coinciding with the regional foliation, which was less prominent on the diagrams based on satellite images and field measurement (Attanayake 1999).

While all such observations are made, the question is, how do they relate to the productivity of wells situated on or near lineaments? The answer to that question is solved empirically, in other words, by analysing well yields in relation to prominence and tectonic nature of lineaments, distance from lineaments, lineament direction, density, lengths and interconnectivity.

Several authors (e.g. Greenbaum, 1992; Chilton and Foster, 1995; Sander et al., 1996) mention that the analysis may be cumbersome because well-testing methods and well development are not uniform, and sources may not enable standardization, in addition to positional error of well sites and lineaments, as discussed below.

When the number of wells are plotted against the distance from lineaments, often the graph shows a peak at a distance of about 100 to 300 m and the curve declines for larger distances (e.g. Savane et al., 1995). It is not clear whether this can be explained solely by preference for a well location not too close to a river (flooding, dense vegetation, etc.) or whether other factors play a role.

### 10.9.3 *Prominence and type of lineaments and well yields*

Wells located on or near long and prominent lineaments could be highly productive (see the Review by Waters et al. 1990), but not necessarily so in the case of mineral (or clay) filling and erosion (Greenbaum, 1987).

Neogene rifting and faulting in Eritrea on the western flank of the Red Sea produced a variety of shear zones and normal faults and fractures roughly orthogonal to the former. These fractures are dilatational and although at places filled with clastic sediments and highly altered basaltic and felsic dykes, they have considerable potential for groundwater production, particularly since they are long and their trend takes them from areas of high elevation with regionally the highest precipitation to lowland semi-arid areas (Drury et al., 2001).

Sander et al. (1996) placed for prospective sites more weight on prominent lineaments interpreted from Landsat TM images in an area west of Lake Volta, Ghana, than the less prominent lineaments from air photos. These gave the highest weight of 2.5 for sites close to Landsat TM lineaments and the lowest weight of 1 to the least air photo lineament on a subjective scale.

Buckley and Zeil (1984) noted in Botswana that most of the prominent features were shear zones, but the main groundwater circulation was through less obvious tensional fractures. The larger tensional fractures could achieve yields of up to  $20 \text{ m}^3\text{h}^{-1}$ , but only  $35 \text{ m}^3\text{h}^{-1}$  from the smaller fractures.

Lineaments were differentiated into potential shear and tensional fractures by Boeckh (1992) and the intersection of the two were selected for geophysical survey and drilling in an area in Burkina Faso.

#### *Well yield versus distance from lineaments and intersections*

Plotting of well yields against distance from lineament will throw light on the significance of lineaments in terms of groundwater productivity. However, this is easier said than done in a meaningful manner for a number of reasons. Firstly, the data set of boreholes has to be fairly large and the well performance tests have to be comparable. In many cases only air lift tests are available, in fewer cases specific capacities are known, and in still fewer cases can transmissivity be determined for the entire data set. As is well known, air-lift tests tend to overestimate well performance.

A second source of uncertainty pertains to accuracy of location. The coordinates of most wells in crystalline areas were determined before the days of GPS by interpolation on map coordinates and if GPS was used in more recent surveys, the settings could have been faulty. Furthermore pixel size and accuracy of georeference plays a role. As illustrated by Sander (1997), in some fracture zones, wells placed precisely on a fracture fill may have low yield, but wells placed a little distance away can have high yields. .

Thirdly, it may be difficult to judge the hydrogeological setting related to well performance, such as saturated regolith thickness versus fracture zone; inclined fractures versus vertical ones; association of lineament and type of fracture (tensional, width of fractured zone, etc.). Furthermore recharge conditions influence well yields.

Using LANDSAT MSS images (60 x 80 m resolution) Schowengerdt et al. (1981) found a correlation between specific capacity and lineament density of verified fractures and faults. However, the total lineament length in an area with 2.4 km radius around each well was negatively correlated with specific capacity ( $n = 42$ ,  $r = 0.14$ ), and a negative correlation coefficient was obtained for transmissivity ( $n = 14$ ,  $r = 0.67$ ).

Most hydrogeologists believe that the chance of success is greater close to lineaments (e.g. Waters et al., 1990; Gustafsson, 1994; Galanos and Rokos, 2006; Solomon and Quiel, 2006; Sander 2007). However, there are studies that caution against generalization of this rule of thumb.

Magowe and Carr (1999) found in western Botswana no statistically significant correlation between median well yield and distance to lineament, but the correlation with distance to lineament intersections was significant at the 95% level.

Greenbaum (1992) noted that 90% of almost 300 boreholes in SE Zimbabwe were located within 150 m from lineaments. However, attempts to correlate the yield with recorded distance to the lineament were inconclusive, possibly due to inaccuracy of location of bore hole and/or pump test data, according to the author.

Density contouring was done for two directions of lineaments believed to be associated with the youngest open fractures in a granite-gneiss catchment in southern India and the result was compared with well yields by Srinivasan Rao et al. (2000). They found the highest yield ( $> 12 \text{ m}^3\text{h}^{-1}$ ) and lowest water table fluctuation at intersections in high-density areas in moderately weathered pediplain, while yields decreased ( $2\text{--}10.8 \text{ m}^3\text{h}^{-1}$ ) in areas with lower density in pediplains and valley fills. In the pediments and low residual outcrop-hillocks (Tors) having no lineaments the yields were  $< 2 \text{ m}^3\text{h}^{-1}$  and water tables fluctuated by over 16 m.

#### 10.9.4 Lineament azimuth and well yields

Tectonic models (e.g. Larsson, Boeckh, op.cit.) postulate that lineaments in the tensional direction and those in the direction of the shear fractures may have different hydraulic properties. It is therefore worthwhile to analyse wells yields against the azimuths of lineaments.

Each area has its own tectonic and geomorphological history and type of crystalline rocks and therefore results of the analysis differ, as the following studies demonstrate.

The tectonic setting of lineaments and the hydrogeology of a large catchment in northern Cote d'Ivoire on crystalline rocks was investigated by Biémi et al. (1995). The lineament direction (NW-SE) gave the most productive wells ( $6\text{--}14 \text{ m}^3\text{h}^{-1}$ ) and along that direction seismic activities had been reported, while the N-S direction – a known regional tectonic direction – came second in productivity, as shown in Table 10.1. It is noteworthy that

<i>% of wells</i> <i>6–14 m<sup>3</sup> h<sup>-1</sup></i>	<i>Lineament</i> <i>direction</i>	<i>% of wells</i> <i>3–6 m<sup>3</sup> h<sup>-1</sup></i>
63	NW – SE	21
25	N – S	21
12	E – W	14
0	NE – SW	43

Table 10.1 Yield and lineament direction, catchment in northern Côte d'Ivoire. Source: Biémi et al. (1995).



the authors remark that few wells had been found near lineaments with a N-S direction because of the difficulty of observing the direction on air photos.

The contrast for the percentages of high and low yielding wells (0 and 43%) for the NE-SW direction is not explained in the text, although a borehole with a yield above  $3 \text{ m}^3\text{h}^{-1}$  can be considered as successful for a hand-pump. The use of hand-pumps usually avoids over-pumping and depletion of the aquifer.

In SE Zimbabwe only limited correlation existed between successful boreholes and the main lineament directions. Using a lower cut-off of  $0.9 \text{ m}^3\text{h}^{-1}$  for the yield of the well, there was minor improvement in the success rate and four azimuth directions (Greenbaum, 1992).

For a sub-area in the Voltaian Sedimentary Basin, west of Lake Volta, where groundwater is dominated by secondary porosity, Sander et al. (1996) found that wells situated close to major lineaments interpreted from Landsat TM were all successful ( $> 0.6 \text{ m}^3\text{h}^{-1}$ ), but in another sub-area that association was not clear.

### 10.9.5 Analysis approaches

Probabilistic approaches to analyse the occurrence of well yields in an area in N. Sri Lanka have been used by Hansmann et al. (1992). First, the influence of individual factors, such as distances to valleys, lineaments, drainage divides, on high well yields is analysed. Other factors, such as rock types, intersections of lineaments and lineament densities, were not thought to be relevant in the particular area of study. Results were used to determine weights for the a priori probability in the so-called 'weights of evidence modelling' (Bonham-Carter et al. 1988), based on Bayes' rule. The result is a map showing spatial units with the a posteriori probability of high yielding wells.

Bayesian statistics were used by Sander (1997), who assigned prior probability values for groundwater occurrences based on expert opinion. The highest expert ratings were given to lineaments derived by interpretation of satellite images and of aerial photographs. Perennial and ephemeral streams had the lowest ratings, while topographic lineaments and dry season vegetation took an intermediate position.

A series of a-posteriori maps were produced showing the effect of factors and weights used, which included in one area also lithology.

The randomness of lineaments in local areas around springs with high discharges was tested by using the formula for relative entropy by Galanos and Rokos (2006). They found that high spring discharges were associated with low entropy values. Spring discharges and borehole yields were used in a statistical analysis of the effect of lineaments in the crystalline rocks (including marble) of the Greek island of Naxos. Springs with high discharges had a greater probability of occurrence where lineaments fall into only a few of the 18 classes or lineament orientation that were differentiated and that high discharge springs are related to the  $50\text{--}80^\circ$  orientation in that area. Furthermore, successful boreholes occurred close to lineaments with the mentioned orientation.

Analysis of the hydrogeological significance of fractures/lineaments is complicated by the fact that numerical variables (yields, number of springs, etc) have to be combined with categories (rock type, orientation classes) or to tectonic phases. Pacheco and Alencão (2002) compiled first the fracture-fault lengths and orientations (from aerial photographs and geological maps) and springs (topographic maps, field work) and derived spring density ( $\text{no. km}^{-2}$ ) and number of springs  $\text{km}^{-1}$  in each lithologic hard rock unit in the area studied and per orientation class (18 in total). After that, cross tabulation was done to combine the numerical variables with the categories and the conditional probabilities of the combinations were calculated, and plotted as line plots against orientation classes. Such plots are considered as spectra. The spectra for total number of springs, directions and intrinsic density, which depends on number of springs  $\text{km}^{-1}$  in a fracture family of given strike, and angle  $\theta$  (the angle between  $\sigma_1$  and the strike of the fracture), were normalized and then decomposed. The decomposition was done to allow separation into individual spectra (line-plots), one related exclusively to fracture lengths and one to present day stress field orientation. A graphical method 'peak matching' was used with the decomposed spectra to link observed spring frequencies to their most influential structural parameters. The result of the analysis enabled conclusions on the relations between springs, fracture orientation, structure and tectonic phases.

Lachassagne et al. (2001) used multicriteria (discriminant) analysis of collected data, including lineament mapping, concerning the structure and functioning of a hard rock aquifer in a catchment in France, and produced a hierarchical map of groundwater resource potential in order to identify areas for field prospecting aimed at siting high yield wells or well fields.

## 10.10 Hydrogeological mapping and use of GIS procedures

The few studies mentioned in the previous section all make use of GIS functionalities to implement specific approaches. GIS functionalities are briefly mentioned in Chapter 3.

For crystalline basement terrain two overlapping approaches (A and B) are possible:

### *Approach (A)*

A hydrogeological *base map* is prepared using image interpretation. The main contents, apart from topography and drainage systems, are as follows.

Interpreted hydrogeomorphological terrain units, which are generally complex and thus contain associations, as discussed above. Transfer of the map into a GIS implies that the attributes of each unit are contained in a database. In other words, complex entities (i.e. units), based on image interpretation with hydrogeological knowledge attached are entered into the GIS. This differs from the approach where complex units are created purely from single data layers in the GIS. Such data layers may not be available in many of the large crystalline basement areas.

Interpreted lineaments should be added, possibly as a separate layer.

It is assumed that the overall meteorological conditions (precipitation, P, and evapotranspiration, ET) do not change much in the investigated area. If so, a separate layer may be prepared of P-ET and used in the analysis and characterization of the terrain units.

The base map with terrain units has to be transformed into a hydrogeological map, requiring hydrogeological characterization of the units by using data from bore-well logs and observations in the field concerning nature and depth of regolith (especially when many open wells exist), supplemented by information from the users of the wells concerning fluctuations or estimated yields. Attributes or combination of attributes of the units can be compared with yield data or estimated yields. For example, well yields in terrain units with weathering depths exceeding a given threshold, gentle slopes and low dissection could be compared with well yields in units of different nature, that is, different sets of attributes. This process may lead to merging of units or sub-differentiation of units, for which re-interpretation of the images is required. Once the hydrogeological properties are assessed, the hydrogeomorphological units may be termed hydrogeological units.

The lineaments may be classified according to their productivity prospect, depending on the result of the analysis using well yields with additional information such as presence of vegetation along the lineament, and, if available, ground geophysical data. It is tempting to use a GIS functionality to transform the lineament map into a lineament density map and to consider zones with high density as favourable ones. However, Sander (2007) expresses doubts because within such a zone, wells can be dry and a difference of several tens of metres can be in some areas mean the difference between a successful and a dry well.

The areas irrigated by groundwater as derived by, for example, NDVI transform may be added as an indication of productivity and drafts.

Finally, other elements of standard hydrogeological maps (water quality, etc.) should be added.

The advantage of this procedure is that experience gained during the survey and analysis finds its expression on the map, which is based essentially on an image interpretation map with specific relevant features added.

### *Approach (B)*

Another approach is to enter separate data layers in the GIS, such as: a slope map; a geological map, reclassified according to estimated permeability or specific yields; a map with the drainage lines and divides; a soil map, with outcrops as separate units; a land cover map; a lineament map; possibly a map with (P-ET0) if there are significant differences, and so on.

Some of these aspects can be obtained by remotely sensed data including SRTM-DEM data (land cover, updating of geological maps, drainage lines, outcrops, slope-steepness maps).

The hydrogeological evaluation of combinations of the individual map layers may be done by assigning empirical weights or scores to each of the categories of each layer and the final map is usually prepared by summation (e.g. Solomon and Quiel, 2006). This map is supposed to give an indication of favourable zones for groundwater exploration. This method is a flexible one, but the problem lies in the determination of the weights, which

can be subjective, unless sufficient data exists to check the outcome and iteratively adjust the weights. This is seldom the case for all combined units.

It is evident that a hybrid approach can be adopted between the two approaches A and B, depending on quality and consistency of the layers in the GIS.

## 10.11 Summary and conclusions

In crystalline basement terrain groundwater is stored in the fractured zone and in the weathered zone (or regolith) and therefore image interpretation should consider both aspects. Under given climatic conditions, groundwater recharge, that is, rainwater that reaches storage, is determined by local topography, land cover and associated drainage features and the nature of the weathered zone, which is influenced by present and past climatic conditions interacting with mineral and physical properties of the various crystalline rocks. These interactions have governed the geomorphological development, and therefore differentiation of geomorphological terrain units is implicitly a differentiation of potential hydrogeological terrain units. Land cover and soils are associated with the geomorphology. The term potential refers to the fact that hydrogeological field data must support the hydrogeological characterization of the units. Examples of such segmentation of the terrain into units interpreted on images have been included.

Well yields of boreholes in the weathered zone and in large fractures are, broadly speaking, of comparable magnitude, although high yielding wells are generally associated with large fractures, which can often be related to lineaments that can be interpreted on images. Attention is given to the visual interpretation aspects for tracing of lineaments, which is to some degree subjective, but no automated methods are advocated. Image scale influences the detection of large to small lineaments and so does the type of image processing method used (filtering).

Geological background knowledge concerning basic structural aspects is introduced and illustrated to support lineament detection and assessment, although there are contrasting views with regard to the hydrogeological significance of the use of tectonical models.

Because of the importance of the regolith, image interpretation for studying aspects of the regolith are discussed, requiring knowledge of geomorphological development as influenced by overall climatic conditions of the past. Examples are provided of lineaments and evident fractures extending into the regolith, while other examples show full obliteration of lineaments under a regolith cover.

Several examples of pediments are included because they have a specific hydrogeological environment. Groundwater seepage appearing at the surface in crystalline terrain in the so-called dambos (or marigots in Francophone countries) of Africa can be observed on images and some hydrogeological characteristics are discussed.

Recharge conditions are discussed and the examples include one from ophiolite terrain with large-scale images.

Practical application of image interpretation for well siting is illustrated by two examples; the first one assumes no prior local knowledge and the second one shows the results of image interpretation with follow-up by geophysical survey and drilling.

Sections on analysis have been included to review results of studies attempting to relate lineament properties to well yields. The section on GIS mentions an approach for a comprehensive hydrogeological study when thematic map data is incomplete and information relies overly on image data and terrain units, and the classical GIS approach of combination of single data layers.

## References

- Armand, C., Legac, H., Souisseau, B. and Thibault, J. 1983. Recherches et solutions retenues pour l'alimentation en eau potable de la ville d'aribinda. *Hydrogeologie de l'ingenieur*, Vol. 3, pp. 159–69.
- Attanayake, A.N.B. 1999. Analysis of fractures in a granitic terrain and their tectonic and hydrogeological implications: A study from Sardon catchment area, Salamanca Province, Spain. M.Sc. Thesis, ITC Enschede, The Netherlands.

- Bannert, D. 1969. Luftbildkartierung des Lineationsnetzes vom Ries und seiner Umgebung. *Geologica Bavarica*, Vol. 61, München, pp. 379–84.
- Barker, R.D., White, C.C. and Houston, J.F.T. 1992. Borehole siting in an African accelerated drought relief project. E.P. Wright and W.G.E. Burgess (eds) *Hydrogeology of crystalline basement aquifers in Africa*. Geological Society Special Publ. No. 66, pp. 183–210.
- Bième, J., Jourda, J.P., Deslandes, S. and Gwyn, H. 1995. Positionnement, productivité et gestion des forages en milieu fissure de Côte d'Ivoire par télédétection et système d'information géographique. *Remote sensing and water resources*, Proceedings of the international workshop, Montpellier, France, 1995, FAO, Rome, 1997, FAO Corporate Document Repository [http://www.fao.org/documents/show\\_cdr.asp?url\\_file=/docrep/W7320B/w7320b00.htm](http://www.fao.org/documents/show_cdr.asp?url_file=/docrep/W7320B/w7320b00.htm).
- Boeckh, E. 1992. An exploration strategy for higher-yield boreholes in the West Africa crystalline basement. E.P. Wright and W.G.E. Burgess (eds) *Hydrogeology of crystalline basement aquifers in Africa*. Geological Society Special Publ. No. 66, pp. 87–100.
- Bonham-Carter, G.F., Agterberg, F.P. and Wright, D.F. 1988. Integration of geological data sets for gold exploration, Nova Scotia. *Photogrammetric Eng. And Remote Sensing*, Vol. 54(11), pp. 1585–92.
- Buckley, D.K. and Zeil, P. 1984. Fractured rock aquifers in eastern Botswana. Challenges in African Hydrology and Water Resources. Proceedings of the Harare Symp. July 1984. IAHS Publ. No. 144, pp. 26–33.
- Caruthers, R.M. and Smith, I.F. 1992. The use of ground electrical survey methods for siting water-supply boreholes in shallow crystalline basement aquifers in Africa. E.P. Wright and W.G.E. Burgess (eds) *Hydrogeology of crystalline basement aquifers in Africa*. Geological Society Special Publ. No. 66, pp. 203–20.
- Chilton, P.J. and Foster, S.S.D. 1995. Hydrogeological characterisation and water-supply potential of basement aquifers in tropical Africa. *Hydrogeology Journal*, Vol. 3, No. 1, pp. 36–49.
- Cook, P.G. 2003. A guide to regional groundwater flow in fractured rock aquifers. CSIRO-Australia, [http://www.lwa.gov.au/downloads/publications\\_pdf/PX020312.pdf](http://www.lwa.gov.au/downloads/publications_pdf/PX020312.pdf).
- Dewandel, B., Lachassagne, P., Boudier, F., Al-Hattali, S., Ladouche, B., Pinault, J-L. and Al Suleiman, Z. 2005. A conceptual hydrogeological model for ophiolite hard-rock aquifers in Oman based on a multiscale and multidisciplinary approach. *Hydrogeology Journal*, Vol. 13(5–6), pp. 708–26.
- Drury, S.A., Peart, R.J. and Deller, M.E.A. 2001. Hydrogeological potential of major fractures in Eritrea. *Journal of African Earth Sciences*, Vol. 32, pp. 163–77.
- Dutatre, P., King, C., Motti, E. and Pointet, T. 1990. Utilisation de l'imagerie SPOT en prospection hydrogéologique au Burkina Faso: Le petite irrigation à partir des eaux souterraines des milieux fissures. *Hydrogéologie*, No. 2, pp. 145–54.
- Galanos, I. and Rokos, D. 2006. A statistical approach in investigating the hydrogeological significance of remotely sensed lineaments in the crystalline mountainous terrain of the island of Naxos, Greece. *Hydrogeology Journal*, Vol. 14(8), pp. 1569–81.
- Greenbaum, D. 1987. *Lineament studies in Masvingo Province, Zimbabwe*. BGS Technical Report MP/87/7/R.
- Greenbaum, D. 1992. Structural influences on the occurrence of groundwater in SE Zimbabwe. E.P. Wright and W.G.E. Burgess (eds) *Hydrogeology of crystalline basement aquifers in Africa*. Geological Society Special Publ. No. 66, pp. 77–85.
- Gustafsson, P. 1994. SPOT satellite data for exploration of fractured aquifers in semi arid area in southeastern Botswana. *Hydrogeology Journal*, Vol. 2(2), pp. 9–18.
- Hansmann, B.C., Meijerink, A.M.J. and Kodituwakku, K.A.W. 1992. An inductive approach for groundwater exploration. *ITC Journal* 1992/93, pp. 269–76.
- Hazell, J.R.T., Cratchley, C.R. and Jones, C.R.C. 1992. The hydrogeology of crystalline aquifers in northern Nigeria and geophysical techniques used in their exploration. E.P. Wright and W.G.E. Burgess (eds) *Hydrogeology of crystalline basement aquifers in Africa*. Geological Society Special Publ. No. 66, pp. 155–82.
- Jaroszewski, W. 1984. *Faults and Fault Tectonics*. Ellis Horwood, Chichester.
- Kaila, K.L., Roy Chaudhury, K., Reddy, P.R., Krishna, V.G., Haro Narain, Sabbotin, S.I., Sollogub V.B., Chekonov, A.V., Kharechko, G.E., Lazarenko, M.A. and Ilchenko, T.V. 1979. Crustal structure along Kavali-Udipi profile in the Indian Peninsular shield from Deep Seismic Sounding. *Journal Geological Society of India*, Vol. 20, pp. 307–33.
- Kellgren, N. and Sander, P. 2000. Benefits of incorporating remote sensing techniques as a methodological

- approach for improving borehole siting in fractured rock aquifers. O. Sililo (ed.) *Groundwater: Past Achievements and Future Challenges*. Proc. 30th IAH Congress, Cape Town, S. Africa, Balkema Publ., pp. 193–98.
- Lachassagne, P., Wyns, R., Bérard, P., Bruel, T., Chéry, L., Coutand, T., Desprats, J.F. and Le Strat, P. 2001. Exploitation of high yields in hard rock aquifers: Downscaling methodology combining GIS and multicriteria analysis to delineate field prospecting zones. *Groundwater*, Vol.39, No.4, pp. 569–81.
- Larsson, I. 1968. Ground water in Precambrian rocks in southern Sweden. E. Ericsson, Y. Gustafsson and K. Nilsson (eds) *Groundwater Problems*. Oxford, Pergamon Press, pp. 23–41
- Larsson, I. 1972. Ground water in granite rocks and tectonic models. *Nordic Hydrology*, Vol. 3, pp. 111–29.
- Lattman, L.H. 1958. Technique of mapping geologic fracture traces and lineaments on aerial photographs. *Photogrammetric Engineering*, Vol. 24, pp. 568–76.
- Lattman, L.H. and Parizek, R.R. 1964. Relationship between fracture traces and the occurrence of groundwater in carbonate rocks. *Journal of Hydrology* Vol. 2, pp. 73–91.
- Leopold, L.B., Wolman, M.G. and Miller, J.P. 1964. *Fluvial Processes in Geomorphology*. Freeman, San Francisco.
- Mackel, R.M. 1985. Dambos and related landforms in Africa – an example for the ecological approach to tropical geomorphology. *Zeitschrift für Geomorphologie*, 52, pp. 1–52.
- Magowe, M. and Carr, J.R. 1999. Relationship between lineaments and ground water occurrence in western Botswana. *Ground Water* 37 (22), pp. 282–86.
- McFarlane, M.J. 1989. Dambos- their characteristics and geomorphological evolution in parts of Malawi and Zimbabwe, with particular reference to their role in hydrogeologic regime of surviving areas of African Surface. Groundwater exploration and development in crystalline basement aquifers, Commonwealth Science Council Publication 1, pp. 254–310.
- McFarlane, M.J. 1992. Groundwater movement and water chemistry associated with weathering profiles of the African surface in parts of Malawi. E.P. Wright and W.G.E. Burgess (eds) *Hydrogeology of crystalline basement aquifers in Africa*. Geological Society Special Publ. No. 66, pp. 101–29.
- Maréchal, J.C. 1999. Observation des massifs cristallines alpines au travers des ouvrages souterrains. 1. Caractérisation de la conductivité hydraulique à l'échelle du massif. *Hydrogéologie*, No. 1, 21–32.
- Meijerink, A.M.J., Rao, D.P. and Rupke, J. 1984. Stratigraphy and structural development of the Precambrian Cuddapah Basin, SE India. *Precambrian Research*, 26, pp. 57–104.
- Mudzinhwa, B. 1999. Hard rock hydrology of the Nyatsime catchment, Zimbabwe. Unpubl. M.Sc thesis, ITC, Enschede, The Netherlands.
- O'Leary, D.W., Frieman, J.D. and Pohn, H.A. 1976. Lineaments, linear, lineations, some standards for old terms. *Bull. Geol. Society of America*, Vol 87, pp. 1463–69.
- Omorinbola, E.O. 1982. Verification of Some Geohydrological Implications of Deep Weathering in the Basement Complex of Nigeria. *Journal of Hydrology*, Vol. 56(3–4).
- Reul, K. Anwendung der Luftbildgeologie bei der Grundwasserschließung. Gwf Munchen 114, Heft2, pp. 3–15.
- Ruhland, M. 1973. Méthode d'étude de la fracturation naturelle des roches associée à divers modèles structuraux. *Bulletin des Sciences Géologiques*, Vol. 26, pp. 91–113.
- Pacheco, F. and Alenção, A. 2002. Occurrence of springs in massifs of crystalline rocks, northern Portugal. *Hydrogeology Journal*, Vol. 10(2), pp. 239–53. [http://www.fao.org/documents/show\\_cdr.asp?url\\_file=/docrep/W7320B/w7320b00.htm](http://www.fao.org/documents/show_cdr.asp?url_file=/docrep/W7320B/w7320b00.htm)
- Sami, K. 1996. Evaluation of the variations in borehole yield from a fractured Karoo aquifer, Spouth Africa. *Groundwater*, Vol 34(1), pp. 114–20.
- Sander, P., Chesley, M.M. and Minor, T.B. 1996. Groundwater assessment using remote sensing and GIS in a rural groundwater project in Ghana; Lessons learned. *Hydrogeology Journal*, Vol. 4(3), pp. 40–49.
- Sander, P. 1997. Water-Well Siting in Hard-Rock Areas: Identifying Promising Targets Using a Probabilistic Approach. *Hydrogeology Journal*, Vol. 5(3), pp. 32–43.
- Sander, P. 2007. Lineaments in groundwater exploration: a review of applications and limitations. *Hydrogeology Journal*, Vol. 15(1), pp. 71–74.
- Savane, I., Goze, B. and Biéme, J. 1997. Evaluation des ressources en eau dans le socle par l'étude des fractures à l'aide des données Landsat (basin d'Odienné, Côte d'Ivoire). Remote sensing and water resources, Proceedings of the International Workshop, Montpellier, France, 1995, FAO, Rome, 1997, FAO Corporate Document Repository.

- Schowengerdt, R., Babcock, E.M., Ethridge, L. and Glass, C.E. 1979. Correlation of geologic structure inferred from computer enhanced Landsat imagery with underground water supplies in Arizona. M. Deutsch, D.R. Weisnet and A. Rango (eds), *Satellite Hydrology. Proceedings of 5th Pecora Memorial Symp. Remote Sensing*, Sioux Falls, 1979. Amer. Water Research Association, Minneapolis.
- Singhal, B.B.S. and Gupta, R.P. 1999. *Applied Hydrogeology of Fractured Rocks*. Kluwer Acad. Publ. Dordrecht.
- Solomon, S. and Quiel, F. 2006. Study using remote sensing and GIS in the central highlands of Eritrea. *Hydrogeology Journal*, Vol. 14(5), pp. 729–41.
- Sporry, R. 2004. Geophysical techniques in groundwater investigations, V.S. Kovalevski, G.P. Kruseman and K.R. Rushton (eds) *Groundwater Studies*, IHP Series on Groundwater No. 3, UNESCO, pp. 133–83.
- Sreedevi, P.D., Subrahmanyam, K. and Ahmed, S. 2005. Integrated approach for delineating potential zones to explore for groundwater in the Paguru River Basin, Cuddapah District, A.P., India. *Hydrogeology Journal*, Vol. 13(3), pp. 534–43.
- Srinivasa Rao, Y., Reddy, T.V.K. and Nayudu, P.T. 2000. Groundwater targeting in a hard rock terrain using fracture-pattern modeling, Niva River Basin, Andhra Pradesh, India. *Hydrogeology Journal*, Vol. 8, pp. 494–502
- Stefouli, H. and Osmaston, H.A. 1983. The remote sensing of geologic linear features using Landsat: matching analytical approaches to practical applications. Proc. 10th Int. Conf. Remote Sensing Society.
- Taylor, R. and Howard, K. 2000. A tectono-geomorphic model of the hydrogeology of deeply weathered crystalline rock: Evidence from Uganda. *Hydrogeology Journal*, Vol. 8(3), pp. 279–94.
- Teme, S.C. and Oni, S.F. 1991. Detection of groundwater flow in fractured media through remote sensing techniques- Some Nigerian cases. *Journal of African Earth Science*, Vol. 12, No. 3, pp. 461–66
- Thomas, M.F. 1974. *A study of weathering and landform development in warm climates*. Macmillan, London.
- UNESCO, 1984. *Groundwater in Hard Rocks*. Studies and Reports in Hydrology, No. 33. Project 8.6 of IHP, UNESCO, Paris.
- Verstappen, H.Th. 1983. *Applied Geomorphology: Geomorphological Surveys for Environmental Development*. Elsevier, Amsterdam.
- Waters, P., Greenbaum D., Smart P.L. and Osmaston H. 1990. Applications of remote sensing to groundwater hydrology. *Remote Sensing Reviews*, Vol. 4(2), Harwood Academic Publishers GmbH, pp. 223–64.
- Wolski, P. 1999. Application of reservoir modelling to hydrotopes identified by remote sensing. ITC Publ. No. 69.
- Wise, D.U. 1982. Linesmanship and the practice of Linear Geo-art. *Bull. Geol. Society of America* Vol. 93, pp. 886–88.
- Wright, E.P. 1992. The hydrogeology of crystalline basement aquifers in Africa. E.P. Wright and W.G.E. Burgess (eds) *Hydrogeology of crystalline basement aquifers in Africa*. Geological Society Special Publ. No. 66, pp. 1–27.

# Remotely sensed data and groundwater modelling

## 11.1 Introduction

Groundwater modelling is considered nowadays as a very useful tool in support of groundwater management. The reliability of groundwater modelling is largely constrained by the quality of input data. However, the techniques of input data acquisition are still much less developed compared to the numerical modelling tools. This is because standard, point-sampling methods are expensive, time consuming and inefficient due to the common problems of heterogeneity of subsurface medium. Can remote sensing contribute to better quality of input data for groundwater modelling and thereby improve its reliability? This chapter presents a review of the current applicability and potential of the remote sensing technique, and surface and near-surface geophysics, as input data source for numerical groundwater modelling.

Lillesand and Kiefer (2004) describe remote sensing as ‘the science and art of obtaining information about an object, area, or phenomenon through the analysis of data acquired by a device that is not in contact with the object, area, or phenomenon under investigation’. This definition implies that not only the acquisition of information from space (in the visible, infrared, microwave and radio-wave, magnetic and gravity fields) but also depth-wise, that is, non-invasive acquisition of information from the near-surface or the ground surface about the subsurface by various geophysical techniques, belongs to remote sensing science. This assumption will be maintained in this chapter.

Remote sensing applications in surface hydrology such as, for example, estimation of rainfall, DEM derivatives, evapotranspiration, land cover and snow cover are quite well known nowadays (Schmugge et al., 2002) and are increasingly used in surface water modelling. Because of the coupling of surface runoff with groundwater models (e.g. Bauer et al., 2006), remotely sensed data is therefore implicitly used for numerical groundwater studies. However, remote sensing applications in numerical groundwater modelling *per se* are less well known, probably because of the depth penetration problem, despite some promising applications and good development perspectives.

Examples of the use of simple (cross-sectional) groundwater flow models in relation to image interpretation have been given in Chapter 7 (section 7.3.5) and Chapter 8 (section 8.3.2), while the method of Gandiotti for estimation of submarine groundwater discharge is given in Chapter 5 (section 5.2.3).

One way of transforming remotely sensed data, in conjunction with meteorological and available hydrometric data, into quantified characterization of groundwater flow in data scarce areas, is to first identify terrain units or complexes, that were termed as (groundwater) hydrotopes by Meijerink et al. (1997) and Wolski (1999). A hydrotope is a specific set of interrelated terrain features that governs near-surface processes – surface runoff, infiltration, percolation and evapotranspiration – and subsurface processes, influenced by overall head distribution, specific yield and permeability. Relative recharge (infiltration) is evaluated from rock/soil associations, and a conceptual model for the groundwater flow systems is made, using available hydrogeological data and image interpretation of features associated with groundwater. Reservoir or tank modelling was used for the quantitative description. A configuration of parallel or serial linear and non-linear (quasi-linear) reservoirs is made to mimic the flow systems in a hydrotope.

Wolski (1999) applied this approach to a hard rock catchment in Zimbabwe (Chapter 10, section 10.4.4) and to an area with thick Kalahari sands in Zambia (Chapter 7, section 7.3.5). He was able to accurately simulate base flows of a river hydrograph in the hard rock catchment and water level hydrographs of dambos depending on groundwater levels in the sand area. However, a limitation of the approach is the difficulty in a priori determination of model parameters, and therefore its use for regionalization (Wolski, 1999).

A review of remote sensing applications yielding quantitative data for groundwater studies – chiefly pertaining

to the US – is given by Becker (2006), who concludes, ‘At present, the best that can be achieved with satellite sensors is to determine spatial distribution of groundwater discharge and recharge areas, storage changes over vast areas, or measurement of surface water heads in large river bodies’. These subjects, besides others, have been discussed in various chapters in this book.

LeBlanc et al. (2003, 2007) used a variety of remote sensing data from multiple sensors for a regional numerical groundwater model of Lake Chad. They used thermal data (Meteosat and NOAA-AVHRR) and multi-spectral data (Modis, Landsat TM) for determining recharge and discharge areas, aspects of aquifer geometry and lateral flow with bordering aquifers. Large and rapidly changing features, such as extent of the lake and the floodplains were monitored by low-resolution sensors (Meteosat, NOAA-AVHRR) and smaller features, such as ponds and paleochannels by high-resolution data (Landsat TM). SRTM data was used for elevations in conjunction with data from topographic maps. Image enhancement techniques were used for image interpretation (paleochannels, former shoreline deposits, extent and boundary-type of aquifers, and spectral classifications). Multi-spectral data processing was also successfully used for definition of discharge and recharge areas based on surface indicators including terrain analysis, monitoring of vegetation activity and mapping of infiltration capacity (Tweed et al., 2007).

In a review emphasizing numerical groundwater modelling, Brunner et al. (2007) mention briefly some specific applications of various sensors, and pointed out that ‘The bulk of remote sensing data relevant for groundwater modelling are data which allow quantifying the distribution of recharge and discharge’. They describe several examples where such was the case, and discussed an interesting stochastic approach to coupling remotely sensed information with groundtruth data. Hendrick-Franssen (2006) applied a stochastic inverse modelling method, whereby model calibration was constrained by DEM data and recharge potential from remote sensing. The examples in the review of Brunner et al. (2007) pertain to: (a) a study by Brunner (2005), who verified a groundwater model with phreatic evaporation derived by remote sensing; (b) a study by Wacker et al. (2005), who used geomagnetic data and lineament analysis of images to map compartments and fractures with different transmissivity for improvement of the performance of an existing numerical groundwater model of the dolomite aquifer studied.; and (c) the assessment of relative recharge using satellite derived rainfall and evapotranspiration and comparison with recharge determined by the chloride method (Brunner et al., 2004).

## 11.2 Remote sensing data

Remote sensing (RS) techniques provide non-invasive spatial or even spatio-temporal information about surface and subsurface of a medium. The RS data are cost effective as a primary data source for groundwater modelling but also as a tool for extrapolating data acquired with other, potentially invasive methods. There are many types of remote sensing techniques, which differ in their applicability to groundwater modelling. The important questions are: which groundwater modelling steps can remote sensing techniques contribute to, to which input data types, and how? The following discussion will address these questions.

Remote sensing provides a valuable source of data contributing to the setting up of groundwater models. Space-borne and/or air-borne images are an inexpensive source of data. Ground-based remote sensing (i.e. geophysics) is usually more expensive than space and airborne remote sensing but is typically more accurate and still cheaper than invasive methods (e.g. borehole drilling).

As mentioned in the first chapter (Introduction), some of the information obtained by remote sensing is qualitative in nature and the transformation into quantities of water has to be accomplished in a second step. However, image data is in many cases the only source for providing spatial distributions, because point measurements are usually limited.

Space-borne and air-borne techniques have limitations with regard to depth penetration. Ground-based geophysical methods are more suitable for depth-wise characterization of the subsurface but are limited with regard to spatial characterization. The best approach is therefore to integrate space-borne, airborne and ground based RS sensing techniques combined with field measurements, as discussed by Lubczynski and Gurwin (2005). For a transient groundwater modelling study of a hard rock catchment in Spain, authors used Landsat TM and SPOT images to detect fracture patterns (lineaments), shown in Figure 11.1. This information was integrated with geophysical data, drilling, pumping tests, automated water level recording and estimation of the actual evapotranspiration using satellite data.



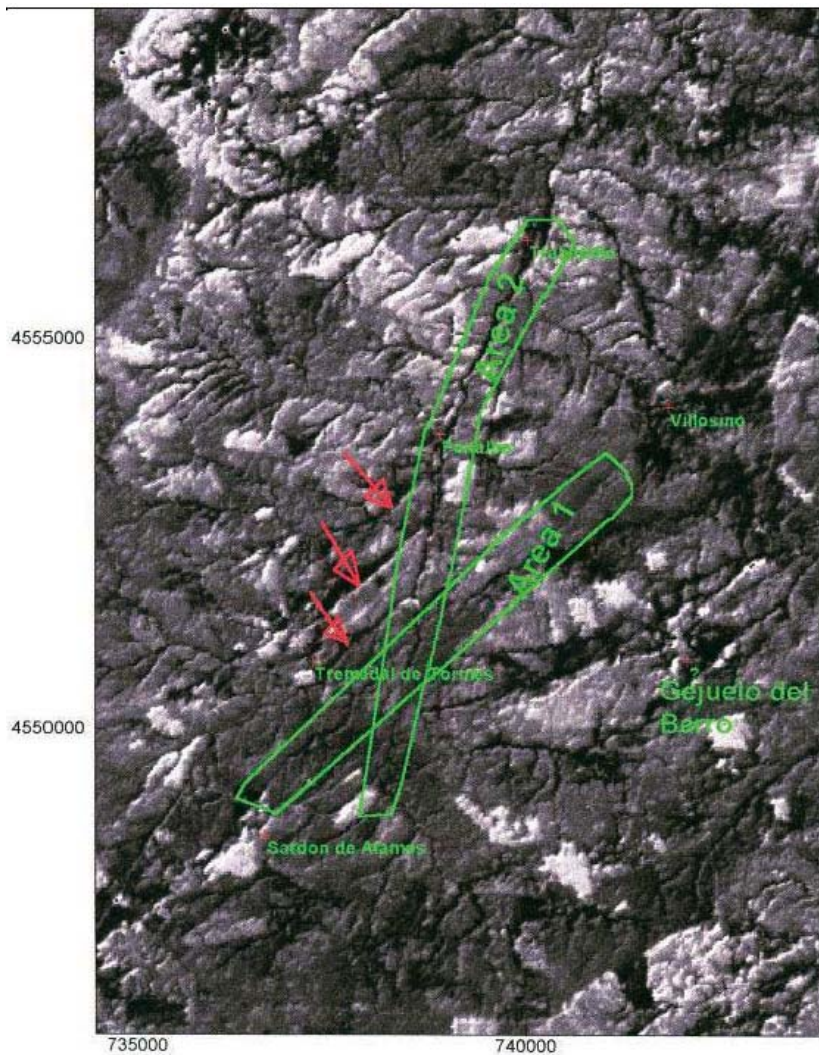


Figure 11-1

TM band 7 enhanced with 5 x 5 high-pass filter of the granite Sardon study area in Western Spain. Areas 1 and 2 represent location of major lineaments; the arrows indicate shorter segments parallel to the NE-SW lineament. The orientations of the lineaments are consistent with the regional fault systems. The lineament areas were used in the numerical groundwater model (Lubczynski and Gurwin, 2005) as the areas of enhanced aquifer transmissivity.

Space-borne or airborne data provide information on changes of features that influence hydrological processes or the measurement of water quantities, such as:

- Land cover/land-use and their changes, using mainly multi-spectral, radar and thermal images (Chapters 2, 4 and 5)
- Upscaling of tree transpiration with the aid high resolution images; vegetation density and groundwater (Chapter 14)
- Groundwater recharge, using multi-spectral, thermal images and radar data (Chapter 14)
- River drainage and flow; appearance of water in ephemeral river beds, occurrence of transmission losses (Chapters 7, 13 and 14) observed on airphotos and multi-spectral images; inflow of groundwater in rivers and coastal waters using thermal images (Chapter 5); lake levels using radar altimetry (Chapter 4). Empirical hydraulic geometry of river width and discharge relations may be used for the estimation of base flow in alluvial channels
- Areal rainfall, using multi-spectral, thermal and radar data (Chapter 14)
- Moisture of the surface soil measured by active and passive radar (Chapter 4)
- Deformation of the land surface related to recharge and extraction of groundwater, based on radar interferometry (Chapter 4)
- Estimation of evapotranspiration using thermal and multi-spectral images (Chapters 12 and 14)
- Change of saturated storage in large aquifers by satellite gravity measurement (Chapter 14), and for aquifers of smaller size by local gravity measurement on the ground (van Lanen et al., 2006).

Ground based remote sensing is used either for specific data acquisition concerning the subsurface, especially for the hydrostratigraphy, or for verification of space and airborne remote sensing data.

The set-up of any groundwater model consists of the following tasks: (0) defining the model's purpose; (1) defining the conceptual model; (2) setting up the numerical model; (2a) laying out a grid; (2b) defining model boundaries; (2c) defining hydrostratigraphic boundaries; (2d) defining aquifer parameters; (2e) defining groundwater fluxes; (2f) evaluating sink and sources (3) model calibration, validation and (4) preparing and running simulation or prediction scenarios. Remote sensing can contribute mainly to points 1 and 2. The role of remote sensing in model calibration is limited, but in some cases the surface features associated with groundwater outflow can be used, as is discussed and illustrated Chapter 7, section 7.3.5.

### 11.3 Defining the conceptual model

A conceptual model is a schematic, simplified representation of a 'real-world' system, in this case a groundwater flow system. This representation can have various forms, such as:

- Hard copy or digital projection of a flow system using cross-sections and/or 2D maps, eventually 3D distributions of various model input components. Such a projection of a flow system helps to understand and build up the conceptual model based on data from various sources; this option is typically used if collection and analysis of hydrogeological data is done by others than those that perform numerical modelling.
- Pictorial representations of groundwater systems are an explicit expression of a mental process, based on archive data and field experience. The 'brain' concept can be then implemented directly in a numerical model (for example MODFLOW, McDonald and Harbough, 1988) using pre-processing tools, such as, for example, the relatively simple modelling environment of PMWIN (Processing Modflow) interfaced with standard GIS tools (ArcGIS, ILWIS etc.). This type of solution is the most efficient in cases of less complicated models but only if the same person compiles hydrogeological data and performs the groundwater modelling.
- Use of sophisticated modelling packages, for example, GMS (EMS 2007), equipped with a built-in GIS pre-processor that allows internal construction of a conceptual model, which is finally converted in an automated manner to the numerical model. This solution is efficient in case of complex models with large amount of data (Gurwin and Lubczynski 2005) but is restricted to the relatively small community of hydrogeologists skilled in the efficient use of such sophisticated, modelling packages.
- RS data is very useful in setting up conceptual models, regardless of the applied approach (as explained above), particularly in data scarce areas, where maps and databases may not be adequate. In data-rich industrialized areas, RS data is also useful, providing opportunities for efficient spatio-temporal data upscaling with links to field based measurements.

### 11.4 Setting up a numerical groundwater model

A numerical model is a mathematical, simplified representation of the conceptual model; it is always a simplified representation of field reality. Depending on the task and data available, numerical models can be 1, 2 or 3D. Remote sensing contributes to the spatial or spatio-temporal data of the 2D and 3D numerical models.

In setting up numerical groundwater models it is appropriate to use all available information, which often comes from a variety of types of data sources. Among those sources remotely sensed data have an important role mainly because of their spatial nature. RS data can be imported into modelling environments either in its original form (e.g., a certain band of a geo-referenced satellite image, or colour composite as background for setting up a grid) or in its processed form (e.g. evapotranspiration map based on the remote sensing solution of the energy balance).

Figure 11.2 shows an example of the grid of a groundwater model superimposed on an image that is the result of image fusion between a false colour composite of three Landsat TM bands and an image of the second derivative of the aeromagnetic total field intensity. In this image subsurface geological features covered by sand are enhanced, for example, the lineament along the northern boundary of the model area. This lineament represents the Kadimotse fault which is a contact between impermeable metamorphic gneisses and sedimentary sandstone rocks forming Ntane aquifer (Lubczynski, 1996).

Remote sensing data transfer to a modelling package is dependent upon the type of software modelling environment. In cases of complex software modelling environments such as, for example, GMS package, the main strategy is to move all relevant, point, vector and raster data into the modelling environment. Sophisticated groundwater modelling packages are well adapted to specific subsurface data processing such as, for example, 2D and 3D interpolations, stochastic simulations etc. However, their GIS capability of matrix operations is not adapted yet to complex and complicated matrix operations required, for example, in RS solutions of soil moisture and evapotranspiration. Such data processing tasks still have to be realized in GIS, and transferred afterwards to the modelling environments.

In less sophisticated modelling environments such as PMWIN, the strategy of data transfer is different. All the remote sensing data is rather pre-processed in the GIS environment and then the output is interactively (by import-export options) linked to the modelling environment.

The choice of a strategy for data pre-processing is constrained by the modelling package used and in fact depends entirely upon the preference of the modeller. It stands to reason that less sophisticated modelling environments are more efficient in solving simple modelling problems with small data sets whereas complex modelling environments are more suitable for complex modelling problems with large data sets.



**Figure 11-2** Numerical model grid build over the integrated image of Landsat TM false colour composite (bands 4, 7, 1) with the second vertical derivative of the aeromagnetic total field intensity (Lubczynski et al., 1996). Grid cells with triangles represent northern inflow.

### 11.4.1 Model grid

The first step in setting up a numerical model is to generate a model grid. Such a grid has to be well adjusted to the model domain. This means grid type (e.g. rectangles in finite difference method or triangles in finite element method), grid size, orientation and spatial coverage.

Model grids of numerical groundwater models are nowadays generated automatically by modelling packages (codes). Such generation is preferably done on top of the imported selected map of the study area or on top of the imported remote sensing image, as shown in Figure 11.2. Importing maps and/or images to modelling environments is also useful for geo-referencing of the grid, which automatically links available database information (e.g. borehole data) with the model domain.

The type of model grid is defined already at the stage of modelling code selection. Finite difference models have regular, rectangular grid structures whereas finite element models have irregular, mostly triangular grid structures. Most groundwater agencies nowadays select finite difference models (e.g. MODFLOW) because of their simplicity, but also because their grids tie directly to standard coordinate systems used not only by local maps but also by geo-referenced images, thereby facilitating easy data exchange between model and external data source. Grids skewed with respect to standard coordinate systems are rarely used.

The size of a grid depends upon the problem statement, data available and expected accuracy, but also on complexity of natural conditions. For example, areas with large hydraulic gradients, abundance of hydraulic barriers, wells or springs, require finer grids. In principle, the resolution of an image used for defining the grid should be higher than the expected grid size. This particularly refers to the regional or intermediate models that are likely to be refined at a later stage, required for working out groundwater management options. A single band geo-referenced image may be sufficient to define grid size during the preliminary evaluation of the complexities in the model domain. The degree of uniformity of a terrain, as interpreted on images, influences the grid size and its variability in size. In case of topographically or geologically variable terrains, stereoscopic images are recommended. Topography can be observed on stereo images or be visualized using SRTM data (see Chapter 3).

Most of the model pre-processing codes (e.g. PMWIN) have the possibility to import geo-referenced images. Such images often need to be processed before they can be used as background for the model. Some of the modelling codes have some image processing options; however, for more complicated image processing options, additional GIS functionalities can be used.

The model grid does not need to be uniform. Sometimes it is useful and computer memory-efficient to refine the model locally. Grid refining options are now available in nearly all modelling packages. Good adjustment of grid density to the degree of complexity of the model domain, including local grid refinements, is one of the modelling challenges. Grid density depends on the local hydrogeological complexity of the area, such as fractured hard rock areas that can be studied on images. Areas with local groundwater flow systems require fine grids. Such local systems are found where the terrain consists of either small hills or fossil, broad dune ridges, where recharge is sufficient to create a topography of the groundwater surface or where small depressions occur, taking the form of evaporative sinks in hot climates caused by shallow groundwater. The pattern of shallow groundwater occurrences may be evident from the combination of topography, land cover, emergence of water at the surface (NIR bands) and thermal contrasts (Chapters 5 and 14 contain examples). Furthermore, permeable zones such as weathered and fractured zones in crystalline or karst terrain, particularly their discreet increments, may be represented in a groundwater model by a fine mesh.

However, there are cases where standard optical RS information is not applicable in grid design. This typically applies to deeper aquifers where only specific RS methods can be used. A good example is the case of the Kalahari Serowe groundwater model, where the hydrostratigraphy of the layers and the spatial position of the hydraulic barriers (faults and dolerite dykes) constraining grid are hidden under a >50 m sand cover, but could have been revealed (see Figure 11.2) by an airborne magnetic survey (SGAB, 1988). This was possible because of favourable geology, that is, the presence of basalt, to which aeromagnetics surveys are sensitive. In many other areas similar subsurface assessment is not possible.

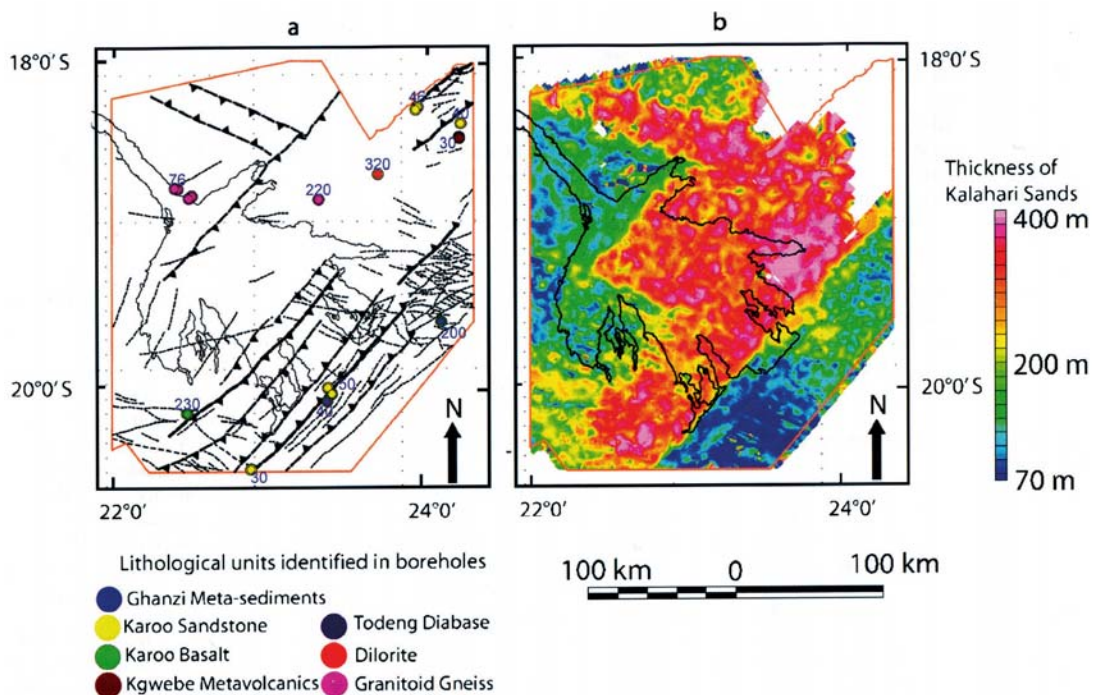
### 11.4.2 Setting model boundaries

Selection of appropriate model boundary conditions is the most critical step in development of a numerical groundwater model. The most reliable are physical model boundaries, in other words, 2D features, such as impermeable rock contacts, surface water bodies, groundwater outcrops and so on. Most of those features, when exposed, can be delineated on satellite images or aerial photographs, often requiring some additional image processing to enhance visibility.

When certain model boundaries (e.g. contact between permeable and impermeable rocks) are below a substantial overburden, it may be difficult, if not impossible to locate and evaluate them using image data. Geophysical surveying and test drilling may then be directed to the zone where such boundaries are expected, based on geologic reasoning using the synoptic view offered by the images.

Airborne geophysical surveys can offer relevant information contributing to the assignment of boundary conditions or presence of compartments within the aquifer in case of rocks with large magnetic susceptibility (e.g. basalt). Examples of successful application of airborne magnetic surveys are known from, for example, Botswana, where magnetic contrast between basalt and sandstone was used to depict internal and external model boundaries (Dijk et al., 1996; SGAB, 1988; Wacker et al., 2005). It may be noted that in a particular case, the Pala Road aquifer in Botswana (Figure 11.2), most of the faults revealed by an aeromagnetic survey could be traced on Landsat TM images as lineaments in the sandy overburden (Van Dijk et al., 1996).

Airborne magnetic survey can provide not only structural information but also thickness of the Kalahari Sands, as in the example from the Okavango Delta in Botswana presented in Figure 11.3.



**Figure 11-3** Determination of aquifer thickness from airborne magnetic survey: a) structural patterns extracted from aeromagnetic data. The orange outline represents the boundary of the study area; the thin solid black line represents the boundary of the Okavango Delta; the thick black lines represent faults (triangles point in the direction of throw); the dotted lines represent faults with unknown throw direction; b) Estimated thickness of Kalahari Sand aquifer in metres.

Lithological discrimination of model boundaries and salinity of groundwater can be defined with other methods, such as airborne electromagnetic surveys. An example of such a survey in the same Delta Okavango area is presented in Figure 11.4. In this figure, patches of fresh water have been located in an environment where saline groundwater is dominant (Masedi, 2003). Resistive buried fresh water channels are shown in blue and saline waters in red, delineating boundaries between fresh and saline waters.

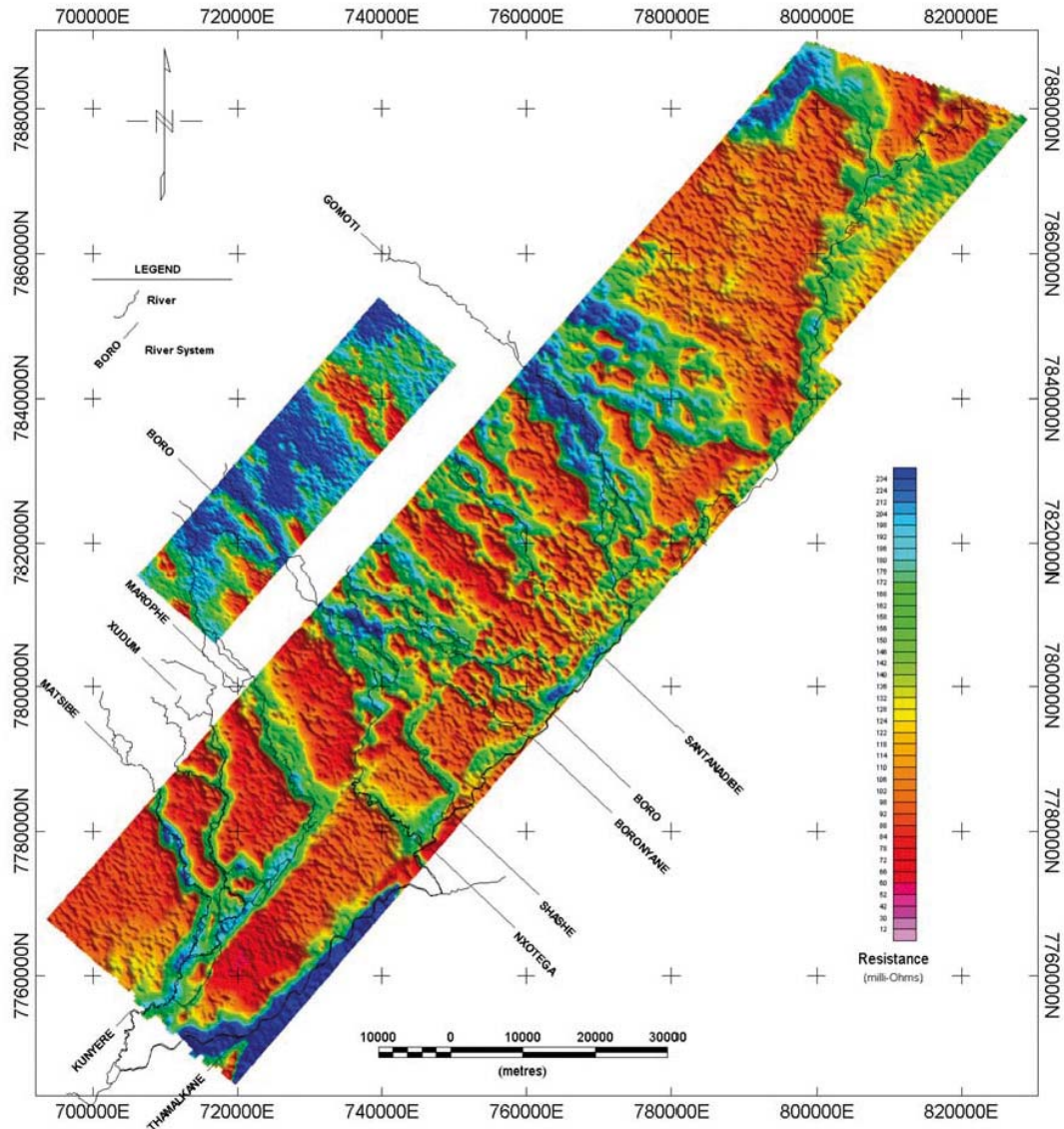


Figure 11-4 Airborne electromagnetic data set of Botswana. Resistive buried fresh water channels in blue between ‘Boro’ and ‘Santanadbe’ and saline water in red.

Source: Masedi, 2003

**11.4.3 Spatial input data (model parameters)**

Spatial input data refers to time invariant data type, assigned to each cell of a model grid. In numerical groundwater flow models these data types are: hydrostratigraphic boundaries of layers and parameters such as hydraulic conductivity, transmissivity (for confined aquifers only), specific yield and specific storage, but not the potentiometric surface, which is time variant. Each of such data types is represented in the numerical model by a discrete representation in a form of data matrix constrained by the model grid.

*Hydrostratigraphic boundaries (top and bottom model boundaries)*

Setting up a model refers not only to areal (planar) system discretization but also to profile (vertical) discretization. This is done by defining the number of layers and the shape of layers, in other words, the spatial configuration of the aquifer tops and bottoms. The more layers, the more complicated the model solution is. The simplest solution is represented by one layer model referred to as 2D planar model. The shape of layers is typically assigned in the models through interpolation from the available point data within the modelling environment, if there are no

reasons to assume discontinuities (e.g. absence of lineaments, uniform aeromagnetic data, and so on). The shape of layers is not always explicitly present in the models. In case of confined aquifers it is often 'hidden' within the model parameters such as transmissivity ( $T=KD$ ) and confined storativity ( $S_c=S_sD$ ) where  $K$  and  $S_s$  are respective rock specific constants such as hydraulic conductivity and specific storage and  $D$  is the layer thickness.

Standard remote sensing has limited application in vertical layer discretization because only the land surface is sensed. An exception of this is radar remote sensing that in dry sands can penetrate up to some 2 m depth (Chapter 4). Deeper information useful for layer discretization, besides borehole data, is provided by ground remote sensing (ground geophysics). An exception is the information coming from airborne geophysics, for example, airborne magnetic surveys, but that data is constrained by the presence of magnetic rocks, while airborne electromagnetic surveys are constrained by contrasts in rock resistivity.

Surface geophysical methods are the most suitable for depth-wise scanning of subsurface as input for distributed groundwater models. These methods however are time consuming and therefore less efficient and more expensive in use than space RS methods. Considering the large spatial data demands of the models, the benefit/cost related efficiency of the method in spatial data acquisition is a major concern in using ground-based geophysical methods. Several types of surface geophysical methods are most suitable for spatial definition of hydrostratigraphic boundaries: electrical resistivity surveying, 'active' electromagnetic methods, refraction seismic method and ground penetration radar method.

The most common are 'active' electromagnetic (EM) methods (resistivity methods and time domain electromagnetic) that apply an electrical current or electromagnetic field to the ground and sense contrasts in rock resistivity between layers with depth. The advantage of these methods is their simplicity, low cost and relatively large penetration depth (dependent upon rock resistivity) whereas the disadvantage is that it is a time consuming operation and has uncertainty, which is related to depth evaluation due to equivalence error. It is generally accepted that EM is the best method in hard rock terrain to locate deep weathered zones and fractures. EM surveys are typically done at selected places after interpretation of images for lineaments and position and extent of weathered zones.

The refraction seismic method uses a seismic shock (explosion for deeper penetration or strong hammer blow for shallow measurement) to measure by geophones the seismic wave velocity dependent upon the layer elastic property and density, both controlling various seismic velocities. The advantage of that method is the highest spatial (planar and depth-wise) resolution among surface geophysical techniques and its generally large depth penetration particularly in cases of large seismic velocity contrast. The disadvantage is the high cost of the survey and uncertainty due to velocity inversion, minimum layer thickness, and so on.

The ground penetration radar (GPR) method is probably the most efficient of the ground geophysical methods in terms of speed of data acquisition but it is appropriate only for imaging of high resistivity rocks, with good permittivity contrast (Al-Shuhail, 2006). This is a serious limitation with regard to the variety of rocks that can be investigated. Most GPR applications are focused on discrimination between wet and dry rock layers.

The most appropriate for hydrostratigraphy assessment and suitable for nearly all rock conditions is the new magnetic resonance sounding (MRS) method, discussed below. Due to the large cost of the MRS instrument and of the survey itself, the MRS is not considered yet as a hydrostratigraphic mapping tool. However, with MRS technology development this may change.

### *Hydraulic conductivity/aquifer transmissivity*

Aquifer hydraulic conductivity ( $K$ ) is typically deduced from borehole pumping tests and hydraulic rock sample analysis, but it may also be assessed by flow net analysis. Non-invasive geophysical methods are not yet very effective in hydraulic conductivity determination. Several electric methods, for example, EM and resistivity profiling have been useful in mapping clay-enriched zones with locally reduced ( $K$ ). However as other standard geophysical methods, they do not provide absolute ( $K$ ) values.

The most appropriate geophysical method is the relatively new magnetic resonance sounding (MRS) method (Lubczynski and Roy, 2003, 2004). This is because the analysed MRS signal amplitude is directly linked with groundwater content and MRS signal decay with  $K$  (so also with  $T$ ) because the MRS decay time constant describes mobility of water (extractability of water) in the rock matrix (Lubczynski and Roy, 2004). That correlation has still an empirical form not generalized for various hydrogeological conditions. If applied in unknown environments where MRS verification has not been done before, it requires calibration. Such calibration is typically

performed by making several MRS soundings at locations with reference (K) for example, from pumping tests to establish area-specific, decay time constant to hydraulic conductivity conversion functions. After such calibration MRS can be used in the ‘calibrated area’ for direct determination of not only (K) but also (T) because MRS enables also discrimination of hydrostratigraphic layers. Neither space-borne nor air-borne applications to determine subsurface K/T are not known as yet.

### *Storage coefficient*

The storage coefficient of an aquifer largely influences transient model calibration and model predictions, which are very important in groundwater management. Standard methods of acquisition of the storage coefficient are pumping test when pumping well (+pump) and observation well are already available, or less accurately with, for example, laboratory analysis of disturbed samples. Therefore, promising developments in hydro-geophysical methods such as MRS and gravimetric methods are very important in the context of rapidly increasing groundwater modelling applications.

MRS is the most suitable geophysical method to obtain aquifer storage, but also to derive a storage coefficient for groundwater modelling. This is because the subsurface water content is directly and physically related with MRS signal amplitude, which can be directly converted to storage coefficient (Lubczynski and Roy, 2003). The advantage of MRS as compared to other geophysical methods is because:

- MRS is water selective, that is, the measured signal originates from water only (this is the main advantage of the MRS method as compared to other geophysical methods);
- The relation between the measured signal amplitude and the water content is straightforward and physically-based so it does not need pump test verification as in case of K/T in MRS assessment
- MRS provides an integrated (averaged) signal so the storage coefficient is also averaged from the volume of up to  $10^6 \text{ m}^3$ , the latter corresponding with a loop area of approximately  $10^4 \text{ m}^2$ . The loop area refers to the area encompassed by the loop of electrical wire on the ground surface used for transmitting – downward – the excitation pulse and for analysing the upward MRS- relaxation signal to derive the water content (porosity).

The main MRS disadvantages are the relatively large cost of the instrument and that the survey is quite time consuming taking on average about half a day. Besides, current MRS applications are restricted to low noise locations, but it is expected that this problem will be overcome in the near future.

The principle of gravimetric methods refers to the observation that porous material has a lower density than massive rock and that water saturation increases the density of a porous rock. In contrast to MRS, gravimetric surveys focus not on the evaluation of aquifer storage but on the change of storage in time. Such change, when applied as model input and calibrated in transient mode, can lead to evaluation of aquifer storage coefficient. Next to the ground version, the gravimetric method has its airborne and recently also spaceborne (GRACE) versions.

Two GRACE satellites in tandem orbit were launched in March 2002. The two satellites, with precisely recorded inter-distance, measure the gravity field of the Earth at the resolution of  $\sim 300 \times 300 \text{ km}$ , with monthly or longer intervals. The difference between the two GRACE global gravity fields, after corrections for other external effects, at different periods yields a time variable component of subsurface water storage. That component combines, surface water, unsaturated moisture and groundwater (Chapter 14).

Airborne gravimetric surveys can, in principle, also be used for measuring changes in groundwater storage. These surveys are very expensive and are known practically only from mineral exploration. To our knowledge such surveys are not practised yet. This is because in order to measure change of storage of groundwater multi-temporal gravimetric data acquisition is required, at prohibitive expense.

Ground-based gravimeter measurements have the advantage that water storage change can be measured with high temporal resolution. Such short-term gravity variation, which has to be corrected for a number of effects (e.g. polar motion, Earth tides) was found by van Lanen et al. (2006) to be highly correlated with medium and high rainfall reflecting quick distribution of water near the gravimeter. The authors expect that the observed varying gravity will reflect groundwater storage change if the different groundwater flow processes at their site (from stream, shallow subsurface flow from hill slopes and direct infiltration) each with its own time constant can be accounted for.



Out of the two presented methods suitable for aquifer storage assessment, the MRS method is more direct and more accurate, but restricted to surface applications only. The gravimetric method is restricted to evaluation of storage change (not the storage as whole) and is less accurate than MRS, but has a large potential in airborne and space borne data acquisition, being therefore particularly suitable for storage change assessment over large areas.

## 11.5 Spatio-temporal model input data

Spatio-temporal model input data is a data type that is assigned to each cell and varies in time. Temporally variable data is used only in numerical transient models. There are two types of transient models:

- (1) Fully-transient models, with temporally variable groundwater fluxes (groundwater evapotranspiration and groundwater recharge), temporally variable aquifer storage (defined by temporally variable potentiometric surface) and temporally variable contribution of external sources and sinks (well abstraction, irrigation return flow, etc.)
- (2) Quasi-transient models with temporally variable aquifer storage (defined by temporally variable potentiometric surface) and with temporally variable contribution of external sinks and sources.

In transient models not only space but also time is discretized into stress periods. For each stress period and each data type, separate spatio-temporal data matrixes have to be assigned, all demanding extensive data acquisition. To which extent then remote sensing can contribute to satisfy such a demand?

### 11.5.1 Potentiometric surface (hydraulic head)

Potentiometric data are critical in groundwater modelling solutions because they determine hydraulic gradients and thus directions of groundwater flow. Even small data acquisition errors, in order of centimetres, may result in wrong modelling solutions. Therefore very high accuracy in acquisition of that particular data type is required, higher in areas with gentle gradients and relatively lower in areas with steep groundwater gradients.

Point hydraulic head measurements are the most direct and straightforward measurements. They are often considered in groundwater modelling protocol as control or reference data to which other data types (e.g. parameters, fluxes) are fitted in the process of model calibration. The standard way of obtaining potentiometric data is by measurement of the groundwater level in wells or preferably drilled piezometric holes typically referenced nowadays by accurate ( $\pm 2$  cm) differential ground positioning systems. Remote sensing methods have little to offer for measurement of heads with high precision. However, field observations of piezometric levels may be expensive and the density and locations of observation wells and peizometers often leave much to be desired.

Images can be used for locating places where the phreatic groundwater table intersects with the surface, as evidenced by the appearance of water in ephemeral river beds or in exfiltration areas or in seepage zones (dam-bos), but the elevation of such emergence places has to be determined by other means.

Airborne and spaceborne radar returns from a (shallow, less than a few metres) groundwater surface could be used, at least in theory, after accounting for returns or backscatter from other objects above the groundwater table. In practice this will limit the application to circumstances of low surface roughness, arid conditions and a homogeneous unsaturated zone of limited thickness, in 'radar transparent' media such as clean sands, clean quartzite or clean igneous rocks, in other words, devoid of clay, graphite and so on. This ability however has not been yet investigated in various rock types and conditions and there is very little known about the accuracy of such assessment. Reutov and Shutko (1992) describe how microwave remote sensing (i.e. passive radar) data can be used for the estimation of the groundwater table in a specific dry soil case study case.

Ground penetrating radar (GPR) seems to be the most suitable geophysical tool for efficient groundwater table depth assessment. Like airborne microwave assessment, GPR use is restricted to dry, resistant, 'radar-transparent' media conditions with permittivity contrast between saturated and unsaturated zone (which, due to the presence of capillary fringe is not always clear). The accuracy of GPR assessment depends upon the frequency of the antenna used. The lower the frequency, the higher the penetration depth is, but at the expense of accuracy in the shallow part of the subsurface. Recent developments have seen very promising efficient and accurate GPR

assessment made using a monostatic antenna on the ground (Lambot et al., 2004) and very recently from aircraft (Lambot et al., 2006).

If field conditions are not suitable for the use of GPR, other techniques such as electric and/or seismic survey can be used, not for quantitative groundwater depth assessment but only for extrapolation of piezometric field measurements. Airborne gravity and airborne electromagnetic methods have also potential for groundwater depth assessment but due to the large cost of surveys, such potential has not yet been well investigated.

The most accurate, non-invasive assessment of groundwater table depth seems to be possible with MRS techniques. An advantage of this type of assessment is not only in its superior accuracy (<1 m depending mainly upon the signal to noise ratio, rock type and depth of groundwater table) but also in its integrated response from the quadratic loop size (in order of 50 x 50 m to 100 x 100 m) comparable with most common cell sizes of groundwater models. The MRS technique however is not yet widely used for such application, mainly because it is too expensive and too time consuming to be efficient in surveys focused on groundwater table assessment only. Besides, MRS technology is still restricted to sites with low noise.

### 11.5.2 *Evapotranspiration*

Discharge of groundwater (also in groundwater models) can take place not only by outflow from the aquifer ( $Q_g$ ) but also by groundwater evapotranspiration ( $ET_g$ ).  $ET_g$  flux consists of direct evaporation from the groundwater table called groundwater evaporation ( $E_g$ ) and/or of groundwater uptake by deep-rooting trees called groundwater transpiration ( $T_g$ ).  $ET_g$  can be a significant component of groundwater balance particularly in arid and semi-arid countries, so disregarding or underestimating it may lead to serious groundwater modelling errors (Lubczynski and Gurwin, 2005).

So far there is no direct way to estimate  $ET_g$  or to extract it from total evapotranspiration (ET) that can be derived from micrometeorological measurements on the ground or with a RS solution of the energy balance. ET in general differs from  $ET_g$  (the one used in groundwater modelling), although in dry seasons, particularly in arid and semi-arid locations with thin unsaturated zone characterized by low retention capacity, the assumption  $ET_g \sim ET$  is often permitted. Whenever such an assumption cannot be made, any ET can always be used as guideline to spatially redistribute  $ET_g$  (Lubczynski and Gurwin, 2005) that finally would be undergoing the model calibration process.

The gist of the surface energy balance method for assessment of ET using satellite data (SatSEB) is discussed in Chapter 14. At this point, it may be remarked that the accuracy of all RS solutions of energy balance was confirmed in wet areas or irrigated areas, but was shown to be insufficient in dry areas with diverse vegetation and topography, where the SatSEB solution error was too high to be applicable in circumstances of very low fluxes (but could well be used for  $ET_g$  extrapolation purpose in such areas) but was successfully applied in groundwater modelling of the irrigated sites.

An attempt to apply microwave C-band SAR radar data to calculate ET of arid playas was also made but it gave evaporation rates of 2–3 times those measured at the evaporating pan and about 4–9 times those estimated using a radiation model of evaporation calibrated using meteorological station measurements (Wadge and Archer, 2003).

### 11.5.3 *Groundwater recharge*

Recharge (R) is the amount of water that reaches the groundwater table in contrast to net recharge that represents the difference between recharge and groundwater evapotranspiration ( $R_n = R - ET_g$ ). Groundwater recharge is probably the most difficult and often the most uncertain data type used in groundwater modelling. There is as yet no remote sensing based method to evaluate recharge directly in a quantitative way. However, the RS and GIS methods can contribute to recharge assessment at least indirectly through:

- scaling up recharge assessed with other methods using GIS modelling (Lubczynski and Gurwin 2005; Shaban, 2006)
- GIS-based solution of water balance with some input of RS technique (e.g. vegetation)
- RS-based assessment of P and ET followed by spatial mapping of P-ET further used for scaling up chloride based recharge estimates (Brunner et al., 2004)

- stochastic modelling of the P-ET using recharge measurements as modelling reference (Hendrics-Franssen, 2006)
- RS-based determination of soil moisture applied as input for unsaturated recharge models (e.g. HYDRUS) or as input for saturated-unsaturated groundwater models (see Chapter 14 for remarks).

Direct, quantitative RS assessment of recharge seems to be feasible only with the ground-based MRS technique, which, if installed in situ in the logging mode, can provide tomographic 3D water content scans of the subsurface down to 100–150 m. Currently however, the MRS technology allows only 1D water content scans in a logging mode and 3D in a field profiling mode, but this is evolving rapidly.

#### ***11.5.4 Contribution from sinks and sources***

Sinks and sources are known in groundwater modelling protocol as man-driven water losses or additions from or to the aquifer system. An example of a sink is a well while an example of a source could be seepage from irrigation canals and field losses of surface water irrigation to the underlying aquifer.

In many aquifers used for irrigation, the loss of groundwater, in other words, the difference between the amount pumped from aquifer and the ET of the irrigated fields, is not known. As mentioned above, ET however can be estimated by using a SatSEB method, or alternatively, by mapping irrigated acreage and crops using multi-spectral classification and using empirical crop water use factors. This way the irrigation loss can be estimated that in groundwater modelling represents the source. Sinks of groundwater are not detectable with remote sensing.

Remote sensing cannot contribute to well management but can attempt to control irrigation losses in space and in time.

#### ***11.5.5 River discharge in ungauged catchments***

River discharges, particularly river base flows, are critical for reliable model solutions. Various techniques exist to separate the base flow from the total flow, as expressed by the hydrograph of the river. The total base flow over a given period is the outflow of groundwater via the river. The hydrograph of the base flow is important in transient model calibration, because the use of that data substantially reduces the number of degrees of freedom of the calibrated model.

In cases of ungauged catchments, the base flow can be estimated by field surveys (including spot measurements, visual observation and enquiring), hydrological simulation modelling or by regionalization methods. Remote sensing techniques provide substantial data input (e.g. land cover, vegetation density, rainfall, DEM data and derivatives) for such models (Dubayah et al. 2000; Mazvimavi, 2004).

## **11.6 Summary and conclusions**

Numerical groundwater modelling is an important tool for groundwater management, because the effects of exploitation of aquifers can be simulated, but also effects of climatic change on the groundwater resource and the fate of groundwater pollution. The models require spatial data input and in many regions such data is scarce. Remote sensing can provide a part of the input, especially when data from geological and hydrogeological surveys and from geophysical surveys, airborne or on the ground are included.

References to modelling studies using remote sensing are made. The major steps in setting up a groundwater model are discussed, starting with defining the conceptual model. The role of remote sensing, including geophysics, in deciding on a model grid, aquifer boundaries and some spatial parameters are explained and partly illustrated.

Transient modelling is even more data intensive because time series are needed. To some degree remote sensing can assist in such data acquisition, such as groundwater evaporation using satellite data. However, limitations are mentioned such as the measurement of piezometric levels.

The role of magnetic resonance sounding (MRS) is emphasized because it is the only tool that can measure the presence of subsurface water and may provide some hydrogeologic parameter values.

References to other chapters have been made where several subjects are discussed and illustrated.

## References

- Al-Shuhail, A.A. 2006. Mapping the surface of a shallow groundwater system using GPR: A case study in eastern Saudi Arabia. *The Leading Edge*, Vol. 25(6), pp. 738–40.
- Bauer P, Gumbricht T and Kinzelbach W. 2006. A regional coupled surface water/ground water model of the Okavango Delta, Botswana. *Water Resources Research*, 42, W04403, doi:10.1029/2005WR004234Vol.
- Becker, M.W. 2006. Potential for satellite remote sensing of ground water. *Groundwater*, Vol. 44(2), pp. 306–18.
- Bernard, J., Lemine M., Diagana, B. and Ricolvi M. 2003. Combination of electrical resistivity and magnetic resonance sounding data for mapping an aquifer layer in Mauritania. <http://heritagegeophysics.com/papers/NMRMauritania.pdf>.
- Brunner, P. 2005. Sustainable agriculture in the Yanqi Basin, China. Ph.D. Thesis ETH, Zurich, No. 16210.
- Brunner, P., Bauer, P., Eugster, M. and Kinzelbach, W. 2004. Using remote sensing to regionalize local precipitation recharge rates from the chloride methods. *Journal of Hydrology*, Vol. 294(4), pp. 241–50.
- Brunner, P., Hendricks Franssen, H.J., Kgotlhang, L., Bauer-Gottwein, P., Kinzelbach, W. 2007. How can remote sensing contribute in groundwater modelling? *Hydrogeology Journal* Vol. 15(1), pp. 5–18.
- Dijk, P.M., Lubczynski, M.W., Farr, J.L. and Gaabake, G.G. 1996. Application of RS, GIS and groundwater modelling techniques in recharge evaluation at Palla Road, Botswana. Conference ‘The application of remotely sensed data and GIS in environmental and natural resources assessment in Africa’ in Harare, March.
- Dubayah, R.O, Wood, E.F., Engman, E.T., Czajkowski, K.P., Zion, M. and Rhoads, J. 2000. Remote sensing in hydrological modelling. E.T. Engman and G.A. Schulz (eds) *Remote Sensing in Hydrology and Water Management*, Springer Verlag.
- EMS-Environmental Modelling System. 2007. GMS – Groundwater Modelling Software. <http://www.ems-i.com/GMS/gms.html>.
- Gurwin, J. and Lubczynski, M.W. 2005. Modelling of complex multi-aquifer systems for groundwater resources evaluation – Swidnica study case (Poland). *Hydrogeology Journal* Vol. 13(4), pp. 627–39.
- Hendricks-Franssen, H.J.W.M., Brunner, P., Kgotlhang, L. and Kinzelbach, W. 2006. Inclusion of remote sensing information to improve groundwater flow modelling in the Chobe region. IAHS, ModelCARE (Redbook series).
- Leblanc, M., Razack, M., Daborne, D., Mofor, L., Jones, C. 2003. Application of Meteosat thermal data to map soil infiltrability in the central part of the Lake Chad Basin, Africa. *Geophys Res Lett* 30(19), Art. No.1998.
- LeBlanc, M., Favreau, G., Tweed, S., Leduc, C., Razack, M. and Mofor, L. 2007. Remote sensing for groundwater modeling in large semiarid areas: Lake Chad Basin, Africa. *Hydrogeology Journal*, Vol. 15(1), pp. 97–100.
- Lillesand, T.M., Kiefer, R.W. and Chapman, J.W. 2004. *Remote Sensing and Image Interpretation* 5th edn. John Wiley & Sons.
- Lambot, S., Slob, E., Van den Bosch, I., Stockbroeckx, B., Scheers, B. and Vanclooster, M. 2004. Estimating soil dielectric properties from monostatic GPR signal inversion in the frequency domain, *Water Resources Research*, 40, W04205.
- Lambot, S., Weiermüller, L., Huisman, J., Vereecken, H., Vanclooster, M. And Slob, E. 2006. Analysis of air-launched ground-penetrating radar techniques to measure the soil surface water content, *Water Resources Research*, 42, W11403.
- Lanen, H.A.J. van, Dijkma, R., Hasan, S., Kroner, C. and Troch, P.2006. Monitoring and modelling distributed water storage to understand local gravity at Moxa, Germany. *Geophysical Research Abstracts*, Vol. 8, 06516.
- Lubczynski, M.W. Gumirehete, R. Gaabake, G.G. 1996. Application of automated inverse modelling technique in calibration of steady state groundwater flow model at Palla Road, Botswana. MODEL CARE 96 Proceedings, IGWMC, pp. 137–44.
- Lubczynski, M.W. and Gurwin, J. 2005. Integration of various data sources for transient groundwater modelling with spatio-temporally variable fluxes—Sardon study case, Spain. *Journal of Hydrology*, Vol. 306(1–4), pp. 1–26.
- Lubczynski, M.W. and Roy, J. 2003. Hydrogeological interpretation and potential of the new magnetic resonance sounding (MRS) method. *Journal of Hydrology*, 283/1–4, pp. 19–40.
- Lubczynski, M. W. and Roy, J. 2004. Magnetic resonance sounding: new method for ground water assessment. *Ground Water*, Vol. 42(2), pp. 291–303.

- Masedi, G.V. 2003. Modelling recharge from river infiltration – Thamalakane River, Botswana; MSc Thesis, ITC, Enschede, The Netherlands [www.itc.nl]
- Mazvimavi, D., Meijerink, A.M.J. and Stein, A. 2004. Prediction of base flow from basin characteristics: a case study from Zimbabwe. *Hydrological Sciences Journal / Journal des Sciences Hydrologiques*, Vol. 49(4), pp. 703–15.
- McDonald, MG and Harbough, AW. 1988. A modular three-dimensional finite difference groundwater flow model. *US Geol Surv Tech Water Resour Invest.*, Book 6(Chapter A1).
- Meijerink, A.M.J., Lubczynski, M.W. and Wolski, P. 1997. Remote sensing, hydrologic response simulation and hydrotopes. Proc. Int. Conf. Regionalization in Hydrology, IAHS, Braunschweig, Germany, pp. 169–72.
- Reutov, E.A. and Shutko, A.M. 1992. Estimation of the depth to a shallow water-table using microwave radiometry. *International Journal of Remote Sensing*, Vol. 13(12), pp. 2223–32.
- Schmugge, T.J., Kustas, W.P., Ritchie, J.C., Jackson, T.J., Rango, A. 2002. Remote sensing in hydrology. *Advances in Water Resources*, 25, pp. 1367–85.
- SGAB. 1988. Serowe groundwater resources evaluation. Swedish Geological Co. Report for Department Geological Survey, Botswana.
- Shaban, A., Khawlie, M. and Abdalla, C. 2006. Use of GIS and remote sensing to determine recharge potential zones; the case of occidental Linanon. *Hydrogeology Journal*, Vol. 14 (4), pp. 433–43.
- Tweed, S.O., Leblanc, M., Webb, J.A. and Lubczynski, M.W. 2007. Remote sensing and GIS for mapping groundwater recharge and discharge areas in salinity prone catchments, southeastern Australia. *Hydrogeology Journal*, 15(1), pp. 75–96.
- Wacker, S., Webersberger, S., Kgotlhang, L. and Kinzelbach, W. 2005. Modelling the fractured aquifer near Kanye, Botswana. Report to the Department of Water Affairs, Gaborone, Botswana (ETH Zurich).
- Wolski, P. 1999. Application of reservoir modelling to hydrotopes identified by remote sensing. PH.D. thesis and ITC Publ. No. 69.

# Remotely sensed information for groundwater management

## 12.1 Introduction

Groundwater management pertains to a broad field and several aspects have been selected to describe how information obtained by remote sensing can be of assistance in planning and monitoring sustained use of groundwater.

The traditional assessment of sustainable groundwater use or 'safe yield' considered the long-term balance between recharge and drafts, and the obvious management option was to control drafts from aquifers. In view of the interactions between groundwater and surface water, upstream-downstream relations within river basins and environmental water requirements, the concept of 'safe yield' has to be placed in a wider context. For a discussion of sustainable use of groundwater, we refer to Sophocleus (2000), who presented a synthesis of water sustainability issues from the hydrologic perspective, which includes groundwater-dependent ecosystems, and discusses water-use policies and planning horizons. Eamus et al. (2006) emphasize the need for a functional methodology for determining the groundwater regime needed to maintain the health of groundwater-dependent ecology.

Remote sensing plays an important role in refining the spatial patterns of rainfall and assessment of water use by crops and natural vegetation, and their monitoring – all key elements for working out sustained groundwater use, as will be discussed below.

A number of applications of remote sensing in groundwater management will be discussed in this chapter, starting with subjects which pertain to the direct use of the data, such as assessment of scope for further groundwater development in crystalline basement area, or estimation of the net draft from an aquifer. A watchdog function is shown, by matching the actual groundwater use determined by remote sensing against water rights. Other subjects pertain to an indirect use of remotely sensed data related to groundwater contamination and groundwater management plans.

Developments in satellite hydrology make it possible to take stock of the actual water use of various land covers (water accounting) and when matched with spatial rainfall patterns, partly derived by remote sensing, allow identification of patterns of groundwater recharge and loss.

The role of remote sensing in groundwater modelling, which is an important instrument in groundwater management, is discussed in Chapter 11.

Alleviation of shortages of groundwater by managed aquifer recharge is a management option and a separate chapter (Chapter 13) is devoted to image interpretation for selection of sites for schemes aiming at recharge by impeding and diverting flash floods of small to moderately sized catchments in semi-arid regions.

For discussion of general aspects of groundwater management we refer to websites with links to their publications, of such international organizations dealing with (ground)water as, the International Water Management Institute (IWMI), UNESCO Water Sciences, Food and Agricultural Organization (FAO) and World Bank (WB) and International Association of Hydrogeologists (IAH). A special issue of the *Journal of Hydrogeology* (2006) is devoted to social and economic aspects of groundwater governance.

## 12.2 Scope for further groundwater development

### 12.2.1 Introduction

A report of the International Water Management Institute (IWMI) by Shah et al. (2000) draws attention to the importance of groundwater for irrigated food production in India and to the threat posed by water depletion to production because of groundwater mining. According to IWMI (WPB-undated): 'Recent research shows that groundwater irrigation has surpassed surface irrigation as the primary source of food production and income generation in many rural areas (in India). The key question for policy makers and planners in many regions in the

world is how to tap this resource without exhausting the supply. The mind-set and water management skills need to shift from resource development to resource planning.’

The importance of groundwater for irrigation, as a proportion of total irrigation water use and volume ranked for 8 countries, is shown in Table 12.1.

Rank	Country	Irrigated area	Irrigation water use	Proportion groundwater	Groundwater use for irrigation
		Mha	km <sup>3</sup> /yr	%	Km <sup>3</sup> /yr
1	India	50.1	460	53	244
2	China	48.0	408	18	73
3	Pakistan	14.3	151	34	51
4	Iran	7.3	64	50	76
5	Mexico	5.4	61	27	16
6	Bangladesh	3.8	13	69	9
7	Argentina	1.6	19	25	5
8	Morocco	1.1	10	31	3

Table 12-1

Groundwater use for irrigation.

Source: IAH/briefings

In the case of the hard rock terrain of south-central India where thousands of borehole wells and open wells exist, problems due to groundwater overexploitation are not infrequent. Some decades ago, supplementary irrigation was practiced from open wells using animal traction for water lift. During years of drought and low recharge, the groundwater table reached the bottom of the wells or declined a little below them, but during years of average rainfall the groundwater level recovered. Depending on the local situation, some 2 to 5 ha were irrigated per well or well cluster, as can be measured on aerial photographs taken in the 1960s. With the advent of rural electrification and agricultural credit, rapid expansion of well drilling took place and supplementary irrigation was replaced by full irrigation of areas much larger per well than the few hectares of former times. The result was a drastic drop in the groundwater level, and accompanying reduction of the water yields with due consequences for the farming community. At places, the irrigated acreage is now more or less reduced to the former one, but with high lifting costs. In order to avoid or minimize the hazard through such instruments as loans, subsidies, water pricing or taxation, legislation tuned to the hydrogeological situation of the particular area, and other possible measures, spatial patterns of permissible drafts for a sustainable use of groundwater should be known. The next section illustrates that remotely sensed images can be used to assess the situation in a simple manner.

### 12.2.2 Rapid appraisal of scope for groundwater development in crystalline areas

It can be expected that greater use of groundwater will be made for irrigation in hard rock areas. The experience of the hard rock Rayalaseema area India, one of the worst affected areas suffering from decline of the groundwater level, is a warning for other semi-arid hard rocks where irrigation by groundwater is not yet so intensive. Marechal et al. (2003) used the water table fluctuation method to study the groundwater balance in a part of this area and they found that during a year of normal rainfall the water table dropped by 1.2 m due to irrigation.

According to a study by Premananth and Liyanapatabendi (1994) of the hard rock terrain of Anuradhapura district, Sri Lanka, which has an annual rainfall of 1,280 mm, for every acre irrigated by groundwater, 34 to 37 acres of recharge area are needed for sustained groundwater use. Their ratio seems to be high in comparison with what can be observed on images of southern India with much lower rainfall. The case from Sri Lanka appears rather atypical.

To give an estimate of how much groundwater can be pumped for irrigation without mining the resource is not easy because of the difficulty in estimating some of the factors in the water budget, as will be discussed below. A simple solution is to make a rapid inventory of the total irrigated area per hydrogeological terrain unit (such units are discussed e.g. in the chapters on Crystalline Rocks and Alluvial Areas) and compare the results with field data on the behaviour of the groundwater level, for example by interviewing well owners.

Figure 12.1 shows an NDVI image of a hard rock terrain in the Rayalaseema area of southern India, from 1982 (Landsat MSS), during the initial phase of the expansion of the number of wells and irrigated acreage. About 8 to 10% of the total area shown in the figure, depending on what NDVI threshold is adopted, consists of irrigated fields.

An estimate of the crop water requirement for the irrigated fields can be made. This estimate should include

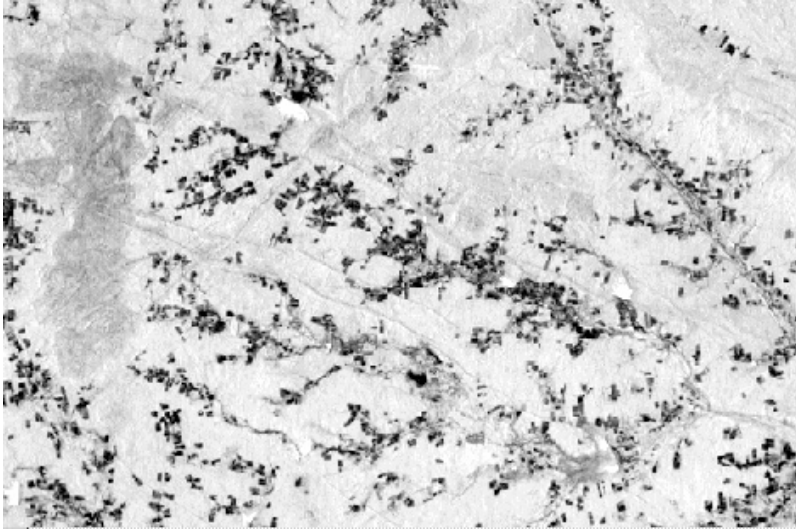


Figure 12-1

Landsat MSS-NDVI image of a hard rock terrain, showing fields (dark tones) mainly irrigated by groundwater during the initial period (1982) of expansion of well-irrigation which led later on to a drastic decline of the groundwater level.

the amount of water, which has to be applied after the long dry season to bring the rooting depth of the soil up to the field capacity, the crop water requirement during the various crop development stages using crop water factors, and monthly potential evapotranspiration (ET<sub>0</sub>). A conservative estimate works out to be around 500 mm for a single cropping season from end of May till early November. During that period ET<sub>0</sub> is around 1,050 mm while effective precipitation (P – estimated runoff) is around 500 mm in the growing season, leaving a deficit of 550 mm. It can be argued that this amount has to be supplied by irrigation from groundwater.

Recharge during the rainy period may be estimated, albeit with relatively low accuracy, as percentages of monthly effective rainfall, varying from 0% for the first rainy month to 30% for the only month (September) with a very small surplus (P-ET<sub>0</sub>). The recharge estimate is 60 mm, which is close to the average of 10% given by the Central Groundwater Board of India for crystalline terrain.

Since 10% of the area is irrigated and deficit and recharge are more or less in balance, it can be concluded that there is not much scope for further expansion. In other words, further groundwater development is probably not sustainable, unless groundwater augmenting measures are implemented.

It may be remarked that more detailed consideration of the amount of irrigation water used without field data is difficult because it is unknown how much of that water is captured in the vadose zone, where during the long dry season, soil moisture has been depleted by gravity, by uptake of weeds and by upward capillary flux.

## 12.3 Estimation of the net draft

If measures are planned to stop groundwater mining, it is obvious that the amount and pattern of groundwater used for irrigation, if irrigation is the main groundwater use, has to be determined. This task is a common problem in the practice of groundwater management or groundwater studies if a large number of wells with no or poor registration exist. By using remote sensing the spatial pattern of actual groundwater use can be estimated, as an alternative to doing so by a well inventory in field.

### 12.3.1 Groundwater use by estimation of crop water use with empirical method

Using multi-spectral images not only can the irrigated areas be mapped but also the crop types, as discussed in the chapter on Image Processing (Chapter 2, section 2.7.5). The accuracy of the crop type classification depends on a number of factors, but with proper sample sets is usually in the order of 80% of fields with a given crop correctly classified.

For example, a crop classification survey using Landsat TM in the Sana'a Basin, Yemen, where many fields have a small size and therefore the mixed pixel problem is encountered, gave good results. The accuracy of results for the two dominant irrigated crops, grapes and qat were 93% and 87% respectively. For the class 'mixed cereals and other crops' the accuracy was 81%, but for orchards only 53%. The last category, orchards, is usually difficult



to classify because there is no closed canopy and spectral reflectance from the ground is highly variable, depending on proportion of weeds and bare soil.

With crop acreage data, an estimate of the crop water consumption can be made using the cropping calendar and Kc factors (Doorenbos and Pruitt, 1984; Allen et al. 2000) for the individual crops. The Kc factor gives the crop water use as a fraction (normally between 0.3 and 1.1) of the crop reference evapotranspiration. By working out the consumptive use for the different crop stages and crop types a more accurate estimate is obtained than is the case in rapid appraisal method mentioned above, where aggregated data was used.

The total amount of groundwater used by the crops is roughly equal to the pumped amount. The assumption is that irrigation water percolating below the root zone of the crops returns fully to the groundwater body. As mentioned in the previous section, this may not be the case if important soil moisture changes occur at the start and end of the growing season. Effective rainfall during the growing season has to be accounted for because it is not likely that farmers pump water when rainfall was sufficient.

### ***12.3.2 Groundwater use by estimation of crop water use with surface energy balance method***

An alternative use of remotely sensed data for the estimation of the draft is to use the surface energy balance (SEB) method to calculate the actual evapotranspiration (ETa). Chapter 11 (Image Data and Groundwater Modelling) mentions some groundwater studies where use was made of the SEB method. Some essentials of the SEB method are given in Chapter 14, section 14.3.

In section 12.4 below, a system is described for which the SEB method provided information to enable effective monitoring of groundwater use. The meteorological data for the area of application and the adequate number of Landsat TM images available, made it possible to obtain results of sufficient accuracy.

The SEB method was also used for estimating the drafts in the Sana'a Basin and is included here to mention the potential, but also to discuss problems encountered.

The falling groundwater level in the Sana'a Basin became a matter of concern when results of a preliminary groundwater model (Foppen, 1996) indicated that the sandstone aquifer of the basin would be depleted in a few decades. Only crude estimates of the total draft were available and a well survey met with difficulties of various natures. Therefore, an attempt was made to estimate the total draft by the actual evapotranspiration (ETa) of the irrigated area for the year 2000 with the aid of SEBAL (Bastiaanssen et al., 1998), a Surface Energy Balance Algorithms for Land, based on remote sensing data and a minimum of ground data. The irrigated areas of the Sana'a Basin are shown by way of an NDVI image in Figure 12.2. The simple NDVI transform provides a good overview of where the areas irrigated by groundwater (white tones) are located.

The accuracy of the application of the SEB method to the Sana'a Basin was hampered by absence of proper air temperature data in the various parts of the plain and the valleys surrounded by cliffs. Also important in the method is the difference between air temperature and the surface temperature as recorded on the thermal images, after radiometric and atmospheric correction. Incoming radiation for the year 2000 was measured at a central place in the basin.

A main limitation was that only three cloud-free Landsat TM images (60 m resolution for the thermal band) were available during the irrigation season of the year 2000. A linear interpolation was used for the ETa between overpass dates, a too simplistic method. A study by Gieske and Meyninger (2005) using the frequent images of NOAA for an irrigated area in Turkey indicated considerable variation in daily ETa based on SEB during periods of several consecutive days. A remedy is averaging, but the frequent NOAA images could not be used in case of the Sana'a Basin because of the poor spatial resolution of the NOAA images.

Results of the Sana'a Basin study could only be verified by comparing crop water consumption in areas with contiguous grape fields (an important crop in the area) based on the ETa satellite data and the listed Kc factors for overpass dates.

However, a figure for the estimate of the total draft was obtained and the quantified pattern of groundwater use was mapped. A small part of the basin with ETa values is shown in Figure 12.3.

Some questioned the results because the total estimated draft, estimated on the basis of the total ETa, turned out to be much lower than earlier thought. It would be therefore useful to continue the study based on SEB whereby use can be made of data from high resolution satellites launched after 2000 (ASTER), having more frequent overpasses and to complement field measurements, particularly air temperature measurements in the various parts of the basin.

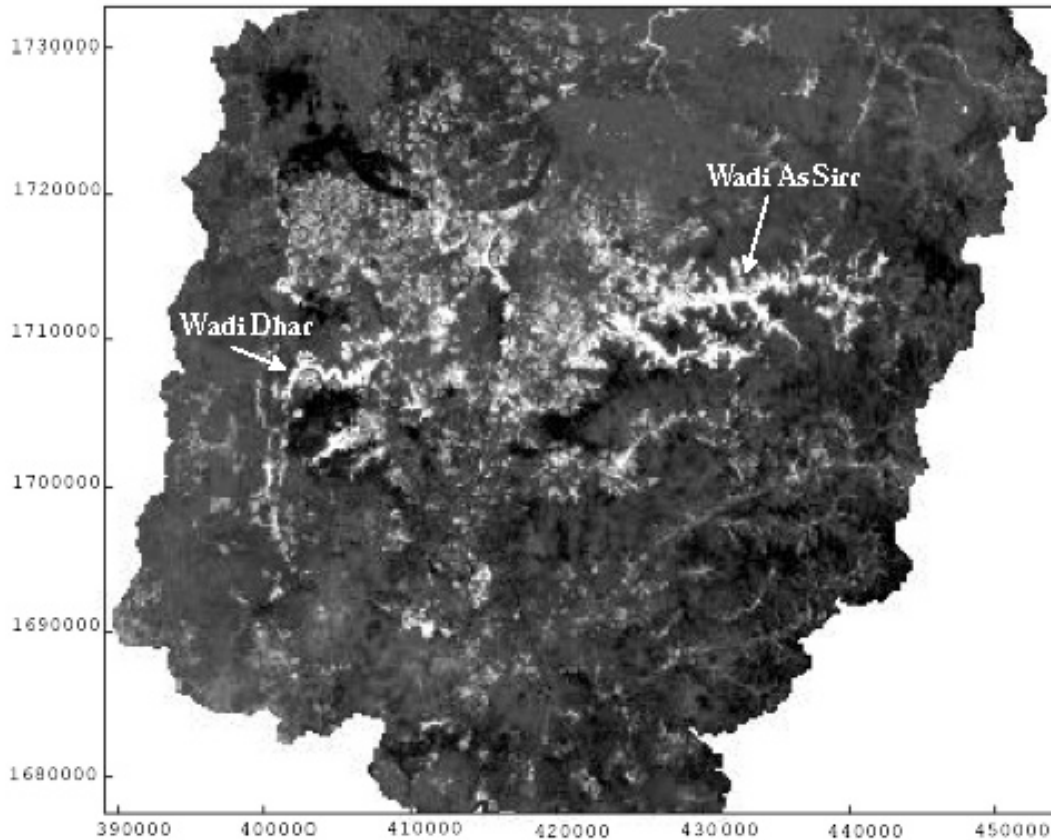


Figure 12-2 NDVI image of Landsat TM, year 2000, during the growing season of Sana'a Basin, Yemen. With this image a mask was prepared for aggregating the calculated actual evapotranspiration, see next figure below. The density of such areas is a first proxy of groundwater drafts.

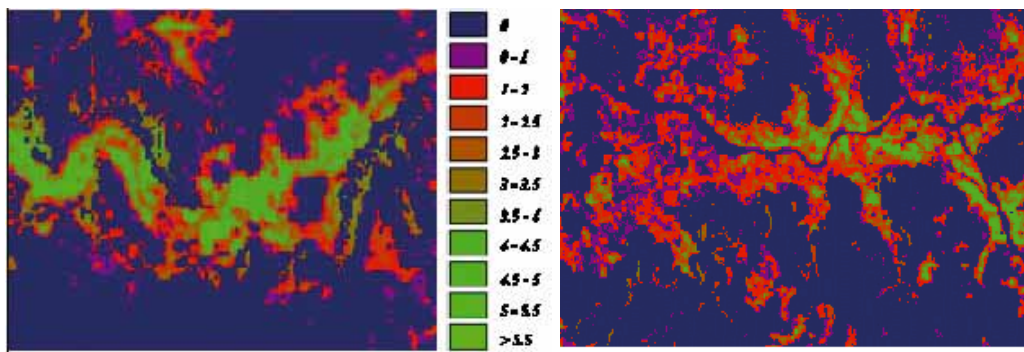


Figure 12-3 Daily actual evapotranspiration ( $\text{mm d}^{-1}$ ) calculated with Surface Energy Balance method using Landsat TM image of 13 May 2000 of Wadi Dhar and Wadi As Sirc, tributaries to Sana'a Basin, Yemen. The study was made to estimate total draft in the entire basin.

Source: Timmermans and Meijerink, 2002.

## 12.4 Examples of groundwater monitoring and economic aspects

### 12.4.1 Monitoring

In some countries groundwater-permits or water-rights specify allowed drafts and size of area irrigated. In some countries, where the practice is advanced, permitted groundwater use is determined on the basis of groundwater modelling results, but a general problem is observing whether users do not exceed their groundwater rights, even when water meters are in place. This observation can be achieved with the aid of remote sensing.

It is possible to map the irrigated area by remote sensing (NDVI transform or near infrared band of images during the dry season when crops depend on irrigation, see example above), but also to obtain an indication of how much water is used. The surface energy balance (SEB) method can be used to determine the actual water use for irrigation. The gist of the SEB method is discussed in Chapter 14, but here an example of actual application for monitoring actual groundwater use is given for an aquifer in the Guadiana catchment in Spain (Anon., 1999).

Using several Landsat TM images during the irrigation season, and standard meteorological data supplemented by measurement of incoming radiation, a SEB method (SEBAL, Bastiaanssen, 1998) was used to determine the actual evapotranspiration (ET<sub>a</sub>) loss from the irrigated fields during satellite overpass. For the estimate of ET<sub>a</sub> for period between overpasses an interpolation method was used, based on measured potential evapotranspiration and rainfall.

In this manner the seasonal and annual total ET<sub>a</sub> was obtained and shown on a map based on a georeferenced Landsat TM, to be compared with the permitted groundwater abstraction rate. The particulars of each farmer, their water rights and permitted irrigated area were captured in a GIS. In fact, a user-friendly monitoring system was made for the water authority with which they could query pertinent questions with regard to individual users or aggregate use for the aquifer. Groundwater level data was included in the system. Figure 12.4 shows a part of one of the screens of the system, namely a query for all entries where more water was used than allowed. The table lists the actual irrigated area (left column), the registered area (2nd column), and the actual versus the allowed water consumption (3rd and 4th column) of all users that had exceeded the allowed amount (names masked here). Particulars of the water licence appeared on the part of the screen not shown here. The system included a function with which the operator could click on a name, resulting in a map showing the location of the farm and associated irrigated lands.

Obviously, this tool using remotely sensed data helps the water authority to take proper action.

Query executed: List of expedientes[Overexploited(water)](Order by expediente)[records 566]

Query parameters: Expediente: 156425659, 1566 3, 1566 5, 1566 6; CLAS\_MAS

IRRIGATED AREA (l)	REGISTERED (ha)	WATER CONSUMP	ALLOWED WATER	1st Surname	2nd Surname	NAME	ID	ESTATE
1	1	6000	4278				0550	ARD
19.6875	6	51406.25	17406				0450	NADA
2.25	2.65	13687.5	11336.7				0550	ARRE
11.75	6	29656.25	17406				0550	ARRE
10.5	7.6	30218.75	19044.4				0248	LOME
19.25	20	39306.25	30742				0612	YA Gr
20.5	20.57	43656.25	39610.68				0612	YA Gr
2.375	1.87	18812.5	7999.86				0551	QZD I
2.5	2.57	19125	10994.46				0493	JRPA
10.25	20.66	43875	39747.84				0611	ERTU
7.375	6.64	57625	18381.36				0243	NOS
2	2.51	13937.5	10737.78				0373	NOS
4.4375	3	16750	12834				0441	NOS
4.375	8.46	26250	21155.04				0613	RRAS
6.0125	8.4	34687.5	21063.6				0609	NGUE
26.3125	10	140468.75	23502				0609	RRES
17.375	23	57687.5	43314				0611	JMOS
16.1875	16	33093.75	32646				0610	JMOS
4	13	30625	28074				0612	HILLAI
9.5	22	50687.5	41790				0580	ZAN

Figure 12-4 Screen of a groundwater management system, after query for those owners of water rights, who had exceeded the allowed amount. The groundwater consumption was based on calculation of the actual evaporation using a surface energy balance equation and sequential Landsat TM data. The parcels of each individual owner can be shown on a map.

### 12.4.2 Economic aspects

A possible measure to reduce groundwater drafts in case of declining groundwater table is to allocate water. This is easier said than done in practice, but a helpful step is to prepare a map showing where groundwater is used, preferably with the quantity and what the economic benefits are. Those in charge of water allocation may then decide, for example, to reduce allocation where the water has low economic returns.

It is common in many countries that no detailed spatial overview exists. By mapping the areas irrigated by groundwater and classification of crop types using remote sensing, a first step is made. This has to be followed by an economic assessment of the returns, based on field survey and use of available data, which may be available in aggregated form per administrative unit.

Such a study was undertaken for the Naivasha area in Kenya and the following salient aspects are derived from Becht et al. (2006). Lake Naivasha is situated in a hydrogeological saddle position with subsurface outflow to the south, see Figure 12.5. The freshwater nature of the terminal lake is attributed to the outflow of groundwater. The lake is fed by groundwater and by the Malewa River and the smaller Gilgit River. Since the 1970s, development of commercial farms in the area around the lake has taken place. A drop in the level was attributed to pumping of groundwater around the lake and from the lake itself, but from the side of the commercial water users it was pointed out that the lake levels had also been lower for some period in the past before development took place. To resolve the issue of man-made versus natural causes, a model was made, which simulated successfully the lake levels since they were recorded, from 1900 onwards. The curves for simulated and observed lake levels started to diverge from the early 1980s, providing evidence for the effect of pumping.

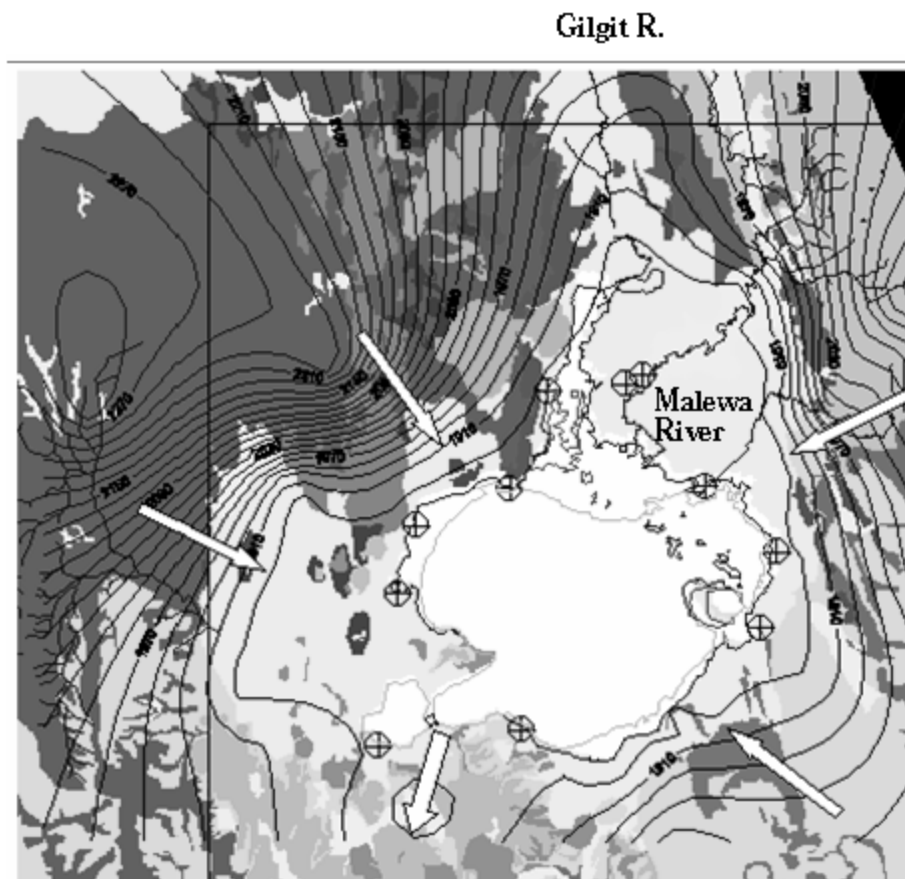


Figure 12-5 Groundwater contours, flow directions around Lake Naivasha, Kenya with surface geology in grey tones.

Source: Becht (pers. comm.)

After that an inventory was made of the expansion of commercial farms using sequential images supplemented by a GPS survey for the latest update, as well as a land use survey, partly based on remotely sensed data. With these maps a survey was made to assess the economic returns for the various crops and these were matched with the

known abstraction rates to calculate the monetary returns per m<sup>3</sup> of water (bar chart of Figure 12.6) and to show the spatial pattern (upper right map of Figure 12.6). Similarly, a map was produced that showed the abstractions per farm.

These documents, whereby remotely sensed data are merged with data from other sources, provide a very useful means for water authorities to plan or execute measures to minimize further drop of the lake level, under consideration of the economic aspects. One option is to reduce water allotment for low value crops.

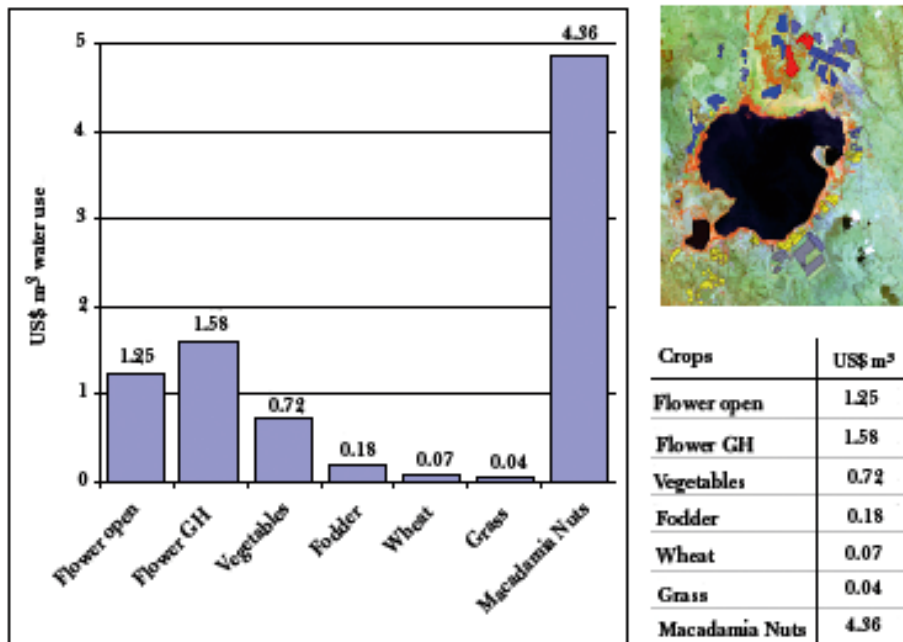


Figure 12-6 Economic return per m<sup>3</sup> for the irrigated crops by commercial farms around Lake Naivasha, Kenya.  
Source: Becht et al., 2006

## 12.5 Pollution of groundwater by urban development

### 12.5.1 Urban development

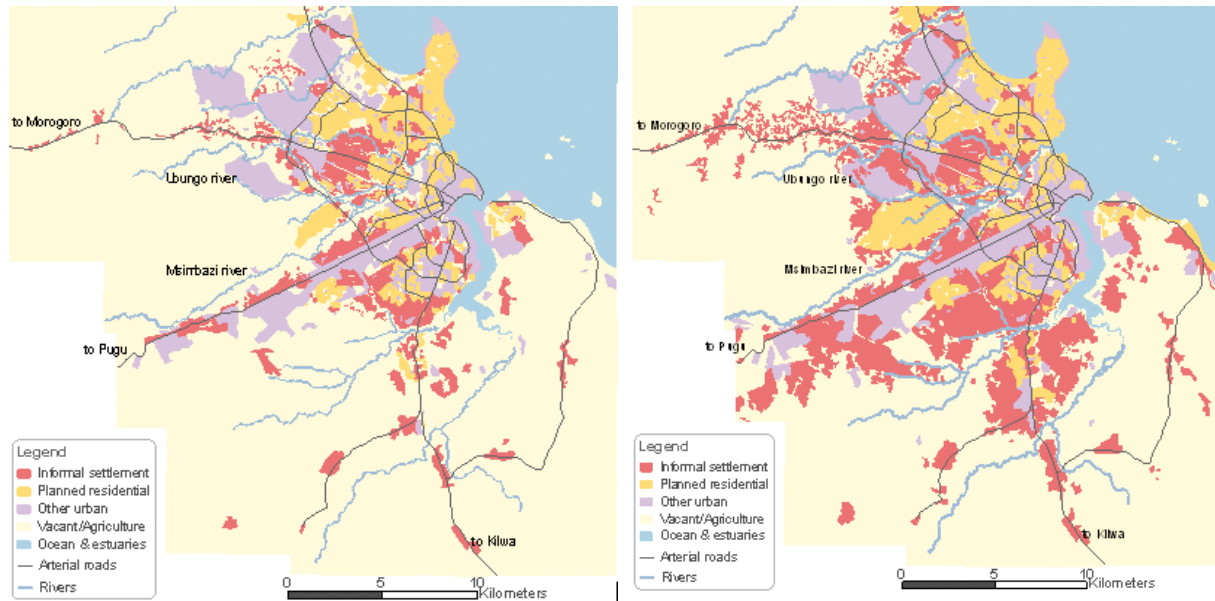
Many of the cities in the developing world have grown during the last decades and will continue to do so. Typical of this rapid development is the lack of sewage systems while household waste and industrial waste is ‘disposed of’ in waste pits and other places in parts of the cities. For a study of the pollution of the groundwater below the urban areas it is important to know the spatial pattern of pollutant load in order to work out remedial measures. In other words, is it possible to estimate the total amount of waste in the waste disposal pits and if so, can the history be traced? The latter is important for understanding changes in contamination records (if existing) and for transient groundwater modelling. The answer to the question is affirmative, but only in an indirect manner.

### 12.5.2 Mapping urban growth

The most accurate, but time consuming method, is to use sequential aerial photography to map the growth of urban areas, because of the high spatial resolution and stereoscopic interpretation for differentiating type of urban land use. However, as explained in Chapter 3 (Geometric Aspects), the interpretations have to be transposed onto the topographic base maps in use, which may require mono-plotting in case of hilly terrain.

However, there may be no sufficient sequential coverage of airphotos, and therefore multi-spectral or panchromatic satellite images can be used to fill the gaps. For the more recent situations the high-resolution (1 to 5 m) satellite images can be used.

As an example, the growth of the city of Dar es Salaam, Tanzania, between 1982 and 1998 compiled from airphotos and satellite images and other sources is shown in Figure 12.7.



**Figure 12-7** Mapping the growth of Dar es Salaam using satellite images and airphotos. Left: 1982, right: 1998.

Source: Sliuzas, 2004

The 1972 Landsat MSS images, also available in digital format, are usually the first satellite images available. The MSS pixel size is 60 by 80 m, which was chosen to comply with the character sizes of the IBM lineprinters of that time as output medium. The resolution and the difficulty of obtaining training sets based on former field truth impede the accuracy of automated classification. Visual interpretation of georeferenced, resampled images (e.g. 80 x 80 m) with edge enhancement filtering will probably give the best results for tracing developments using more recent satellite images.

As no sewage system exists in many of the newer unplanned extensions, the growth was accompanied by pollution of the groundwater below the extensions.

### 12.5.3 Urban land use and spatial pattern of population density

The urban type of land use, such as residential areas with different densities (planned and unplanned), city centres with offices and shops, industrial areas and areas with mixed types of land use have to be known before pollution loading can be assigned to the urban land use categories. Interpretation of airphotos or high-resolution satellite images, preferably in stereo, facilitates the recognition of the urban land use types.

Multi-spectral classification using lower resolution images (20–30 m) is more difficult because the sample sets will show much overlap in the feature space, which is understandable because of the mixed pixel problem, due to mixtures of roofs of different materials, gardens, paved and unpaved roads, bare soil, and so on. However, by compiling good training sets and including probabilistic elements in the classification (Gorte, 2000), reasonable accurate mapping can be achieved. Figure 12.8 shows categories of urban land use based on multi-spectral classification of a SPOT image of the city of Dar es Salaam.

For estimation of pollution loading it is useful also to estimate the spatial pattern of population densities. The latter are, at best, available from census data per city district, but if the average density per urban land use category is known, the multi-spectral map can be transformed into a population density map, whereby calibration is possible through aggregation with a GIS using census data and city districts.

By counting houses per unit area in the various categories on high-resolution images and by applying an average number of inhabitants per house more accurate mapping can be done.

Figure 12.9 shows a small part of an unplanned extension of the city of Dar es Salaam on an airphoto (hand held camera on light aircraft). Various urban land use types were photographed to obtain more accurate information on urban land use types made by multi-spectral classification of the city.

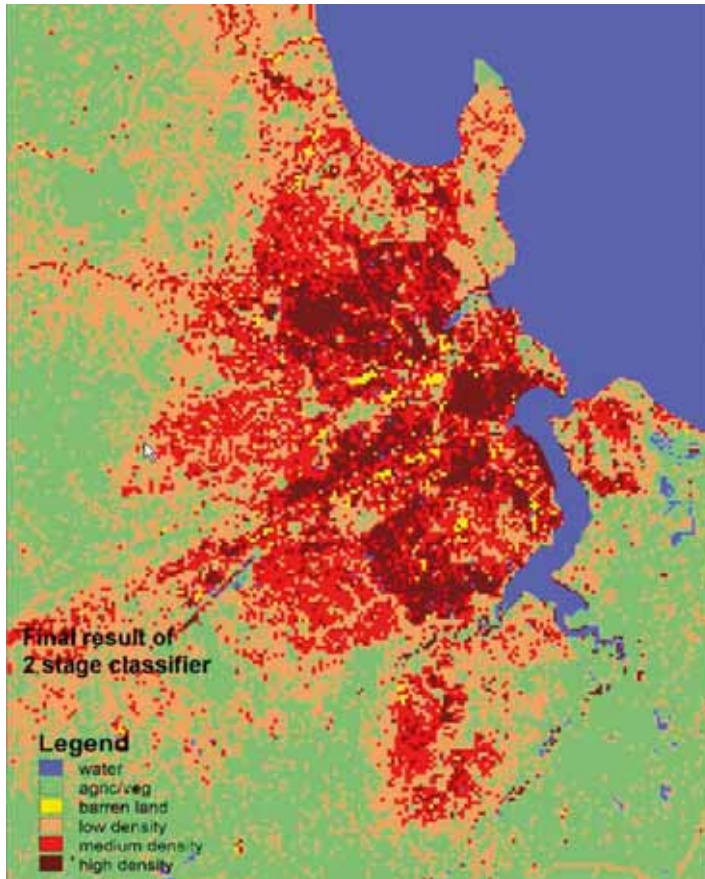


Figure 12-8

Urban land use map based on spectral classification of Dar es Salaam using a SPOT image. Such classifications can be a starting point for estimation of the spatial pattern of pollution loading and can also be used for stratified sampling for more refined estimates, based on large scale images (see Figure 12.9).

Source: Sliuzas, 2004



Figure 12-9

Large-scale airphoto made with hand held camera from light aircraft of part of high density, unplanned extension of Dar es Salaam, Tanzania. Such photos were used for sampling population density and can be used for estimation of the pollution loading to groundwater.

Source: Sliuzas, 2004

With this preparatory work based on remote sensing, the pollution loading can be assigned to the map after the (estimated) average waste disposal per household in the various residential categories is known. For the areas with licensed industries the records at the municipality can be used for assessing the amount and manner of waste disposal. The mapping of industrial areas is of course important because of the non-organic waste produced.

By comparing the map with estimated pollution loading with a map showing the groundwater flow systems, depth of vadose zone and water quality data at sample points – including base flow derived from urban areas, a good overview of the contamination situation is obtained. Furthermore, it will become evident where additional sampling or monitoring of the groundwater quality has to be done.

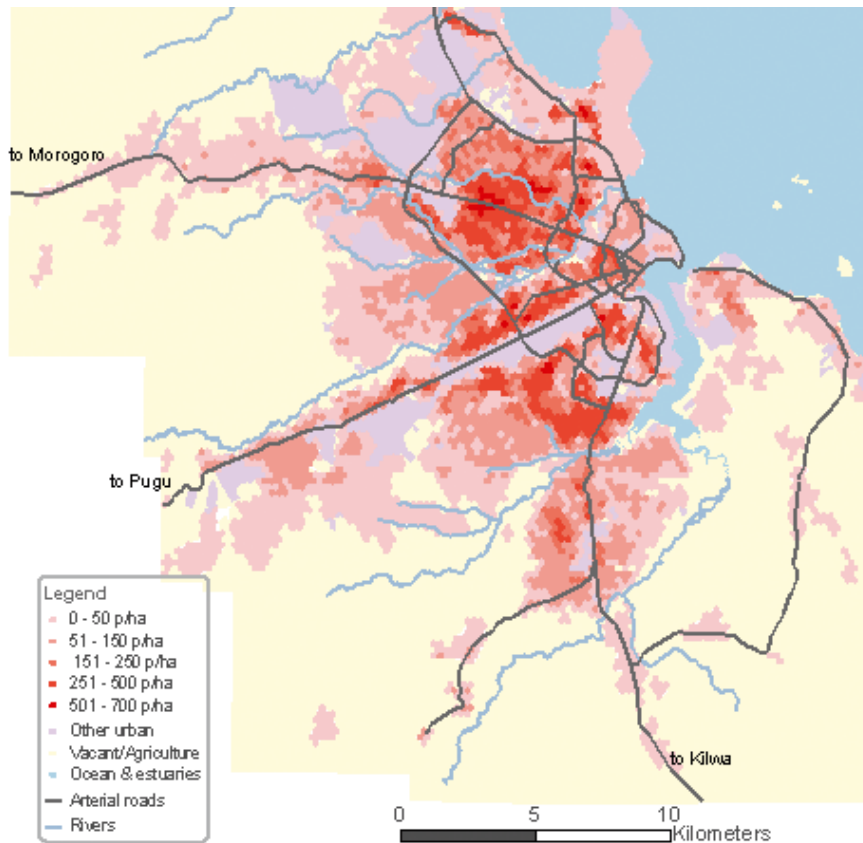


Figure 12-10

Mapping population density using satellite images and large-scale airphotos in sample areas. Such maps can be used for estimating pollution loading in areas where sewage systems are absent.

Source: Amer (in prep.)

## 12.6 Pollution of groundwater by agriculture and vulnerability of groundwater to contamination

### 12.6.1 *Non-point pollution*

The contribution of remote sensing in taking stock of the contaminant load in agricultural lands by agro-chemicals is limited to land use classification. An overview of effect of agriculture on groundwater is given by Vbra and Romijn (1986).

By multi-spectral classification (Chapter 2, Image Processing) a differentiation can be made for fields with perennial crops, such as orchards and plantations, fields where always the same crop is grown, such as rice lands, and fields where crop rotation is practiced. This differentiation is required because for each type different agrochemicals are used. Availability of images at various dates during the cropping season will facilitate the classification and improve accuracy. For example, it may be difficult to classify a crop as rice correctly if only a single image is available, because the spectral signature of the rice crop can be similar to some other land covers. However, the typical sequence of puddling and inundation, young crop, mature crop and harvested rice crop



causes drastic changes in spectral properties and this offers the possibility of identifying the rice crop or other crops by Boolean operators using sequential classification, if the cropping calendar is known.

Irrigated lands should be differentiated from rain fed croplands, because the leaching requirement enhances percolation of agro-chemicals to the groundwater. An NDVI image of the dry season, recorded when rain fed crops have been harvested, will show crops on irrigated lands, if the growing season for irrigated crops is longer than that of rain fed crops. There are of course other indicators for irrigated lands, such as topography and field patterns and fields with relatively low surface temperatures on thermal images.

After agricultural land cover classification the next step is assessment of the type and quantity of agro-chemicals used and to assess their fate in the vadose and saturated zone.

	<i>DRASTIC</i>	<i>Pesticide DRASTIC</i>
Depth to the water table	5	5
Net Recharge	4	4
Aquifer material	3	3
Soil type	2	5
Topography	1	3
Impact of the vadose zone	5	4
Hydraulic Conductivity	3	2

Table 12-2 Weights for DRASTIC factors

Remotely sensed images can be used to assist in the assessment of the vulnerability of groundwater to contamination. The vulnerability may be defined as: ‘The sensitivity of groundwater quality to an imposed contaminant load, which is determined by the intrinsic characteristics of the aquifer’ (van Duijvenbooden and Waegeningh, 1987). Various systems of vulnerability evaluation and ranking have been developed and applied in the past, for example, Aller et al. (1987), Foster (1987) and for carbonate terrain, Daly et al. (2002).

The index of vulnerability of the DRASTIC method (Aller et al., 1987) corresponds to the weighted average of 7 values corresponding to 7 hydrogeological factors, forming the acronym. In Table 12.2 the DRASTIC factors are presented together with the weights respectively for normal DRASTIC applications and for DRASTIC pesticide applications.

A value between 1 and 10 is attributed to each parameter, depending on local conditions. High values correspond to high vulnerability. The attributed values are obtained from tables, which give the correspondence between local hydrogeological characteristics and the parameter value. Next, the local index of vulnerability is computed through multiplication of the value attributed to each parameter by its relative weight, and adding up all seven products. Image interpretation can be helpful in identifying and mapping some of the factors of the method in case of absence of adequate thematic maps.

In some areas indirect information on the depth to the groundwater table can be obtained through remote sensing, particularly when the depth is shallow (see Chapters 5, 7 and 14).

It is difficult to interpret soil type on remotely sensed images, but soil boundaries can be identified through the relationship of soil units and physiography (and lithology). By physiography what is meant here is geomorphology with information from vegetation and land use added. Availability of such interpretation maps speeds up the soil survey.

A digital elevation model (DEM) (Chapter 3, section 3.2), such as SRTM data (Chapter 4, section 4.2) enables mapping of the topographic factor.

It is evident that presence of significant pollution loading and high vulnerability forms a large pollution risk. A limitation of the vulnerability mapping of the DRASTIC approach is that flow of groundwater is not considered, while areas with shallow groundwater tables are usually due to exfiltration of groundwater flow systems where the water originates from surrounding areas with higher elevation.

For karst terrain, remote sensing data – particularly stereo airphotos – information with respect to soil cover,

sinkholes and other solution landforms, presence of (unsaturated) epikarst and occurrence of non-karstic bedrock can be obtained, as is illustrated in the chapter on Limestone Terrain.

### 12.6.2 *Specific point pollution*

Scrutiny of stereo airphotos and high-resolution images can reveal sources of point pollution such as mining dumps and other waste sites. A systematic scrutiny of the images is often the only way to obtain an overview of potential point pollution sources or small areas with concentration of contaminants because records are usually incomplete and illegal dumps may exist.

Van Eeckhout et al. (1996), describe the use of historical aerial photographs and thermal infrared images for studying a waste site.

## 12.7 Groundwater dependent ecosystems, water accounting

In addition to management of productive aquifers, a need for the preservation of groundwater dependent ecosystems is recognized.

Vegetation that is entirely or highly dependent on groundwater usually comprises a small fraction of the total area, but these ecosystems have an importance far in excess of their geographical extent. The need for comprehensive groundwater management plans has been formulated to conserve terrestrial vegetation that survives dry periods by water uptake from deep roots (vadose and saturated zone), ecosystems depending on base flow, transient perched water tables and wetland systems. Hatton and Evans (1998) give a framework for Australia.

Both groundwater level rise and decline cause changes in ecology, including agriculture. In Chapter 7, section 7.3.6, the water logging and salinization problems in Argentina due to increase in rainfall and rise of groundwater level were illustrated by means of sequential images. Such problems also exist in Australia, where the land use change from native vegetation, notably eucalyptus forest, to rangeland and cropland caused a rise in the water table. In other areas, pumping of groundwater led to a lowering of the groundwater surface, with consequences for the base flow in rivers, wetlands and groundwater dependent vegetation.

One of the first important steps in groundwater management at different scales is to take stock of the situation in generally heterogeneous terrain, and to do an analysis of trends.

### 12.7.1 *Taking stock*

The role of remote sensing in the process of making a groundwater management plan is substantial, particularly when no thematic maps of appropriate scale are available or in need of updating:

Satellite data provide DEMs and in addition to elevation, drainage networks, a slope steepness map and slope aspect map can be generated.

Vegetation associations can be classified using multi-spectral data at various scales. Global monitoring of vegetation properties (NDVI) can be readily obtained from the internet so that the seasonal and year-to-year variations can be analysed, in conjunction with (global) data sets of rainfall and temperature, also available on the internet. However, such global data sets have resolutions of > 500 m, hence, gallery forests and other vegetation associations related to local groundwater occurrences need to be studied with the aid of medium-to-large resolution systems.

Heterogeneous terrain in terms of geomorphology and geology with varied vegetation can be differentiated into hydrogeological terrain units that contain also the soil distribution (see the discussion in Chapter 10, sections 10.2 and 10.11). Such mapping should be supported by GIS operations, and some of the units can be derived by GIS operations using digitized geology, DEM data and, in some cases, multi-spectral land cover classification.

The comparison of vegetation cover with terrain units provides a first and preliminary overview of groundwater dependents ecosystems, and diagnostic elements can be used, to name a few:

- disappearance and density of gallery forests on alluvium indicate conditions where streams are losing their water to the surrounding aquifer
- the reverse situation suggests emergence of groundwater

- vegetation fringes along breaks of slope could be related to exfiltration areas of local groundwater systems
- lines of vegetation along the contour on slopes may point to perched groundwater, particularly in low dipping strata that contain permeable layers
- lineaments or incised local valleys with vegetation, in contrast to sparse vegetation on interfluves, suggest presence of groundwater
- broad valley bottoms with a grass-herbaceous cover surrounded by interfluves with savannah or forest cover indicate shallow groundwater table in the valley bottom, at least seasonally
- typical meandering rivers (i.e. their geometric parameters adhere to power laws) are associated with perennial river flow, having less fluctuation in discharge than braiding rivers or most other river types
- decreasing widths of ephemeral river beds in semi-arid areas in the upper part of an alluvial fans indicate that the groundwater level is well below the surface, but a pattern of small sinuous rivers and vegetation response on the lower alluvial fan signifies a shallow groundwater level.

During the course of hydrologic field investigations in a given area, such diagnostic aspects can be established, especially with the support of hydrometric data, and used for extrapolation on the basis of image interpretation.

By combining processed data derived from various sensors (multi-spectral, thermal, radar backscatter and radar-based DEMs and possibly gamma-ray images) with hydrometric data in a GIS, the hydrogeological situation can be shown in the form of maps, which form basic documents for management actions. Münch and Conrad (2007) used Landsat TM images of different times (winter rainfall, after wet year, end of dry season) and aerial photographs to classify vegetation and compared these with topographic factors (depressions, slope steepness, flow accumulation and relative slope position) and the estimates groundwater depth. The latter was prepared with the DEM and point level data, using Bayesian kriging, justified because of good correlation between topographic elevations and the phreatic levels.

Tweed et al. (2007) followed a somewhat similar approach, as mentioned in Chapter 3, section 3.6.

### ***12.7.2 Study of trends using sequential images***

Land cover change affects the land hydrologic cycle of which groundwater is a component. Old images (aerial photos, Landsat MSS, etc.) are often the only source to map the land cover at early times and trends in land cover change using sequential series of images may be compared with existing long-term hydrometric data. As mentioned above, for a productive aquifer the trend in acreage irrigated by groundwater will be related to a trend in the piezometric level.

Even when no hydrometric data exists, sequential images may be used in some specific cases to estimate variations in groundwater discharges as the example of the Amboseli springs in Kenya illustrates (Chapter 14).

Changes in areas with phreatophyte vegetation are an indication of changes in groundwater; a decrease of area and vegetation density not due to cutting indicates lowering of the table and vice versa. However, salinization due to an increase of the groundwater level affects the density and is accompanied by change of species. The recognition and mapping of species and their associations requires large-scale images, and high-resolution multi-spectral satellite images of recent date. For the former situation only airphotos are usually available and for species recognition these should be of large scale (1: 20,000 or less) as discussed in Chapter 14.

The hydrologic implication of general land cover changes is usually limited to qualitative assessment based on empirical rules. Nearly everywhere a change of native vegetation cover to cropland increases surface runoff, hence, less water is available for infiltration and recharge, unless effective soil and water conservation measures have been taken. Forests use more water than grass (Bosch and Hewlitt, 1984) and deforestation may be associated with a rise in the groundwater table, as the Australian experience has shown. However, for tropical areas, the relation between deforestation and base flow is not clear (Bruynzeel, 1990) and the net effect of land cover changes on groundwater may not be known because of lack of local empirical data.

### ***12.7.3 Water accounting***

The art of water accounting is to classify water balance components into water use categories that reflect the consequences of human interventions in the hydrologic cycle (Molden, 1997). Groundwater management plans, especially those at river basin scale, may benefit from water accounting, namely the use of groundwater by the variety of land covers, including natural and semi-natural vegetation, rain fed crops and irrigated crops. The ability to esti-

mate actual evapotranspiration (ET<sub>a</sub>) by satellite data offers the possibility to obtain such estimates. A time series of satellite images is required to aggregate ET<sub>a</sub> values over monthly, seasonal or yearly periods as well as a multi-spectral classification of the land cover. An example for a semi-arid area in Kenya is provided by Farah (1991). Coupling this to a map with groundwater depths allows an appraisal of water use from the vadose and saturated zones.

If areas with phreatophyte vegetation have been identified, it is possible to compare their water use with vegetation deriving moisture mainly from the vadose zone; this aspect is of importance for a groundwater management plan. Although contrasting evidence exists of the accuracy of the SatSEB method in heterogeneous terrain under dry conditions, at least the patterns generated are of interest.

When combined with rainfall, a map showing water surplus and deficit on a pixel basis can be made with implications for recharge, as discussed in Chapter 14.

## 12.8 Summary and conclusions

Groundwater management covers many fields, ranging from the socio-economic domain to the bio-physical domain. For some fields remote sensing contributes to the provision of data and in a few cases decisions can be made on the basis of image data.

In semi-arid hard rock regions where groundwater is limited in quantity because it occurs in fractured rocks and the weathered zone, there is a risk of over-exploitation of groundwater for irrigation. Determining the actual proportion of the land under such irrigation using satellite images and making some simple water budget calculations, can give some indication of whether or not there is scope for further development of the groundwater resource.

For many aquifers there is no or non-reliable data concerning the actual amount of water pumped. This can be estimated using remote sensing in two ways; the first consists of the determination of acreages under irrigation and the crop types using multi-spectral images and application of empirical crop water use factors. The second is to calculate the actual evaporation with the surface energy balance method based on satellite data. The actual evapotranspiration is the amount of groundwater lost from the aquifer. The historical development of irrigated acreage of an aquifer can be estimated by using a time series of satellite images starting in the early 1970s and the trend can be compared with the trend in groundwater levels.

Systems have been developed for practical management of groundwater based on satellite data. Such systems, embedded in GIS allow the manager to query for those farmers who have used more water than their permit allows and to locate the culprits.

By combining satellite data, GIS functions and agricultural production data, information can be offered to decision makers for selecting management options, as the case concerning the groundwater use by commercial farms around a Ramsar lake demonstrates.

Satellite images are a unique source for estimating pollution loading of groundwater in the rapidly expanding cities with unplanned extensions, although in an indirect manner. Multi-spectral classification of urban land use can be made after which pollution values are assigned to the categories. Trends in urban growth can be established by using historical images. The information thus obtained should be compared with hydrochemical field data. In a similar fashion images can be used for agricultural non-point pollution. High-resolution images and thermal data have been used for locating point pollution.

Traditionally, management of groundwater in productive aquifers consisted of attempting to limit drafts to the 'safe yield', that is, the long-term recharge of groundwater. Nowadays, it is realized that a more comprehensive approach has to be adopted and groundwater is studied in its full spatial pattern to establish links between recharge areas, exploitation areas and outflow of groundwater in rivers. The studies of groundwater dependent ecosystems and the development of the water accounting approach are a sign of this awareness and remote sensing data provides much of the spatial data needed to take stock of the situation. The ability to calculate the patterns of actual evaporation based on satellite data is a step forward in this endeavour.

Relationships between vegetation and groundwater are discussed in Chapter 14, and a separate chapter (Chapter 13) is devoted to the important subject of managed aquifer recharge in semi-arid areas.

## References

- Ahmad, M.D., Bastiaanssen, W.G.M. and Feddes, R.A. 2002. Sustainable use of groundwater for irrigation: a numerical analysis of subsoil water flux, *Irrigation and Drainage* 51(3), pp. 227–41
- Anon. 1999. Application of Space Techniques for the Integrated Management of a River Basin Water Resources (ASTIMwR). Final Report, January 1999, European Commission, Direct. Gen. XII, Centre for Earth Observation, IVth Framework ENVA-CT 96-0366.
- Allen, R.G., Pereira, L.S., Raes, D. and Smith, M. 1998. Crop evapotranspiration. Guidelines for computing crop water requirements. FAO Irrigation and Drainage Paper No. 56. FAO, Rome.
- Aller, L., Bennet, T., Lehr, J.H. and Petty, R.J. 1987. DRASTIC: a standardized system for evaluating groundwater pollution potential using hydrogeological settings, US EPA Report 600/2-85/018.
- Bastiaanssen, W.G.M., Menenti, M., Feddes, R.A. and Holtslag, A.A.M. 1998. A remote sensing surface energy balance equation for land (SEBAL). 1. Formulation. *Journal of Hydrology*, Vols. 212–13, pp. 198–212.
- Bastiaanssen, W.G.M., Pelgrum, H., Wang, J., Ma, Y., Moreno, J.F., Roerink, G.J. and van der Wal, T. 1998. A remote sensing surface energy balance equation for land (SEBAL). 2. Validation. *Journal of Hydrology*, Vols. 212–13, pp. 213–29.
- Becht, R. and Harper, D.M. 2002. Towards understanding of human impact upon the hydrology of Lake Naivasha, Kenya. *Hydrobiologia*, Vol. 488(1-3), pp. 1–11.
- Becht, R., Odada, E.O. and Higgings, S. 2006. Lake Naivasha experience and lesson learned brief. Management of lakes and their basins for sustained use; Lake Basin Managers and Stakeholders: Intern. Lake Env. Comm. Found., Kusatsu, Japan, pp. 277–89. [www.ilec.or.jp/Ibmi2/reports/17\\_Lake Naivasha\\_27February2006.pdf](http://www.ilec.or.jp/Ibmi2/reports/17_Lake_Naivasha_27February2006.pdf)
- Bosch, J.M. and Hewlett, J.D. 1982. A Review of Catchment Experiments to Determine the Effect of Vegetation Changes on Water Yield and Evapotranspiration. *Journal of Hydrology*, Vol. 55(1–4), pp. 3–23.
- Bruynzeel, L.A. 1990. Hydrology of moist tropical forests and effects of conversion: a state of knowledge review. UNESCO/ITC/LAHS/Free University, Amsterdam.
- Daly, D., Dassargues, A., Drew, D., Dunne, S., Goldscheider, H., Neale, S., Popescu, J. and Zwahlen, F. 2002. Main concepts of the ‘European approach’ to karst-groundwater vulnerability assessment and mapping. *Hydrogeology Journal*, Vol. 10(2), pp. 340–45.
- Duijvenbooden, W. van and Waegeningh, H.G. van. 1987. Vulnerability of Soil and Groundwater to Pollutants, Proceedings and Information No. 38 of the International Conference held in the Netherlands, in 1987, TNO Committee on Hydrological Research, Delft, The Netherlands.
- Eeckhout van, E., Pope, P., Rofer, C., Becker, N. and Wells, B. 1996. Environmental waster site characterization utilizing aerial photographs and satellite imagery: Three sites in New Mexico, USA. XVII ISPRS Congress, Vienna July 1996. Comm. VII, Working Group I and <http://www.lanl.gov/source/orgs/d/d4/energy/docs/96-1172.pdf>.
- Farifteh, J., Farshad, A. and George, R.J. 2006. Assessing salt-affected soils using remote sensing, solute modelling and geophysics. *Geoderma*, 130, pp. 191–206
- Foster, S.S.D. 1987. Fundamental concepts in aquifer vulnerability, pollution risk and protection strategy, in W. van Duijvenbooden and H.G. van Waegeningh (eds), Vulnerability of Soil and Groundwater to Pollution, Proceedings and Information No. 38 of the International Conference held in the Netherlands, TNO Committee on Hydrological Research, Delft, The Netherlands.
- Foppen, J.A.W. 1996. Evaluation of the effects of groundwater use on groundwater availability in the Sana’a Basin. SAWAS Techn. Rep. No. 5, Volume II: Data Availability. National Water and Sanitation Authority, Sana’a, Yemen & TNO, The Netherlands.
- Gieske, A.S.M. and Meyniger, W. 2005. High density NOAA time series of ET in Gediz, Turkey. *Irrigation and Drainage Systems* 19, pp. 285–99
- Gorte, B.G.H. 2000. Land-use and catchment characteristics. G.A. Schultz and E.T. Engman (eds) *Remote Sensing in Hydrology and Water Management*, Springer Verlag, pp. 133–56.
- Hatton, T and Evans, R. 1998. Dependence of ecosystems on groundwater and its significance to Australia. Occasional Paper No 12/98, Land and Water Resources Research and Development Corporation, CSIRO Australia. [www.lwa.gov.au/downloads/publications\\_pdf/PR980270.pdf](http://www.lwa.gov.au/downloads/publications_pdf/PR980270.pdf)
- Hess, L.L., Melack, J.M., Filoso, S. and Wang, Y. 1995. Delineation of inundated area and vegetation along the

- Amazon floodplain with the SIR-C synthetic aperture radar. *IEEE Transac. Geoscience Remote Sensing*, 33, pp. 896–904.
- Hydrogeology Journal*. 2006, Vol.14 (3). Social and Economic Aspects of Groundwater Governance. Special Issue.
- Israel M, Mufid-al-hadithi, Singhal D.C. and Bhism K. 2006. Groundwater recharge using a surface electrical resistivity method in the Himalayan foothill region, India. *Hydrogeology Journal*, Vol. 14 (1-2):44-50.
- IWMI. The socio-ecology of groundwater in India. IWMI Water Policy Brief. [www.iwmi.cgiar.org](http://www.iwmi.cgiar.org).
- Kasische, E.S., Melack, J.M. and Bobson, M.C. 1997. The use of imaging radars for ecological applications – a review. *Remote Sensing of the Environment*, 59, pp. 141–56.
- Leblanc, M, Leduc, C., Razack, M, Lemoalle, J., Dagerne, D., Mofor, L., Servat, E., Wadji, N., Christian, L. and Ahmed, S. 2003. Applications of remote sensing and GIS for groundwater modeling of large semi-arid area: example of Lake Chad basin, Africa. IAHS Publ. No.278:186-192. Hydrology of Mediterranean and semi-arid regions, Montpellier 1–4 April.
- Maréchal, J.C., Galeazzi, L, Dewandel, B. and Ahmed, S., 2003. Importance of irrigation return flow on the groundwater budget of a rural basin in India. IAHS Publ. No. 278, pp. 62–67. Hydrology of Mediterranean and semi-arid regions, Montpellier 1-4 April.
- Meijerink, A.M.J., Gieske, A.S.M. and Vekerdy, Z. 2005. Surface energy balance using satellite data for the water balance of a traditional irrigation-wetland system in SW Iran. *Irrigation and Drainage Systems*, Vol. 19, pp. 89–105.
- Metternicht, E.J. and Zinck, J.A. 2003. Remote Sensing of soil salinity: potentials and constraints. *Remote Sensing of the Environment*, 85 (1.25), pp. 1–20.
- Molden, D. 1997. Accounting for water uses and productivity. SWIM Paper 1. IIMI, Colombo, Sri Lanka.
- Muhamed, Y.A., Savenije, H.H.G., Bastiaanssen, W.G.M. and van der Hurk, B.J.J.M. 2005. New lesson on the Sudd hydrology learned from remote sensing and climate modeling. *Hydrol. Earth Science Discussions*, 2, pp. 1503–35. Europ. Geosciences Union, and: [www.copernicus.org/EGU/hess/hessd/2/1503/hessd-2-1503\\_p.pdf](http://www.copernicus.org/EGU/hess/hessd/2/1503/hessd-2-1503_p.pdf).
- Munch, Z. and Conrad, J. 2007. Remote sensing and GIS based determination of groundwater dependent ecosystems in the Western Cape, South Africa. *Hydrogeology Journal*, Vol. 15(1), pp. 19–28.
- Paulsson, B. 1992. Urban applications of satellite remote sensing and GIS analysis. World Bank, Urban Management Program (UMP).
- Pope, K.D., Rejmankova, E. and Paris, J.F. 2001. Spaceborn imaging radar-C (SIR-C) observations of groundwater discharge and wetlands associated with the Chicxolub impact crater, northwestern Yucatan Peninsula, Mexico. *Bull. Geol. Soc. of America*, Vol. 113(3), pp. 403–16.
- Premananth, K.L.L. and Liyanapatabendi, T. 1994. Groundwater depletion due to agrowells. 20th WEDC Conference.
- Shah, T, Molden, D., Shaktivadel, R. and Seckler, D. 2000. The global groundwater situation; Overview of opportunities and challenges. IWMI, Colombo, Sri Lanka.
- Sliuzas, R.V. 2004. Managing informal settlements: a study using geo-information in Dar es Salaam, Tanzania. ITC Dissertation no. 112, 309 pp.
- Sophocleous, M.A. 2000. From safe yield to sustainable development of water resources – the Kansas experience. *Journal of Hydrology*, Vol. 235(1-2), pp. 27–43.
- Sophocleous, M.A. 2002. Interactions between groundwater and surface water: the state of science, *Hydrogeology Journal*, Vol. 10, pp. 52–67.
- Travaglia, C. and Macintosh, H. 1997. Wetlands monitoring by ERS-SAR data: A case study: Lake Bangweulu wetland system, Zambia. RSC Series 69, FAO, Rome.
- Tweed, S.O., Leblanc, M., Webb, J.A. and Lubczynski, M.W. 2007. Remote sensing and GIS for mapping groundwater recharge and discharge areas in salinity prone catchments, southeastern Australia. *Hydrogeology Journal*, 15(1), pp. 75–96.
- Vbra, J. and Romijn, E. 1986. Impact of agricultural activities on groundwater. *International Contributions to Hydrogeology*, No. 5, Balkema Publ. Dordrecht, Netherlands.
- Winter, T.C., Harvey, J.W., Franke, O.L. and Alley, W.M. 1999. Ground water and surface water: a single resource. US Geological Survey Circular No. 1139, Denver, Colorado.

# Site selection for managed aquifer recharge

## 13.1 Introduction

### 13.1.1 Artificial recharge

The augmentation of the groundwater resource by artificial recharge is an important groundwater management aspect in semi-arid regions, where water is a scarce commodity and where many aquifers have declining groundwater levels. Therefore artificial recharge schemes have been constructed in many countries and many more will be needed. Managed Aquifer Recharge (MAR) has many bio-physical and socio-economic aspects. This text concentrates on the use of remote sensing for site selection for a few types of schemes.

Managed aquifer recharge can be described as the recharge of groundwater induced by man through constructions for ponding runoff, be it channel flow or sheetwash. A great variety of types of artificial recharge schemes exist.

Some traditional systems, such as the spate irrigation system of Yemen and other countries, may contribute to recharge although their primary function is soil moisture storage. Similarly the thousands of shallow reservoirs (tanks) in the valleys of hard rock terrain of, for example, India and Sri Lanka, used for gravity surface irrigation, recharge groundwater in valleys.

The present systems may consist of trenches and low earth dams with or without spillways requiring relatively low initial investment to sophisticated systems with inflatable diversion dams, gravel filled infiltration trenches, treatment facilities of inflow water and so on.

For artificial recharge a large number of aspects have to be considered, such as the quantity and quality of the water available for recharge, the properties of the soil, vadose zone and aquifer, hydraulic engineering consideration, maintenance of systems and socio-economic considerations.

These aspects have been discussed by, for example, Huisman and Oltshoorn (1983), Bouwer (2002) and in the proceedings of international recharge symposia that were held in California in 1988 and in Florida in 1994 (American Society of Civil Engineers, Reston, Virginia, US), in Amsterdam (Peters, 1998) and Adelaide (Dillon, 2002), see [www.iah.org/recharge](http://www.iah.org/recharge). Furthermore the Hydrogeology Journal devoted a special issue to artificial recharge (Vol. 10, No. 1, February 2002), and the Proceedings of the ISMAR 2005 symposium in Berlin have been distributed by UNESCO (2005).

Gale et al. (2006) give an overview of schemes in India, their performance and socio-economic aspects. Saraf and Chaudhury (1998) discuss some examples whereby remote sensing data is integrated in a GIS for groundwater exploration in general but also site selection for artificial recharge.

This text is limited to a discussion and illustration of how remotely sensed images can make a contribution to selecting potentially suitable places for two categories of artificial recharge schemes:

- Ponding of runoff within the drainage system itself
- Diversion of ephemeral runoff into ponding basins; flood-spreading.

The first category is based on retardation of runoff by way of weirs and small dams or sand storage dams in the channels. The second category is of interest because of the substantial quantities of water that can be made to infiltrate by diversion of stream runoff and in particular the runoff from flash floods in semi arid regions, also known as flood water harvesting.

The ephemeral runoff is usually lost into the sea, playas or desert plains and is a source of water to supplement the groundwater resource, which is usually over-exploited in drier regions.

Catchments that range in size from a few tens of km<sup>2</sup> to a few hundred km<sup>2</sup> are typical of catchments that generate sufficient amounts of episodic runoff and where peak flow is not so large as to make intake structures very expensive, possibly prohibitively so. There are a great many such smaller catchments and usually runoff and other

data are lacking or scanty. The problem is how to select the best area and site in a given region for a flood-spreading scheme.

Because of the many factors to be considered, screening of all areas is needed to select the most promising areas for field investigation. An attempt is made here to describe and illustrate how remote sensing can assist in the screening process, at reconnaissance level. The text relies heavily on examples from Iran, where many of such schemes have been constructed.

Water from perennial rivers is also diverted for artificial recharge, but such schemes are usually in regions where a number of data sources exist and the role of remote sensing is more limited than is the case for the numerous potential sites for flood-spreading in data scarce regions.

In the effort to augment groundwater resources to sustain irrigated agriculture or drinking water supplies, it may be remarked that flood-spreading schemes can have important collateral benefits for flood damage mitigation, thereby enhancing the economic benefits.

### 13.1.2 Some economic considerations

Keller et al. (2000) discuss the various forms of storage of water. They consider groundwater storage as having high conservation potential, operational flexibility and reliability, but low adequacy because of the limited amount of water stored during the lifetime of a recharge scheme in comparison to storage of surface water in a large reservoir. On a worldwide basis, large dams have comparatively low costs per 1,000 m<sup>3</sup> stored: up to US\$ 32 against US\$ 110 for small- and medium-sized dams. Data from Gleich (1993) put the costs of artificial groundwater recharge per 1,000 m<sup>3</sup> at US\$ 190 for low storage schemes and US\$ 230 for high storage schemes.

In a later study by Kheirkhah (2005) for a flood-spreading site in Iran at Chandab, construction and maintenance costs, including desilting— valid for Iranian conditions – of a flood-spreading scheme amounted to some € 80 per 1,000 m<sup>3</sup> for a low storage canal cum overflow basin type of scheme (explained below), to €106 for a large scheme of the same type. Calculations, with simplification, were made for a lifetime of all schemes of 50 years. For the deep basin type with large storage at the same site the costs were around €105, see Table 13.1. Site 1 pertains to an infiltration area in the upper fan, in two parts; Site 2 is a larger area extending in a downslope direction, also in two parts.

The Chandab site was selected out of several other sites in the vicinity after screening. This is because of many favourable conditions considered in a DSS analysis, which used a spatial extension of the Analytical Hierarchy Process (mentioned below) as part of the multi-criteria decision-making.

Scheme type		Main criterion		Total costs	Main criterion		Life-time (years)	Cost per m <sup>3</sup> water (€)	
		Costs (€1,000)			Benefits			Without flood mitigation benefit	Considering flood mitigation benefit
		Sub-criterion	Sub-criterion		Sub-criterion	Sub-criterion			
Canal and Basin	Deep Basin Type Site	Construction	Maintenance	Harvested water (1,000 m <sup>3</sup> )	Flood mitigation (€1,000)				
Site I, Part 1		114	394	508	6,321	0	45	0.0803	0.0803
Site I, Part 2		124	381	505	5,087	0	37	0.0993	0.0993
Site II		267	1,004	1,272	10,227	0	50	0.1244	0.1244
Site I, Part 1+ Part 2		238	775	1,013	11,408	1,254	37-45	0.0888	-0.0211
Site I + Site II		505	1,780	2,285	21,635	2,312	37-50	0.1056	-0.0012
Deep Basin Scheme		981	2,032	3,013	28,606	3,922	50 >	0.1053	-0.0318

**Table 13-1** Estimates of costs and benefits for all alternative schemes in Chandab area, Iran, with end and without reduced flood damages in the area downstream of the recharge site. Source: Kheirkhah, 2005.



A cost-benefit analysis was also made for the Chandab area, considering a main benefit – namely flood mitigation; this was because frequent damage from floodwaters and sediment occurred in the lower alluvial area. The scheme was designed for diversion of large discharges, as shown in Table 13.1; in doing so, the cost per cubic m of water was strongly reduced.

## 13.2 Recharge schemes based on ponding of runoff within the drainage system

The basic idea of this type of managed aquifer recharge is the retardation and ponding of runoff behind check dams (if the discharges are relatively small), weirs or sand storage dams in sandy or gravely river beds. High flows spill over the weir or dam and prevent sedimentation of clays and silts, so that the ponded water can percolate to shallow alluvial aquifers or into the weathered or fractured zone, with minimal evaporation loss. In the case of sand dams, the intention is to let sand accumulate upstream of the dam to increase the storage volume; also the dam may be heightened from time to time.

Another possibility is the construction of small reservoirs in the watershed with the objective of letting water infiltrate below the reservoir or releasing water into the riverbed downstream of the dam in a gradual manner. The disadvantages of small reservoirs are (1) the high evaporation losses and reduced infiltration due to clay accumulation, despite the greater water depth than is the case with sand storage dams or with weirs and (2) the substantial costs.

Potential sites for these and other schemes can be selected on the basis of image interpretation.

River width can be determined and may differ from what is shown on topographic maps. The river stability can be determined using sequential images – usually old aerial photographs (or topomaps) and recent satellite imagery. From the pattern of shifts, sites that are stable in plan can be selected, to avoid the expense of river training.

Presence and extent of phreatic alluvial aquifers adjoining the river can be determined on images. Relatively thin alluvium, say 10 to 20 m thickness, of limited extent is important for groundwater occurrence and may support irrigated agriculture, but is often not shown adequately on geologic maps. The images can also be inspected for presence of outcrops in riverbeds bordered by alluvium. If outcrops are found, the alluvial cover is not much deeper than the elevation of the outcrops, but deeper regolith may be present in fractured zones.

Inspection of the channel shape and banks, preferably using stereo airphotos, gives indirect information on the permeability of the deposits. Channels in cohesive (clay rich) material tend to have a smaller width-to-depth ratio than channels in non-cohesive (sand, gravel) deposits.

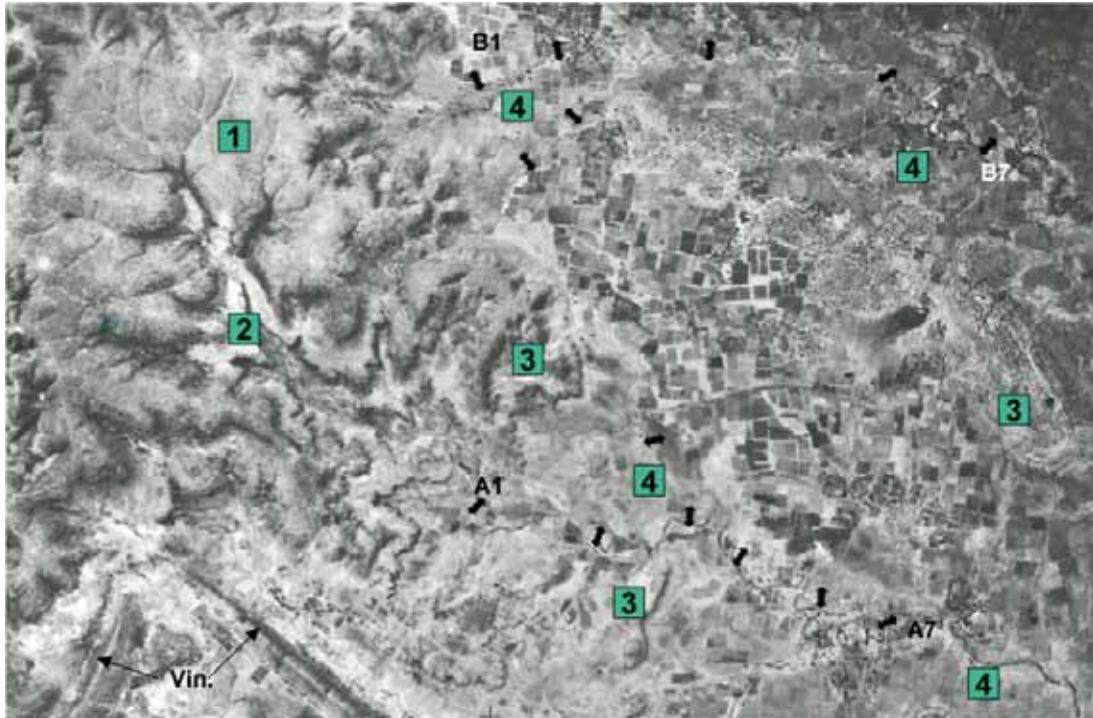
In hard rock terrain, alluvium may overlie weathered or fractured rocks. By recharging the alluvium the fractured zone will also be recharged. Lineament pattern and density in the rocks adjoining the river or alluvial belt can be studied on images (see Chapter 10). It can be assumed that the lineament characteristics occur below the alluvium; possibly the density may be somewhat higher because valleys tend to be formed in areas of weakness due to higher joint and fracture densities. Of particular interest are large lineaments that may cross the alluvium because locating a weir just downstream of such a lineament is helpful in recharging the fractured zone formed by the lineament.

It is quite important to identify on images the extent of agricultural lands, which benefit from groundwater irrigation. As mentioned in chapters 2 and 12, stock can be taken of the acreage and location of irrigated fields by using an NDVI image of the growing season some weeks after the rainy period is over. By taking crop water use factors, an estimate of the total drafts can be made with a repercussion on setting priorities for artificial recharge.

### *Example: Recharge in small catchments on flood basalts, India*

Two small catchments or watersheds (A and B) are shown on a high resolution panchromatic image of central India, Figure 13.1, which details four flat lying Deccan trap flows (numbers in boxes) overlaying folded quartzite and slate of the Vindhyan Formation (Vin). The low-lying areas with the cultivated fields (some are irrigated by groundwater, small parcels, some trees present) are of interest. Soils are rich in clay (black cotton soil or vertisol) and recharge takes place mainly at the onset of rains when the deep cracks are open. The cracks close when the soil is wet and infiltration then is very low.

The wells, many of them wide-diameter open wells, have low yields and derive water mainly by fracture flow.



**Figure 13-1** Example of small watersheds in Deccan Trap country, showing possible locations (A1-7, B1-7) of weirs or low dams to recharge groundwater near locations with agricultural and irrigated fields. Deccan trap flows (nos 1 to 4) overly quartzite and slate of the Vindhyan Formation. Flow no. 4 is weathered. Groundwater occurs mainly in fractures and in vesicular basalt, as was observed in open wells in the field. High resolution panchromatic image. Distance E-W is 10 km.

The groundwater table is shallow (2 to 8 m) in the weathered area of flow 4 and the rivers of catchment A and B have base flow in the downstream part at the time the image was taken. It is difficult to detect fractures in the weathered area (flow 4), but fractures can be seen in the upper area of flow 1.

An artificial recharge scheme could consist of ponding surface runoff at locations in the vicinity of agricultural fields and particularly where irrigation is present. In both catchments possible locations (A1 to A7, B1 to B7) have been indicated. Monsoon showers can generate much runoff, therefore the weirs or low dams have to be strong. The idea is that by retardation of the flow and some ponding, the water recharges the fracture system, as was shown in some other areas in Deccan Trap country in India by the Central Groundwater Board of India.

The drainage network, presence of thick soils, agricultural fields and irrigated areas are shown in a synoptic view offered by the image.

#### *Example: Artificial recharge in larger semi-arid catchment*

The next example from Gujarat, western India, shows an area where at places permeable alluvial aquifers of limited depth are found adjoining larger ephemeral rivers with wide sandy beds. In order to augment recharge of the shallow aquifers, weirs and sand dams can be constructed (as was done in the AGRAR project). Some potential sites have been indicated in the Figure 13.2, which is a TM false colour with edge enhancement for all 3 bands (TM 5, 3 and 1). Some locations are chosen at upstream parts of alluvial areas with irrigated fields; two locations are along the contact zone of the granite and the metamorphic rocks. At one location a large fracture seems to cross the river, as indicated.

## 13.3 Recharge schemes based on diversion of flash flows

### *13.3.1 Flood-spreading schemes: Concepts and types*

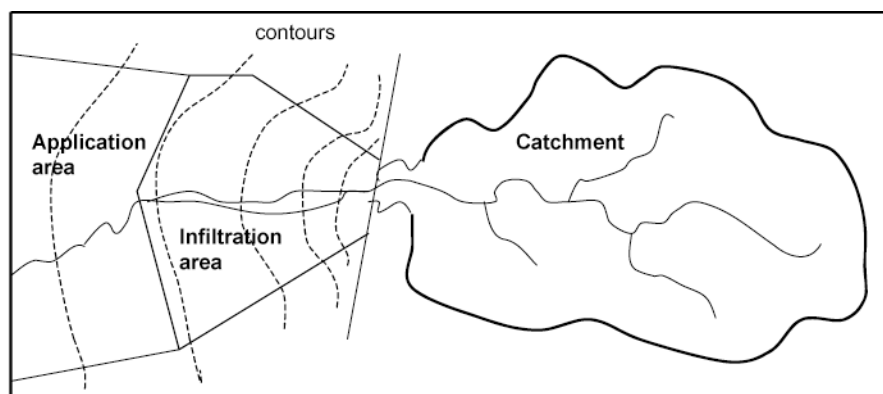
First, a few concepts should be mentioned.



**Figure 13-2** Dhamni River in north Gujarat, India, with possible recharge sites for weirs or sand dams (black arrows). All. = alluvium, (c) = contact zone metamorphics and granites. White arrow indicates site on lineament (fracture, F). Sites and alternatives need to be checked in the field. Distance E-W is 14 km. Landsat ETM+ image

The ‘catchment’ refers to the topographic catchment (or river basin) upstream of the point of artificial diversion (intake), as shown in Figure 13.3. Runoff will increase with increasing catchment area.

The ‘infiltration area’ is the permeable terrain close to the ephemeral river to which flash floods are diverted by way of an intake or diversion structure for infiltration and percolation to the groundwater body in an aquifer.



**Figure 13-3** Sketch showing the functional areas

There can be a transitional area between the catchment outlet and suitable places for the intakes, as is the case on many alluvial fans. The diversion of floodwater of ephemeral rivers needs an intake structure that feeds the conveyance canal, which has normally a capacity that is much less than the peak flow in the ephemeral riverbed. In

other words, only a part of the flood flow can be diverted per intake, but more intakes along the river are possible. The size of the infiltration area depends on the capacity of the conveyance canals and the infiltration properties of the infiltration area.

The 'application area' is the area, which benefits from the artificial recharge. It is usually the agricultural area downstream of the recharge scheme, irrigated by groundwater of the recharged aquifer or could be a remote location in case the water is used for drinking water.

### *Types of flood-spreading schemes*

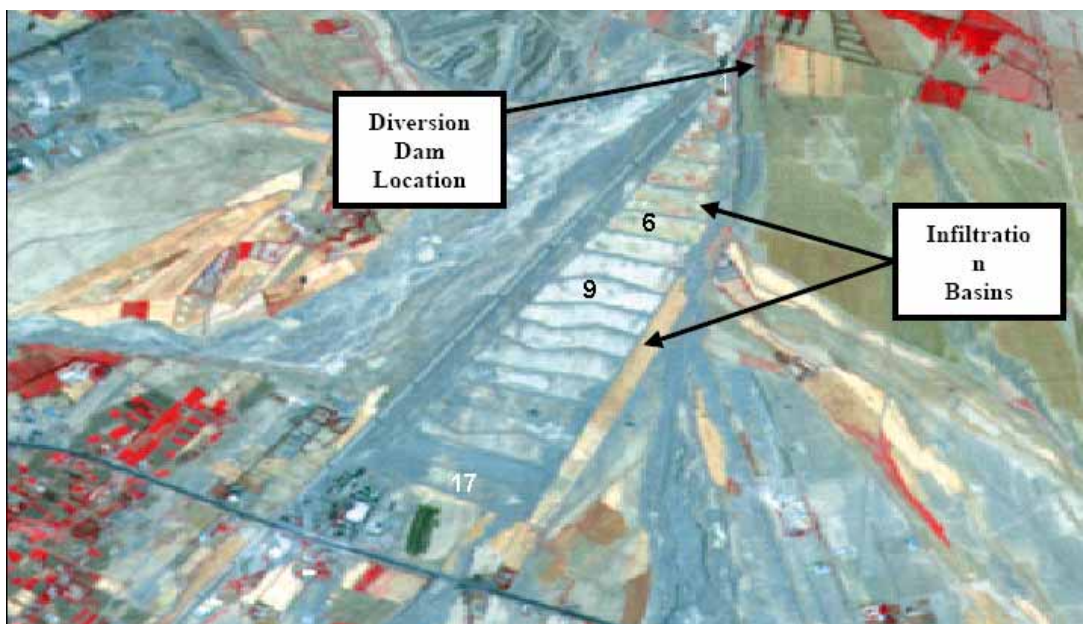
Although there is a great variety in the layout of schemes, three main types may be differentiated.

#### *1. The deep basin type*

This type consists of a cascade of deep basins, separated by spillways. The system is fed by water diverted from the river through a supply canal that starts at an intake structure. The advantages of this type are the relatively large depths of water, causing more rapid infiltration, hence less evaporation loss, and the sediment trap formed by the uppermost basins. The disadvantage is the larger investment cost per m<sup>3</sup> recharged water.

Figure 13.4 shows an example of this type, located on the apex of a large alluvial fan of the Jaj Rud (Rud = river) in northern Iran. The first six basins are filled with sediment up to the internal spillways. Episodic inundation reaches up to the ninth basin, the remainder are not yet functioning. Total inflow depends largely on the duration of flood flow in the main river.

It is interesting to note that in the basins filled with sediment, rich in clay and silt, substantial infiltration contributing to recharge still took place, as was shown by Kheirkhah (2005) using a calculation model that accounted for inflow, extent and water depth in each of the cascade of basins and evaporation loss.



**Figure 13-4** Aster image of the Soghesar flood-spreading scheme (deep basin type), north Iran. Basins no.1 to 6 are filled up with sediment, mainly fine-grained but still having an important recharge function. Diverted water reached basin no.9. Source: Kheirkhah, 2005

#### *2. The canal-overflow basin type*

From the intake structure and supply canal water enters into one or more wide and shallow infiltration canals dug along the contour. The lower side of the infiltration canal acts as an overflow. That flow is ponded by a small dyke further down the slope. The advantage of this type is the relatively low initial investment per m<sup>3</sup> of recharged water. Disadvantages are limited depths of water and widespread sedimentation, whereby the heavy textured sediments reduce infiltration. Figure 13.5 shows a sketch of the outlay and Figures 13.15, 13.20 and 13.21 show such schemes on Landsat TM images.

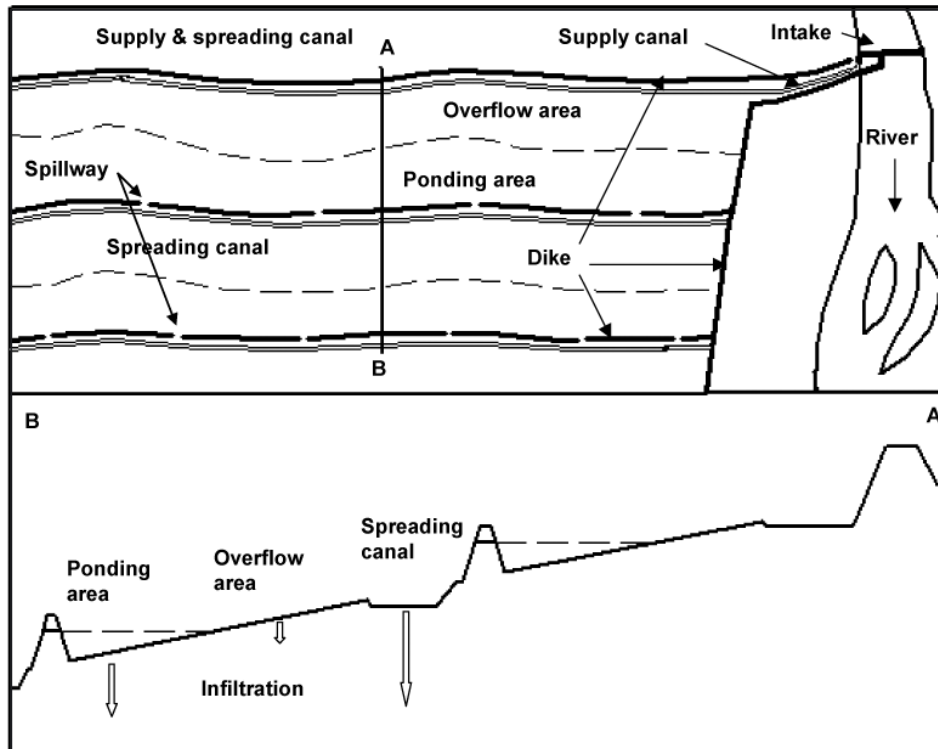


Figure 13-5 Sketch showing lay-out of canal-overflow basin type of flood-spreading scheme for groundwater recharge. Size of arrows gives relative recharge contribution of components.

### 3. The long dyke type

The objective of this type is to pond water that flows over wide areas, such as often occurs on the middle and lower parts of alluvial fans. The dykes have spillways to let the water pass to the next downstream dyke (Figure 13.6), similar to the canal-overflow basin type. This is the only feasible type of artificial recharge scheme for such fans with a wide zone of active channels, as shown in the image in Figure 13.10. Depending on the materials used for the dykes and spillways, initial costs are not so high, but sedimentation of clay and silt can reduce effectiveness, and in some cases fully stop the recharge (section 13.3.3.) unless desilting and ripping is done.

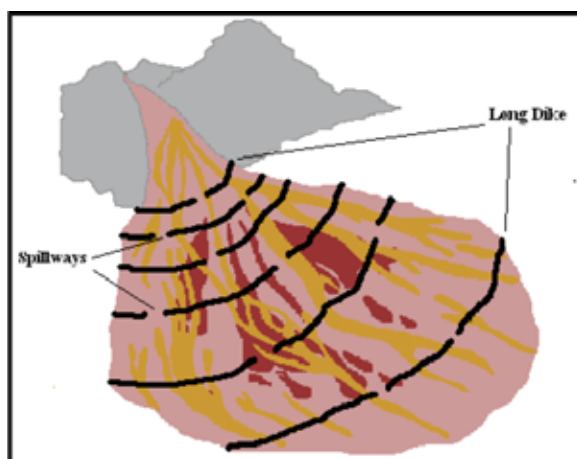


Figure 13-6 Schematic view of the 'long dike' type of floodwater spreading scheme. Source: Kheirkah, 1995

### Recharge efficiency

Evaporation losses within a scheme determine recharge efficiency, in other words, the ratio of amount of water diverted and the amount reaching the groundwater depends on evaporation loss. The efficiency of the canal-overflow basin type depends on the properties of the site (slopes, soil permeability) and amount of inflow, as shown in Figure 13.7. The high efficiency with low inflow is due to the fact that most water stays in the supply

cum spreading canal (see Figure 13.5), which is cleared by desilting. For larger inflows the effects of clay and silt sedimentation in the infiltration basins upslope of the dykes, which are not desilted, play a role. The deep basin type has high efficiency because of larger depths of water and full desilting operations.

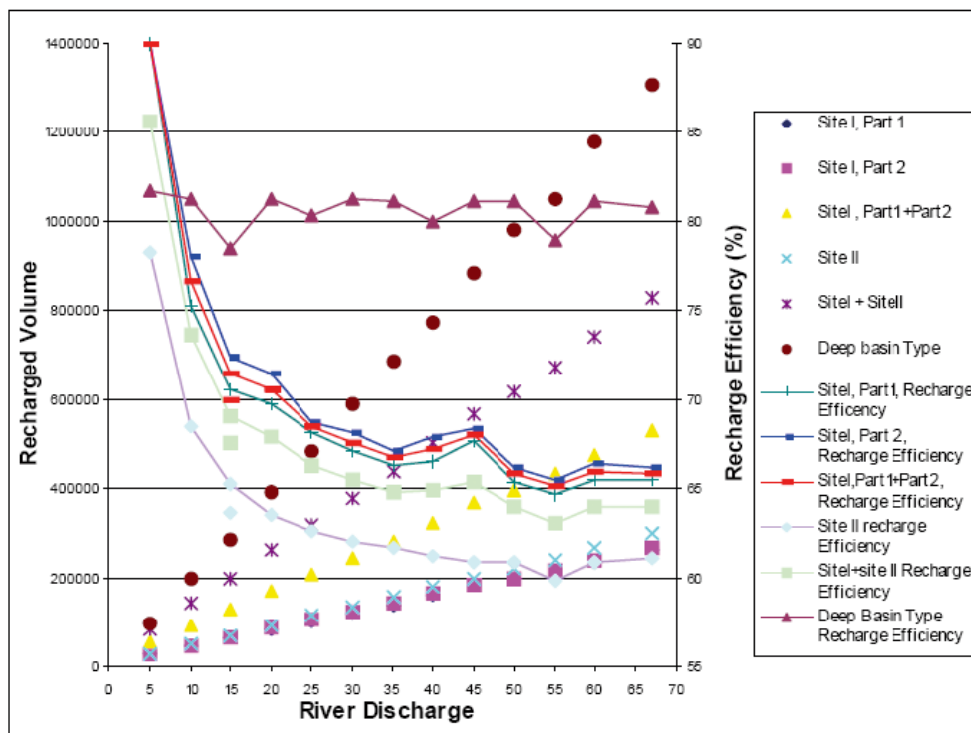


Figure 13-7 Relationship between river discharge ( $\text{m}^3 \text{s}^{-1}$ ), recharged water volume ( $\text{m}^3$ ) and recharge efficiency for alternative schemes for single runoff events of different magnitude for the Chandab area, Iran. Source: Kheirkhah, 2005.

Esfandiari-Baiat and Rahbar (2004) found that during nine flood events, 886,000  $\text{m}^3$  water entered a canal-cum-basin type of scheme in south-eastern Iran and 83.5% of that amount recharged the groundwater. Such high efficiencies can occur also in other type of schemes (Gale, 2006).

### 13.3.2 Procedure for selection of suitable areas and sites for flood-spreading schemes

The full procedure consists of three stages:

- (1) Screening at reconnaissance level resulting in potentially suitable areas
- (2) Evaluation of potentially suitable areas
- (3) Working out global designs and options.

This approach is efficient in the sense that no further data needs to be gathered and worked from areas and sites that will not be retained during further scrutiny. It must be remembered that in a given region where schemes are planned, a great many locations need to be considered at least in principle. Furthermore, the multitude of factors to be considered requires a multi-criteria evaluation. The level of detail of information and data needed increases from stage 1 to stage 3.

#### *Multi-criteria evaluation*

Since a multitude of factors have to be considered with data of different nature and format (qualitative, including 'expert opinion', and quantitative data), a method must be used by which a formal evaluation can be made to obtain the most promising sites. Fernández-Escalante et al. (2006) in a multi-criteria analysis of MAR used three different sets of indicators; one set for the environment related to the impact of man, another set for the quality of

environment and resources and a third set to describe the level of social and political involvement in environmental matters and resources.

Out of several methods in use for Decision Support Systems, Saaty's (1980) Analytical Hierarchy Process (AHP) was used for evaluation and selection of the most promising sites for flood water spreading schemes for groundwater recharge by Kheirkhah (1995), with a strong input of remotely sensed data.

The term 'analytical' in the AHP method refers to the breakdown of any abstract or material entity into its constituent elements, for example, available runoff, properties of an infiltration area, and so on.

In view of the complexity, a hierarchical ordering of factors or criteria facilitates the evaluation. For example, the factor or criterion 'available water' can be divided into number of runoff events and corresponding discharges, and chemical quality of the water. The AHP method requires the breakdown into a hierarchy of clusters, termed main criteria, sub-criteria and main indicators.

AHP is a process that helps the decision maker, rather than being a model to provide the 'right' answer. The process consists of making comparisons of every pair of criteria. A linguistic expression of the relative importance of one member of a comparison pair relative to another is given (e.g. equal preference, weak preference, to absolute preference) and a number ranging from 1 to/including 9 is assigned. The preferences can be based on qualitative criteria, which could be based on experience with existing recharge schemes or on quantitative data, for example, model results. A matrix of preferences for each pair-wise comparison (e.g. slope classes for the infiltration area, or number of runoff events) is made, from which the geometric mean and the relative importance are calculated. Starting at the lowest level of 'indicators' the obtained 'relative importances' are used for similar pair-wise comparison at the next higher level and thus provides a way for aggregation.

The AHP process can be applied to all stages mentioned above, but is particularly useful at stages 2 and 3.

### *Screening*

The first judgement of the suitability of an 'area', discussed above, for a possible flood-spreading scheme is based on:

- features of the catchment that influence runoff and sediment load
- presence of an aquifer with a suitable infiltration area
- characteristics of the application area, such as suitability for and presence of groundwater irrigated agriculture and whether or not flood damages occur.

The strength of remote sensing images in the screening process is the synoptic view, which allows a first judgement of the main factors to single out the most promising areas. Generic data of qualitative nature is used for the factors to be considered, and most of them can be obtained by interpretation of remote sensing images, provided local knowledge, geologic and topographic maps are available.

### *Evaluation of potentially suitable areas*

The areas that have passed through the 'screening sieve' are subjected to further scrutiny, whereby the number of criteria and indicators are expanded in the attempt to narrow the search for the most suitable areas or sites.

Remotely sensed data is used for the estimation of runoff and sediment load (some methods are explained later) in ungauged ephemeral rivers, stability of the river and development of irrigated agriculture using sequential images, presence of shallow groundwater and associated salinity, land use and so on, as will be illustrated below. At this stage more field information is required than at the screening stage, particularly concerning the aquifer and infiltration area.

### *Working out global design and options*

The last stage consists of working out designs for the infiltration areas of selected 'sites' after the multi-criteria analysis of stage 2. By considering one or two types of schemes that are best suited for the particular area, by using different sizes of schemes, and by working out global costs and benefits, options can be offered to the decision maker. Finally, out of the options, a choice has to be made for the engineering plan.

The full procedure for flood-spreading schemes for semi-arid Iran for groundwater recharge has been described and illustrated by Kheirkhah (2005), who structured the hierarchical set-up of criteria and used spatial AHP, that is, AHP procedures implemented and adjusted to GIS operations. The interpretation of remote sensing images provided in his study important information for the assessment of runoff, sediment from the selected catchments, intake locations and general nature and extension of the infiltration area.

Here, we will concentrate on the interpretation of remote sensing images for obtaining information on factors or criteria, which are important for finding suitable areas for artificial recharge schemes based on flood water spreading.

## 13.4 Main factors

The main factors that have to be considered in the screening process and the area selection are:

Water:

- Amount of episodic runoff that can be diverted
- Magnitude of natural recharge by transmission loss
- Stability of the river
- Water quality
- Permeable infiltration areas
- Presence of suitable aquifers below infiltration areas
- Flood damages.

Sediment:

- Order of magnitude of the sediment yield
- Composition of the sediment load.

Topography and land use:

- Slope and dissection of the infiltration area
- Space for infiltration areas.

### 13.4.1 *Episodic catchment runoff*

The amount of water potentially available for artificial recharge needs to be known and it is assumed here that no gauged data are available for the many ephemeral rivers that are of interest. Hence, an estimate has to be made.

#### *Aspects of catchment runoff*

As mentioned above, the capacity of the conveyance channel forms a threshold for the flow diverted at the intake. The distribution in time of the runoff, as given by the hydrograph, is important because of the limiting capacity of the intake. A typical hydrograph of an ephemeral river of a semi-arid catchment of a few tens to hundreds km<sup>2</sup> is sketched in Figure 13.8. A logarithmic scale for discharge  $Q$  was used, because recession curves tend to be straight lines on such diagrams. Particularly noteworthy is the rapid rise up to the peak flow and the rapid recession of the direct runoff. Such a flood may pass within one or two days, depending on rainfall duration and catchment size. A relatively long recession of the delayed flow may occur if the catchment has areas with permeable zones of shallow thickness, such as fractured and well jointed outcrops, colluvial, fluvial and other superficial deposits. For the generation of delayed flow the vertical permeability of the top zone that gets temporary saturation should be much less than the lateral or horizontal permeability. Although the volume of the delayed flow is usually less than that of the direct runoff, it lasts longer and all of it may be diverted, as is indicated in the sketch. The total runoff volume below the threshold is available for recharge.

Ideally, typical hydrographs of small, medium and large runoff events should be studied, but available discharge data is often limited to daily discharges, so that for the smaller catchments only hydrographs of the



medium or larger events can be compiled. The simplest approach to obtain the hydrograph shape for a catchment is to plot dimensionless hydrographs (using  $Q/Q_{\text{peak}}$  and  $t/t_{\text{base}}$ ) on top of each other and draw an average hydrograph for a few runoff classes. The averaged hydrographs can then be used for estimating how much water is likely to enter the infiltration area, after noting the frequency of occurrence of runoff events in each class.

All other things being equal, catchments that generate much delayed flow are preferred to catchments that convert rainfall in direct or fast runoff only.

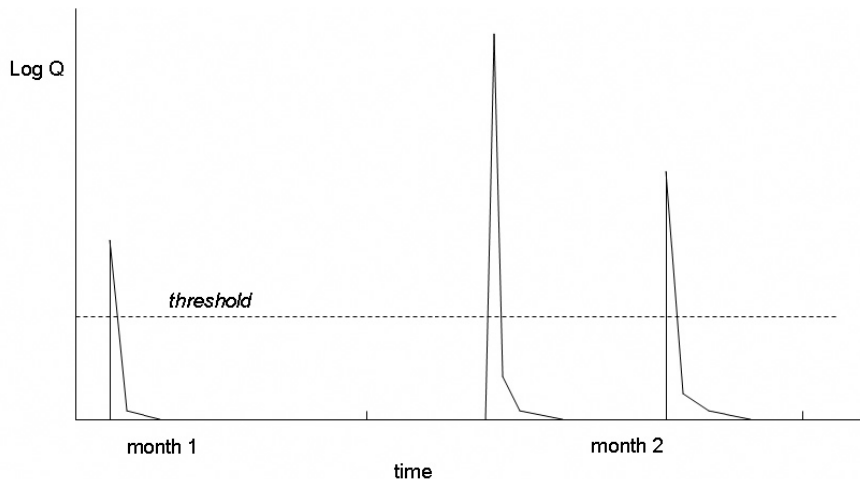


Figure 13-8

Sketch of typical hydrographs of semi arid catchment with low permeability. Volume of flow below threshold (i.e. capacity of conveyance canal) is available for recharge

#### Use of runoff data from gauged catchments in the region

If no records are available for the catchment under consideration, perhaps the best way to estimate runoff is to use discharge records from smaller catchments in the area of interest with sizes of a few  $\text{km}^2$  to several hundred of  $\text{km}^2$ . The runoff events may be grouped in classes and the number of occurrences within each class be noted. A frequency graph can be prepared, which usually shows frequent occurrence of small runoff events and fewer larger events. Since the length of the discharge record is known, the average frequency of runoff in each class is known.

The catchment properties of the ungauged catchment under investigation are compared with those of the gauged ones and runoff is estimated on the basis of similarity, chiefly by judging overall catchment permeability. Of the gauged catchments, runoff statistics should be analysed and related to catchment permeability. The latter could be defined as the percentage of permeable surfaces (light textured alluvial and colluvial deposits, windblown sands, karstic limestone, highly fractured sandstone with sandy soil, volcanic rocks with large surface depression storage, and so on). Relief and drainage density has to be taken into account, because runoff tends to be high on steep slopes and channel networks (even integrated rill and first order drainage lines) are created by and facilitate fast runoff.

A good example of this approach is given in a systematic study of a large number of catchments in the Sahel by Rodier (1975). Annual runoff coefficients were related to rainfall frequencies, for categories of catchment permeability and catchment size in three broad isohyetal zones in the Sahel. Catchment permeability was described by drainage density and degree of integration of the drainage network, rock type, nature soils and deposits and relief. Aerial photographs are included in Rodier (1975) to illustrate areas of typical permeability. Table 13.2 shows annual runoff coefficients of medium sized catchments ( $40\text{--}300 \text{ km}^2$ ) in the Sahel in the  $100\text{--}300 \text{ mm}$  annual rainfall zone. The data is mainly derived from Rodier, who had to use short-term discharge data.

The differences due to permeability are appreciable.

Permeability	Dry year	Median year	Wet year
Impermeable - low permeability	0-5	10-20	20-20
Medium permeability	0-5	3-10	15-20
Permeable	0	1-2	10-15

Table 13-2 Runoff coefficients (%) depending on catchment permeability and rainfall. Data mainly taken from Rodier, 1975.

In case small reservoirs are present in the area, these should be visited to assess whether the capacity matches the catchment runoff, whereby estimates of the frequency and magnitude of overflows through the spillway may have to be made. Local information is often the only source.

The data thus obtained should be compared with the design criteria for the reservoir and with catchment characteristics, and the result could be used for estimates of runoff in catchments where floodwater diversion for artificial recharge is planned.

Runoff data from micro-catchments should not be used for the estimation of runoff in catchments sufficiently large for flood water harvesting because it is known that runoff coefficients decrease rapidly when catchment size increases from tens of m<sup>2</sup> or a few hectares to a size of few km<sup>2</sup> or more.

*Estimation of runoff when no gauged data is available*

A common problem is that catchment rainfall may not be known because of low density of rain gauges. In such cases synthetic rainfall series may be developed using data from nearby stations.

In addition, runoff data of an approximate nature can be obtained by interviewing local inhabitants, shepherds in particular, about the frequency of runoff events, duration of recessions and high water levels. By using the slope area method for estimating peak flows based on the Manning equation, an estimate of peak flows can be made and compared with those obtained by the SCS method or other methods.

In most semi-arid regions soil maps may not be available for the assessment of the hydrologic condition in the SCS method and therefore the images have to be interpreted to delineate soil unit boundaries, including the outcrops and areas with thin soil cover. Interpretation has to be followed up by field checking because it is difficult to assess the nature of the soils and thus their hydrologic properties by using image data only. In particularly, the presence of strong sealing of the upper few millimetres of the soil, due to dispersion of soil aggregates and compaction by raindrops, is not interpretable on images, but has a strong effect on runoff. Surface sealing is common

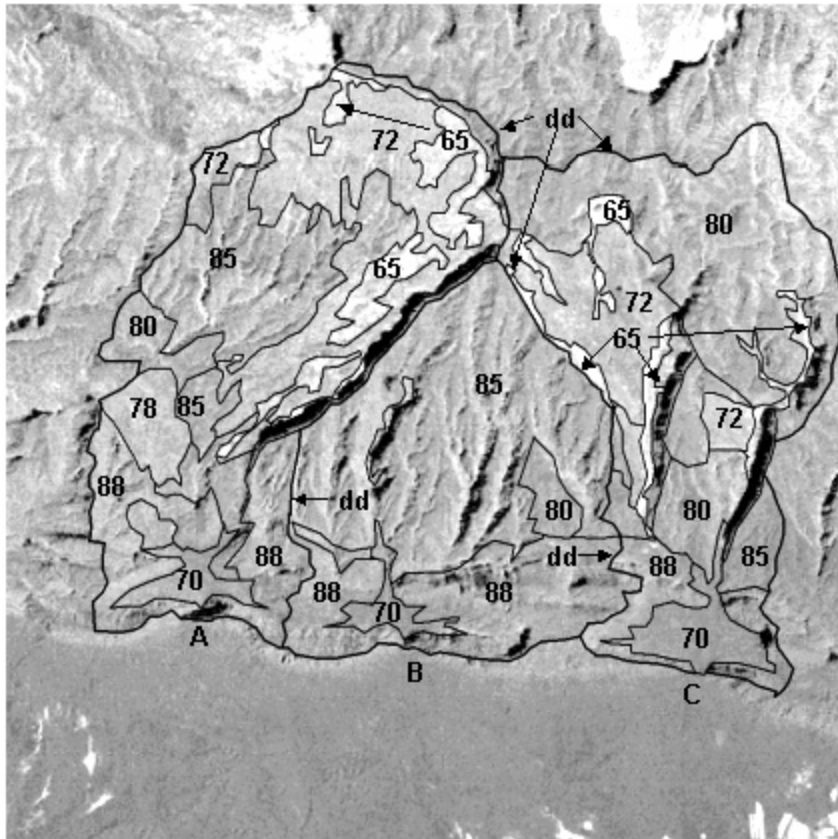


Figure 13-9

Terrain units consisting of combination of hydrological soil condition and vegetation condition, indicated by estimated curve number. NDVI image Landsat TM. Black zones are cliffs in full shadow.

in semi-arid areas on tilled land and in areas with rangeland vegetation having poor canopy cover and appreciable grazing pressure.

In the SCS method, the soil hydrologic condition and the vegetation condition are separate entries for selecting a curve number. However, in most semi-arid rangelands there exists a close association between the kind and thickness of soil and the vegetation density and therefore terrain units may be interpreted on images, which combine the two.

Figure 13.9 shows an example of such an interpretation of a small catchment in south-central Iran. The boundaries of the hydrologic soil units are drawn on the basis of an understanding of the interaction of rock type, weathering and soil formation, erosion and deposition processes, details of the topography such as slope forms, degree of dissection and land cover (natural vegetation, crop lands, etc).

One difficulty is that the method does not provide information on the proportion of direct runoff to delayed flow, and this aside, the curve number method should be applied to the smaller catchments only.

By visual interpretation, preferably of stereo images, the proportion of permeable deposits in a catchment (colluvial zones, accumulation glacial deposits, river terraces, and so on) that store and release rainwater could be determined. Such deposits increase catchment permeability, which tends to lower runoff coefficients (e.g. Table 2.1), but increases delayed runoff, which usually has low turbidity and therefore does not contribute much to sedimentation within a flood-spreading scheme.

### ***13.4.2 Magnitude of natural recharge by transmission loss***

In the selection of suitable sites, it should be realized that a large part of the flood runoff may infiltrate in sandy and gravelly ephemeral river beds (i.e. transmission loss), and therefore either the search is diverted to other areas, or the design of an artificial recharge scheme is adjusted.

Figure 13.10 shows an alluvial fan in central Iran, where important transmission losses occur in the wide active ephemeral riverbed. It can be noted that the riverbed ceases to exist. Some water may be lost in the form of sheet wash, but most is infiltrated. Only a few minor culverts were constructed along the road, while south of the road no major channel is found.

Another example is shown in Figure 13.11 from northwestern China, which illustrates that the runoff from the catchments in the hills in the south is nearly fully infiltrated in the alluvial fans, because only faint signs of sediment and water entering the cultivated area can be seen.

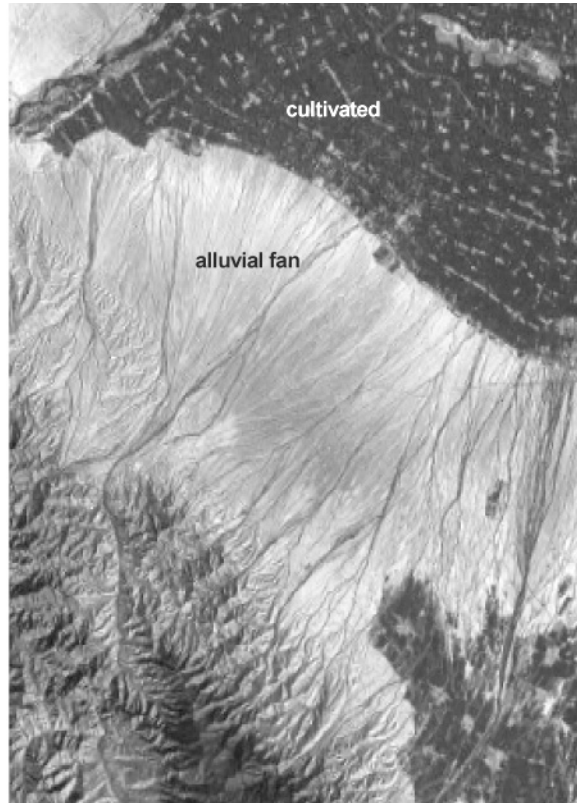
In such cases it is doubtful whether a recharge scheme in the alluvial fans serves much purpose, because the floodwaters infiltrate without human interference and expenditure.

The literature (Walters, 1990; Sorman and Abdulrazzak, 1993) mentions amounts of water lost in wadi beds during flood events. However, little information was found concerning groundwater table rises due to transmission loss. The importance of this can be shown by comparing water table rises in observation wells situated close to active beds with those further away. Figure 13.12 shows an area in southern Iran (north of Bander Abbas, see also Figure 2.18, Chapter 2) that contains an alluvial aquifer in a shallow syncline. Locations of observation wells are shown on the PC 4 image, which displays the fresh sands and gravels of the active riverbeds, which are episodically flooded by flash flows from the mountains in the west. The ephemeral rivers flow in a relatively narrow incised channel in the west, but spread out when the central part of the syncline is reached. In the diagram of Figure 13.13, increases of the groundwater level in the observation wells are shown, due to transmission losses during episodic flooding. Rises of a few metres have been observed only in wells close to the active river beds, namely wells nos 1, 4, 5, 6 and 8. The largest rises occurred in well no. 5, which is located close to a flood-spreading scheme consisting of large basins. Wells nos 7 and 10 show a somewhat deviating fluctuation because of the influence of the – saline – main river in the northeast. Note that on the permeable, dissected alluvial fans (well no. 2) the water table rise was very small and that along the flexured southern margin of the aquifer where Pliocene shale and fine-grained sandy beds are found, there was no response at all (well no. 3).

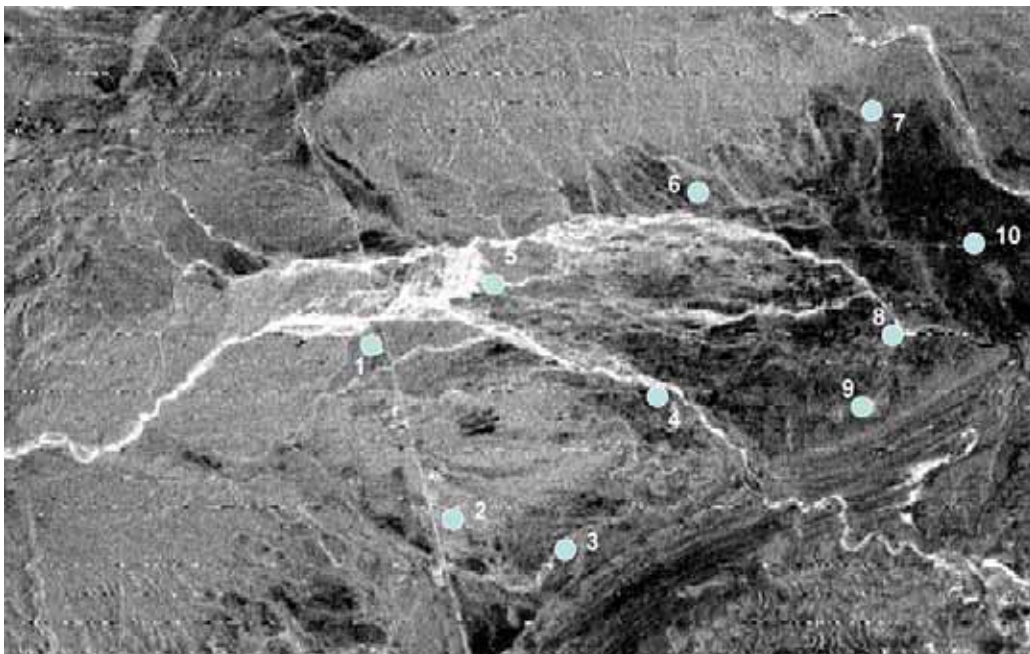
Another example of transmission loss can be found in the discussion of the Eastern Zanjan valley, Chapter 7, section 7.4.5.



**Figure 13-10** Alluvial fan with large active part where most of runoff is lost by transmission loss, except runoff of largest floods. Note absence of drainage lines south of road. TM, band 5. Central Iran. Distance EW is 8.5 km.



**Figure 13-11** Runoff from catchment in the hills in the south is infiltrated in the alluvial fans by transmission loss. No appreciable traces of sediment and water can be observed in the cultivated area. Landsat TM image, NE China. Distance EW is about 6 km.



**Figure 13-12** Locations of well locations in relation to recent sand and gravel deposits of active drainage system, episodically flooded by flash flows. For hydrographs see next Figure 13.13. TM PC4 image is selected for display of recent deposits. Distance EW is 17.5 km

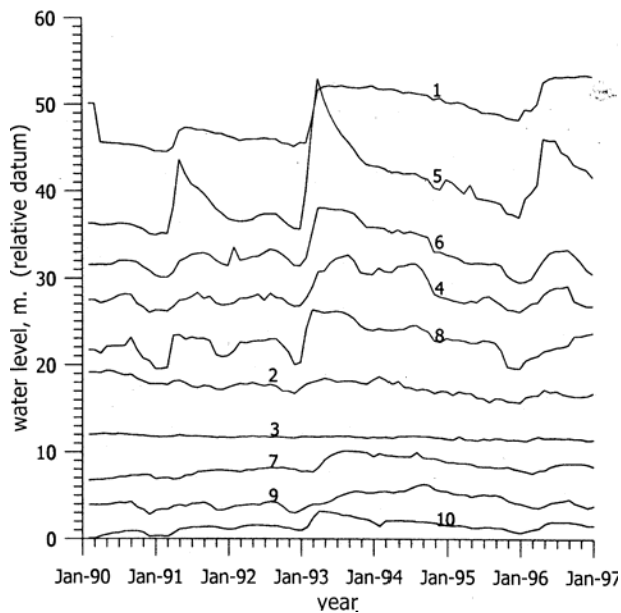


Figure 13-13

Rises of groundwater table of wells shown in Figure 13-12, due to transmission loss during short episodic flows in ephemeral active riverbeds.

### 13.4.3 Stability of the river

#### *Stability in plan*

Intake structures are expensive, especially when using concrete. Costs can be reduced by using gabions, but these need to be replaced usually after large floods. It is evident that an intake should be located at a stretch where the river is stable in plan.

This is not so when on an image the river splits up in two or more active or sub-recent branches, as is shown in Figure 13.19 (below). In this example, the river has a comparatively large sediment load consisting of fine-grained materials because most of the rocks of the large catchment consist of shale and mudstone. Apart from considerations of permeability and salinity, an intake requires very expensive river training works, giving this fan a low score in the screening, possibly even excluding it as a suitable area.

When sediment splays can be observed right at the apex of the fan, the intake may be positioned at the place where the river leaves the outcrops of the hill or mountain. However, this may necessitate a relatively long supply canal, possibly with drop structures, to carry water to a lower position because the upper alluvial fan may be too steep for economical construction of a scheme. A good location is usually found on the transition of an incised river on the upper alluvial fan and the middle fan. The water can be easily diverted to the middle or upper-middle part of the fan where surface and subsurface permeability is high.

Sequential imagery with sufficient time lapse is of course very useful for estimating the stability in plan, at least for the period between the two images. Vertical stability of the riverbed is discussed in the section on sediment yield, below.

### 13.4.4 Chemical water quality

#### *Water for diversion*

Flash floods are a direct response to rainfall and there is therefore little time to accumulate salts. In other words, the chemical water quality is generally suitable for infiltration if there are no man-made pollution sources in the catchment. Assessment of water quality aspects is a matter of field and laboratory investigation, but in some cases some information can be obtained by remote sensing. Figure 13.14 shows a salt diapir in the form of a large hill that is bordered by a bahada (coalescing alluvial fans) or accumulation glacia, which contains pebbles and finer particles of salt, which are also transported to the riverbed from where they are further taken downstream for some distance, rendering the water saline. During flood flows, substantial dilution occurs, but during recessional flows the river water is too saline for diversion and usually there is no provision for closing the conveyance canal at the intake of a scheme.

Furthermore, the alluvial deposits of the saline river contain salt particles, rendering the river water and the groundwater in the deposits saline and unsuitable for irrigation or drinking.

The land use can give a clue as to whether the river water that feeds an aquifer is of sufficient quality for irrigation. If irrigated agricultural fields exist on the fluvial deposits, the water is probably suitable



Figure 13-14

Salt dome intruded in folded rocks, with bahada (glacis or coalescing fans) with gravels and pebbles of salt entering the river, which has saline water. TM band 5 South Iran. Distance EW is 10.3 km.

### *Salinization / alkalization*

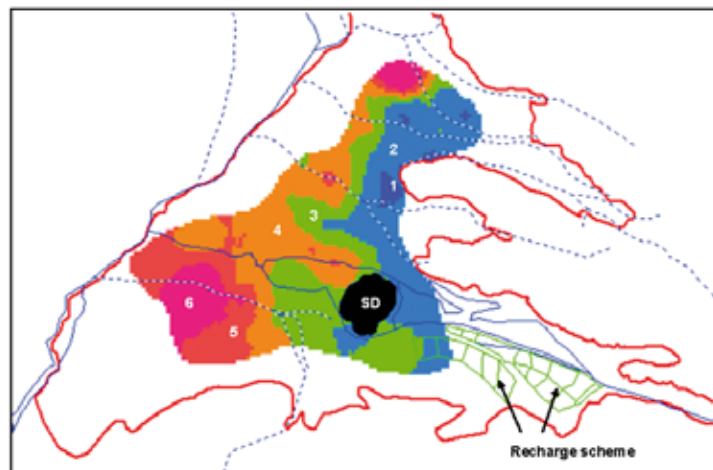
Much more common than saline intake water is the presence of saline water at the lower parts of the alluvial fan. On its slow passage through the fan, the total salt content of the groundwater tends to increase. At the lower part of the fan the groundwater table can be at shallow depth and within the influence of capillary rises take place in the heavy textured soils causing salinization of the soils (Metternich and Zinck, 2002). The problem is often aggravated by (over)application of irrigation water from surface streams or reservoirs to fields in the middle to lower part of the fan.

Figure 13.19 (below) shows such an area. The light tones on the lower fan are due to efflorescence of salt at the surface, which signifies the last stage of salinization. This means that agricultural fields just upslope of the salt area are at risk and often show lower vegetation densities, as would be apparent on a false colour composite or NDVI image. Comparison of images of different dates make it possible to map the progress of the process, after applying correction methods for comparing images, discussed in Chapter 2 (section 2.7). An artificial recharge scheme may aggravate the salinity problem by a rise in the groundwater table, as does the return water from irrigation using external surface water. Therefore, if a flood-spreading scheme is planned in areas with a salinity hazard, the recharge scheme should be accompanied with a pumping scheme that uses the recharge water fully, but avoids an upsurge of the brackish water interface.

In the example of Figure 13.14, fluvial deposits derived from a salt dome rendered the river water saline. However, the presence of a salt dome may not prohibit the construction of recharge scheme, as the following example shows. Figure 13.15 shows an ASTER image (NIR) of a local alluvial aquifer in southern Iran, consisting of alluvial fan deposits, a salt dome and a recharge scheme upstream of the dome. The electrical conductivity (EC) line of  $4,000 \mu\text{S cm}^{-1}$  drawn in Figure 13.15 is based on interpolation of the EC of groundwater in agricultural wells, shown in Figure 13.16 (modified, after Hossainipour, 2000). The map shows only limited influence of the salt dome on the pattern of salinity of groundwater downstream of the dome. It can be noted that on the image, presence of irrigated agricultural fields coincide roughly with the salinity pattern.



**Figure 13-15** Alluvial aquifer of Sarchahan Plain, salt dome (SD) and flood-spreading scheme (FS), south Iran. West of white line, electrical conductivity of groundwater is  $> 4,000 \mu\text{S}$ , east of line EC is less. Agricultural area (irrigated by groundwater) coincides roughly with  $\text{EC} < 4,000 \mu\text{S}$ , while the salt dome has minor influence on groundwater quality distribution. Landsat ETM



**Figure 13-16** Kriged distribution of electrical conductivity (EC), average of 1988–1998 period, of groundwater in agricultural wells for central part of the total aquifer. SD is the salt dome. EC class 1 =  $< 2,000 \mu\text{S cm}^{-1}$  and successive classes in steps of  $1,000 \mu\text{S cm}^{-1}$ . Pattern shows effect of transmission loss in upper and middle reaches on groundwater water quality. Recharge scheme was constructed during the observation period.  
Source: Modified after Hossainipoor, 2000

### 13.4.5 Permeable infiltration areas

Most of the suitable areas for flood-spreading schemes in semi arid regions consist of alluvial fans or coarse-grained fluvial deposits. In Chapter 7 (section 7.4), alluvial fan deposits and other fluvial deposits have been described and illustrated.

The land cover reflects the change of facies of alluvial fan deposits. The upper-middle alluvial fan usually has rangeland vegetation because of the low water-holding capacity of the sandy or gravelly soils and deep groundwater table, while on the lower fan with heavy textured soils, agricultural fields are found, see, for example, Figure 13.20 (below).

Other coarse-grained fluvial or alluvial deposits can occur in the form of accumulation terraces, possibly some of them buried by younger deposits.

Agricultural fields are often found on fluvial deposits. This does not necessarily imply that the subsurface deposits are heavy textured. Usually, terrace deposits near mountain fronts have coarse-grained bed load deposits at some depth, which become fine-grained to the top, reflecting the deposition of suspended load before the river shifted or started to incise. Furthermore on older terrace deposits soil formation took place whereby the less resistant minerals decomposed into clay.

In case an image of alluvial deposits shows many traces of former braided riverbeds and overflow deposits it is likely that most of the top-soil is coarse-grained and permeable and therefore potentially suitable for a recharge scheme. In cases where the alluvial area is cultivated and shows no signs of fluvial deposits, it is likely that a fine-grained soil is present. For the deep basin type of scheme this may not be a problem if coarse-grained deposits are found below the soil. It must be remarked that simulation studies using 1D soil moisture models and some field experiments have shown that certain fine-grained soils may have acceptable infiltration capacities (Kheirkhah, 2005). Much depends on the type of clays. In case many other factors are found to be favourable in the screening process, areas with heavier textured soils may be retained provisionally and should be subjected to field tests, preferably pond infiltration tests.

Tectonism and past climates influence the nature of fanglomerates (i.e. alluvial fan deposits), as discussed in Chapter 7.

Impeding layers could be present at or below the surface, even with older upper fans, as is shown in Figure 13.17. In this example, a lime crust (l. c.) was developed on older, slightly tilted alluvial fans. In the upper fan a wide canal was dug (arrow 1) into which river water was diverted. The decline of the water level in the canal after closure of the intake was so little that the experiment was abandoned, because of the impermeable nature of the crust. However, an observation well at location 1, close to the recent alluvium (*r.all*) in the active river bed, showed an annual increase of groundwater level of 1 to 4 m. due to recharge by transmission loss during the spring period (see also the Eastern Zanzan case, Chapter 7, section 7.4.5). Small earth dams (arrow 2) were constructed to pond runoff generated on the fan itself. It is doubtful whether this measure will contribute to groundwater recharge.

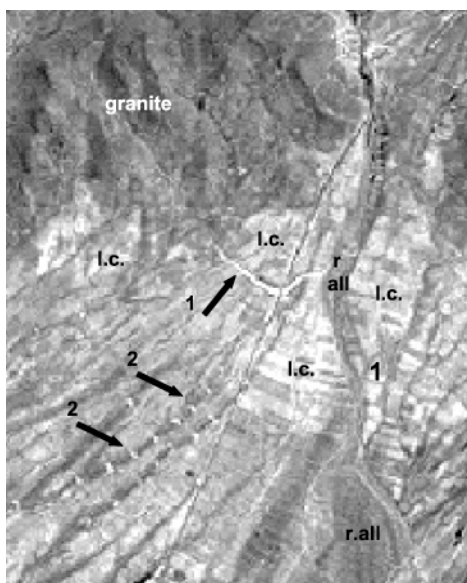


Figure 13-17

**Infiltration canal (arrow 1) dug in upper alluvial fan. Because of presence of impermeable lime crust (l.c.) no infiltration took place.**

**Small earth dams in shallow dissection valleys of the older fan (arrows 2) aim at ponding local runoff for infiltration.**

**In fact, recharge of the aquifer takes place by transmission loss in the recent alluvium of the river (*r.all*), as evidenced by a well at location 1.**

**TM band 3, Zaker river, Zanzan valley, N. Iran.**

**Distance EW is 5 km. Landsat TM**



### 13.4.6 Presence of suitable aquifers below infiltration areas

Thickness and aquifer drainage are important aspects in the screening process, and these factors require an 'in-depth' interpretation of the images. It is true that images show the surface features, but by applying knowledge about the geology and the geomorphological history of the region, deductions can be made. Of course, for the final selection drilling data and geophysical work is needed, but the search for promising areas can be narrowed down, saving time and money.

#### *Permeability*

A prime condition for a recharge scheme is the permeability of the aquifer, which has to be in connection with or in the proximity of an ephemeral river. Therefore, generally coarse-grained fluvial deposits and in particular alluvial fans are suitable areas. If these are of sufficient thickness, say, some tens of metres or more, there is sufficient storage capacity for the recharge water. If not, the alluvial deposits should be overlaying permeable aquifers of non-alluvial nature, such as permeable sandstones and some volcanic rocks (rhyolite tuffs, porous lava flows, and so on) and possibly karstic limestone. The latter case has the complication that it may not be known where the recharge water actually goes.

Alluvial fan deposits (fan A) with overall low permeability are shown in Figure 13.18. The catchment rocks consist predominantly of argillaceous suites (shale, mudstone, soft marl). The relatively gentle gradient of the fan is adjusted to the nature of the deposits and magnitude of discharges. The poor permeability, the unstable river and salinity hazard (mentioned earlier) lead to a very low suitability ranking in the screening process.



**Figure 13-18** Large alluvial fan (A) consists of deposits rich in clays and silts because of catchment lithology and has relatively gentle gradient. Small fan B has coarse-grained deposits due to presence of limestones and sandstones in catchment and has relatively steep gradient. Whitish tones correspond to salt efflorescence at surface, saline soils without efflorescence indicated. Landsat ETM false colour (bands 7, 4 and 2), South Iran. Distance EW is 6.5 km.

In contrast, deposits of smaller fan B are permeable because of the catchment lithology (limestone, sandstone and conglomerate) and the relatively steep gradient of the fan.

### *Thickness of alluvial aquifers*

Alluvial aquifers of sufficient thickness occur generally in subsidence areas, which can be of local nature and in areas where due to climatic change or sea level rise deposition took place.

A climatic phase causing deposition results in the building up of fluvial plains with extensions into the tributary valleys. Later climatic events may have induced incision leading to formation of fluvial terraces. A contiguous and sizeable cover of alluvial deposits suggests that the alluvial deposits could be thick, particularly in the central parts. Presence of outcrops in the riverbed is a sign of limited thickness because they indicate the level of erosion prior to the alluvial accumulation.

Late Tertiary and Quaternary tectonism has caused in many parts of the world the accumulation of fluvial deposits. They often occur as fanglomerates because uplift and subsidence, separated by faults or narrow flexure zones created breaks in the gradients of the rivers, as discussed in Chapter 7. Two examples of the interpretation of the (neo)tectonic setting are discussed below, to illustrate that aquifer thickness can be judged to some degree using common geologic reasoning.

It should be remarked that interpretation of thickness, due to a climatic cause or a tectonic one, remains a matter of conjecture in the absence of geophysical survey data and drilling logs. However, an idea may be formed that helps in the screening process of finding potentially suitable areas for flood-spreading schemes, because areas with possibly thin alluvial deposits will obtain a lower score.

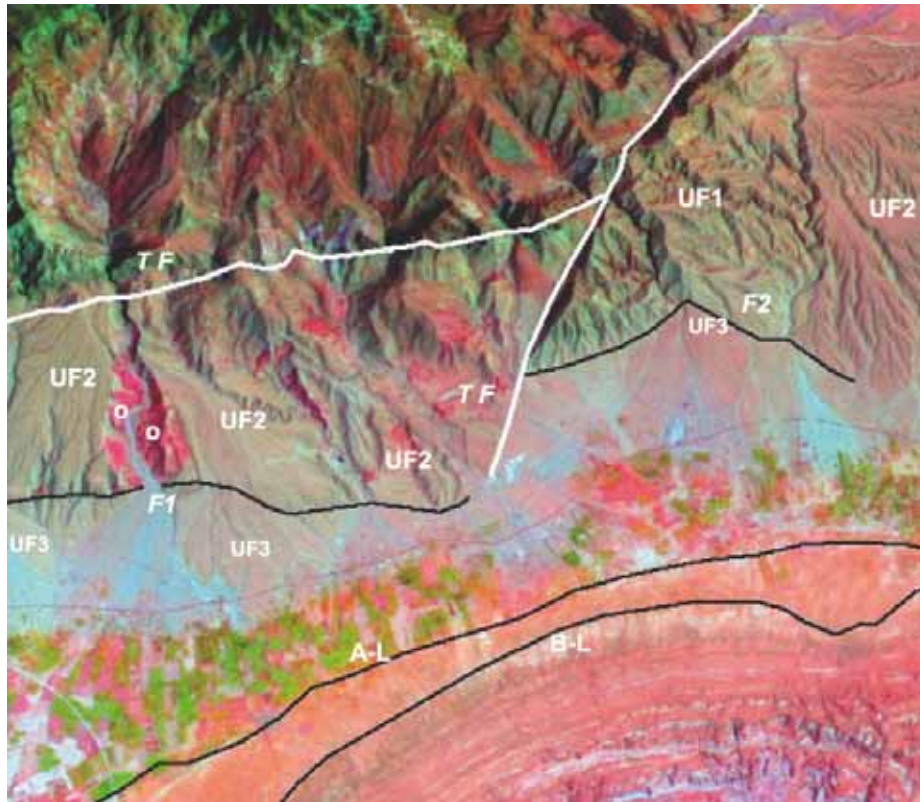
The first example, Figure 13.19 pertains to an area in southern Iran with clear evidence of neo-tectonic uplifts, but little subsidence. The aquifer area can be recognized by the presence of agricultural fields, which are irrigated by groundwater. The large and high anticlinal structure in the north includes resistant rocks (sandstone, conglomerate and limestone) from which the coarse-grained alluvial fan deposits have been derived. On the southern flank of the anticline the fanglomerates have been uplifted and successions of uplifts can be derived from the degree of dissection of the fans. However, the fans north of the normal fault (F1) have a thickness of < 20 m or so, because at various places (only two indicated) in incised valleys it can be seen that they overlie rocks of low resistance (shale and soft marl).

The eroded anticline in the south consists of impermeable rocks of low resistance and the outcrops are separated from the alluvial aquifer by a glacis (not cultivated) with thin deposits overlaying the impermeable rocks. By extending the erosional glacis surface below the alluvium in the central part of the valley in a geologic cross section, it is likely that little thickness develops up to the faults. However, the western and eastern part of the alluvial area opens up and is bordered by dipping older fanglomerates, suggesting an increase in thickness of the alluvium in these parts.

A second example, from south-central Iran, shows a subsidence area, which terminates against an east-west striking fault, Figure 13.20. That fault is covered by alluvium, and is drawn on the strength of the outcrops at a few places just south of the east-west river. South of that fault up to the hogback with near vertically dipping rocks in the south, is a glacis with thin alluvial deposits, generally of argillaceous composition, overlying impermeable soft rocks.

The interesting part for managed aquifer recharge is the alluvial fan forms by the river, which drains the syncline in the north (S). An eroded flank of a syncline, partly covered by local fan deposits, forms the northern part of the alluvial area, without signs on the image of faulting or flexuring. It thus seems that the subsidence took place in the form of tilting with a dip south, till the fault is reached. In fact geophysical data confirms this interpretation. The alluvial fan deposits have the classical facies change, from very coarse-grained deposits in the upper part to sandy deposits in the middle part and fine-grained (fine sands to clay) deposits in the lower part.

This area, Gareh Bygan, is well known in Iran for one of the first canal cum overflow basin types of schemes, scheme no. 1, indicated on the image and described by Kowsar (1992). The small dark sinuous lines are tree-lined spreading canals. Areas 2 and 3 are further extensions with the same type of scheme, while scheme no. 4 makes use of local runoff from the mountain front. Scheme no. 3 is located on the deposits of local fans, which are of a different nature than those of the large alluvial fan. Increase of irrigated agriculture has taken place after construction of the artificial recharge scheme, but at the time of writing no hydrogeologic evaluation was available.



**Figure 13-19** Interpretation of neo-tectonic setting and relative depth of aquifer. Large anticlinal structure in the north is bounded by thrust faults (TF) and by faults (F1 and F2). Anticline in south with impermeable rocks is bounded by contact (B-L). Southern aquifer limit is (AL). Uplifted fans (UF) are differentiated according their relative age (1 is oldest). Aquifer is relatively shallow, particularly in the central area and is bounded by fault F1 in the western part because of outcrops (o) exposed on valley walls below uplifted fanglomerates. Northern aquifer limit in eastern part extends below uplifted fans. Recent fans have bluish tones and recharge takes place by transmission loss. Recharge schemes on the recent fans will have the additional benefit of flood mitigation. Landsat ETM, false colour of bands 7, 4, 2. Distance EW is 15 km.



**Figure 13-20** Subsidence area bordered in south by a fault, note outcrops (O) and in the north by the flank of syncline (S), axis shown. Thickness of fanglomerates in central part of subsidence area is >100m. Alluvial cover is shallow south of the fault (glacis) and in the area with local fans. 1 = oldest canal-overflow basin type of flood-spreading scheme, scheme 2 is more recent, scheme 3 is under construction, while scheme 4 makes use of local runoff. Flash flows from the river draining the syncline are diverted. River is unstable between schemes no's 1 and 2. Irrigated agriculture benefits from groundwater recharge. Gareh Bygan area south-central Iran. TM band 8 (14.25 m resolution). Distance EW=14.8 km.

### 13.4.7 Sediment

#### Quantity

A substantial sediment load is common of ephemeral river discharges in semi-arid terrain, and part of the suspended load (sands and finer fractions) will enter the recharge scheme. Much sedimentation of clay and silt reduces the recharge efficiency and raises costs of desilting and adjustment of internal spillways in the canal cum overflow basin type of scheme.

Figure 13.21 shows hybrid types of flood-spreading schemes. The northern scheme consists of an upper basin (added as a stilling basin) and the remainder is the canal and overflow basin type. The southern scheme has an upper basin and long dykes. A simple experiment with a container floating in inundation water in the northern scheme indicated that no infiltration took place. However, the test pit method before sedimentation showed infiltration of  $8.5 \text{ md}^{-1}$ . In the southern scheme the experiment with the container showed limited infiltration of  $0.01 \text{ md}^{-1}$  after sedimentation while a test pit method before construction gave  $0.093 \text{ md}^{-1}$ . Also in this scheme a stilling basin was added.

The catchment lithology of the southern scheme consists of limestone and granite, which have low erodibility and produce relatively large amounts of coarse-grained sediment. In the catchment of the northern scheme, some 15% of the catchment area consists of marl; the remaining is limestone and granite. Possibly, the presence of marl has increased the amount of silt and clay in the runoff to account for the lower infiltration.



**Figure 13-21** Alluvial fans SE of Yazd, central Iran, showing two types of recharge schemes on the non-dissected part of the alluvial fans. Schemes were constructed to augment groundwater, which is brought to Yazd city (not shown) by means of long qanats. Clay accumulation (30 to 40 cm) in the Basin cum canal type of scheme proved to be impermeable. The coarse-grained deposits in the long dike type of scheme were more permeable during test period but had significant evaporation loss. Image shows the difficulty of positioning and designing intakes because of flash flows. The dissected part of the upper fan is not suitable because infiltration-overflow canals along contours will be very sinuous.  
Source: Google Earth

It is therefore important to consider the magnitude of the sediment load in the screening process. A problem is that sediment yields in semi-arid areas vary much from a few tens of  $\text{tonkm}^{-1}\text{y}^{-1}$  to several tens of thousands of  $\text{tonkm}^{-1}\text{y}^{-1}$ , depending on catchment lithology and dynamic geomorphology. In fact, there is no upper limit for the solid load because debris flows and mudflows can occur (see Figure 7.19, Chapter 7).

Apart from spatial variation of the sediment yield in the smaller catchments, there is a large temporal

variation. For example, Inbar (1962) reports an event in a semi-arid catchment, which caused the annual yield to be  $60,000 \text{ ton km}^{-1}$ , against a normal yield of  $6,000$  to  $8,000 \text{ ton km}^{-1}$ .

Sediment yields are discussed in, for example, Hadley et al. (1985).

Figure 13.22 shows strong deposition on the alluvial fan of catchment (B), in southern Iran, where landslides occurred in the soft rocks in the core of the anticlinal structure.

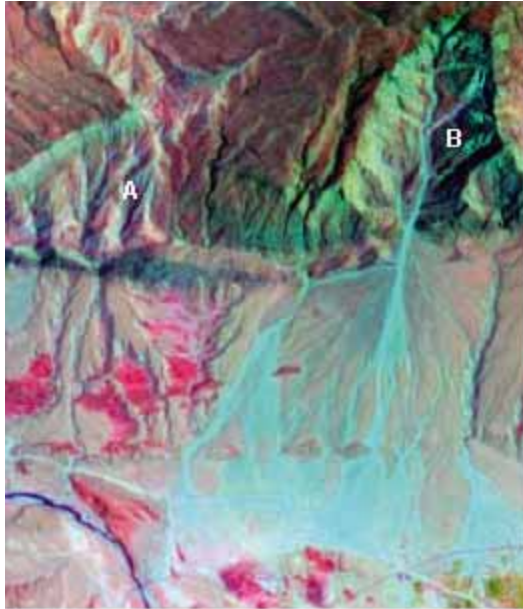


Figure 13-22

**Landsat TM image (false colour) showing catchment B with high sediment load, due to mass wasting and catchments around A with less sediment load.**

**Note large width of river of catchment B in the hills and sediment splays downstream. Distance E-W is 9.7 km.**

Such landslides are usually episodic events, but when they happen, a sudden increase in the sediment yield occurs, after which the yield tends to decline gradually. Landslides often cause debris flows, which leave unsorted deposits on the fans, in other words, mixtures of boulders, pebbles sands and clay.

Large widths of riverbeds in comparison to catchment size can be observed on images, and it is a sign of large amounts of coarse material being supplied to the channel network by landslides or ravine development. The entrained materials cannot be transported by the runoff and therefore the riverbed starts aggrading, whereby the width increases.

It is obvious that the catchment and fan of area B will not be considered as favourable in the screening process. It should be noted that the adjoining catchments near (A) have a much lower sediment yield, as can be judged from the size of the channels. It is difficult to predict if, where and when landsliding will take place without detailed studies, but presence of landslides may be taken as sign that more may occur or that they may be re-activated by heavy rainfall and tremors.

In areas with excessive sediment loads, intake structures, supply canals and infiltration or spreading canals of recharge schemes will be rapidly choked with sediment and lose their function in case of aggradation. Obviously, such areas have a low suitability or are not suitable for MAR schemes.

### *Composition*

It should be noted that the sedimentation features on an image pertain mainly to the deposition of the bed load, which is coarse-grained and permeable. Saltation load during flood events consist of sand fractions but most of the solid load is transported as suspended load. As the gradient of alluvial fans decrease in downstream direction as well as the discharge because of transmission losses, first sands are deposited and on the lower fan silts and clays by overbank wash.

However, when the catchment rock consists predominantly of argillaceous rocks (shale, mudstone, soft marl), even at the upper fan the deposits can have low permeability (see Figure 13.18), because the solid load of the river is argillaceous while shale and mudstone pebbles carried as bed load can decompose upon exposure.

At the intake of a flood-spreading scheme all three types of loads will be diverted, but the hydraulic design of the intake can minimize diversion of bed load. In the spreading channels the saltation load will settle and further downstream also part of the suspended load, the remainder will reach the ponding areas.

For a first estimate of the suspended load, the study of Heusch and Lillières-Lacroix is helpful. Based on data from the Mahgreb (NW Africa) they determined the average and median values of the turbidity (saltation and suspended load) as a function of rock type in the catchment, Table 13.3a.

With increasing rainfall and runoff, the turbidity decreases, see Table 13.3b, due to the protection of vegetation to erosion, but the sediment yield increases because of more runoff.

<i>No. of catchments</i>	<i>Dominant lithology</i>	<i>Average</i>	<i>Median</i>
9	Marl	30.2	31
13	Marl-schist	15,5	9.2
12	Marly limestone and Marls-sandstone	9.9	8.7
10	Loam, schist	6.4	5.7
13	Limestone, dolomite	2.5	2.6
11	Sandstone, micaschist	1.8	1.2

**Table 13-4a** Influence of catchment lithology on turbidity of rivers in NW Africa. Source: Heusch and Lillières-Lacroix (1971).

Furthermore, methods such as those of the Pacific Southwest Inter-Agency Committee (PSIAC, 1968) sediment yield prediction procedure can be used for an estimate of the sediment yield (Johnson and Gebhardt, 1982), whereby geomorphological and vegetation factors can be estimated by image interpretation.

<i>Catchment type</i>	<i>Annual Rainfall (mm)</i>	<i>Annual runoff</i>		<i>Turbidity (g/l)</i>
		<i>Mm</i>	<i>% of rainfall</i>	
Sub-desert	326	15.8	4.8	16.9
Semi-arid zone	477	52.7	11	11.3
Sub-humid zone	692	171	24.7	7.6
Humid mountains	1,031	467	45.3	5.5

**Table 13-4b** Rainfall, runoff and turbidity in NW Africa. Source: Heusch and Lillières-Lacroix (1971).

### 13.4.8 Topography and land use

#### *Slope and dissection of the infiltration area*

Slope steepness is an important factor in the selection of sites, because on steeper gradients construction costs of schemes increase. Ponding areas (see Figure 13.5) are relatively small on steeper slopes and erosion may take place in the overflow areas of the canal-overflow basin type of scheme.

Unless photogrammetry with large scale aerial photographs or high-resolution satellite images can be used, the slope has to be determined by field surveying in order to obtain the required accuracy, assuming that a Lidar survey for a single recharge scheme of limited size is too expensive. Topographic maps and STRM data (Chapter 4, 4.6.1) provide an overall measure for the slope steepness of use in the screening at reconnaissance level and crude estimates can be made by image interpretation (see e.g. the steep fan B and the gentle fan A of Figure 13.18).

For the screening process the degree of dissection is important and dissection can be judged by image interpretation, particularly by using stereo high-resolution images. Strongly dissected fans can also be observed on medium resolution images (e.g. Figure 13.19, UF1 and UF2).

A network of incised drainage lines as can be found on upper alluvial fans and fluvial terraces, may prevent the construction of spreading canals and ponding dykes (curvature too strong), and complicates the construction of the deep basin type.

### *Land use, infrastructure*

In the screening process, land use is an important factor, in some cases a decisive one. Infiltration areas of recharge schemes are generally not planned on lands with valuable infrastructure, such as irrigated areas, settlements and so on. Sufficient space for infiltration areas on rangelands can be easily assessed by image interpretation.

In the application area of a scheme, the presence of arable and irrigable lands should be interpreted using land use pattern and crop response as an indication of suitability of the soil for irrigated crops. Most MAR schemes are constructed for the benefit of irrigated agriculture.

The order of magnitude of possible damages to infrastructure by flooding can also be estimated by image interpretation. As discussed earlier, flood damage mitigation can have an important impact on the economics of a scheme.

The images allow assessment of the accessibility of potential sites, and accessibility plays a role in the overall costs.

### **13.4.9 Flood damages**

In many of the images shown above (e.g. Figures 13.10, 13.12, 13.15, 13.18, 13.19 and 13.20) it can be observed that flash flows and sediment can reach infrastructure and agricultural fields, causing damage. Mitigation of flood damages can be achieved by reduction of the flow through diversion to infiltration basins in recharge areas.

Remotely sensed images can play an important role in the inventory of the total damage, as was shown by Maathuis et al. (1997) in a damage survey following the devastating floods of June 1996 in central Yemen, whereby affected areas were mapped using multi-scale images, taken before and after the flood. After the survey, the recommendation was made to construct a flood-spreading scheme in the area shown in Figure 13.23 to reduce the damages further downstream but also to alleviate the declining groundwater level in the alluvial aquifers in the valleys, due to pumping for irrigation.

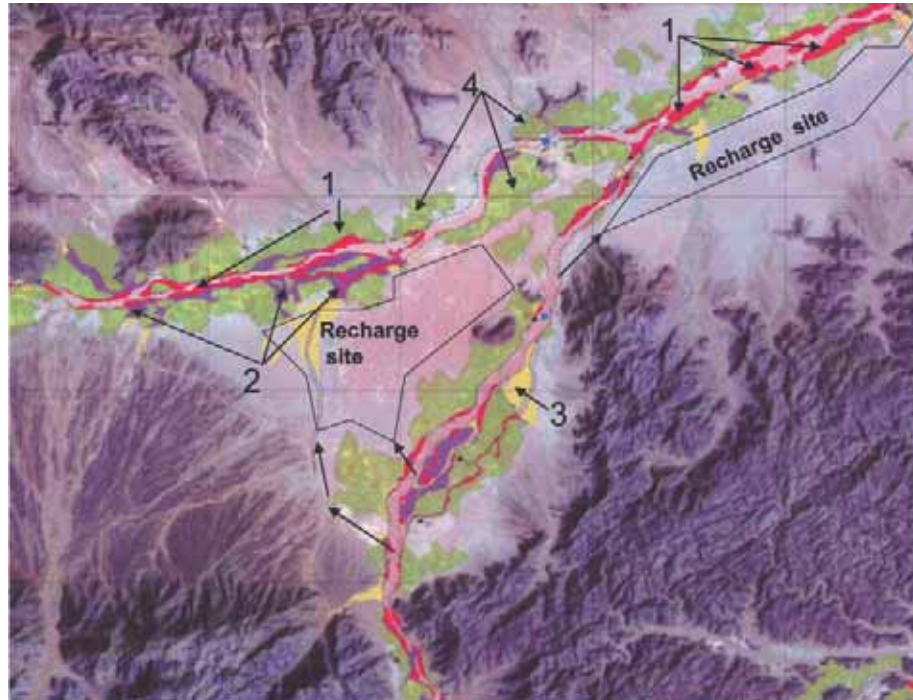


Figure 13-23

Permeable alluvial area suitable for recharge and flood storage, shown on flood damage survey map made after devastating June 1996 floods in north Yemen, Wadi Markha upstream of Wasit.

Red areas (1) fields and infrastructure destroyed by erosion; Purple areas (2) fields destroyed by sedimentation; Yellow areas (3) sedimentation, Green areas (4) irrigated fields.

Damage survey map by multi-scale images taken after flood of all affected wadis; interpretation results shown on background of Landsat TM image. Distance E-W is 14 km.

Flood damage mitigation plays an important role in cost-benefit analysis, whereby the construction and maintenance costs are compared with the benefits obtained by water for agricultural production or drinking water and reduced costs of flood damage, as main factors.

The estimates of damage within the affected areas need field investigation, but this can be done at areas and places potentially affected by the floods as interpreted on images. Furthermore, with high-resolution images objects can be identified, such as buildings, roads, canals and so on.

Kheirkhah (2005) looked at the construction costs and maintenance costs of flood-spreading schemes of different magnitude and type at a particular site (Chandab area, north-central Iran) and the benefits of using recharged water and reduced flood damage as main criteria. He differentiated the potential infiltration area into Site 1 being the upper part of an alluvial fan of more limited dimension than a larger Site 2 on the downslope side of Site 1. Each of the two sites was divided into two parts. These sites were delineated on the basis of remotely sensed images, and soil permeability data were available. The total runoff for diversion was estimated using the curve number method (SCS) with remote sensing input and available discharge estimates made at catchment outlet just upstream of the infiltration area. Calculations were made up to  $67 \text{ m}^3 \text{ s}^{-1}$ , being the maximum capacity of the intake and supply canal feasible for the site. Recharge to groundwater was estimated using 1D soil moisture modelling, by considering permeability and depth of inundated water in the various parts and types of scheme.

Various 'alternative' options pertaining to size and two types of schemes, the deep basin type and the canal cum overflow basin type, were considered. The results are shown in Table 13.4, which shows high costs per unit of recharge water when small amounts of water are diverted. Costs per unit of water decrease are the least for the simple, small sized canal cum basin type. For larger amounts of water diverted (up to  $30 \text{ m}^3 \text{ s}^{-1}$ ) and associated larger developed infiltration areas, costs per unit of water stabilize. According to Kheirkhah (2005), for the larger schemes, which are effective for flood damage mitigation, the total estimated benefits outweigh the total costs. This conclusion is of course particular to the Chandab area.

Scheme	Main criterion Costs (€1,000)			Main criterion			Costs per $\text{m}^3$ of recharged water (€)	
	Sub-criterion		Total costs	Sub-criterion		Life-time (years)	Without flood mitigation	With flood mitigation
Canal and Basin type	Construction	Maintenance		Harvested water ( $1,000 \text{ m}^3$ )	Flood mitigation (€1,000)			
Site I, Part 1	114	394	508	6,321	0	45	0.080	0.080
Site I, Part 2	124	381	505	5,087	0	37	0.099	0.099
Site II	267	1,004	1,272	10,227	0	50	0.124	0.124
Site I, Part 1+ Part 2	238	775	1,013	11,408	1,254	37-45	0.088	-0.021*
Site I + Site II	505	1,780	2,285	21,635	2,312	37-50	0.105	-0.001*
Deep Basin Scheme	981	2,032	3,013	28,606	3,922	50 >	0.105	-0.032

\* total benefits outweigh costs

Table 13-4 Cost and benefit estimation of various alternative schemes for Chandab Area. After Kheirkhah (2005).

### 13.4.10 The screening process

The synoptic view offered by satellite images makes it possible to rapidly assess whether or not an area has promise for a possible scheme.

Generally, the catchment size, coupled to presence of an aquifer (generally alluvial aquifer) is the first aspect to be considered. The images are then checked for aspects, which may exclude the area from further consideration, such as excessive sediment loads, lack of space for infiltration areas and specific to parts of Iran – presence



of salt domes causing saline water in the river. Relative severity of flooding and characteristics of the application area is another aspect that should be noted, for reasons mentioned earlier.

It may be decided to subject a reduced number of areas for more detailed interpretation concerning the sediment load and composition, catchment runoff, details of potential infiltration areas and possible salinity hazard.

Multi-criteria analysis, such as AHP, can be used, but for screening at reconnaissance level simpler methods may suffice, such as weighted addition of scores for the main factors.

Experience has shown that in many semi-arid regions not too many areas have favourable conditions with regard to most of the main factors. It is wise to discuss the screening results with other persons having experience in selection or construction of flood-spreading schemes, in order not to disregard areas that may well score well in the analysis of stage 2, for which field information has to be included.

## 13.5 Summary and conclusions

In order to augment groundwater resources in dry regions use can be made of river water, generally ephemeral flows. Amongst a variety of schemes, two categories are discussed and illustrated; (1) flow retardation and storage in small structures across streams within a catchment, and (2) flood-spreading schemes.

The use of remote sensing in selection of sites for the first category of schemes concentrates on the identification of aquifers along stream courses, presence of fractures and land use.

The second category has more complexities because a variety of factors have to be considered, such as: runoff amount and water quality, sediment load and characteristics, nature and thickness of aquifers, nature and availability of infiltration areas and possible mitigation of flood damages.

A multi-criteria approach for screening the suitability of areas and sites in three phases is discussed. Within a given region a large number of possible catchments and sites will have to be examined, while in many dry regions little thematic data of sufficient detail is available.

Most of the screening at the first phase – at reconnaissance level – can be done by visual image interpretation, provided the interpreter has hydrogeological and geomorphological background knowledge. Introduction to such subjects are given.

Promising areas are retained in the screening process for further scrutiny at the second phase, where remote sensing can provide some of the specific data needed; the same is true for the last phase, which focuses on sites in areas that have the best promise.

Screening is an efficient method for site selection because of avoidance of redundant data collection.

Three types of flood spreading schemes are discussed: (a) the canal and overflow basin type, (b) the deep basin type and (c) the long dyke type. Visual interpretation of images can identify which of these types is the most suitable for a given area. Remotely sensed images illustrate how the various factors can be judged.

In the evaluation and image interpretation during the screening it is useful to bear in mind some economic considerations with regard to trade-off between size of scheme and costs. A study based on an Iranian case study, following the multi-criteria approach, showed that the ratio of scheme-costs per cubic metre of water recharged for two types of flood-spreading schemes versus benefits by reduction of flood damages, due to diversion of flood water into the recharge scheme, was low for the larger schemes at a particular site

## References

- Bouwer, H., 1989. Effect of water depth in groundwater recharge basins on infiltration. *Journal of Irrigation and Drainage Engineering*, Vol. 115(4), pp. 556–67.
- Bouwer, H., 1996. Issues in artificial recharge. *Water Science and Technology*, Vol. 33, pp. 381–90.
- Bouwer, H., 2002. Artificial recharge and engineering. *Hydrogeology Journal*, Vol.10(1), pp. 121–42.
- Das, D. 2006. Development of fresh water sources in some parts of the arsenic contaminated areas of West Bengal (eastern India) through artificial recharge: a remote sensing and geographical information system approach. Topic 7, ISMAR 2005, Proc. 5th Intern. Symp. Management of Aquifer Recharge, Berlin, IHP-VI, *Series on Groundwater*, No. 13, UNESCO.
- Esfandiari-Baiat, M. and Rahbar, G. 2004. Monitoring of inflow and outflow rate from Kaftari artificial recharge of

- groundwater system in Dorz-Sayban region in south-eastern Iran. I.N. Gale (ed.) *Strategies for managed aquifer recharge (MAR) in semi-arid areas*. [www.iah.org/recharge](http://www.iah.org/recharge) and [www.unesco.org/water/ihp](http://www.unesco.org/water/ihp).
- Fernández-Escalante, A.E., García-Rodríguez, M. and Villaroya-Gil, F., 2006. Use of environmental indicators in a multicriteria analysis of the impact of MAR on groundwater dependent wetlands. Topic 7, ISMAR 2005, Proc. 5th Intern. Symp. Management of Aquifer Recharge, Berlin, IHP-VI, *Series on Groundwater* No. 13, UNESCO.
- Gale I.N., (Ed), 2005. *Strategies for managed aquifer recharge (MAR) in semi-arid areas*. [www.iah.org/recharge](http://www.iah.org/recharge) and [www.unesco.org/water/ihp](http://www.unesco.org/water/ihp).
- Gale, I.N., Macdonald, D.M.J., Calow, R.C., Neumann, I., Moench, M., Kulkarni, H., Mudrakharta, S. and Palanisami, K. 2006. Managed Aquifer Recharge: an assessment of its role and effectiveness in watershed management. *British Geological Survey*, Commissioned Report, CR/06/107N.
- Gleick, P. 1993. *Water in Crisis: a guide to fresh water resources*. Oxford Univ. Press, Oxford, UK.
- Hadley, R.F., Lal, R., Onstad, Walling, D.E. and Yair, A. 1985. *Recent developments in erosion and sediment yield studies*. Techn. Doc. In Hydrology, UNESCO-IHP, Paris.
- Heusch, B. and Milliès-Lacroix, A. 1971. Une méthode pour estimer l'écoulement et l'érosion dans un bassin. Application au Maghreb. *Mines et Géologie*, No. 33, Rabat, pp. 21–39.
- Hossainipoor, H.K. 2000. Water quality analysis of the Sarchahan Plain aquifer, Hormozgan, Iran. M.Sc thesis, ITC, Enschede, The Netherlands.
- Huisman, L. and Olthoorn, T.N. 1983. *Artificial Groundwater Recharge*. Pitman, Boston.
- Metternich, G.I. and Zinck, J.A. 2002. Remote Sensing of soil salinity: potentials and constraints. *Remote Sensing of Environment*, 85, (2003), pp. 1–20.
- Inbar, M. 1972. A geomorphic analysis of a catastrophic flood in a Mediterranean basaltic watershed. Paper presented to 22nd International Geographical Congr., Montreal, Canada.
- Johnson, C.W. and Gebhardt, K.A. 1982. Predicting sediment yields from sagebrush rangelands. Proc. Workshop on estimating erosion and sediment on rangelands. US Dept. Agric. ARM-W-26, pp. 145–56.
- Kheirkah, M.Z. 2005. Decision support system for floodwater spreading site selection in Iran. ITC, Enschede, The Netherlands, Publ. No. 122.
- Maathuis, B.H.P., Meijerink, A.M.J. and Timmermans, W.J. 1997. The June 1996 flood in Central Yemen studied by aerospace imagery. River Flood Disasters. Proc. ICSU SC/IDNDR. IHP/OHP-Berichte.Sonderheft 10, Koblenz 1997, pp. 107–26.
- Pacific Southwestern Inter-Agency Committee (PSIAC). 1968. Report of the water management subcommittee on factors affecting sediment yield in the Pacific southwest area. USDA Forest Service.
- Rodier, J.A. 1975. Evaluation de l'écoulement annuel dans le Sahel tropical Africain. Travaux et Documents de l'ORSTOM, No. 46, Bondy, France.
- Saathy, T.L. 1980. *The Analytic Hierarchy Process*. McGraw Hill, New York.
- Saraf, A.K and Chaudhury, P.R. 1998. Integrated remote sensing and GIS for groundwater exploration and identification of artificial recharge sites. *Intern. J. of Remote Sensing*, Vol. 19(10), pp. 1825–41.
- Slack, R.B. and Welch, R. 1980. Soil Conservation Service Runoff Curve Number Estimates from Landsat Data. *Water Resources Bulletin*, Vol. 16(5), pp. 887–93.
- USDA-SCS. 1985. *National Engineering Handbook*, Section 4L: Hydrology. Washington, DC: USDA-SCS.
- Sorman, A.U., Abdulrazzak, M.J. 1993. Infiltration-recharge through wadi beds in arid regions. *Hydrological Sciences Journal*, Vol. 38(3), pp. 173–86.
- Walters, M.O. 1990. Transmission losses in arid region. *Journal of Hydraulic Engineering* Vol. 116(1), pp. 129–38.

# General themes

## 14.1 Introduction

The role of remote sensing in a number of cross-cutting themes will be discussed that have a relation with ground-water and are independent of the geological nature of the terrain, namely: Rainfall, Evapotranspiration, Vegetation, Recharge, Soil Moisture, Gravity data for groundwater storage changes in large aquifers and Hyperspectral imaging.

These applications make use of various sensors or their combinations. Reference is made to sections in earlier chapters where aspects of the themes have been mentioned and illustrated.

## 14.2 Rainfall

### 14.2.1 Introduction

Most aquifers are in relatively flat terrain and correlation coefficients of annual or monthly rainfall between stations some tens of km apart are sufficiently high to be used for interpolation. Hence a water budget for an aquifer on an annual or monthly basis can be made using rainfall station data.

However, in dry regions with deep groundwater, recharge is often limited to large rainfall amounts occurring over a few days and such events may happen only once, on average, in one or two decades. An insight into the rainfall pattern during such events would be welcome. Furthermore, paucity of rainfall data affects the runoff estimates of ungauged catchments required for design of artificial groundwater recharge schemes and the spatial pattern of averaged recharge.

Considering the poor density of rain gauges in many parts of the world and associated poor data availability and consistency, methods have been developed to use easily available multi-spectral and thermal satellite images to improve determination of spatial rainfall. An overview is given by Collier (2000).

### 14.2.2 Qualitative rainfall patterns

In groundwater studies, the simplest method for improving seasonal or annual isohyetal maps is to plot rainfall stations on a vegetation index map and adjust isohyets, assuming that the natural or semi-natural vegetation density reflects rainfall amount. Adjustments for land use have to be made. The result will be more accurate than that based on mere interpolation of data with wide spacing between stations.

An example of a localized area with higher rainfall than the surrounding, as evidenced by the vegetation response on a NDWI image is shown in Figure 14.1. An NDVI image (not shown) shows the same pattern. There are no reasons to account for the denser vegetation on the basement plateau due to relief, geology, geomorphology and overall soil properties.

The dense vegetation in the hills in the east is due to orographic rainfall and ecologists believe that the forest type on the hills points to rainfall at the higher altitudes of >1,000 mm annually. The area is located in NW Kenya for which no standard rain gauge data are available. Global TRRM data indicates that rainfall three months prior to the satellite overpass was low (<20 mm/month).

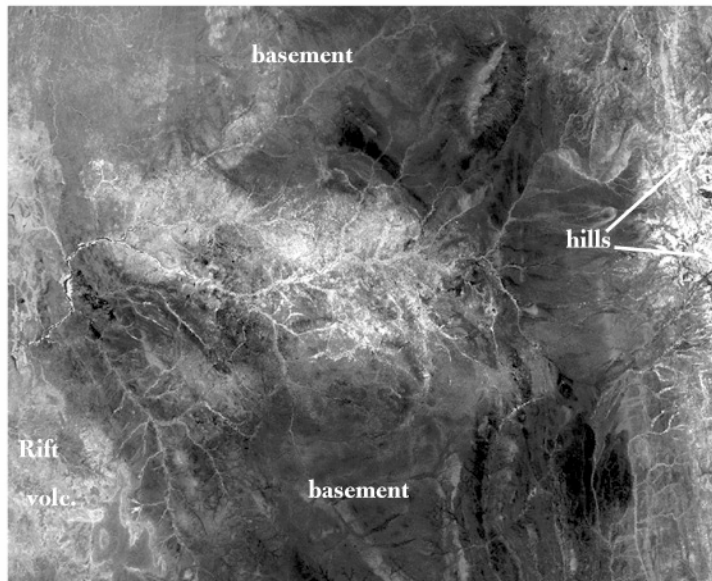


Figure 14-1

Area around Baragoi, N. Kenya

NDWI image of part of the gently undulating basement complex with localized area of higher rainfall, as reflected by the vegetation wetness, due to rainfall, not captured by rain gauges.

On western side are the Rift valley volcanics. Eastern margin shows high hills with forest vegetation and water vegetation content due to orographic rainfall.

Landsat ETM+ 27 Jan 2000

Distance E-W is 50 km.

### 14.2.3 Estimation of rainfall amounts

#### *Visual and thermal data*

For estimation of daily rainfall, use is made of the visual bands to detect cloud patterns using reflectivity and the thermal band is used for obtaining the temperature of clouds, whereby the 'cold cloud duration' and temperature thresholds are important parameters. The accuracy of the determination of the spatial rainfall depends on a number of factors related to type of clouds and their development, requiring empirical relations which are time dependent, availability of rain gauge data, success in differentiating snow cover from cloud cover, and so on.

Despite the relatively low accuracy of daily rainfall measurement by satellite data, applied to large areas only, it can be stated that use of satellite data always results in an improvement of the spatial rainfall estimate if gauge density is low. Correlation coefficients of satellite-based rainfall with station data are in the range of about 0.5 to 0.7, depending on the region and method used. Such estimates are routinely used for crop forecasting in Africa and hydrologic forecasting in large river basins (Grimes and Diop, 2003), even if simplified methods are used.

Low cost receivers and software for PCs make it now possible to make rainfall estimates using the METEOSAT-8 (MSG) at a decentralized level. Maathuis et al. (2006) described the system, which includes a low cost disk antenna and demonstrated the hydrological functionality with a local station in Uganda.

#### *Microwave remote sensing*

The Tropical Rainfall Measuring Mission (TRMM) was the first satellite with the specific purpose of measuring rainfall in the tropics by employing active radar. The advantage of radar for precipitation measurement is that actual rainfall is sensed physically.

Real time, quick looks are available on the internet, and all TRMM products are archived and distributed by Goddard Distributed Archive Center (DAAC) [trmm.gsfc.nasa.gov/dir dat a.html]

The TRRM rainfall information provided can be used for relating short episodes of heavy rainfall to, for example, groundwater rises in boreholes when no rain gauge data is available.

However, TRRM will be decommissioned by the end of 2006 while the Global Precipitation Mission, a concerted effort of several Space Agencies will start by the end of the decade.

#### *Composite systems*

The methods for rainfall prediction based on infrared data and based on microwave data (passive) have limited accuracy. A combination of the two improves the validity of prediction.

NOAA's Climate Prediction Centre implemented an improved version of Africa-RFE rainfall data. The frequent (30 minutes) infrared data of geostationary Meteosat is used for observing cold cloud top temperatures and this is combined with data of two specific microwave sensors and data from about 1,000 ground rainfall stations is used to remove bias. Daily totals in mm at an approximate resolution of 10 km are summed up to provide decadal estimates, but warm cloud precipitation estimates are not included (CPC FEWS-NET).

## 14.3 Evapotranspiration

### 14.3.1 Hydrogeological applications

Setting up a groundwater budget requires estimating the loss of groundwater by capillary rise if groundwater is at shallow depths and groundwater uptake by vegetation, which in some semi-arid environments may reach depths of tens of metres or even more. This loss is the actual evapotranspiration (ET<sub>a</sub>), which now can be assessed by a satellite data-based surface energy balance method with a minimum of ground data (termed here: SatSEB, for differentiation with SEB based on ground station data).

Some applications of SatSEB in groundwater studies are mentioned in the section 14.5 on recharge, section 14.6.2 on soil moisture, and in Chapter 12. In this section the gist of the method is mentioned, the results of some comparative studies, and attention is drawn to a new and much simplified method.

It is noteworthy that satellite data can be used for groundwater recharge estimates. Brunner (2004) used satellite-derived ET<sub>a</sub> for estimation of groundwater recharge patterns by subtracting rainfall (also derived by satellite data) from ET<sub>a</sub> (using Roerink's method, see below) with a series of 47 satellite images (NOAA-AVHRR) over a period of 9 years for a part of Botswana. The relative recharge obtained in this manner was correlated with recharge estimates based on the chloride method.

Traditionally it is difficult, if not impossible, to obtain the spatial patterns of the actual evapotranspiration. Usually ET<sub>a</sub> is estimated by making a water balance in an aggregated manner, whereby ET<sub>a</sub> is the remaining term, containing the errors of the other terms.

### 14.3.2 Surface energy balance

Only the gist of this method is mentioned; for proper discussion of the multi-step procedure, requiring radiometric and atmospheric corrections, the reader is referred to the references in this section.

The surface energy balance states that:

$$R_n - (H + L_e + G_o) = 0 \quad (a)$$

where,  $R_n$  is the net radiation at the surface,  $H$  the latent heat flux,  $L_e$  the sensible heat flux and  $G_o$  the ground heat flux, all in the same units ( $W\ m^{-2}$ ). The equation is deceptively simple, because the determination of the terms is no easy matter. It is important to remark that algorithms have been developed that require, apart from multi-spectral satellite data, including thermal band(s), only standard meteorological data.

Equation (a) can be expressed as latent heat flux by considering evaporative fraction ( $\Lambda$ ) and net available energy ( $R_n - G_o$ ):

$$L_e = \Lambda (R_n - G_o) \quad (b)$$

where

$$\Lambda = L_e / (R_n - G_o) = L_e / (L_e + H) \quad (c)$$

For  $R_n$ , net radiation, the difference between incoming and outgoing radiation at the surface, multi-spectral and thermal satellite data is used to determine the albedo, or short wave reflection ( $0.3-3\ \mu$ ) and the long wave (thermal) radiation ( $3,100\ \mu$ ). Together they constitute outgoing energy not available for evapotranspiration. The outgoing radiation is a function of the surface temperature, in other words, the kinematic temperature of soil and canopy surface and their emissivity.

Incoming radiation is the product of exo-atmospheric radiation, depending on sun-earth astronomical relations for which tables exist, and the atmospheric transmittance ( $\tau$ ). It has to be measured on the ground or estimated from empirical equations.

The simplest form for H, latent heat flux, is:

$$H = \rho_a C_p / r_{ah} (T_0 - T_a) \quad (d)$$

where  $\rho_a$  is the density of air,  $C_p$  the heat capacity of air,  $T_0$  the aerodynamic surface temperature,  $T_a$  the air temperature at a reference height within the surface layer, and  $r_{ah}$  the aerodynamic resistance to heat transport. However, the determination of  $T_0$  and  $r_{ah}$  is difficult. A linear relationship between the radiometric surface temperature, which is obtained for the thermal image and the aerodynamic surface temperature is not always valid, but this relation is used for internal calibration purposes in dividing the available energy over the turbulent fluxes. A practical solution for this partitioning is given below.

The thermal band(s) data of satellite sensors are used, because the surface temperature is a key element in the determination of H, but some additional data is needed for some parameter-lean models, namely SEBS (Su, 2002) or SEBAL (Bastiaanssen et al., 1998). The additional data needed are (interpolated) station data of air temperature, relative humidity, wind speed and NDVI.

The ground heat flux  $G_o$  is the smallest quantity in the surface energy budget and is either measured or is estimated as a fraction of  $R_n$  taking into account presence of leaves through a satellite-based vegetation index.

For a discussion and implementation of the multi-step procedure and options for obtaining parameter values, the reader is referred to Kustas et al., 1996; Bastiaanssen, 1998a; Menenti, 2000a; Roerink et al., 2000 and Su, 2005.

A long-standing problem was the estimation of H in the absence of well instrumented sites, because the  $H(T_0)$  relationship is not unique. A practical way to overcome the problem of relating source height to radiometric surface temperature is by selecting manually on the images the driest and wettest locations (pixels). By model inversion, a temperature difference  $\Delta T_{air}$  is obtained, which is required for the matching of the range of H in given turbulent conditions. For a fully wet pixel,  $H \approx 0$ , and for a dry pixel with no or negligible evaporation,  $Le \approx 0$ . Roerink et al. (2000) describe a simplified method whereby the fraction of net energy consumed by evaporating water is determined from a pixel-wise plot of surface temperature versus albedo.

### 14.3.3 Simplified, semi-automated approach

It may be remarked that a recent study (Timmermans et al. under review, 2007) offers a simplified and automated approach based on the surface energy balance, requiring only a cloud free and atmospherically corrected radiometric surface temperature image. The evaporative fraction is redefined as:  $\Lambda = (T_{max} - T_0) / (T_{max} - T_{min})$  where,  $T_{max}$  is taken as the hottest pixel in the image,  $T_{min}$  as the 0.5% lowest temperature on the image to avoid extreme conditions, using the histogram. It is assumed that pixels having the latter value are transpiring at potential rate. Furthermore, simple relationships are used for atmospheric transmissivity and atmospheric emissivity. Surface albedo is assumed to be a linear function of  $T_0$  and the long wave radiation components using  $T_{min}$  in combination with nominal values for emissivity, while  $G_o$  is assumed to be a simple linear function of  $\Lambda$ . Having obtained values for each pixel of  $\Lambda$ ,  $R_n$ ,  $G_o$ , equation (b) can be solved for  $Le$ , being equivalent to the actual evapotranspiration (ETa).

Results of the simplified method, termed DATTUTDUT, have been compared with ETa obtained in two well-instrumented test areas of heterogeneous terrain and with another area under irrigation, for which a time series of ETa was available, obtained by various field methods. The simplified method performed as well as the single source model and two versions of a dual source model. The latter evaluates soil evaporation and transpiration separately. For the irrigated area the simplified method produced results that were closer to ETa based on an overall water budget than results of available single source model data.

### 14.3.4 From instantaneous ETa to time series

The net available energy in equation b is originally an instantaneous value, valid for satellite overpass time. Conversion to a daily value is straightforward for cloud free days only. For periods between overpasses the assumption is made, based on experimental evidence, that the evaporative fraction (equation c) remains constant, on the condition that soil moisture does not change much. The day-to-day variation of  $Le$  is best overcome by temporal integration (averaging or accumulation) using satellite time series; MODIS, METEOSAT-S-G or NOAA

AVHRR offer such series, but at spatial resolutions of 500 m or more. Examples of the variation of ETa using satellite data for successive days or weeks are given by Farah (2004) and Gieske and Meyninger (2005).

### 14.3.5 Accuracy and outlook

To assess the accuracy of the daily ETa calculated by SatSEB models is not simple, because it requires an accurate measurement of the spatial observations of ETa. Droogers and Kite (2002) discuss the varying results obtained in an area in Turkey, depending on methods used.

Lysimeters would be ideal, but not many exist, and these must be of a large size, preferably larger than the pixel size of the thermal sensor used (60 m or 90 m for Landsat or Aster). For time series with coarse resolution sensors the required size of a lysimeter is beyond practical limits.

The latent heat flux can be obtained from data of flux towers (fast thermo couples) or by scintillometers, but that data pertains to the footprint of the instruments and it is not always clear as to what exactly the footprint is, which varies with weather conditions.

Results of a dual layer SatSEB model and a single layer model were compared with a handful of flux tower observations by Timmermans et al. (2007). In general, there was reasonable agreement between the output of the two types of models, but spatial intercomparisons yielded relatively large discrepancies, which were attributed to land cover.

Timmermans et al. (under review) compared results of three models with this type of field data in three experimental sites in the US and concluded that accuracy was acceptable (mean absolute per cent difference ranged from 22 to 16, but some difficulties with the accuracy of the flux tower data were mentioned).

Validation of satellite based ETa calculations using data of meteorological fields stations in dry regions with savannah vegetation is hampered by the doubtful accuracy of the Bowen ratio or the temperature gradient method in such areas. Their use is appropriate in more humid regions. In semi-arid climates these methods seem to overestimate ETa, as was found by Obakeng (2007) who used many well-instrumented field stations situated some 10–20 km apart over the Serowe aquifer in Botswana. The annual ETa calculated from the station data by the two mentioned methods surpassed the annual rainfall. He also showed that transpiration from 30 by 30 m plots with dense tree stands, measured by sapflow was of an order of magnitude lower than the ETa station data. A single layer SEB algorithm, using Landsat TM and NOAA AVHRR of the Serowe area (Timmermans and Meijerink, 1999), yielded rates that were comparable to the ETa station data, but are far too high as well. However, it must be remarked that operator interference plays a role in the model used.

Finally, SatSEB model results have been compared with water balance analysis. A close agreement was found by Bastiaanssen and Bandara (2001) between results of a single layer SEB model for a medium-sized catchment in Sri Lanka and a conventional water balance, determined independently. Timmermans et al. (2007) noted that their simplified model had on average only 0.3 mm daily difference with a preliminary water budget described by Kite and Droogers (2000).

It is hoped that if results of more studies become available, the performance of the SatSEB methods for different terrain, vegetation and climatic conditions will be known. In any case, knowing the ETa pattern is helpful and in case of discrepancies with well-established water balances, scaling may be applied between near zero values for permanently dry surfaces to values that are close to potential evapotranspiration values valid for wet surfaces.

## 14.4 Vegetation and groundwater

### 14.4.1 Introduction

In the practice of siting wells, use is often made of the local knowledge of certain tree species as indicators for presence of groundwater. Tree and other plant associations may be related to groundwater occurrences at various depths, seepage zones, perched water tables and salinity of groundwater, as is, for example, discussed and illustrated for South Africa by Colvin et al (2003), and for Botswana by Kruck (1990) and by Ringrose et al. (2005). Obakeng (2007) used tracers to prove water uptake by savannah trees from large depths, even from groundwater at 76 m in Kalahari sands and he discusses the effect of water use by trees on net recharge and a regional water balance.

Once such relationships are known, remotely sensed images can be used to map the patterns. However, recognition of tree species and spectral classification requires usually high-resolution images, as will be mentioned below.

If such images are not available, multi-spectral classification techniques with medium-resolution (20–30 m) satellite data can be tried, but spatial heterogeneity of plant communities and effect of soil background may limit the accuracy of the result, because spectral clusters are likely to show significant overlap (see Chapter 2). Spectral unmixing methods may be applied, but the results may not have the desired accuracy.

Vegetation density can be mapped using vegetation indices (Chapter 2, section 2.9) at various resolutions, but it is difficult to separate grass and shrub vegetation with relatively shallow root systems in the vadose zone from trees with deeper roots, which may reach the saturated zone.

By grouping all species across biomes with the exclusion of croplands, Canadell et al. (1996) computed mean maximum rooting depths of  $7.0 \pm 1.2$  m for trees and  $5.1 \pm 0.8$  m for shrubs and  $2.6 \pm 0.1$  m for herbaceous plants.

Deep roots are most likely to occur in seasonally dry, semi-arid to humid tropical regions under savannah or thorn-scrub vegetation or under seasonally dry semi-deciduous to evergreen forests (Schenk and Jackson, 2005). Rooting depths of several tens of metres in semi-arid regions have been reported (Dell et al., 1983, Obakeng, 2007). Therefore, identification of tree and shrub vegetation in dry areas on images implies evapotranspiration from the vadose zone and possibly the saturated zone.

However, the net vegetation effect on recharge and evapotranspiration is complex because of many interactions in the processes involved. For example, under vegetation more infiltration may take place due to protection of the soil surface (no sealing), organic matter content of the soil and biological activities, but this may not necessarily lead to more recharge because plants take up water. This uptake depends on species and environmental factors and has to be determined (so far) by field experiments. The SatSEB methods aim at replacing these expensive field experiments, but as mentioned the accuracy of the result in diverse environments is not yet known.

A systematic study of the relationship between woody vegetation and groundwater up to 50 m depth, in an area in semi-arid Botswana using remote sensing (Landsat TM), was done by Ringrose et al. (1998). They used two vegetation criteria: (1) density of woody vegetation and (2) classes containing deep-rooted species and related results to lithology and to geomorphic units. TM bands 1, 5 and 7 were found to give the best results for classification, rather than transformed images (NDVI, PC). Compared with groundtruth, the vegetation density classes were found to be 85% correct and the classes with deep rooted species were 69% correctly classified. The distribution of dense vegetation was indicative for high potential geomorphic aquifers for 3 out of 5 cases (60%), while the distribution of classes with deep-rooted species were regarded as being only 20% successful in locating high potential aquifer sources. Dense woody classes tended to select aquifers in topographically higher areas, and deep-rooted species low lying areas, such as fossil valleys. Authors mention that man-made disturbance of the woody vegetation and the 30 m resolution of the TM data for classifications with species could have affected the results.

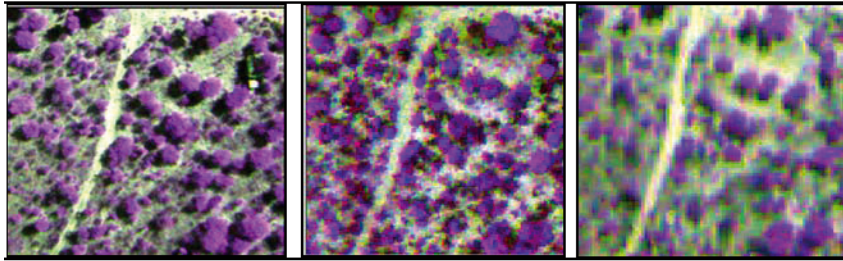
#### 14.4.2 *Species recognition and water use*

A study of the role of savannah trees in recharge and possible loss of groundwater by transpiration requires the identification of species. Transpiration measurements on trees (by sapflow or otherwise) have revealed much variation between species. Rates can vary from a small fraction of  $\text{mm}\cdot\text{d}^{-1}$  to a few  $\text{mm}\cdot\text{d}^{-1}$  (Thornburn et al., 1993, Obakeng, 2007) while in some cases in Australia and Botswana, no variation across seasons was found, indicating that environmental factors govern the process rather than evaporative demand. Important differences in sapflow-based transpiration rates were found not only between species but also within species.

Measurements made on individual trees have to be upscaled to areal estimates and to do so, the density of the species has to be known and hence high-resolution imagery is required. Multi-spectral classification may be used if the canopies are so large that they fully cover pixels and the trees are in leaf. The deterioration of recognition criteria such as crown size and structure as a function of pixel resolution is illustrated in Figure 14.2, which shows savannah trees with spatial resolutions of 30 cm obtained by a digital multi-spectral aerial camera and resolutions of 60 cm and 1 m, obtained by increasing the flying height.

High-resolution satellite images can be used for mapping of tree species. Kimani et al. (2007) added the 1 m resolution panchromatic band to the resampled 4 m resolution spectral bands of Ikonos. The false colour composite of the NIR, Red and Green band is shown in Figure 14.3 (left-hand image) and the composite of the





**Figure 14-2** False colour of savannah trees by digital aerial camera at resolutions of 30 cm (left), 60 cm (centre) and 1 m (right).  
Source: Kimani et al., 2007.

same bands of the aerial camera, at the same scale, is shown on the right-hand image. The images were used for classification of species using multi-spectral and object oriented classification.

The results demonstrated that the highest accuracy was obtained by the 30 cm resolution images.

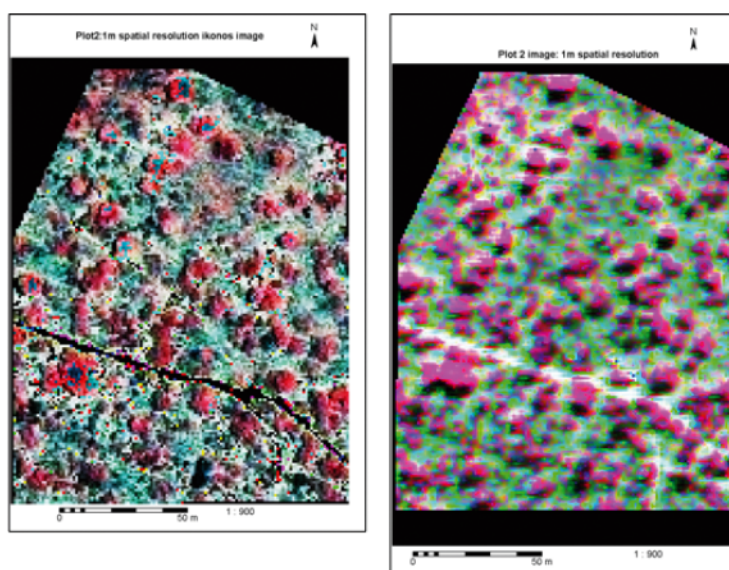
For the 1 m resolution images, the best result was achieved by using an object-oriented classification for the airborne images, but this was only slightly better than a maximum likelihood classification.

These investigations were made for upscaling sapflow measurements, first to the level of canopy area and then to the level of plots which measured 30 x 30 m. Annual plot transpiration rates were found to vary from 3 to 71 mm, depending on species and density. ETa estimates ranged, depending on location in the Serowe aquifer from 509 to 655 mm using the Bowen ratio-SEB and from 386 to 481 mm with the temperature gradient-SEB method. These values are higher than the mean annual rainfall of 437 mm. Therefore the validity ETa estimation of the two methods based on meteorological data for the savannah vegetation in Botswana has to be questioned. Moran et al. (1989) pointed out that the Bowen ratio cannot be applied to large, diverse areas.

It may be noted that a 1 layer SatSEB algorithm using a dry season Landsat and a NOAA-AVHRR image for pixels with medium to dense vegetation in the same area yielded values that also surpass the annual rainfall when the daily SatSEB ETa was multiplied with the number of days in a year (Timmermans and Meijerink, 1999).

Also interesting are the results of tracer studies in the area, which proved deep water uptake by several tree species up to a depth of 70 m from the phreatic surface in the Serowe area (Obakeng, 2007). However, there does not seem to be a relationship between deep groundwater depth and density of woody savannah vegetation, not with dry season ETa (SatSEB) in the thick Kalahari sands of the area investigated.

The above discussion shows that the inventory of species by remote sensing requires high-resolution data and that the next step, the estimation of water use, is complex. The two-layer SatSEB approach offers the possibility of separating soil evaporation from evapotranspiration by vegetation. However, the resolution of the thermal band (at best 60 m for satellite sensors) excludes the use for estimating ETa for tree species, unless uniform species occupy large areas. The latter is not the case for (semi)natural vegetation, especially not in dry regions.



**Figure 14-3**

Savannah vegetation in Botswana.

Left: false colour image of pan-sharpened Ikonos (1 m resolution)

Right: False colour image obtained by digital aerial camera (1m resolution).

Source: Kimani et al., 2007.

### 14.4.3 Areal estimates of evapotranspiration by other methods

Before the advent of the SatSEB approaches, satellite NDVI images were used for estimating large area evapotranspiration, based on relationships between NDVI and leaf area index (LAI), and interpolated meteorological station data with adjustment for topography and microclimate (Pierce et al. 1993).

Water use by phreatophytes on and near floodplains in arid and semi-arid areas in the US has been determined by a two-stage approach. First, the areal extent of vegetation associations using groundwater was determined by multi-spectral classification. After that the Bowen ratio SEB method with data from field meteorological stations was used to estimate ET<sub>a</sub> for each class (Lazniac, 2006). Instead of multi-spectral classification, vegetation density classes may be differentiated. DeMeo et al. (1993) in a study of phreatophyte evapotranspiration in Death Valley, US used the Soil Adjusted Vegetation Index (SAVI) with a temporal series of 6 Landsat TM images to distinguish classes of vegetation density to map evaporative groundwater discharge areas. Groundwater depths varied from near surface to 6 m. Annual evapotranspiration rates varied from 180 mm for sparse low vegetation to some 925 mm for dense vegetation. At the height of the growing season the rate was about 6 mm.d<sup>-1</sup>. DeMeo et al. (1993) found little difference between the Bowen ratio-SEB values and those derived by eddy correlation. In this case the Bowen ratio for estimating evapotranspiration was used because measurement was made over homogeneous areas surrounding the instruments, while the shallow groundwater surface (0 to 6 m b.g.l.) permitted high transpiration rates, contrary to the conditions in Botswana mentioned above.

### 14.4.4 Plant indicators for groundwater quality

Presence of agricultural fields with good crops, as evidenced by NDVI, in areas affected by salinity due to shallow groundwater are an indication of the presence of shallow groundwater with low salinity below the fields. Hyperspectral imaging (section 14.9, below) offers possibilities of improved determination of plant species and may be applied to surveying areas where relationships between salinity of shallow groundwater and vegetation types are known.

Spatial successions of vegetation types can be related to depth to groundwater and to salinity gradients, as described by Kruck (1990) for Botswana and other places. Figure 14.4 shows the relation between salinity and vegetation type.

## 14.5 Recharge

### 14.5.1 Interpretation, qualitative approaches

Recharge of groundwater is a key issue because the sustained use of groundwater depends on recharge. A comprehensive treatment of recharge issues and case studies is given in Lerner et al. (1990).

In the preceding chapters, several examples have been given concerning recharge. In general, recharge is strong if terrain units receive runoff from surrounding areas (run-on), such as ephemeral river beds, depressions in fossil dune areas, karst depressions, some lava flows, areas with ephemeral flood spreading over permeable deposits, such as sands and tuffs, and so on.

Such areas can be interpreted by close inspection of images, preferable high-resolution stereo-images. The intensity of the run-on may be estimated by judging the relative permeability of the catchment areas in conjunction with rainfall data. A high drainage density in the catchment (channels, gullies, large rills) indicates fast runoff, hence ponding may be negligible and time for infiltration on the slopes is limited. Incised drainage lines and poor development of colluvial zones at the foot of slopes are associated with high runoff. Estimation of runoff is discussed in Chapter 13, section 13.3.3.

If recharge is limited to rainfall recharge, the permeability of the soil and subsoil has to be assessed and this requires field observations, after delineating soil units aided by image – assuming that no adequate soil maps are available.

In many textbooks, the drainage density is considered to be inversely related to permeability. This may be so in some areas, but one has to be aware of the fact that resistance to erosion, *i.e.* drainage incision, under present and past climatic conditions also affects drainage density. For example, semi- or unconsolidated permeable sand

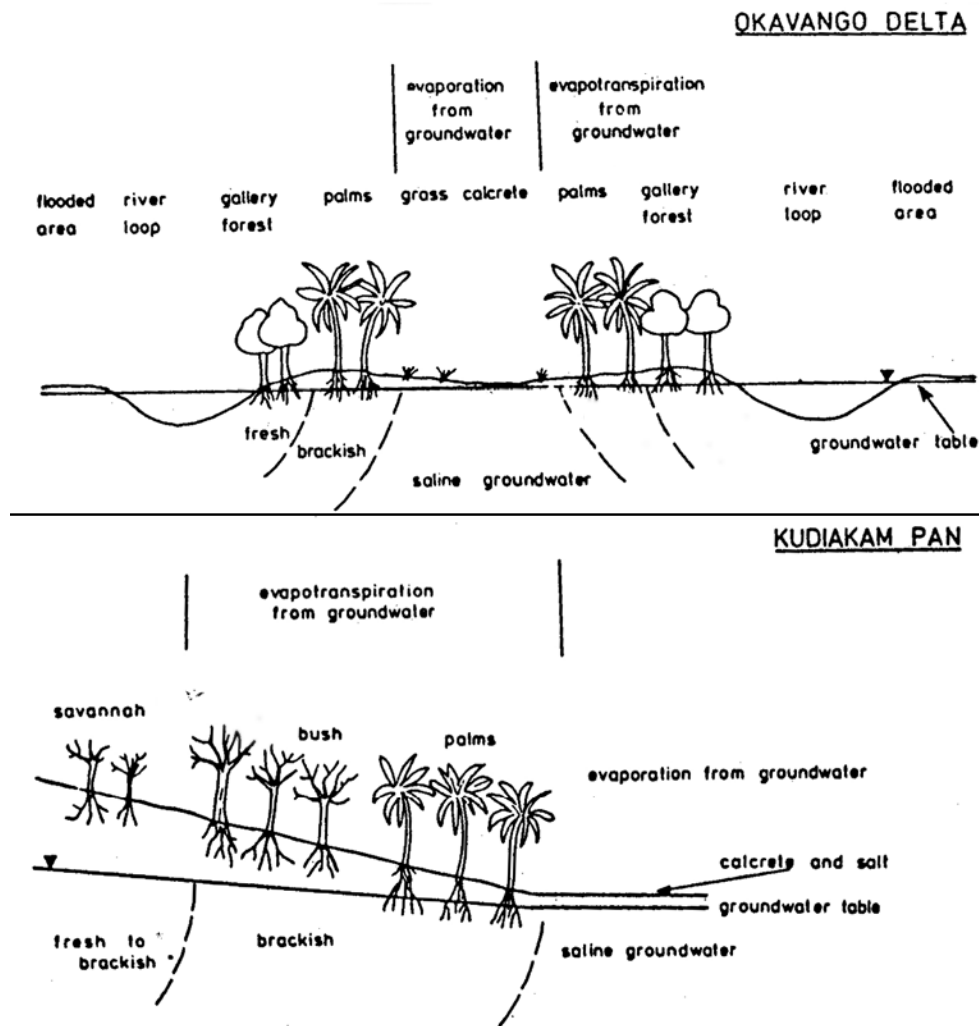


Figure 14-4 Relations between vegetation type and salinity of groundwater, Okavango, Botswana.  
Source: Kruck, 1990.

deposits may have a drainage density of near zero in an environment that is free of incision, but the same sands may have a drainage density of tens of  $\text{km.km}^{-2}$  when dissected by head ward erosion along, for example, river terrace bluffs. Hard, massive but impermeable basalts often have a very low drainage density because of their resistance to incision, not because of their permeability. Furthermore joint/fracture densities and even schistosity can influence drainage densities because they influence the erodibility of the rocks. Therefore, no simple and unique relations between drainage density and permeability exist.

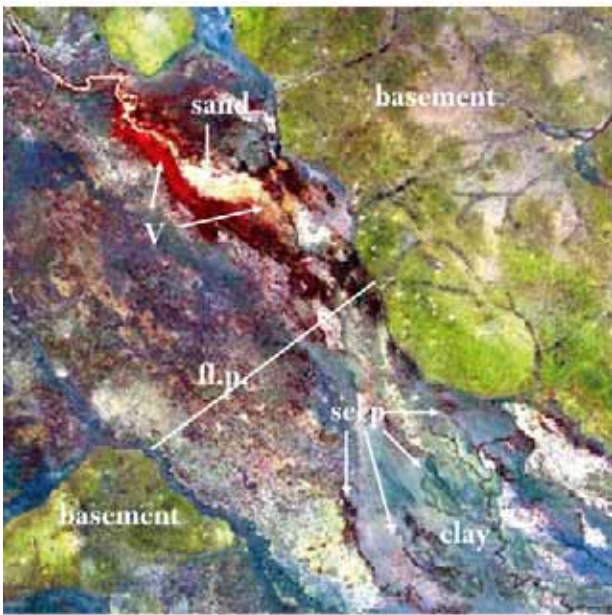
The interpretation of recharge has to rely on judging the effect of soil successions along the slopes from divide to channel (catena), the details of valley floors and drainage lines and the erosion history. Obviously, the presence of thick overburdens as evidenced by subdued landforms, are more favourable for recharge than areas with rock outcrops, particularly the smooth surfaces of inselbergs. Differences in overburden and recharge in two adjoining areas due to lithology (gabbro and peridotite) are shown in Chapter 10, section 10.7.

Depression areas collect runoff while water depth enhances infiltration and therefore potentially, recharge. However, clays may have accumulated in depressions, and depending on their mineralogical composition and physical properties, the clays can have low permeability, impeding recharge.

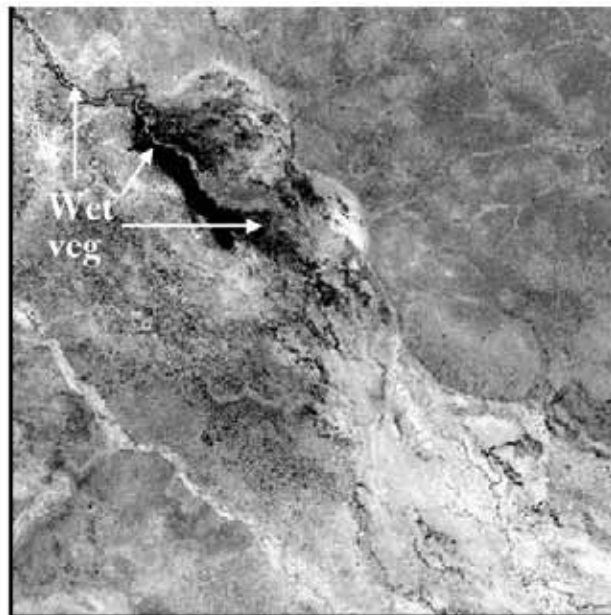
### 14.5.2 Locating areas with strong recharge

Areas with evident important recharge, in combination with presence of an aquifer can often be interpreted in a straightforward manner.

For example, Figure 14.5 (southern Kenya) shows mainly crystalline basement and alluvium of ephemeral drainage systems. The dry sandy riverbed and the sand splay of the largest system can be seen on the false colour image (Figure 14.5a, Landsat ETM+, bands 4, 3 and 1 in red, green and blue). Important recharge takes place in the area with red tones (green forest vegetation) along the riverbed and the sand splay, which indicate that flood spreading takes place. Further downstream silts and clays are deposited in the lower part of the floodplain, where grass and salt tolerant herb vegetation acts as a filter, because of reduction of the flow velocity due to spreading and transmission loss. The change of sands to silt-clay deposition is accompanied by a decrease of the depth of the groundwater table, because seepage pattern (*seep* in Figure 14.5a) can be observed. However absence of lush, green vegetation suggests that the groundwater is saline (as is indeed the case, sedges and salt tolerant species are found on the floodplain). High vegetation water content is shown on the NDWI image (Figure 14.5b, here in black tones).



**Figure 14-5a** False colour of Landsat ETM+ (bands 4, 3 and 1) of crystalline basement and alluvial deposits in a floodplain (fl.p.) in southern Kenya. Strong episodic recharge takes place in area with red tones and sand splay.  
Distance E-W is 13.2 km.



**Figure 14-5b** NDWI image of same area showing high vegetation wetness in area with flood spreading and transmission loss and low wetness in downstream floodplain with clay deposition and salinity, despite shallow groundwater table, note seepage channels (*seep*) on left image.

Depth to bedrock cannot be determined by interpretation, but the observed width, the interpreted aggradation and absence of outcrops in the floodplain make it likely that the saturated thickness and volume, maintained by the high recharge, is sufficiently developed to sustain substantial yields of good quality groundwater in the area with high vegetation wetness.

Also to be noted is the medium NDWI values of vegetation growing on the weathered zone of the basement rocks, suggesting the presence of soil moisture. Other examples of recharge in various types of geologic terrain are illustrated in chapters 7, 8, 9, 10 and 13.

In semi-arid or arid terrain average annual recharge is generally very limited, in the order of a few  $\text{mm}\cdot\text{y}^{-1}$ , or less. However, substantial recharge may take place during episodic heavy rainfall and shortly after such events from floodwaters infiltrating into floodplains and possibly from water stagnating in depressions. Such areas can be identified by remote sensing, as is illustrated in Figure 14.6. Pre-flood and post-flood images were combined using Principal Component transform and the colour combination is made by selecting those PCs that showed best the floodplains inundated during the flood. It is likely that most of the recharge took place by transmission loss in the floodplains rich in sandy materials. Most of the water accumulated in the temporary lake (in yellow) could have been lost by evaporation because the pre-flood images showed a dry lake bed composed probably of clayey deposits.

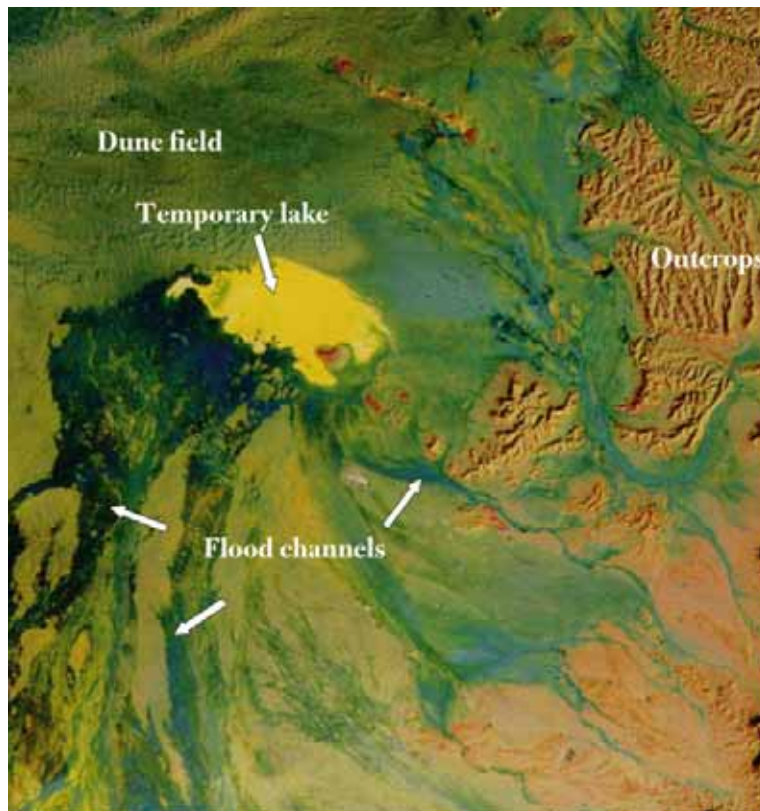


Figure 14-6

Temporary lake and flood plains after the June 1996 flood in Ramlat As Sab'atayn depression in central Yemen, causing episodic recharge of the desert area by transmission loss.

Image is made of PCs 2, 5 and 8 of pre-flood Landsat TM (6 bands) and post-flood IRS LISS-III (3 bands).

Distance E-W is 45 km.

Source: Maathuis et al., 1997.

### 14.5.3 Mapping of relative recharge units

Units with relative recharge can be mapped by image interpretation, followed by quantification estimates using conventional data, such as the chloride method, water table fluctuation or incorporation of the relative recharge pattern in the calibration of a groundwater model. Either terrain units, grouping geomorphology, lithology and cover, are differentiated as recharge units, or the units may be derived by a GIS procedure with weighted factors (see Shaban, 2006). The latter procedure, *mutatis mutandis*, forms the core of groundwater vulnerability mapping with approaches such as DRASTIC or similar ones (Chapter 12, section 12.7).

Terrain units with strong recharge, due to high permeability and runoff as mentioned earlier, can be emphasized. Examples are colluvial fringes around large and bare outcrops, ephemeral river beds near mountain fronts, where the bed materials tend to be coarse grained, most wind blown sand sheets, non-inundated karst depressions and so on.

Because of the subjectivity involved in estimating relative recharge of composite terrain units, it may be wise to use few classes only.

The amount of recharge may be estimated with the aid of a soil moisture model. When soil data is scanty, a simple model, (e.g. the Thornthwaite and Mather monthly soil moisture budget method) may be used. Apart from rainfall and potential evapotranspiration data, information about rooting depth (i.e. effective soil depth) and water holding capacity (WHC) of the soil as related to texture, has to be estimated in such approaches. Rooting depths may be judged by vegetation classification based on multi-spectral data, while WHC estimates may be based on terrain analysis using visual interpretation supplemented by field observation if soil maps are not available. If some recharge data is available the model may be calibrated, but the difficulty is to judge whether the rooting depth or the WHC has to be adjusted.

### 14.5.4 Patterns of rainfall recharge with satellite based rainfall and evapotranspiration

The pattern of groundwater recharge in dry regions can be estimated using only satellite data available on the internet and some point recharge data determined by field methods.

Patterns of relative recharge were obtained by Brunner et al. (2004) at regional scale in a semi-arid area by subtracting actual evapotranspiration (ETa) from rainfall (P), both obtained by satellite data. A total of 47 useable NOAA-AVHRR images of the period 1990–2000 were processed with the method of Roerink et al. (2000) to estimate spatial actual evapotranspiration. Spatial rainfall data was obtained from an internet source METEOSAT 5 based FEWS, (see section on rainfall) for the corresponding period. As the author remarks, neither the P nor the ETa estimates are accurate, but the pattern after subtraction of ETa from P of images of such a long period gives a good indication of the relative recharge pattern in time. The contents of the time averaged (P-ETa) maps were correlated with point recharge determined by the chloride method ( $R^2$  of 0.74 and 0.78 for logarithmic regression for two areas).

Because of the correlation the (P-ETa) map with relative values could be rescaled to absolute values.

## 14.6 Soil moisture

### 14.6.1 Multi-spectral, thermal and gamma radiation data

Images are interpreted in a hydrogeological context, in other words, surface features related to soil moisture are analysed in terms of geomorphology, relative groundwater depths and vegetation patterns, not by quantitatively relating soil moisture to reflectivity, which is too variable in space and time.

In the preceding text examples are given of wet soils related to shallow groundwater tables, either by reflectivity (Chapter 2, Image Processing) or by patterns due to groundwater emergence (section 14.7.4 and Chapter 7, section 7.4), or vegetation response indicating presence of water in fractures of hard rock terrain by NDVI images (Figures 2.21 and 10.14). The water content of vegetation, estimated by a simple NDWI transform, could be an indicator for soil moisture and presence of groundwater (Figure 14.5, above), because during dry periods the water content of the vegetation must be derived from the rooting depth in the soil and weathered or fractured zone. SPOT VEGETATION provides decadal (10-days) images of NDVI, and the Moderate Resolution Imaging Sensor (MODIS) is used for the purpose. Data sets covering the world are available through the internet.

Thermal images have been used in a qualitative sense in groundwater studies (see Chapter 5, Thermal Images) to identify shallow groundwater and moist soils because evaporation of moist areas cools the surface. However, interpretation may be confounded by the emissivity of other surfaces and by vegetation in areas where groundwater is deep.

Attempts have been made to relate surface temperature to volumetric soil moisture content. By observing the diurnal temperature change a relationship between the change and soil moisture can be made, provided the thermal conductivity and heat capacity of the soil is known. Diurnal changes can be obtained from low-resolution meteo-satellites. Furthermore, the method is limited to bare soil conditions.

Ahmed and Bastiaanssen (2003) related relative soil moisture content of the root zone, assumed to be 1 m, to the evaporative fraction (equation c, section Evapotranspiration) using an empirical function developed in soil moisture-evaporation-biomass studies (Schott, 2002):

$$\theta / \theta_s = e^{((\Lambda - 1) / 0.42)}$$

where  $\theta$  is volumetric soil moisture and  $\theta_s$  is saturated soil moisture. Using the equation, soil moisture maps can be made using satellite data.

The differences in gamma radiation of dry and wet soils can be observed on low altitude airborne surveys, but quantitative estimates of soil moisture require calibration flight lines to determine soil moisture background values. Furthermore, repeated surveys would be required for monitoring soil moisture change and therefore place this system out of practical bounds in hydrogeology.

### 14.6.2 Soil moisture and recharge, a discussion

Remotely sensed soil moisture monitoring is now feasible, by radar and by microwave remote sensing as discussed in Chapter 4 (Radar Images), but data pertains to the uppermost soil only and the expected accuracy still has to be established. It has been suggested to couple satellite-based surface soil moisture monitoring to recharge models.

The interest of soil moisture in hydrogeology concentrates on moisture flux in the vadose zone that deter-

mines groundwater recharge, but also possible loss of groundwater by an upward flux. Infiltration is influenced by soil moisture, particularly when swelling clays are present in the soil, while the unsaturated hydraulic conductivity that governs the passage of water down the vadose zone varies by several orders of magnitude with the moisture content of the medium. Even with knowledge of topsoil moisture, derived by microwave remote sensing, it is difficult to predict in dry regions how much, if any, of that moisture reaches deep groundwater tables. Coupling of surface soil moisture with physical 1D soil moisture modelling may not be fruitful for several reasons:

- The spatial resolution of the microwave sensors is poor (about 25 x 25 km<sup>2</sup>) while within this size appreciable differences in vadose zone properties may exist. For example, in thick Kalahari sand deposits, which are considered as uniform in terms of grain size and layering is absent, appreciable differences in deep soil moisture profiles were found (Obakeng, 2006) at sites about 5 to 10 km apart.
- Practical implementation of 1D soil models (e.g., HYDRUS, SWATR) require the use of pedotransfer functions, but an extensive study by Wagner et al. (2001) demonstrated the poor performance of such functions when compared with measured hydraulic conductivity.
- Many species of dry region vegetation have deep roots and the root function in the 1D models is as yet a matter of conjecture, while processes such as hydraulic lift and preferential flow are not included in the soil moisture models.

Recharge to deeper groundwater in semi-arid regions is usually in the order of mm and accuracy of both remote sensing input and models, due to uncertainty in parameter values, do not match with such small amounts.

Recharge models such as EARTH (Van der Lee and Gehrels, 1990) simulate vadose zone processes in terms of linear reservoirs in a lumped fashion. Similarly, the well-known groundwater modelling MODFLOW packages simulate upward unsaturated flow as a simple linear function. Such approaches, which have proven their worth in hydrogeology, do not need surface soil moisture data.

There is much to say for exploring the performance of soil moisture models of a more simple nature than those based on the Richard's equation to simulate recharge, when remotely sensed soil moisture data (e.g. SWI) and land cover is included.

The loss of groundwater by upward flux can be significant when the groundwater table is within the capillary zone and moisture gradient is maintained by surface evaporation and transpiration. It can be expected that the remotely sensed soil moisture monitoring provides useful information for the mapping of areas with shallow groundwater and for groundwater budgets of such areas.

## 14.7 Wetlands, areas with shallow groundwater tables

### 14.7.1 Introduction

A wetland (i.e. area that is seasonally or permanently wet) can be (1) a groundwater recharge area if fed by surface runoff and a piezometric surface that slopes away from the wetland, (2) a groundwater discharge area if the piezometric surface slopes towards the wetland and (3) a flow-through area where groundwater inflow equals groundwater outflow. Hybrid situations are commonly found in the larger wetlands.

Many wetlands are located in areas with little relief and are shallow, thus small changes in water depth have a large effect on their extent and water balance. The interaction between surface water and groundwater in wetlands has various degrees of complexity.

For example, the left-hand sketch of Figure 14.7 shows the effect of inundation and drying on groundwater in a situation found at the islands of higher ground in the Okavango delta, described by Wolski and Savenije (2006). Flooding causes recharge (R), and evapo(transpi)ration (E), in the floodplain will be much reduced during the dry season, while in the islands (E) depends on root uptake of water.

The middle figure shows a large and a small wetland due to groundwater flow systems; the wetness condition of the wetlands, as observed on images, is linked to groundwater fluxes in the upland, due to rainfall recharge. The inset map (right figure) shows bank storage in case surface water inflow in the larger wetland raises the water level.

Furthermore, wetlands are difficult to survey in the field and hydrometric data is often scarce. Therefore, studies of wetlands make use of remotely sensed images, not only for the reconstruction of the history, but also for quantitative studies. In many cases the historical monitoring record can only be established by time series of air-photos and multi-spectral images, starting with the first Landsat MSS images from 1972.

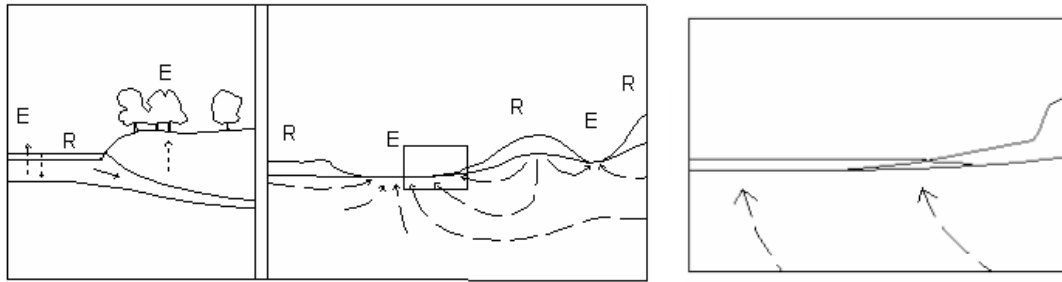


Figure 14-7 Sketches showing some groundwater-surface water interactions

Leblanc et al. (2003) used maps and remotely sensed images integrated in a GIS to map pertinent characteristics and features in terrain that reveal or influence recharge and discharge processes for a regional transient groundwater model of the large Quaternary aquifer of Lake Chad. Satellite data with good spatial resolution was used to locate areas where ponding at the end of the wet season favoured recharge (ephemeral beds, depressions). With low-resolution Meteosat thermal images and NDVI images based on NOAA-AVHRR areas with surface water, both open water and water under aquatic vegetation were determined and in those areas exchanges with the aquifer were modelled. Wherever the lake dried up, these exchanges stopped and evaporation processes were applied to the aquifer.

### 14.7.2 Mapping of wetlands

Many wetlands have shallow water depths, with the consequence that variability in rainfall and evapotranspiration results in highly dynamic patterns of inundation, desiccation and vegetation adjustments. This dynamic behaviour makes use of the frequent images provided by meteo-satellites attractive, accepting the low resolutions.

Wetlands in warm climates are relatively cool at daytime and therefore their extent can be determined on thermal daytime images. Leblanc (2003) used thermal images of Meteosat and NOAA AVHRR images to determine the extent of Lake Chad for a regional groundwater model. However, in some cases there may be little contrast on thermal images between wetland vegetation and upland vegetation.

The wetland can then be mapped by making use of thermal inertia, as shown in Chapter 5 (Thermal Images). Travaglia et al. (1995) used thermal images (NOAA AVHRR) at midday and nighttime for wetland mapping. Roshier and Rumbachs (2004) used NOAA AVHRR for temporary wetlands during a wet period in semi-arid Australia and used a spectral matching method because of confusion between such elements as salt-crustured surfaces and others and turbid or clear water. By comparing results with a classification based on Landsat TM data, an underestimation of 61% was noted, due to the presence of narrow zones of inundation, having about the same or small dimension as the NOAA-AVHRR images (about 1 km).

NOAA AVHRR data was used by Birkett (2000) to map the changes in the extension of Lake Chad and the corresponding elevation of the lake was determined by Topex-Poseidon altimeter data (see Chapter 4, section 4.7). Vekerdy and Dost (2006) demonstrated how the dynamics of a large wetland on the border of Iran and Afghanistan (Sistan wetlands) can be monitored over a long period, 1976–2005, using ASTER, Landsat MSS, TM, ETM, IRS, MODIS and AVHRR images, whereby image-scarce periods were supplemented by quicklooks.

To minimize the effect of mixed (partly wet, partly dry) pixels a spectral unmixing method may be used. Verhoeve and Wulf (2002) modelled the value of each pixel of SPOT VEGETATION images (1 km resolution) as a linear combination of land cover spectra present in the image and their respective fractions to map wetlands.

Radar images are also useful for wetland mapping because water surfaces without waves do not give backscatter (black on a radar image) while for moist soils the di-electric constant causes reduction of the backscatter. Dense vegetation on waterlogged areas differs from that of well-drained surroundings and since much of the radar backscatter is influenced by vegetation structure, the combination of wet soils and specific vegetation associations allows mapping of such waterlogged areas.

An additional advantage of active radar in studying wetlands is that the L and P bands can detect water below a woody forest canopy. Hess et al. (1995) found that presence of water below the canopy increases backscatter by ground-trunk two-bounce scattering, while in non-woody wetlands, a decrease of backscatter may occur because of the forward specular scattering of the pulse signal. Pope et al. (2001) mapped wetlands and seasonal flooding of



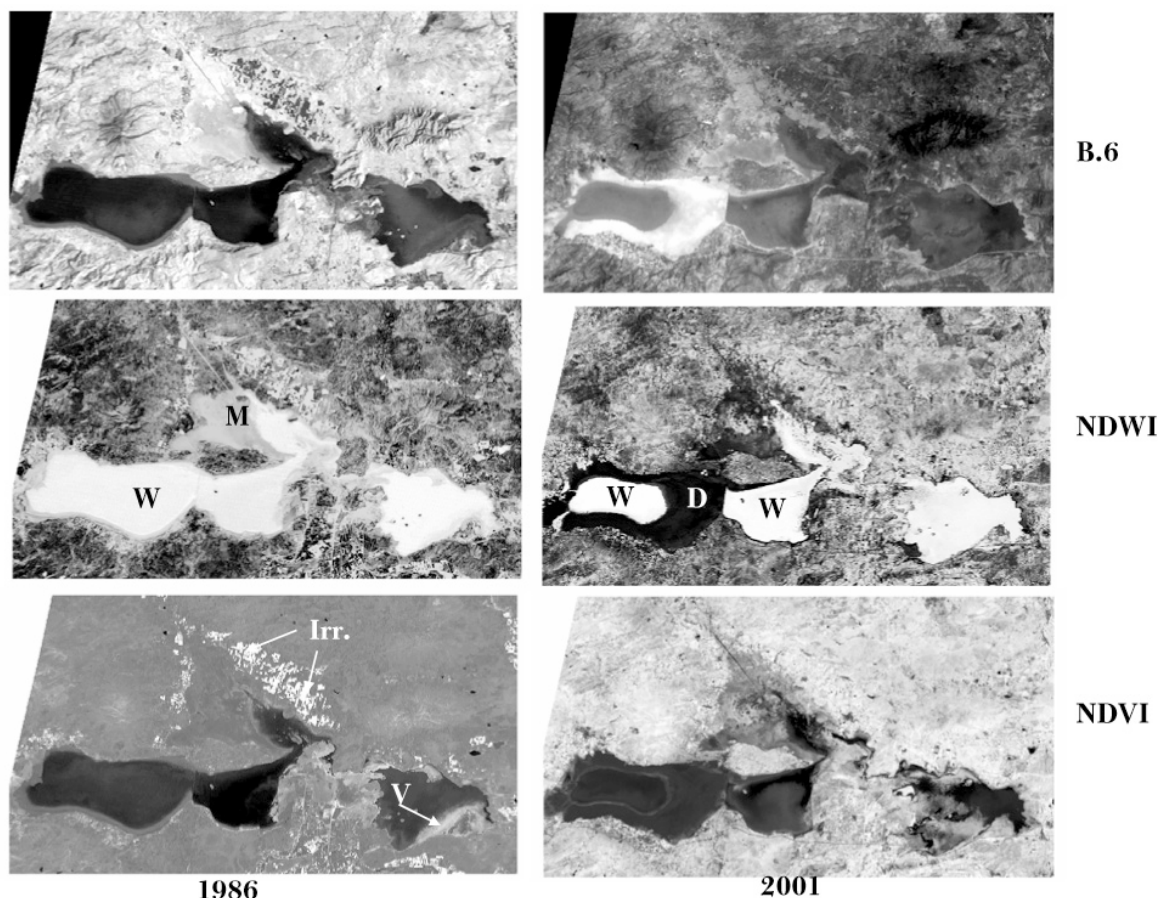
an impact crater using radar-C (SIR-C) images with concurrent chemical water sampling and found three major zones of groundwater discharge. An example of the use of radar for such mapping by visual interpretation is given by, for example, Travaglia and Macintosh (1997) who used multi-temporal radar images to study the dynamics of a large wetland in Zambia.

Radar and multi-spectral images have been used for wetland mapping. Töyrä et al. obtained the best result for freshwater wetland mapping with the combination of a Radarsat image (low angle) and a SPOT image.

In mapping wetlands with multi-spectral images the highly differing spectral reflectance of various surfaces in and around the wetland should be considered. In case of shallow water aquatic plants, floating or rooted may be present, clear and turbid water, dry and wet mudflats and so on. A problem is often that no groundtruth can be obtained for earlier images and one has to rely on best judgement of features observed on images or their transformed products, as is discussed in the following example.

In Figure 14.8, the Cuitzeo wetland in central Mexico, the dynamics of inundation and vegetation on Landsat images of March 1986 and August 2001 are shown by way of thermal images, NDVI and NDWI transforms. For the latter, histogram equalization was applied in order to have an equitable distribution of grey tones over the full range of NDWI values. The area around (M) is a part of the lake bottom, which episodically is inundated; the groundwater is at a relatively shallow depth, as can be noted on the NDWI response in a part of that area. Crops irrigated with groundwater (Irr.) have high contrast with the dry vegetation and soils/rocks on the thermal image of 1986. Aquatic vegetation is indicated with (V) on the NDVI image of 2001. The lake is fed mainly by surface runoff, but partly by groundwater flowing towards the wetland from the higher ground around the lake.

In order to estimate the evapotranspiration loss, for example, for a groundwater budget using sequential images, a good approach is first to prepare a mask of the maximum extension of the lake area by visual interpretation, by using the information of the thermal band 6 of 1986 and the NDVI image of 2001. The mask can then be placed on other images to exclude responses outside the lake area. Inspection of the lake area may show that the



**Figure 14-8** Lake Quitzeo, Central Mexico. Landsat TM, March 1986 (left side) and Landsat ETM, August 2001 (right side). Linear stretch to thermal band (B.6) and NDVI, histogram equalization to NDWI. Images show complexities of decision for evaporating surface area. Distance E-W is 51.8 km.

NDVI image does not discriminate – as expected – between bare, dry soil and water. The NDWI image seems to have the least confusion as to open water surface and moist lake bottom with or without aquatic vegetation. To determine the area with maximum (potential) evapotranspiration, a threshold value for high NDVI values (white tones) has to be adopted. The dark tones (D) on the NDWI image corresponds to dry surface areas and evaporation will be low. For areas in the medium range NDWI values a fraction of the potential evapotranspiration rate may be adopted. Note the differences in NDVI values and NDWI values in the southeastern lake area and the area around (M).

Mendoza et al. (2006) describe the water surface fluctuations in this wetland and the relation with rainfall and temperature.

A rapid assessment of vegetation and open water dynamics can be obtained by colour coding NDVI images of different seasons, as is illustrated in Figure 14.9, showing a MSS NDVI image of a small part of the Sudd wetland in Sudan. By using additive colour theory, the composite image of three dates can be interpreted in a simple fashion, as indicated in the subscript of the figure.



Figure 14-9

Colour coded Landsat MSS, NDVI images of 3 different dates:

Date 1 coded in green

Date 2 coded in red

Date 3 coded in blue

Interpretation, using additive colour theory, in wetland area:

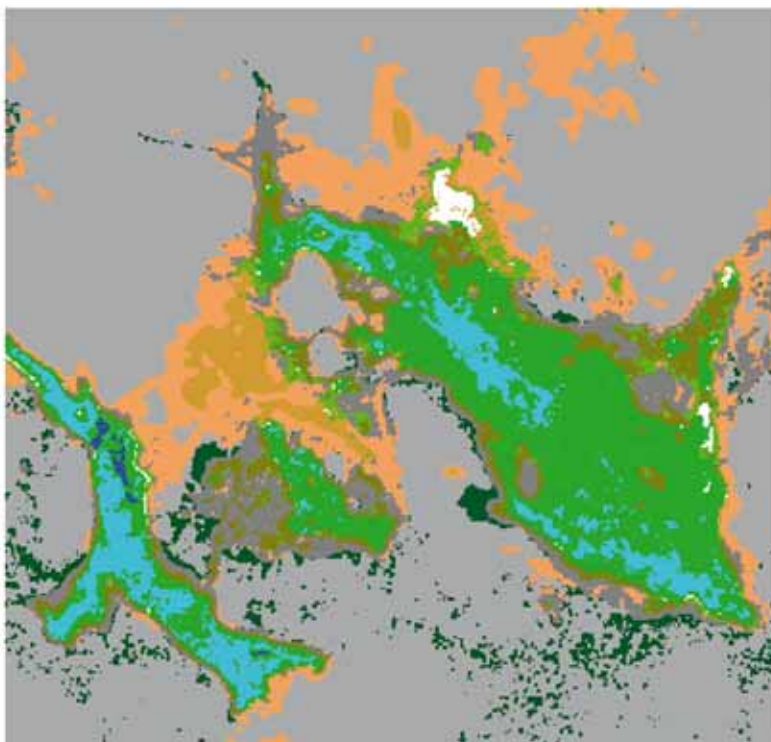
Black = open water, all dates

White = dense green vegetation, all dates

Yellow = vegetation during date 1 and 2

Green = vegetation only during date 1, open water during other two dates

Magenta = vegetation during date 2 and 3



Legend

- 1: Bare soil
- 2: Trees & bush
- 3: moist soil, sparse vegetation
- 4: Mod. dense grass/shrub, moist soil
- 5: Open grass/shrub
- 6: Grass/shrub, wet soil
- 7: Waterlogged, grass/shrub
- 8: Open, deep water
- 9: Deep marsh, dense vegetation
- 10: Not classified

Figure 14-10

Classification of saturated and moist areas of groundwater fed wetlands in Amboseli, Kenya

Distance E-W is 11 km.

Landsat ETM image.

Combination of the thermal and visual bands made it possible to discriminate areas with different moisture contents under partial or full vegetation cover, open water and vegetation growing in water in the flat area with the groundwater-fed springs of the Amboseli marshes, Kenya, shown in Figure 14.10. In this example classification was done by using cross tabulation using NDVI data and thermal data, with suitable adjustment of the class intervals on both.

The legend units have been arranged in groups of more or less increasing order of evapotranspiration loss. The class 'Bare soil' pertains to dry surface conditions with very low evaporation.

### ***14.7.3 Estimation of wetland evapotranspiration***

Groundwater recharge or discharge is an important factor in the water balance of wetlands and therefore the actual evapotranspiration term has to be determined or estimated, also when the wetland is a flow-trough type.

The simplest, but approximate way, is to equate the evapotranspiration of wet areas to the potential or crop reference evapotranspiration (PET). General agreement exists that the Penman-Monteith method (see Allen et al., 1998) is a suitable method for the calculation of PET. In case only temperature data is available, the Hargreaves equation may be used. The seasonal course of the extent of wet areas can be determined with satellite images.

A somewhat more refined estimate can be obtained by differentiating various land cover classes in a wetland to assign a coefficient to PET. For some types of vegetation  $ET_a$  may be higher as the crop reference (or potential) evapotranspiration, as the tables of the crop coefficient ( $K_c$ -FAO) show, due to aerodynamic effects. For water hyacinth and paddy,  $K_c = 1.2$ , but unfortunately no other wet vegetation types are listed. For open water, low and even vegetation, not short of water the  $K_c$  factor will be close to unity.

In case of partial drying up of the wetland, vegetated parts supported by groundwater or soil moisture, should be differentiated from non-vegetated, non-inundated bottomlands. At the beginning of the drying period a  $K_c$  value of 1 may be assumed, but that value will decrease – most likely exponentially – depending mainly on soil texture and depth of water table.

A thermal image may be helpful in the estimation of dryness of the surface, because evaporation of water brought to the surface by capillary rise lowers the surface temperature. The dried bottom land of wetlands usually has various spectral signatures due to different moisture contents, organic matter of the soil, dried algae and plant remains and soil textures.

Quantification of the evapotranspiration could be done by field measurement (Bowen ratio, eddy correlation) as was done in phreatophyte studies mentioned above, but at substantial cost. A cost effective alternative is to use a SatSEB method to assess the evapotranspiration. Muhamed et al. (2005) did so for the large Sudd marshes in Sudan with a time series of NOAA-AVHRR images

Monthly water balances for the Shadegan wetland and the upland irrigated area were estimated using SatSEB data in SW Iran. The contribution of capillary rise from shallow groundwater in the irrigated area was estimated by noting the actual evapotranspiration rates in rangelands around irrigated and wetland areas (Meijerink et al. 2005).

Brunner (2005, 2007) coupled SatSEB data to a groundwater model in a low-lying, partly irrigated area in China and was able to determine the evaporative flux from groundwater.

### ***14.7.4 Interpretation of shallow groundwater conditions***

In areas where no adequate piezometric maps exist, areas with groundwater at shallow depth in dry regions can be interpreted by combining information from various sources. Topographic depressions derived from SRTM or other DEM data can be compared with dry and wet season vegetation densities, and to reflectivity variations associated with wet and dry soils. Global NDVI monitoring provides such data on vegetation dynamics. Seasonally perched water tables may exist if ephemeral channels end in depressions and vegetation is found after the rainy periods but not in the dry season. The presence of man-made drainage channels, seen on high-resolution images, indicates water logging. The presence of salt efflorescence in low-lying areas is usually due to capillary rise from shallow groundwater. Extended periods of high surface soil moisture content during dry weather obtained from microwave remote sensing (global monitoring) may also be related to shallow groundwater, but the resolution is about 25 km<sup>2</sup>, too coarse for undulating terrain where shallow groundwater may occur in small areas or valleys.

Emergence of groundwater in dry riverbeds points to the intersection of the groundwater level and riverbed,

as is illustrated in Figure 14.11. The aerial photo (original scale 1:64,000) shows an embayment with regolith and alluvium overlying metamorphic rocks of low permeability. In the hilly terrain valleys are dry, but it is likely that groundwater from the large hinterland (not shown) flows through major fractures to the low area, which is also recharged by transmission loss during flow events. It can be safely assumed that the groundwater surface at the intersection can be extrapolated with a gentle gradient up to the steep rise of the hills.

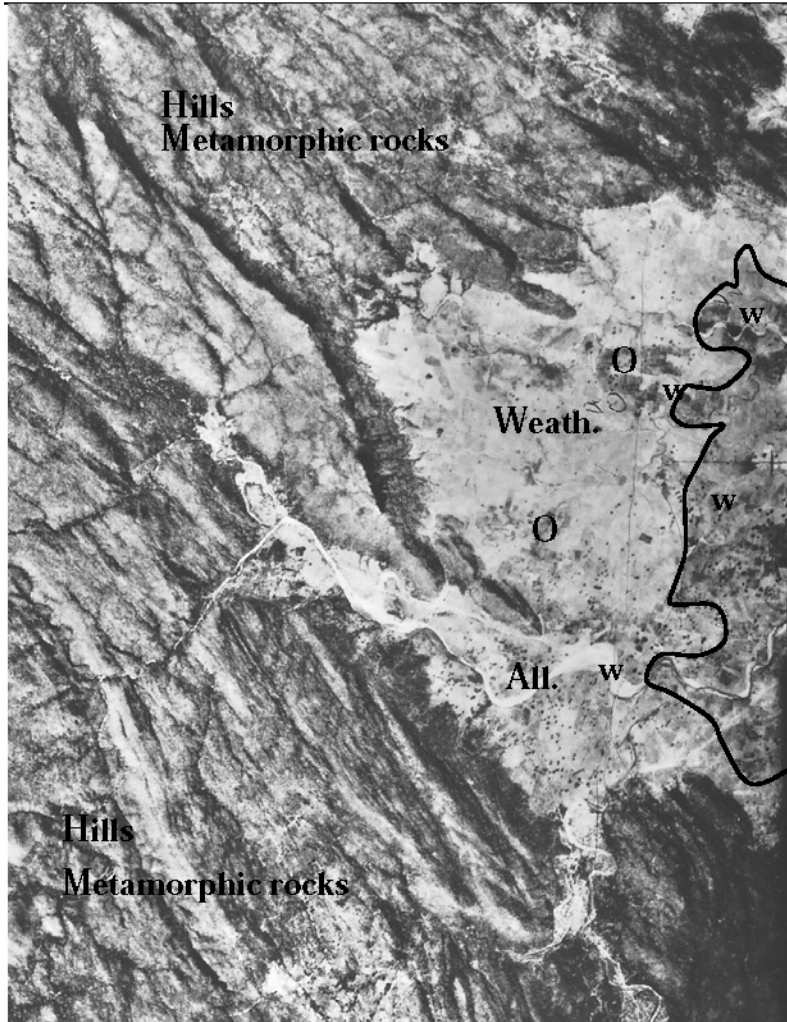


Figure 14-11

**Emergence of groundwater as indication of shallow groundwater table in weathered/alluvial area, aerial photograph.**

**Full area shown consists of high grade metamorphic rocks (low permeability). Rivers in hills and alluvial fringe are ephemeral.**

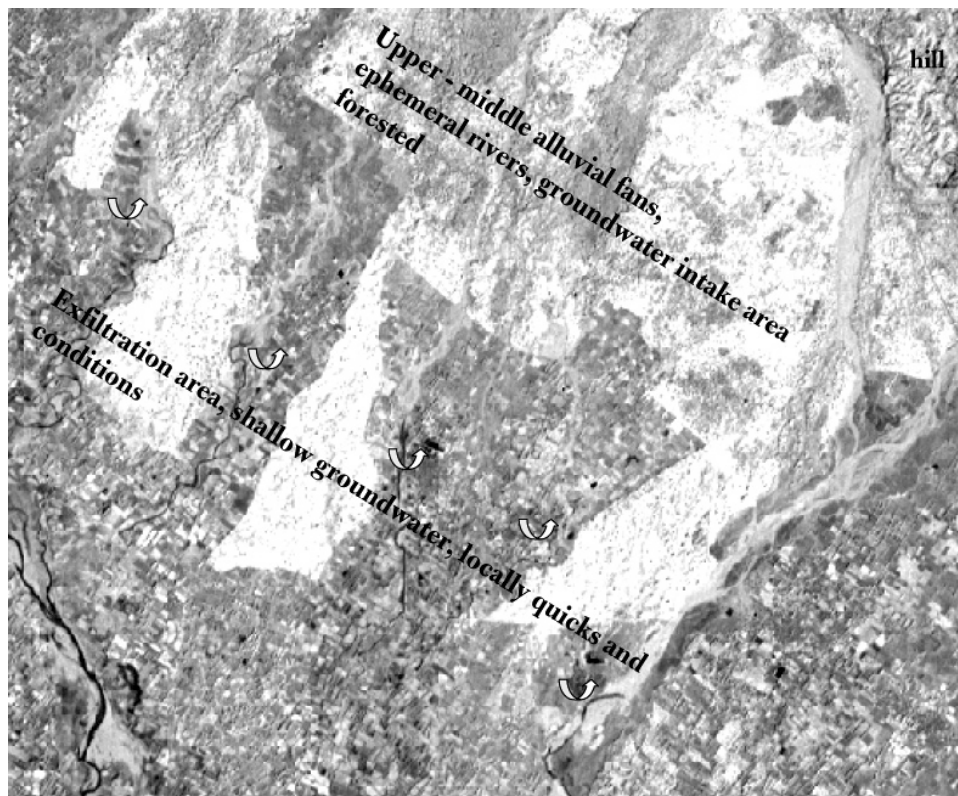
**Groundwater emerges at a few points (w) and area with shallow groundwater (darker tones) is delineated.**

**O = outcrops.**

**Distance E-W is 6.4 km.**

**High resolution panchromatic image.**

In some cases shallow groundwater is found at places or zones where it is expected because a groundwater flow system can be interpreted, as is illustrated in Figure 14.12, which shows the near infrared band of an ASTER image of an alluvial area in north India. It may be remembered that the near infrared band is suited for detecting water at the surface because of absorption of light even when the water depth is a few mm. As can be seen on the image, emergence of groundwater can be observed in the riverbeds, which are dry in the upstream part. In fact, the upper part of the area shown in the figure is a groundwater intake area, where recharge takes place by rainfall (some 1,500 mm annually) and by transmission loss of runoff from the hills in the ephemeral riverbeds. The transition of the alluvial area and the hills can be considered as a no-flow boundary because of the presence of thick shale beds, dipping south (not shown). In the upwelling or exfiltration zone of the groundwater flow system; just downstream of the line indicated by curved arrows, locally quicksand conditions occur. Incidentally, this caused a problem to the foundations of towers of a high-tension electric transmission line. The simplest solution here was to shift the alignment of the line to upstream of the emergence zone. In the entire area between the emergence points and the river in the southwest, the groundwater is shallow and the groundwater contours follow the gently sloping topography.



**Figure 14-12** Aster Image (VNIR band) of alluvial area in north India. Groundwater that infiltrated in the upper part emerges in the exfiltration area. Curved arrows indicate groundwater emergence or spring zone. In the riverbeds just downstream of spring zone, locally quicksand conditions exist because of upward pressure of groundwater. Distance E-W is 10 km.

### 14.7.5 Salinization/alkalinisation

Saline areas are generally associated with evaporation of shallow groundwater, brought to the surface by capillary flow or by evaporation of surface water in depressions. Salt crusts signify an end stage of salinization, and the crusts can usually be easily recognized by the high reflectance of the crust. Figure 13.18 in Chapter 13 (Site Selection for Managed Aquifer Recharge) shows a Landsat TM false colour image of the large alluvial fan/inland delta in S. Iran, where the salt crust is apparent. From the poor crop responses upstream of salt flats salt affected soils can be inferred. Considering the hydrogeological setting it can be assumed that the incipient salinization is due to capillary rise from shallow groundwater, but the level of salinization cannot be assessed from the false colour image.

A variety of sensors (e.g. aerial photographs, satellite- and airborne multi-spectral sensors, microwave sensors, video imagery, airborne geophysics, hyperspectral sensors, and electromagnetic induction meters) and approaches are used for identification of salt-affected areas. These are reviewed by, for example, Metternicht and Zinck (2003) and by Farifteh et al. (2006) and both reviews contain abundant references.

Various image processing techniques have been used in discriminating salt affected soils, such as spectral classification methods (supervised and clustering), Principal Component transforms whereby the first four components proved to be useful, band ratioing, and image fusion of images of different resolution, as well as other methods. Also approaches whereby prior information, such as contextual landscape information, groundwater quality, etc. is included, usually in a GIS environment, have proven to increase the accuracy of the mapping.

Of special interest for groundwater management is the monitoring of the status of salination/alkalinisation in relation to irrigation. A lowering of the groundwater table by pumping may be desired to reduce capillary rise, but also groundwater irrigation using deep sources may increase soil salinity in case of perched water tables or in depressional areas. The past development of salinity/alkalinity often relies on the use of satellite images.

However, to monitor the levels of salinity/alkalinity using remote sensing data alone has much uncertainty,

because spectral signatures of affected soils are influenced by volunteer vegetation, moisture content and mineral mixtures, which can vary in time. Furthermore, the images have to be mutually comparable. That can be achieved by radiometric correction, whereby it is assumed that standard atmospheres are valid, and to some extent by normalization methods (see Chapter 2, sections 2.5.1 and 2.7).

As Metternicht and Zinck (2003) mention ideally the monitoring should consider the salt affected soil as a 3D body, while the remote sensing techniques give 2D (surface) data. Reconstruction of the trend in salinity/alkalinity therefore requires historical field and laboratory data of soils, groundwater levels and quality.

However, since accuracies in detecting salinity by remote sensing methods are reasonable, sequential images can be used to detect main trends.

## 14.8 Groundwater status measured by satellite gravity data

The principle of measuring changes in the mass of the groundwater body, expressed by depth to water table, is based on corresponding changes in the gravity field. Variations in this field affect the distance between two GRACE (Gravity Recovery and Climate Experiment) satellites launched in 2002, and that distance is measured with great precision. GRACE data include 30-day estimates of gravity fields, as well as profiles of air mass, density, pressure, temperature, water vapour, and ionospheric electron content throughout the 5-year duration of the mission.

By examining a GRACE-derived gravity model from each of the two time periods (e.g. consecutive months), it will be possible to calculate, for a particular region, if the change in total water mass has been calculated and related successfully to results of water balance models of large basins (e.g. Seo et al, 2005). Rodell and Famiglietti (2002) pointed out that if effects of moisture in the vadose zone and the atmosphere could be eliminated, monitoring of groundwater storage change is possible using GRACE data. They indicated that uncertainty in storage change determination would be much lower than the actual changes measured by conventional means in the High Plains aquifer of the mid-US. In a later study, Rodell et al. (2007) indeed found reasonably good results between GRACE observations and phreatic water levels for the very large basin (900,000 km<sup>2</sup>) they studied, but not for two smaller basins, about half the size of the former.

## 14.9 Use of hyperspectral images

The multi-spectral sensor systems discussed so far have relatively broad wavelength bands and therefore spectral variations are averaged so that particular diagnostic characteristics cannot be used. Hyperspectral imaging (also termed imaging spectrometry and imaging spectroscopy) record images in a large number of narrow spectral bands (some systems >100), usually less than 10 to 20 nm (1  $\mu\text{m}$  = 1,000 nm). For example, a mineral like kaolinite shows a sharp dip in the spectral curve around 1.4  $\mu\text{m}$ , but much higher reflectances at 1.3 (or 1.6)  $\mu\text{m}$ . This contrast can be visualized by taking the ratio of the bands at, for example, 1.4 and 1.6  $\mu\text{m}$ .

The detailed spectral curves obtained by such systems are usually compared with spectral reflectance curves of minerals or specific soil surfaces, measured in the field or in a laboratory. Radiometric correction and atmospheric correction (section 2.7.3.) have to be done to obtain absolute reflectance values. For the comparison spectral matching algorithms have been developed to deal with the high-dimensional spectral data sets. Pixel reflectance values are the result of the contribution of various ground classes (e.g. minerals, plant species, etc.) and for retrieval of desired feature various methods for spectral unmixing are used.

No further details are given here because, so far, application of hyperspectral data has been limited to the observation of features indirectly related to groundwater. Hyperspectral imaging was used for discrimination of various types of carbonate rocks, which could contribute to the knowledge of karst, and to mapping of various types of saline soils. Salinity is often associated with shallow groundwater and the analysis of hyperspectral data may give relations with quality of shallow groundwater. When combined with DEM data, saline groundwater seeps can be detected (Taylor et al., 2001).

Hyperspectral data has proved to be useful for recognizing and mapping vegetation. Verbeiren et al. (2003) studied riparian wetness in groundwater exfiltration areas with hyperspectral data. As discussed in Chapter 14, section 14.4, improved recognition of phreatophytes species or vegetation associations is important for groundwater budget studies.

Precipitated minerals in streambeds, such as iron sulphate, iron hydroxide and iron oxide in river beds can be associated with the pH of the base flow at the time of deposition and thus to the groundwater feeding the base flow. Submarine groundwater discharge (Chapter 5, section 5.2.3) is generally detected by thermal images, but phytoplankton, sediment and dissolved organic matter contents of groundwater flowing out in the sea can have subtle differences with those of seawater and hyperspectral imaging may show such differences.

Airborne hyperspectral instruments have long been used (since the 1970s) but were beyond the scope of the average groundwater study. The recent Hyperion satellite system has 220 bands in the range of 0.4 to 2.5  $\mu\text{m}$ , a spatial resolution of 30 m and an image covers 7.5 by 100 km land area. It can be expected that the new data will find applications in groundwater along the lines mentioned above, or others.

## 14.10 Summary and conclusions

In many areas rain gauges are few while there may be spatial variations in rainfall, the source of groundwater recharge. In semi-arid regions the pattern of vegetation density may reflect qualitative differences in rainfall. Satellite image data can be used to improve spatial rainfall quantitatively, and internet sources provide such information.

A step forward in satellite hydrology is the possibility to estimate actual evapotranspiration (ET<sub>a</sub>). In this chapter the gist of the method is discussed and its use for groundwater budgets is pointed out and discussed earlier in the book (Chapter 12).

Groundwater management requires a comprehensive approach that includes groundwater dependent vegetation and wetlands. Vegetation can be identified and mapped by remote sensing at different scales, and relations with groundwater occurrences and water quality may exist, as is discussed in reference to studies. The use of (deep) groundwater by trees in semi-arid areas has attracted attention and field studies are undertaken to measure the transpiration rates. However transformation of such measurements to areal values require upscaling and images with high spatial resolution are required.

An important issue in hydrogeology of dry regions is the estimation of groundwater recharge. The patterns of recharge in such a region were mapped by satellite rainfall and evapotranspiration data, and these were related to recharge determined by the chloride method. Relative recharge patterns can be mapped by detailed geomorphological interpretations concerning topography, runoff and properties of the surface materials. The relative pattern of episodic recharge after floods can be mapped by using overpasses of imaging satellites shortly after floods.

High levels of soil moisture may be related to shallow groundwater occurrences and may lead in dry areas to soil salinity. Multi-spectral and thermal images can be used to detect areas with shallow groundwater by visual interpretation and by using relationships with vegetation, if placed in a hydrogeological context. The use of radar and microwave remote sensing for soil moisture is discussed in Chapter 4, but here the potential use of surface soil moisture for recharge estimation is discussed. Difficulties are expected in the results of coupling surface soil moisture to 1D soil moisture models, based on Richard's equation, in case of deep groundwater.

Wetlands have special surface-groundwater interactions and are important in groundwater budgets. Various sensors have been used to study wetlands and the mapping of wetlands is discussed and illustrated.

Satellite gravity data has recently been used for detecting changes of groundwater storage in very large aquifers, but the processing of the data is complex.

Hyperspectral imaging has promise for detailed studies of features that are indirectly associated with groundwater, but has as yet been little applied. This may change with the availability of hyperspectral satellite data.

## References

- Ahmed, M.D. and Bastiaanssen, W.G.M. 2003. Retrieving soil moisture storage in the unsaturated zone from satellite imagery and bi-annual phreatic surface fluctuations. *Irrigation and Drainage Systems*, Vol. 17(3), pp. 141–61.
- Ahmed, M.D., Bastiaanssen, W.G.M. and Feddes, R.A. 2005. A new technique to estimate net groundwater use across large irrigated areas by combining remote sensing and water balance approaches. *Hydrogeology*

- Journal*, Vol. 13(5–6), pp. 653–64.
- Allen, R.G., Pereira, L.S., Raes D. and Smith, M. 1998. Crop evapotranspiration: Guidelines for computing crop water requirements. FAO Irrigation and Drainage Paper 56.
- Bastiaanssen, W.G.M., Menenti, M., Feddes, R.A. and Holtslag, A.A.M. 1998a. A remote sensing algorithm for land (SEBAL). 1. Formulation. *Journal of Hydrology*, 212–13, pp. 198–212.
- Bastiaanssen, W.G.M., Pelgrum, H., Wang, J., Ma, Y., Moreno, J.F., Roerink, G.J., van der Wal, T. 1998b. A remote sensing algorithm for land (SEBAL). 2. Validation. *Journal of Hydrology*, 212–13, pp. 213–29.
- Bastiaanssen, W.G.M. and Bandara, K.M.P.S. 2001. Evaporative depletion assessments for irrigated watersheds in Sri Lanka, *Irrigation Science*, Vol. 21(1), pp. 1–15.
- Brunner, P., Bauer, P., Eugster, M. and Kinzelbach, W. 2004. Using remote sensing to regionalize local precipitation recharge rates obtained from the chloride method. *Journal of Hydrology* Vol. 294(4), pp. 241–50.
- Brunner, P. 2005. Sustainable agriculture in the Yangi Basin, China. PH.D. Thesis ETH, Zurich No. 16210.
- Brunner, P., Hendricks-Franssen, H.-J., Kgotlhang, L. and Kinzelbach, W. 2007. Remote sensing in groundwater modelling. *Hydrogeology Journal*, Vol. 15(1), pp. 5–18.
- Canadell, J., Jackson, R.B., Ehleringer, J.R., Mooney, H.A., Sala, O.E. and Schulze, E.D. 1996. Maximum rooting depth of vegetation types at the global scale. *Oecologia*, Vol. 108, pp. 583–95.
- Ceccato, P., Flasse, S., Tarantola, S., Jacquemond, S. and Gregoire, J. 2001. Detecting vegetation water content using reflectance in the optical domain. *Remote Sensing of Environment*, Vol. 77, pp. 22–33.
- Collier, C.G. 2000. Precipitation. G.A. Schultz and T.Engman (eds) *Remote Sensing in Hydrology and Water Management*, Springer Verlag, pp. 111–32.
- Colvin, C., LeMaitre, D. and Hughes, S. 2003. Assessing terrestrial groundwater dependent ecosystems in South Africa. WRD Report No. 1090-2/2/03. CSIR, South Africa.
- Dell, B., Bartle, J.R. and Tacey, W.H. 1983. Root occupation and root channels of Jarrah forest subsoils. *Australian Journal of Botany*, Vol. 31(3), pp. 183–204.
- DeMeo, G.A., Laczniak, R.J., Boyd, R.A., Smith, J.L. and Nylund, W.E. 2003, Estimated ground-water discharge by evapotranspiration from Death Valley, California, 1997–2001: US Geological Survey Water-Resources Investigations Report 034254.
- Droogers, P. and Kite, G. 2002. Remotely sensed data used for modelling at different hydrological scales. *Hydrological Processes*, Vol. 16(8), pp. 1543–56.
- Farah, H.O., Bastiaanssen, W.G.M. and Feddes, R.A. 2004. Evaluation of the temporal variability of the evaporative fraction in a tropical watershed, *Int. J. of Applied Earth Observation and Geoinformation*, 5, pp. 129–40.
- Farifteh J., Farshad A. and George R.J. 2006. Assessing salt affected soils using remote sensing, solute modelling and geophysics. *Geoderma*, 130(3–4), pp. 191–206.
- Gao, B. 1996. NDWI—a normalized difference water index for remote sensing of vegetation liquid water from space. *Remote Sensing of Environment*, 58, pp. 257–266.
- Gieske, A. and Meijninger, W. 2005. High density NOAA time series of ET in the Gediz Basin, Turkey. *Irrigation and Drainage Systems*, 19, pp. 285–99.
- Grimes, D.I.F. and Diop, M. 2003. Satellite based rainfall estimation for river flow forecasting in Africa. Part I. Rainfall estimates and Hydrological forecasts. *Hydrological Sciences*, Vol. 48(4), pp. 567–84.
- Hatton, T.J. and Nulsen, R.A. 1999. Towards achieving functional ecosystem mimicry with respect to water cycling in southern Australian agriculture. *Agroforestry Systems*, Vol. 45 (1–3), pp. 203–14.
- Hess, L.L., Melack, J.M. and Filoso, S. 1995. Delineation of inundated area and vegetation along the amazon floodplain with the sir-c synthetic-aperture radar. *IEEE T Geoscience Remote Sensing*, 33 (4), pp. 896–904.
- Kimani, J.M., Hussin, Y.A., Lubczynski, M.W., Chavarro, D. and Obakeng, O.T. 2007. Mapping Savannah Trees in Kalahari Using High Resolution Remotely sensed Images and Object-Oriented Classification
- Jackson, T.J. 2003. Measuring soil moisture using passive microwave remote sensing. *Hydrological Processes*, Vol.6.
- Jhorar, R.K., Bastiaanssen, W.G.M., Feddes, R.A. and van Dam, J.C. 2002. Inversely estimating soil hydraulic functions using evapotranspiration fluxes. *Journal of Hydrology*, 258(1), pp. 198–213.
- Kruck, W. 1990. Application of remote sensing for groundwater prospecting in the Third World. Proceedings Intern. Symp. Remote Sensing and Water Resources, Enschede, The Netherlands, IAH & Neth.Soc.R.S., pp. 455–64.
- Kustas, W., Humes, K., Norman, J. and Moran, M. 1996. Single and dual source modeling of surface energy fluxes



- with radiometric surface temperature. *Journal of Applied Meteorology*, Vol. 35, pp. 110–21.
- Kwarteng, A., Homewood, P. and Mettraux, M. 2005. Remote sensing of the modern carbonate system of the Bar Al Hikman Peninsula, Oman. Geoscience and Remote Sensing Symposium, IGARSS '05, Proceedings, IEEE International.
- Laczniaik, R., Smith, J., LaRue, J. and deMeo, G.A. 2006. Annual ground-water discharge from areas of spring-fed riparian vegetation along the eastern margin of Death Valley, 2000–02. US Geol. Survey Scientific Investigations Report 2006-5145. <http://pubs.usgs.gov/SIT/2006/5218/pdf/sir20065218.pdf>
- Leblanc, M., Leduc, C., Razack, M., Lemoalle, J., Dagonne, D. and Mofor, L. 2003. Applications of remote sensing and GIS for groundwater modelling of large semiarid areas; example of Lake Chad Basin, Africa. *Hydrology of the Mediterranean and Semiarid Regions*, Proceedings Int. Symp. Montpellier 2003, IAHS Publ. No. 278, pp. 186–192.
- Lerner, D.N., Issar, A.S. and Simmers, I. 1990. Groundwater recharge—a guide to understanding and estimating natural recharge. *IAH-International Contributions to Hydrogeology*, Vol. 8, Heinz Heise Verlag, Hannover.
- Lubczynski, M.W. 2000. Groundwater evapotranspiration- underestimated component of the groundwater balance in a semi-arid environment; Serowe case Botswana. *Past Achievements and Future Challenges*, Balkema Publ., pp. 199–204.
- Maathuis, B.H.P., Timmermans, W.J., Kingma, N.C. and Meijerink, A.M.J. 1997. Flood damage and hazard assessment, June 1996 floods, Central Yemen. Comm. Report. ITC, Enschede, The Netherlands.
- Maathuis, B., Retsios, V., Lasry, F. and Schilling, M., 2006. Installation, setup and use of a low cost c-band Meteosat-8 ground receiving station in Rwanda. 6th International Conference, Earth Observation and Geoinformation Sciences in Support of Africa's Development, 30 October – 2 November, 2006, Cairo, Egypt. African Association of Remote Sensing of the Environment Conference Proceedings.
- Meijerink, A.M.J., Gieske, A.S.M and Vekerdy, Z., 2005. Surface energy balance using satellite data for the water balance of a traditional irrigation-wetland system in SW Iran. *Irrigation and Drainage Systems*, 19, pp. 89–105.
- Mendoza, M.-E., Bocco, G. and Bravo, M. 2006. Predicting water surface fluctuations of continental lakes, a GIS and RS based approach in central Mexico. *Water Resources Management*, Vol. 20(2), pp. 291–311.
- Menenti, M. 2000. Evaporation. G.A. Schultz and T.Engman (eds), *Remote Sensing in Hydrology and Water Management*, Springer Verlag, pp. 157–88.
- Metternich, G.I. and Zinck, J.A. 2003. Remote sensing of soil salinity: potentials and constraints. *Remote Sensing of Environment*, Vol. 85(1), pp. 1–20.
- Muhamed, Y.A., Savenije, H.H.G., Bastiaanssen, W.G.M. and van der Hurk, B.J.J.M. 2005. New lesson on the Sudd hydrology learned from remote sensing and climate modeling. *Hydrol. Earth Science Discussions*, 2: 1503–35. Europ. Geosciences Union., and: [www.copernicus.org/EGU/hess/hessd/2/1503/hessd-2-1503\\_p.pdf](http://www.copernicus.org/EGU/hess/hessd/2/1503/hessd-2-1503_p.pdf)
- Mohamed, Y.A., Savenije, H.H.G and Bastiaanssen, W.G.M. 2006. New lessons on the Sudd hydrology learned from remote sensing and climate modelling, *Hydrology and Earth System Sciences*, 10(4), pp. 507–18.
- Moran, M.S., Jackson, R.D., Raymond, L.H. and Gay, L.W. 1989. Mapping surface energy balance components by combining Landsat Thematic mapper and ground-based meteorological data. *Remote Sensing of the Environment*, Vol. 30, pp. 77–88.
- Obakeng, O.T. 2007. Soil moisture dynamics and evapotranspiration at the fringe of the Botswana Kalahari, with emphasis on deep rooting vegetation. Dissertation No. 141. ITC, Enschede, The Netherlands.
- Pierce, L.L., Walker, J., Dowling, T.L., McVicar, T.R., Hatton, T.J., Running, S.W., Coughlan, J.C. 1993. Ecohydrological Changes in the Murray-Darling Basin. III. A Simulation of Regional Hydrological Changes. *Journal of Applied Ecology*, Vol. 30(2), pp. 283–94.
- Pope, K.O., Rey-Benayas, J.J. and Paris, J.F. 1994. Rader remote sensing of forest and wetland ecosystems in the central American tropics. *Remote Sensing of the Environment*, Vol. 48, pp. 205–19.
- Qi, J., Chehbouni, A., Huerte, A.R., Kerr, Y.H., and Sorooshian, S. 1994. *A modified soil adjusted vegetation index: Remote Sensing Environment*, Vol. 48, pp. 119–126.
- Ringrose, S., Jellema, A., Huntsman-Mapila, P, et al. 2005. Use of remotely sensed data in the analysis of soil-vegetation changes along a drying gradient peripheral to the Okavango delta. *International Journal of Remote Sensing*, Vol. 26(19), pp. 4293–319.
- Ringrose, S., Vanderpost, C. and Matheson, W. 1998. Evaluation of vegetative criteria for near-surface ground-

- water detection using multi-spectral mapping and GIS techniques in semi-arid Botswana. *Applied Geography*, 18, pp. 331–54.
- Rodell, M. and Famiglietti, J.S., 2002. The potential for satellite based monitoring groundwater storage changes using GRACE; the High Plains aquifer, central US. *Journal of Hydrology*, Vol. 263(1–4), pp. 245–56.
- Roerink G.J., Su, Z. and Menenti, M. 2000. S-SEBI: a simple remote sensing algorithm to estimate the surface energy balance. *Physics and Chemistry of the Earth, Part B2* 2, Vol. 35(2), pp. 147–57.
- Roshier, D.A. and Rumbachs, R.M., 2004. Broad-scale mapping of temporary wetlands in arid Australia. *Journal of Arid Environments*, Vol. 56(2), pp. 249–63.
- Shaban, A, Khawlie, M and Abdallah, C. 2006. Use of remote sensing and GIS to determine recharge potential zones: the case of Occidental Lebanon. *Hydrogeology Journal*, 14(4)pp. 433–43.
- Schenk, H.J and Jackson, R.B. 2005. Mapping the global distribution of deep roots in relation to climate and soil characteristics. *Geoderma*, 126, pp. 126–40.
- Seo, K.-W., Wilson, C.R., Famiglietti, J.S., Chen, J.L. and Rodell, M. 2006. Terrestrial water mass load changes from Gravity Recovery and Climate Experiment (GRACE), *Water Resour. Res.*, 42, W05417, doi:10.1029/2005WR004255.
- Su, Z., 2002. The Surface Energy Balance System (SEBS) for estimation of turbulent heat fluxes at scales ranging from a point to a continent. *Hydrol. Earth Sys. Sci.*, Vol. 5(1), pp. 85–99.
- Su, Z., 2005. Estimation of the surface energy balance. M.G. Anderson and J.J. McDonnell (eds) *Encyclopedia of Hydrological Sciences: Vol. 2*. Chichester, John Wiley & Sons, pp. 731–52.
- Taylor, G.R., Hemphill, P., Currie, D., Broadfoot, T. and Dehaan, R.L. 2001. Mapping dryland salinity with hyperspectral imagery. *Geoscience and Remote Sensing Symposium, IGARSS '01. IEEE 2001 International*. Vol. 1, pp. 302–04.
- Timmermans, W.J., Kustas, W.P., Anderson, M.C. and French, A.N. 2007. An intercomparison of the Surface Energy Balance Algorithm for Land (SEBAL and the Two-Source Energy Balance (TSEB) modelling schemes. *Remote Sensing of the Environment* (2006), doi:10.1016/j.rse.2006.11.028.
- Timmermans, W.J., Meijninger, W.M.L., Kustas, W.P., Gieske, A.S., de Bruin, H.A.R. and French, A.N. 2007. DATUTDUT: Operational monitoring of water and heat fluxes. Under review.
- Timmermans, W.J. and Meijerink, A.M.J. 1999. Remotely sensed actual evapotranspiration: implications for groundwater management in Botswana. *International Journal of Applied Earth Observation and Geoinformation*, Vol 3–4, pp. 222–33.
- Travaglia, C., Kapetsky, J.M. and Righini, G. 1995. Monitoring wetlands for fisheries by NAOO\_AVHRR LAC thermal data. *FAO RSC Series 68*, FAO, Rome.
- Travaglia, C. and Macintosh, H. 1997. Wetlands monitoring by ERS-SAR data; a case study Lake Bangweulu wetland system, Zambia. *FAO RSC Series 69*, FAO, Rome.
- Thorburn, P.J., Hatton, T.J. and Walker, G.R. 1993. Combining measurements of tree water use and stable isotopes of water to determine groundwater discharge from forests. *Journal of Hydrology*, 150, pp. 563–87.
- Van der Lee, J. and Gehrels, J.C., 1990. Modelling aquifer recharge: introduction to the lumped parameter model EARTH. Free University, Amsterdam.
- Vekerdy, Z. and Dost, R.J.J. 2006. History of environmental change in the Sistan Basin based on satellite image analysis: 1976–2005. Geneva and Enschede, United Nations Environmental Programme (UNEP) and ITC. <http://postconflict.unep.ch/publications/sistan.pdf>
- Verhoeye, J. and De Wulf, R. 2000. Sub-pixel mapping of sahelian wetlands using multi-temporal SPOT VEGETATION images. [vegetation.cnes.fr/vgtprep/vgt2000/verhoeye.pdf](http://vegetation.cnes.fr/vgtprep/vgt2000/verhoeye.pdf)
- Verbeien, B., Batelaan, O., Hung, L.Q. and De Smedt, F. 2003. Hyperspectral mapping of riparian wetness gradients. *CASI-SWIR 2002 Workshop*, Bruges, Sept.
- Wagner B, Tarnawski, V.R., Hennings, V., Müller, V., Wessolek, G. and Plagge, R. 2001. Evaluation of pedo-transfer functions for unsaturated soil hydraulic conductivity using an independent data set. *Geoderma*, Vol. 102, pp. 275–97.
- Wolski, P and Savenije, H.H.G. 2006. Dynamics of floodplain-island groundwater flow in the Okavango Delta, Botswana. *Journal of Hydrology*, Vol. 320(3–4), pp. 283–301.

## Appendix 1: List of acronyms

ADEOS	ADvanced Earth Observing Satellite
ALI	Advanced Land Imager
AMSR-E	Advanced Microwave Scanning Radiometer for EOS
AP	Aerial Photograph
AP	Andhra Pradesh
ASAR	Advanced Synthetic Aperture Radar
ASTER	Advanced Spaceborne Thermal Emission and Reflection Radiometer
ATCOR	Atmospheric Correction and Haze Reduction for ERDAS IMAGINE
AVHRR	Advanced Very High Resolution Radiometer
AVNIR	Advanced Visible and Near Infrared Radiometer
BRGM	Bureau de Recherche Géologiques et Minières
CCD	Charge-coupled Devices
DEM	Digital Elevation Model
DN	Digital Number
EM	Electro Magnetic
EO	Earth Observation satellite system
EOS	Earth Observing System
ERS	European Remote Sensing Satellite
ESA	European Space Agency
ET	Evapotranspiration
ET <sub>a</sub>	Actual Evapotranspiration
ET <sub>g</sub>	Groundwater Evapotranspiration
FAO	Food and Agriculture Organization (United Nations)
FEWS	Famine Early Warning System
GIS	Geographic Information System
GPS	Ground Positioning System
GPR	Ground Penetrating Radar
GRACE	Gravity Recovery and Climate Experiment
GREEN	Green band
HGU	HydroGeomorphological Unit
HIS	Hue Intensity Saturation (colour scheme)
IAH	International Association of Hydrogeologists
ILWIS	Integrated Land and Water Management System (software)
INSAR	Interferometric Synthetic Aperture Radar
IRS	Indian Remote sensing Satellite
ITC	International Institute for Geo-information Science and Earth Observation
IWMI	International Water Management Institute
Landsat TM	Landsat Thematic Mapper
Landsat ETM(+)	Landsat Enhanced Thematic Mapper
Landsat MSS	Landsat MultiSpectral Scanner
LOWTRAN	Low Resolution Transmission (model)
JERS	Japanese Earth Resources Satellite
JPL	Jet Propulsion Laboratory
LAI	Leaf Area Index
LIDAR	LIght Detection And Ranging
MERIS	MEdium Resolution Imaging Spectrometer

MODFLOW	MODular three-dimensional finite-difference ground-water FLOW model
MODIS	Moderate Resolution Imaging Spectroradiometer
MODTRAN	MODerate resolution atmospheric TRANsmission
MP	Madhya Pradesh
MRS	Magnetic Resonance Sounding
MSAVI	Modified Soil Adjusted Vegetation Index
NASA	National Aeronautics and Space Administration
NDVI	Normalized Difference Vegetation Index
NDWI	Normalized Difference Water Index
NIR	Near Infrared
NOAA	National Oceanic and Atmospheric Administration
PC	Principal Component
PC	Personal Computer
PET	Potential Evapotranspiration
PMWIN	Processing Modflow (software) for WINDows
RADAM	RADAr of AMazonia
RED	Red band
RGB	Red Green Blue (colour scheme)
RMSE	Root Mean Square Error
RS	Remote Sensing
SAR	Synthetic Aperture Radar
SatSEB	Satellite data based SEB
SAVI	Soil Adjusted Vegetation Index
SEB	Surface Energy Balance
SGD	Submarine Groundwater Discharge
SIR	Spaceborne Imaging Radar
SLAR	Side Looking Airborne Radar
SPOT	Satellite Probatoire d'Observation de la Terre
SRTM	Space Shuttle Topographic Mission
SWIR	Short Wavelength Infra-Red
TIN	Triangulated Irregular Network
TIR	Thermal Infrared
TOA	Top of Atmosphere
TRMM	Tropical Rainfall Measuring Mission
UNESCO	United Nations Educational, Scientific and Cultural Organization
USGS	United States Geological Survey
UTM	Universal Transverse Mercator (projection)
VNIR	Visible and Near Infra-Red
VWC	Vegetation Water Content

# Appendix 2: Overview of sensors

## Commonly used medium resolution multi-spectral satellite images in hydrogeology

For imaging radar systems, see Chapter 4.

Landsat-7 ETM+ (Landsat-4 and 5 TM, no band 6)	
<i>Band and spatial resolution</i>	<i>Range (<math>\mu\text{m}</math>)</i>
1 (30 m)	0.45–0.52
2 (30 m)	0.52–0.60
3 (30 m)	0.60–0.69
4 (30 m)	0.76–0.90
5 (30 m)	1.55–1.75
7 (30 m)	2.08–2.35
6 (60 m)	10.4–12.5
8 (15 m) Panchromatic	0.52–0.90

Advanced Land Imager EO-1 ALI	
<i>Band and spatial resolution</i>	<i>Range (<math>\mu\text{m}</math>)</i>
1 (30 m)	0.43–0.45
2 (30 m)	0.45–0.515
3 (30 m)	0.525–0.605
4 (30 m)	0.63–0.69
5 (30 m)	0.775–0.805
6 (30 m)	0.845–0.890
7 (30 m)	1.2–1.3
8 (30 m)	1.55–1.75
7 (30 m)	2.08–2.35
Pan (10 m)	0.48–0.69

Terra system: Advanced Spaceborne Thermal Emission and Reflection Radiometer ASTER	
<i>Band and spatial resolution</i>	<i>Range (<math>\mu\text{m}</math>)</i>
1 (15 m) VIS	0.52–0.60
2 (15 m) VIS	0.63–0.69
3 (15 m) NIR 3N and 3B*	0.76–0.86
4 (30 m) SWIR	1.600–1.700
5 (30 m) SWIR	2.145–2.185
6 (30 m) SWIR	2.185–2.225
7 (30 m) SWIR	1.235–2.285
8 (30 m) SWIR	2.295–2.365
9 (30 m) SWIR	2.360–2.430
10 (90 m) TIR	8.125–8.475
11 (90 m) TIR	8.475–8.825
12 (90 m) TIR	8.925–9.275
13 (90 m) TIR	10.25–10.95
14 (90 m) TIR	10.95–11.65

\* N = nadir, B = backward images for stereo

Terra System: Moderate Resolution Imaging Spectroradiometer, MODIS	
<i>Band and spatial resolution</i>	<i>Range (<math>\mu\text{m}</math>)</i>
1 (250 m)	0.620–0.670
2 (250 m)	0.841–0.876
3 (500 m)	0.459–0.479
4 (500 m)	0.545–0.565
5 (500 m)	1.230–1.250
6 (500 m)	1.628–1.652
7 (500 m)	2.105–2.155
8–36 (1,000 m)	0.405–14.385

Indian Remote Sensing Satellite IRS-1D, LISS-III sensor	
<i>Band and spatial resolution</i>	<i>Range (<math>\mu\text{m}</math>)</i>
Pan (5.4 m)	0.50–0.75
2 (23.5 m)	0.52–0.59
3 (23.5 m)	0.62–0.68
4 (23.5 m)	0.77–0.84
5 (66 m)	1.55–1.70

Note: IRS-P7 with LISS-IV sensor, bands 2, 3 and 4 will have resolution of 6 m and 23.5 m for b5.

Système Pour l'Observation de la Terre (SPOT)	
<i>Band and spatial resolution</i>	<i>Range (<math>\mu\text{m}</math>)</i>
SPOT-5	
Pan 2.5 m or 5 m	0.48–0.71
1 (10 m)	0.50–0.59
2 (10 m)	0.61–0.68
3 (10 m)	0.78–0.89
4 (20 m)	1.58–1.75
SPOT-4	
Monospectral (10 m)	0.61–0.68
1 (20 m)	0.50–0.59
2 (20 m)	0.61–0.68
3 (20 m)	0.78–0.89
4 (20 m)	1.58–1.75
SPOT-1, 2, 3	
Pan (10 m)	0.50–0.73
1 (20 m)	0.50–0.59
2 (20 m)	0.61–0.68
3 (20 m)	0.78–0.89

### Low resolution systems (mentioned in text)

NOAA Advanced Very High Resolution Radiometer (AVHRR). NOAA 14, 15 and 16 are operational at present	
<i>Band and spatial resolution</i>	<i>Range (<math>\mu\text{m}</math>)</i>
1 (1 km*)	0.58–0.68
2 (1km*)	0.725–1.10
3A (NOAA 15–16) (1 km*)	1.58–1.64
3B (1 km*)	3.55–3.93
4 (1 km*)	10.3–11.3
5 (1 km*)	11.5–12.5

\* In fact 1.1 km at nadir, > 1.1 km for off-nadir pixels, resampled to 1 km.

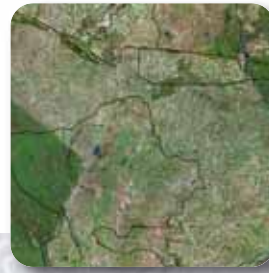
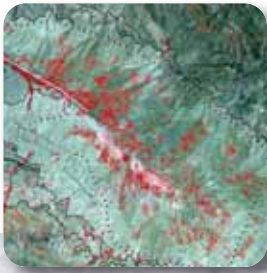


## INTERNATIONAL HYDROLOGICAL PROGRAMME (IHP)

IHP is UNESCO's international scientific cooperative programme in water research, water resources management, education and capacity-building, and the only broadly-based science programme of the UN system in this area.

IHP's primary objectives are:

- to act as a vehicle through which Member States, cooperating professional and scientific organizations and individual experts can upgrade their knowledge of the water cycle, thereby increasing their capacity to better manage and develop their water resources;
- to develop techniques, methodologies and approaches to better define hydrological phenomena;
- to improve water management, locally and globally;
- to act as a catalyst to stimulate cooperation and dialogue in water science and management;
- to assess the sustainable development of vulnerable water resources;
- to serve as a platform for increasing awareness of global water issues.



The importance of satellite observation of the Earth was recognized at the World Summit on Sustainable Development in Johannesburg in September 2002. A plan of implementation was produced and adopted by heads of state, that highlighted the need for global satellite observations. Water resources management is one of the areas of application that greatly affects people's safety, well-being and livelihoods. Use of satellite remote sensing for groundwater studies is particularly challenging, because much of the useful information identified by satellites is revealed indirectly, for example, through surface vegetation or fracture zones.

This book is written for those who wish to become acquainted with the use of remote sensing for groundwater studies, be it for exploration of well sites, evaluation of groundwater resources, or management of groundwater. Written from the point of view of a hydrogeologist-practitioner, it does not require prior knowledge of remote sensing.

Part I deals with image processing methods of use for groundwater studies and contains chapters on the use of thermal and radar images in hydrogeology.

Part II discusses and illustrates the hydrogeological interpretation of images of the main types of geologic terrain with examples found in warm climates.

Part III concentrates on the use of remote sensing for groundwater management, modelling, managed aquifer recharge, and various cross-cutting themes, such as, evapotranspiration, vegetation, recharge, soil moisture, wetlands, and deals with new sensor technologies.

Today, many satellite images can be downloaded free of charge and open source software for remote sensing and GIS is accessible on the internet. Remote sensing technology is now accessible to anyone working on groundwater-related investigations.

This book is a contribution toward the TIGER initiative of space agencies, international organizations and various African institutions that aims to develop sustainable satellite-based information services in Africa. UNESCO is working in cooperation with the European Space Agency to strengthen capacities of local partners to apply these techniques and hence develop technical sustainability.